ISSN: 1411-9420 (print); 2460-1578 (online)

Indonesian Journal of Chemistry

Vol. 23, No. 4, August 2023

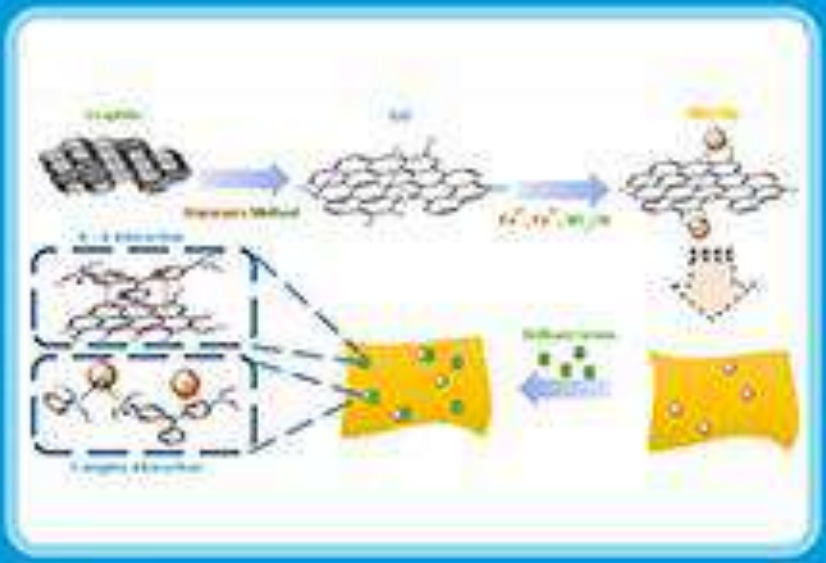

Accredited by RISTEK-BRIN
No. 85/M/KPT/2020

Indones. J. Chem. | Vol. 23 | No. 4 | PP 899-1196 | Yogyakarta August 2023

Characterization of Botanical Parts of *Erythrina crista-galli* Using Pyrolysis-Gas Chromatography/Mass Spectrometry and Multivariate Analysis

Abd. Wahid Rizaldi Akili[1], Ari Hardianto[1], Jalifah binti Latip[2], Maya Ismayati[3], and Tati Herlina[1*]

[1]*Department of Chemistry, Faculty of Mathematics and Natural Sciences, Universitas Padjajaran, Jl. Raya Bandung Sumedang Km 21 Jatinangor, Sumedang 45363, Indonesia*

[2]*School of Chemical Sciences and Food Technology, Faculty of Science and Technology, Universiti Kebangsaan Malaysia, Selangor 46300, Malaysia*

[3]*Research Center for Biomass and Bioproducts, National Research and Innovation Agency (BRIN), Jl. Raya Bogor Km 46, Cibinong 16911, Indonesia*

* ***Corresponding author:***

email: tati.herlina@unpad.ac.id

Received: August 27, 2022
Accepted: April 20, 2023

DOI: 10.22146/ijc.77325

Abstract: Erythrina crista-galli *is commonly used in folk medicines for its pharmacological properties which are associated with the bioactive compounds. Profiling botanical parts of* E. crista-galli *is an exciting topic and essential to uncover the similarity and clustering based on their chemical content. The botanical parts of* E. crista-galli, *including bark, flowers, leaves, roots, and twigs, were subjected to pyrolysis-gas chromatography/mass spectrometry. The samples were pyrolyzed using a multi-shot pyrolyzer. The relative abundance of the pyrolysate was subjected to multivariate analysis,* i.e., *principal component analysis (PCA) and hierarchical cluster analysis (HCA). The scree plot for PC.1, PC. 2, and PC. 3 accounted for 36.5%, 27.2%, and 20.3%, respectively. Together, the first three PCs explain 84% of the total variance. The PCA allows characterizing the roots of* E. crista-galli *by the highest relative abundance of lignin G, followed by the twigs, bark, and leaves, while the flowers had the least relative abundance of lignin G. The HCA allows to cluster the botanical parts of* E. crista-galli *into three different clusters based on their chemical component similarity,* i.e., *flowers-leaves, twigs, and roots-bark. In conclusion, Py-GC/MS analysis can be used in conjunction with multivariate data analysis to characterize the botanical parts of* E. crista-galli.

Keywords: E. crista-galli*; pyrolysis-GC/MS; multivariate analysis; principal component analysis; hierarchical clustering analysis*

■ INTRODUCTION

Erythrina (Fabaceae) is a large genus comprising around 200 species [1]. They are commonly used in folk medicines in Asian, African, and South American countries due to their pharmacological properties. One of the *Erythrina* species, *E. crista-galli*, was traditionally used as a wound healing and sedative. Meanwhile, people in Indonesia used *E. crista-galli* for malaria treatment by stewing the leaves and barks [2]. Additionally, *E. crista-galli* was also reported to have laxative, hypertensive, and diuretic activities. The botanical parts of *E. crista-galli* have various bioactivity; for example, the aerial parts of *E. crista-galli* have analgesic and anti-inflammatory activities; the root has antibacterial and antifungal activities, the bark has antibacterial, antimycobacterial, and antifungal activities; the leaves have antibacterial, antifungal, antivirus, animal repellent, and cytotoxic activities; while the flowers show antimutagenic activity [3]. These efficacies are associated with the metabolites constituents, which may unevenly spread within the botanical parts of *E. crista-galli*, as reported for some other species [4-5]. Thus, profiling the botanical parts of *E. crista-galli* is an exciting topic and essential to uncover

the similarity and the clustering of every botanical part based on their chemical content.

Various methods can be used for metabolite profiling, such as gas chromatography (GC) [6], high-performance liquid chromatography (HPLC) [7], gas chromatography coupled to mass spectrometry (GC-MS) [8], gas chromatography coupled to time-of-flight mass spectrometry (GC-TOF-MS) [9], ultra-performance liquid chromatography coupled to time-of-flight mass spectrometry (UPLC-TOFMS) [10], and pyrolysis-gas chromatography/mass spectrometry (Py-GC/MS) [5]. Among these methods, Py-GC/MS has the advantage that it is a fast analysis method, it requires simple sample preparation and a small amount of sample. Py-GC/MS can analyze diverse metabolite species, including high molecular weight metabolites, which in turn provides the opportunity to analyze the whole compound including primary and other metabolites [11].

Pyrolysis works by applying heat greater than the energy of specific bonds so that the molecule will fragment in a reproducible way. The fragments produced are then separated by the capillary column of the GC to produce the pyrogram. The interpretations of resulting pyrograms require detailed knowledge of the pyrolysis behavior of the desired compounds. This poses extreme difficulty for the global elucidation of metabolites, but since the Py-GC/MS of complex matrices results in a complex mixture of volatile fragments of the original sample, the resulting pyrogram can be used very effectively as a fingerprint of that particular sample. The analysis of the fingerprint pattern of these samples is often accomplished by the use of multivariate statistical techniques, which can be used to reveal relationships between samples and correlations between variables [12]. Two of the most used multivariate techniques to explore similarities and hidden patterns among samples are principal component analysis (PCA) and hierarchical cluster analysis (HCA) [13].

When the variables in a data set are highly correlated, which suggests data redundancy, PCA is extremely beneficial. PCA can be used to reduce the original variables into a smaller number of new variables called principal components that explain the majority of the variance in the original variable due to this redundancy [14]. PCA can also provide visualization to look for grouping in a data set. However, this method does not explicitly define clusters, and this is where the HCA method comes in [15]. HCA is a method to determine the underlying structure of observations by repeating a procedure that associates or dissociates each object until they are all processed wholly and equally. This method divides samples from a data set into groups that are related to one another [16]. Therefore, in our study, we use HCA in addition to PCA to explore similarities and hidden patterns among different parts of *E. crista-galli*.

In this study, Py-GC/MS was applied to characterize the botanical parts (bark, flowers, leaves, roots, and twigs) of *E. crista-galli*. The result obtained from Py-GC/MS was then subjected to PCA and HCA multivariate analysis to distinguish between parts of *E. crista-galli* based on their whole chemical component. The PCA and HCA analyses were performed in the R programming language. To the best of our knowledge, this is the first study that aimed to characterize five different parts of the *E. crista-galli* plant based on their whole metabolites using Py-GC/MS and to cluster these different parts of *E. crista-galli* based on their metabolite fingerprint similarity.

■ EXPERIMENTAL SECTION

Materials

Materials used were the botanical parts of *E. crista-galli*, including bark, flowers, leaves, roots, and twigs, that were collected from Bandung, West Java, Indonesia. These plant materials have been determined at the Laboratory of Agricultural Production Technology & Services, Agricultural Cultivation Department, Faculty of Agriculture, Universitas Padjajaran, under voucher specimen number 1020.

Instrumentation

The equipment used in this study was eco-cup SF PY1-EC50F, glass wool, multi-shot pyrolyzer (EGA/PY-3030D) interfaced with GC/MS system QP-2020 NX (Shimadzu, Japan) equipped with an SH-Rxi-5Sil MS column with electron impact of 70 eV.

Procedure

Pyrolysis-GC/MS measurement

Py-GC/MS was performed on several botanical parts of *E. crista-galli plants* (*i.e.,* bark, flowers, leaves, roots, and twigs). About 500 µg of samples were analyzed by Py-GC/MS. It was put in eco-cup SF PY1-EC50F and covered by glass wool. Furthermore, the eco-cup was pyrolyzed at 500 °C for 6 s using a multi-shot pyrolyzer (EGA/PY-3030D) which was interfaced (interface temperature 280 °C) with a GC/MS system QP-2020 NX (Shimadzu, Japan) equipped with an SH-Rxi-5Sil MS column (30 m × 0.25 mm i.d. film thickness 0.25 µm), with electron impact of 70 eV and helium as a carrier gas. The pressure was 20.0 kPa (15.9 mL/min, column flow 0.61 mL/min). The temperature profile for GC was as follows: 50 °C held for 1 min. Then the temperature increased until 280 °C (5 °C/min), and 13 min at 280 °C. Products resulting from the pyrolysis were identified by comparing their retention times and mass spectra data with NIST LIBRARY 2017.14. The identified pyrolysates were further compared with the literature [17].

Multivariate analysis

In this study, we performed two multivariate analyses, PCA which was followed by agglomerative hierarchical clustering or Hierarchical Clustering on Principal Components (HCPCs). Pyrograms of the botanical parts were assigned a matrix (row i, column k). The botanical parts were assigned as observations (i), whereas pyrolysis products were as descriptors (k). Mean centering and scaling were applied to the matrix during the preprocessing stage. The mean centering procedure was performed to maintain the important variation. The scaling step was employed due to the different scales of pyrolysis products.

An orthogonal linear transformation was applied to the matrix to produce principal components [18]. F_s (resp. G_s) indicates the coordinate vectors of the samples (resp. pyrolysis products), which can be expressed as Eq. (1) and (2):

$$F_s(i) = \frac{1}{\sqrt{\lambda_s}} \sum_k x_{ik} m_k G_s(k) \quad (1)$$

$$G_s(k) = \frac{1}{\sqrt{\lambda_s}} \sum_k x_{ik} p_i F_s(i) \quad (2)$$

whereas $F_s(i)$ and $G_s(k)$ represent the coordinates of the botanical part i and pyrolysis product k on the axis s. Notation λ_s is the eigenvalue corresponding to the axis s. Notations of m_k and p_i are the weights associated with pyrolysis product k and the botanical part i, respectively, whereas x_{ik} refers to the matrix (row i, column k). The first PCs responsible for at least 80% variance were retained and subjected to agglomerative hierarchical clustering. The most similar individual observations i were agglomerated iteratively based on the pairwise distance of Ward's criterion. The number of clusters was selected according to the hierarchical tree. PCA and HCPC were computed in the R programming language environment using FactoMineR [19]. The results were visualized using factoextra [20] or ggplot2 [21]. Leave-one-out cross-validation (LOOCV) computation for PCA was performed using chemometrics [22].

■ RESULTS AND DISCUSSION

Pyrolysis Products of the Botanical Parts of *E. crista-galli*

The chemical compositions of bark, flowers, leaves, roots, and twigs of *E. crista-galli* were analyzed by Py-GC/MS. This analysis method produces a pyrogram that plots retention time to its relative intensity. The resulting pyrograms from the analysis of botanical parts of *E. crista-galli* are given in Fig. 1.

According to the resulting pyrogram (Fig. 1), 93 pyrolysis products (pyrolysates) were identified by comparing their retention times with mass spectra data with NIST LIBRARY 2017.14. Table 1 shows pyrolysates and their relative intensities in each sample. The most abundant pyrolysates belong to polysaccharides, followed by lignins and extractives. This finding is unsurprising since polysaccharides and lignins are the main constituents of plant materials [23]. In softwood, polysaccharides such as cellulose and hemicellulose compose 41–50 and 11–33% of the biomass, respectively, while lignin constitutes 19–30%. The cellulose and

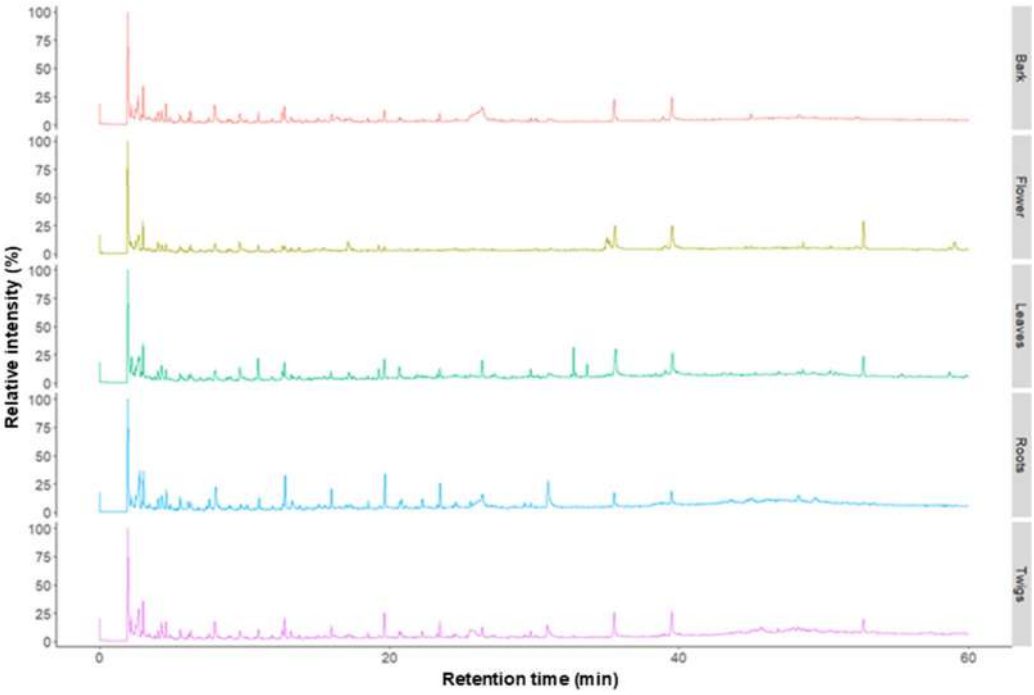

Fig 1. Pyrogram comparison of 5 botanical parts of *E. crista-galli*

Table 1. Pyrolysis products and their relative abundance

t_R (min) [a]	Pyrolysis product	SI (%) [b]	Molecular formula	Relative abundance (%)				
				Roots	Flowers	Leaves	Bark	Twigs
			Polysaccharide					
1.927	ammonium carbamate	98	$CH_6N_2O_2$	15.230	25.440	18.070	18.690	17.380
2.177	2-oxopropanal	88	$C_3H_4O_2$	3.690	1.590	4.830	4.610	3.030
2.343	2-methylpropanal	95	C_4H_8O	-	-	0.800	0.330	0.830
2.472	butane-2,3-dione	91	$C_4H_6O_2$	1.810	1.030	1.240	1.470	6.470
2.585	3-methylbutanoic acid	74	$C_5H_{10}O_2$	-	2.800	-	-	-
2.768	acetic acid	96	$C_2H_4O_2$	9.700	2.980	4.390	6.150	0.660
2.918	2,5-dihydrofuran	87	C_4H_6O	0.840	0.370	0.510	0.580	4.840
2.977	1-hydroxypropan-2-one	98	$C_3H_6O_2$	-	4.830	4.030	4.920	0.400
3.015	1-hydroxypropan-2-one	97	$C_3H_6O_2$	5.090	-	-	-	0.490
3.267	2-oxobutyl acetate	84	$C_6H_{10}O_3$	0.360	-	-	-	1.250
3.409	2,3-dihydro-1,4-dioxine	82	$C_4H_6O_2$	0.720	-	0.620	0.760	3.000
3.823	1-methylpyrrole	92	C_5H_7N	0.380	-	0.450	0.550	2.100
4.034	3-methylpenta-1,4-diene	84	C_6H_{10}	1.470	2.120	1.190	1.440	0.470
4.285	1-nitropropan-2-one	83	$C_3H_5NO_3$	2.430	1.830	2.500	2.090	1.160
4.603	methyl 2-oxopropanoate	96	$C_4H_6O_3$	2.330	0.890	0.920	2.260	0.700
4.861	5-(cyclohexylmethyl)pyrrolidin-2-one	83	$C_{11}H_{19}NO$	0.470	-	-	0.940	1.380
5.534	furan-2-carbaldehyde	90	$C_5H_4O_2$	1.320	0.570	0.570	1.200	0.820
6.100	2-hydroxycyclohexyl acetate	81	$C_8H_{14}O_3$	0.960	-	0.570	0.740	4.120
6.268	2-oxopropyl acetate	95	$C_5H_8O_3$	1.180	0.620	0.760	1.610	-
7.367	4,4-dimethyl-5-oxopentanenitrile	77	$C_7H_{11}NO$	0.250	-	-	-	-
7.564	2*H*-furan-5-one	91	$C_4H_4O_2$	1.170	-	-	0.720	-
7.964	cyclopentane-1,2-dione	90	$C_5H_6O_2$	-	2.630	2.510	4.840	-

t_R (min) [a]	Pyrolysis product	SI (%)[b]	Molecular formula	Relative abundance (%)				
				Roots	Flowers	Leaves	Bark	Twigs
8.009	4,5-dimethyloctane	83	$C_{10}H_{22}$	4.780	-	-	-	-
8.812	ethenyl propanoate	79	$C_5H_8O_2$	-	-	-	0.230	-
8.951	5-methylfuran-2-carbaldehyde	84	$C_6H_6O_2$	0.410	-	-	0.540	-
9.063	3-methylcyclopent-2-en-1-one	93	C_6H_8O	0.280	-	-	0.390	-
10.960	2-hydroxy-3-methylcyclopent-2-en-1-one	88	$C_6H_8O_2$	-	1.410	3.120	1.590	1.450
11.013	2-hydroxy-3-methylcyclopent-2-en-1-one	97	$C_6H_8O_2$	1.440	-	-	-	-
12.773	4-methoxyphenol (*p*-cresol)	96	$C_7H_8O_2$	-	1.530	-	-	-
13.277	cyclopropylmethanol	88	C_4H_8O	1.200	0.770	0.740	0.830	1.030
13.370	3-methylbutyl 2-methylpropanoate	80	$C_9H_{18}O_2$	0.410	0.480	-	-	-
13.690	3-hydroxy-2-methylpyran-4-one	89	$C_6H_6O_3$	-	-	-	0.320	-
13.802	3-ethyl-2-hydroxycyclopent-2-en-1-one	89	$C_7H_{10}O_2$	0.530	0.800	0.420	0.430	0.600
14.272	1,4-dioxaspiro[2.4]heptan-5-one	80	$C_5H_6O_3$	0.430	-	-	-	-
15.130	7-methyl-1,4-dioxaspiro[2.4]heptan-5-one	87	$C_6H_8O_3$	0.610	-	-	0.570	-
17.024	1,4:3,6-dianhydro-α-D-glucopyranose	91	$C_6H_8O_4$	0.590	-	-	0.660	-
17.185	2,3-dihydro-1-benzofuran	91	C_8H_8O	-	3.980	1.620	0.540	-
17.330	2,3-anhydro-D-mannosan	91	$C_6H_8O_4$	0.260	-	-	0.720	-
27.036	6,7-dimethoxy-1-[(*E*)-2-phenylethenyl]-1,2,3,4-tetrahydroisoquinoline	77	$C_{19}H_{21}NO_2$	0.220	-	-	-	0.260
30.117	3*H*-[1]benzofuro[3,2-d]pyrimidin-4-one	77	$C_{10}H_6N_2O_2$	-	-	-	0.520	0.370
31.110	tetradecanoic acid	91	$C_{14}H_{28}O_2$	-	-	-	-	0.920
32.728	7,11,15-trimethyl-3-methylidenehexadec-1-ene	94	$C_{20}H_{38}$	-	-	3.680	-	-
33.651	7,11,15-trimethyl-3-methylidenehexadec-1-ene	89	$C_{20}H_{38}$	-	-	1.680	-	-
35.045	(*E*)-octadec-6-enyl acetate	90	$C_{20}H_{38}O_2$	-	2.790	-	-	-
35.527	hexadecenoic acid	94	$C_{16}H_{32}O_2$	2.400	7.920	7.560	6.060	6.170
39.482	octadecanoic acid	93	$C_{18}H_{36}O_2$	1.850	9.290	6.250	5.860	5.930
46.895	dotriacontane	94	$C_{32}H_{66}$	-	-	0.510	-	0.620
48.570	tetracontane	88	$C_{40}H_{82}$	-	1.390	0.890	-	0.240
52.731	dotriacontane	95	$C_{32}H_{66}$	-	8.470	3.830	-	3.010
	Total			64.810	86.530	74.260	73.160	69.700
			Lignin G					
12.806	guaiacol	97	$C_7H_8O_2$	4.370	-	2.800	2.700	3.450
16.006	4-methylguaiacol	96	$C_8H_{10}O_2$	1.960	-	0.860	1.770	2.050
18.545	4-ethylguaiacol	94	$C_9H_{12}O_2$	0.740	-	-	0.400	0.570
19.697	4-vinylguaiacol	93	$C_9H_{10}O_2$	4.840	0.670	2.650	1.880	3.920
20.821	eugenol	94	$C_{10}H_{12}O_2$	1.070	-	0.330	0.470	0.860
21.092	4-propylguaiacol	89	$C_{10}H_{14}O_2$	0.240	-	-	0.480	-
22.280	*cis*-isoeugenol	83	$C_{10}H_{12}O_2$	1.190	-	-	-	1.030

t_R (min) [a]	Pyrolysis product	SI (%)[b]	Molecular formula	Relative abundance (%)				
				Roots	Flowers	Leaves	Bark	Twigs
23.508	*trans*-isoeugenol	95	$C_{10}H_{12}O_2$	3.120	-	1.100	1.330	2.480
24.584	acetoguaiacone	96	$C_9H_{10}O_3$	0.810	-	-	-	0.190
25.603	guaiacylacetone	92	$C_{10}H_{12}O_3$	0.670	-	-	-	0.880
29.322	(*E*)-4-(3-hydroxyprop-1-en-1-yl)-2-methoxyphenol	91	$C_{10}H_{12}O_3$	0.640	-	-	-	0.320
30.973	(*E*)-4-(3-hydroxyprop-1-en-1-yl)-2-methoxyphenol	92	$C_{10}H_{12}O_3$	6.940	-	-	1.210	3.800
	Total			26.590	0.670	7.740	10.240	19.550
			Lignin H					
9.731	phenol	98	C_6H_6O	0.650	2.770	2.260	1.760	1.460
11.901	2-methylphenol	94	C_7H_8O	-	0.660	0.450	0.650	11.893
12.642	*p*-cresol	96	C_7H_8O	0.820	1.550	1.690	2.220	12.579
	Total			1.470	4.980	4.400	4.630	25.932
			Lignin S					
20.707	syringol	94	$C_8H_{10}O_3$	0.810	-	1.710	0.630	0.950
23.320	4-methylsyringol	90	$C_9H_{12}O_3$	0.350	-	0.560	-	0.510
26.422	4-vinylsyringol	93	$C_{11}H_{14}O_4$	0.980	-	2.560	3.110	1.270
28.507	*cis*-4-propenylsyringol	83	$C_{11}H_{14}O_3$	0.170	-	-	0.330	-
28.720	syringaldehyde	92	$C_9H_{10}O_4$	0.210	-	-	-	-
29.782	*trans*-4-propenylsyringol	92	$C_{11}H_{14}O_3$	0.560	-	1.060	0.530	0.990
31.320	syringylacetone	92	$C_{12}H_{16}O_4$	-	-	-	-	0.410
	Total			3.080	0.000	5.890	4.600	4.130
			Extractive and others					
6.380	*o*-xylene	92	C_8H_{10}	-	-	0.570	-	-
10.169	2,2-diethyl-3-methyl-1,3-oxazolidine	88	$C_8H_{17}NO$	0.680	-	-	0.450	-
16.419	2-(hydroxymethyl)-2-nitropropane-1,3-diol	83	$C_4H_9NO_5$	-	-	-	1.760	-
19.262	1*H*-indole	92	C_8H_7N	-	1.250	1.470	-	-
21.897	3-methyl-1*H*-indole	96	C_9H_9N	-	-	0.400	0.410	-
26.275	3,4-diacetyloxy-6,8-dioxabicyclo[3.2.1]octan-2-yl acetate	82	$C_{12}H_{16}O_8$	-	-	-	1.310	-
27.026	pentadecan-1-ol	85	$C_{15}H_{32}O$	-	-	-	0.210	-
32.85	3,7,11,15-tetramethylhexadec-2-ene	94	$C_{20}H_{40}$	-	-	0.500	-	-
34.833	(*Z*)-18-octadec-9-enolide	93	$C_{18}H_{32}O_2$	-	0.460	-	-	-
34.963	(8*Z*)-1-oxacycloheptadec-8-en-2-one	91	$C_{16}H_{28}O_2$	-	1.820	-	-	-
35.188	(*Z*)-18-octadec-9-enolide	90	$C_{18}H_{32}O_2$	-	2.730	-	-	-
38.401	phytol (alkenol)	96	$C_{20}H_{40}O$	-	-	0.400	0.630	
38.995	(9*Z*,12*Z*,15*Z*)-octadeca-9,12,15-trienoic acid	85	$C_{18}H_{30}O_2$	-	-	-	0.530	-
39.068	(7*Z*,10*Z*,13*Z*)-hexadeca-7,10,13-trienal	90	$C_{16}H_{26}O$	-	-	0.930	-	-
39.88	hexadecanamide	88	$C_{16}H_{33}NO$	-	-	0.660	-	-
44.976	6,7-dimethoxy-1-phenyl-3,4-dihydroisoquinoline	61	$C_{17}H_{17}NO_2$	-	0.630	-	0.950	-
45.688	2,6,10,15,19,23-pentamethyl-2,6,18,22-tetracosatetraen-10,15-diol	86	$C_{30}H_{54}O_2$	-	-	-	-	1.330

t_R (min) [a]	Pyrolysis product	SI (%)[b]	Molecular formula	Relative abundance (%)				
				Roots	Flowers	Leaves	Bark	Twigs
48.224	(*E*)-3,3'-dimethoxy-4,4'-dihydroxystilbene	91	$C_{16}H_{16}O_4$	1.510	-	-	-	0.970
48.284	methyl 2-phenylquinoline-7-carboxylate	67	$C_{17}H_{13}NO_2$	-	-	-	0.830	-
49.421	clionasterol	93	$C_{29}H_{50}O$	1.870	-	-	-	-
50.815	squalene	95	$C_{30}H_{50}$	-	-	0.500	-	-
50.404	heptacosyl heptafluorobutyrate	95	$C_{31}H_{55}F_7O_2$	-	-	-	-	0.530
	Total			4.060	6.890	5.430	7.080	2.830

[a] SI (%) = Similarity index based on NIST 2017 library (%)
[b] t_R (min) = retention time in minutes

hemicellulose contents in the hardwood are 39–53 and 19–36%, respectively, while lignin is 17–24%. Meanwhile, the percentages of cellulose and hemicellulose in the herbaceous plants are 24–50 and 12–38%, respectively, whereas lignin is 6–29% [24].

Based on Table 1, carbohydrates generate several classes of compounds during pyrolysis, such as anhydrous sugars, carbonyls, lactones, furans, pyrans, carboxylic acids, and esters [17]. The examples of anhydrous sugars are 1,4:3,6-dianhydro-α-D-glucopyranose and 2,3-anhydro-D-mannosan, whereas those of carbonyls are 2-oxopropanal and butane-2,3-dione.

During the Py-GCMS analysis, lignin is fragmented into its monomers: H (*p*-hydroxyphenyl unit), G (guaiacyl unit), and S (syringyl unit). The concentration of lignin and its monomeric composition change between plant species, tissues, cell types, and different cell wall layers during development [25]. Based on the relative abundance (%) of lignin monomers, among the 5 botanical parts of *E. crista-galli*, the twigs have the highest total lignin content (45.59%), followed by roots (23.56%), bark (18.26%), and leaves (18.03%), while flowers have the lowest total lignin content (5.56%). Lignin accumulates in the cell walls of specialized cell types to enable plants to stand upright and conduct water and minerals [26]. Twigs provide mechanical support and transport water, carbohydrates, and nutrients [27]. This explains why the twigs have the highest total lignin content among the other botanical parts of *E. crista-galli*.

Py-GC/MS provides a complete overview of global metabolite fingerprints to characterize botanical parts of *E. crista-galli*. Through pattern recognition analysis, the multivariate data obtained from Py-GC/MS analysis can be useful to provide information on how each botanical part of *E. crista-galli* is different from one another based on the metabolite fingerprint. Therefore, we coupled the Py-GC/MS results with multivariate analysis in the next step.

Multivariate analysis is concerned with datasets having several response variables for each observational or experimental. The commonly used multivariate data analysis for pattern recognition are PCA and HCA. These are examples of unsupervised learning techniques in which the objective is to identify previously unknown structures in the data set, as well as to identify clusters in a given dataset without using class membership information in the calculations [28].

Multivariate Analysis

Multivariate analysis with all pyrolysis products

PCA is a statistical method that can be used to visualize information in a data set by describing how each sample differs from another, which variables contribute significantly to this difference, as well as to identify sample patterns. In our research, in order to easily identify which metabolite contribute to the similarity or differences between 5 botanical parts of *E. crista-galli* based, we use the relative abundance data of metabolites as variables for PCA analysis, as done by several previous studies [29].

PCA minimizes the data dimension by creating the so-called principal components (PCs), which are linear combinations of the variables in the data set to

summarize the data [30]. Fig. 2(a). shows the scree plot, which is a line plot of the principal components along with the percentage of explained variance from the principal component analysis of the data set. Cross-validation was subjected to the data set in order to determine the number of PCs that should be retained in order to account for most of the data variability. The result from cross-validation suggests that at least the first three PCs should be retained to fulfill a variance of 80% (Fig. 2(b)).

Fig. 3 shows the score plot of the botanical parts of *E. crista-galli* on PC.1, PC.2, and PC.3. PC.1 accounts for 36.5% of the total variance, while PC.2 27.2% and the PC.3 20.3%. Together, the first three PCs explain 84% of the total variance. Each PC can be described by the origin variables (Rts). Variables described the best in each PC can be identified by the correlation coefficient and the coordinates of the botanical parts on a PC. Correlation coefficients are calculated for all the variables, followed by testing the significance of each correlation coefficient and sorting the variables from the most to the less correlated. The most significant variables then describe each PC; such a method is beneficial for interpreting the dimensions with many variables [20]. Table 2 shows a list of significantly correlated variables to PC.1, 2, and 3 from the PCA.

According to Table 2, eugenol, 4-ethylguaiacol, *trans*-isoeugenol, and (*E*)-4-(3-hydroxyprop-1-en-1-yl)-2-methoxyphenol are pyrolysates that have a positive correlation to PC.1. Therefore, samples with a high score

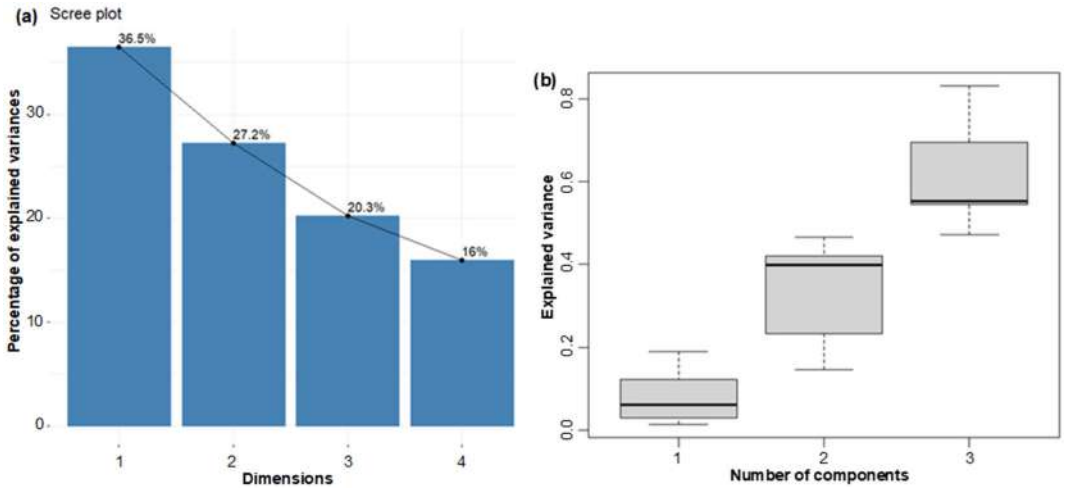

Fig 2. (a) Scree plot and (b) box plot of cumulative variances resulted from leave-one-out cross-validation

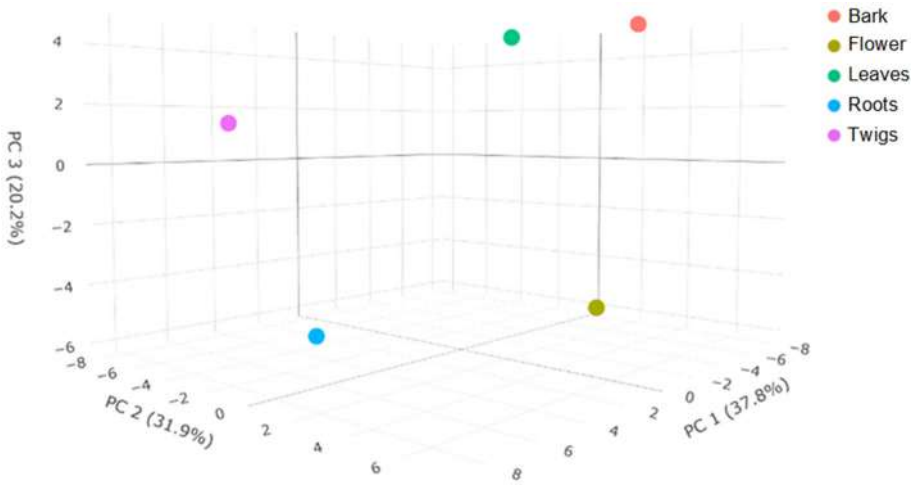

Fig 3. PCA score plot of botanical parts of *E. crista-galli* on PC.1, PC.2, and PC.3

Table 2. List of significantly correlated variables to PC.1, PC.2, and PC.3

t_r (min)	Corr.	*p*-value	Pyrolysis product	Origin
			PC.1	
20.821000	0.979400	0.003541	eugenol	Lignin-G
18.545000	0.978600	0.003747	4-ethylguaiacol	Lignin-G
23.508000	0.970400	0.006087	trans-isoeugenol	Lignin-G
30.973000	0.934900	0.019742	(*E*)-4-(3-hydroxyprop-1-en-1-yl)-2-methoxyphenol	Lignin G
9.731000	-0.992500	0.000776	phenol	Lignin-H
			PC.2	
6.268000	0.974000	0.005015	1-(acetyloxy)-2-propanone	Linear ketone derivatives
			PC.3	
26.422000	0.924300	0.024734	4-vinylsyringol	Lignin-S
13.370000	-0.966000	0.007472	3-methylbutyl 2-methylpropanoate	Linear ketone derivatives

on PC.1 will have a high relative abundance of these pyrolysis products. On the other hand, phenol has a negative correlation to PC.1. Thus, any sample with a high score on PC.1 will have a low relative abundance of that pyrolysis product. For PC.2, only 1-(acetyloxy)-2-propanone has a significant positive correlation to the second latent variable. Meanwhile, for PC.3, 4-vinylsyringol and 3-methylbutyl 2-methylpropanoate are positively and negatively correlated to the third latent variable, respectively.

The PCA score plot (Fig. 3) shows that roots have the highest score on PC.1, followed by twigs, bark, leaves, and flowers. Revering to Table 2, most of the significantly correlated variables on PC.1 come from the pyrolysis products of lignin G. Roots have the highest score on PC.1, while flowers have the lowest score. Thus, roots are characterized by high lignin G content, whereas flowers are low lignin G content, which is also confirmed by Table 1. Similarly, since the bark owns a high score on PC.2, it has the highest relative abundance of 1-(acetyloxy)-2-propanone, whereas twigs have the lowest relative abundance of this pyrolysis product.

Visualization provided by PCA score plots may facilitate clustering in pyrolysis product data. Nonetheless, PCA does not explicitly define clusters. More formal approaches can be used by clustering methods. Cluster analysis divides observations into groups that are related to one another. In terms of specific characteristics, each group or cluster is homogeneous and should be distinct from others. The closeness of two objects is expressed by similarity or dissimilarity, which can be computed by mathematical methods, and eventually displayed in a dendrogram based on the features of individual objects [30]. HCPC is a clustering approach that allows to combine principal component method, hierarchical clustering, and partitioning clustering method to identify clusters within a data set. The combination of the principal component method along with the clustering method is useful in a situation where the data set contains multiple continuous variables. The PCA can be used to reduce the dimension of the data, and then clustering can be performed on the PCA result [15].

From the PCA and LOOCV analysis, at least the first three PCs should be retained to cover 80% of the variance (Fig. 2). Therefore, we performed the HCPC analysis from the first three (84% total variance) and four principal components (100% total variance). Fig. 4 shows the dendrogram of botanical parts of *E. crista-galli* resulting from HCPC analysis.

HCPC analysis from the first three and four principal components shows that the botanical parts of *E. crista-galli* are divided into three different clusters. Fig. 4 show that in HCPC analysis with the first three PCs, cluster 1 consists of flower, cluster 2 consists of leaves and bark, and cluster 3 consists of twig and root, whereas in HCPC analysis with four PCs, Cluster 1 consists of flowers and leaves, cluster 2 consists of twigs and cluster 3 consists of roots and bark. Since the first four PCs cover 100% variability, HCPC analysis from the first four PCs is used to cluster botanical parts of *E. crista-galli*.

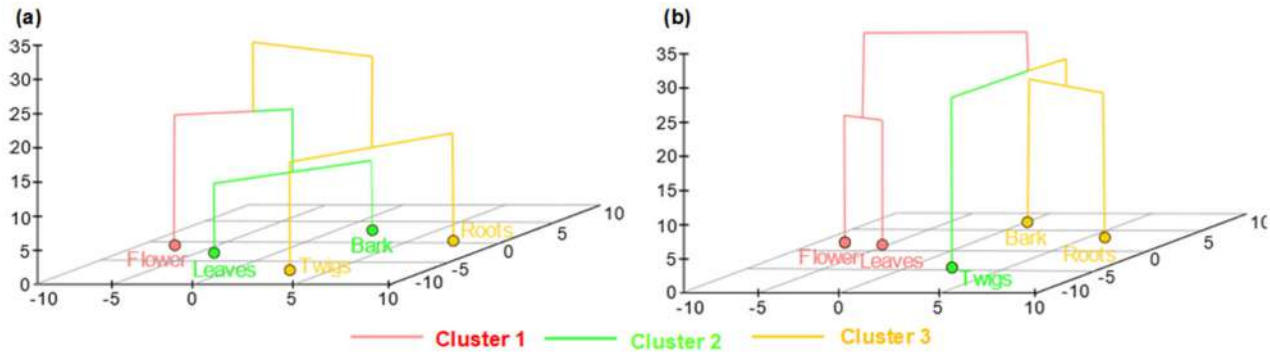

Fig 4. Hierarchical clustering on the factor map of botanical parts of *Erythrina crista-galli* with (a) three PCs and (b) four PCs. Clusters 1, 2, and 3 are denoted by pink, green, and yellow, respectively

Table 3. Variables that describe the most each cluster

t_R (min)	Mean in category	Overall mean	*p*-value	Pyrolysis product	Origin
				Cluster 1	
19.2620	1.3600	0.5440	0.046681	1*H*-indole	Unknown
				Cluster 2	
50.4040	0.5300	0.1060	0.045500	heptacosyl heptafluorobutyrate	Extractive/Unknown?
45.6880	1.3300	0.2660	0.045500	2,6,10,15,19,23-pentamethyl-2,6,18,22-tetracosatetraen-10,15-diol	Unknown
31.3200	0.4100	0.0820	0.045500	syringylacetone	Lignin-S
31.1100	0.9200	0.1840	0.045500	tetradecanoic acid	Linear ketone derivatives
11.9010	11.8900	2.7306	0.045795	2-methylphenol	Lignin-H
2.9180	4.8400	1.4280	0.046366	2,5-dihydrofuran	Furan derivatives
12.6420	12.5700	3.7718	0.046617	*p*-cresol	Lignin-H
2.4720	6.4700	2.4040	0.047257	2,3-butanedione	Linear ketone derivatives
				Cluster 3	
15.1300	0.5900	0.2360	0.045707	7-methyl-1,4-dioxaspiro[2.4]heptan-5-one	Lactone derivatives
17.0240	0.6250	0.2500	0.046065	(1*S*,3*R*,6*R*,7*R*,9*R*)-2,5,8-trioxatricyclo[4.2.1.03,7]nonan-9-ol	Anhydro sugars
4.6030	2.2950	1.4200	0.046812	methyl 2-oxopropanoate	Linear ketone derivatives
8.9510	0.4750	0.1900	0.048895	5-methylfuran-2-carbaldehyde	Cyclopentenone derivatives

Table 3 shows a list of variables that describe the most exact cluster. Variables that are significantly associated with specific clusters have higher mean category values than the overall mean. Thus, it could be said that cluster one (*i.e.,* flowers and leaves) is characterized by the higher content of 1*H*-indole pyrolysate. 1*H*-indole is assumed to be a minor pyrolysis product that originated from protein [31] or extractive as an alkaloid after fragmentation of the pyrolysis process and was detected by Py-GC/MS [32]. 1*H*-Indole is produced by the pyrolysis of the amino acid tryptophan. It undergoes thermal degradation at a temperature above 800 °C. Three main pyrolysates of indole are phenylacetonitrile, 2- methylbenzonitrile, and 3-methylbenzonitrile which formed due to the opening of the pyrrole ring [25]. Since, in our research, the pyrolysis was performed at the temperature of 500 °C, the indole might not undergo a pyrolytic reaction. That's why 1*H*-indole (retention time, t_R = 19.267 min) and 3-methyl-1-*H*-indole (t_R = 21.897 min) pyrolysate are still detected. Those pyrolysates might also indicate the presence of indole alkaloids such as 1*H*-indole-3-propanamide,

abrine, and hypaphorine (Fig. 5) that has been identified in *Erythrina* genus [33]. Since indole pyrolysate is associated with the presence of indole alkaloids, the flowers and leaves contain a higher amount of indole alkaloids compared to the other clusters.

Other pyrolysates that could indicate the presence of alkaloids are 6,7-dimethoxy-1-phenyl-3,4-dihydroisoquinoline (t_R = 44.976 min) and methyl 2-phenylquinoline-7-carboxylate (t_R = 48.284 min). Isoquinoline is one compound that is very stable at elevated temperatures. It undergoes pyrolysis at a temperature above 900 °C to produce benzene, toluene, naphthalene, phenanthrene, and anthracene, as well as the isomer of the other quinoline, indole, and several nitriles, including benzonitrile, and several isomers of cyanostyrene and cyanonaphthalene [25].

Cluster 2 (*i.e.,* twigs) is characterized by a higher relative abundance of heptacosyl heptafluorobutyrate, 2,6,10,15,19,23-pentamethyl-2,6,18,22-tetracosatetraen-10,15-diol, syringylacetone, tetradecanoic acid, 2-methylphenol, 2,5-dihydrofuran, *p*-cresol, and 2,3-butanedione pyrolysate. Heptacosyl heptafluorobutyrate and 2,6,10,15,19,23-pentamethyl-2,6,18,22-tetracosatetraen-10,15-diol were detected at the end of pyrogram as minor pyrolysis products from amino acids of lignocellulose biomass samples [34]. Cluster 3 (*i.e,* roots and barks) is characterized by a higher relative abundance of 7-methyl-1,4-dioxaspiro[2.4]heptan-5-one, (1*S*,3*R*,6*R*,7*R*,9*R*)-2,5,8-trioxatricyclo[4.2.1.03,7]nonan-9-ol, methyl 2-oxopropanoate, and 5-methylfuran-2-carbaldehyde pyrolysate.

Tables 2 and 3 show that the distribution of samples in the score plot of PC.1, PC.2, and PC.3, as well as the clustering, are mainly influenced by the polysaccharide and lignin content in those samples. This is mainly true since polysaccharides and lignin are relatively abundant compared to extractives in higher plants, whether in softwood, hardwood, or even in herbaceous plants [24].

Multivariate analysis with only extractive pyrolisate

The second principal component analysis was performed on the relative abundance (%) of extractive pyrolysates. Fig. 6 shows the score plot of the samples for the second PCA.

For the second principal component analysis, PC.1 and PC.2 account for 37.8 and 31.9% of the total variance, respectively, while PC.3 contributes to 20.2% of the total variance. Together the first three PCs account for 89.9% of the total variance. The analysis shows that phytol (t_R = 38.401 min) is the variable that significantly correlated to PC.1 (corr. = 0.938, p val. = 0.0179). Since bark has the highest score on PC.1, therefore it has the highest relative abundance of phytol.

Indole (t_R = 19.262 min) is the pyrolysate that is significantly correlated to PC.2 (corr. = −0.949, *p*-value = 0.0136) and the correlation of indole with PC.2 is negative. Thus, samples with the smallest score in PC.2 (*i.e.*, leaves and flowers) have the highest relative abundance of this pyrolysate. (*Z*)-18-Octadec-9-enolide, (8*Z*)-1-oxacycloheptadec-8-en-2-one, and (*Z*)-18-Octadec-9-enolide are pyrolysates that significantly correlated to PC.3 with correlation value of −0.925. Since the correlation value is negative, indicating samples that have a positive value on PC.3 will have a small relative abundance of those pyrolysates.

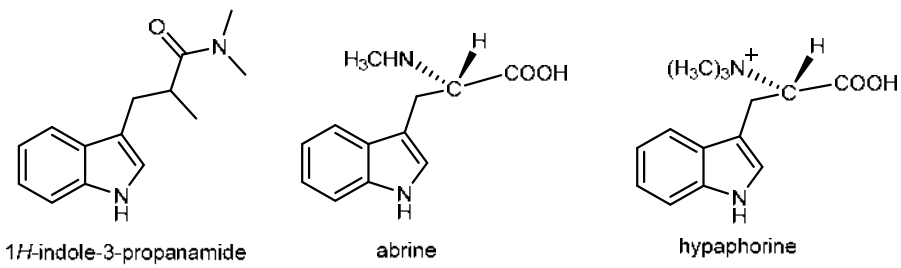

Fig 5. Indole alkaloids identified in *Erythrina*

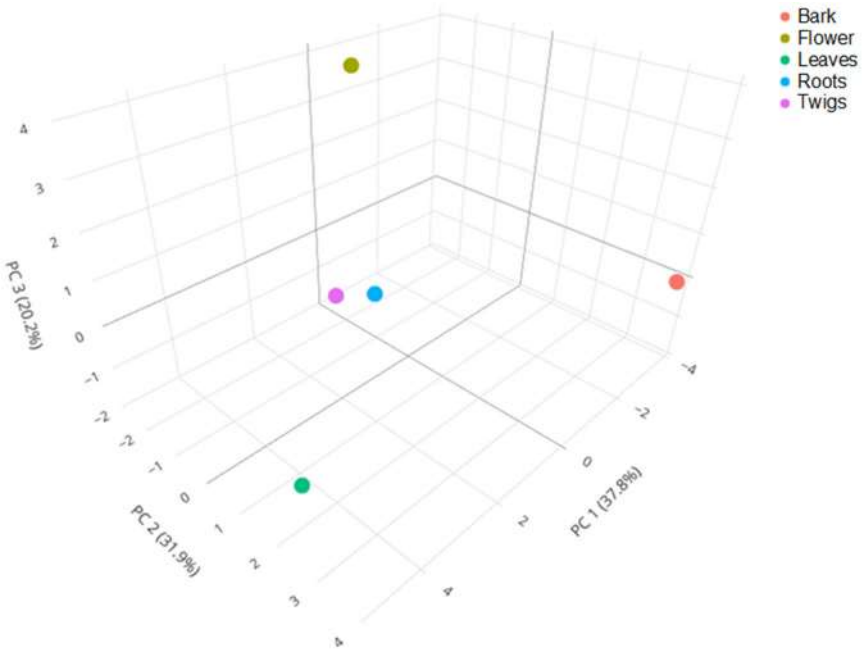

Fig 6. Score plot of botanical parts of *E. crista-galli* for the second principal component analysis

CONCLUSION

Py-GC/MS analysis can be used in conjunction with multivariate data analysis to characterize the botanical parts of *E. crista-galli*. The Py-GC/MS shows that most pyrolysis products or pyrolysate are originated from polysaccharides and lignin. PCA shows that the roots of *E. crista-galli* is characterized by the highest relative abundance of lignin G, while the flowers have the least relative abundance of lignin G. Hierarchical cluster analysis shows that the botanical parts of *E. crista-galli* are clustered in three different clusters based on their similarity. Cluster 1 consists of flowers and leaves and is characterized by the higher content of indole pyrolysate. Cluster 2 consist of twigs and characterized by higher relative abundance of heptacosyl heptafluorobutyrate, 2,6,10,15,19,23-pentamethyl-2,6,18,22-tetracosatetraen-10,15-diol, syringylacetone, tetradecanoic acid, 2-methylphenol, 2,5-dihydrofuran, *p*-cresol, and 2,3-butanedione pyrolysate, and cluster 3 consist of roots and barks is characterized with higher relative abundance of 7-methyl-1,4-dioxaspiro[2.4]heptan-5-one, (1*S*,3*R*,6*R*,7*R*,9*R*)-2,5,8-trioxatricyclo[4.2.1.03,7]nonan-9-ol, methyl 2-oxopropanoate, and 5-methylfuran-2-carbaldehyde pyrolysate.

ACKNOWLEDGMENTS

The authors are grateful to the Universitas Padjadjaran for providing funds through the Outstanding Padjadjaran Postgraduate Scholarships (BUPP) scheme and Academic Leader Grant (ALG) by Tati Herlina (No. 1959/UN6.3.1/PT.00/2021).

AUTHOR CONTRIBUTIONS

Conceptualization, Tati Herlina and Ari Hardianto; Data curation, Abd. Wahid Rizaldi Akili and Maya Ismayati; Formal analysis, Ari Hardianto, Abd. Wahid Rizaldi Akili, Jalifah binti Latip, Maya Ismayati, Tati Herlina; Funding acquisition, Tati Herlina; Investigation, Maya Ismayati, Abd. Wahid Rizaldi Akili; Methodology, Ari Hardianto, Tati Herlina, and Maya Ismayati; Software, Abd. Wahid Rizaldi Akili and Ari Hardianto; Validation, Maya Ismayati, Ari Hardianto, and Tati Herlina; Visualization, Abd. Wahid Rizaldi Akili and Ari Hardianto; Writing – original draft, Abd. Wahid Rizaldi Akili and Ari Hardianto; Writing – review & editing, Tati Herlina, Jalifah binti Latip and Ari Hardianto.

REFERENCES

[1] Tan, Q.W., Ni, J.C., Fang, P.H. and Chen, Q.J., 2017, A New Erythrinan alkaloid glycoside from the seeds

of *Erythrina crista-galli*, *Molecules*, 22 (9), 1558.

[2] Fahmy, N.M., Al-Sayed, E., El-Shazly, M., and Singab, A.N., 2018, Comprehensive review on flavonoids biological activities of *Erythrina* plant species, *Ind. Crops Prod.*, 123, 500–538.

[3] Kaushal, A., Sharma, M., Navneet, N., and Sharma, M., 2020, Ethnomedicinal, phytochemical, therapeutic and pharmacological review of the genus *Erythrina*, *Int. J. Bot. Stud.*, 5 (6), 642–648.

[4] Kim, D.S., Na, H., Kwack, Y., and Chun, C., 2014, Secondary metabolite profiling in various parts of tomato plants, *Korean J. Hortic. Sci. Technol.*, 32 (2), 252–260.

[5] Yang, H., Huang, Z., Huang, Y., Dong, W., Pan, Z., and Wang, L., 2015, Characterization of Chinese crude propolis by pyrolysis-gas chromatography/mass spectrometry, *J. Anal. Appl. Pyrolysis*, 113, 158–164.

[6] Youssef, F.S., Mamatkhanova, M.A., Mamadalieva, N.Z., Zengin, G., Aripova, S.F., Alshammari, E., and Ashour, M.L., 2020, Chemical profiling and discrimination of essential oils from six *Ferula* species using GC analyses coupled with chemometrics and evaluation of their antioxidant and enzyme inhibitory potential, *Antibiotics*, 9 (8), 518.

[7] Tanuwidjaja, I., Svečnjak, L., Gugić, D., Levanić, M., Jurić, S., Vinceković, M., and Fuka, M.M., 2021, Chemical profiling and antimicrobial properties of honey bee (*Apis mellifera* L.) venom, *Molecules*, 26 (10), 3049.

[8] Ikram, M.M.M., Ridwani, S., Putri, S.P., and Fukusaki, E., 2020, GC-MS based metabolite profiling to monitor ripening-specific metabolites in pineapple (*Ananas comosus*), *Metabolites*, 10 (4), 134.

[9] Duan, S.G., Hong, K., Tang, M., Tang, J., Liu, L.X., Gao, G.F., Shen, Z.J., Zhang, X.M., and Yi, Y., 2021, Untargeted metabolite profiling of petal blight in field-grown *Rhododendron agastum* using GC-TOF-MS and UHPLC-QTOF-MS/MS, *Phytochemistry*, 184, 112655.

[10] Qian, Y., Wang, Y., Sa, R., Yan, H., Pan, X., Yang, Y., and Sun, Y., 2013, Metabolic fingerprinting of *Angelica sinensis* during growth using UPLC-TOFMS and chemometrics data analysis, *Chem. Cent. J.*, 7 (1), 42.

[11] Picó, Y., and Barceló, D., 2020, Pyrolysis gas chromatography-mass spectrometry: Focus on organic matter and microplastics, *TrAC, Trends Anal. Chem.*, 130, 115963.

[12] Traoré, M., Kaal, J., and Martínez Cortizas, A., 2018, Chemometric tools for identification of wood from different oak species and their potential for provenancing of Iberian shipwrecks (16th-18th centuries AD), *J. Archaeol. Sci.*, 100, 62–73.

[13] Szczepanik, M., Szyszlak-Bargłowicz, J., Zając, G., Koniuszy, A., Hawrot-Paw, M., and Wolak, A., 2021, The use of multivariate data analysis (HCA and PCA) to characterize ashes from biomass combustion, *Energies*, 14 (21), 6887.

[14] Greenacre, M., Groenen, P.J.F., Hastie, T., D'Enza, A.I., Markos, A., and Tuzhilina, E., 2022, Principal component analysis, *Nat. Rev. Methods Primers*, 2 (1), 100.

[15] Wehrens, R., 2020, *Chemometrics with R Multivariate: Data Analysis in the Natural and Life Sciences*, Springer-Verlag, Berlin, Heidelberg.

[16] Madala, N.E., Piater, L.A., Steenkamp, P.A., and Dubery, I.A., 2014, Multivariate statistical models of metabolomic data reveals different metabolite distribution patterns in isonitrosoacetophenone-elicited *Nicotiana tabacum* and *Sorghum bicolor* cells, *Springerplus*, 3 (1), 254.

[17] Moldoveanu, S.C. 2020, *Analytical Pyrolysis of Natural Organic Polymers*, Elsevier Science, New York, US.

[18] Husson, F., Le, S., and Pagès, J., 2017, *Exploratory Multivariate Analysis by Example Using R*, 2nd Ed., Chapman and Hall/CRC, New York, US.

[19] Husson, F., Josse, J., Le, S., and Mazet, F., 2016, Package 'factominer', *An R package*, 96, 698.

[20] Kassambara, A., 2016, *Practical Guide to Principal Component Methods in R*, STHDA.

[21] Wickham, H., 2016, *ggplot2: Elegant Graphics for Data Analysis*, Springer, Cham, Switzerland.

[22] Garcia, H., and Filzmoser, P., 2017, *Multivariate Statistical Analysis using the R package*

chemometrics, Vienna University of Technology, Austria.

[23] Kang, X., Kirui, A., Dickwella Widanage, M.C., Mentink-Vieger, F., Cosgrove, D.J., and Wang, T., 2019, Lignin-polysaccharide interactions in plant secondary cell walls revealed by solid-state NMR, *Nat. Commun.*, 10 (1), 347.

[24] Tarasov, D., Leitch, M., and Fatehi, P., 2018, Lignin-carbohydrate complexes: Properties, applications, analyses, and methods of extraction: A review, *Biotechnol. Biofuels*, 11 (1), 269.

[25] Decou, R., Labrousse, P., Béré, E., Fleurat-Lessard, P., and Krausz, P., 2020, Structural features in tension wood and distribution of wall polymers in the G-layer of *in vitro* grown poplars, *Protoplasma*, 257 (1), 13–29.

[26] Blaschek, L., Champagne, A., Dimotakis, C., Nuoendagula, C., Decou, R., Hishiyama, S., Kratzer, S., Kajita, S., and Pesquet, E., 2020, Cellular and genetic regulation of coniferaldehyde incorporation in lignin of herbaceous and woody plants by quantitative Wiesner staining, *Front. Plant Sci.*, 11, 00109.

[27] Yan, Z., Li, P., Chen, Y., Han, W., and Fang, J., 2016, Nutrient allocation strategies of woody plants: An approach from the scaling of nitrogen and phosphorus between twig stems and leaves, *Sci. Rep.*, 6 (1), 20099.

[28] Granato, D., Santos, J.S., Escher, G.B., Ferreira, B.L., and Maggio, R.M., 2018, Use of principal component analysis (PCA) and hierarchical cluster analysis (HCA) for multivariate association between bioactive compounds and functional properties in foods: A critical perspective, *Trends Food Sci. Technol.*, 72, 83–90.

[29] Park, Y.J., Baek, S.A., Choi, Y., Kim, J.K., and Park, S.U., 2019, Metabolic profiling of nine *Mentha* species and prediction of their antioxidant properties using chemometrics, *Molecules*, 24 (2), 258.

[30] Ebeling, B., Vargas, C., and Hubo, S., 2013, Combined cluster analysis and principal component analysis to reduce data complexity for exhaust air purification, *Open Food Sci. J.*, 7 (1), 8–22.

[31] Kebelmann, K., Hornung, A., Karsten, U., and Griffiths, G., 2013, Intermediate pyrolysis and product identification by TGA and Py-GC/MS of green microalgae and their extracted protein and lipid components, *Biomass Bioenergy*, 49, 38–48.

[32] El Hayany, B., El Fels, L., Dignac, M.F., Quena, K., Rumpel, C., and Hafidi, M., 2021, Pyrolysis-GCMS as a tool for maturity evaluation of compost from sewage sludge and green waste, *Waste Biomass Valorization*, 12 (5), 2639–2652.

[33] Rambo, D.F., Biegelmeyer, R., Toson, N.S.B., Dresch, R.R., Moreno, P.R.H., and Henriques, A.T., 2019, The genus *Erithrina* L.: A review on its alkaloids, preclinical, and clinical studies, *Phytother. Res.*, 33 (5), 1258–1276.

[34] Chen, H., Xie, Y., Chen, W., Xia, M., Li, K., Chen, Z., Chen, Y., and Yang, H., 2019, Investigation on co-pyrolysis of lignocellulosic biomass and amino acids using TG-FTIR and Py-GC/MS, *Energy Convers. Manage.*, 196, 320–329.

Green Synthesis and Electrochemical Study of Undoped and Doped Al_2O_3 Nanoparticles Using *Hibiscus rosa-sinensis* Leaves Extract

Farzana Haider*, Gul Asimullah Khan Nabi, Kiran Shah, Kafeel Ahmad Khan, and Haseeba Khan

Department of Chemistry, Bacha Khan University, Charsadda, 24420, Khyber Pakhtunkhwa, Pakistan

* ***Corresponding author:***

tel: +92-09-3349096322
email: unsty36@gmail.com

Received: August 31, 2022
Accepted: May 13, 2023

DOI: 10.22146/ijc.77418

Abstract: *In the present work, nanoparticles of Al_2O_3, Cu-Al_2O_3, and Ni-Al_2O_3 were prepared using* Hibiscus rosa-sinensis *plant leaf extract through co-precipitation method. The prepared nanomaterials were characterized through TGA, EDX, SEM, UV-Vis, XRD, and FTIR instruments. The electrochemical behavior of Al_2O_3, Cu-Al_2O_3, and Ni-Al_2O_3 has been studied in DMF solution in the potential ranges from −1.5 to 1.5 V. The nanoparticles are thermally stable, according to the TGA, and the XRD patterns revealed that all the Al_2O_3, Cu-Al_2O_3, and Ni-Al_2O_3 particles were crystalline, with the mean sizes of 12.44, 34.61, and 31.63 nm, respectively. The cyclic voltammogram showed a cathodic peak (E_{pc}) at 0.49 V with an anodic counterpart (E_{pa}) at 0.49 V [$E_{1/2}$ = 1.748 V]. The optical band gaps of Al_2O_3, Cu-Al_2O_3, and Ni-Al_2O_3 were 3.8, 3.2 and 3.65 eV, owed a cathode. It is observed that the electrochemical behavior of Ni-Al_2O_3 was identical to that of Al_2O_3 and Cu-Al_2O_3. The anodic and cathodic peak values rise with the scan rate. The one-electron oxidation and reduction processes are reversible, as seen by the shifting cathodic peak value toward higher negative values. All cycles exhibit absorption has a constant anodic current. This result indicated the diffusion-based redox process.*

Keywords: *cyclic voltammogram; electrochemical behavior; co-precipitation method; Al_2O_3;* Hibiscus rosa-sinensis

INTRODUCTION

With potential applications in industries range starting cosmetics to electronics, the area of nanotechnology and nanoscience are rapidly expanding for biological, physical, chemical, and phenomena at the sub-atomic and atomic level [1-9]. Scientists are working hard to discover new technologies through nanosciences and nanotechnology that are involved in the creation of new materials with distinctive and better properties [10-12]. Nanoparticles (NPs) are synthetic particles produced by nanotechnology. NPs are increasingly being used in medicine, catalysis, cosmetics, dyes, and biosensing fields [6].

Outstanding physicochemical characteristics are found in NPs. When compared to other approaches, the synthesis and stability of NPs made from plants are both quicker and more stable [13]. Because there are so many plants, they are easily accessible, have an advantage over physical and chemical methods, and are simple to work with [14]. Additionally, there are no hazardous chemicals used in the production process. Natural capping agents derived from plants are useful for the production of NPs [15]. Doping is an important parameter used for NPs due to the reformation of physicochemical properties of metal oxide, which has large applications, especially in the electrochemical field [16].

Many processes are applied in the fabrication of NPs, together with electrochemistry, electrical devices, and catalysis [17]. In several branches of chemistry, cyclic voltammetry has emerged as a prominent and popular electro-analytical technique. By adjusting the electrode potential of an electrochemical cell, the redox reaction occurring on the electrode can be managed. Therefore, it is essential to study the electrochemical reactions that take place at electrode/electrolyte contact. By methodically analyzing the current-voltage data of a specific

electrochemical cell, cyclic voltammetry is a potent tool for studying the electrochemical behavior of a system. Voltammetric techniques are widely used by inorganic, physical, and biological chemists for a wide range of applications, including basic research on oxidation and reduction processes in various media, adsorption on surfaces, mechanisms of electron transfer and reaction, the kinetics of electron transfer processes, transport, speciation, and thermodynamic properties of solvated species [18].

The research interest of our group is to synthesize NPs using plants which are easily approachable, non-toxic, cheap, and safe. Scientists around the world are working on different plants for the synthesis of NPs, but the *Hibiscus rosa-sinensis* plant is not used up till now. The NPs were synthesized using the co-precipitation method using *H. rosa-sinensis* leaves extract in this study.

■ EXPERIMENTAL SECTION

Materials

Aluminium(III) nitrate, copper(II) nitrate, dimethyl sulfoxide (DMSO), nickel(II) nitrate, potassium chloride, and *H. rosa-sinensis* leaves were the ingredients employed in the manufacture of undoped and copper doped aluminium oxide (Al_2O_3) NPs. All chemicals came from the Sigma Aldrich firm and were utilized without any further processing. Aluminium(III) nitrate solution was prepared by taking 10 mL of aluminium(III) nitrate (1.06 M) and dissolved in 50 mL of deionized water to give 1 mM solution.

Instrumentation

A Gallenkamp thermal stirrer was used for the batch experiments (ZHWY-200B, ZHICHENG Analytical Co. Ltd). The metal solution was filtered through a Whatman filter paper No. 1 (Millipore Corp., Bedford, and Mass). A double-beam UV–visible spectrophotometer (UV-1800 240 V, Shimadzu Corporation) was used for the determination of NPs. Additionally, the particles underwent calcination in a muffle furnace (JFF 2000). The functional groups contained in the solution were examined by using FTIR (Perkin Elmer, resolution at 4 cm^{-1} in a range of diffusion reflect an assembly and KBr). Through EDX (INCA-200) and SEM (JSM-5910, JEOL), respectively, the particles' elemental composition and surface morphology were examined. TGA was used to do the thermal studies of the particles (25–800 °C). Electrochemical characterizations of NPs were done by cyclic voltammetry. The cyclic voltammetric Potentiostate DY 2300 model was used to obtain a cyclic voltammogram. The electrochemical workstation consisted of a cell containing three electrodes: the calomel electrode was used as the reference electrode, the graphite electrode was used as the working electrode, and the gold electrode was used as the counter electrode. XRD analysis was performed at Cu Kα radiation = 1.5406, using the 2 ranges of 20–80° with a step width of 0.02" and step time of 2.40 s [19].

Procedure

Preparation of H. rosa-sinensis *leaves extract*

Fresh *H. rosa-sinensis* plant leaves were collected from District Charsadda. The leaves of the plant were washed several times with water to remove the dust particles and then sun-dried for 10 min to remove the residual moisture. After that, the leaves were shaded and dried for two weeks. Finally, dried leaves were ground into fine powder form. The extract was prepared by placing 20 g of finely powdered leaves, adding to 200 mL of double distilled water and boiling for 30 min. The extract was cooled to room temperature and filtered. The filtered extracts were stored in a refrigerator to be used for further experiments [20].

Synthesis of Al_2O_3 NPs

Using the green combustion approach and leaf extract from the *H. rosa-sinensis* plant as fuel, Al_2O_3 NPs were prepared. A 40 mL of aluminum(III) nitrate solution 1 mM was combined with 10 mL of *H. rosa-sinensis* plant extract. The muffle furnace was preheated at 200 ± 5 °C. The sample is then taken in a clay crucible and put in a muffle furnace. In roughly 2–3 min, the mixture burnt completely, yielding undoped Al_2O_3 NPs. The sample (ash) was then filtered to remove any leftover ash made from plant extract. The ash was cleaned with deionized water multiple times to remove impurities. The generated NPs were also calcinated for 2 h at 200 ± 5 °C to achieve purity. The characterization

results showing the Al_2O_3 NPs are fine and accurate, which were kept in an airtight container for further study [20].

Synthesis of copper-doped Al_2O_3 NPs

Using the green combustion technique and the leaf extract of *H. rosa-sinensis* as fuel, Cu-doped Al_2O_3 NPs were precipitated. In 40 mL of double-distilled water, 1 mM of aluminium(III) nitrate and 1.305 g of copper(II) nitrate trihydrate ($Cu(NO_3)_2{\cdot}3H_2O$) were combined with 10 mL of *H. rosa-sinensis* leaf extract. Using a magnetic stirrer and continual stirring at 2000 rpm, the solution was homogenized for 2 to 5 min. Firstly, the temperatures are set to 200 ± 5 °C and then start combustion. The sample was heated to 200 ± 5 °C in a muffle furnace before being placed in a clay crucible (with the aid of a long iron sample holder). Cu-doped Al_2O_3 NPs were produced as a result of the mixture burning within 2 to 3 min. Ashes from the plant extract were removed from the mixture through filtering, and pollutants were eliminated through rinsing with double-distilled water. To achieve purity, the produced NPs underwent 2 h calcination at 200 ± 5 °C. The output, which was light greenish Cu-doped Al_2O_3 NPs kept in an airtight container, was satisfactory [19].

Synthesis of nickel-doped Al_2O_3 NPs

Utilizing the green combustion technique and *H. rosa-sinensis* leaf extract as fuel, Ni-doped Al_2O_3 NPs were created. A 10 mL of *H. rosa-sinensis* leaf extract was combined with 1 mM of aluminum(III) nitrate, 1.305 g of nickel(II) nitrate, and 40 mL of double distilled water. A magnetic stirrer was used to mix the solution continuously for 2 to 5 min at 2000 rpm. At the start of combustion, the temperature of the muffle furnace (Neycraf™ JFF 2000 furnace) is 200 ± 5 °C. Following that, the sample was taken in a clay crucible and heated to 200 ± 5 °C in a muffle furnace. The mixture burnt entirely in 2 to 3 min, resulting in Ni-doped Al_2O_3 NPs. The resulting mixture was filtered to remove any ash from the plant extract before being cleaned with double-distilled water to remove any impurities. The synthesized NPs underwent a 2 h calcination procedure to obtain purity. As a result, fine, white Ni-doped Al_2O_3 NPs were created and stored in an airtight container [19].

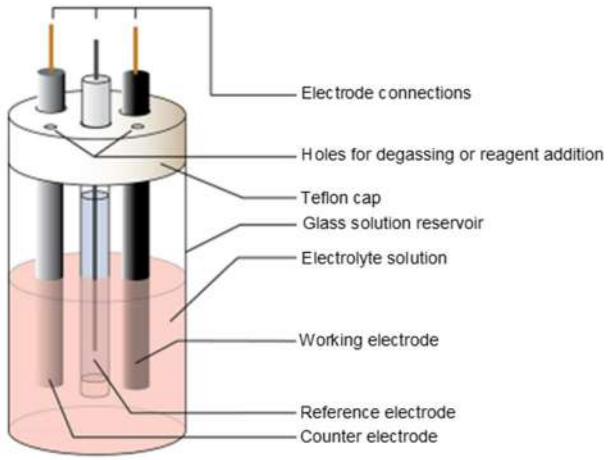

Fig 1. Schematic representation of an electrochemical cell for CV experiments

Procedure for electrochemical measurement (solution)

KCl solution was commonly employed as the inner solution for the reference electrode or as supporting electrolytes in the sample solution during cyclic voltammetry. Prepared Al_2O_3 NPs weighing 0.006 g were dissolved in 10 mL of DMSO solvent. A few drops of KCl solution were then added to this mixture. Similarly, for the 2 mM solution of Ni-doped Al_2O_3 NPs, the generated doped particle powder weighing 0.007 g was diluted in 10 mL of DMSO solvent. This solution was supplemented with a few drops of KCl solution. Likewise, for the 2 mM solution of Cu-doped Al_2O_3 NPs, the obtained doped particle powder weighing 0.007 g was diluted in 10 mL of DMSO solvent. A few drops of KCl solution were added to this combination. These carefully prepared solutions were integral to the subsequent electrochemical measurements.

Cyclic voltammetry

A schematic representation of an electrochemical cell is presented in Fig. 1.

■ RESULTS AND DISCUSSION

Characterization

SEM analysis

SEM analysis was employed in order to determine the size and morphologies of Al_2O_3, Cu-Al_2O_3 and Ni-Al_2O_3 NPs. SEM analysis of Al_2O_3, Cu-Al_2O_3, and Ni-

Al_2O_3 NPs. Fig. 2(a), (b) and (c) are taken within the range of 1 µm with the magnification of 10,000×, at an accelerating voltage of electron beam of 20 kV which are exhibited. Fig. 2(a), (b) and (c) shows the typical SEM images of Al_2O_3, Cu-Al_2O_3, and Ni-Al_2O_3 NPs. It is observed that Al_2O_3, Cu-Al_2O_3 and Ni-Al_2O_3 are of spherical morphology and have narrow diameter distributions (50–80 nm). However, Al_2O_3 NPs show aggregation (Fig. 2(a)), while Cu-Al_2O_3 and Ni-Al_2O_3 NPs are uneven and homogeneously scattered, as shown in Fig. 2(b, c).

EDX analysis

The EDX spectrum of Al_2O_3 demonstrates a strong link between O and Al with element weights of 59.35% and 40.65%, confirming the formation of Al_2O_3 NPs. Al_2O_3 NPs doped with Cu, the EDX spectrum reveals a prominent band of O, Al, S, Cl, and Cu with element weight of 58.79%, 38.67%, 0.82%, 0.35%, and 4.27% confirming the synthesis of Cu doped Al_2O_3 NPs. While Al_2O_3 NPs doped with Ni, the EDX spectrum reveals a prominent band of C, O, Al, K, and Ni with element weight of 8.04%, 46.22%, 39.67%, 0.72%, and 5.36% confirming the sample contains Ni doped Al_2O_3 NPs (see Table 1).

XRD analysis

Fig. 3(a), (b), and (c) shows the results of the XRD examination of Al_2O_3, Cu-Al_2O_3, and Ni-Al_2O_3 NPs. Cu-Al_2O_3, Ni-Al_2O_3, and Al_2O_3 sample crystallization took place at 350 °C calcinating temperatures. The samples exhibit high crystallinity, which shows that contaminants have been removed and a crystalline phase has formed. According to the XRD examination, tetragonal Al_2O_3 particles were produced with good crystallinity. The crystal sizes for Cu-Al_2O_3, Ni-Al_2O_3, and Al_2O_3 NPs, were with diameters of 12.44, 34.61, and 31.63 nm, exhibit high crystallinity, which shows that contaminants have been

Table 1. EDX of Al_2O_3, Cu-Al_2O_3, and Ni-Al_2O_3

	Element	Weight (%)	Atomic (%)
Al_2O_3	O K	59.35	71.12
	Al K	40.65	28.88
	Totals	100.00	100.00
Cu-Al_2O_3	O K	55.89	68.51
	Al K	38.67	28.11
	S K	0.82	0.50
	Cl K	0.35	0.19
	Cu K	4.27	2.69
	Totals	100.00	100.00
Ni-Al_2O_3	C K	8.04	12.69
	O K	46.22	54.78
	Al K	39.67	27.88
	K K	0.72	0.35
	Ni K	5.36	4.29
	Totals	100.00	100.00

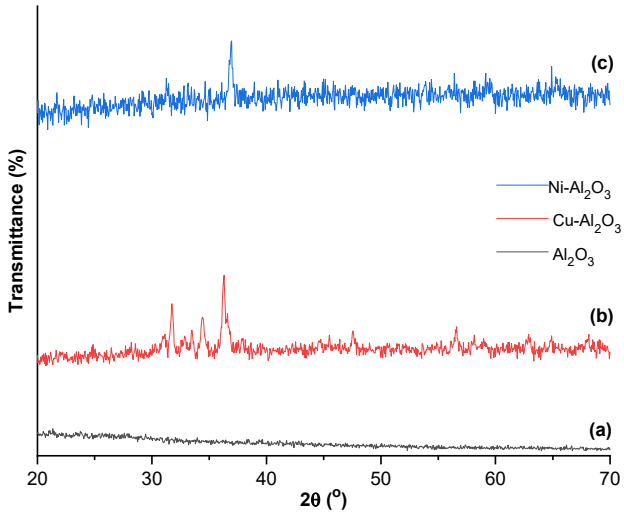

Fig 3. XRD Analysis of (a) Al_2O_3, (b) Cu-Al_2O_3, and (c) Ni-Al_2O_3

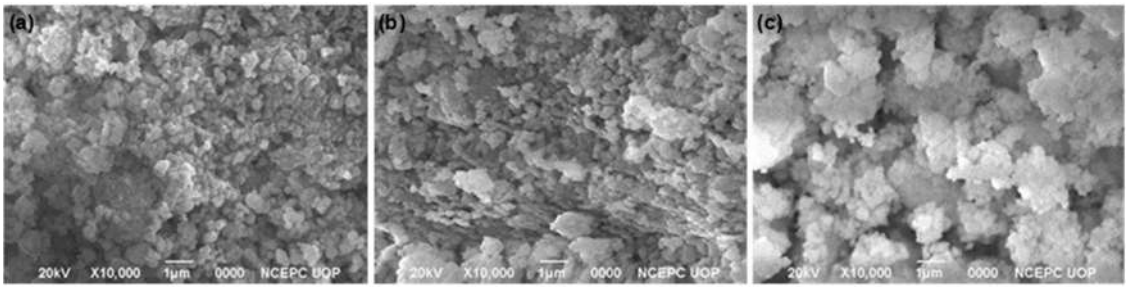

Fig 2. SEM images of (a) Al_2O_3, (b) Cu-Al_2O_3, and (c) Ni-Al_2O_3

removed and a crystalline phase has formed. According to the XRD examination, tetragonal Al_2O_3 particles were produced with good crystallinity. The crystal sizes for Cu-Al_2O_3, Ni-Al_2O_3, and Al_2O_3 NPs, were with diameters of 12.44, 34.61, and 31.63 nm, respectively. It was discovered that the amount of additive had a significant impact on the nanocrystalline Al_2O_3 crystalline size effect. The growth in crystallite size is caused by the doping's continued addition. The increase in crystallite size with the increased addition of the doped. The observed pattern has a number of sharp peaks orientation in the planes (110), (020), (101), (022), (200), (111), (211), (220), (002), (310), (112), (301), and (202) at different angles (2θ) indicating that higher crystallinity of the material. No peaks of extra impurity crystalline phases have been detected. All strong and sharp diffraction peaks obtained are approved by the formation of Al_2O_3. The experimental XRD pattern shows diffraction lines of cassiterite Al_2O_3 (ICDD PDF no. 88-0287). The crystallite size (D) was calculated by the measurement of the diffraction line and applying the Debye Scherrer formula, Eq. (1) [21];

$$D = \frac{0.94\lambda}{\beta \cos\theta} \quad (1)$$

where λ is the wavelength of α radiations, β the full width at half maximum of the peaks corresponding to the plane, and θ the angle obtained from 2θ value corresponding to a maximum intensity peak in the XRD pattern. The size of crystalline NPs can be estimated by the amount by which the X-ray line is sharp.

FTIR analysis

Fig. 4 shows the Fourier transform infrared (FTIR) spectra of the synthesized Al_2O_3 as well as doped Cu-Al_2O_3 and Ni-Al_2O_3 NPs. The FTIR spectrum of Al_2O_3 and Cu-Al_2O_3 and Ni-Al_2O_3 NPs shows the carbonyl group (C=O), stretching C=C aromatic ring, C-OH stretching vibrations, and C-I hydrogen compound at 1653, 1416.34, 1329.98, 1043.71, 814.21, and 541.53 cm^{-1}, respectively [22]. The FTIR analysis clearly shows that plant chemicals are adsorbed on the surface of metal NPs and act as capping, stabilizing, and protecting agents, as shown in Fig. 4(a-c).

TGA analysis

Fig. 5(a), (b) and (c) shows the TGA analysis for Al_2O_3, Cu-Al_2O_3, and Ni-Al_2O_3 NPs was performed within the temperature range (25–800 °C). This study was performed in the nitrogen environment at a speed of 15 °C/min to analyze the weight loss of the samples. The weight loss caused by moisture was excluded at 100 °C. Thus, the total weight loss in Cu-Al_2O_3 was 44.57% up to 800 °C, 21.22% in Ni-Al_2O_3, and 62.66% in Al_2O_3 NPs were observed. Cu-Al_2O_3 and Ni-Al_2O_3 loosed less weight due to the presence of more functional groups [23-24].

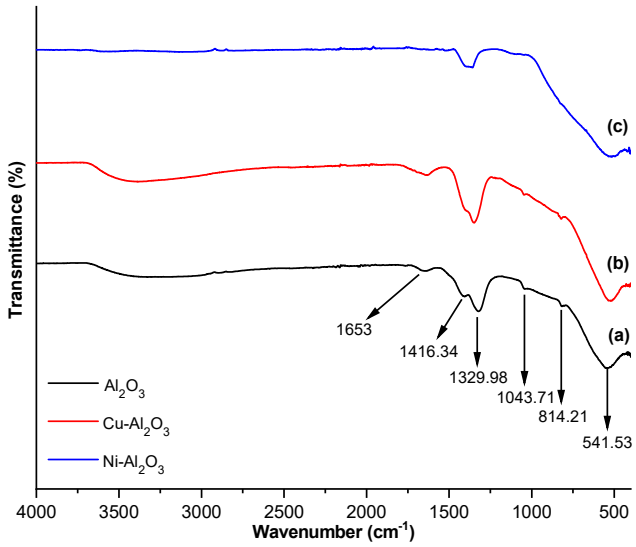

Fig 4. FTIR spectra of (a) Al_2O_3 and (b) Cu-Al_2O_3, (c) Ni-Al_2O_3 NPs

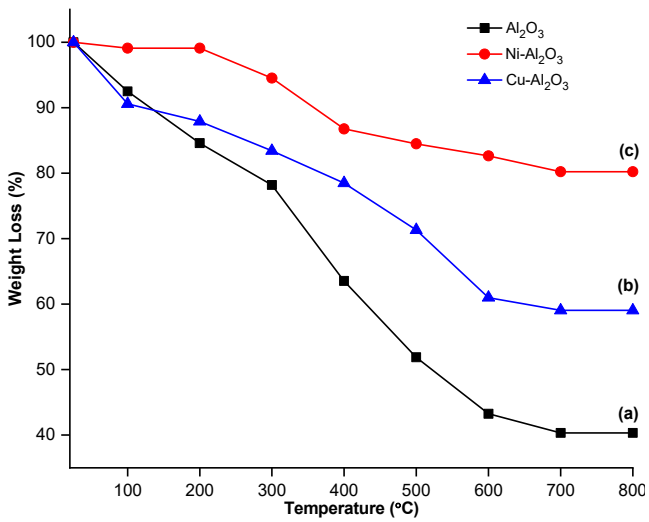

Fig 5. Thermal gravimetric analysis of (a) Al_2O_3 and (b) Cu-Al_2O_3, (c) Ni-Al_2O_3 NPs

UV-Vis and Optical Band Energy

UV-Vis absorption spectra and optical band gap energy of Al_2O_3, Cu-Al_2O_3, and Ni-Al_2O_3. The spectra show strong absorption peaks at 303, 324 and 300 nm for Al_2O_3, Cu-Al_2O_3 and Ni-Al_2O_3. This is due to electron photoexcitation from the valence band to the conduction band. The direct optical band gap energy (E_g) of Al_2O_3, Cu-Al_2O_3 and Ni-Al_2O_3 is calculated using the Tauc relation, Eq. (2) and (3);

$$(\alpha h\nu)^2 = \beta(h\nu - E_g) \quad (2)$$

where β is constant, and α is the absorption coefficient, and it is determined using the following relation:

$$\alpha(\lambda) = 2.303TA \quad (3)$$

where A and T are the absorbances and the thickness of the prepared sample, respectively. Fig. 6 represents the plot of $(\alpha h\nu)^2$ against hν of Al_2O_3, Cu-Al_2O_3 and Ni-Al_2O_3. The direct optical band gap energy E_g is calculated by extrapolating the linear portion of the plot with photon energy (hν) [25]. As shown values of E_g are 3.8, 3.2 and 3.65 eV.

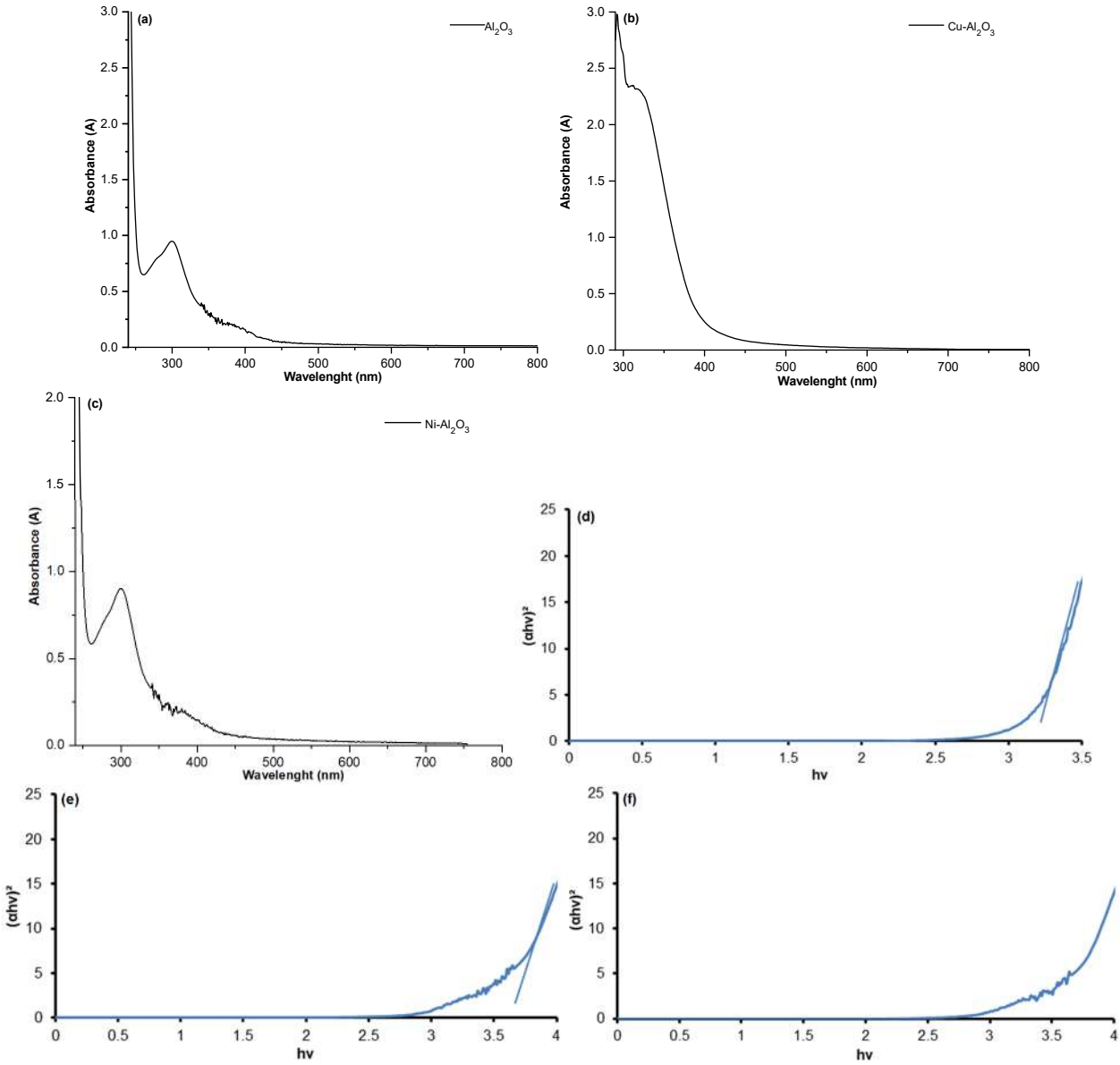

Fig 6. UV-Vis Spectra of (a) Al_2O_3, (b) Cu-Al_2O_3 and (c) Ni-Al_2O_3 and optical band gap of (d) Al_2O_3, (e) Cu-Al_2O_3 and (f) Ni-Al_2O_3

Electrochemical Studies

The electrochemical behavior of the metal NPs undoped Al_2O_3, doped Cu-Al_2O_3 and Ni-Al_2O_3 have been studied in DMF solution. Fig. 7 shows the cyclic voltammogram of metal NPs Al_2O_3, doped Cu-Al_2O_3 and Ni-Al_2O_3, in DMF solution with potential ranges of −1.5 to 1.5 V. The electrochemically irreversible reduction peak observed at 0.524 V is due to the reduction of Al_2O_3, doped Cu-Al_2O_3 and Ni-Al_2O_3 center. This value is in agreement with those observed in the related Al_2O_3, doped Cu-Al_2O_3 and Ni-Al_2O_3 Schiff base complexes. The irreversibility of the redox processes can be attributed to the instability of the reduced species in DMF solvent. By expanding the cyclic voltammogram potential range and monitoring the cyclic voltammogram of 1, 2 and 3 from −1.5 to 1.5 V, one reduction wave at −1.5 to 1.5 V. The cyclic voltammogram shows a cathodic peak (E_{pc}) at 0.49 V with an anodic counterpart (E_{pa}) at 0.49 V [$E_{1/2}$ = 1.748 V]. The electrochemical behavior and the data are in agreement with those reported for related Al_2O_3, doped Cu-Al_2O_3 and Ni-Al_2O_3 [26]. From the cyclic voltammogram, it is clear that the electroactive species reduced and then oxidized. In the forward scan, the species lost electrons and becomes reduced. In reverse scan, the species gained electrons and became oxidized. The oxidation and reduction take place on the working electrode. At a 2 V/s scan rate, the voltammogram was completed very quickly, which showed the electrical energy stored in electroactive species.

Voltammogram of Polycyclic

To obtain 5 cycles voltammogram for Al_2O_3, Cu-Al_2O_3 and Cu-Al_2O_3 at room temperature and pressure, the potentiostat was operated at 0.05 V with a potential range of −1.5 V to +1.5 V. The redox process was based on adsorption-regulated or diffusion controlled, which multicycles assist in explaining. If the anodic current drops in several cycles, adsorption takes place. The redox process was diffusion-based if the anodic current continued to flow unaltered [27].

Fig. 8(a) displays the Al_2O_3 voltammogram with 5 back-to-back cycles and a scan rate of 0.05 V. The voltammogram demonstrated that the anodic current was not constant, proving that absorption was taking place. All cycles that exhibit absorption have a constant anodic

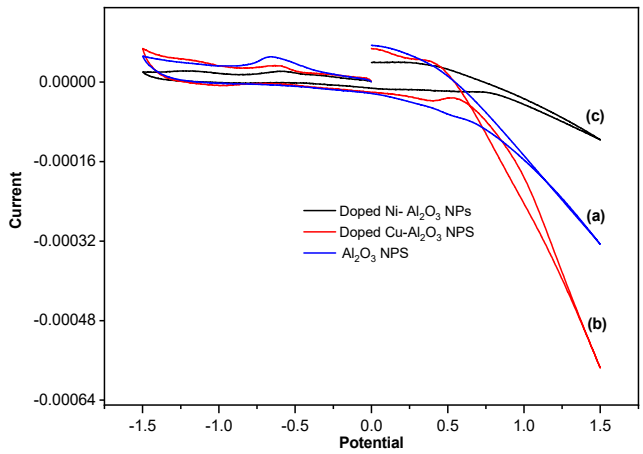

Fig 7. Cyclic voltammogram of (a) Al_2O_3, (b) Cu-Al_2O_3, and (c) Ni-Al_2O_3 NPs with scan rate of 2 V/s

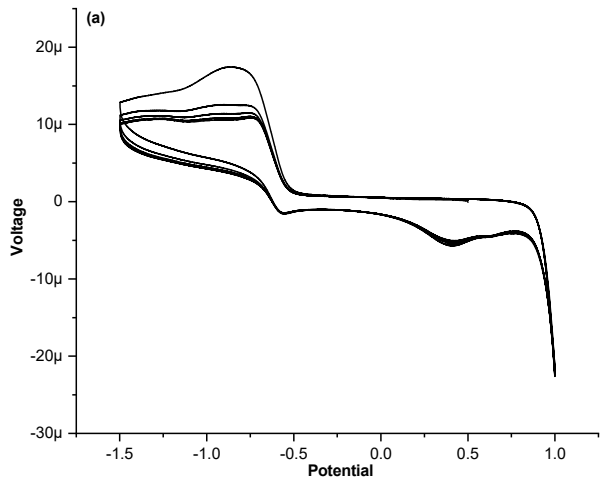

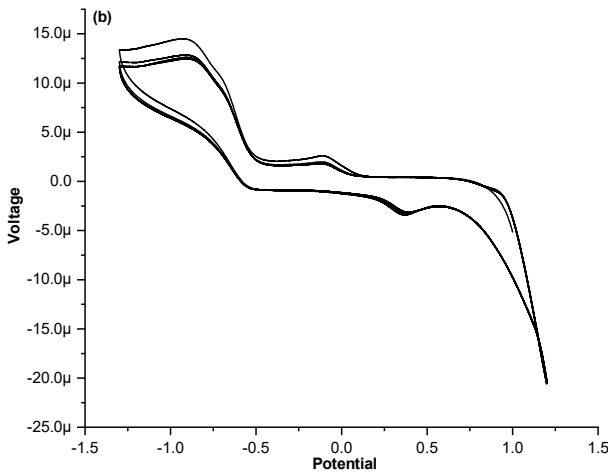

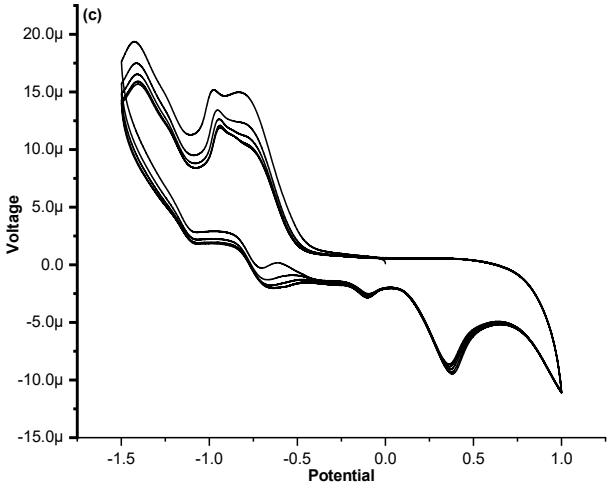

Fig 8. Cyclic voltammogram of (a) Al_2O_3, (b) Cu-Al_2O_3 and (c) Ni-Al_2O_3 at 0.05 V scan rate

current. The values of anodic and cathodic currents are essentially constant. This showed that the redox process was diffusion based.

At a scan rate of 50 mV, Fig. 8(b) shows a 5 cyclic voltammogram of Cu-Al_2O_3. The voltammogram made it evident that the anodic current stayed constant, indicating a diffusion control redox mechanism. Because each Cu-Al_2O_3 molecule had a similar amount of anode surface area to employ, the current stayed constant. The intricate molecule does not stick to the anode's surface but is desorbed from the surface.

The potentiostat was operated for 5 cyclic voltammograms at a 0.05 V scan rate for Ni-Al_2O_3 in order to demonstrate the adsorption base redox process. The anodic current remained constant, as seen in Fig. 8(c), demonstrating a diffusion-controlled redox mechanism. Each Ni-Al_2O_3 molecule had a similar amount of anode surface area to employ, making the current stay constant. The intricate molecule does not adhere to the anode's surface, because each complicated molecule readily donates electrons at the anode, and the current was produced.

Voltammogram of Different Scan Rates

The Al_2O_3 voltammogram was displayed in Fig. 9(a) at various scan speeds. The cathodic potential value changes to the negative side as the scan rate value rises, whereas the anodic peak goes to the positive side. Reversible mechanisms of oxidation and reduction existed because the heterogeneous rate constant values are high.

The voltammogram of Cu-Al_2O_3 at various scan speeds is shown in Fig. 9(b). With an increase in scan rate,

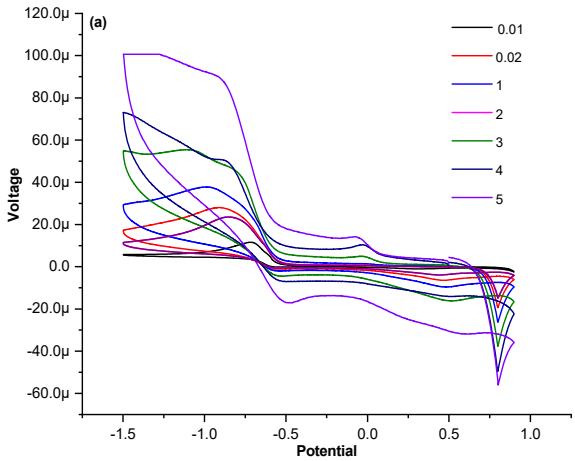

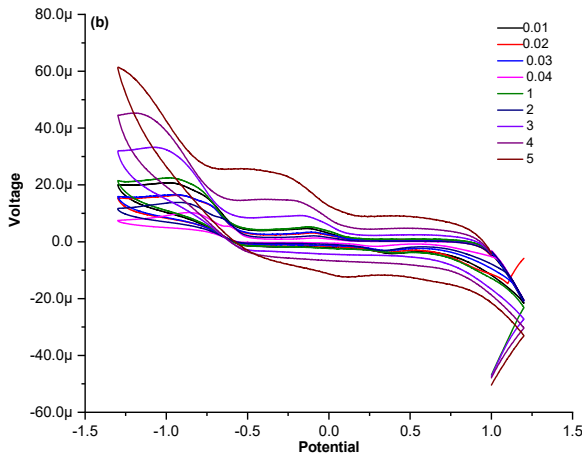

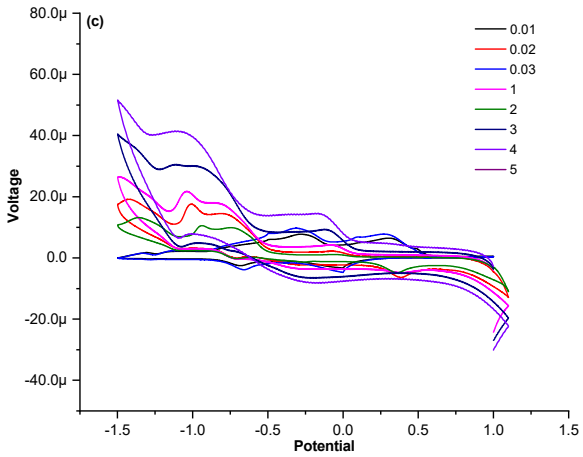

Fig 9. Voltammogram of (a) Al_2O_3, (b) Cu-Al_2O_3 and (c) Ni-Al_2O_3 at 0.05V scan rate at various scan rates

the anodic potential value shifts toward a more positive value and the cathodic potential value toward a more negative side. It demonstrated that the mechanism is reversible. The Ni-Al_2O_3 voltammogram was displayed in Fig. 9(c) at various scan speeds. The electrochemical behavior of Ni-Al_2O_3 was identical to that of Al_2O_3 and Cu-Al_2O_3. The anodic and cathodic peak values rise with the scan rate. The one-electron oxidation and reduction processes are reversible, as seen by the shifting cathodic peak value toward higher negative values.

CONCLUSION

The present work presented using *H. rosa-sinensis* plant leaf extract, Al_2O_3, Cu-Al_2O_3, and Ni-Al_2O_3 NPs were prepared through co-precipitation method. The synthesized particles were analyzed using different techniques EDX, XRD, FTIR, and UV-Vis. The phase structure and surface area of the prepared photocatalyst were investigated using XRD. The shape and composition of Al_2O_3, Cu-Al_2O_3, and Ni-Al_2O_3 NPs were analyzed through SEM and EDX techniques. The cyclic voltammogram shows a cathodic peak (E_{pc}) at 0.49 V with an anodic counterpart (E_{pa} at 0.49 V [$E_{1/2}$ = 1.748 V] within potential ranges from −1.5 to 1.5 V. The electrochemical behavior and the data are in agreement with those reported for related Al_2O_3, Cu-Al_2O_3, and Ni-Al_2O_3. It is noted that the intricate molecule does not adhere to the anode's surface as each molecule readily donates electrons at the anode, and the current was produced.

AUTHOR CONTRIBUTIONS

Farzana Haider provided methodology, supervision, and financial support. Gul Asimullah Khan Nabi curated data and contributed to writing and editing. Kiran Shah conducted investigations and prepared the original draft. Kafeel Ahmad Khan reviewed and edited the content. Haseeba Khan provided co-supervision and assisted with writing and reviewing.

REFERENCES

[1] Vinardell, M.P., Sordé, A., Díaz, J., Baccarin, T., and Mitjans, M., 2015, Comparative effects of macro-sized aluminum oxide and aluminum oxide nanoparticles on erythrocyte hemolysis: Influence of cell source, temperature, and size, *J. Nanopart. Res.*, 17 (2), 80.

[2] Huguet-Casquero, A., Gainza, E., and Pedraz, J.L., 2021, Towards Green Nanoscience: From extraction to nanoformulation, *Biotechnol. Adv.*, 46, 107657.

[3] Pathak, M., Pathak, P., Khalilullah, H., Grishina, M., Potemkin, V., Kumar, V., Majee, R., Ramteke, P.W., Abdellattif, M.H., Shahbaaz, M., and Verma, A., 2021, Green synthesis of silver nanoformulation of *Scindapsus officinalis* as potent anticancer and predicted anticovid alternative: Exploration via experimental and computational methods, *Biocatal. Agric. Biotechnol.*, 35, 102072.

[4] Ingle, A.P., Duran, N., and Rai, M., 2014, Bioactivity, mechanism of action, and cytotoxicity of copper-based nanoparticles: A review, *Appl. Microbiol. Biotechnol.*, 98 (3), 1001–1009.

[5] Erenler, R., Gecer, E.N., Hosaflioglu, I., and Behcet, L., 2023, Green synthesis of silver nanoparticles using *Stachys spectabilis*: Identification, catalytic degradation, and antioxidant activity, *Biochem. Biophys. Res. Commun.*, 659, 91–95.

[6] Schrand, A.M., Rahman, M.F., Hussain, S.M., Schlager, J.J., Smith, D.A., and Syed, A.F., 2010, Metal-based nanoparticles and their toxicity assessment, *WIREs Nanomed. Nanobiotechnol.*, 2 (5), 544–568.

[7] Brouwer, H., Van Oijen, F.L.N., and Bouwmeester, H., 2023, "Potential human health effects following exposure to nano- and microplastics, lessons learned from nanomaterials" in *Present Knowledge in Food Safety*, Eds. Bouwmeester, H., Knowles, M.E., Anelich, L.E., Boobis, A.R., and Popping, B., Academic Press, Cambridge, US, 590–605.

[8] O'Shaughnessy, P.T., 2013, Occupational health risk to nanoparticulate exposure, *Environ. Sci.: Processes Impacts*, 15 (1), 49–62.

[9] Luyts, K., Napierska, D., Nemery, B., and Hoet, P.H.M., 2013, How physico-chemical characteristics of nanoparticles cause their toxicity: complex and unresolved interrelations, *Environ. Sci.: Processes Impacts*, 15 (1), 23–38.

[10] Malakar, R., Kanel, S.R., Ray, C., Snow, D.D., and Nadagouda, N.M., 2021, Nanomaterials in the environment, human exposure pathway, and health effects: A review, *Sci. Total Environ.*, 759, 143470.

[11] Ma, N.L., Zhang N., Yong, W.T.L., Misbah, S., Hashim, F., Soon, C.F., Lim, G.P., Peng, W., and Sonne, C., 2023, Use, exposure and omics characterisation of potential hazard in nanomaterials, *Mater. Today Adv.*, 17, 100341.

[12] Monisha, B., Sridharan, R., Kumar, P.S., Rangasamy, G., Krishnaswamy, V.G., and Subhashree, S., 2023, Sensing of azo toxic dyes using nanomaterials and its health effects - A review, *Chemosphere*, 313, 137614.

[13] Karlsson, H.L., Cronholm, P., Hedberg, Y., Tornberg, M., De Battice, L., Svedhem, S., and Wallinder, I.O., 2013, Cell membrane damage and protein interaction induced by copper containing nanoparticles–Importance of the metal release process, *Toxicology*, 313 (1), 59–69.

[14] Aruna, A., Nandhini, R., Karthikeyan, V., and Bose, P., 2014, Synthesis and characterization of silver nanoparticles of insulin plant (*Costus pictus* D. Don) leaves, *Asian J. Biomed. Pharm. Sci.*, 4 (34), 1–6.

[15] Khan, M.Z.H., Tareq, F.K., Hossen, M.A., and Roki, M.N.A.M., 2018, Green synthesis and characterization of silver nanoparticles using *Coriandrum sativum* leaf extract, *Int. J. Eng. Sci.*, 13 (1), 158–166.

[16] Pirasteh, M., Isfahani, T.M., and Pourghobadi, Z., 2022, Electrochemical codeine sensor based on carbon paste electrode/HKUST-1, *Mater. Res. Express*, 9, 095008.

[17] Ken, D.S., and Sinha, A., 2020, Recent developments in surface modification of nano zero-valent iron (nZVI): Remediation, toxicity and environmental impacts, *Environ. Nanotechnol., Monit. Manage.*, 14, 100344.

[18] Joshi, P.S., and Sutrave, D.S., 2018, A brief study of cyclic voltammetry and electrochemical analysis, *Int. J. ChemTech Res.*, 11 (9), 77–88.

[19] Naz, F., Nabi, G.A.K., Nawaz, A., Ali, S., and Siddique, M., 2022, A novel approach for the photocatalytic degradation of binary dyes mixture using SnO_2 nanoparticles as a catalyst, *J. Cluster Sci.*, 34 (4), 2047–2066.

[20] Sumesh, K.R., and Kanthavel, K., 2019, Green synthesis of aluminium oxide nanoparticles and its applications in mechanical and thermal stability of hybrid natural composites, *J. Polym. Environ.*, 27 (10), 2189–2200.

[21] Tas Anli, S., Ebeoglugil, M.F., and Celik, E., 2020, Effect of dopant elements on structure and morphology of SnO_2 nanoparticles, *J. Aust. Ceram. Soc.*, 56 (2), 403–411.

[22] Nasrollahzadeh, M., Issaabadi, Z., and Sajadi, S.M., 2019, Green synthesis of Cu/Al_2O_3 nanoparticles as efficient and recyclable catalyst for reduction of 2,4-dinitrophenylhydrazine, Methylene blue and Congo

red, *Composites, Part B*, 166, 112–119.

[23] Changmai, M., Priyesh, J.P., and Purkait, M.K., 2017, Al_2O_3 nanoparticles synthesized using various oxidizing agents: Defluoridation performance, *J. Sci.: Adv. Mater. Devices*, 2 (4), 483–492.

[24] Younes, N., Kashyout, A.E.H.B., Shoueir, K., and El-Kemary, M., 2022, Palladium doped tungsten oxide nanoparticle nanocomposite for sensitive detection of CO_2 and LPG gases, *J. Mater. Res. Technol.*, 19, 2633–2644.

[25] Ismail, R.A., Zaidan, S.A., and Kadhim, R.M., 2017, Preparation and characterization of aluminum oxide nanoparticles by laser ablation in liquid as passivating and anti-reflection coating for silicon photodiodes, *Appl. Nanosci.*, 7 (7), 477–487.

[26] Chebout, O., Trifa, C., Bouacida, S., Boudraa, M., Imane, H., Merzougui, M., Mazouz, W., Ouari, K., Boudaren, C., and Merazig, H., 2022, Two new copper(II) complexes with sulfanilamide as ligand: Synthesis, structural, thermal analysis, electrochemical studies and antibacterial activity, *J. Mol. Struc.*, 1248, 131446.

[27] Raccichini, R., Amores, M., and Hinds, G., 2019, Critical review of the use of reference electrodes in Li-ion batteries: A diagnostic perspective, *Batteries*, 5 (1), 12.

Fabrication of Dye Sensitized Solar Cell (DSSC) Using Combination of Dyes Extracted from Curcuma (*Curcuma xanthorrhiza*) Rhizome and Binahong (*Anredera cordifolia*) Leaf with Treatment in pH of the Extraction

Pirim Setiarso*, Rifanda Viantiano Harsono, and Nita Kusumawati

Department of Chemistry, Faculty of Mathematics and Natural Sciences, Universitas Negeri Surabaya, Jl. Ketintang, Surabaya 60231, Indonesia

** Corresponding author:*

email: pirimsetiarso@unesa.ac.id

Received: September 20, 2022
Accepted: June 8, 2023

DOI: 10.22146/ijc.77860

Abstract: *Research on Dye Sensitized Solar Cell (DSSC) fabrication has been carried out using a combination of dyes extracted from* Curcuma xanthorrhiza *and* Anredera cordifolia*. Each dye was extracted by treating pH 1 to 13 and then characterized using UV-Vis spectroscopy. The band gap energy was determined by using the cyclic voltammetric method. The UV-Vis spectrum of* C. xanthorrhiza *extract reveals the presence of curcumin components. The UV-Vis spectrum of* A. cordifolia *indicates the presence of chlorophyll and a trace of anthocyanin.* C. xanthorrhiza *extract had the least band gap energy in the acid phase, pH 1, at 0.66 eV, and the alkaline phase, pH 13, at 0.43 eV. The minimum band gap energy of* A. cordifolia *extract was determined to be 0.96 eV in the acid phase, pH 7, and 0.65 eV in the alkaline phase, pH 12. When* A. cordifolia *and* C. xanthorrhiza *extracts were mixed, with the best composition ratios being pH 7:pH 1 (3:2 ≈ pH 1.7) and pH 12:pH 13 (1:4 ≈ pH 12.6). The composition of this mixture was applied to the DSSC resulting in an efficiency of 0.096 and 0.147%, respectively.*

Keywords: Curcuma xanthorrhiza*; Anredera cordifolia; pH; extract; DSSC*

INTRODUCTION

The demand for energy around the world is increasing every day, and this trend will continue in the future. Therefore, efforts to develop renewable energy sources continue to be made, such as energy from the sun, wind, and water, which are widely available in nature at low cost [1-3]. This motivates researchers to explore energy sources that are clean, practical, renewable, abundant, and environmentally friendly. One of the promising renewable energy sources is solar cells, also known as photovoltaic solar cell to harvest solar energy [4]. Solar energy is one of the energies that can be converted into other energies [5-7]. Sunlight can be converted into electrical energy using solar cells by converting solar radiation directly into a source of electrical energy [8-9].

Dye Sensitized Solar Cells (DSSC) were first discovered by Michael Grätzel and Brian O'Regan in 1991. DSSC continues to develop until the manufacture of Nitrogen-doped carbon nanotubes grafting rutile TiO_2 nanofilms, which is carried out by Belkhanchi et al. [10]. The DSSC device consists of a conductive glass, a semiconductor oxide material, a dye as a photosensitizer, an electrolyte, and a counter electrode [11-12]. Currently, the most efficient dye sensitizer used for electron transfer in DSSC is a polypyridyl ruthenium(II) complex compound, with an overall photovoltaic conversion efficiency of 10% [13]. DSSC has attracted wide attention both scientifically and industrially due to their easy manufacture, low cost, versatility, and wide range of dyes [4].

The working principle of DSSC will be briefly explained as follows. Sunlight with a certain intensity can penetrate into the dye layer because the layer of conductive glass and semiconductor crystals can be easily penetrated by visible light. If the energy of the photon hits the energy gap of the dye molecule, which is the difference between the highest electron-filled

molecular orbital (HOMO) and the lowest empty molecular orbital (LUMO), the dye will absorb it, promoting one electron from HOMO to LUMO. The light energy can cause the excitation of one electron from HOMO to LUMO in the dye molecule. The excited electrons will then be injected into the conduction band of the semiconductor then collected by the conductive glass of the anode. These electrons flow towards an inert counter electrode and are collected by the conductive glass at the cathode. Then the electrons will be captured by the redox pair electrolyte and will return to the dye for regeneration [11]. An illustration of the working principle of DSSC is shown in Fig. 1.

Recently, many DSSC studies have explored sources of natural dyes as promising sensitizers. Besides being easy to obtain, natural dyes are also cheap and environmentally friendly. Natural dyes could come from plants, such as flowers, leaves, fruit, fruit skins, and vegetables. Natural pigments that have been studied to date include anthocyanins, chlorophyll, betacyanins, betaxanthins, betalains, and beta-carotene [14]. Natural dyes can be extracted directly from plants with a variety of solvents and a variety of treatments. DSSC fabricated using extracts from plants of saffron, mallow, red onion, and oregano has an efficiency of 0.51, 0.45, 0.54, and 0.51, respectively [15]. Previous studies have also reported that DSSC fabricated using extracts from pandan leaves has an efficiency of 0.35% [16] and spinach leaves of 0.002% [17].

Many studies in the world also focus research on semiconductor materials. Research on semiconductors is expected to increase the efficiency of DSSC, which also

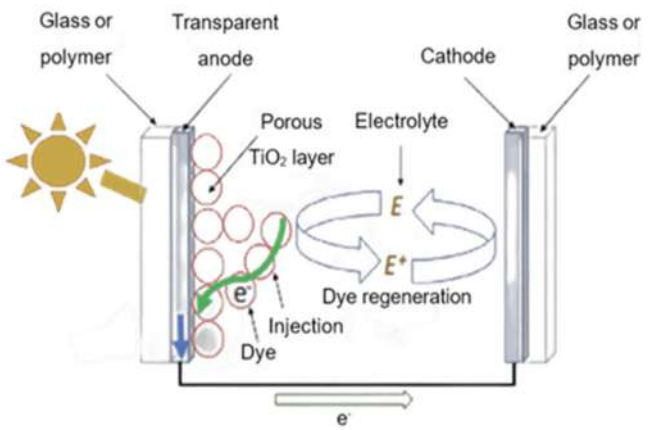

Fig 1. Working principle of DSSC [18]

considers the dye molecules that can easily bind to the layer.

Until now, the most frequently used semiconductor is TiO_2 because it is stable, easy to obtain, and non-toxic [19]. In addition, the dye can also bind easily to the TiO_2 layer to improve the performance of the DSSC. Semiconductors besides TiO_2, there are also other materials such as ZnO [20], SnO_2 [21], ZnO-CdS [22], ZnO-Fe_2O_3 [23], and TiO_2-Ag [24].

The purpose of this study was to determine the performance efficiency of DSSC using dyes extracted from *Curcuma xanthorrhiza* and *Anredera cordifolia*. Each sample was optimized for pH in the extraction process to determine the smallest band gap energy. From here, the smallest band gap will be varied in the mixing composition, and the smallest band gap energy will be sought again. Then, it will be used for DSSC fabrication. Measurement of band gap energy using Cyclic Voltammetry (CV) method, and for the characterization of compounds using UV-Vis spectrophotometry.

■ EXPERIMENTAL SECTION

Materials

TiO_2 powder obtained from Sigma Aldrich. NaOH, KI, and polyethylene glycol (PEG 1000) were purchased from Merck. Demineralization water purchased from CIMS. Ethanol and acetonitrile were purchased from Fulltime. *C. xanthorrhiza* rhizome and *A. cordifolia* leaves were bought from local markets in Pabean-Surabaya, with curcumin concentration varying from 1.0–2.4% in the extract of *C. xanthorrhiza* rhizome and chlorophyll content ranging from 20 to 24 mg/L in the extract of *A. cordifolia*. Carbon pencil 2B (Faber-Castell), Kimwipes KIMTECH (PT Indolab Utama) and cudle wax (Aladin, PT Elos Bintang Selamat). Iodine (I_2) was purchased in VWR Chemicals. ITO conductive glass was purchased from Ali Jaya Lab. HNO_3 was obtained from Emsure while HCl was purchased from SAP Chemicals.

Instrumentation

Calibrated digital pH meter (ATC), used to adjust pH. A rotary evaporator (Buchi R-300) is used to evaporate the solvent resulting from the extraction. UV-Vis spectroscopy (Shimadzu 1800) was used to

characterize the compounds produced from the extraction of *C. xanthorrhiza* and *A. cordifolia*. The band gap energy was determined using a Voltammetry (797 VA Computrace). DSSC performance test using 10-watt LED lamp (509.554 mW/cm^2), multimeter, potentiometer, and other supporting tools.

Procedure

Extraction of C. xanthorrhiza *rhizomes*

The obtained *C. xanthorrhiza* is then peeled off and washed with water until clean. *C. xanthorrhiza* that has been cleaned, cut into small pieces, and then dried using an oven. *C. xanthorrhiza* was extracted using the maceration method. The dried *C. xanthorrhiza* is reduced in size by breaking it, then macerated using ethanol with a ratio of 1:10 (sample:solvent). Optimization of the extraction is done by adjusting the pH from 1 to 13. Adjust the pH by adding HCl and NaOH. Maceration was carried out in dark conditions and protected from light for ± 24 h. The extraction results were then filtered using filter paper. The obtained filtrate is concentrated using a rotary evaporator.

Extraction of A. cordifolia *leaves*

The leaves were obtained from the *A. cordifolia* plant, which was separated from the stem. Then the *A. cordifolia* leaves were cleaned with a tissue that had been moistened with a little water and then cut into small pieces. The extraction process for *A. cordifolia* leaves was the same as for *C. xanthorrhiza* rhizomes.

Preparation of TiO_2 paste

TiO_2 paste was prepared based on the procedure from previous research [25], with a slight modification by adding PEG 1000. A 1.15 g TiO_2 powder was added with 1.5 g PEG 1000. Then 1.5 mL HNO_3 was added to the mixture and stirred for ± 30 min until evenly distributed. After that, let it stand for ± 10 min until the paste is stable.

Preparation of working electrode

The working electrode was prepared following the procedure from previous work [26], with slight modifications. The prepared TiO_2 paste was coated onto the ITO glass on the conductive side. Paste the coating using the Doctor Blade method, with an area of 2 cm × 1.5 cm. Then the glass is heated at 450 °C using a hot plate for 30 min. The sintering product is left to stand until the temperature returns to normal. TiO_2 coating that exceeds the active area of 2 cm × 1.5 cm is removed with ethanol-soaked laboratory wipes.

The finished glass is then soaked in color pigments extracted from *C. xanthorrhiza* and *A. cordifolia* for 24 h. Soaking is done in a dark place away from light. After soaking, color pigments that exceed the active area are removed with ethanol-soaked laboratory wipes.

Preparation of counter electrode

The counter electrode was made following the procedure from previous research [27], with some modifications. ITO glass was made with a deposition size of 2 cm × 1.5 cm using tape. A 2B pencil graphite is shaded on ITO glass, then the tape is removed. ITO glass which has been shaded with pencil graphite, is heated over a burning candle. After that, wait until the temperature decreases, and trim the edges using ethanol-soaked laboratory wipes.

Preparation of electrolyte

The electrolyte solution was made by dissolving 8.3 g of KI and 1.27 g of I_2 in 100 mL of ethylene glycol. To avoid direct sunlight, the solution was stored in a dark place.

Assembly of dye-sensitized solar cell

The DSSC circuit starts from the working electrode, then stacked with the opposing electrode, clamped left and right with a paperclip. After that, the electrolyte solution is dripped on the edges, occasionally opening the paper clip gap to make it easier for the electrolyte to enter it.

Characterization and measurement

The results of *A. cordifolia* and *C. xanthorrhiza* extracts which optimized for pH values, were divided into two ranges is at pH 1 to 7 (considered as the acid phase), and at pH 8 to 13 (considered as the alkaline phase). Characterization of extracted compounds using UV-Vis spectrophotometry. Then the band gap energy is determined using CV method, with a potential range of -1 to 1 V and a scan rate of 20 mV/s.

Characterization of DSSC is determined from the value of V_{oc}, I_{sc}, P_{in}, FF, and efficiency. To test the

performance of DSSC using a potentiometer 250 kΩ. For the light source, a LED lamp 10 watt is used with a light intensity of 509.554 mW/cm^2. The overall performance of the cell was determined by FF. The FF (Eq. (1)) and cell efficiency (η) (Eq. (2)) were calculated using the following formula [28];

$$FF = \frac{V_{max} \times I_{max}}{V_{oc} \times I_{sc}} \quad (1)$$

$$\eta = \frac{FF \times V_{oc} \times I_{sc}}{P_{in}} \times 100\% \quad (2)$$

where V_{max} = maximum output voltage, I_{max} = maximum output current, I_{sc} = short circuit current, V_{oc} = open circuit voltage, and P_{in} = input power 509.554 mW/cm^2.

■ RESULTS AND DISCUSSION

UV-Vis Spectroscopic Characterization of *C. xanthorrhiza*

Results of *C. xanthorrhiza* extract with pH treatment did not show a significant shift in wavelength. In the pH range of 1–7 (Fig. 2(a)), the resulting wavelength is around 424 nm. This compound tends to be stable and maintains its structure in acidic conditions [29]. A peak with a maximum wavelength of 422 nm was found at pH 8–11 (Fig. 2(b)). At pH 8–11 (Fig. 2(b)), the resulting wavelength is around 422 nm, pH 13 has shifted to 419 nm and there are signs of the appearance of small absorption at a wavelength of 438 nm. This is a characteristic of curcumins in *C. xanthorrhiza*. Electron excitation of the π→π* transition occurs in the absorption band in the visible light range, not the n→π* transition, which is proven by theoretical studies [30-31]. Although not significant, curcumin at pH 8–12 experienced a hypochromic or blue shift effect caused by the influence of solvents. At pH 13, a shoulder peak occurs at 438 nm. Alkaline hydrolysis causes the degradation of curcumin, resulting in ferulic acid and feruloyl methane fractions, which reduce absorbance [32-33]. This is supported by the research of Sinha et al. [34] and Pourhajibagher et al. [35] who reported that curcumin extracts in ethanol show variable wavelengths around 350–470 nm due to the degradation of curcumin compounds at the pH above 11.

UV-Vis Spectroscopic Characterization of *A. cordifolia*

Results of the *A. cordifolia* extract will be presented in this study. Treatment of pH extract under acidic conditions did not show a significant wavelength shift. It can be seen in Fig. 3(a), the treatment of pH 1–7 on the extract showed the same peak pattern. The absorption peaks appear at 664, 436, and 412 nm, which reflect the characteristics of the chlorophyll a [35-36]. Theoretically, chlorophyll will lose the central magnesium atom in its structure under acidic conditions, which is called pheophytin. The green color has faded, turning yellow [37-38]. From the spectrum in Fig. 3(a), it can be predicted that the presence of chlorophyll a that lost a central magnesium atom is called pheophytin a because

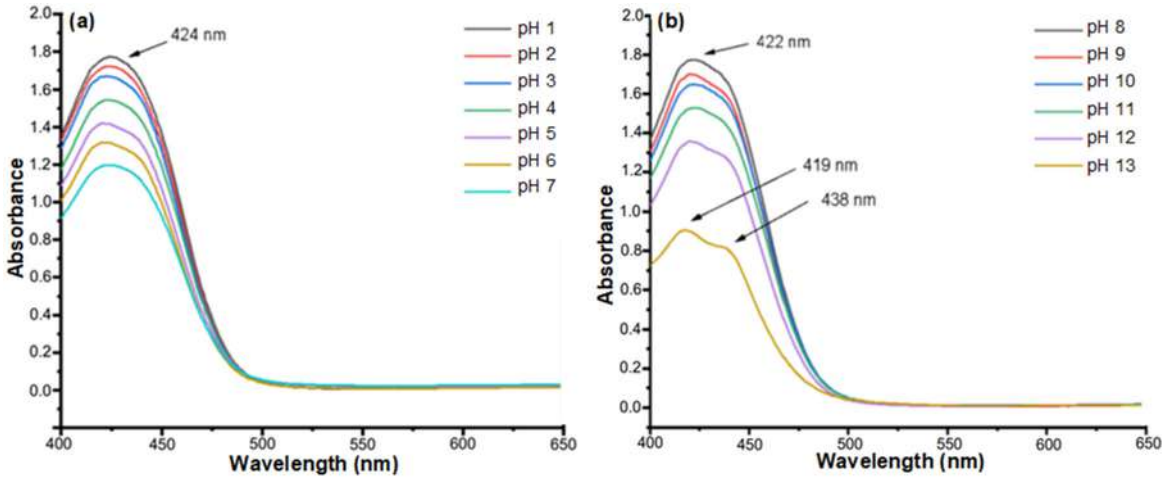

Fig 2. The spectrum of *C. xanthorrhiza* extract (a) pH 1 to 7 and (b) pH 8 to 13

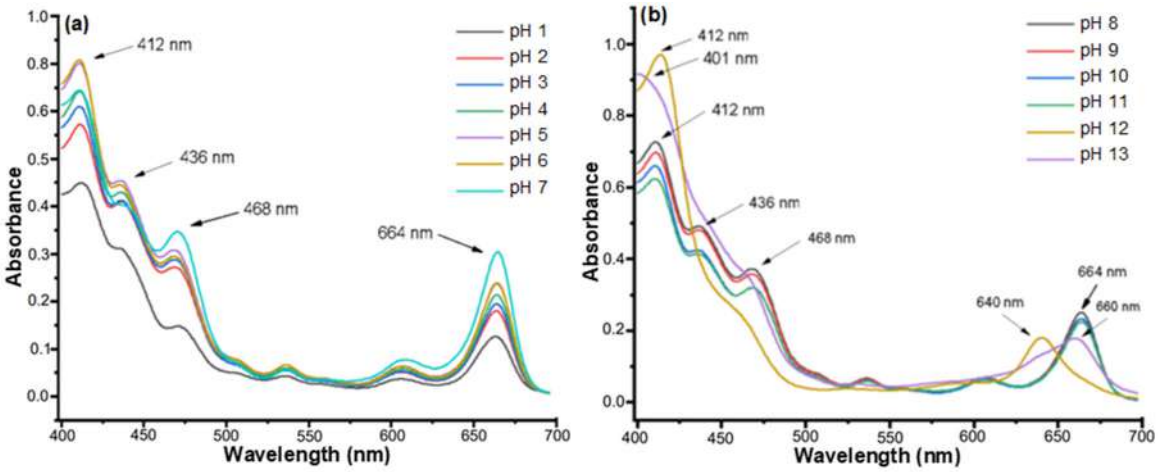

Fig 3. The spectrum of *A. cordifolia* extract (a) pH 1 to 7 and (b) pH 8 to 13

chlorophyll a absorbs red light at approximately 662 nm and violet light at approximately 430 nm. Then the absorption peak appears at 468 nm, which indicates the presence of anthocyanin molecules [39]. However, the treatment of pH 1–7 affects the absorbance. Where the increase in pH from 1 to 7, the absorbance also increases. The increase in absorbance is related to the number of molecules or the concentration of chlorophyll a that has been extracted. Then it can be seen in Fig. 3(b), there is no shift in wavelength at pH 8–11. The absorption pattern is still the same with pH 1–7. However, there was a decrease in absorbance at pH 8–11. This is related to the quantity of molecules or the concentration of chlorophyll a that is extracted less. At pH 12 there is a change in the wavelength absorption. The resulting wavelengths are 640 and 412 nm. Predictably this absorption is an intact chlorophyll b with a central magnesium atom. At pH 12 there was also no absorption peak at a wavelength of 468 nm, which indicated that anthocyanin compounds were not extracted at this pH. At pH 13, the resulting wavelengths are 660 and 401 nm. There is a shift of 664 to 660 nm. Predictably at the top is the presence of an intact chlorophyll a with magnesium as the central atom. Besides that, there is a shift in the absorption of the wavelength at the peak of 412 to 401 nm. This is related to the chlorophyll a which is hydrolyzed into chlorophyllide a and phytol group [40-41].

Band Gap Determined of Cyclic Voltammetry

The band gap energy of the extraction results with pH treatment was determined by the CV method. Measurements were made at a scan rate of 20 mV/s at a potential range of −1 to 1 V. The band gap energy was determined from the difference between HOMO and LUMO values. If the difference between the HOMO and LUMO values is getting smaller, the better the quality of the extracted dye. The ability to regenerate dyes shows the ease of electron transfer from electrolyte I^-/I_3^- to the HOMO band of the substance. This is related to the easier process of excitation of dye electrons from the valence band to the conduction band; with sufficiently small energy, the electrons can be excited. The conduction band is affected by the TiO_2; which the effect of TiO_2 will be in line with the energy of the LUMO dye compound, the easier it is for electron injection. The values calculated in the equation below involve 4.40 eV as the standard energy level of iodine electrolyte below the vacuum level (b). Thus, the HOMO, LUMO, and band gap energy values can be calculated by Eq. (3-5) [42].

$$E_{HOMO} = -e\left(E_{ox} + 4.40\right)eV \quad (3)$$

$$E_{LUMO} = -e\left(E_{red} + 4.40\right)eV \quad (4)$$

$$E_g = E_{LUMO} - E_{HOMO} \quad (5)$$

The HOMO value is correlated with the oxidation state (oxidation peak), while the LUMO is correlated with the reduction state (reduction peak) of the CV [34]. The CV can be seen in Fig. 4. This research will study the combination of dye mixtures and compositions. The band gap energy values are summarized in Table 1. In the range of pH 1 to 7, the best band gap energy of *C.*

xanthorrhiza extract was at pH 1 of 0.66 eV. While in the pH range 1 to 7, the best band gap energy is found at pH 7 of 0.96 V. The *A. cordifolia* extract in the range of pH 8 to 13 has the best band gap energy at pH 13 of 0.43 eV. Meanwhile, in the range of pH 8 to 13, the best band gap energy at pH 12 is 0.65 eV. Of all the dye extraction results with pH variations that have been described, all of them have the potential to become sensitizers in DSSC. However, the band gap energy is taken from this optimum pH to be used for mixing variations. Characterization was also carried out by UV-Vis spectroscopy and voltammetry. The bandgap energy of TiO_2 is 3.2 eV [43]. The LUMO TiO_2 energy has been determined to be −4.00 eV [44]. So that the excitation of electrons from the dye will be easier to inject into the TiO_2 layer when exposed to light. Therefore, the dye produced in this study has the potential as a DSSC sensitizer and is expected to increase DSSC efficiency. Electrons are injected into the conduction band of the porous semiconductor layer because the LUMO of the dye has a higher energy level than that of the conduction layer. Suggesting that the electron injection from these LUMOs to the TiO_2 conduction band is possible. Use of TiO_2 for a variety of benefits, including it is stable, can be used as an electrode in photoelectrochemical systems operating at high temperatures, is inexpensive, non-toxic, and has good optical properties that aid the injection of excited dye electrons into the semiconductor [44].

UV-Vis Spectroscopic Characterization of Mixed Extracts

This characterization is viewed from the best band gap energy determined by the previous CV method. In this study, the extract was mixed in two parts, acid and alkaline. Under acidic conditions, the extracts of pH 7 and 1 were mixed, while in alkaline conditions, the extracts

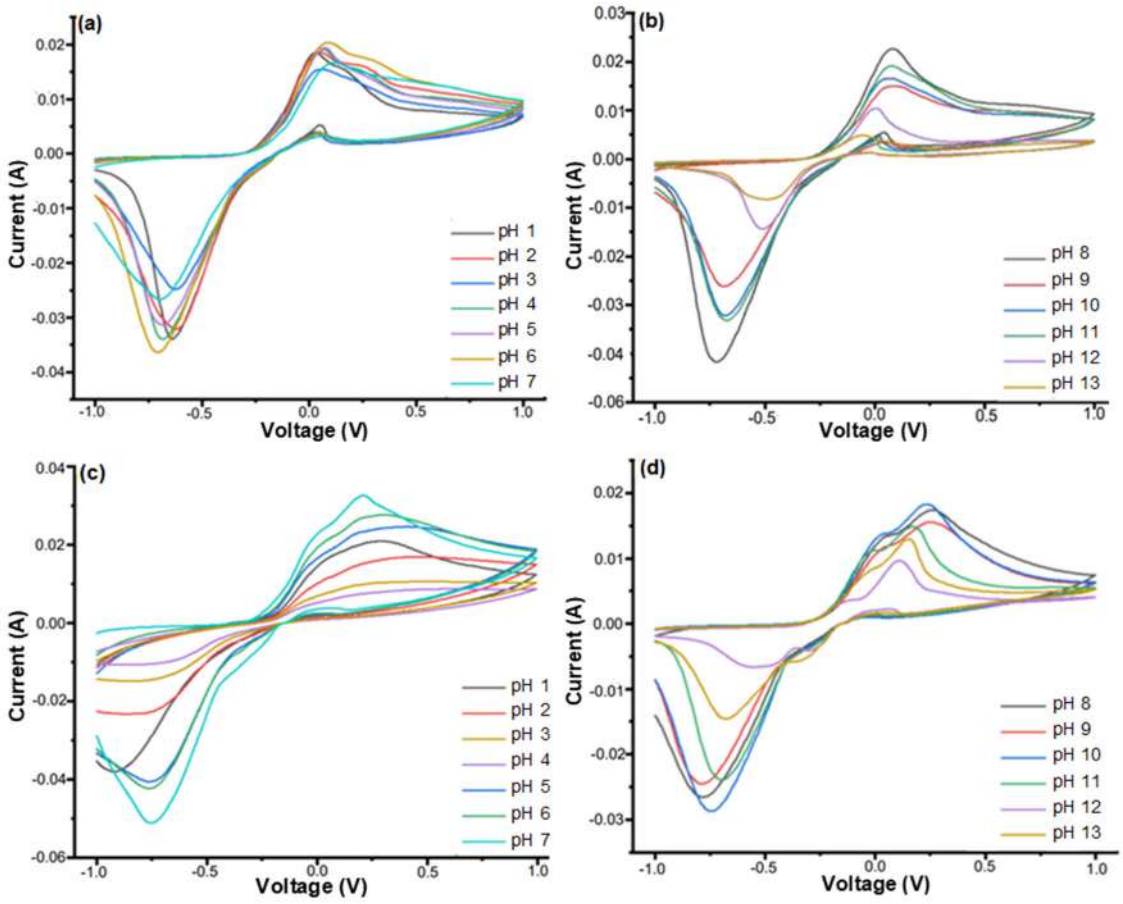

Fig 4. Cyclic voltammogram of *C. xanthorrhiza* extract (a) pH 1 to 7 (b) pH 8 to 13, and *A. cordifolia* extract (c) pH 1 to 7, (d) pH 8 to 13

Table 1. Energy band gap between HOMO and LUMO, extraction results with variations in pH

pH	*C. xanthorrhiza* extract			*A. cordifolia* extract		
	HOMO (eV)	LUMO (eV)	Band gap (eV)	HOMO (eV)	LUMO (eV)	Band gap (eV)
1	-4.42	-3.76	0.66	-4.69	-3.48	1.21
2	-4.45	-3.78	0.67	-4.69	-3.65	1.04
3	-4.46	-3.78	0.68	-4.67	-3.64	1.03
4	-4.46	-3.71	0.75	-4.66	-3.64	1.02
5	-4.47	-3.71	0.76	-4.69	-3.70	0.99
6	-4.48	-3.69	0.79	-4.61	-3.63	0.98
7	-4.51	-3.70	0.81	-4.60	-3.64	0.96
8	-4.48	-3.68	0.80	-4.66	-3.62	1.04
9	-4.48	-3.72	0.76	-4.65	-3.62	1.03
10	-4.47	-3.72	0.75	-4.63	-3.66	0.97
11	-4.47	-3.72	0.75	-4.57	-3.70	0.87
12	-4.41	-3.89	0.52	-4.50	-3.85	0.65
13	-4.34	-3.91	0.43	-4.49	-3.83	0.66

were mixed with pH 12 and 13. The mixture was varied in the composition ratio of 1:4, 2:3, 1:1, 3:2, and 4:1 (*A. cordifolia* extract: *C. xanthorrhiza* extract).

The results of mixing extract pH 7 and 1 with a composition ratio of 1:4, 2:3, 1:1, 3:2, and 4:1 resulted in the final pH being 1.2, 1.5, 1.6, 1.7, and 2.0. UV-Vis spectrum resulting from a mixture of pH 7 and 1 with various composition ratios can be seen in Fig. 5. The spectrum which is generated from the entire composition mixture shows the dominance of curcumin molecules. The resulting absorption peak is 423 nm, and for a mixture of 4:1, composition is 422 nm. Almost no visible signs of the presence of chlorophyll molecules. This is because the ethanol solvent does show a more suitable level of polarity in the curcumin molecule than in chlorophyll. Basically, the curcumin molecule produces a higher concentration when extracted using ethanol than chlorophyll. Chlorophyll has a side chain called phytol in which there are many methyl functional groups, thus reducing the polarity when extraction using ethanol solvent. If seen, indeed, the curcumin molecule produces a relatively higher absorbance in the previous characterization than chlorophyll.

The results of mixing extract pH 12 and 13 with a composition ratio of 1:4, 2:3, 1:1, 3:2, and 4:1 resulted in the final pH is 12.6, 12.4, 12.3, 12.2, and 12.1. UV-Vis spectrum

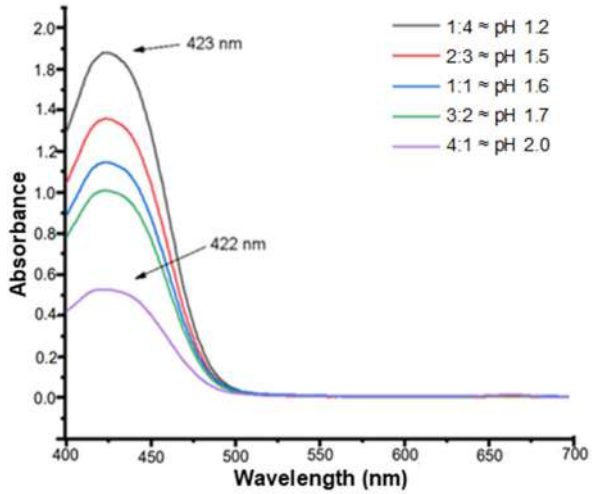

Fig 5. UV-Vis spectrum mixture composition *A. cordifolia* pH 7 and *C. xanthorrhiza* pH 1

resulting from a mixture of pH 12 and 13 with various composition ratios can be seen in Fig. 6. The spectrum which resulted is still the same as before, namely the dominance of curcumin molecules and no signs of the presence of chlorophyll molecules. A mixture of 1:4 composition resulted in a strong peak at 417 nm and a shoulder peak at 439 nm. At a mixture of 2:3 and 1:1 composition, it resulted in a strong peak at 417 nm and a broad peak at 438 nm. Then a mixture of 3:2 composition resulted in an absorption peak at 419 nm, and no shoulder peak appeared as in the previous

composition. Finally, the 4:1 composition mixture only produces an absorption peak at 417 nm, and the shoulder peak that appears is not too strong and sharp. This shows that the composition mixture only shifts the absorption peak slightly so that it experiences a bathochromic effect on the shoulder peak and a hypochromic effect on the strong peak.

Determination Band Gap of Mixed Extracts

This characterization is based on the best band gap energy determined by the previous CV method on each dye that has the best pH for acidic and alkaline conditions. In acidic conditions, *A. cordifolia* extract with pH 7 and *C. xanthorrhiza* extract with pH 1 were combined, while in alkaline conditions, *A. cordifolia* extract with pH 12 was combined with *C. xanthorrhiza* extract with pH 13. Each of these combinations varied with composition ratios of 1:4, 2:3, 1:1, 3:2, and 4:1 (*A. cordifolia* extract: *C. xanthorrhiza* extract). The CV can be seen in Fig. 7.

In a mixture of extracts pH 7 and 1, the best band gap was obtained at a composition of 3:2 with a final pH of 1.7. pH 1.7 is the most optimal concentration in the extract mixture. This is because at this pH, it has the lowest band gap among the other mixtures, as shown in Table 2. The smaller the band gap in the mixture, the easier the dye electron excitation process from the valence band to the conduction band will be, so the quality of the mixed dye will be better. When exposed to light, the electrons will be excited properly and consequently inject into the TiO_2 layer. Higher concentration could cause an obstacle to the total electron excitation process, so the excitation does not take place optimally.

The results of measurements of HOMO-LUMO energy and energy band gap *A. cordifolia* extract mixture (pH 7) and *C. xanthorrhiza* extract (pH 1) as well as a mixture of *A. cordifolia* extract (pH 12) and *C. xanthorrhiza* extract (pH 13) were determined by voltammetry can be seen in Tables 2 and 3.

The best bandgap composition in the mixed extract pH 12 and 13, a composition of 1:4, was found with a final pH of 12.6. The molecular concentration at pH 12.6 is considered the most optimal. The curcumin molecules extracted at pH 13 were less, therefore the composition

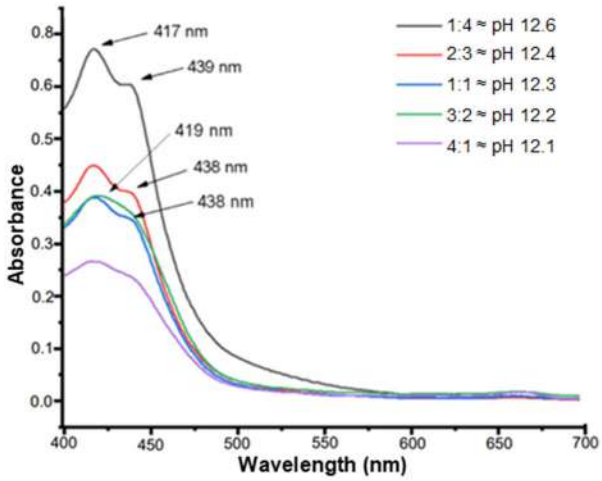

Fig 6. UV-Vis spectrum mixture composition *A. cordifolia* pH 12 and *C. xanthorrhiza* pH 13

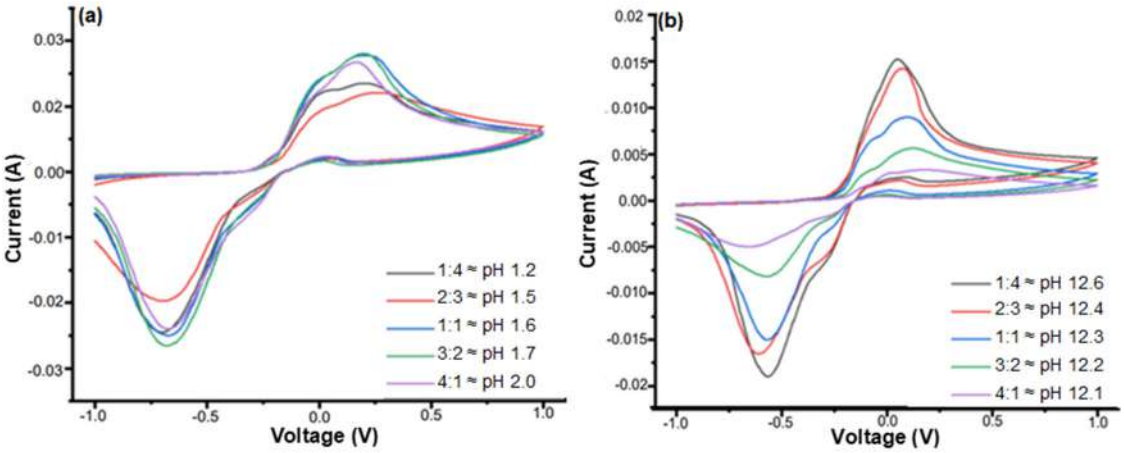

Fig 7. Cyclic voltammogram mixture composition (a) *A. cordifolia* pH 7 and *C. xanthorrhiza* pH 1 (b) *A. cordifolia* pH 12 and *C. xanthorrhiza* pH 13

Table 2. HOMO, LUMO, and band gap mixture pH 7 and 1

Mixture composition	Mixture of *A. cordifolia* extract (pH 7) and *C. xanthorrhiza* extract (pH 1)		
	HOMO (eV)	LUMO (eV)	Band gap (eV)
1:4 ≈ pH 1.2	-3.70	-4.60	0.90
2:3 ≈ pH 1.5	-3.70	-4.66	0.96
1:1 ≈ pH 1.6	-3.73	-4.60	0.87
3:2 ≈ pH 1.7	-3.73	-4.57	0.84
4:1 ≈ pH 2.0	-3.72	-4.60	0.88

Table 3. HOMO, LUMO, and band gap mixture pH 12 and pH 13

Mixture composition	Mixture of *A. cordifolia* extract (pH 12) and *C. xanthorrhiza* extract (pH 13)		
	HOMO (eV)	LUMO (eV)	Band gap (eV)
1:4 ≈ pH 12.6	-3.83	-4.45	0.62
2:3 ≈ pH 12.4	-3.79	-4.47	0.68
1:1 ≈ pH 12.3	-3.83	-4.50	0.67
3:2 ≈ pH 12.2	-3.73	-4.57	0.69
4:1 ≈ pH 12.1	-3.74	-4.58	0.84

of the mixture at pH 12.6 was more abundant than *C. xanthorrhiza* extract. The composition ratio between chlorophyll b and curcumin molecules is optimum in this composition because it has a smaller band gap than *C. xanthorrhiza* extract or *A. cordifolia* extract. In a mixture of these compositions, both can excite electrons well when exposed to light.

DSSC Performance Sensitized from Mixture Selected Compositions of Dyes

DSSC performance was tested using a 10-watt LED lamp with a light intensity of 509.554 mW/cm^2. The distance between the lamp and the DSSC is 4 cm. Measurement of DSSC performance using a potentiometer as reported by Setyawati et al. [45]. Characterization includes V_{oc}, I_{sc}, Fill Factor, and efficiency. The summary and characterization of the I-V curve of the DSSC can be seen in Table 4 and Fig. 8.

In this study, a mixture of pH 7 and 1 extracts was selected at a ratio of 3:2 with a pH of 1.7. This combination resulted in cell parameters of I_{sc} = 2.5 μA, V_{oc} = 320 mV, and FF = 1.83, with a maximum cell efficiency of 0.096%. Under acidic conditions, curcumin molecules tend to be stable and maintain their structure. However, in the extraction process, the pH treatment affected the concentration of the extracted curcumin molecules, so the best was chosen [46]. Meanwhile, chlorophyll in acidic conditions affects the release of a magnesium atom as the central atom of the chlorophyll complex. In addition, the presence of anthocyanins was detected at this pH when extracted. This is associated with the greater steric hindrance when mixing, which will affect the binding to the TiO_2 layer, and also the injection of electrons into the TiO_2 layer when exposed to light. The structure of the anthocyanins may influence DSSC performance. For example, if the structure includes

Table 4. Characterization DSSC mixture of the best composition *A. cordifolia* extract and *C. xanthorrhiza* extract

Extract mixture (pH)	Composition ratio	V_{oc} (mV)	I_{sc} (μA)	FF	Efficiency (%)
7 and 1	3:2 ≈ pH 1.7	320	2.5	1.83	0.096
12 and 13	1:4 ≈ pH 12.6	407	3.3	1.67	0.146

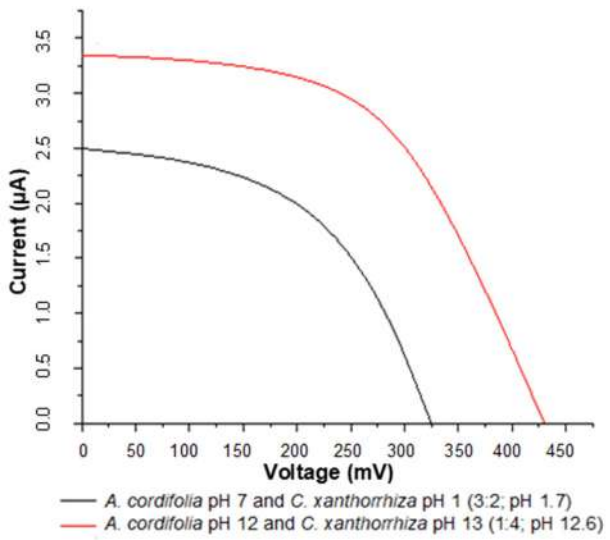

Fig 8. I-V Curves DSSC mixture of the best composition *A. cordifolia* extract and *C. xanthorrhiza* extract

a longer R group, the steric hindrance for the anthocyanin to form a bond with the oxide surface of the TiO_2. As a result, it efficiently blocks the molecule from chemical adsorption on the TiO_2 film layer. Therefore, in this study, the best pH was also selected, and the best mixture composition was also selected to produce optimal efficiency when used as a dye sensitizer in DSSC.

Under alkaline conditions, a mixture of pH 12 and 13 was chosen with a ratio of 1:4 to produce a final pH of 12.6, to be used as a dye sensitizer in DSSC. In the alkaline phase, curcumin molecules have hydrolysis so that they are degraded. This causes a change in the chromophore group, which results in a change in visible light absorption, resulting in a smaller band gap for electron excitation. Then chlorophyll at this pH is predicted as pure chlorophyll without anthocyanins, and also, the central magnesium atom cannot be separated. So that when mixing, the steric resistance that occurs is smaller than that of the acidic phase. This makes the process of chemical bonding by the dye functional groups to the TiO_2 layer easier, and also, when exposed to light, it will be easier to inject electrons into the TiO_2 layer. At this stage, the selection of the best composition is also carried out to obtain optimal efficiency and sensitivity to sunlight. In alkaline conditions, the best combination of *A. cordifolia* extract pH 12 with *C. xanthorrhiza* extract pH 13 is a ratio of 1:4 with a final pH of 12.6. The composition of this combination has the smallest band gap energy that has been determined by cyclic voltammetry and also characterized using UV-Vis spectroscopy. The observed cell parameters from this combination were I_{sc} = 3.3 μA, V_{oc} = 407 mV, and FF = 1.67, with the maximum cell efficiency obtained being 0.146%.

CONCLUSION

Sensitized DSSC from extracts of *C. xanthorrhiza* and *A. cordifolia* with pH treatment has been successfully fabricated. The UV-Vis spectrum shows that the extracted pigment contains curcumin and chlorophyll compounds. The pH treatment also showed a shift in the characteristics of the absorption peak associated with changes in the chromophore and auxochrome groups in the molecule. The band gap energy of the extracted dye, by pH treatment, was determined using cyclic voltammetry. These two dyes have the potential to be applied as DSSC sensitizers. The best mixture of these two dyes (*A. cordifolia* extract:*C. xanthorrhiza* extract) was found at pH 7 and 1 with a composition of 3:2 ≈ pH 1.7, producing V_{oc}, I_{sc}, FF, and η, of 320 mV, 2.5 μA, 1.83, and 0.096%, respectively. Then at pH 12 and 13 with a composition of 1:4 ≈ pH 12.6, it produced V_{oc}, I_{sc}, FF, and η, of 407 mV, 3.3 μA, 1.67, and 0.146%, respectively.

AUTHOR CONTRIBUTIONS

Rifanda Viantiano Harsono and Pirim Setiarso contributed to the extraction of curcuma rhizome and binahong leaves as well as the fabrication of DSSC. Nita Kusumawati contributed to the UV-Vis analysis. In addition, this article manuscript was written by all authors.

REFERENCES

[1] Mamur, H., Dilmaç, Ö.F., Begum, J., and Bhuiyan, M.R.A., 2021, Thermoelectric generators act as renewable energy sources, *Cleaner Mater.*, 2, 100030.

[2] Silva, N., Fuinhas, J. A., and Koengkan, M., 2021, Assessing the advancement of new renewable energy sources in Latin American and Caribbean countries, *Energy*, 237, 121611.

[3] Dong, F.Y., Xu, S., Guo, W., Jiang, N.R., Han, D.D., He, X.Y., Zhang, L., Wang, Z.J., Feng, J., Su, W., and Sun, H.B., 2020, Solar-energy camouflage coating with varying sheet resistance, *Nano Energy*, 77, 105095.

[4] Ndeze, U.I., Aidan, J., Ezike, S.C., and Wansah, J.F., 2021, Comparative performances of nature-based dyes extracted from Baobab and Shea leaves photo-sensitizers for dye-sensitized solar cells (DSSCs), *Curr. Res. Green Sustainable Chem.*, 4, 100105.

[5] Nan, H., Shen, H.P., Wang, G., Xie, S.D., Yang, G.J., and Lin, H., 2017, Studies on the optical and photoelectric properties of anthocyanin and chlorophyll as natural co-sensitizers in dye sensitized solar cell, *Opt. Mater.*, 73, 172–178.

[6] Behar, O., Peña, R., Kouro, S., Kracht, W., Fuentealba, E., Moran, L., and Sbarbaro, D., 2021, The use of solar energy in the copper mining processes: A comprehensive review, *Cleaner Eng. Technol.*, 4, 100259.

[7] Tsvetkov, N.A., Krivoshein, U.O., Tolstykh, A.V., Khutornoi, A.N., and Boldyryev, S., 2020, The calculation of solar energy used by hot water systems in permafrost region: An experimental case study for Yakutia, *Energy*, 210, 118577.

[8] Damayanti, R., Hardeli, H., and Sanjaya, H., 2014, Preparasi dye sensitized solar cell (DSSC) menggunakan ekstrak antosianin ubi jalar ungu (*Ipomea batatas* L.), *Sainstek: J. Sains Teknol.*, 6 (2), 148–157.

[9] Khan, M.I., Farooq, W.A., Saleem, M., Bhatti, K.A., Atif, M., and Hanif, A., 2019, Phase change, band gap energy and electrical resistivity of Mg doped TiO_2 multilayer thin films for dye sensitized solar cells applications, *Ceram. Int.*, 45 (17, Part A), 21436–21439.

[10] Belkhanchi, H., Ziat, Y., Hammi, M., Laghlimi, C., Moutcine, A., Benyounes, A., and Kzaiber, F., 2021, Nitrogen doped carbon nanotubes grafted TiO_2 rutile nanofilms: Promising material for dye sensitized solar cell application, *Optik*, 229, 166234.

[11] Job, F., Mathew, S., Rajendran, R., Meyer, T., and Narbey, S., 2020, An investigation on the performance of dye-sensitized solar cell at various light intensities, *Mater. Today: Proc.*, 43, 3386–3390.

[12] Güzel, R., Yediyıldız, F., Ocak, Y.S., Yılmaz, F., Ersöz, A., and Say, R., 2020, Photosystem (PSII)-based hybrid nanococktails for the fabrication of BIO-DSSC and photo-induced memory device, *J. Photochem. Photobiol., A*, 401, 112743.

[13] Bej, S., Ghosh, P., Majumdar, G., Murmu, N.C., and Banerjee, P., 2020, "Design and Synthesis of New Ruthenium Coordination Complex as Efficient Dye in DSSC Like Alternative Energy Resources with a Bird's Eye View on Strategies Towards GHGs Mitigation" in *Encyclopedia of Renewable and Sustainable Materials*, Eds. Hashmi, S., and Choudhury, I.A., Elsevier, Oxford, UK, 395–410.

[14] Wang, X.F., and Kitao, O., 2012, Natural chlorophyll-related porphyrins and chlorins for dye-sensitized solar cells, *Molecules*, 17 (4), 4484–4497.

[15] Jalali, T., Arkian, P., Golshan, M., Jalali, M., and Osfouri, S., 2020, Performance evaluation of natural native dyes as photosensitizer in dye-sensitized solar cells, *Opt. Mater.*, 110, 110441.

[16] Siddick, S.Z., Lai, C.W., and Juan, J.C., 2018, An investigation of the dye-sensitized solar cell performance using graphene-titania (TrGO) photoanode with conventional dye and natural green chlorophyll dye, *Mater. Sci. Semicond. Process.*, 74, 267–276.

[17] Rahul, R., Singh, S., Singh, P.K., Kakroo, S., Hachim, D.M., Dhapola, P.S., and Khan, Z.H., 2021, Eco-friendly dye sensitized solar cell using natural dye with solid polymer electrolyte as hole transport material, *Mater. Today: Proc.*, 34, 760–766.

[18] Cruz, H., Pinto, A.L., Lima, J.C., Branco, L.C., and Gago, S., 2020, Application of polyoxometalate-ionic liquids (POM-ILs) in dye-sensitized solar cells (DSSCs), *Mater. Lett.: X*, 6, 100033.

[19] Kishore Kumar, D., Kříž, J., Bennett, N., Chen, B., Upadhayaya, H., Reddy, K.R., and Sadhu, V., 2020, Functionalized metal oxide nanoparticles for efficient dye-sensitized solar cells (DSSCs): A review, *Mater. Sci. Energy Technol.*, 3, 472–481.

[20] Sakai, N., Miyasaka, T., and Murakami, T.N., 2013, Efficiency enhancement of ZnO-based dye-sensitized solar cells by low-temperature $TiCl_4$ treatment and dye optimization, *J. Phys. Chem. C*, 117 (21), 10949–10956.

[21] Pari, B., Chidambaram, S., Kasi, N., and Muthusamy, S., 2014, Recent advances in SnO_2 based photo anode materials for third generation photovoltaics, *Mater. Sci. Forum*, 771, 25–38.

[22] Ansir, R., Shah, S.M., Ullah, N., and Hussain, M.N., 2020, Performance of pyrocatechol violet and carminic acid sensitized ZnO/CdS nanostructured photoactive materials for dye sensitized solar cell, *Solid-State Electron.*, 172, 107886.

[23] Sebehanie, K.G., 2017, Comparative study of ZnO/Fe_2O_3 nanocomposite sensitized with natural pigments for dye sensitized solar cell, *Int. J. Hybrid Inf. Technol.*, 10 (1), 199–214.

[24] Ibrayev, N., Serikov, T., Zavgorodniy, A., and Sadykova, A., 2018, The effect of the DSSC photoanode area based on TiO_2/Ag on the conversion efficiency of solar energy into electrical energy, *IOP Conf. Ser.: Mater. Sci. Eng.*, 289, 012024.

[25] Mensah-Darkwa, K., Agyemang, F.O., Yeboah, D., and Akromah, S., 2020, Dye-sensitized solar cells based on graphene oxide and natural plant dye extract, *Mater. Today: Proc.*, 38, 514–521.

[26] Syafinar, R., Gomesh, N., Irwanto, M., Fareq, M., and Irwan, Y.M., 2015, Chlorophyll pigments as nature based dye for dye-sensitized solar cell (DSSC), *Energy Procedia*, 79, 896–902.

[27] Hölscher, F., Trümper, P., Juhász Junger, I., Schwenzfeier-Hellkamp, E., and Ehrmann, A., 2019, Application methods for graphite as catalyzer in dye-sensitized solar cells, *Optik*, 178, 1276–1279.

[28] Narasimha Rao, B., Padma Suvarna, R., Giribabu, L., Raghavender, M., and Ramesh Kumar, V., 2018, PEO based polymer composite with added acetamide, NaI/I_2 as gel polymer electrolyte for dye sensitized solar cell applications, *IOP Conf. Ser.: Mater. Sci. Eng.*, 310, 012012.

[29] Yoon, S.J., Lim, I., Kim, J.H., Adhikari, S., Lee, W.Y., Lee, J.K., Shrestha, N.K., Ahn, H., Han, J.W., and Han, S.H., 2016, Deprotonated curcumin as a simple and quick available natural dye for dye sensitized solar cells, *Energy Sources, Part A*, 38 (2), 183–189.

[30] Zsila, F., Bikádi, Z., and Simonyi, M., 2003, Molecular basis of the Cotton effects induced by the binding of curcumin to human serum albumin, *Tetrahedron: Asymmetry*, 14 (16), 2433–2444.

[31] Kim, H.J., Kim, D.J., Karthick, S.N., Hemalatha, K.V., Justin Raj, C., Ok, S., and Choe, Y., 2013, Curcumin dye extracted from *Curcuma longa* L. used as sensitizers for efficient dye-sensitized solar cells, *Int. J. Electrochem. Sci.*, 8 (6), 8320–8328.

[32] Leung, M.H.M., Colangelo, H., and Kee, T.W., 2008, Encapsulation of curcumin in cationic micelles suppresses alkaline hydrolysis, *Langmuir*, 24 (11), 5672–5675.

[33] Wang, Y.J., Pan, M.H., Cheng, A.L., Lin, L.I., Ho, Y.S., Hsieh, C.Y., and Lin, J.K., 1997, Stability of curcumin in buffer solutions and characterization of its degradation products, *J. Pharm. Biomed. Anal.*, 15 (12), 1867–1876

[34] Sinha, D., De, D., and Ayaz, A., 2018, Performance and stability analysis of curcumin dye as a photo sensitizer used in nanostructured ZnO based DSSC, *Spectrochim. Acta, Part A*, 193, 467–474.

[35] Pourhajibagher, M., Plotino, G., Chiniforush, N., and Bahador, A., 2020, Dual wavelength irradiation antimicrobial photodynamic therapy using indocyanine green and metformin doped with nano-curcumin as an efficient adjunctive endodontic treatment modality, *Photodiagn. Photodyn. Ther.*, 29, 101628.

[36] Al-Alwani, M.A.M., Ludin, N.A., Mohamad, A.B., Kadhum, A.A.H., and Sopian, K., 2017, Extraction, preparation and application of pigments from *Cordyline fruticosa* and *Hylocereus polyrhizus* as sensitizers for dye-sensitized solar cells, *Spectrochim. Acta, Part A*, 179, 23–31.

[37] Yang, M., Zhu, S., Jiao, B., Duan, M., Meng, Q., Ma, N., and Lv, W., 2020, SlSGRL, a tomato SGR-like protein, promotes chlorophyll degradation downstream of the ABA signaling pathway, *Plant*

Physiol. Biochem., 157, 316–327.

[38] Heaton, J.W., and Marangoni, A.G., 1996, Chlorophyll degradation in processed foods and senescent plant tissues, *Trends Food Sci. Technol.*, 7 (1), 8–15.

[39] Hosseinnezhad, M., Rouhani, S., and Gharanjig, K., 2018, Extraction and application of natural pigments for fabrication of green dye-sensitized solar cells, *Opto-Electron. Rev.*, 26 (2), 165–171.

[40] Kaewsuksaeng, S., 2011, Chlorophyll degradation in horticultural crops, *Walailak J. Sci. Technol.*, 8 (1), 9–19.

[41] Hörtensteiner, S., and Kräutler, B., 2000, Chlorophyll breakdown in oilseed rape, *Photosynth. Res.*, 64 (2), 137–146.

[42] Çakar, S., Atacan, K., and Güy, N., 2019, Synthesis and characterizations of TiO_2/Ag photoanodes for used indigo carmine sensitizer based solar cells, *Celal Bayar Univ. J. Sci.*, 15 (1), 23–29.

[43] Onah, E.O., Offiah, S.U., Chime, U.K., Whyte, G.M., Obodo, R.M., Ekechukwu, O.V., Ahmad, I., Ugwuoke, P.E., and Ezema, F.I., 2020, Comparative photo-response performances of dye sensitized solar cells using dyes from selected plants, *Surf. Interfaces*, 20, 100619.

[44] Hayat, A., Shivashimpi, G.M., Nishimura, T., Fujikawa, N., Ogomi, Y., Yamaguchi, Y., Pandey, S.S., Ma, T., and Hayase, S., 2015, Dye-sensitized solar cells based on axially ligated phosphorus-phthalocyanine dyes, *Appl. Phys. Express*, 8 (4), 047001.

[45] Setyawati, H., Darmokoesoemo, H., Ningtyas, A.T.A., Kadmi, Y., Elmsellem, H., and Kusuma, H.S., 2017, Effect of metal ion Fe(III) on the performance of chlorophyll as photosensitizers on dye sensitized solar cell, *Results Phys.*, 7, 2907–2918.

[46] Ramirez-Perez, J., Maria, C., and Santacruz, C.P., 2019, Impact of solvents on the extraction and purification of vegetable dyes onto the efficiency for dye-sensitized solar cells, *Renewables: Wind, Water, Solar*, 6 (1), 1.

Bioanalytical Method Validation of Metformin Hydrochloride in Human Plasma by HPLC-UV for Preliminary Population-Based Pharmacokinetic Modeling Study

Dimas Adhi Pradana[1,2*], Erna Kristin[2], Akhmad Kharis Nugroho[3], Dwi Aris Agung Nugrahaningsih[2], Mustofa Mustofa[2], and Ari Wibowo[1]

[1]*Department of Pharmacy, Universitas Islam Indonesia, Jl. Kaliurang km. 14, Yogyakarta 55584, Indonesia*

[2]*Department of Pharmacology and Therapy, Faculty of Medicine, Public Health, and Nursing, Universitas Gadjah Mada, Jl. Farmako, Sekip Utara, Yogyakarta 55281, Indonesia*

[3]*Faculty of Pharmacy, Universitas Gadjah Mada, Sekip Utara, Yogyakarta 55281, Indonesia*

* ***Corresponding author:***

email: dimas.pradana@uii.ac.id

Received: September 21, 2022
Accepted: June 13, 2023

DOI: 10.22146/ijc.77903

Abstract: *This study aims to validate the method for measuring metformin hydrochloride plasma concentrations using High-Performance Liquid Chromatography (HPLC). This research performed chromatography on a 250 mm 4.6 mm 5 µm purosphere® Star RP-18 column at ambient temperature with a UV detector system at 233 nm. The mobile phase components were 70% phosphate buffer (KH_2PO_4) (10 mM), sodium dodecyl sulfate (0.3 mM), and 30% acetonitrile. It was pumped at an isocratic flow rate of 1.2 mL/min. Metformin HCl and ranitidine HCl (internal standard) were extracted using acetonitrile. The calibration curve was linear (R^2 = 0.9998) in the 0.18–6 µg/mL concentration range. The lower limit of quantification (LLOQ) was 0.18 µg/mL. For intraday accuracy and precision, the percent difference and the coefficient of variation were less than 4 and 7%, and for inter-day were lower than 8 and 6%. The recovery average was 100.96%. The short-term plasma stability test was stable at 24 h at ambient temperature, and the long-term stability test was steady for 30 d at −20 °C. It was also stable after three freeze-thaw cycles. The method meets selectivity, sensitivity, linearity, accuracy, precision, recovery, carryover, and stability requirements and can be applied to population-based pharmacokinetic modeling.*

Keywords: *human plasma; HPLC-UV; metformin HCl; pharmacokinetic; validation*

■ INTRODUCTION

Metformin hydrochloride (metformin HCl) is the recommended starting therapy for diabetes type 2 [1-2] and also for prediabetes and diabetes prevention [3]. It can be used as monotherapy or in combination with insulin or other glucose-lowering treatments [4-5]. In addition, metformin controls gestational diabetes caused by polycystic ovarian syndrome and shows early promise as an anticancer drug [6-7] and anti-aging [7]. Metformin HCl has a chemical name of 1,1-Dimethylbiguanide hydrochloride, a molecular formula of $C_4H_{11}N_5$•HCl, and a molecular weight of 165.62 g/mol [8]. Therefore, monitoring metformin plasma levels are critical for investigating the medication's pharmacokinetics/pharmacodynamics modeling, pharmacogenomics, and therapeutic drug monitoring to achieve a better clinical result for the patient.

Various chromatographic techniques are currently available for metformin HCl analysis in human plasma. A literature review conducted by Kaur et al. states that the High-Performance Liquid Chromatography (HPLC) method is a reasonably good method for analyzing plasma metformin levels compared to other methods such as High-Performance Thin-layer Chromatography (HPTLC), Hydrophilic Interaction Liquid Chromatography HILIC-MS/MS, Liquid Chromatography tandem mass spectrometric (LC-MS-MS), Ultra-High Performance Liquid Chromatography

(UPLC). It is because the HPLC method can separate and quantify metformin levels, has a fast analysis time, minimizes the use of organic solvents, and is affordable for clinical testing of metformin, as mentioned above. The study recommends developing HPLC methods to focus on developing new extraction methods, mobile phases, and adsorbent materials for HPLC separation [9]. LC-MS-MS has better sensitivity than HPLC-UV, but as long as the HPLC-UV method can determine metformin levels according to therapeutic concentrations, this method can still be used according to the objectives of the study [10-11]. However, LC-MS-MS is also not optimal for clinical applications due to the high cost and limited availability of the necessary equipment in clinical laboratories [12].

Several studies have used HPLC-UV to analyze metformin in dosage form and human plasma [12-17]. Because of the need to minimize disruptions while minimizing analyte loss, metformin extraction and purification from human plasma is sometimes the most challenging step in bioanalysis [12-15]. Organic liquid-liquid extraction is an easy, accurate, and effective way to prepare samples for most drugs. However, metformin's high polarity makes the extraction more difficult including its extraction from biological matrices that become more complicated [12-13], and several previous studies reported that this method produces a longer running time [13,18]. Therefore, protein precipitation has been the preferred sample preparation approach to address metformin extraction's difficulty. However, this method's time retention is too short, has poor recovery [19] and is ineffective in removing endogenous interferences [18-19].

Another problem that occurred in several previous studies was the use of a relatively narrow range of calibration curves [12,14,18], thus not covering the range of metformin plasma therapeutic levels of 0.4–5 μg/mL [20-21]. Based on these problems, the current study was conducted to modify the extraction method and mobile phase and adjust the calibration curve range to estimate metformin plasma levels in patients with diabetes mellitus so that it is expected to produce better validity parameter results, especially for metformin concentration needs in pharmacokinetic modeling studies. In addition, FDA guidelines state that full validation should be performed on developing new bioanalytical methods or revisions/modifications of existing bioanalytical methods [22].

This study aims to validate a simple and effective metformin plasma extraction technique for plasma concentration measurement by HPLC-UV. The method needs to be validated because there are modifications in the extraction method to get a better recovery test, modifications in the composition of the mobile phase to get a shorter running time, and ranitidine as an internal standard. The study reports on the accuracy, precision, linearity, sensitivity, Lower Limit of Quantification (LLOQ), carryover, selectivity, and stability in stock solutions, human plasma, three freeze-thaw cycles, and results of applying this method in preliminary population-based pharmacokinetic modeling using Monolix 2023R1 software.

■ EXPERIMENTAL SECTION

Materials

Metformin HCl and ranitidine HCl (the internal standard) were secondary reference standards sourced from the National Agency of Drug and Food Control of Indonesia. Acetonitrile and potassium dihydrogen phosphate (KH_2PO_4) were purchased from Merck, Germany. Sodium dodecyl sulfate (SDS) was purchased from Sigma-Aldrich, and sterile water for injection from Ikapharmindo (Indonesia). In addition, human plasma was taken from healthy volunteers who had signed an informed consent agreement. The Medical and Health Research Ethics Committee (MHREC), Faculty of Medicine, Public Health and Nursing, Universitas Gadjah Mada approved the study with the reference number: KE/FK/0217/E.C./2021 and conducted it following the Declaration of Helsinki. A preliminary population-based pharmacokinetic modeling study involved 17 patients with type 2 diabetes mellitus receiving 500 mg of metformin every 12 h as a monotherapy.

Instrumentation

Metformin HCl plasma concentration was measured using Shimadzu High-Performance Liquid Chromatography (HPLC) LC-10AD VP manual

injection with a U.V. detector system at 233 nm. The separation was performed on purosphere® Star RP-18 end-capped 250 mm 4.6 mm 5 μm from Merck Germany. The mobile phase was a phosphate buffer (70%) and acetonitrile (30%) mixture. The phosphate buffer consisted of 10 mM potassium dihydrogen phosphate (KH_2PO_4) and 0.3 mM sodium dodecyl sulfate (SDS) at pH 5.2. Analyses were run at a 1.2 mL/min flow rate, and injection volumes were 20 μL at room temperature column. The recorder system used is Shimadzu Class-VP version 6.1 software. A preliminary study of population-based pharmacokinetic modeling was conducted with Monolix 2023R1 software from Lixoft.

Procedure

The metformin assay method used in this study is a modification of several previously published methods developed by Amini et al. and Gabr et al. [12-13] with changes to the extraction method, composition, and procedure of preparation of the mobile phase and the concentration range of the calibration curve and quality control samples considering the therapeutic range of metformin in plasma in diabetes mellitus patients.

Plasma calibration standards and quality control samples

Metformin HCl and ranitidine HCl standard solutions were made by dissolving 10 mg of each reference standard in 10 mL of distilled water to yield a final concentration of 1000 μg/mL and storing them at −20 °C. Metformin HCl working solution was created by diluting aliquots of the standard solutions with distilled water to obtain final levels of 60, 40, 20, 10, 5, 2.5, and 1.8 μg/mL. These solutions were utilized to create plasma calibration standards in the 0.18 to 6.0 μg/mL linear calibration range. The lower limit of quantification (LLOQ), Quality Control Low (QCL), Quality Control Medium (QCM), and Quality Control High (QCH) plasma samples were produced with 0.18, 0.54, 3.0, and 4.5 μg/mL concentrations, respectively.

Extraction procedure

A volume of 500 μL of plasma containing metformin HCl was mixed with 50 μL ranitidine HCl and 1 mL acetonitrile in a test tube. A 2 min vortexing procedure was followed by a 10 min centrifugation step at 10,000 rpm. Then, the supernatant was taken and the second extraction process was performed for the remaining residue by adding 1 mL acetonitrile and conducting the same vortexing and centrifugation procedure. Finally, the supernatant from the first and second extractions were combined and evaporated with nitrogen (N_2). The resulting dry extract was reconstituted with 500 μL of phosphate buffer: acetonitrile (70:30) and vortexed for 3 min. It was then filtered using a 0.45 μm syringe filter, and 20 μL was administered into a previously equilibrated HPLC system.

Assay validation

Assessment for the validation of the analytical method refers to the guidelines from the US Food and Drug Administration (FDA) and European Medicines Agencies (EMA) [22-23]. The specificity was determined by comparing metformin and internal standard-containing samples' chromatograms to those of blank samples. In addition to the calibration standards curve, further tests were conducted to establish intra-day and inter-day assay precision and accuracy, selectivity, sensitivity, recovery, carryover, and stability. Besides the LLOQ concentration, which should be at most 20% of the coefficient of variation (CV) and percentage of difference (% diff), the acceptance criterion for the CV and % diff should be at most 15% [22-23].

Preliminary population-based pharmacokinetic modeling study

Seventeen patients with type 2 diabetes mellitus who received Metformin HCl 500 mg twice daily in 12 h intervals as monotherapy were subjected to periodic blood sampling. Metformin blood levels were determined at two sampling points for each patient. The first sampling of all subjects was carried out at pre-dose/just before taking metformin. The second collection was carried out randomly at one of the times chosen between the time ranges of 0.5, 1, 2, 3, 4, 6, 8, and 10 h post-dose [20,24]. Modeling population-based pharmacokinetic parameters was performed using the monolix 2023R1 software [25]. A volume of 500 μL of plasma samples were taken from patients, and extracted in the same methods described above.

RESULTS AND DISCUSSION

Method Development

The significant modification from the previous study [12-15,18-19,26] concerns the extraction method, composition, and preparation procedure of the mobile phase, as well as the concentration range of the calibration curve and quality control samples, taking into account the therapeutic range of metformin in the plasma of the patients with diabetes mellitus. Optimization of several alternative extraction methods was carried out in the preliminary study, including protein precipitation with trichloroacetic acid and acetonitrile. However, this method was less effective in removing the peaks of endogenous plasma compounds causing them to coincide with the peaks of metformin. Furthermore, liquid-liquid extraction was carried out with acetonitrile added with 100 µL NaOH 8 M to alkalinize the pH. However, the metformin peak results obtained were less symmetric. Finally, the extraction was conducted in a more straightforward method and by only using acetonitrile as the solvent without alkalizing the pH with NaOH and without adding acetic acid. In addition, we also performed evaporation with nitrogen gas to produce dry extracts to concentrate the concentration of analytes, because in bioanalytic studies, it is challenging to quantify small amounts of the drug in plasma with the tailing factor level still according to the recommendations.

A preliminary study was also conducted to optimize the mobile phase's performance. Initially, a combination of acetonitrile and sterile water for injection was used with various compositions. As a result, metformin appeared in a short retention time because it is a highly polar compound. However, in the early minutes, a peak of endogenous compounds will also appear in the plasma and can interfere with metformin peaks [19]. In modifying the mobile phase composition, phosphate buffer was used with SDS admixture. SDS is an anionic surfactant that can be a quasi-stationary phase that can delay the appearance of metformin peaks to a more optimal retention time [27]. SDS will form micelles above the critical micelle concentration, resulting in a pseudo-stationary phase that can partition components/analytes according to their partition coefficient [28]. The final mobile phase components were 70% phosphate buffer (KH_2PO_4) 10 mM, sodium dodecyl sulfate (0.3 mM), and 30% acetonitrile. Pure acetonitrile and its water (buffering) mixtures have unique chromatographic extraction characteristics and significant applications [29]. Fig. 2 shows an excellent peak symmetry, and both the analyte and internal standard were effectively separated at 4.8 and 6.7 min retention times with running time at 8 min. This result is better than previous references [12-15,19], which show a longer running time, thus less efficient. The resulting retention time was optimal, not too fast, so it did not coincide with endogenous plasma compounds. It was under 8 min, so it was efficient and suitable for laboratory and clinical pharmacokinetics services.

Method Validation

System suitability test

Table 1 demonstrates that the HPLC-UV system satisfies all suitability test parameters. Resolution and relative retention parameters indicate that plasma matrices containing metformin and ranitidine (internal standard) are well separated. The tailing factor (TR) level also meets the requirements to guarantee accuracy in quantifying the area of the metformin peak [30]. The column used also has good efficiency based on the value of the Plate Number (N) and HETP parameters [30].

Table 1. System suitability test

No.	Parameters	Acceptability criteria [30]	Metformin	Ranitidine [IS]
1.	Capacity factor (k')	> 2	3.94	5.83
2.	Resolution (Rs)	> 2	3.8	5.93
3.	Tailing factor (TF)	≤ 2	1.39	1.38
4.	Relative retention (α)	> 1	2	1.39
5	Plate number (N)	> 2000	2526.4	2125
6	Height Equivalent Theoretical Plate (HETP)	0.01–1	0.098	0.117

Selectivity

Six individual plasma samples were analyzed by chromatography to examine the possibility of endogenous compounds in plasma that could interfere with the appearance of metformin hydrochloride peaks and internal standards. As illustrated in Fig. 2(a), no endogenous plasma peak interfered with the elution of metformin or ranitidine. It is generally considered that there are no interfering components when the analyte's response is less than 20% of LLOQ and the internal standard is less than 5% [22]. The result shows no significant interfering components at the retention time of the analyte and internal standards of the blank matrix.

Lower limit of quantification [LLOQ]

LLOQ was the least amount at which repeatability was within 20% of CV, and the measured concentration was within 20% of the actual attention [22-23]. Determining the LLOQ value was conducted using the response method's standard deviation and the calibration curve's slope [31]. In this study, we decided on the LLOQ value at 0.18 μg/mL with the CV values being 6.542% and % diff of 0.905%, which is better than the previous study reported by Ningrum et al. [19]. The LLOQ value set at 0.18 μg/mL indicates that the method can meet the sensitivity requirements in the analysis of metformin because the range of metformin levels in plasma is 0.4–5 μg/mL [20,24].

Linearity

The standard calibration curve was drawn using seven spiking metformin plasma levels (0.18, 0.25, 0.5, 1, 2, 4, 6 μg/mL), including the LLOQ. The standard curve is based on the metformin level series (x) versus the chromatogram area ratio of the metformin to ranitidine (y). The correlation coefficient was 0.9998 with the linear regression equation y = 0.1595x + 0.0043. Fig. 1 displays the calibration curve from metformin spiked in human plasma. Several previous studies employed a calibration curve with a relatively limited range that did not correspond well with plasma metformin levels, particularly in the upper range (above 2 μg/mL) [12,14,18]. In addition, some studies had linearity with an R^2 value under 0.999 [14,18].

Accuracy and precision

Accuracy refers to the proximity of the obtained concentration value to the actual concentration of the analyte, expressed as a percentage difference (% diff). Precision refers to the similarity of repeated individual analyte measurements, denoted by the coefficient of variation (CV). The acceptance limits for % diff, and CV are 20% for LLOQ and 15% for QCL, QCM, and QCH [22-23]. Table 2 shows intra- and inter-day accuracy and precision data for measuring metformin in human plasma. For intraday accuracy and precision, the percent difference was less than 4%, and the coefficient of variation was less than 7%. The results were below 8 and 6% on day-to-day accuracy and precision. Fig. 2 shows

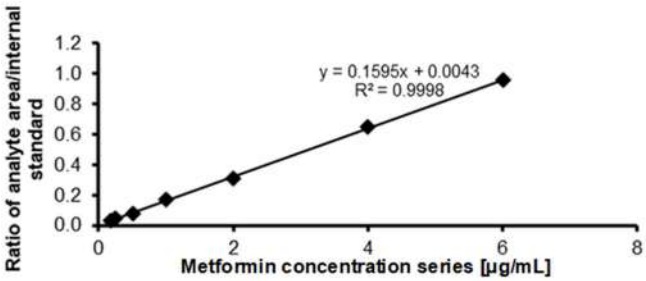

Fig 1. Spiked plasma metformin calibration curve

Table 2. The intra- and inter-day accuracy and precision plasma spiking metformin

	Intra-day (n = 5)		Inter-day (n = 5)			
			Day 2		Day 3	
Conc. (μg/mL)	Accuracy (% diff)	Precision (% CV)	Accuracy (% diff)	Precision (% CV)	Accuracy (% diff)	Precision (% CV)
0.18	0.905	6.542	2.663	1.301	-3.893	5.305
0.54	3.059	4.509	5.879	1.125	7.723	3.095
3	-3.295	3.295	-3.877	2.014	-0.397	1.782
4.5	0.415	2.008	-5.931	2.996	-0.622	2.264

The acceptance limits for % difference [% diff] and CV are below 20% for LLOQ and < 15% for QCL, QCM, and QCH [22-23]

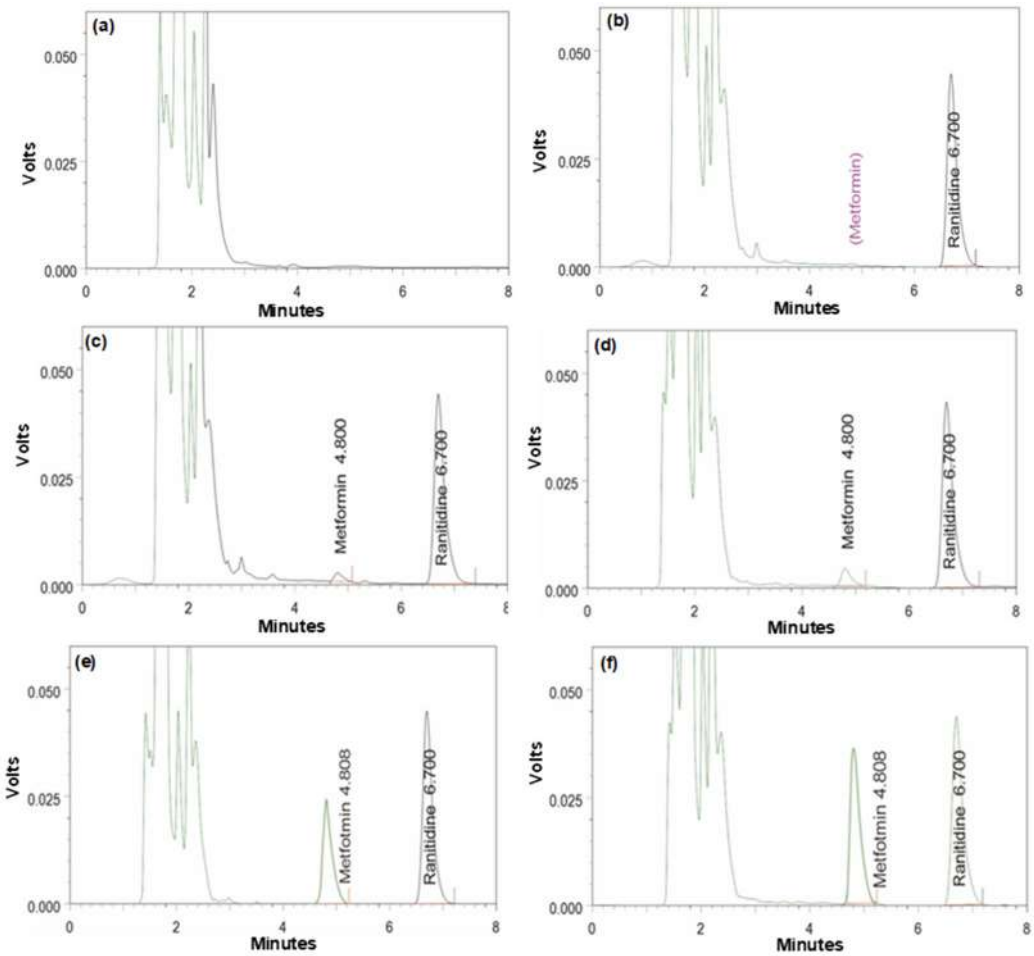

Fig 2. Chromatograms for a blank plasma sample (a), a zero sample (blank+internal standard 10 µg/mL) (b), spiking plasma metformin LLOQ sample (c), spiking plasma metformin QCL sample (d), spiking plasma metformin QCM sample (e) and spiking plasma metformin QCH sample (f). Zero, LLOQ, QCL, QCM, and QCH samples were spiked with the ranitidine 10 µg/mL as the internal standard

an example of a chromatogram peak from LLOQ, QCL, QCM, and QCH samples.

Recovery

Recovery is a term that relates to an analytical process's extraction efficiency, expressed as the ability to recover a predetermined amount of analyte from a sample after sample extraction and processing, and is measured in terms of recovery percentage. The acceptance limit for % recovery is 80–120% for LLOQ and 85–115% for QCL, QCM, and QCH [31]. Table 3 shows the average recovery of LLOQ, QCL, QCM, and QCH, which ranged from 96.159–104.905%. The relative recovery ranged between 92.749–99.352% (LLOQ), 102.327–109.778% (QCL), 95.357–102.524% (QCM), and 101.477–106.714% (QCH).

Table 3. Metformin plasma recovery

Conc. (µg/mL)	Mean recovery (n = 3)	SD	% CV
0.18	96.159	3.307	3.439
0.54	104.905	4.223	4.025
3	98.693	3.609	3.657
4.5	104.078	2.619	2.516

The acceptance limits for % difference [% diff] and CV are below 20% for LLOQ and < 15% for QCL, QCM, and QCH [22-23]

The result indicated that the extraction method produced a better recovery test than the previous study by Gabr et al., with complex liquid-liquid extraction (recovery ranging from 93.7–88.5%) [13], Ningrum et al., that used a simple protein precipitation method (recovery ranged

from 59.98–93%) [19], and Nielsen et al., that used a solid-phase extraction (recovery ranged 80–88%) [14].

Carryover

After injecting the high concentration standard, carryover should not exceed 20% of the LLOQ and should not exceed 5% for the internal standard [22-23]. Results show that the average metformin level after injecting blank samples after a high concentration (6 μg/mL) was 0.038 μg/mL (not greater than the LLOQ value of 0.18 μg/mL) and 0.051% for the internal standard (lower than 5%).

Stability

Every step in the sample preparation and analysis and the storage conditions employed should be examined to verify that the analyte concentration does not change. The stability tests that were carried out were stock solution storage stability (Table 4) and plasma storage stability (Table 5).

Stability in stock solution (short and long term). The stock solution was tested for stability for 24 h at ambient temperature and 30 d under freezing (−20 °C). Testing was conducted using QCL and QCH samples. Table 4 shows that the stock solution stability test was excellent, as demonstrated by the accuracy value (% diff) and precision (CV) being less than 15%. In conclusion, the metformin stock solution was steady at ambient temperature for 24 h and after 30 d under freezing (−20 °C).

Stability in human plasma

(i) **Short term stability.** Stability testing with QCL and QCH samples was conducted at 25 °C for baseline and after 24 h (Table 5). As a result, the concentration of metformin HCl in plasma remained constant for 24 h at room temperature because both CV and % diff was less than 15%.

(ii) **Long term stability.** Two QCL and QCH plasma samples were subjected to stability testing at −20 °C storage conditions for 0, 7, and 30 d. Table 5 informs that the accuracy value (% diff) was −11.324% (QCL) and −8.753% (QCH), and the precision (CV) was 0.853% (QCL) and 1.925% (QCH) after 30 d at −20 °C storage. Therefore, metformin plasma spiking was steady for 30 d at −20 °C.

(iii) **Freeze and thaw stability.** The effect of three freeze/thaw cycles on the plasma metformin concentrations of the QCL and QCH samples in duplicate was evaluated. Table 6 shows that after three freeze/thaw cycles, the accuracy value (% diff) was 0.535% (QCL) and 4.75% (QCH), respectively. The precision parameter (CV) was 1.89% (QCL) and 1% (QCH). The results show a good test for three freeze/thaw cycles from accuracy and precision parameters.

The stability test results on stock solutions and human plasma showed results that met the stability criteria, both under short-term and long-term (30 d) storage conditions. The stability criteria following FDA and EMEA guidelines were % diff and CV below 15% [22-23]. For the short-term stability test, storage at room temperature for 24 h was carried out to ensure that the metformin HCl stock solution and metformin HCl in human plasma were stable during the analysis. Meanwhile, the results of long-term stability testing both in stock solutions and human plasma showed long-lasting results in storage at −20 °C for 30 d. The method also offers sample stability after three freeze-thaw cycles.

Table 4. Short and long-term stock solution stability

Conc. (μg/mL)	After 24 h at room temperature (n = 3)		After 30 d at −20 °C (n = 3)	
	% diff	% CV	% diff	% CV
0.54	-1.486	4.118	-4.086	9.391
4.5	-4.246	0.672	-1.163	2.712

Note: acceptance criteria limit % diff and CV are below 15% [22-23]

Table 5. Stability of metformin in human plasma

Conc. (μg/mL)	Room temperature				In −20 °C					
	Baseline		After 24 h		After 24 h		After 7 d		After 30 d	
	% diff	% CV	% diff	% CV	% diff	% CV	% diff	% CV	% diff	% CV
0.54	0.616	2.201	-4.946	6.505	-5.883	0.760	-8.416	0.971	-11.324	0.853
4.5	0.24	0.415	-1.482	0.606	1.222	0.600	1.020	0.312	-8.753	1.925

Note: acceptance criteria limit % diff and CV are below 15% [22-23]

Table 6. Freeze/thaw stability test

Conc. (μg/mL)	After three freeze/thaw cycles (n = 3)	
	% diff	% CV
0.54	-0.79	1.896
4.5	5.53	1

Note: acceptance criteria limit % diff and CV are below 15% [22-23]

Application in Preliminary Population-Based Pharmacokinetic Modeling Study

Metformin concentrations in human plasma samples were collected from 17 type two diabetes mellitus patients who received metformin HCl 500 mg twice daily in 12 h intervals as monotherapy. Fig. 3 shows the chromatogram profile of metformin in the patient's plasma, which looks similar to the chromatogram profile during the method validation test. Preliminary population-based pharmacokinetic modeling studies were done using Monolix 2023R1 software. Fig. 4 shows the profile of the level-versus-time curve of 17 patients based on a population. Plasma sampling was conducted

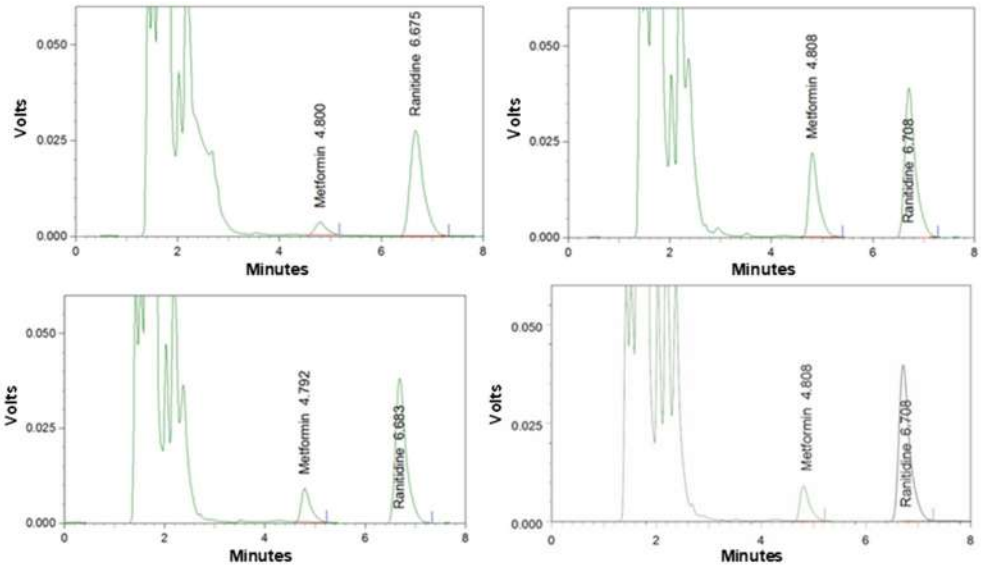

Fig 3. Representative chromatograms from diabetes mellitus patients receiving metformin 500 mg twice daily with spiking internal standard 10 μg/mL

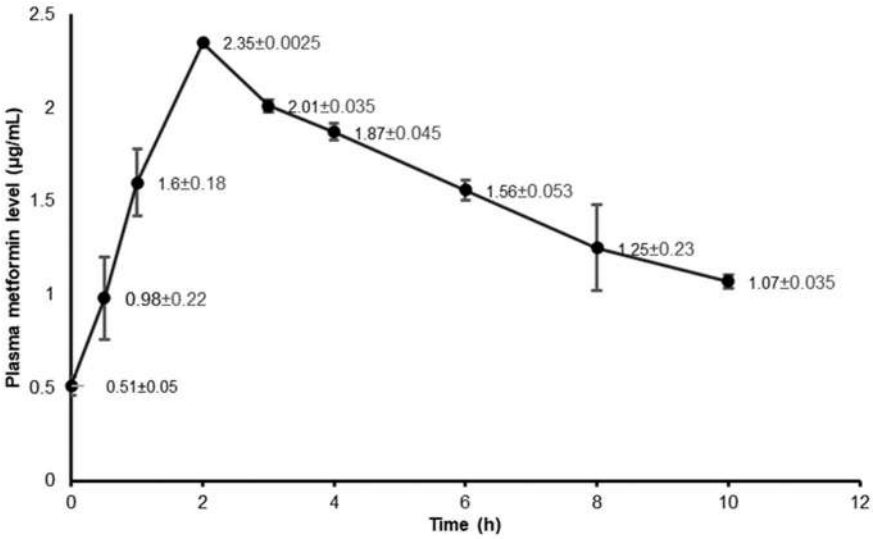

Fig 4. Population-based plasma metformin levels (± error standard) vs. time from 17 diabetes mellitus patients receiving metformin 500 mg twice daily

Table 7. Population-based pharmacokinetics parameters from 17 types two diabetes mellitus 500 mg twice daily

Parameters	Value	SE	RSE (%)
ka_pop (h^{-1})	0.751	0.147	19.648
V_pop (L)	209.567	14.049	6.704
k_pop (h^{-1})	0.165	0.0138	8.387
C_{max}_pop* (μg/mL)	2.35	0.0025	0.106
C_{min}_pop* (μg/mL)	0.51	0.05	9.8

SE: Standard error
RSE: relative standard error
ka_pop: absorption rate constant from the population
V_pop: apparent volume of drug distribution in the body from the population
k_pop: elimination rate constant from the population
C_{max}: maximum plasma drug concentration from the population
C_{min}: minimum plasma drug concentration from the population
*: values based on population-based metformin plasma level curve profiles versus time created by Monolix 2023R1 (Fig. 4)

twice as blood sampling from each patient will be combined in 1 observation data curve. The curves of plasma metformin level versus time indicate ideal pharmacokinetic phases, namely the absorption, peak, and elimination phases. Table 7 informs the value of population pharmacokinetic parameters from the Monolix 2023R1 software processing results using the pharmacokinetics structural model. The pharmacokinetic structural model equation used is as follows: Cc =Cc0 + (ka*amtDose/(V*(ka-k))*(exp(-k*t)-exp(-ka*t))) with the PK model definition; Cc = pkmodel(ka, V, k).

Curves of metformin plasma level versus time and population parameter values from an initial population-based pharmacokinetic study exhibited encouraging results. In addition, it demonstrates that the method can be utilized in a population-based pharmacokinetic study.

CONCLUSION

The method performed in the current study meets the requirements for selectivity, sensitivity, linearity, accuracy, precision, recovery, carryover, and stability requirements based on EMA and FDA guidelines. The modifications in the extraction method obtained a better recovery test and the composition of the mobile phase obtained a shorter running time. A preliminary population-based pharmacokinetic study showed promising results from the curve of metformin plasma levels versus time and population parameter values. Furthermore, it shows that this method can be applied in a population-based pharmacokinetic study in diabetes mellitus patients who receive metformin 500 mg every 12 h as monotherapy.

ACKNOWLEDGMENTS

The researchers would like to extend their appreciation to the Directorate of Research and Community Service at the Universitas Islam Indonesia for financing the research in the form of the Basic Research Grant (Grant number 004/Dir/DPPM/70/Pen.Unggulan/XII/2020) and the Pharmacology and Therapy Laboratory, Faculty of Medicine, Public Health and Nursing, Universitas Gadjah Mada, for supporting the facilities in this research.

AUTHOR CONTRIBUTIONS

Dimas Adhi Pradana: Methodology, Investigation, Resources, Data Curation, Writing (original draft). Erna Kristin: Conceptualization, Methodology, Writing (review and editing). Akhmad Kharis Nugroho: Conceptualization, Methodology, Writing (review and editing). Dwi Aris Agung Nugrahaningsih: writing (review and editing). Mustofa: Conceptualization, Methodology, Writing (review and editing). Ari Wibowo: Methodology, Writing (review and editing).

REFERENCES

[1] Shurrab, N.T., and Arafa, E.S.A., 2020, Metformin: A review of its therapeutic efficacy and adverse effects, *Obes. Med.*, 17, 100186.
[2] Sanchez-Rangel, E., and Inzucchi, S.E., 2017, Metformin: Clinical use in type 2 diabetes, *Diabetologia*, 60 (9), 1586–1593.
[3] Hostalek, U., Gwilt, M., and Hildemann, S., 2015, Therapeutic use of metformin in prediabetes and diabetes prevention, *Drugs*, 75 (10), 1071–1094.
[4] Flory, J., and Lipska, K., 2019, Metfonim in 2019, *JAMA*, 321 (19), 1926–1927.
[5] Indonesian Association of Endocrinologists (Perkeni), 2019, *Consensus on Type-2 Diabetes Mellitus Control and Prevention*, Jakarta, Indonesia.

[6] Johnson, N.P., 2014, Metformin use in women with polycystic ovary syndrome, *Ann. Transl. Med.*, 2 (6), 56.

[7] Podhorecka, M., Ibanez, B., and Dmoszyńska, A., 2017, Metformin - Its potential anti-cancer and anti-aging effects, *Postepy Hig. Med. Dosw.*, 71, 170–175.

[8] Center for Drug Evaluation and Research, 2013, *Chemistry review(s): ActoPlus MET™ XR (pioglitazone HCl/metformin HCl extended release) Tablets*, Application Number 22-024, Lincolnshire, UK.

[9] Kaur, G., Garg, S., Sharma, P., and Sud, D., 2021, A review on high-performance liquid chromatographic methods for the determination of metformin, *Curr. Anal. Chem.*, 17 (6), 754–767.

[10] Fachi, M.M., Leonart, L.P., Cerqueira, L.B., Pontes, F.L.D., de Campos, M.L., and Pontarolo, R., 2017, A systematic and critical review on bioanalytical method validation using the example of simultaneous quantitation of antidiabetic agents in blood, *J. Chromatogr. B*, 1055-1056, 61–71.

[11] Mohamed, D., Elshahed, M.S., Nasr, T., Aboutaleb, N., and Zakaria, O., 2019, Novel LC-MS/MS method for analysis of metformin and canagliflozin in human plasma: Application to a pharmacokinetic study, *BMC Chem.*, 13 (1), 82.

[12] Amini, H., Ahmadiani, A., and Gazerani, P., 2005, Determination of metformin in human plasma by high-performance liquid chromatography, *J. Chromatogr. B*, 824 (1-2), 319–322.

[13] Gabr, R.Q., Padwal, R.S., and Brocks, D.R., 2010, Determination of metformin in human plasma and urine by high-performance liquid chromatography using small sample volume and conventional octadecyl silane column, *J. Pharm. Pharm. Sci.*, 13 (4), 486–494.

[14] Nielsen, F., Christensen, M.M.H., and Brøsen, K., 2014, Quantitation of metformin in human plasma and urine by hydrophilic interaction liquid chromatography and application to a pharmacokinetic study, *Ther. Drug Monit.*, 36 (2), 211–217.

[15] Abdessadek, M., Tadmori, A.E., El-Attari, A., Diarra, M., Magoul, R., Ajdi, F., El-Ouezzani, S., and Khabbal, Y., 2015, Simple HPLC-UV method for determination of metformin in human plasma and erythrocytes application to therapeutic drug monitoring, *Int. J. Pharm. Pharm. Sci.*, 7 (11), 35–39.

[16] Nikam, N., Maru, A., Jadhav, A., and Malpure, P., 2019, Analytical method development and validation of metformin hydrochloride by using RP-HPLC with ICH guidelines, *Int. J. Trend Sci. Res. Dev.*, 3 (3), 415–419.

[17] Gedawy, A., Al-Salami, H., and Dass, C.R., 2019, Development and validation of a new analytical HPLC method for simultaneous determination of the antidiabetic drugs, metformin and gliclazide, *J. Food Drug Anal.*, 27 (1), 315–322.

[18] Chhetri, H.P., Thapa, P., and Van Schepdael, A., 2014, Simple HPLC-UV method for the quantification of metformin in human plasma with one step protein precipitation, *Saudi Pharm. J.*, 22 (5), 483–487.

[19] Ningrum, V.D.A., Wibowo, A., Fuaida, I., Ikawati, Z., Sadewa, A.H., and Ikhsan, M.R., 2018, Validation of an HPLC-UV method for the determination of metformin hydrochloride in spiked-human plasma for the application of therapeutic drug monitoring, *Res. J. Pharm. Technol.*, 11 (6), 2197–2202.

[20] Li, L., Guan, Z., Li, R., Zhao, W., Hao, G., Yan, Y., Xu, Y., Liao, L., Wang, H., Gao, L., Wu, K., Gao, Y., Li, Y., 2020, Population pharmacokinetics and dosing optimization of metformin in Chinese patients with type 2 diabetes mellitus, *Medicine*, 99 (46), e23212

[21] Kajbaf, F., De Broe, M.E., and Lalau, J.D., 2016, Therapeutic concentrations of metformin: A systematic review, *Clin. Pharmacokinet.*, 55 (4), 439–59.

[22] U.S. Department of Health and Human Services Food and Drug Administration, Center for Drug Evaluation and Research (CDER), and Center for Veterinary Medicine (CVM), 2018, *Bioanalytical Method Validation: Guidance for Industry*, Silver Spring, Maryland, USA.

[23] Committee for Medicinal Products for Human Use, 2022, *ICH Guideline M10 on Bioanalytical Method Validation*, European Medicines Agency, Amsterdam, Netherlands.

[24] U.S. Department of Health and Human Services Food and Drug Administration, Center for Drug Evaluation and Research (CDER), and Center for Veterinary Medicine (CVM), 2022, *Population Pharmacokinetics: Guidance for Industry*, Silver Spring, Maryland, USA.

[25] Traynard, P., Ayral, G., Twarogowska, M., and Chauvin, J., 2020, Efficient pharmacokinetic modeling workflow with the MonolixSuite: A case study of remifentanil, *CPT: Pharmacometrics Syst. Pharmacol.*, 9 (4), 198–210.

[26] Harahap, Y., Dianpratami, K., Wulandari, M., and Rahmawati, R., 2012, Validation of metformin hydrochloride in human plasma by HPLC-photo diode array (PDA) for application of bioequivalence Study, *J. Life Sci.*, 6, 20–27.

[27] Niraula, T.P., Bhattarai, A., and Chatterjee, S.K., 2014, Sodium dodecyl sulphate: A very useful surfactant for scientific investigations, *J. Knowl. Innovation*, 2 (1), 111–113.

[28] Patyra, E., and Kwiatek, K., 2021, Application of micellar mobile phase for quantification of sulfonamides in medicated feeds by HPLC-DAD, *Molecules*, 26 (13) 3791.

[29] Rudakov, O.B., Rudakova, L.V., and Selemenev, V.F., 2018, Acetonitrile as tops solvent for liquid chromatography and extraction, *J. Anal. Chromatogr. Spectrosc.*, 1, 883.

[30] Center for Drug Evaluation and Research (CDER), 1994, *Reviewer Guidance: Validation of Chromatographic Methods*, Rockville, Maryland, USA.

[31] International Council for Harmonisation, 2022, *ICH Guideline Q2(R2) on Validation of Analytical Procedures*, European Medicines Agency, Amsterdam, Netherlands.

Identification of Volatile Compounds of Oil Palm Flower (*Elaeis guineensis* Jacq.) with Gas Chromatography and Mass Spectrometry Based on the Difference in Time

Fizrul Indra Lubis[1,2], Sudarjat Sudarjat[3], Ichsan Nurul Bari[3], and Unang Supratman[4*]

[1]*Agricultural Science, Faculty of Agriculture, Universitas Padjadjaran, Jl. Raya Bandung-Sumedang Km. 21, Jatinangor, Sumedang 45363, Indonesia*

[2]*Sulung Research Station, PT Sawit Sumbermas Sarana Tbk. Citra Borneo Indah Group, Jl. H. Udan Said No. 47, Pangkalan Bun 74113, Indonesia*

[3]*Department of Plant Pests and Diseases, Faculty of Agriculture, Universitas Padjadjaran, Jl. Raya Bandung-Sumedang Km. 21, Jatinangor, Sumedang 45363, Indonesia*

[4]*Department of Chemistry, Faculty of Mathematics and Natural Sciences, Universitas Padjadjaran, Jl. Raya Bandung-Sumedang Km. 21, Jatinangor, Sumedang 45363, Indonesia*

**** Corresponding author:***

email: unang.supratman@unpad.ac.id

Received: October 27, 2022
Accepted: June 13, 2023

DOI: 10.22146/ijc.78682

Abstract: *The pollination process in oil palm is assisted by the insect* Elaeidobius kamerunicus*, which occurs when male and female flowers bloom producing volatile compounds that act as attractants. This study aims to identify volatile compounds in oil palm flowers based on differences in times with gas chromatography mass spectrometry (GC-MS). The research steps include determining the time of the release of volatile compounds in oil palm flowers, extracted using steam distillation, and identification by GC-MS. There are different times of the release of volatile compounds for each type of oil palm flower. Three times by male flowers, at 08:00 am, 11:00 am and 14:00 pm, with the highest volatile compounds at 14:00 pm. Meanwhile, female flowers occurred at 09:00 am, 12:00 am and 15:00 pm, with the highest volatile compounds at 12:00 am. The results of the GC-MS analysis showed that 21 and 19 volatile compounds were identified, with a total of 38 different types. Estragole compounds were dominant in both types of flowers and did not show significant differences in the area sum values at each time of observation. These results indicated the importance of estragole compound for the pollination process in oil palm.*

Keywords: Elaeis guineensis Jacq.*; estragole; palm oil; volatile compounds*

INTRODUCTION

Oil palm (*Elaeis guineensis* Jacq.) is one of the plantation commodities that has an important role in economic development and is a source of foreign exchange for the country. The productivity and land area of oil palm continues to increase every year, from 22.5 million and 4.5 million tons in 2010 to 44.8 million and 8.9 million tons in 2020 [1]. The development of oil palm area and productivity in Indonesia is influenced by several factors, one of which is the role of the oil palm pollinating insect (SPKS) *Elaeidobius kamerunicus* Faust which was introduced in March 1983. In general, there was an increase in pollination efficiency, so the fruit set value increased from 11.27 to 75.56%, and there was an increase in other production components such as bunch weight and crude palm oil per Ha [2].

The pollination process by *E. kamerunicus* occurs when male and female flowers bloom, producing volatile compounds that act as attractants. Several studies reported that the volatile compound that acts as an attractant for *E. kamerunicus* is estragole [3-5]. Estragole is an allylphenol derivative compound formed through the shikimate (phenylpropanoid) pathway. In addition to estragole, it is suspected that there are other volatile

compounds that act as attractants. Anggraeni et al. [3] analyzed the volatile compounds of male oil palm flowers at the 100% flowering stage. The results showed that there were compounds of palmitic acid, 4-tetradecyl chloroacetate, estragole, and 1-dodecyne. Meanwhile, female flowers contain 4-tetradecyl chloroacetate, palmitic acid, farnesol, and squalene compounds. Muhamad Fahmi et al. [4] identified volatile compounds from oil palm flowers on different soil types. There were 10 compounds identified, estragole was found to be the main compound in sandy soil (37.49%), clay (30.71%), and peat soil (27.79%). Other compounds such as 9,12-octadecadionic acid and *n*-hexadecanoic acid were found as the main compounds in peat (27.18% and 7.45%), sandy soil (14.15% and 9.31%); and clay (30.23% and 4.99%). The interaction between oil palm and *E. kamerunicus* benefits both plants and pollinating insects, *E. kamerunicus* gets food from male flowers and then carries pollen to female flowers [6]. Based on Anggraeni et al. [3], *E. kamerunicus* is active foraging during the day and peaks at 10:00–11:00 am. Until now, there has been no research that has identified the volatile compound content of oil palm flowers at different times, in the morning, afternoon and evening. GC-MS is a powerful instrument for identifying volatile compounds from plants [7-9]. This study aims to identify the content of volatile compounds in male and female flowers of oil palm based on differences in that time with the GC-MS.

■ EXPERIMENTAL SECTION

Materials

The palm flower was collected from the collecting observational data, and research samples were Batu Kotam (111°30'6.1"E2°18'39.9"S) and Rangda area (111°36'59.7664"E 2°18'47.7493"S) in West Kotawaringin, Central Kalimantan, Indonesia. The oil palm flower extraction process was carried out at the Sulung Research Station Laboratory, Central Kalimantan. Analysis of volatile compounds was carried out at the Central Laboratory, Universitas Padjadjaran, Jatinangor, West Java, Indonesia. The materials used were anthesis (≥ 75%), female receptive oil palm flowers (≥ 75%), distilled water, 4-allylanisole (98%, Sigma-Aldrich), *trans*-anethole (99%, Sigma-Aldrich), anisole (99%, Merck), methyl eugenol (98%, Sigma-Aldrich), ethyl oleate (90%, Sigma-Aldrich), and dichloromethane (99.8%, Merck).

Instrumentation

Tiger Select Portable VOC Detector (ION Science Ltd.) was performed to analyze volatile compounds in palm flowers and gas chromatography-mass spectrometry (GC-MS) type Agilent 7 890 A was carried out to investigate volatile compounds from extract from steam distillation.

Procedure

This research process goes through several stages. The first stage was observing oil palm flowers in the field to determine the time of the release of volatile compounds. The second step is to extract volatile compounds from oil palm flowers by using a steam distillation technique. The last stage is the identification of the types of volatile compounds by using GC-MS.

Determination of release of volatile compounds

Detection of the level and time of the release of volatile compounds was carried out by using a portable VOC detector on 10 samples of male and female oil palm flowers with blooming criteria ≥ 75%. Portable VOC detectors are used for specific applications for spot-checking and measuring for such a volatile or gas compound. Observations were made on three sample points with an interval of 60 min from 07:00 am–17:00 pm [3].

Extraction of volatile compounds from oil palm flowers

The volatile compounds of oil palm flowers were obtained by using a steam distillation apparatus [7]. Determination of the timing of flower sampling based on the pattern of the release of the highest volatile compounds from the detection results in the field. Distillation materials to obtain volatile compounds were 1 kg of male and female flowers and 4 L of distilled water [10]. The distillation process was carried out for 4 h [7] at room temperature (± 25 °C) and chiller temperature (below 20 °C) [11-12].

Identification of volatile compounds using GC-MS

The results of the distillation were then analyzed using GC-MS to determine the composition of volatile compounds in oil palm flowers [10]. Analysis of the composition of volatile compounds begins with the preparation of the distillate, which is taken as much as 1 mL and injected into the GC-MS with a split ratio of 1:50 using the hot-needle technique. Several dilution experiments were carried out on the sample to be injected so that the compound with the smallest percentage could be read. The temperature of the injection area and the transfer line used at the interface set is 325 °C, with the ion source adjusted to a temperature of 200 °C. The carrier gas used is helium (He 99.99%), with a constant flow rate of 1 mL/min. The initial oven temperature was at 50 °C for 2 min, after which it was raised to 200 °C at 10 °C/min, which was then equilibrated for 3 min, before the next sample injection. The mass spectrum was recorded at one scan per second with a mass detection range of *m/z* 40–470 amu. Chromatograms and mass spectra were evaluated using GC/MSD 5977B with a limit of fit 80%. Data acquisition and processing were carried out using the NIST 17 mass spectral library. The concentration of the studied compound was calculated from the peak area in the total ion chromatogram. The relative abundance was obtained from the electronic integration of the measurements and the average results of three replicates [13].

■ RESULTS AND DISCUSSION

Time Pattern for the Release of Volatile Compounds in Palm Flower

Determination of the time pattern for the release of volatile compounds emitted by male and female flowers of oil palm at 07:00 am to 17:00 pm using the VOC detector showed differences for each type of oil palm flower (Fig. 1). There are three times for the release of volatile compounds by male flowers, namely at 08:00 am, 11:00 am, and 14:00 pm, with the highest release at 14:00 pm. Meanwhile, the three times for the release of volatile compounds in female flowers occurred at 09:00 am, 12:00 am and 15:00 pm. The peak of the release of the highest volatile compounds occurred at 12:00 am. This will be marked by a stronger floral aroma when in the field. The release of volatile compounds in male flowers was higher than that of female flowers, seen at the peak of the release of volatile compounds by male flowers of 0.610 ppm, while in female flowers, it was 0.056 ppm.

Identification of Volatile Compounds in Male Palm Flowers by GC-MS Based on the Time

The results of volatile compounds based on the time of the release of volatile compounds in male flowers were identified using GC-MS. The results of the GC-MS analysis identified 13 compound peaks at 8:00 am (Fig. 2), 7 compound peaks at 11:00 am (Fig. 3) and 14 compound peaks at 14:00 pm (Fig. 4). Based on the detected peaks,

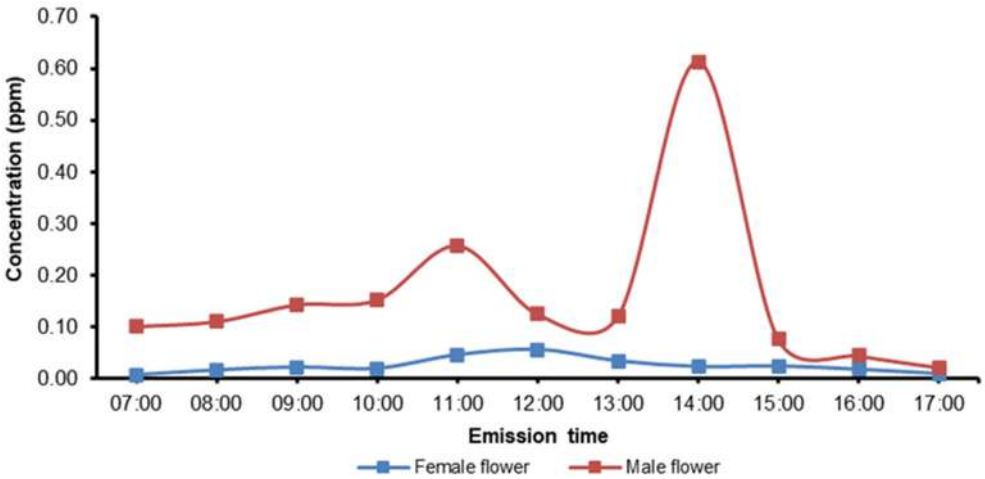

Fig 1. Time pattern for the release of volatile compounds from oil palm flowers

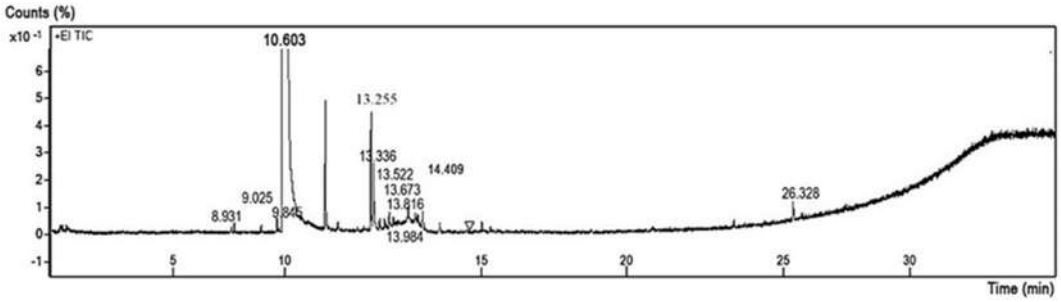

Fig 2. Chromatogram of male flowers at 08:00 am

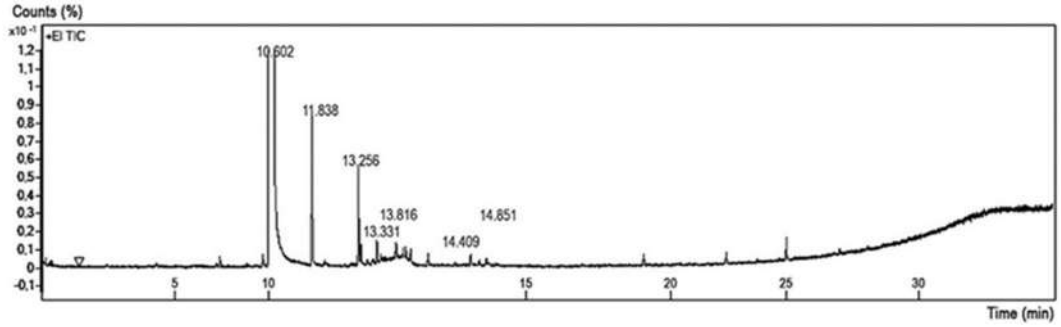

Fig 3. Chromatogram of male flowers at 11:00 am

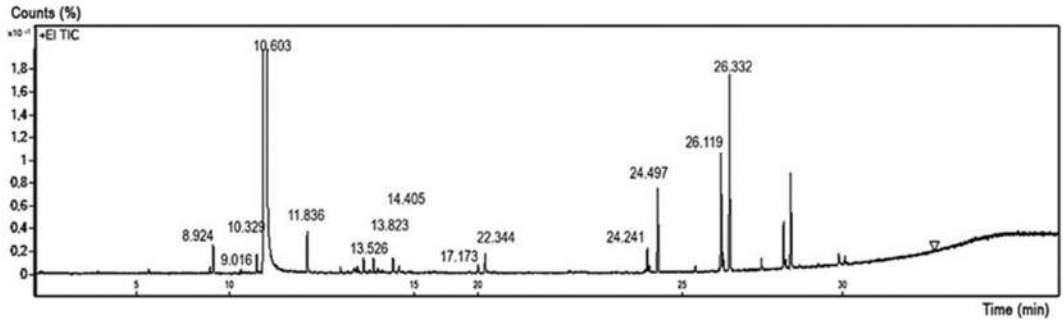

Fig 4. Chromatogram of male flowers at 14:00 pm

the dominant volatile compound in oil palm flowers for all observation times was estragole.

Identification of GC-MS on the sample at 8:00 am obtained the highest peak compound with a retention time (RT) of 10.603 min and a sum area of 99.66, which is suspected to be estragole (Fig. 2). In addition, other peaks were identified, these compounds were 2-propenamide, nonanal, 1-ethenyl-4-methoxybenzene, anethole, 1-ethenyl-1-methyl-2,4-bis(1-methylethenyl)cyclohexane, methyl eugenol, germacrene D, 3-methyl-6-(1-methyl ethylidene)cyclohexene, γ-elemene, α-farnesene, 1-(2-Acetoxyethyl)-1-(4-methylpent-4-enyl)-2-(1-methyl ethenyl)cyclobutane, and hexamethylcyclotrisiloxane (Table 1).

The dominant estragole compound was identified at 11:00 am with RT 10.602 min and area sum 99.65 (Fig. 3). Six other compounds identified were anethole, 1-ethenyl-1-methyl-2,4-bis(1-methylethenyl)cyclohexane, methyl eugenol, 4-(2,6,6-trimethyl-1-cyclohexen-1-yl)-2-butanone, 1-ethenyl-1-methyl-2,4-bis(1-methylethenyl) cyclohexane, and 1,5-dimethyl-8-(1-methylethenyl)-1,5-cyclodecadiene (Table 2). There are 14 peaks at 14:00 am, with the highest peak at RT 10.603 min and a sum area of 98.33 which is suspected to be estragole compound (Fig. 4). Meanwhile, other peaks are linalool, nonanal, 1-methoxyadamantane, (1*S*,2*E*,6*E*,10*R*)-3,7,11,11-tetramethylbicyclo[8.1.0]-undeca-2,6-diene, 2-butanone, 4-(2,6,6-trimethyl-1-cyclohexen-1-yl),

Table 1. List of volatile compounds of male flowers samples at 08:00 am

Peak	Compound	Start	RT (min)	End	Height	Area	Area sum	%Area
1	2-Propenamide	8860	8.931	8952	963	1851	0	0.00
2	Nonanal	8976	9.025	9057	1833	3201	1	0.01
3	1-Ethenyl-4-methoxybenzene	9826	9.845	9899	1295	2063	1	0.01
4	Estragole	10450	10.603	11066	4730275	39799003	10000	99.66
5	Anethole	11800	11.840	11888	22181	35322	9	0.09
6	1-Ethenyl-1-methyl-2,4-bis(1-methylethenyl)cyclohexane	13220	13.255	13298	20171	30331	8	0.08
7	Methyl eugenol	13304	13.336	13390	10844	18611	5	0.05
8	Germacrene D	13482	13.522	13565	1893	3928	1	0.01
9	3-Methyl-6-(1-methylethylidene)cyclohexene	13649	13.673	13705	1849	3080	1	0.01
10	γ-Elemene	13792	13.816	13870	2725	5612	1	0.01
11	α-Farnesene	13924	13.948	13983	1644	3558	1	0.01
12	1-(2-Acetoxyethyl)-1-(4-methylpent-4-enyl)-2-(1-methylethenyl)cyclobutane	14358	14.409	14436	2707	5769	1	0.01
13	Hexamethylcyclotrisiloxane	26293	26.328	26371	3452	6965	2	0.02

Table 2. List of volatile compounds of male flowers samples at 11:00 am

Peak	Compounds	Start	RT (min)	End	Height	Area	Area sum	%Area
1	Estragole	10458	10.602	11125	4710964	37728112	10000	99.65
2	Anethole	11806	11.838	11890	39044	63305	17	0.17
3	1-Ethenyl-1-methyl-2,4-bis(1-methylethenyl)cyclohexane	13226	13.256	13288	24758	36233	10	0.10
4	Methyl eugenol	13313	13.331	13361	4119	5843	2	0.02
5	4-(2,6,6-Trimethyl-1-cyclohexen-1-yl)-2-butanone	13792	13.816	13876	5811	10247	3	0.03
6	1-Ethenyl-1-methyl-2,4-bis(1-methylethenyl) cyclohexane	14339	14.409	14474	3911	8957	2	0.02
7	1,5-Dimethyl-8-(1-methylethenyl)-1,5-cyclodecadiene	14824	14.851	14902	3489	6125	2	0.02

trans-β-Ionone, pentadecanal, nonadecane, 1-docosene, nonadecane, and 5-eicosene (Table 3).

The interpretation of the main peak of the mass spectrum in the male flower sample at 8.00 am was obtained at a retention time of 10.603 min. The mass spectrum of the compound at the main peak *m/z* = 148, the molecular ion is thought to have fragmented with the release of ($C_2H_3^{\bullet}$), yielding (M-27) at *m/z* = 146. The peak at *m/z* = 77 probably appears due to the loss of the group ($CH_3O^{\bullet}$) produce (M-31). The compound is thought to be estragole (Fig. 5).

Meanwhile, the chromatogram peak in male flower samples at 11.00 am with a retention time of 10.602 min was a compound with the molecular formula $C_{10}H_{12}O$. The mass spectrum showed that the molecular mass of the compound was 148 and showed a molecular ion peak at *m/z* 148 followed by fragments at *m/z* 148, 121, 77, 65, and 51 (Fig. 6). The peak of the chromatogram on male flower samples at 14:00 pm obtained a retention time of 10.603 min is suspected to be estragole compounds. The mass spectrum showed molecular ion peaks at *m/z* 148 with fragments at *m/z* 148, 121, 77, and 51 (Fig. 7).

Identification of GC-MS Volatile Compounds Based on Time of the Release of Female Palm Flowers

The results of the samples that have been isolated by steam distillation technique are separated between the oil and water phases, then identified using GC-MS to determine the content of volatile compounds. The results of GC-MS showed that 10 compound peaks were identified in the female flower sample at 9:00 am (Fig. 8), 14 compound peaks at 12:00 am (Fig. 9) and 9 compound peaks at 15:00 pm (Fig. 10).

Table 3. List of volatile compounds of male flowers samples at 14:00 pm

Peak	Compounds	Start	RT (min)	End	Height	Area	Area sum	%Area
1	Linalool	8898	8.924	8957	2266	3720	1	0.01
2	Nonanal	8981	9.016	9054	11440	17638	6	0.06
3	1-Methoxyadamantane	10297	10.329	10370	7462	14154	5	0.05
4	Estragole	10465	10.603	10874	4731972	27998331	10000	98.33
5	Estragole	11806	11.836	11887	16406	27216	10	0.10
6	(1*S*,2*E*,6*E*,10*R*)-3,7,11,11-Tetramethylbicyclo[8.1.0]undeca-2,6-diene)	13489	13.526	13575	5832	10301	4	0.04
7	4-(2,6,6-Trimethyl-1-cyclohexen-1-yl)-2-butanone	13772	13.823	13869	5902	9793	3	0.03
8	*trans*-β-Ionone	14351	14.405	14448	6037	11085	4	0.04
9	Pentadecanal	17117	17.173	17214	7956	13300	5	0.05
10	Nonadecane	22301	22.344	22389	34569	61392	22	0.22
11	1-Docosene	24195	24.241	24276	47492	77535	28	0.27
12	Nonadecane	24467	24.497	24553	80103	139741	50	0.49
13	5-Eicosene	26092	26.119	26143	17311	24950	9	0.09
14	Nonadecane	26299	26.332	26369	38549	63429	23	0.22

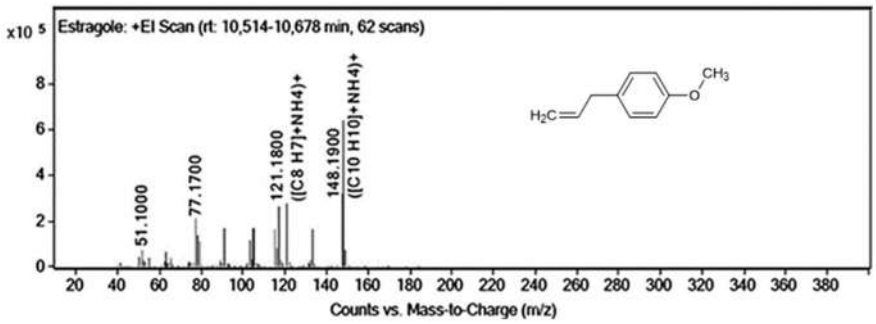

Fig 5. Mass spectrum and structure of estragole in male flower samples at 08:00 am

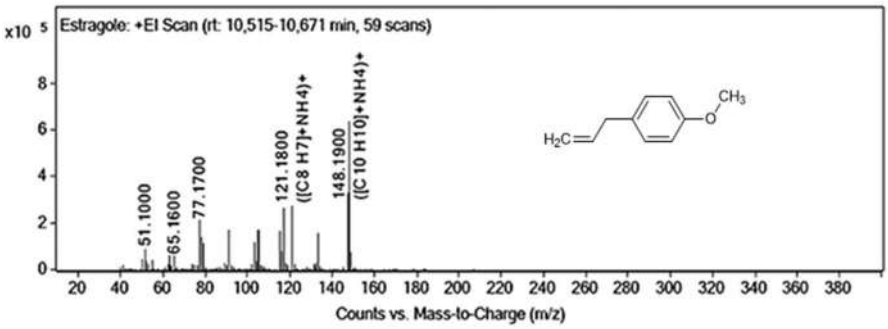

Fig 6. Mass spectrum and structure of estragole in male flowers samples at 11:00 am

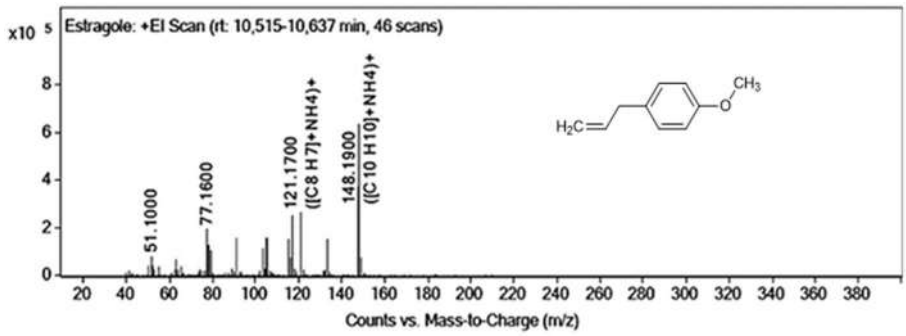

Fig 7. Mass spectrum and structure of estragole in male flowers samples at 14:00 pm

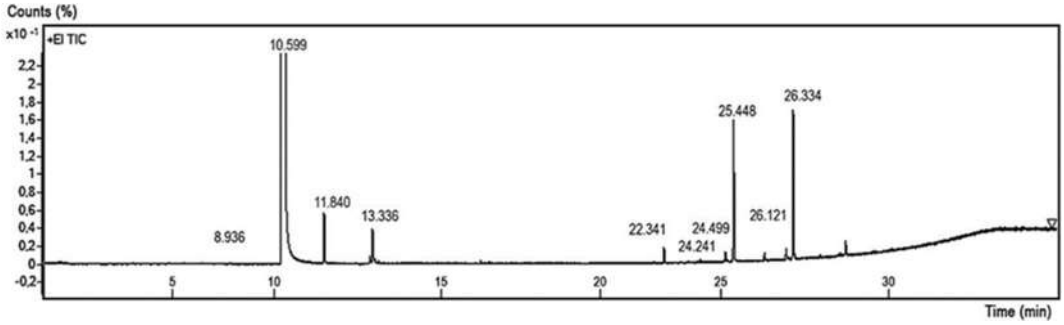

Fig 8. Chromatogram of female flowers at 09:00 am

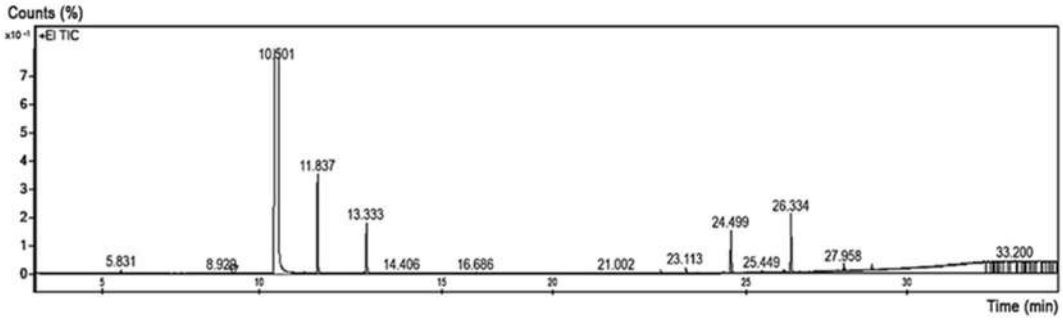

Fig 9. Chromatogram of female flowers at 12:00 am

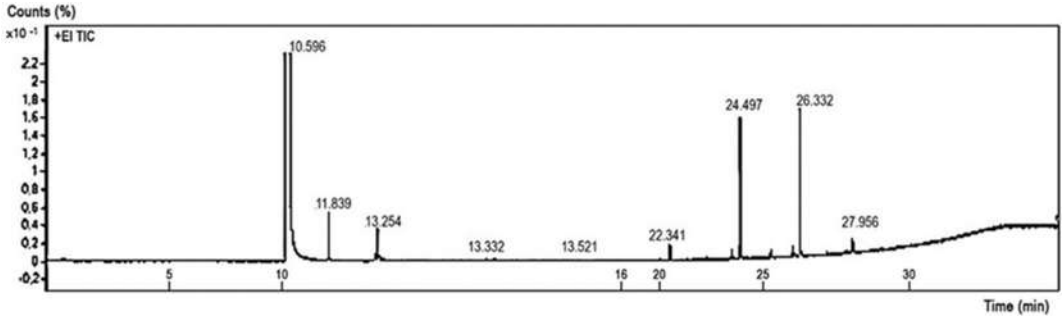

Fig 10. Chromatogram of female flowers at 15:00 pm

The peaks found in female flower samples at 09:00 am occurred at a retention time of 10.599 min with a sum area of 98.91 (Fig. 8). The results of the identification of the peaks are suspected to be estragole compounds. Other compounds identified based on the peak formed included 2-propenamide, anethole, methyl eugenol, hexadecane, 1,1'-(2-methyl-1,3-propanediyl)biscyclohexane, nonadecane, and 1,2,4-benzenetricarboxylic acid, 1,2-dimethyl ester (Table 4).

An increase in the number of peaks was identified at

12:00 am. There are 14 peaks, with the peaks occurring at a retention time of 10.608 min and a sum area of 97.74 which is suspected to be estragole. Other peaks besides estragole are thought to be volatile compounds, namely anisole, 2-propenamide, anethole, methyl eugenol, 2-methyl-3-(3-methyl-but-2-enyl)-2-(4-methyl-pent-3-enyl)-oxetane, 1-butanamenite, hexadecane, ethyl 9-octadecenoate, hexamethylcyclotrisiloxane, nonadecane, and di-*n*-decylsulfone (Table 5).

The peak at 15:00 pm occurred with a retention value of 10.596 min, an area sum of 99.22, and it was suspected that the compound was estragole. Estragole is the dominant compound found in female flowers. Meanwhile, other compounds identified were anethole, 1,5-dimethyl-8-(1-methylethenyl)-1,5-cyclodecadiene, methyl eugenol, 2-(4a,8-dimethyl-2,3,4,5,6, 7-hexahydro-1*H*-naphthalen-2-yl)propan-2-ol, hexadecane, nonadecane, and hexamethylcyclotrisiloxane (Table 6).

Table 4. List of volatile compounds of female flowers at 09:00 am

Peak	Compounds	Start	RT (min)	End	Height	Area	Area sum	%Area
1	2-Propenamide	8890	8.936	8955	699	1536	0	0.00
2	Estragole	10468	10.599	10958	4755799	34816630	10000	98.91
3	Anethole	11805	11.840	11878	26397	43320	12	0.12
4	Methyl eugenol	13309	13.336	13463	17428	35926	10	0.10
5	Hexadecane	22314	22.341	22381	8225	13302	4	0.04
6	1,1'-(2-Methyl-1,3-propanediyl)biscyclohexane	24197	24.241	24273	4871	7830	2	0.02
7	Nonadecane	24456	24.499	24537	74102	127162	37	0.36
8	1,2,4-Benzenetricarboxylic acid, 1,2-dimethyl ester	25407	25.448	25477	4092	6843	2	0.02
9	1,1'-(2-Methyl-1,3-propanediyl)biscyclohexane	26081	26.121	26145	6193	10764	3	0.03
10	Nonadecane	26288	26.334	26390	78296	136393	39	0.39

Table 5. List of volatile compounds of female flowers at 12:00 am

Peak	Compounds	Start	RT (min)	End	Height	Area	Area sum	%Area
1	Anisole	5786	5.831	5870	7120	13291	4	0.04
2	2-Propenamide	8909	8.928	8939	961	1991	1	0.01
3	Estragole	10489	10.501	10683	4752892	34492145	10000	97.74
4	Anethole	11791	11.837	11896	168108	271686	79	0.77
5	Methyl eugenol	13290	13.333	13411	84818	140562	41	0.40
6	2-Methyl-3-(3-methyl-but-2-enyl)-2-(4-methyl-pent-3-enyl)-oxetane	16654	16.687	16733	2031	3351	1	0.01
7	*N*,3-dimethyl-1-butanamenite	20965	21.006	21038	1418	2832	1	0.01
8	Hexadecane	22305	22.343	22391	6243	10796	3	0.03
9	Ethyl 9-octadecenoate	23079	23.114	23178	9513	15750	5	0.04
10	Hexamethylcyclotrisiloxane	23450	23.469	23507	1169	2020	1	0.01
11	Nonadecane	24445	24.499	24563	71008	122503	36	0.35
12	Nonadecane	26271	26.333	26401	98126	175607	51	0.50
13	Di-*n*-decyl sulfone	27930	27.960	27998	11336	20054	6	0.06
14	Hexamethylcyclotrisiiloxane	28779	28.819	28873	8327	15989	5	0.05

Table 6. List of volatile compounds of female flowers at 15:00 pm

Peak	Compounds	Start	RT (min)	End	Height	Area	Area sum	%Area
1	Estragole	10435	10.596	11343	4735482	38092950	10000	99.22
2	Anethole	11796	11.839	11928	31757	50578	13	0.13
3	1,5-Dimethyl-8-(1-methylethenyl)-1,5-cyclodecadiene	13214	13.254	13281	5543	9149	2	0.02
4	Methyl eugenol	13295	13.332	13443	43300	80864	21	0.21
5	2-(4a,8-Dimethyl-2,3,4,5,6,7-hexahydro-1*H*-naphthalen-2-yl)propan-2-ol	13489	13.521	13567	1821	3275	1	0.01
6	Hexadecane	22301	22.341	22382	6666	11918	3	0.03
7	Nonadecane	24462	24.497	24562	38908	66014	17	0.17
8	Nonadecane	26275	26.332	26410	41806	71474	19	0.19
9	Hexamethylcyclotrisiloxane	27918	27.956	28015	3540	6889	2	0.02

The mass spectrum for all-time peaks of the release of volatile compounds in female flowers that occurred at 09:00 am, 12:00 am, and 15:00 pm obtained the main peak *m/z* = 148 which was suspected to be estragole. The fragmentation pattern that occurs based on the mass spectrum for the female oil palm flower samples at 09:00 am, 12:00 pm is *m/z* 148, 121, 77, 51 (Fig. 11 and 12) and the fragmentation pattern for the female oil palm flower at 15:00 pm fragments occurred at *m/z* 148, 121, 77, 65 and 51 (Fig. 13).

Estragole or 1-allyl-4-methoxybenzene is an oxygenated volatile organic compound (OVOC) with the molecular formula $C_{10}H_{12}O$, molecular weight 148.20 g/mol, boiling point 216 °C at 760 mmHg, density 0.946 g/cm^3, liquid at room temperature room, and is optically inactive. Estragole is not classified as a terpenoid compound because it is produced by the phenylpropanoid pathway instead of the terpenoid pathway. Estragole is

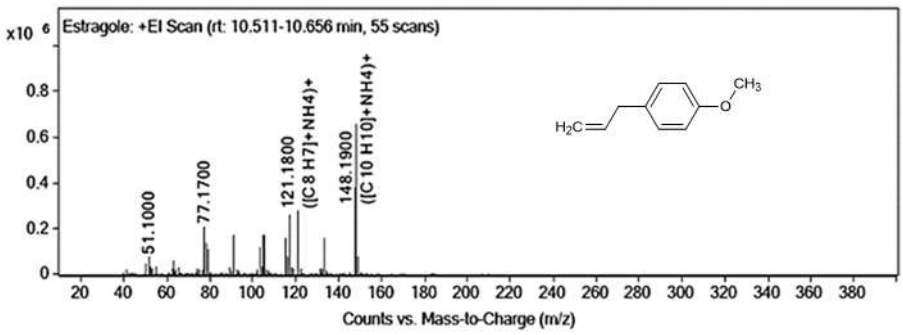

Fig 11. Spectrum and structure of estragole in female flower samples at 09:00 am

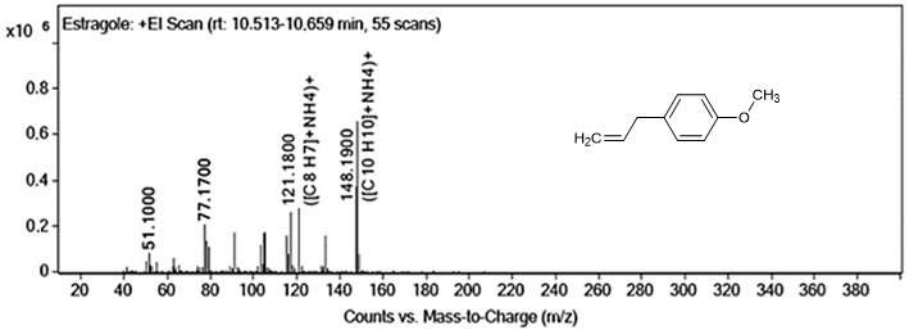

Fig 12. Spectrum and structure of estragole in female flower samples 12:00 am

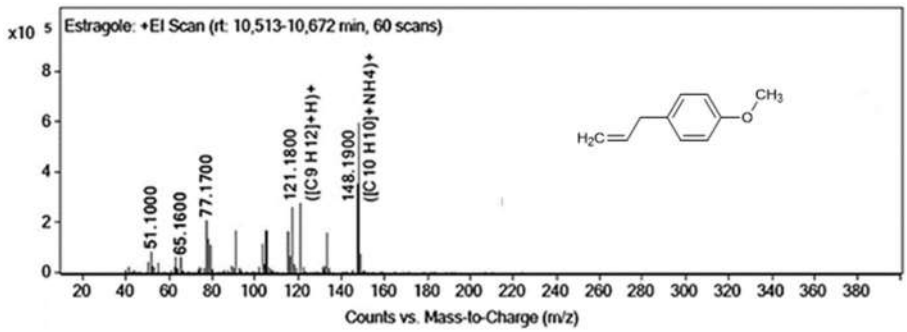

Fig 13. Spectrum and structure of estragole in female flower samples 15:00 pm

found in the essential oils of tarragon and basil plants. Estragole exhibits a carcinogenic effect in mice and can covalently modify DNA. Estragole produced by oil palm plays a role in attracting *E. kamerunicus*. The study conducted by Swaray et al. [14] showed that the stronger aroma of estragole/*p*-methoxyally benzene had the effect of increasing the population density of *E. kamerunicus*.

Anethole is a compound produced through the phenylpropanoid pathway and is an isomer of estragole which has a characteristic anise aroma. Phenylpropene is a class of volatile compounds found in gymnosperms and angiosperms. When removed from flowers, these compounds serve as attractants for pollinators who will detect these compounds through their olfactory system. At high concentrations, this compound shows toxicity to cells which is useful as a defense compound [15].

Anisole is a monomethoxybenzene in which the benzene ring is substituted by a methoxy group. Anisole is a plant metabolite found in *Peristeria elata* and *Ocium gratissimum* plants. Anisole and its derivatives (e.g. *p*-vinyl-anisole, *p*-ethyl-anisole, and *p*-ethylene-anisole) were detected in the rainforest canopy using PTR-MS [16].

Ethyl oleate is a long-chain fatty acid ethyl ester resulting from the formal condensation of the carboxy group of oleic acid with the hydroxy group of ethanol. This compound acts as plant metabolite and acaricide. Ethyl oleate is a natural constituent that can be found in cottonseed oil, linseed oil, peanut oil, coconut oil, and palm kernel oil [17].

Methyl eugenol ($C_{12}H_{24}O_2$) is a phenylpropanoid group compound which is a derivative of eugenol, the shikmiate secondary metabolite biosynthesis pathway between L-phenylaalnine and L-tyrosine [18-19]. This compound is found in several types of plants, including *Melaleuca bracteate*, *O. minimum, O. sanctum,* and *O. tenuiflorum*. According to Kardinan's study [20], methyl eugenol was used as an attractant to attract fruit flies *Bactocera* spp. According to Russo et al. [21] and Jankowska et al. [22], methyl eugenol as an attractant is classified as a "food lure" which attracts male flies for food needs and after consumption it will be synthesized in the body of male fruit flies into pheylpropanoid and coniferyl alcohol compounds which are used as sex pheromones to attract female fruit flies during mating. Methyl eugenol belongs to kairomones which can attract fruit flies *Bactrocera* spp. The male sex is then consumed and processed in the body to produce sex pheromones as a substance that attracts female fruit flies in the mating process [23].

In their life activities, insects communicate them through chemicals called semiochemicals which are divided into two, namely pheromones for communication between individuals within one species and allelochemicals for communication between individuals in different species [24]. Pheromones are divided into several types, such as sex pheromones or sexual stimulation to call the opposite sex; i.e., aggregation pheromones to gather or combine, alarm pheromones that are a sign of danger and alert, epideictic pheromones to indicate the laying area of eggs for female insects to other female insects, territorial pheromones to indicate the territory of certain organisms, and trail pheromones to provide information to the group and other pheromones [25-26]. Allelochemicals consist of allomones (organisms that

release chemical compounds benefit, while those that receive chemical compounds are harmed), kairomones (organisms that release chemical compounds are harmed, while those who receive the benefit), and synomones (organisms that release and receive chemical compounds are equally benefited). Plants produce a bewildering variety of VOCs comprising a great diversity of chemical structures. In addition, diverse metabolic path paths produce various alkanes and low-molecular ethylene, acetaldehyde, acetone, or methanol [25-29]. Volatile compounds from oil palm flowers are thought to belong to the allelochemical type of synomones. The insect *E. kamerunicus* gets food from oil palm flowers and benefits oil palm flowers because it acts as a pollinator that carries pollen from male flowers to female flowers [6].

CONCLUSION

Observation of the release pattern of volatile compounds was carried out at 07:00 am–17:00 pm. The results showed that there were three times of release by male flowers, namely at 08:00 am, 11:00 am and 14:00 pm, with the highest peak release at 14:00 am, while the three peak times for the release of volatile compounds in female flowers occurred at 09:00 am, 12:00 am, and 15:00 pm with the highest peak of the release of volatile compounds occurred at 12:00 am. These results suggest that sunlight effect the volatile compounds release. The results of the GC-MS analysis showed that 21 and 19 volatile compounds were identified from male and female flower samples with a total of 38 different types of compounds. Estragole compounds were dominant in both types of flowers and did not show significant differences in the area sum values at each time of observation. Other compounds identified were consistently present in both types of flowers, namely anetol, 2-propenamide, nonadecane, and methyl eugenol, although with different sum area values.

ACKNOWLEDGMENTS

This study was financially supported by the Ministry of Education and Culture, Innovative and Research Council, Indonesia, Doctoral Research Grant (No. 1318/UN6.3.1/PT.00/2019) by Fizrul Indra Lubis.

REFERENCES

[1] BPS, 2021, *Statistik Kelapa Sawit Indonesia 2020*, Badan Pusat Statistik, Jakarta, 20–25.

[2] Lubis, F.I., Sudarjat, S., and Dono D., 2017, Populasi serangga penyerbuk kelapa sawit *Elaeidobius kamerunicus* Faust dan pengaruhnya terhadap nilai fruit set pada tanah berliat, berpasir dan gambut di Kalimantan Tengah, Indonesia, *Jurnal Agrikultura*, 28 (1), 39–46.

[3] Anggraeni, T., Rahayu, S., Ahmad, I., Esyanti, R.R., and Putra, R.E., 2013, Resources partitioning and different foraging behavior is the basis for the coexistence of *Thrips hawaiiensis* (Thysanoptera: Tripidae) and *Elaeidobius kamerunicus* (Coleoptera: Curculionidae) on oil palm (*Elaeis guineensis* Jacq) flower, *J. Entomol. Nematol.*, 5 (5), 59–63.

[4] Muhamad Fahmi, M.H., Ahmad Bukhary, A.K., Norma, H., and Idris, A.B., 2016, Analysis of volatile organic compound from *Elaeis guineensis* inflorescences planted on different soil types in Malaysia, *AIP Conf. Proc.*, 1784 (1), 060020.

[5] Alves Filho, E.G., Brito, R.S., Rodrigues, T.H.S., Silva, L.M.A., de Brito, E.S., Canuto, K.M., Krug, C., and Zocolo, G.J., 2019, Association of pollinators of different species of oil palm with the metabolic profiling of volatile organic compounds, *Chem. Biodivers.*, 16 (6), e1900050.

[6] Prasetyo, A.E., Purba, W.O., and Susanto, A., 2014, *Elaeidobius kamerunicus*: Application of hatch and carry technique for increasing oil palm fruit set, *J. Oil Palm Res.*, 26 (3), 195–202.

[7] Dewi, L.K., Friatnasary, D.L., Herawati, W., Nurhadianty, V., and Cahyani, C., 2018, Studi perbandingan metode isolasi ekstraksi pelarut dan destilasi uap minyak atsiri kemangi terhadap komposisi senyawa aktif, *RBAET*, 2 (1), 13–19.

[8] Toudert, N., Zakkad, F., Dadda, N., Djilani, A., Dicko, A., and Djilani, S.E., 2021, Phytochemical analysis of bioactive extracts and seed oil of three Euphorbia species from Algerian flora by LC-MS and GC-MS, *Indones. J. Chem.*, 21 (3), 546–553.

[9] Maser, W.H., Purwoko, A., Yuliana, N.D., Lubis,

L.M., and Khatib, A., 2022, GC-MS based metabolite profiling, and antibacterial activity of torch ginger (*Etlingera elatior*) flowers extract, *Indones. J. Chem.*, 22 (4), 1014–1024.

[10] Stratakos, A.C., and Koidis, A., 2016, "Methods for Extracting Essential Oils" in *Essential Oils in Food Preservation, Flavor and Safety*, Eds. Preedy, V.R. Academic Press, San Diego, US, 31–38.

[11] Akdağ, A., and Öztürk, E., 2019, Distillation methods of essential oils, *Selçuk Univ. Fen Fak. Fen Derg.*, 45 (1), 22–31.

[12] Ma'sum, Z., and Proborini, W.D., 2016, Optimasi proses destilasi uap essential oil, *Jurnal Reka Buana*, 1 (2), 105–109.

[13] Mustapa, M.A., Guswenrivo, I., Zurohtun, A., Khairul Ikram, N.K., and Muchtaridi, M., 2023, Analysis of essential oils components from aromatic plants using headspace repellent method against *Aedes aegypti* mosquitoes, *Molecules*, 28 (11), 4269.

[14] Swaray, S., Rafii, M.Y., Amiruddin, M.D., Ismail, M.F., Jamian, S., Jalloh, M., Oladosu, Y., Mohamad, M.M., Marjuni, M., Kalopo, O.K., and Chukwu, S.C., 2021, Assessment of oil palm pollinating weevil (*Elaeidobius kamerunicus*) population density in biparental *dura* × *pisifera* hybrids on deep peat-soil in Perak State, Malaysia, *Insects,* 12 (3), 221.

[15] Mostafa, S., Wang, Y., Zeng, W., and Jin, B., 2022, Floral scents and fruit aromas: Functions, compositions, biosynthesis, and regulation, *Front. Plant Sci.*, 13, 860157.

[16] Schurr, L., Masotti, V., Geslin, B., Gachet, S., Mahé, P., Jeannerod, L., and Affre, L. 2022, To what extent is fennel crop dependent on insect pollination?, *Agric., Ecosyst. Environ.*, 338 (6), 108047.

[17] National Center for Biotechnology Information, 2022, *PubChem Compound Summary for CID 5363269, Ethyl oleate*, https://pubchem.ncbi.nlm.nih.gov/compound/Ethyl-oleate, accessed on May 23, 2022.

[18] Santos-Sánchez, N.F., Salas-Coronado, R., Hernández-Carlos, B., and Villanueva-Cañongo, C., 2019, "Shikimic Acid Pathway in Biosynthesis of Phenolic Compounds" in *Plant Physiological Aspects of Phenolic Compounds*, Eds. Soto-Hernández, M., García-Mateos, R., and Palma-Tenango, M., IntechOpen, Rijeka, Croatia.

[19] Tangpao, T., Krutmuang, P., Kumpuoun, W., Jantrawut, P., Pusadee, T., Cheewangkoon, R., Sommano, S.R., and Chuttong, B., 2021, Encapsulation of basil essential oil by paste method and combined application with mechanical trap for oriental fruit fly control, *Insect*, 12 (7), 633.

[20] Kardinan, A., 2019, Prospek insektisida nabati berbahan aktif metil eugenol ($C_{12}H_{24}O_2$) sebagai pengendali hama ulat buah *Bactrocera* spp. (Diptera: Tephritidae). *Perspektif,* 18 (1), 16–27.

[21] Russo, A., Pollastri, S., Ruocco, M., Monti, M.M., and Loreto, F., 2022, Volatile organic compounds in the interaction between plants and beneficial microorganisms, *J. Plant Interact.,* 17 (1), 840–852.

[22] Jankowska, M., Rogalska, J., Wyszkowska, J., and Stankiewicz, M., 2017, Molecular targets for components of essential oils in the insect nervous system: A review, *Molecules*, 23 (1), 34.

[23] Li, A.S., Iijima, A., Huang, J., Li, Q.X., and Chen, Y., 2020, Putative mode of action of the monoterpenoids linalool, methyl eugenol, estragole, and citronellal on ligand-gated ion channels, *Engineering*, 6 (5), 541–545.

[24] Jones, P.L., and Agrawal, A.A., 2017, Learning in insect pollinators and herbivores, *Annu. Rev. Entomol.*, 62, 53–71.

[25] Conchou, L., Lucas, P., Meslin, C., Proffit, M., Staudt, M., and Renou, M., 2019, Insect odorscapes: From plant volatile to natural olfactory scenes, *Front, Physiol.*, 10, 00972.

[26] Jardine, K.J., Fernades de Souza, F.V., Oikawa, P., Higuchi, N., Bill, M., Poras, R., Niinemets, Ü., and Chambers, J.Q., 2017, Integration C_1 and C_2 metabolism in tress, *Int. J. Mol. Sci.*, 18 (10), 2045.

[27] Pickett, J.A., and Khan, Z.R., 2016, Plant volatile-mediated signalling and its application in agriculture: Successes and challenges, *New Phytol.*, 212 (4), 856–870.

[28] Jardine, A.B., Jardine, K.J., Fuentes, J.D., Martin, S.T., Martins, G., Durgante, F., Carneiro, V.,

Higuchi, N., Manzi, A.O., and Chambers, J.Q., 2015, Highly reactive light dependent monoterpenes in the Amazon, *Geophys. Res. Lett.*, 42 (5), 1576–1583.

[29] Vivaldo, G., Masi, E., Taiti, C., Calderalli, G., and Mancuso, S., 2017, The network of plant volatile organic compounds, *Sci. Rep.*, 7 (1), 11050.

Supplementary Data

This supplementary data is a part of a paper entitled "Triterpenoids from the Stem Bark of *Aglaia cucullata* (Meliaceae) and Their Cytotoxic Activity against A549 Lung Cancer Cell Line".

Table of Contents

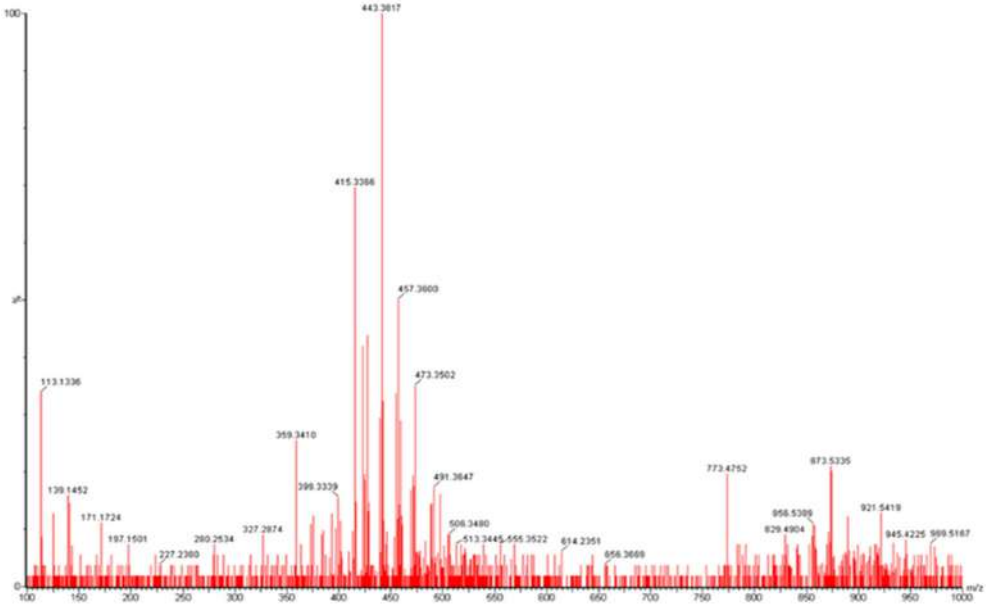

Fig S1. HR-TOFMS spectrum of (**1**)

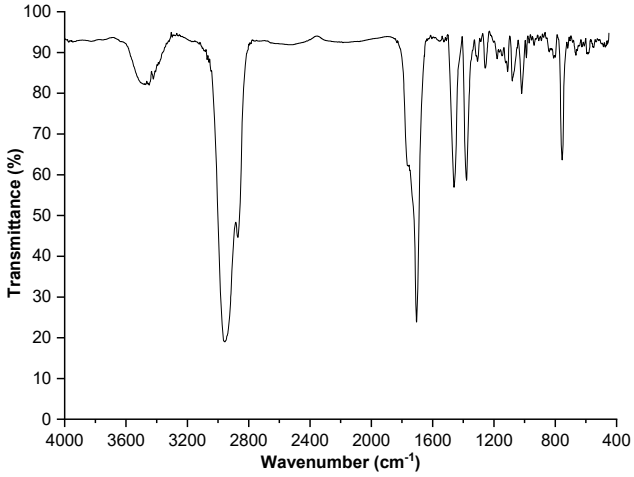

Fig S2. FTIR spectrum of (**1**)

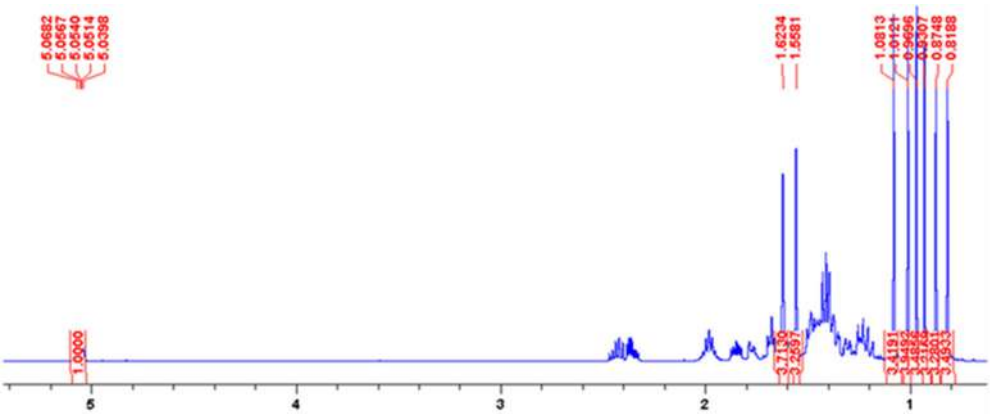

Fig S3. ^{1}H-NMR spectra of (**1**) (500 MHz in $CDCl_3$)

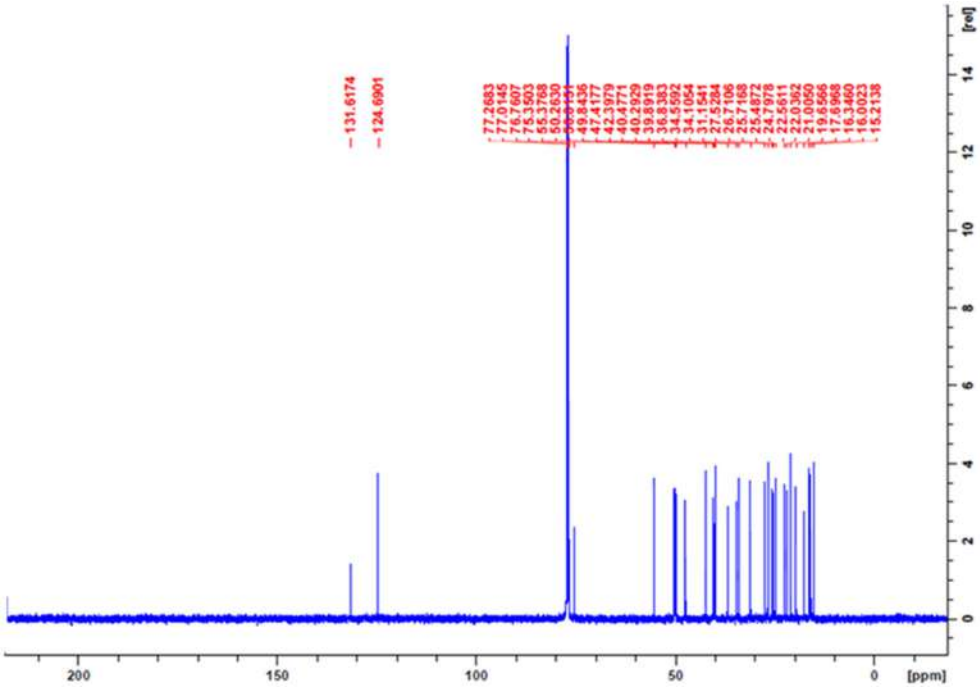

Fig S4. ^{13}C-NMR spectrum of (**1**) (125 MHz in $CDCl_3$)

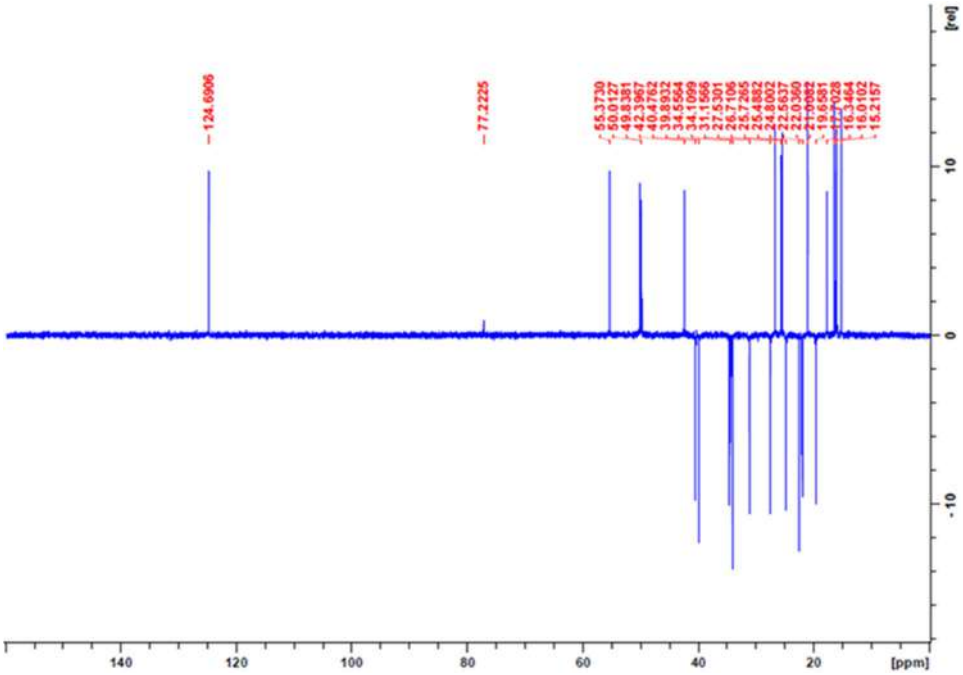

Fig S5. DEPT 135° spectrum of (**1**) (125 MHz in $CDCl_3$)

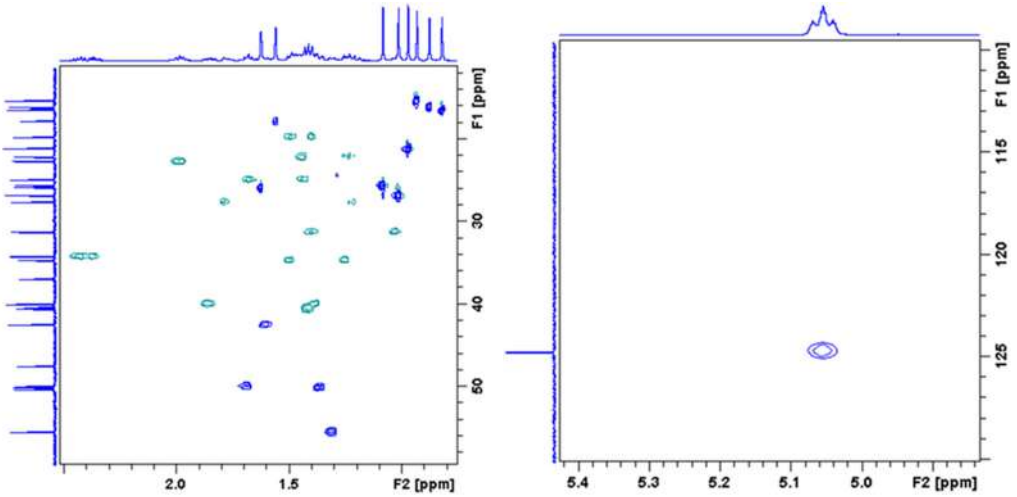

Fig S6. HSQC spectrum of (**1**)

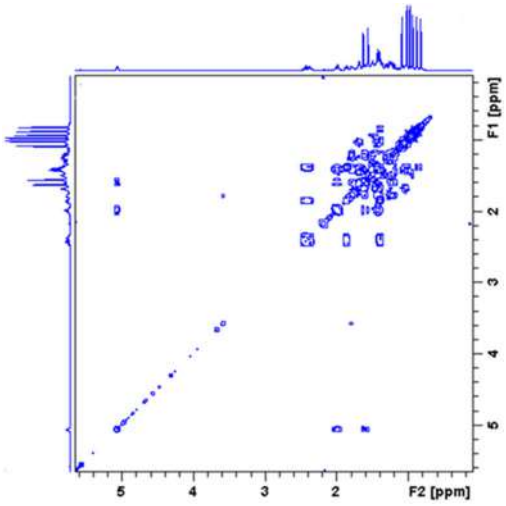

Fig S7. ^{1}H-^{1}H-COSY spectrum of (**1**)

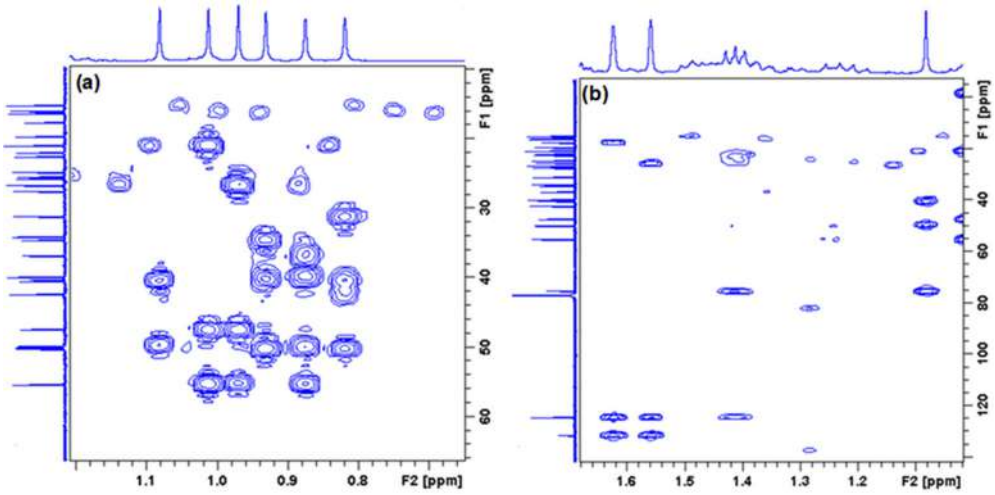

Fig S8. HMBC spectrum of (**1**)

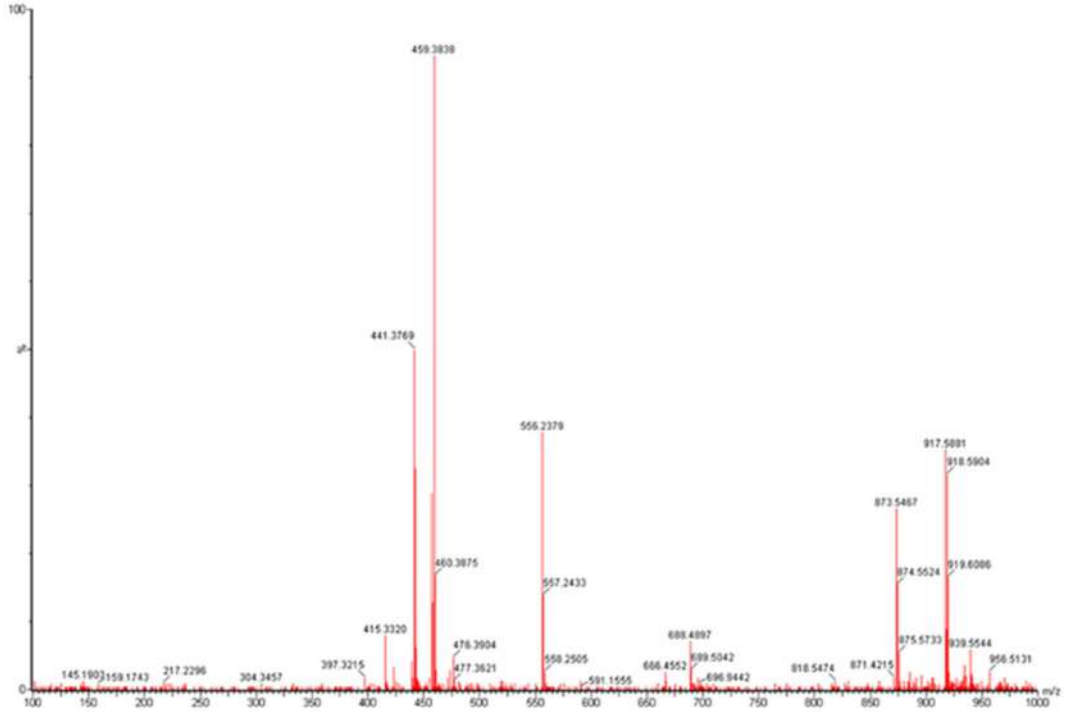

Fig S9. HR-TOFMS spectrum of (**2**)

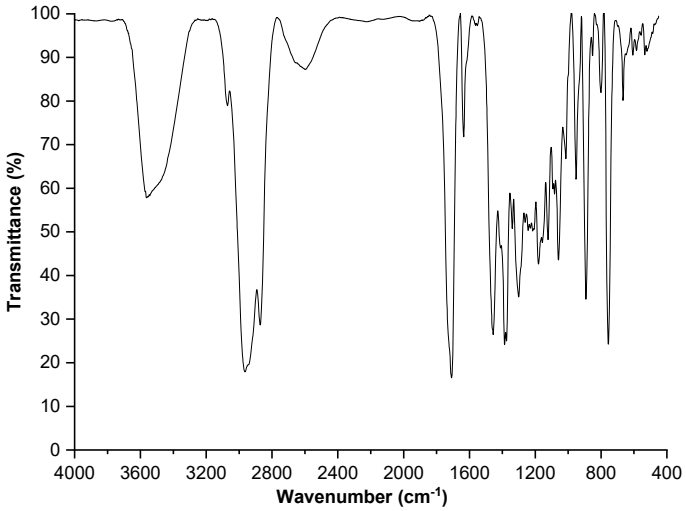

Fig S10. IR spectrum of (**2**)

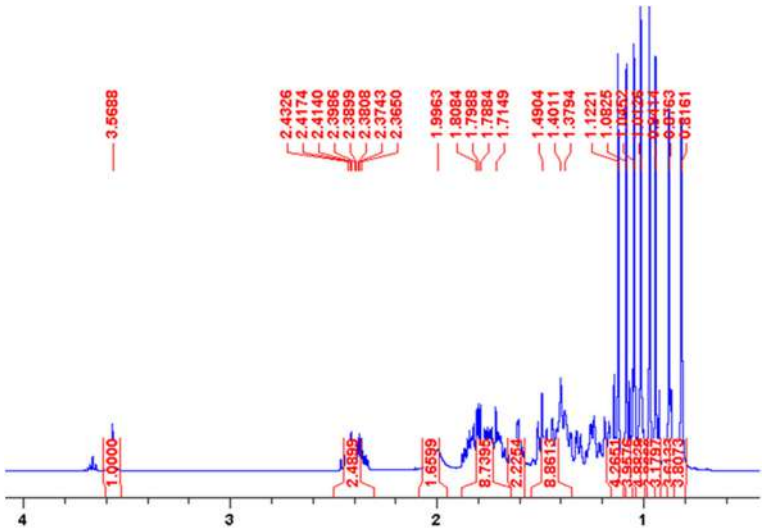

Fig S11. ^{1}H-NMR spectrum of (**2**) (500 MHz in $CDCl_3$)

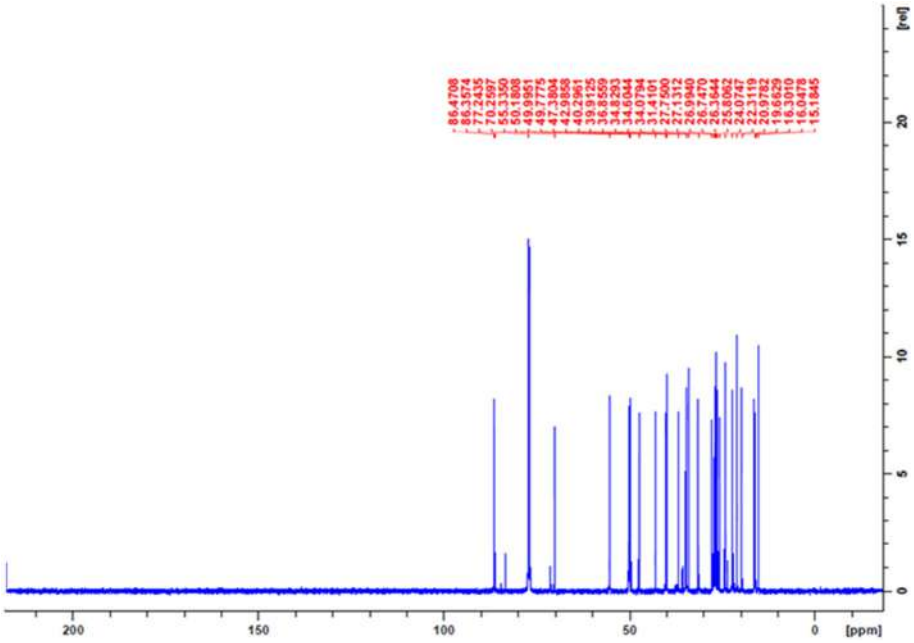

Fig S12. ^{13}C-NMR spectrum of (**2**) (125 MHz in $CDCl_3$)

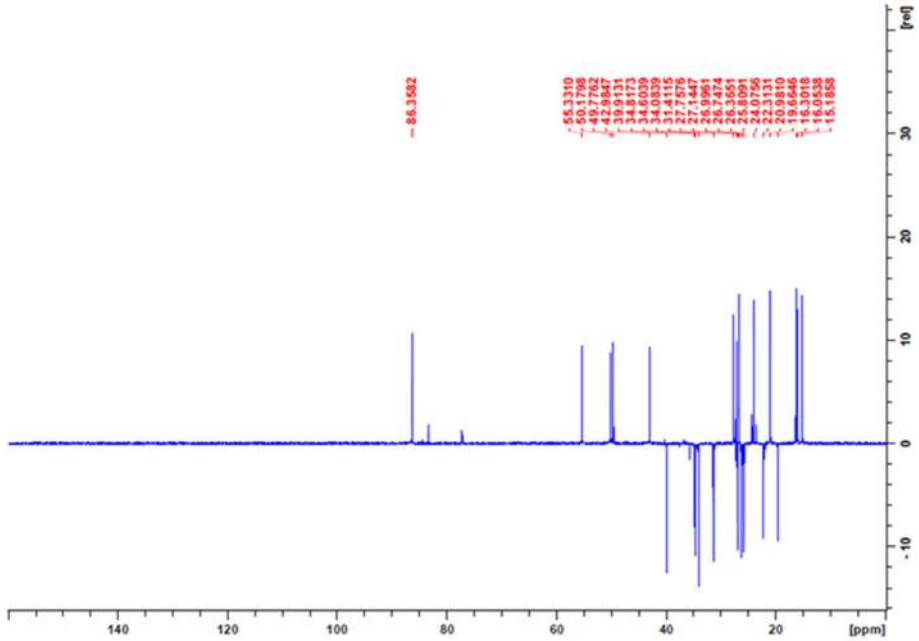

Fig S13. DEPT 135° spectrum of (**2**) (125 MHz in $CDCl_3$)

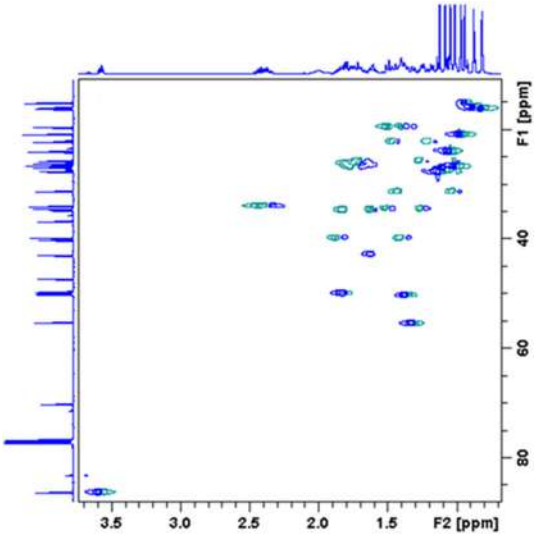

Fig S14. HSQC spectrum of (**2**)

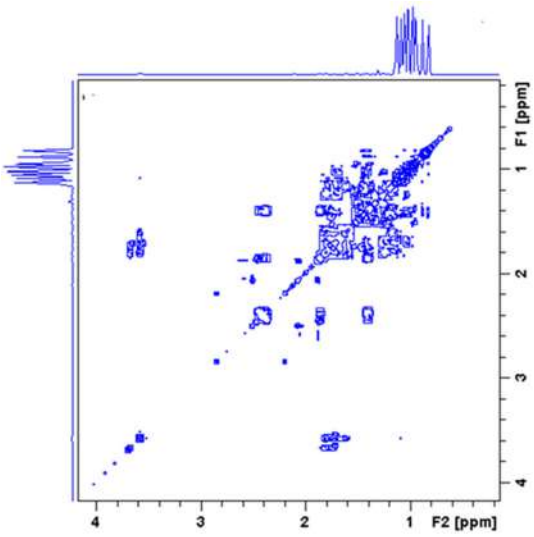

Fig S15. ^{1}H-^{1}H-COSY spectrum of (**2**)

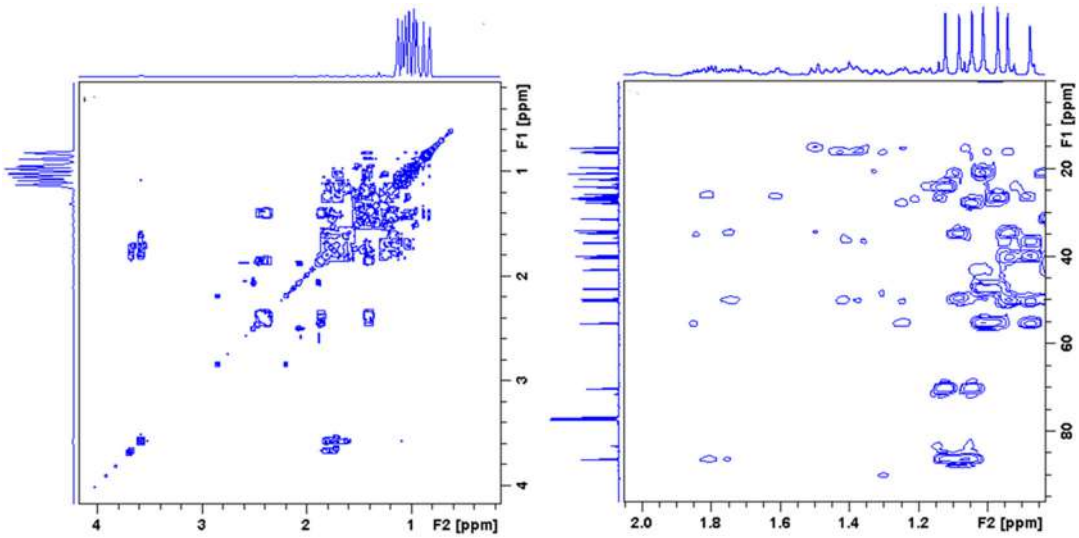

Fig S16. HMBC spectrum of (**2**)

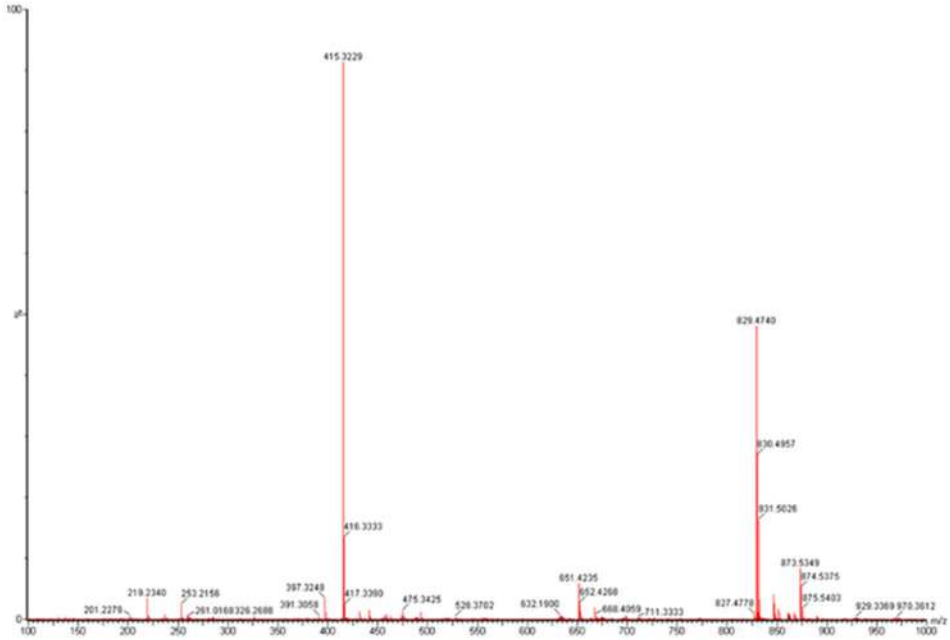

Fig S17. HR-TOFMS spectrum of (**3**)

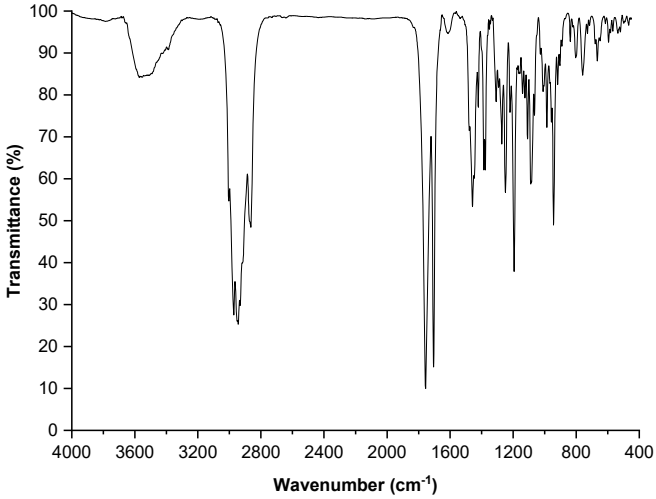

Fig S18. IR spectrum of (**3**)

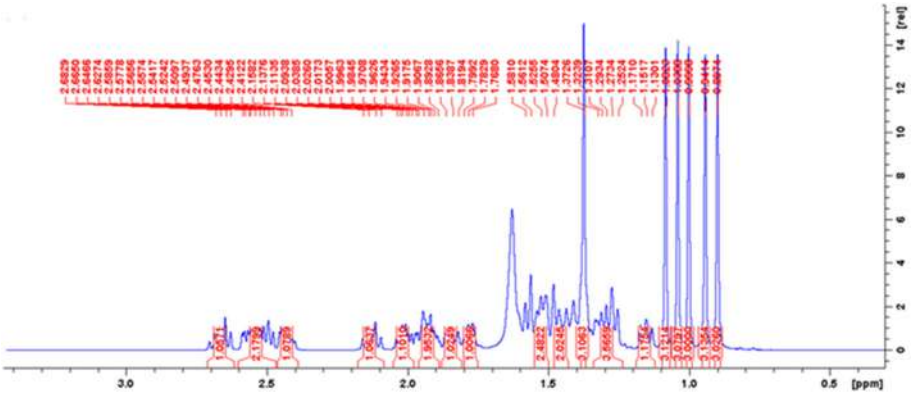

Fig S19. ^{1}H-NMR spectrum of (**3**) (500 MHz in $CDCl_3$)

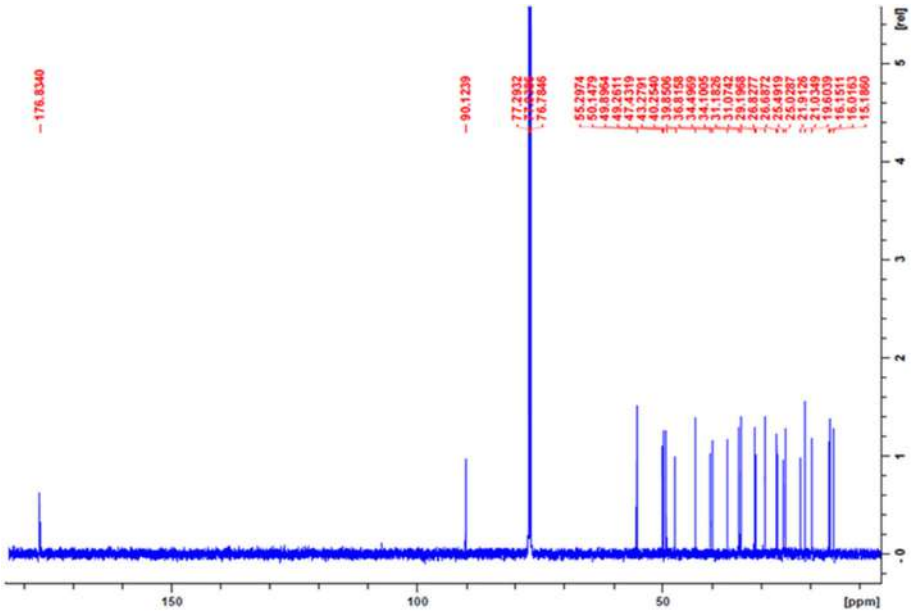

Fig S20. ^{13}C-NMR spectrum of (**3**) (125 MHz in $CDCl_3$

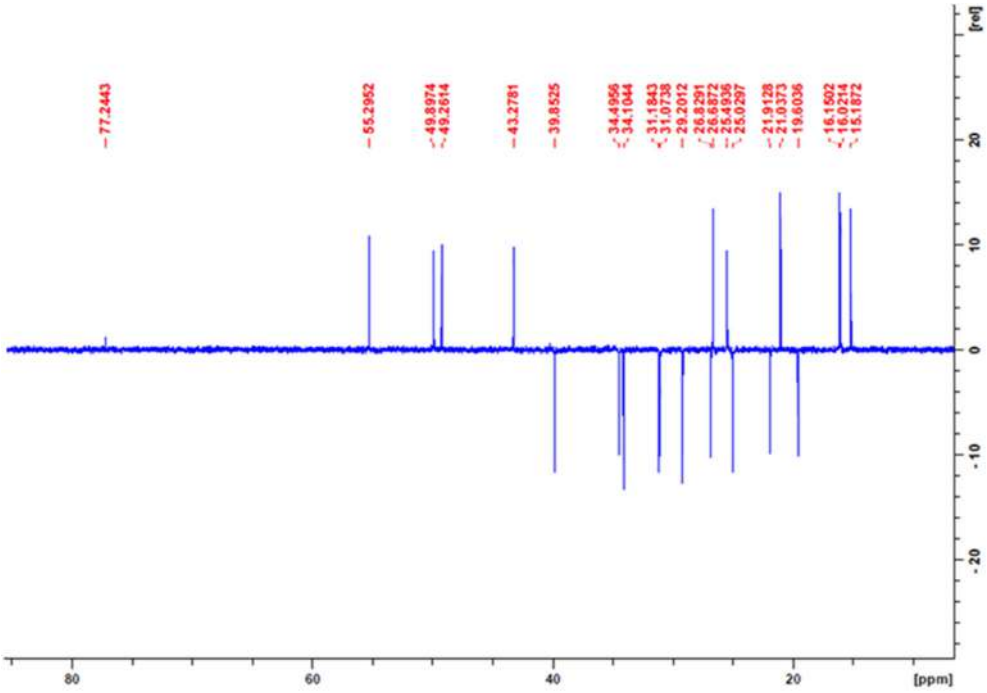

Fig S21. DEPT 135° spectrum of (**3**) (125 MHz in $CDCl_3$)

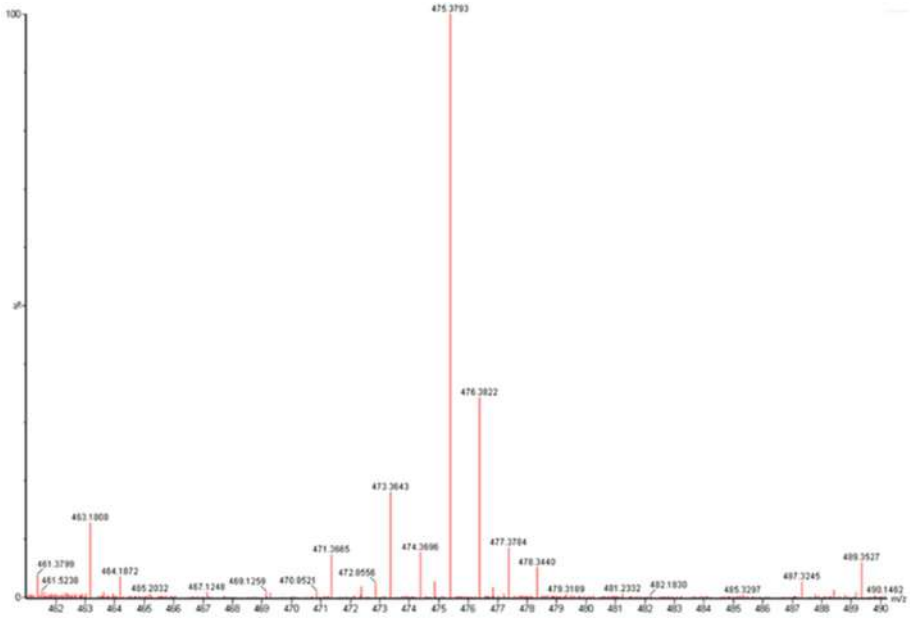

Fig S22. HR-TOFMS spectrum of (**4**)

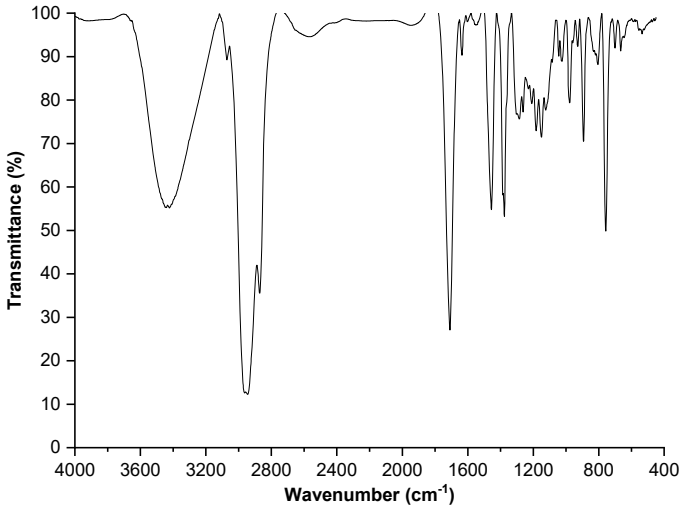

Fig S23. IR spectrum of (**4**)

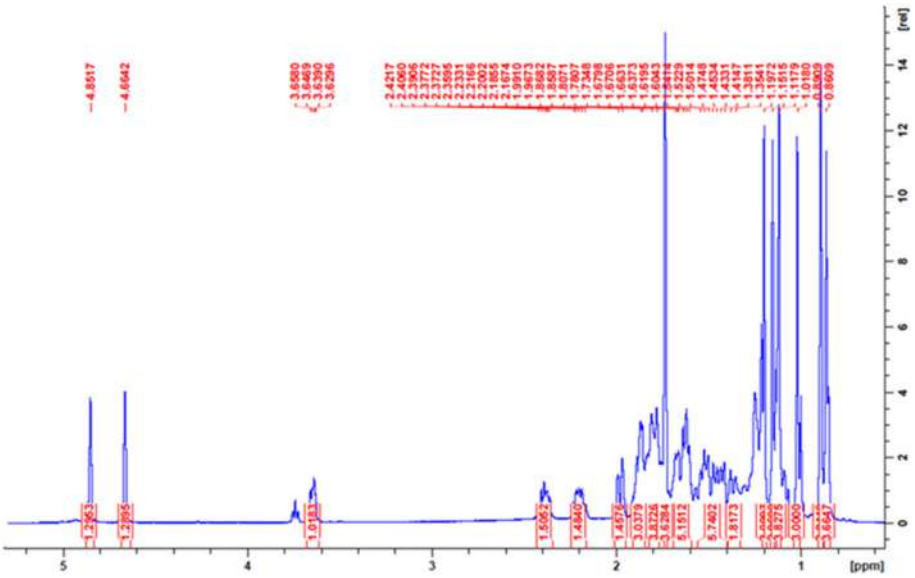

Fig S24. ^{1}H-NMR spectrum of (**4**) (500 MHz in $CDCl_3$)

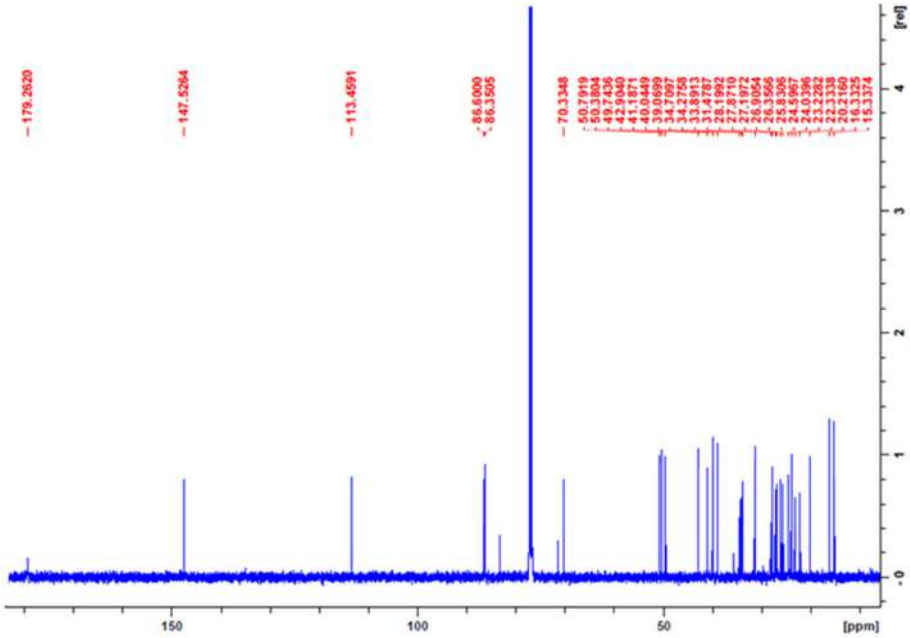

Fig S25. ^{13}C-NMR spectrum of (**4**) (125 MHz in $CDCl_3$)

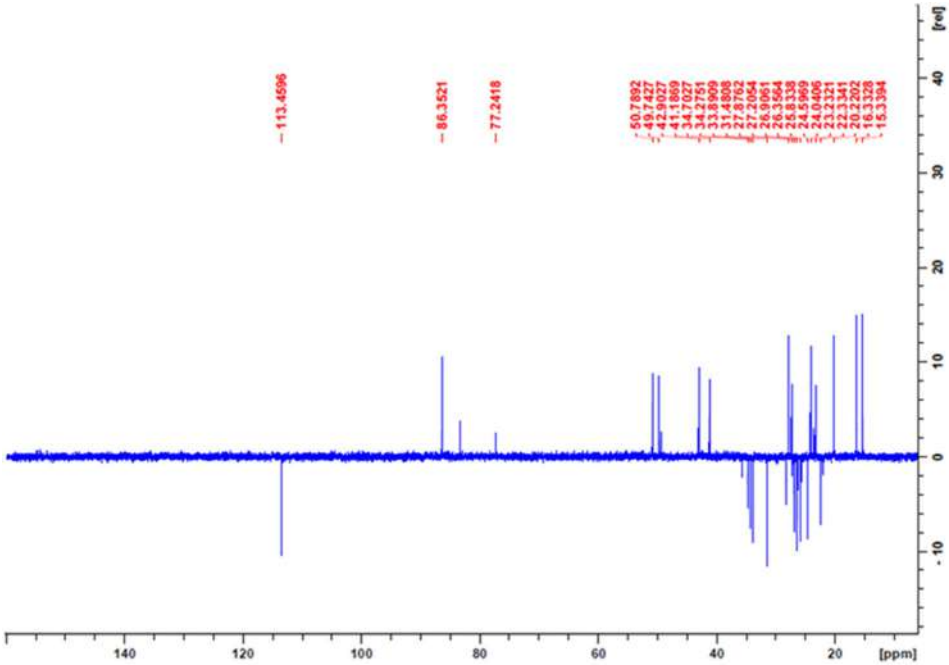

Fig S26. DEPT 135° spectrum of (**4**) (125 MHz in $CDCl_3$)

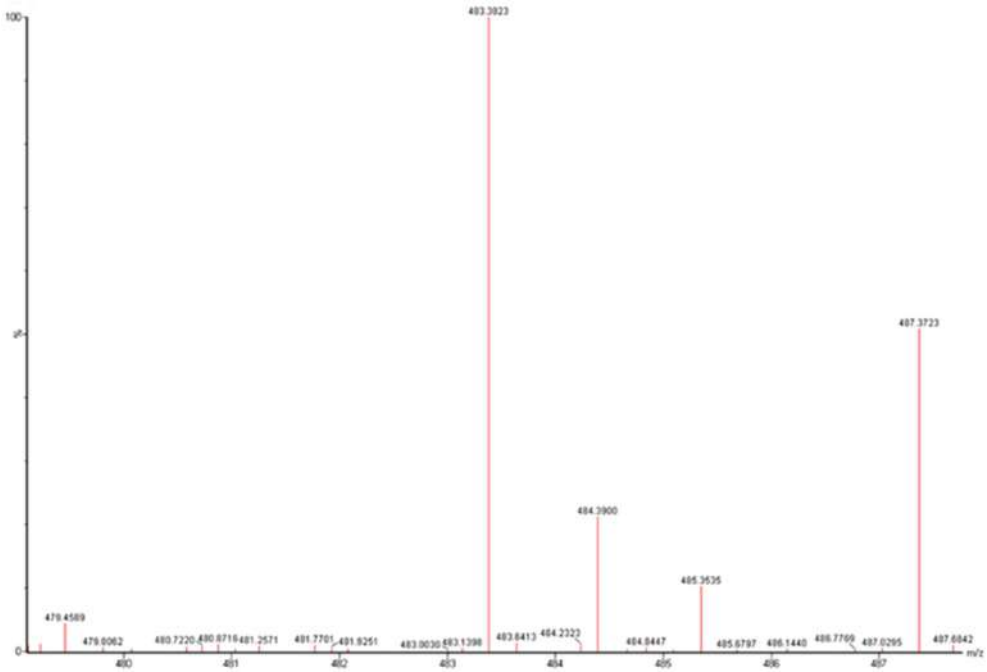

Fig S27. HR-TOFMS spectrum of (**5**)

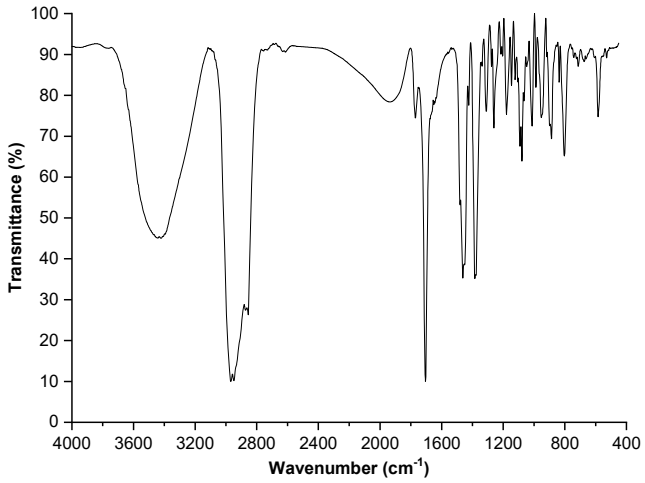

Fig S28. IR spectrum of (**5**)

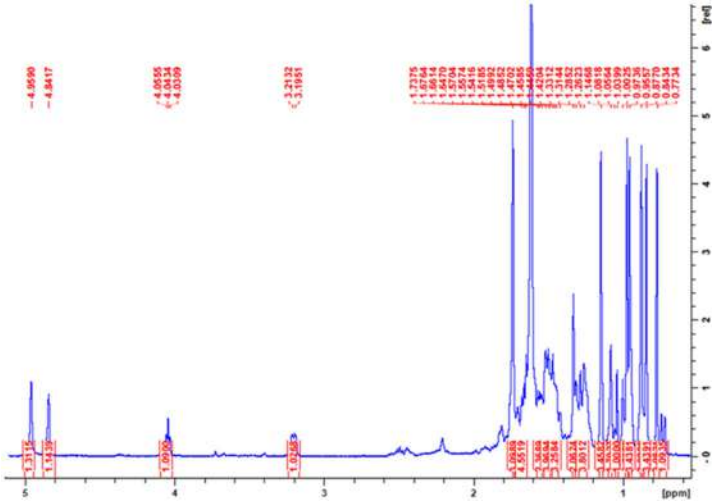

Fig S29. ^{1}H-NMR spectrum of (**5**) (500 MHz in $CDCl_3$)

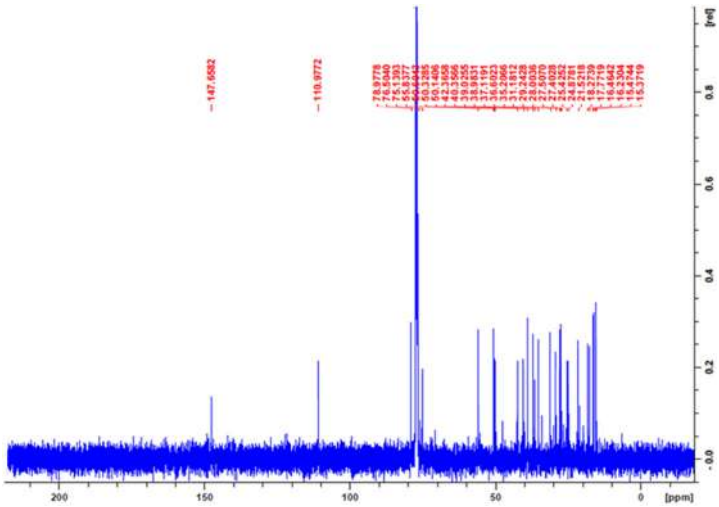

Fig S30. ^{13}C-NMR spectrum of (**5**) (125 MHz in $CDCl_3$)

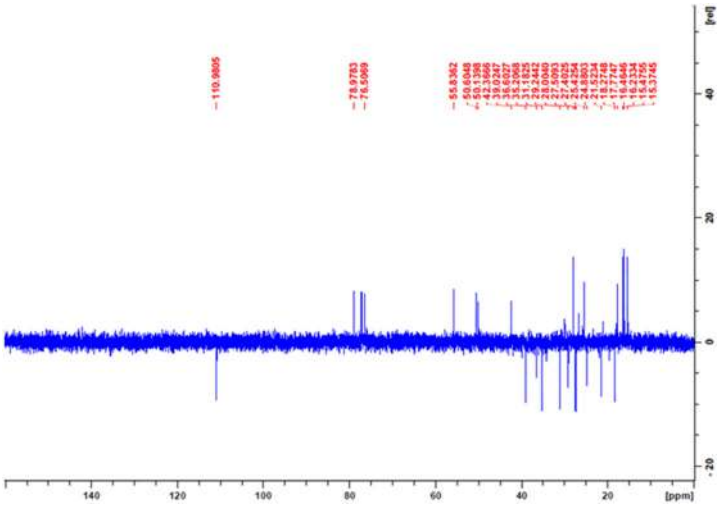

Fig S31. DEPT 135° spectrum of (**5**) (125 MHz in $CDCl_3$)

Triterpenoids from the Stem Bark of *Aglaia cucullata* (Meliaceae) and Their Cytotoxic Activity against A549 Lung Cancer Cell Line

Desi Harneti[1*], Iqbal Wahyu Mustaqim[1], Darwati Darwati[1], Al Arofatus Naini[1], Purnama Purnama[1], Erina Hilmayanti[1], Tri Mayanti[1], Nurlelasari Nurlelasari[1], Shabarni Gaffar[1], Rani Maharani[1], Kindi Farabi[1], Unang Supratman[1,2], Sofa Fajriah[3], Mohamad Nurul Azmi[4], and Yoshihito Shiono[5]

[1]*Department of Chemistry, Faculty of Mathematics and Natural Sciences, Universitas Padjadjaran, Jl. Raya Bandung-Sumedang Km. 21, Jatinangor, Sumedang 45363, Indonesia*

[2]*Central Laboratory, Universitas Padjadjaran, Jl. Raya Bandung-Sumedang Km. 21, Jatinangor, Sumedang 45363, Indonesia*

[3]*Research Center for Pharmaceutical Ingredients and Traditional Medicine, National Research and Innovation Agency (BRIN), Komplek Cibinong Science Center – BRIN, Jl. Raya Bogor Km. 46, Cibinong 16911, Indonesia*

[4]*School of Chemical Sciences, Universiti Sains Malaysia, 11800 Minden, Malaysia*

[5]*Department of Food, Life, and Environmental Science, Faculty of Agriculture, Yamagata University, Tsuruoka, Yamagata 997-8555, Japan*

* ***Corresponding author:***

email: desi.harneti@unpad.ac.id

Received: October 31, 2022
Accepted: March 2, 2023

DOI: 10.22146/ijc.78748

Abstract: *The* Aglaia *species, which contains triterpenoids, is the most numerous in the Meliaceae family. The* A. cucullata *species, of which there are only a few known examples, has received scant research attention. This investigation aims to identify triterpenoids in an* n*-hexane preparation of* A. cucullata *stem bark and evaluate their effects against the A549 lung cancer cell line. Five dammarane-type triterpenoids were isolated from the* A. cucullata *trunk bark, which is (1) (20S)-20-hydroxydammar-24-en-3-one, (2) cabraleone, (3) cabralealactone, (4) eichlerianic acid, and (5) (+)-fouquierol. Their chemical structures were determined using infrared, high-resolution mass spectrometry, and nuclear magnetic resonance, as well as through data comparison of the reported compounds. Compound* ***1*** *was priorly separated from the* Aglaia *genus, compounds* ***2–4*** *were first isolated from the* A. cucullata *species, and compound* ***5*** *has been reportedly isolated from the Meliaceae family and the* Aglaia *genus. All substances were tested for their lethal potential against the A549 lung cancer cell type. A* seco *structure in the A ring of dammarane-type triterpenoid might play an important part in the lethal activity of component 4, which showed the greatest activity with an* IC_{50} *value of 32.17 μM against the A549 lung cancer cell line.*

Keywords: Aglaia cucullate*; cytotoxic activity; lung cancer cell (A549); Meliaceae triterpenoids*

■ INTRODUCTION

Terpenoids, including the crucial triterpenoids, are produced via the acetate/mevalonate route in the cytoplasm and endoplasmic membrane [1-2]. Their carbon structure is made of six isoprene units. Eukaryotic species have been found to contain more than 20,000 triterpenoids [1] and around 200 distinct structures. Higher plants typically contain triterpenoids, which serve as a first line of defense against microbes, parasites, and predators [3-4]. Based on their molecular structure, triterpenoids are categorized as either acyclic [5-6], monocyclic [6-7], bicyclic [8-9], tetracyclic [10-11], pentacyclic [12], or hexacylic [5-6]. There are many potential health benefits associated with triterpenoids, including anti-inflammatory [13-14], antioxidant [15], antibacterial [16-17], antiviral [18-19], antifungal [20-

21], hepatoprotective [20-21], anti-disease Alzheimer's [21], immunomodulatory [22-23], cytotoxic [24], and anticancer [25-26]. *Cedrela* [25], *Turraea* [26], *Entandrophragma* [27], *Azadirachta* [28], *Guarea* [29], *Lansium* [30], *Chisocheton* [31], *Melia* [32], *Dysoxylum* [33], *Toona* [34], and *Aglaia* [35] are all examples of taxa in the Meliaceae family that contain triterpenoids.

A. cucullata (Roxb.) Pellegr, also called Pacific maple, is a mangrove plant that belongs to the *Aglaia* genus [36-37]. *A. cucullata* is a tall tree that grows in coastal forests in tropical regions such as India, Bangladesh, Myanmar, Thailand, Malaysia, and Indonesia [38-39]. This species is widely spread in several regions in Indonesia, including in northern Sumatra and Kalimantan, southern Sulawesi coast, Halmahera, Ambon, Aru, and Irian Jaya [37]. Moreover, the plant's timber is utilized for boat construction, house supports, and fuel wood [38], while the leaves and fruits are for treating diarrhea, dysentery, skin infections, and cardiac diseases by Thai people [40], and as anti-inflammation and rheumatism by Burma people [41]. Flavaglines with cytotoxic activity towards oral human KB, breast cancer cells in human BC, and small cell lung NCI-H187 [40], bisamides [42], kaurane and labdane diterpenoids, and cycloartane triterpenoid with TRAIL resistance-overcoming activity [38] have been isolated through chemical analysis of this species. In our ongoing efforts to search for triterpenoids from the Indonesian *Aglaia* plants, we have further investigated the stem bark of *A. cucullata.* As a result, five triterpenoids (**1**–**5**) were successfully isolated and elucidated. Compound **1** was reported first time in the *Aglaia* genus, compounds **2**–**4** were found in *A. cucullata* for the first time, while compound **5** was discovered for the first time in *Meliaceae* family and *Aglaia* genus. All isolated compounds were assayed against A549 lung cancer cell lines. The detail of isolation, structure elucidation, and cytotoxic activity are described in this article.

■ EXPERIMENTAL SECTION

Materials

The stem bark of *A. cucullata* was obtained from the Manggar River, Balikpapan, East Kalimantan, in December 2020. The plant was examined at the Herbarium Wanariset, Balikpapan (collection No. FF7.20), and stored at the Faculty of Forestry, Universitas Mulawarman.

For extraction, fractionation, isolation, and purification, the following pro analyst and technical grade solvents are utilized: chloroform p.a. (Merck), acetone, methanol (MeOH), ethanol, ethyl acetate (EtOAc), *n*-butanol, *n*-hexane (Sigma-Aldrich), A549 cells were obtained from American Type Culture Collection (ATCC® CCL-185TM, Virginia, USA). Roswell Memorial Park Medium (RPMI) 1640 (Cat. No.11530586, Gibco, USA), 10% Fetal Bovine Serum (FBS, Cat. No.10082147, Gibco), and 1% Penicillin-Streptomycin were used to cultivate the cells (Cat. No. 15140112, Gibco). The cells were incubated at 37 °C in an incubator containing 5% CO_2 (Cat. No. 8000DH, Thermo Fisher Scientific, USA).

Instrumentation

A PerkinElmer Spectrum 100 FTIR spectrometer (PerkinElmer, USA) was utilized to characterize the KBr plate's IR spectrum. Using a Waters Xevo QTOF mass spectrometer (Waters, USA), mass spectra were acquired. Tetramethyl silane (TMS) was used as an internal standard, and NMR spectra were obtained using a Bruker Av-500 spectrometer (Bruker, Germany) at 500 MHz for ^{1}H-NMR and 125 MHz for ^{13}C-NMR. The column chromatography on ODS RF-18 and silica G_{60} was conducted using thin layer chromatography (TLC) on a silica G_{60} GF_{254} (Merck, 0.25 mm) column and a variety of solvent systems (Merck, 70–230 and 230–400 mesh). Spots were discovered using 10% H_2SO_4 in ethanol, which was heated and then examined under UV light at 254 and 365 nm.

Procedure

Extraction and isolation

The pulverized stem bark of *A. cucullata* was macerated in ethanol for 7 d (40 L). Using a rotary vacuum evaporator at 40 °C, the ethanol solvent was evaporated to produce a concentrated ethanol extract residue (523 g). The crude ethanol extract was suspended in a 4:1 ethanol:water mixture and partitioned with each substance to obtain the crude

extracts of *n*-hexane (128 g), EtOAc (35.7 g), and *n*-butanol (13.1 g). The *n*-hexane crude extract was separated by vacuum-liquid chromatography (VLC) on silica G_{60} eluting with *n*-hexane:EtOAc:MeOH (100:0–0:100, 10% v/v) to produce seven fractions (A-G). Fraction C (16.2 g) was further separated by VLC on silica G_{60} and eluted with *n*-hexane:EtOAc (100:0–50:50, 10% v/v) to yield four subfractions (C1-C4). Subfraction C2 (1.28 g) was subjected to column chromatography (CC) on silica gel (230–400 mesh) eluted with *n*-hexane:EtOAc (100:0–80:20, 1% v/v) to produce four subfractions (C2A-C2D). Subfraction C2B (160.8 mg) was further purified with CC over silica gel (230–400 mesh) eluted with *n*-hexane:EtOAc (8:2) to give compound **1** (13.2 mg). Subfraction C2C (562.8 mg) was further separated with CC over silica gel (230–400 mesh) eluted with *n*-hexane:EtOAc (90:10, v/v) to yield five subfractions (C2C1-C2C5). Subfraction C2C2 (243.8 mg) was purified by CC over silica gel (230–400 mesh) eluted with *n*-hexane: EtOAc (85:15, v/v) to yield compound **2** (113.3 mg). In addition, subfraction C4 (12.7 g) was separated using CC on silica gel (70–230 mesh) and eluted with *n*-hexane: EtOAc (100:0–30:70, 2% v/v) to generate ten subfractions (C4A-C4J). Subfraction C4E (2.4 g), which was separated by CC over silica gel (230–400 mesh) and eluted with *n*-hexane: EtOAc (80:20, v/v) to give four subfractions (C4E1-C4E4). Subfraction C4E2 (276.3 mg) was separated using CC silica gel (230–400 mesh) and an isocratic mixture of *n*-hexane, chloroform, and EtOAc (50:40:10, v/v) to give compound **3** (15.5 mg). Subfraction C4E2D (83 mg) was purified by reverse-phase CC on ODS eluted with MeOH: water (80:20, v/v) to give compound **4** (5.3 mg). Subfraction C4E2E (26.7 mg) was purified by CC over silica gel (230–400 mesh) *via* an isocratic mixture of *n*-hexane:chloroform:EtOAc to yield **5** (10.2 mg).

(20*S*)-20-hydroxydammar-24-en-3-one (1). White crystal, m.p. 166–168 °C, IR ν_{max} (cm^{-1}): 3448, 2955, 1704, 1378, 1018. ^{1}H-NMR ($CDCl_3$, 500 MHz) and ^{13}C-NMR spectral data ($CDCl_3$, 125 MHz) are shown in Table 1. HR-TOFMS *m/z* found at 443.3817 $[M+H]^+$ (calculated for $C_{30}H_{51}O_2$, *m/z* = 443.3811).

Table 1. The summary result of NMR signal of (20*S*)-20-hydroxydammar-24-en-3-one (**1**) in $CDCl_3$ (δ in ppm, 500 MHz for ^{1}H and 125 MHz ^{13}C-NMR)

Position	^{13}C-NMR	^{1}H-NMR (ΣH, mult., *J*)	COSY	HMQC	HMBC
1	39.90	1.86 (2H, m)	H2	C1	-
2	34.10	2.37-2.42 (2H, m)	H1	C2	-
3	218.00	-	-	-	-
4	47.40	-	-	-	-
5	55.40	1.32 (1H, m)	H6	C5	-
6	19.70	1.49 (1H, dd, 6.5, 2.4), 1.40 (1H, d, 6.5)	H5/H7	C6	-
7	34.60	1.50 (1H, dd, 7.0, 2.5), 1.26 (1H, d, 7.0)	H6	C7	-
8	40.30	-	-	-	-
9	50.00	1.36 (1H, dd, 9.2, 2.7)	-	C9	-
10	36.80	-	-	-	-
11	22.00	1.45 (1H, dd, 8.5, 2.5), 1.25 (1H, d, 8.5)	H12	C11	-
12	27.50	1.79 (1H, d, 7.9), 1.23 (1H, dd, 7.9, 1.4)	H11/H13	C12	-
13	42.40	1.60 (1H, m)	H12	C13	-
14	50.30	-	-	-	-
15	31.20	1.40 (1H, ddd, 8.2, 6.6, 2.0), 1.03 (1H, dd, 6.6, 2.0)	H16	C15	-
16	24.80	1.69 (1H, dd, 7.0, 4.2), 1.44 (1H, d, 7.0)	H15/H17	C16	-
17	49.80	1.68 (1H, ddd, 9.1, 5.6, 2.1)	H16	C17	-
18	15.20	0.93 (3H, s)	-	C18	C7, C8, C9
19	16.00	0.88 (3H, s)	-	C19	C1, C5, C9, C10
20	75.40	-	-	-	-

Position	^{13}C-NMR	^{1}H-NMR (ΣH, mult., *J*)	COSY	HMQC	HMBC
21	25.50	1.08 (3H, s)	-	C21	C17, C20, C22
22	40.50	1.42 (2H, m)	H23	C22	C24
23	22.60	1.99 (2H, m)	H22/H24	C23	-
24	124.70	5.05 (1H, t, 6.1)	H23	C24	-
25	131.60	-	-	-	-
26	25.70	1.62 (3H, s)	-	C26	C24, C25
27	17.70	1.56 (3H, s)	-	C27	C24, C25
28	26.70	1.01 (3H, s	-	C28	C3, C4, C5
29	21.00	0.97 (3H, s)	-	C29	C3, C4, C5
30	16.40	0.82 (3H, s)	-	C30	C8, C13, C14, C15

Table 2. The summary result of the NMR signal of cabraleone (**2**) in $CDCl_3$ (δ in ppm, 500 MHz for ^{1}H and 125 MHz ^{13}C-NMR)

Position	^{13}C-NMR	^{1}H-NMR (ΣH, mult., *J*)	COSY	HMQC	HMBC
1	39.90	1.88 (1H, dd, 7.8, 2.4), 1.41 (1H, d, 7.8)	H2	C1	-
2	34.10	2.41 (2H, ddd, 6.5, 3.2, 1.6)	H1	C2	-
3	218.00	-	-	-	-
4	47.40	-	-	-	-
5	55.30	1.33 (1H, m)	H6	C5	-
6	19.70	1.50 (1H, dd, 8.2, 4.2), 1.41 (1H, d, 8.2)	H5/H7	C6	-
7	34.60	1.52 (1H, d, 6.5), 1.26 (1H, dd, 6.5, 2.1)	H6	C7	-
8	40.30	-	-	-	-
9	50.20	1.38 (1H, m)	-	C9	-
10	36.90	-	-	-	-
11	22.30	1.47 (1H, m), 1.21 (1H, m)	H12	C11	-
12	27.00	0.99 (2H, m)	H11/H13	C12	-
13	43.00	1.63 (1H, m)	H12	C13	-
14	50.00	-	-	-	-
15	31.40	1.43 (1H, m), 1.04 (1H, m)	H16	C15	-
16	25.80	1.74 (2H, m)	H15/H17	C16	-
17	49.80	1.82 (1H, m)	H16	C17	-
18	15.20	0.94 (3H, s)	-	C18	C7, C8, C9
19	16.10	0.88 (3H, s)	-	C19	C1, C5, C9, C10
20	86.50	-	-	-	-
21	27.10	1.09 (3H, s)	-	C21	C17, C20, C22
22	34.80	1.83 (1H, m), 1.62 (1H, m)	H23	C22	-
23	26.40	1.81 (2H, m)	H22/H24	C23	-
24	86.40	3.57 (1H, dd, 4.6, 9.4)	H23	C24	-
25	70.30	-	-	-	-
26	27.80	1.13 (3H, s)	-	C26	C24, C25
27	24.10	1.05 (3H, s)	-	C27	C24, C25
28	26.80	1.02 (3H, s)	-	C28	C3, C4, C5
29	21.00	0.97 (3H, s)	-	C29	C3, C4, C5
30	16.30	0.82 (3H, s)	-	C30	C8, C13, C14, C15

Cabraleone (2). Colorless needle crystal, m.p. 160–161 °C, IR ν_{max} (cm^{-1}): 3584, 2964, 1708, 1386, 1369, 1058; ^{1}H-NMR ($CDCl_3$, 500 MHz) and ^{13}C-NMR spectral data ($CDCl_3$, 125 MHz) are shown in Table 2. HR-TOFMS *m/z* found at 459.3838 $[M+H]^+$ (calculated for $C_{30}H_{51}O_3$, *m/z* = 459.3838).

Cabralealactone (3). Colorless crystal, m.p. 157–159 °C, IR ν_{max} (cm^{-1}): 2972, 1755, 1704, 1386, 1376, 1084. ^{1}H-NMR, δ_H (ppm): 1.78 (1H, dd, *J* = 7.8, 2.5 Hz, H-1a), 1.42 (1H, d, *J* = 7.8 Hz, H-1b), 2.57 (1H, dd, *J* = 8.5, 3.0 Hz, H-2a), 2.44 (1H, dd, *J* = 8.5, 4.2 Hz, H-2b), 1.32 (1H, t, *J* = 6.3 Hz, H-5), 1.57 (1H, ddd, *J* = 7.5, 6.3, 2.8 Hz, H-6a), 1.51 (1H, dd, *J* = 6.3, 2.8 Hz, H-6b), 1.52 (1H, dd, *J* = 9.0, 2.8 Hz, H-7a), 1.31 (1H, d, *J* = 9.0 Hz, H-7b), 1.46 (1H, d, *J* = 5.6 Hz, H-9), 1.42 (1H, dd, *J* = 8.5, 2.7 Hz, H-11a), 1.13 (1H, ddd, *J* = 8.5, 4.5, 2.7 Hz, H-11b), 1.96 (1H, dd, *J* = 4.5, 2.7 Hz, H-12a), 1.27 (1H, ddd, *J* = 7.8, 4.5, 2.7 Hz, H-12b), 1.57 (1H, dd, *J* = 4.5, 2.0 Hz, H-13), 1.51 (1H, ddd, *J* = 6.0, 4.5, 2.4 Hz, H-15a), 1.15 (1H, dd, *J* = 4.5, 2.4 Hz, H-15b), 1.86 (1H, dd, *J* = 7.0, 2.6 Hz, H-16a), 1.25 (1H, d, *J* = 7.0 Hz, H-16b), 1.17 (1H, dd, *J* = 5.6, 2.4 Hz, H-17), 0.94 (3H, s, Me-18), 1.00 (3H, s, Me-19), 1.37 (3H, s, Me-21), 2.14 (1H, m, H-22a), 1.90 (1H, m, H-22b), 2.65 (1H, m, H-23a), 2.51 (1H, m, H-23b), 1.08 (3H, s, Me-28), 1.04 (3H, s, Me-29), 0.90 (3H, s, Me-30); ^{13}C-NMR spectral data ($CDCl_3$, 125 MHz) are shown in Table 3. HR-TOFMS *m/z* found at 415.3229 $[M+H]^+$, (calculated for $C_{27}H_{43}O_3$, *m/z* = 415.3212).

Eichlerianic acid (4). White crystal, m.p. 165–167 °C, IR ν_{max} (cm^{-1}): 3421, 2968, 1704, 1376, 1260. ^{1}H-NMR: δ_H (ppm): 1.97 (1H, ddd, *J* = 8.5, 6.0, 3.5 Hz, H-1a), 1.53 (1H, dd, *J* = 6.0, 3.5 Hz, H-1b), 2.39 (1H, dd, *J* = 7.8, 3.5 Hz, H-2a), 2.18 (1H, ddd, *J* = 7.8, 6.2, 3.5 Hz, H-2b), 1.96 (1H, dd, *J* = 8.1, 5.6 Hz, H-5), 1.87 (2H, d, *J* = 5.6 Hz, H-6), 1.35 (2H, dd, *J* = 6.8, 5.6 Hz, H-7), 1.45 (1H, dd, *J* = 6.4, 3.2 Hz, H-9), 1.41 (2H, d, *J* = 6.4 Hz, H-11), 1.62 (1H, dd, *J* = 7.3, 4.0 Hz, H-13), 1.43 (2H, dd, *J* = 8.2, 3.5 Hz, H-15), 1.78 (2H, dd, *J* = 7.8, 3.5 Hz, H-16), 1.81 (1H, ddd, *J* = 7.8, 3.5, 2.1 Hz, H-17), 0.89 (3H, s, Me-18), 0.86 (3H, s, Me-19), 1.15 (3H, s, Me-21), 1.54 (2H, d, *J* = 6.4 Hz, H-22), 1.86 (2H, d, *J* = 6.4 Hz, H-23), 3.64 (1H, d, *J* = 5.5 Hz, H-24), 1.20 (3H, s, Me-26), 1.12 (3H, s, Me-27), 4.85 (1H, s, H-28a), 4.66 (1H, s, H-28b), 1.73 (3H, s, Me-29), 1.02 (3H, s, Me-30); ^{13}C-NMR spectral data are shown in Table 3. HR-TOFMS *m/z* found at 475.3793 $[M+H]^+$, (calculated for $C_{30}H_{50}O_4$, *m/z* = 475.3787).

Table 3. NMR data of compounds **3–5*** in $CDCl_3$ (δ in ppm, 125 MHz ^{13}C-NMR)

Position of Carbon	**3** δ_C	**4** δ_C	**5** δ_C
1	39.90	34.30	39.00
2	34.10	28.20	27.50
3	218.00	179.30	78.90
4	47.40	147.50	38.90
5	55.30	50.80	55.80
6	19.60	24.60	18.30
7	34.60	33.90	35.20
8	40.30	40.00	40.40
9	50.20	41.20	50.60
10	36.90	39.10	37.10
11	21.90	22.30	21.50
12	31.00	26.90	24.90
13	43.30	42.90	42.40
14	50.10	50.40	50.30
15	31.20	31.50	31.20
16	26.80	25.80	27.50
17	49.20	49.70	50.10
18	16.10	16.30	15.50
19	15.20	20.20	16.20
20	90.00	86.60	75.10
21	25.50	27.20	25.40
22	25.00	34.70	36.60
23	29.20	26.40	29.20
24	176.70	86.40	76.50
25	-	70.30	147.70
26	-	27.90	110.90
27	-	23.20	17.80
28	26.80	113.50	28.00
29	21.00	24.00	15.40
30	16.00	15.30	16.50

(+)-Fouquierol (5). White colorless crystals, m.p. 147–149 °C, IR ν_{max} (cm^{-1}): 3422, 2945, 1708, 1635, 1376, 1084. ^{1}H-NMR, δ_H (ppm): 1.68 (1H, ddd, *J* = 6.0, 4.5, 2.8 Hz, H-1a), 1.03 (1H, dd, *J* = 4.5, 2.8 Hz, H-1b), 1.65 (1H, ddd, *J* = 7.8, 4.5, 3.4 Hz, H-2a), 1.57 (1H, dd, *J* = 4.5, 3.4 Hz, H-2b), 3.20 (1H, dd, *J* = 6.4, 4.5 Hz, H-3), 0.74 (1H, ddd, *J* = 7.8, 6.4, 2.6 Hz, H-5), 1.54 (1H, ddd, *J* = 7.8, 5.8, 2.5 Hz, H-6a), 1.45 (1H, dd, *J* = 5.8, 2.5 Hz, H-6b), 1.52

(1H, dd, *J* = 6.8, 2.5 Hz, H-7a), 1.29 (1H, d, *J* = 6.8 Hz, H-7b), 1.33 (1H, dd, *J* = 8.5, 4.8 Hz, H-9), 1.49 (1H, ddd, *J* = 9.2, 4.8, 3.4 Hz, H-11a), 1.26 (1H, dd, *J* = 4.8, 3.4 Hz, H-11b), 1.68 (1H, ddd, *J* = 7.9, 4.8, 3.4 Hz, H-12a), 1.46 (1H, dd, *J* = 4.8, 3.4 Hz, H-12b), 1.68 (1H, dd, *J* = 4.8, 1.8 Hz, H-13), 1.46 (1H, ddd, *J* = 8.0, 5.6, 3.2 Hz, H-15a), 1.08 (1H, dd, *J* = 5.6, 3.2 Hz, H-15b), 1.65 (1H, dd, *J* = 6.7, 3.2 Hz, H-16a), 1.57 (1H, ddd, *J* = 7.8, 6.7, 3.2 Hz, H-16b), 1.66 (1H, dd, *J* = 6.7, 3.2 Hz, H-17), 0.96 (3H, s, Me-18), 0.84 (3H, s, Me-19), 1.15 (3H, s, Me-21), 1.47 (1H, d, *J* = 8.9 Hz, H-22a), 1.29 (1H, dd, *J* = 8.9, 4.1 Hz, H-22b), 1.29 (2H, d, *J* = 8.9 Hz, H-23), 4.04 (1H, t, *J* = 6.1 Hz, H-24), 4.96 (1H, s, H-26a), 4.84 (1H, s, H-26b), 1.74 (3H, s, Me-27), 0.97 (3H, s, Me-28), 0.77 (3H, s, Me-29), 0.88 (3H, s, Me-30); ^{13}C-NMR spectral data are shown in Table 3. HR-TOFMS *m/z* found at 483.3823 $[M+Na]^+$ (calculated for $C_{30}H_{52}O_3Na$, *m/z* = 483.3814).

Cytotoxic activity test by Presto Blue assay

Using the Presto Blue cell viability assay, the cytotoxic effect of compounds against A549 lung cancer cells was evaluated. This technique was formerly described by Hutagaol et al. [35]. Cells were cultivated in 96-well microliter plates at a density of 1.7×10^4 cells per well for 24 h in RPMI 1640 media supplemented with 10% (v/v) FBS and 1 L/mL antibiotics. The compounds were introduced to the wells after 24 h. Viability was determined after 96 h by observing the metabolic conversion reduction of resazurin substrate into the pink fluorescent resorufin product produced by viable cells. Using a multimode reader, the Presto Blue assay results were read at 570 nm and the reference at 600 nm. The following concentrations of each compound were tested in DMSO: 3.91, 7.81, 15.63, 31.25, 62.50, 125.00, 250.00, and 500.00 g/mL, with a final concentration of 2% in each well: 3.91, 7.81, 15.63, 31.25, 62.50, 125.00, 250.00, and 500.00 g/mL. Using the linear regression method in Microsoft Excel, IC_{50} values were calculated following two parallel experiments of each compound concentration. Doxorubicin served as the positive experimental control in this study.

■ RESULTS AND DISCUSSION

Five triterpenoid compounds (Fig. 1) were obtained by separating and purifying the *n*-hexane extract from the stem bark of *A. cucullata* using the column chromatography technique.

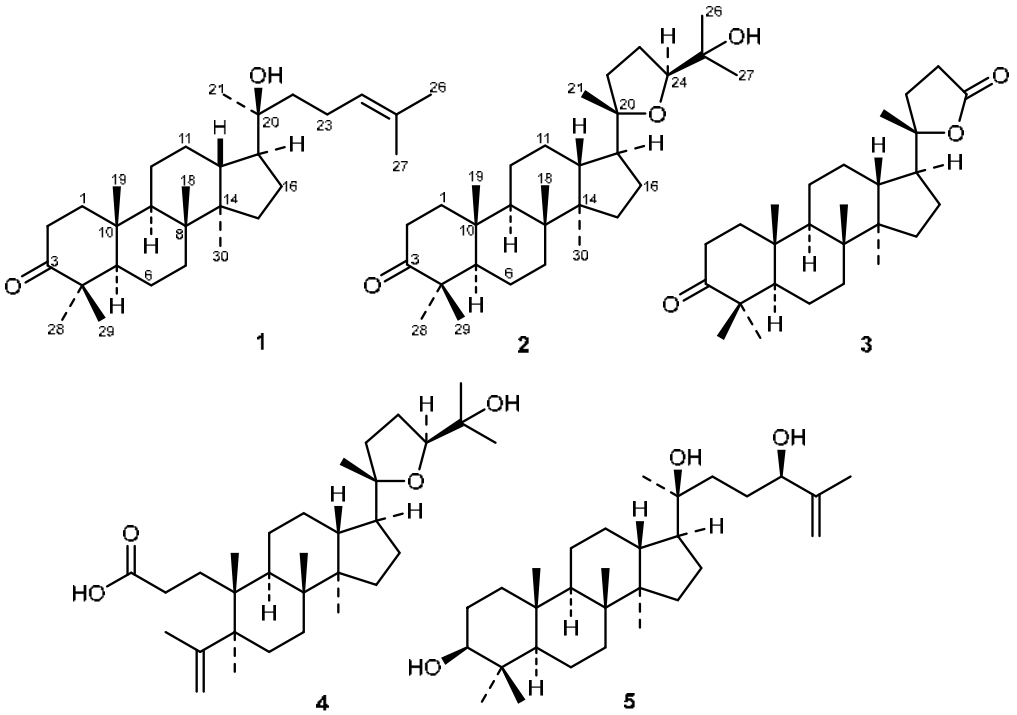

Fig 1. Structures of triterpenoids **1–5**

Compound **1** was isolated as a colorless white crystal. The molecular formula of **1** was determined on HR-TOF-ESI-MS, giving a molecular formula of $C_{30}H_{50}O_2$ (Fig. S1) with *m/z* = 443.3817 as $[M+H]^+$ (calculated *m/z* for $C_{30}H_{51}O_2$ 443.3811), corresponding to six degrees of unsaturation. The IR spectrum (Fig. S2) displayed the existence of hydroxyl (3448 cm^{-1}), aliphatic C–H sp^3 (2955 cm^{-1}), carbonyl (1704 cm^{-1}), ether (1018 cm^{-1}), and *gem*-dimethyl (1378 cm^{-1}) functionalities. The ^{1}H-NMR spectrum (Fig. S3) showed the presence of eight methyls singlet at δ_H/ppm 0.82 (CH_3-30), 0.87 (CH_3-19), 0.93 (CH_3-18), 0.97 (CH_3-29), 1.01 (CH_3-28), 1.08 (CH_3-21), 1.56 (CH_3-27), and 1.62 (CH_3-26), and an olefinic methine at δ_H/ppm 5.05 (1H, t, *J* = 5.0 Hz, H-24). Thirty carbons were revealed through ^{13}C-NMR (Fig. S4) and DEPT (Fig. S5) experiments, which were classified as eight methyls at δ_C/ppm 15.2 (C-18), 16.0 (C-19), 16.4 (C-30), 17.7 (C-27), 21.0 (C-29), 25.5 (C-21), 25.7 (C-26), and 26.7 (C-28), ten methylenes at δ_C/ppm 19.7 (C-6), 22.0 (C-11), 22.6 (C-23), 24.8 (C-16), 27.5 (C-12), 31.2 (C-15), 34.1 (C-2), 34.6 (C-7), 39.9 (C-1), and 40.5 (C-22), four methines (including one sp^2) at δ_C/ppm 124.7 (C-24), 42.4 (C-13), 49.8 (C-17), 50.0 (C-9), and 55.4 (C-5), six quaternary carbons (with two of them are one sp^2 and one oxygenated sp^3 carbons) at δ_C/ppm 131.6 (C-25), 75.4 (C-20), 36.8 (C-10), 40.3 (C-8), 47.4 (C-4), and 50.3 (C-14), and one carbonyl carbon at δ_C/ppm 218.0 (C-3). In the HSQC spectrum data (Fig. S6) presented in Table 1, the proton signals were connected directly to their carbon atoms. The existence of two unsaturated degrees in the primary data indicated that compound **1** was a triterpenoid with a tetracyclic structure. This hypothesis was strengthened by the presence of four aliphatic quaternary carbons devoid of oxygen. The planar structure of **1** was analyzed through the 2D NMR spectra. The ^{1}H-^{1}H COSY spectrum of **1** (Fig. S7) revealed key coupling relationships of H_1/H_2, $H_5/H_6/H_7$, $H_9/H_{11}/H_{12}/H_{13}/H_{17}$, $H_{15}/H_{16}/H_{17}$, $H_{22}/H_{23}/H_{24}$, together with the HMBC correlations (Fig. S8a and S8b) from CH_3-18 to C-7, C-8, C-9; CH_3-19 to C-1, C-5, C-9, C-10; CH_3-30 to C-8, C-13, C-14, C-15; CH_3-28/CH_3-29 to C-3, C-4, C-5, showing that **1** possessed a tetracyclic of the dammarane-type skeleton with the presence of carbonyl at C-3. Furthermore, the hydroxyl attachment at C-20 and olefinic group at C-24/25 in the side chain of **1** was deduced by correlations of CH_3-21 to C-17, C-20, H-22 to C-20, CH_3-26/CH_3-27 to C-24, C-25, and H-22 to C-24. Compound **1** showed δ_C/ppm 75.4 (C-20), 25.5 (C-21), and 40.5 (C-22), which is identical to the 20*S* [43]. Additional analysis and a review of the literature confirmed that compound **1** was (20*S*)-20-hydroxydammar-24-en-3-one compared to those previously reported [44], which was at first isolated from the genus of *Aglaia*.

Compound **2** was acquired as a colorless needle crystal. The molecular formula of **2** was determined as $C_{30}H_{50}O_3$ with six degrees of unsaturation by the analysis of its positive HR-TOF-ESI-MS (Fig. S9) *m/z* = 459.3838 as $[M+H]^+$, calculated for $C_{30}H_{51}O_3$ *m/z* = 459.3838. The IR spectrum (Fig. S10) presented the existence of hydroxyl (3584 cm^{-1}), aliphatic C-H sp^3 (2964 cm^{-1}), carbonyl (1708 cm^{-1}), ether (1058 cm^{-1}), and *gem*-dimethyl (1386 and 1369 cm^{-1}) groups. The ^{1}H-NMR spectrum (Fig. S11) showed the existence of eight methyls singlet at δ_H/ppm 0.82 (CH_3-30), 0.88 (CH_3-19), 0.94 (CH_3-18), 1.01 (CH_3-28), 1.05 (CH_3-27), 1.08 (CH_3-21), and 1.12 (CH_3-26), and one oxygenated methine at δH/ppm 3.57 (1H, dd, *J* = 5.0, 10.0 Hz, H-24). The ^{13}C-NMR (Fig. S12) and DEPT 135° (Fig. S13) spectra of **2** exhibited 30 carbon resonances, including eight methyls at δ_C/ppm 15.2 (C-18), 16.1 (C-19), 16.3 (C-20), 21.0 (C-29), 24.1 (C-27), 26.8 (C-28), 27.1 (C-21), and 27.8 (C-26), ten methylenes at δ_C/ppm 19.7 (C-6), 22.3 (C-11), 25.8 (C-16), 26.4 (C-23), 27.0 (C-12), 31.4 (C-15), 34.1 (C-2), 34.6 (C-7), 34.8 (C-22), and 39.9 (C-1), five methines sp^3 (involving one oxygenated) at δ_C/ppm 86.4 (C-24), 43.0 (C-13), 49.8 (C-17), 50.2 (C-9), and 55.3 (C-5), six quaternary carbons sp^3 (with two of them are oxygenated carbons) at δ_C/ppm 70.3 (C-25), 86.5 (C-20), 36.9 (C-10), 40.3 (C-8), 47.4 (C-4), and one carbonyl carbon at δ_C/ppm 218.0 (C-3). The above data possessed two degrees of unsaturation (one ketone carbonyl and one cyclic by a tetrahydrofuran moiety [45]), indicating four tetracyclic of a triterpenoid framework. The ^{1}H-^{1}H COSY (Fig. S15) correlations of H_1/H_2, $H_5/H_6/H_7$, $H_9/H_{11}/H_{12}/H_{13}/H_{17}$, $H_{15}/H_{16}/H_{17}$ allowed the structural skeleton that is dammarane typed. The HMBC spectrum

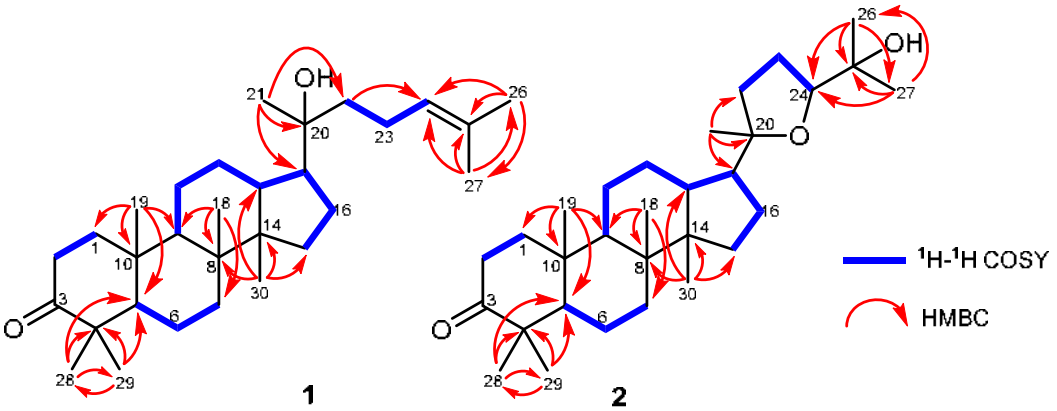

Fig 2. Selected HMBC and ^{1}H-^{1}H COSY correlations of compounds **1** and **2**

(Fig. S16), shows strong correlations (Fig. 2) from CH_3-18 to C-7, C-8, C-9; CH_3-19 to C-1, C-5, C-9, C-10; CH_3-30 to C-8, C-13, C-14, C-15; and CH_3-28/ CH_3-29 to C-3, C-4, C-5 proved the presence of a tetracyclic dammarane-type, as well as the ketonic group positioned at C-3 in **2**. Furthermore, the tetrahydrofuran form in the side chain of **2** was determined through the correlations of CH_3-21 to C-17, C-20, C-22, and CH_3-26/CH_3-27 to C-24, C-25, together with ^{1}H-^{1}H COSY correlations of H_{22}/H_{23}/H_{24} as demonstrated in Fig. 2. Compound **2** provided the chemical shifts of [δ_C/ppm 86.4 (C-24), δ_H/ppm 3.57 (1H, dd, J = 5.0, 10.0, H-24)] and [δ_C/ppm 86.5 (C-20)], referencing to the 20*S* and 24*S* orientations [45-46]. The NMR data comparison of compound **2** with the literature [47] revealed that **2** was cabraleone or 20*S*,24*S*-epoxy-25-hydroxydammar-3-one, which was isolated from *A. cucullata* for the first time.

Compound **3** was obtained as a colorless crystal. The molecular formula of **3** was verified as $C_{27}H_{42}O_3$ based on HR-TOF-ESI-MS (Fig. S17) m/z = 415.3229 as $[M+H]^+$, calculated for $C_{27}H_{43}O_3$ m/z = 415.3212, which described seven degrees of unsaturation. The IR spectrum (Fig. S18) displayed the existence of aliphatic C-H sp^3 (2972 cm^{-1}), carbonyl ester (1755 cm^{-1}), carbonyl ketone (1704 cm^{-1}), *gem*-dimethyl (1386 and 1376 cm^{-1}), and ether group (1084 cm^{-1}). The ^{1}H-NMR spectrum (Fig. S19) showed the presence of six methyls singlet at δH/ppm 0.90 (CH_3-30), 0.94 (CH_3-18), 1.00 (CH_3-19), 1.04 (CH_3-29), 1.08 (CH_3-28), and 1.37 (CH_3-21). These data implied that the oxidative degradation of two side chain methyl groups led to the γ-lactone moiety, resulting in the formation of tris *nor*-triterpenoid compound [48]. The ^{13}C-NMR (Fig. S20) and DEPT 135° (Fig. S21) of **3** exhibited of 27 carbons, assignable to six methyls at δ_C/ppm 15.2 (C-19), 16.0 (C-30), 16.2 (C-18), 21.0 (C-29), 25.5 (C-21), and 26.7 (C-28), 10 methylenes at δ_C/ppm 19.6 (C-6), 21.9 (C-11), 25.0 (C-22), 26.8 (C-16), 29.2 (C-23), 31.0 (C-12), 31.2 (C-15), 34.1 (C-2), 34.5 (C-7), and 39.9 (C-1), four methines sp^3 at δ_C/ppm 43.3 (C-13), 49.3 (C-17), 49.9 (C-9), and 55.3 (C-5), five quaternary carbons sp^3 (including one oxygenated carbon) at δ_C/ppm 90.1 (C-20), 36.8 (C-10), 40.3 (C-8), 47.4 (C-12), and 50.1 (C-14), one carbonyl ester carbon at δ_C/ppm 176.8 (C-24), and one carbonyl ketone carbon at δ_C/ppm 218.0 (C-3). Based on the ^{1}H-NMR, ^{13}C-NMR, DEPT 135° spectra, corresponding to the literature [49], compound **3** was established as the known compound cabralealactone, which was isolated for the first time in the *A. cucullata*.

Compound **4** was isolated as a white crystal. The molecular formula of **4** was determined on HR-TOF-ESI-MS, giving a molecular formula of $C_{30}H_{50}O_4$ (Fig. S22) with m/z 475.3793 $[M+H]^+$ (calculated m/z of $C_{30}H_{51}O_4$ = 475.3787), which revealed six degrees of unsaturation. The IR spectrum (Fig. S23) displayed the existence of hydroxyl (3421 cm^{-1}), aliphatic C-H sp^3 (2968 cm^{-1}), carbonyl ketone (1704 cm^{-1}), *gem*-dimethyl (1376 cm^{-1}), and ether group (1260 cm^{-1}). The ^{1}H-NMR spectrum (Fig. S24) showed the presence of seven methyls singlet at δ_H/ppm 0.86 (CH_3-19), 0.89 (CH_3-18), 1.02 (CH_3-30), 1.12 (CH_3-27), 1.15 (CH_3-21), 1.20 (CH_3-

26), and 1.73 (CH_3-19). The presence of one oxygenated methine in the tetrahydrofuran ring at δ_H/ppm 3.64 (1H, dd, J = 5.5, 9.5 Hz, H-24), and one methylene sp^2 at [δ_H/ppm 4.85 (1H, s, H-28a), 4.66 (1H, s, H-28b)], which are characteristic for a *seco*-dammarane triterpenoid [50]. Compound **4** possessed 30 carbons (Fig. S25 and S26), corresponding to seven methyls at δ_C/ppm 15.3 (C-30), 16.3 (C-18), 20.2 (C-19), 23.2 (C-27), 24.0 (C-29), 27.2 (C-21), and 27.9 (C-26), 11 methylenes (including one sp^2) at δ_C/ppm 113.5 (C-28), 22.3 (C-11), 24.6 (C-6), 25.8 (C-16), 26.4 (C-23), 26.9 (C-12), 28.2 (C-2), 31.5 (C-15), 33.9 (C-7), 34.3 (C-1), and 34.7 (C-22), five methines sp^3 (involving one oxygenated) at δ_C/ppm 86.4 (C-24), 41.2 (C-9), 42.9 (C-13), 49.7 (C-17), and 50.8 (C-5), six quaternary carbons (including one olefinic and two oxygenated) at δ_C/ppm 147.5 (C-4), 70.3 (C-25), 86.6 (C-20), 39.1 (C-10), 40.0 (C-8), and 50.4 (C-14), and one carbonyl of carboxylic acid at δ_C/ppm 179.8 (C-3). Based on the ^{1}H-NMR, ^{13}C-NMR, DEPT 135° spectra, which well-matched with the literature [50], compound **4** was confirmed as the known compound eichlerianic acid, which was isolated for the first time in the *A. cucullata*.

Compound **5** was isolated as a colorless white crystal. Its molecular formula was determined as $C_{30}H_{52}O_3$ with six degrees of unsaturation by the analysis of its positive HR-TOF-ESI-MS (Fig. S27) m/z = 483.3823 as $[M+Na]^+$, calculated for $C_{30}H_{52}O_3Na$ m/z = 483.3814. The IR spectrum (Fig. S28) displayed the existence of hydroxyl (3422 cm^{-1}), aliphatic C-H sp^3 (2945 cm^{-1}), carbonyl ketone (1708 cm^{-1}), olefinic (1635 cm^{-1}), *gem*-dimethyl (1376 cm^{-1}), and ether group (1084 cm^{-1}). The ^{1}H-NMR spectrum (Fig. S29) showed the presence of seven methyls singlet at δ_H/ppm 0.77 (CH_3-29), 0.84 (CH_3-19), 0.88 (CH_3-30), 0.96 (CH_3-18), 0.97 (CH_3-28), 1.15 (CH_3-21), and 1.73 (CH_3-27), two oxygenated methines at δ_H/ppm 3.20 (1H, m, H-3), and 4.04 (1H, t, J = 6.1 Hz, H-24), and one methylene sp^2 at [δ_H/ppm 4.96 (1H, s, H-27a), 4.84 (1H, s, H-27b)]. The ^{13}C-NMR (Fig. S30) and DEPT 135° (Fig. S31) spectra of **5** revealed 30 carbon resonances, including seven methyls at δ_C/ppm 15.4 (C-29), 15.5 (C-18), 16.2 (C-19), 16.5 (C-30), 17.8 (C-27), 25.4 (C-21), and 28.0 (C-28), 11 methylenes (involving one olefinic sp^2) at δ_C/ppm 110.9 (C-26), 18.3 (C-6), 21.5 (C-11), 24.9 (C-12), 27.4 (C-2), 27.5 (C-16), 29.2 (C-23), 31.2 (C-15), 35.2 (C-7), 36.6 (C-22), and 39.0 (C-1), six methines sp^3 (including two oxygenated) at δ_C/ppm 76.5 (C-24), 78.9 (C-3), 42.4 (C-13), 50.1 (C-17), 50.6 (C-9), and 55.8 (C-5), six quaternary carbons (including one olefinic sp^2 and one oxygenated sp^3) at δ_C/ppm 147.7 (C-25), 75.1 (C-20), 37.1 (C-10), 38.9 (C-4), 40.4 (C-8), and 50.3 (C-14). Based on the ^{1}H-NMR, ^{13}C-NMR, and DEPT 135° spectra of compound **5** revealed a good fit to the literature [51], compound **5** was confirmed as the known compound (+)-fouquierol, which was isolated for the first time in the Meliaceae family and *Aglaia* genus.

All isolated compounds **1**–**5** were classified as dammarane-type triterpenoids. In *Aglaia* genus, dammarane-type triterpenoids were commonly found. The modification of dammarane-type triterpenoids, including the A ring opening (such as in compound **4**) and formation of epoxide ring at C-20/C-24 (such as in compounds **2** and **4**), also followed by degradation of three carbon atoms in the side chain to give lactone ring (such as in compound **3**), usually can be found in other species of Aglaia genus [45,48]. The cytotoxic activity of the triterpenoids **1**–**5** was assayed against the A549 lung cancer cell (Table 4) using a method previously reported [52-53]. Doxorubicin (1.08 µg/mL) was used as the positive experimental control in this study. Among all triterpenoid compounds, eichlerianic acid (**4**) had the highest cytotoxic activity, whereas (+)-fouquierol (**5**) showed the lowest cytotoxic activity. Compounds **1** (IC_{50} 142.30 µM) and **4** (IC_{50} 32.17 µM) displayed moderate cytotoxic activity, compounds **2** (IC_{50} 316.40 µM) and **3** (IC_{50} 415.43 µM) showed weak cytotoxic activity, and compound **5** (IC_{50} 1747.63 µM) showed no cytotoxic activity [54]. The IC_{50} value implicated that the existence

Table 4. Cytotoxic activity of compounds **1**–**5**

Compounds	IC_{50} (µM)
(20*S*)-20-hydroxydammar-24-en-3-one (**1**)	142.30
Cabraleone (**2**)	316.40
Cabralealactone (**3**)	415.43
Eichlerianic acid (**4**)	32.17
(+)-fouquierol (**5**)	1747.63
Doxorubicin (+)	1.08

of a *seco* ring in compound **4** greatly enhanced its cytotoxic activity compared to compound **2**. Furthermore, compound **1** had stronger cytotoxic activity than compound **5**, demonstrating that the presence of an olefinic terminal with hydroxyl at C-24 in compound **5** reduced its cytotoxic activity. These findings suggest that the *seco* moiety in the A ring and *gem*-dimethyl attached to quaternary carbon sp^2 at the aliphatic side chain structure play several critical structural features in the cytotoxic activity of dammarane-type triterpenoids.

CONCLUSION

The *n*-hexane preparation of *A. cucullata* stems bark produced five dammarane-type triterpenoids, which were identified as (20*S*)-20-hydroxydammar-24-en-3-one (**1**), cabraleone (**2**), cabralealactone (**3**), eichlerianic acid (**4**), and (+)-fouquierol (**5**). Both compounds **1** and **5** were isolated for the first time from the Meliaceae family and the *Aglaia* genus, respectively. Compound **1** was the first compound to be isolated from the *Aglaia* genus. The cytotoxic potential of substances **1** through **5** was investigated using the A549 lung cancer cell type as a test subject. Among the triterpenoids of the dammarane class, Compound **4** exhibited the highest level of activity, whereas Compound **5** exhibited the lowest level. Increased cytotoxicity in the triterpenoid dammarane type can be attributed to the presence of a *seco* component in the A ring as well as *gem*-dimethyl connected to quaternary carbon sp^2 in the aliphatic side chain. Because of this, the identification of these compounds lays the groundwork for the use of triterpenoid dammarane-type compounds as a therapeutic possibility for the treatment of lung cancer. These compounds have the potential to be developed into lead compounds for the treatment of lung cancer.

ACKNOWLEDGMENTS

This study was financially supported by the Ministry of Education and Culture, Innovative and Research Council, Indonesia, Master Thesis Research (PTM) Grant (No. 1318/UN6.3.1/PT.00/2022) and RKDU 2019 by Desi Harneti.

REFERENCES

[1] Shang, Y., and Huang, S., 2019, Multi-omics data-driven investigations of metabolic diversity of plant triterpenoids, *Plant J.*, 97 (1), 101–111.

[2] Chen, Y., Zhou, B., Li, J., Tang, H., Tang, J., and Yang, Z., 2018, Formation and change of chloroplast-located plant metabolites in response to light conditions, *Int. J. Mol. Sci.*, 19 (3), 654.

[3] Zheng, X., Luo, X., Ye, G., Chen, Y., Ji, X., Wen, L., Xu, Y., Xu, H., Zhan, R., and Chen, W., 2015, Characterisation of two oxidosqualene cyclases responsible for triterpenoid biosynthesis in *Ilex asprella*, *Int. J. Mol. Sci.*, 16 (2), 3564–3578.

[4] Ren, Y., and Kinghorn, A.D., 2019, Natural product triterpenoids and their semi-synthetic derivatives with potential anticancer activity, *Planta Med.*, 85 (11/12), 802–814.

[5] Lim, H.J., Bak, S.G., Lim, H.J., Lee, S.W., Lee, S., Ku, S.K., Park, S.I., Lee, S.J., and Rho, M.C., 2020, Acyclic triterpenoid isolated from *Alpinia katsumadai* alleviates formalin-induced chronic mouse paw inflammation by inhibiting the phosphorylation of ERK and NF-κB, *Molecules*, 25 (15), 3345.

[6] Li, J., Ni, G., Li, L., Liu, Y., Mai, Z., Wang, R., and Yu, D., 2019, New iridal-type triterpenoid derivatives with cytotoxic activities from *Belamcanda chinensis*, *Bioorg. Chem.*, 83, 20–28.

[7] An, X., Wang, J., Yu, X., Wu, H., and Liu, W., 2022, Two new polypodane-type bicyclic triterpenoids from mastic, *Open Chem.*, 20 (1), 267–271.

[8] Stonik, V.A., and Kolesnikova, S.A., 2021, Malabaricane and isomalabaricane triterpenoids, including their glycoconjugated forms, *Mar. Drugs*, 19 (6), 327.

[9] Song, M., Chan, G., Lin, L.G., Li, D., Zhang, K., Zhang, X.Q., Ye, W.C., Li, N., and Zhang, Q.W., 2022, Triterpenoids from the fruits of *Melia azedarach* L. and their cytotoxic activities, *Phytochemistry*, 201, 113280.

[10] Saptanti, K., Heliawati, L., Hermawati, E., and Syah, Y.M., 2022, Pentacyclic triterpenes from the leaves

extract of *Sandoricum koetjape*, *J. Nat. Med.*, 76 (4), 842–848.

[11] Wang, Y.R., Yu, Y., Li, S.M., Liu, W., Li, W., Morris-Natschke, S.L., Goto, M., Lee, K.H., and Huang, X.F., 2018, Salvisertin A, a new hexacyclic triterpenoid, and other bioactive terpenes from *Salvia deserta* root, *Chem. Biodiversity*, 15 (4), e1800019.

[12] Ouyang, X.L., Qin, F., Huang, R.Z., Liang, D., Wang, C.G., Wang, H.S., and Liao, Z.X., 2019, NF-κB inhibitory and cytotoxic activities of hexacyclic triterpene acid constituents from *Glechoma longituba*, *Phytomedicine*, 63, 153037.

[13] Teixeira, F.S., Vidigal, S.S.M.P., Pimentel, L.L., Costa, P.T., Tavares-Valente, D., Azevedo-Silva, J., Pintado, M.E., Fernandes, J.C., and Rodríguez-Alcalá, L.M., 2021, Phytosterols and novel triterpenes recovered from industrial fermentation coproducts exert *in vitro* anti-inflammatory activity in macrophages, *Pharmaceuticals*, 14 (6), 583.

[14] Zhang, J., Zhang, Q., Xu, Y., Li, H., Wang, C., Liu, Z., Liu, P., Liu, Y., Meng, Q., Zhao, F., and Zhao, F., 2019, Synthesis and *in vitro* anti-inflammatory activity of C20 epimeric ocotillol-type triterpenes and protopanaxadiol, *Planta Med.*, 85 (4), 292–301.

[15] Muhammad, D., Hubert, J., Lalun, N., Renault, J.H., Bobichon, H., Nour, M., and Voutquenne-Nazabadioko, L., 2015, Isolation of flavonoids and triterpenoids from the fruits of *Alphitonia neocaledonica* and evaluation of their anti-oxidant, antityrosinase and cytotoxic activities, *Phytochem. Anal.*, 26 (2), 137–144.

[16] Oprean, C., Zambori, C., Borcan, F., Soica, C., Zupko, I., Minorics, R., Bojin, F., Ambrus, R., Muntean, D., Danciu, C., Pinzaru, I.A., Dehelean, C., Paunescu, V., and Tanasie, G., 2016, Anti-proliferative and antibacterial *in vitro* evaluation of the polyurethane nanostructures incorporating pentacyclic triterpenes, *Pharm. Biol.*, 54 (11), 2714–2722.

[17] Hisham Shady, N., Youssif, K.A., Sayed, A.M., Belbahri, L., Oszako, T., Hassan, H.M., and Abdelmohsen, U.R., 2021, Sterols and triterpenes: Antiviral potential supported by *in-silico* analysis, *Plants*, 10 (1), 41.

[18] Innocente, A., Casanova, B.B., Klein, F., Lana, A.D., Pereira, D., Muniz, M.N., Sonnet, P., Gosmann, G., Fuentefria, A.M., and Gnoatto, S.C.B., 2014, Synthesis of isosteric triterpenoid derivatives and antifungal activity, *Chem. Biol. Drug Des.*, 83 (3), 344–349.

[19] Nazaruk, J., and Borzym-Kluczyk, M., 2015, The role of triterpenes in the management of diabetes mellitus and its complications, *Phytochem. Rev.*, 14 (4), 675–690.

[20] Xu, G.B., Xiao, Y.H., Zhang, Q.Y., Zhou, M., and Liao, S.G., 2018, Hepatoprotective natural triterpenoids, *Eur. J. Med. Chem.*, 145, 691–716.

[21] Yu, C.X., Wang, R.Y., Qi, F.M., Su, P.J., Yu, Y.F., Li, B., Zhao, Y., Zhi, D.J., Zhang, Z.X., and Fei, D.Q., 2019, Eupulcherol A, a triterpenoid with a new carbon skeleton from: *Euphorbia pulcherrima*, and its anti-Alzheimer's disease bioactivity, *Org. Biomol. Chem.*, 18 (1), 76–80.

[22] Renda, G., Gökkaya, İ., and Şöhretoğlu, D., 2022, Immunomodulatory properties of triterpenes, *Phytochem. Rev.*, 21 (2), 537–563.

[23] Lehbili, M., Alabdul Magid, A., Kabouche, A., Voutquenne-Nazabadioko, L., Abedini, A., Morjani, H., Gangloff, S.C., and Kabouche, Z., 2018, Antibacterial, antioxidant and cytotoxic activities of triterpenes and flavonoids from the aerial parts of *Salvia barrelieri* Etl, *Nat. Prod. Res.*, 32 (22), 2683–2691.

[24] Jang, E., and Lee, J.H., 2021, Promising anticancer activities of alismatis rhizome and its triterpenes via p38 and PI3k/Akt/mTOR signaling pathways, *Nutrients*, 13 (7), 2455.

[25] Nogueira, T.S.R., Passos, M.S., Nascimento, L.P.S., Arantes, M.B.S., Monteiro, N.O., Boeno, S.I.S., de Carvalho Junior, A., Azevedo, O.A., Terra, W.S., Vieira, M.G.C., Braz-Filho, R., and Curcino Vieira, I.J.C., 2020, Chemical compounds and biologic activities: A review of *Cedrela* genus, *Molecules*, 25 (22), 5401.

[26] Hamid, A.A., Aiyelaagbe, O.O., Negi, A.S., Kaneez, F., Luqman, S., Oguntoye, S.O., Kumar, S.B., and Zubair, M., 2018, Isolation and antiproliferative

activity of triterpenoids and fatty acids from the leaves and stem of *Turraea vogelii* Hook. f. ex benth, *Nat. Prod. Res.*, 33 (2), 296–301.

[27] Happi, G.M., Kouam, S.F., Talontsi, F.M., Zühlke, S., Lamshöft, M., and Spiteller, M., 2015, Minor secondary metabolites from the bark of *Entandrophragma congoënse* (Meliaceae), *Fitoterapia*, 102, 35–40.

[28] Saleem, S., Muhammad, G., Hussain, M.A., and Bukhari, S.N.A., 2018, A comprehensive review of phytochemical profile, bioactives for pharmaceuticals, and pharmacological attributes of *Azadirachta indica*, *Phytother. Res.*, 32 (7), 1241–1272.

[29] Hernandez, V., De Leo, M., Cotugno, R., Braca, A., De Tommasi, N., and Severino, L., 2018, New tirucallane-type triterpenoids from *Guarea guidonia*, *Planta Med.*, 84 (9/10), 716–720.

[30] Matsumoto, T., Kitagawa, T., Ohta, T., Yoshida, T., Imahori, D., Teo, S., bin Ahmad, H.S., and Watanabe, T., 2019, Structures of triterpenoids from the leaves of *Lansium domesticum*, *J. Nat. Med.*, 73 (4), 727–734.

[31] Salam, S., Harneti, D., Maharani, R., Nurlelasari, N., Safari, A., Hidayat, A.T., Lesmana, R., Nafiah, M.A., Supratman, U., Kyle Prescott, T.A., and Shiono, Y., 2021, Cytotoxic triterpenoids from *Chisocheton pentandrus*, *Phytochemistry*, 187, 112759.

[32] Wang, W., Xia, Z., Tian, Z., Jiang, H., Zhan, Y., Liu, C., Li, C., and Zhou, H., 2020, Chemical constituents from the fruits of *Melia azedarach* (Meliaceae), *Biochem. Syst. Ecol.*, 92, 104094.

[33] Naini, A.A., Mayanti, T., and Supratman, U., 2022, Triterpenoids from *Dysoxylum* genus and their biological activities, *Arch. Pharmacal Res.*, 45 (2), 63–82.

[34] Zhang, L., Xia, J., Duan, Y., Wei, K., Gao, R., Li, D., Liu, X., Zhang, T., and Qiu, M., 2021, Toonamicrocarpavarin, a new tirucallane-type triterpenoid from *Toona ciliata*, *Nat. Prod. Res.*, 35 (2), 266–271.

[35] Hutagaol, R.P., Harneti, D., Safari, A., Hidayat, A.T., Supratman, U., Awang, K., and Shiono, Y., 2021, Cytotoxic triterpenoids from the stem bark of *Aglaia angustifolia*, *J. Asian Nat. Prod. Res.*, 23 (8), 781–788.

[36] Meepol, W., Maxwell, G.S., and Havanond, S., 2020, *Aglaia cucullata*: A little-known mangrove with big potential for research, *ISME/GLOMIS Electron. J.*, 18 (1), 4–9.

[37] Duke, N., Sukardjo, S., and Kathiresan, K., 2010, *Aglaia cucullate*, *The IUCN Red List of Threatened Species*, https://www.iucnredlist.org/species/34364/9856175, Accessed on September 30th, 2022.

[38] Ahmed, F., Toume, K., Sadhu, S.K., Ohtsuki, T., Arai, M.A., and Ishibashi, M., 2010, Constituents of *Amoora cucullata* with TRAIL resistance-overcoming activity, *Org. Biomol. Chem.*, 8 (16), 3696–3703.

[39] Pancharoen, R., Sommeechai, M., Maelim, S., Suanpaga, W., Srichaichana, J., Barber, P., and Dell, B., 2021, Phenology of urban trees in a tropical urban forest in Thailand, *Songklanakarin J. Sci. Technol.*, 43 (1), 87–95.

[40] Chumkaew, P., Kato, S., and Chantrapromma, K., 2006, Potent cytotoxic rocaglamide derivatives from the fruits of *Amoora cucullata*, *Chem. Pharm. Bull.*, 54 (9), 1344–1346.

[41] DeFilipps, R.A., and Krupnick, G.A., 2018, The medicinal plants of Myanmar, *PhytoKeys*, 102, 1–341.

[42] Abdelfattah, M.S., Toume, K., Ahmed, F., Sadhu, S.K., and Ishibashi, M., 2010, Cucullamide, a new putrescine bisamide from *Amoora cucullata*, *Chem. Pharm. Bull.*, 58 (8), 1116–1118.

[43] Wang, K.C., Wang, P.H., and Lee, S.S., 1997, Microbial transformation of protopanaxadiol and protopanaxatriol derivatives with *Mycobacterium* sp. (NRRL B-3805), *J. Nat. Prod.*, 60 (12), 1236–1241.

[44] Asai, T., and Fujimoto, Y., 2011, 2-Acety-1-(3-glycosyloxyoctadecanoyl)glycerol and dammarane triterpenes in the exudates from glandular trichome-like secretory organs on the stipules and leaves of *Cerasus yedoensis*, *Phytochem. Lett.*, 4 (1), 38–42.

[45] Roux, D., Martin, M.T., Adeline, M.T., Sevenet, T., Hadi, A.H.A., and Païs, M., 1998, Foveolins A and

B, dammarane triterpenes from *Aglaia foveolata*, *Phytochemistry*, 49 (6), 1745–1748.

[46] Aalbersberg, W., and Singh, Y., 1991, Dammarane triterpenoids from *Dysoxylum richii*, *Phytochemistry*, 30 (3), 921–926.

[47] Hisham, A., Ajitha Bai, M.D., Fujimoto, Y., Hara, N., and Shimada, H., 1996, Complete ^{1}H and ^{13}C NMR spectral assignment of cabraleadiol, a dammarane triterpene from *Dysoxylum malabaricum* Bedd, *Magn. Reson. Chem.*, 34 (2), 146–150.

[48] Oktaviani, D., Sukmawati, W., Farabi, K., Harneti, D., Nurlelasari, N., Darwati, D., Mahari, R., Mayanti, T., Safari, A., and Supratman, U., 2022, Terpenoids from the stem bark of *Aglaia elaeagnoidea* and their cytotoxic activity against HeLa and DU145 cancer cell lines, *Molekul*, 17 (1), 76–84.

[49] Phongmaykin, J., Kumamoto, T., Ishikawa, T., Suttisri, R., and Saifah, E., 2008, A new sesquiterpene and other terpenoid constituents of *Chisocheton penduliflorus*, *Arch. Pharmacal Res.*, 31 (1), 21–27.

[50] Kamarulzaman, F.A., Mohamad, K., Awang, K., and Lee, H.B., 2014, Chemical constituents of *Aglaia lanuginose*, *Pertanika J. Sci. Technol.*, 22 (1), 163–174.

[51] Ren, Y., Anaya-Eugenio, G.D., Czarnecki, A.A., Ninh, T.N., Yuan, C., Chai, H.B., Soejarto, D.D., Burdette, J.E., de Blanco, E.J.C., and Kinghorn, A.D., 2018, Cytotoxic and NF-κB and mitochondrial transmembrane potential inhibitory pentacyclic triterpenoids from *Syzygium corticosum* and their semi-synthetic derivatives, *Bioorg. Med. Chem.*, 26 (15), 4452–4460.

[52] Boncler, M., Rózalski, M., Krajewska, U., Podsędek, A., and Watala, C., 2014, Comparison of PrestoBlue and MTT assays of cellular viability in the assessment of anti-proliferative effects of plant extracts on human endothelial cells, *J. Pharmacol. Toxicol. Methods*, 69 (1), 9–16.

[53] Xu, M., Mccanna, D.J., and Sivak, J.G., 2015, Use of the viability reagent PrestoBlue in comparison with alamarBlue and MTT to assess the viability of human corneal epithelial cells, *J. Pharmacol. Toxicol. Methods*, 71, 1–7.

[54] Sajjadi, S.E., Ghanadian, M., Haghighi, M., and Mouhebat, L., 2015, Cytotoxic effect of *Cousinia verbascifolia* Bunge against OVCAR-3 and HT-29 cancer cells, *J. HerbMed Pharmacol.*, 4 (1), 15–19.

Effect of Addition of NaCl Salt on Extraction of Essential Oil from Lemongrass Leaves by Microwave Hydro-Distillation Method

Fenni Suryanti, Lailatul Qadariyah, and Mahfud Mahfud*

Department of Chemical Engineering, Faculty of Industrial Technology and Systems Engineering, Institut Teknologi Sepuluh Nopember, Surabaya 60111, Indonesia

* ***Corresponding author:***

email: mahfud@chem-eng.its.ac.id

Received: November 5, 2022
Accepted: February 22, 2023

DOI: 10.22146/ijc.78919

Abstract: *Essential oils are compounds extracted from plants and obtained by distillation. Indonesia has many kinds of plant commodities for essential oil production. Among the essential oils that have not been developed in Indonesia is citronella oil which can be extracted from the lemongrass plant this research, we develop Microwave Hydro-Distillation (MHD) method has several advantages over conventional distillation methods: shorter time, higher oil quality and yield. This research proposes to extract citronella oil from lemongrass leaves using the MHD method using aquadest and NaCl solution addition. Operating variables are extraction time (20–180 min), material size (0.5, 1.0, and 1.5 cm), feed-to-solvent ratio (0.1; 0.15; and 0.2 g/mL), and microwave power (300, 450, and 600 watts). The essential oil results are analyzed by GC-MS analysis, specific gravity, refractive index, and solubility. The results showed that it increased with extraction time followed by almost constant conditions, tended to decrease with increasing feed-to-solvent ratio, and increased yield with increasing microwave power. The results from the GC-MS analysis, the active substance content of geraniol was 46.61% and citronellal 5.62%. Additional salt in this method is a green and clean essential oil extraction.*

Keywords: *extraction; essential oil; lemongrass;* Cymbopogon nardus*; Microwave Hydro-Distillation*

■ INTRODUCTION

The variety of biological nature in Indonesia is famous and very abundant. There are essential oil plants that have not been able to be utilized as a whole. Indonesia has to be able to produce around 80 types of essential oil plants that can be traded in the world. Still, only a few kinds of essential oils can be produced by traditional refiners, including patchouli oil, citronella oil, clove oil, cananga oil, eucalyptus oil, sandalwood oil, fragrant root oil and citrus hystrix oil [1]. Essential oil is a high commodity requirement for perfume industries, cosmetics, pharmaceuticals, and food and beverage [2]. Producing primary and secondary products with price fluctuations resistance in the world trade area is highly valuable. However, essential oil production plants in Indonesia have not been adequately developed yet, so essential oil production cannot meet the quality and quantity requirements [3].

Lemongrass is a valuable plant. One of its usefulness is as an essential oil raw material. This plant is easy to cultivate and a significant opportunity for people who want to develop it [4]. Lemongrass plants have a significant potential to cultivate in Indonesia. Furthermore, Indonesia has this plant very abundant as a raw material. Many provinces in Indonesia produce essential oil, such as Nangroe Aceh Darussalam, Lampung, East Java, and West Java, with a total area of 3.492 hectares [5]. There are 2 kinds of variants of lemongrass leaves cultivated in Java, and one is *Cymbopogon winterianus* which is cultivated at West Java and one more is *Cymbopogon nardus* which is cultivated at East Java. They have different chemical compounds, respectively [6-7].

Essential oil extraction commonly uses a conventional method: water or steam distillation [8]. Essential oils are colorless to slightly yellowish and only

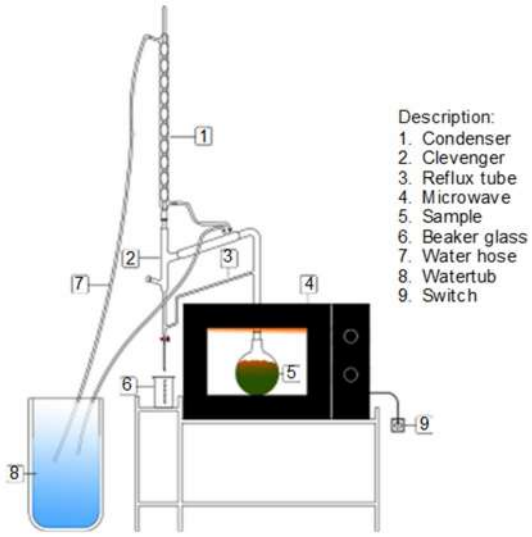

Fig 1. Schematic of MHD method

slightly soluble in water [9]. Extraction of lemongrass essential oil by hydro-distillation is known by people as 7–8 h extraction [10]. Essential oil product handling is also not optimal yet, causing less quality and low prices. The selection of a distillation system based on the leaves and stem of the plant as raw materials to produce higher yield, more efficiency, and avoid burnt leaves [11]. The lack of a system by traditional distillers (Low value of essential oil yield and quality) has to be overcome quickly by developing extraction technology by microwaves, one of which is by MHD method [12-13]. Microwaves are non-ionic electromagnetic waves below radio frequency and above infrared frequency waves, with a frequency distance between 300 MHz and 300 GHz. In the oven, microwaves work at a frequency of 2,450 MHz for general purposes and extraction applications for chemical analysis [14].

For the development of microwave technology, a medium is required to boost the solvent's dielectric coefficient so that it can be optimally absorbed and transformed into thermal energy to increase extracted essential oil and break down protected oil molecules [15-16]. Inorganic salts would cause more damage to the plant tissue's epidermal cells, making the essential oil easier for water vapor to extract and increasing the yield and separation effectiveness of the oil.

This research aims to study the effect of adding NaCl salt on the extraction of lemongrass leaves by the MHD method. This research will review the effect of microwave power, extraction time, the ratio between feed and solvent (F/S), and NaCl level toward extraction yield and oil quality to determine the best value conditions of lemongrass leaves extraction by microwave to produce citronella oil. NaCl salt is very effective in avoiding losses of the heat-sensitive components, especially the main components in essential oil, suit for a cleaner essential oil product to develop the modern essential oil industry [17].

■ EXPERIMENTAL SECTION

Materials

Lemongrass leaves are from *Cymbopogon nardus*, taken from Lumajang, East Java. The leaves have withered for 2 × 24 h to reduce moisture content and minced following the research variable. The research material is based on a dry basis [18]. We used the leaves part based on Feriyanto et al. [19], which yielded higher than stem part yields. To separate between essential oil and its solvent, used *n*-hexane ACS grade (95% pro analysis, CAS No. 110-54-3). NaCl solution made from NaCl 99%.

Instrumentation

The MHD instrumentation scheme was handled by a microwave oven (Electrolux EMM2308X) (Fig. 1), which has dimensions of 50 cm in length, 40 cm in width, and 40 cm in height. The power of the microwave ranges from 0 to 800 W. In this research, the power used was 150, 300, 450, and 600 W. Extraction flask volume 1 L as a glassware of material and solvent carried out the extraction process. Clevenger facilitates the extraction process so that while the process is in progress, solvents that have evaporated and condensed into the liquid phase can return to the extraction flask through the connection on the tool. In addition, the Clevenger is equipped with a Liebig condenser that helps the condensation process from vapors containing extracted oil. The instrumentation also has a Liebig condenser to maximize the cooling system.

Procedure

The MHD used a microwave oven. For the pre-treatment procedure, lemongrass leaves were withered for 2 × 24 h, minced by size according to the variables

(0.5, 1.0, and 1.5 cm), and stored at room temperature ± 30 °C. MHD research procedure is conducted by weighing lemongrass leaves according to the variables (30, 45, and 60 g). Put the weighed lemongrass leaves into the one-neck extraction flask, add 300 mL solvent according to the variables, and flow the water in the cooling system (condenser reflux and Liebig on the Clevenger). Turn on the microwave so that the extraction flask containing raw materials gets exposed to microwave radiation according to operating conditions and research variables. When the first drops come out from the Liebig condenser, it calculates the extraction time starting. Stop the extraction process according to predetermined time variables. The result is in the form of oil and solvent poured into the separator funnel and added *n*-hexane. The mixture between oil and *n*-hexane from the solvent was separated. Oil and n-hexane were separated. The essential oil was kept in a vial bottle at a temperature of 4 °C to prepare and analyze the essential oil obtained.

The experimental variables used in this study are as follows: Microwave power: 300, 450, and 600 W; material measure: 0.5 cm, 1 cm, and 1.5 cm; ratio F/S: 0.1, 0.15, and 0.2 g/mL; solvents: aquadest and NaCl 2% solution; extraction time: 180 min (sampling time every 20 min). Calculation of yield takes account of the moisture content of leaves according to the research by Chen et al. [20], and the yield of citronella oil can be calculated by Eq. (1):

$$\text{Yield}(\%) = \frac{\text{essential oil mass}}{\text{mass of leaves (dry basis)}} \times 100\% \quad (1)$$

Gas chromatography-mass spectrometry (GC-MS) analysis

GC-MS analysis results describe components contained and levels by peaks of components present in essential oil in detail [21]. The analysis was performed using GC-MS (AGILENT 6980N chromatography gas coupled with AGILENT 5973 inert mass spectrometry), carrier gas: Helium. The sample was injected at 250 °C inlet temperature with a split ratio of 1:50. The flow rate inside the GC column was held constant at 1 mL/min.

■ RESULTS AND DISCUSSION

Effect of Time on the Yield of Citronella Oil

The influence of time in the extraction of essentials is that the longer the extraction time, the more the amount of oil is obtained until a state of equilibrium when there is no increase in yield. It was called the optimal extraction time. In traditional distillations, the optimal extraction time 7 approximately h [22], while using a microwave only ranges from 2–3 h.

Effect of Power of the Yield of Citronella Oil

Power is the energy delivered per unit of time (J/s). In microwave extraction, power controls the amount of energy materials will receive to convert into thermal energy. This thermal energy conveys the movement of essential oil from a part of the plant to be extracted very well [23].

Microwave power must be carefully selected to minimize time consumption to obtain a temperature set without reaching excessive temperatures and overpressure. However, increased power with a longer microwave radiation time can lead to solvent loss due to evaporation. The variation of power used for the lemongrass leaves extraction process are 300, 450, and 600 W [24]. Fig. 2 shows the yield for citronella oil increases as long as power increases, at 300 W (1.394%) at power 450 W (2.110%), experiencing an increase in yields. However, at power 600 W (0.904%), the yield of essential oils decreased and tended to be lower than other variables.

Based on the graph, there is a tendency to increase the yield along with the increase in power. The more incredible energy received, the higher yield gets obtained because more energy is converted into the heat of

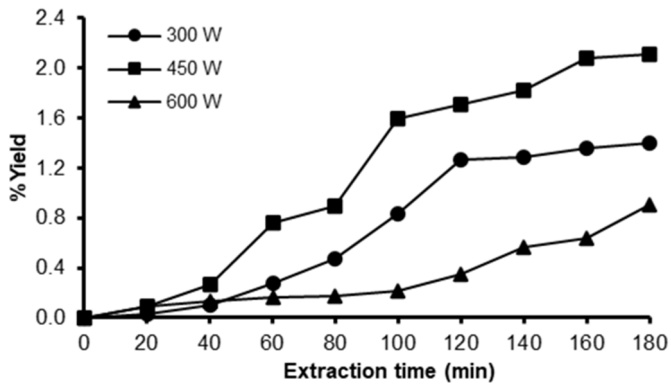

Fig 2. The oil yield function of time for different microwave power

extraction, increasing the extraction yield. The decreasing yield of 600 W caused by the power does not work at an optimum point, and fast evaporation rate increases quickly. This finding may cause the degradation of ingredients that can reduce the yield obtained and damage the composition of essential oil contents [25].

High microwave power will accelerate the heating of the extracted material because linearly, with high power, the higher the heating temperature of the extracted material. High power conveys thermal energy to the material contacted and influences the temperature profile. The oil glands in lemongrass get overheated, breaking the cell walls and lysis process. Oil will diffuse to the solvent and evaporate with the solvent vapor, which is then condensed. High microwave power does not guarantee a high yield because each material has distinct characteristics. Therefore, the best operating conditions are needed to produce high yields and good-quality citronella oil. Based on the experiments that have been carried out in the manufacture of essential oil can be carried out at optimum power for the extraction of citronella oil by the MHD method based on Fig. 2 is 450 W [26].

Effect of Material Size of % Yield of Citronella Oil

Material size variations in the extraction process are 0.5, 1.0, and 1.5 cm long. This size affects the surface area of the material submerged in the solvent. In addition, it also affects the number of material matrices included in one experiment. The effect of material size on yield can be seen in Fig. 3. Fig. 3 shows it can be seen that the yield of citronella oil for a size of 0.5 cm (1.572%) has the highest yield when compared to other sizes, 1.0 cm (0.976%) and 1.5 cm (1.272%). Also, Fig. 3 shows a decrease in the yield of citronella oil as the length of the lemongrass leaves increases. This fact is because the longer the piece of lemongrass, the fewer oil glands are exposed to heat, thereby reducing the surface area of the extracted material so that the smaller the pieces of lemongrass leaves, the more yield is produced. Based on the experiments that have been carried out, optimization in the manufacture of essential oil from lemongrass can be done using a piece of material size of 0.5 cm [27].

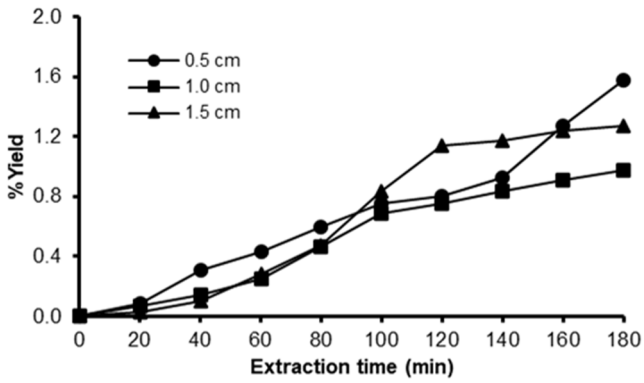

Fig 3. The oil yield function of time for different material sizes

According to the literature, the smaller the size of the extracted material can cause penetration from microwaves to be more effective. Where with the increasingly effective penetration of microwaves in smaller-sized materials, this then causes the extraction efficiency to increase. Based on Fig. 3, it can be seen that the yield of citronella oil for a size of 0.5 cm (1.572%) has the highest yield when compared to other sizes, 1.0 cm (0.976%) and 1.5 cm (1.272%). Where with the increasingly effective penetration of microwaves in smaller-sized materials, this then causes the extraction efficiency to increase [28].

Effect of Feed to the Solvent Ratio of Yield of Citronella Oil

This research was conducted at the ratio of raw materials used per volume of solvents was 0.1, 0.15, 0.2 g/mL, and the mass of material used is 30, 45, and 90 g.

Increasing feed to solvent in the extraction flask causes a yield decrease. It caused by the surface of the material is not exposed to heat optimally. The flask becomes dense, and the heat distribution becomes not optimally spread. The dense flask resists heat transfer between materials so that it decreases extraction energy thermal. Based on Fig. 4, it is found that the optimal yield in the MHD method for citronella oil can be done using the best ratio, where the optimum ratio for the manufacture of citronella oil is about 0.1 g/mL [29].

The volume of the solvent remains constant while the mass of the material changes. It was found that increasing the solid mass can reduce the surface area

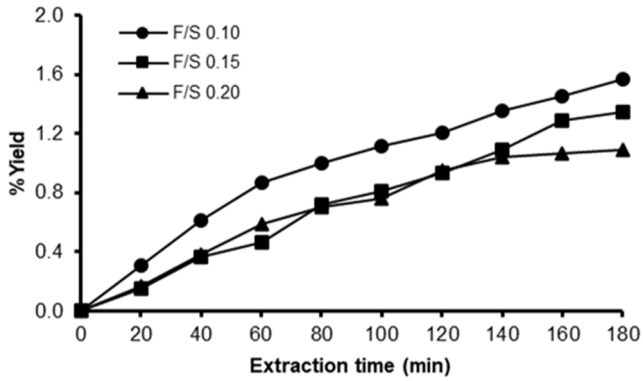

Fig 4. The oil yield function of time for different of feed to solvent ratios (F/S)

available for the solvent to penetrate the plant material and dissolve the target molecules. In general, a lower material-to-solvent (F/S) ratio in extraction techniques can increase the yield of essential oils. The solvent volume should be sufficient to ensure the entire sample is ideally submerged so that the material can expand during extraction [30].

The interaction between power parameters, time, comparison of feeds and solvents, and material size will be discussed in a separate study of optimization and interaction between parameters.

Effect of NaCl Salt Addition on the Yield of Citronella Oil

The best variable for citronella is a material size of 0.5 cm, F/S 0.1, with a material mass of 30 g with a power variation of 300, 450, and 600 W. This research uses NaCl salt to make NaCl 2% solution for the experiment. According to this research, the yield of essential oil increases at NaCl 1–2% and decreases at NaCl concentrations of 3–5% [31].

Another research stated that the yield of essential oil increases in NaCl by 1% and 2.5% but will experience a decrease in yield at NaCl concentrations by 5 and 10%. So from the two research above, variables were selected for extracting clove stem essential oil by the MHD method using NaCl solution 2% [32].

The addition of NaCl accelerates the phenomenon of mass and heat transfer because the addition of NaCl causes the boiling point of water to increase, which can result in the degradation of components, and a hydrolysis reaction occurs [33], so the extraction process can run faster. NaCl act as an electrolyte where NaCl solution consisting of ion moves and rubs against each other due to the influence of electromagnetic waves on the microwave so that the separation of essential oil from water becomes easier [34]. NaCl increases the polarity of the solvent to separate oil from solvent easier.

The selection of solvent is one of the crucial factors that can significantly influence the extraction process using the microwave. The determination of the solvent depends on the solubility of the essential oil, the penetrating power of the solvent, the interaction between the solvent and the matrix of the material, and the dielectric constant [35]. This research used Water and NaCl solutions as solvents because the highest dielectric constant among all solvents is 80.4 and 78 [36]. This fact causes the solvent to have a high capacity to absorb microwaves, and essential oil in lemongrass leaves can be extracted optimally. In this experiment, we used water and added a NaCl solution of 2%.

Fig. 5 shows, on the use of a 2% NaCl solvent, it can be seen that yield increases as the power increases, but there is a decrease in the immense power; yield increases from the power of 300 W (1.094%), 450 W (1.395%) as the power used increases. However, at a power variation of 600 W, there was a decrease (0.988%).

From Table 1, it can be seen that the yield of citronella essential oil has changed at a solvent ratio of 2% NaCl, namely for variables of 300 W (1.394 to 1.094%), 450 W (2.110 to 1.395%), and 600 W (0.904 to 0.988%). The addition of NaCl can affect the dielectric constant to get lower, resulting in the solvent not quickly capturing waves from the microwave so that heating is reduced, this is called dielectric decrement, but this does not happen because dielectric decrement occurs in molarity above 1.5 M. The molarity of the NaCl used is still below that number, so there is no dielectric decrement [37]. This result follows research conducted by Perez et al., where there was a decrease in oil yield from 0% NaCl to 1% NaCl and an increase after adding 2.5% NaCl [32]. The increase in yield, along with the increase in the solvent ratio, is due to the increase in the boiling point of water.

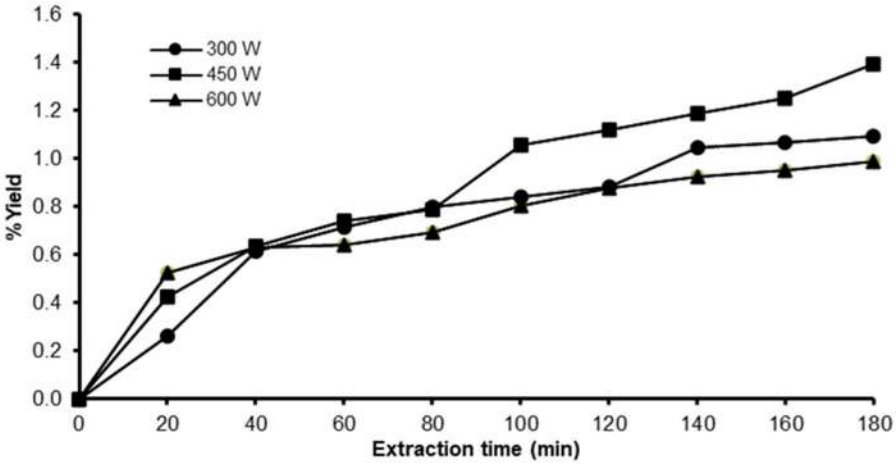

Fig 5. The oil yield function of time for different addition of NaCl 2% solution

Table 1. Comparison of the oil yield between water solvent and 2% NaCl solution

Power	Ratio F/S	Material size (cm)	% Yield (Water)	% Yield (NaCl 2%)
300			1.394	1.094
450	0.1	0.5	2.110	1.395
600			0.904	0.988

Physical Properties of Citronella Oil

The analysis results of the physical properties of citronella oil can be seen in Table 2. The specific gravity of citronella oil processed using the MHD method is 0.896–0.915 g/mL and is close to SNI 06-3953-1995, which is 0.88–0.92 g/mL, meaning essential oil has met quality standards in Indonesia. The specific gravity of citronella oil extracted in this research is almost close to Putri's research [38], whose specific gravity is 0.8640–0.9087. The greater the weight fraction contained in the oil, the greater the density value. The greater the density value, the more components are contained in the substance with a high molecular weight and a long carbon chain [39].

Essential oil dissolves in ethanol 70% at a specific ratio and concentration. The solubility in ethanol of 70% states the ratio of the volume of essential oil and the volume of ethanol of 70% needed to dissolve essential oils. The solubility test on citronella oil obtained the results that the solubility of the citronella oil obtained was following the SNI standard, which was 1:2. This is also reinforced by the results of experiments conducted by Putri [40] that citronella oil dissolves in 70% ethanol in a ratio of 1:2, that is, 1 mL of citronella essential oil is required 2 mL of ethanol, so a clear solution is obtained. The solubility test in alcohol gives an idea of whether an oil is easily soluble or not. The easier the oil is soluble in alcohol, the more polar compounds in the oil. The solubility of alcohol is a principal factor in essential oil testing because it can determine the quality of the essential oil.

The refractive index of citronella oil is 1468, which means that the value of the refractive index of the extracted oil is under the SNI standard, 1466–1475. The refractive index of essential oils is closely related to the

Table 2. Physical properties of citronella oil

Physical properties	SNI 06-3953-1995	Citronella oil
Specific gravity (25 °C)	0.88–0.92	0.896–0.915
Solubility 70% (v/v)	1:2	1:2
Refractive index	1466–1475	1468
Color	Pale yellow to yellowish brown	Pale yellow to yellowish brown

components composed in the resulting essential oil. Similarly, the specific gravity of the essential oil constituent components can affect its refractive index value. The more long-chain components such as sesquiterpenes or oxygen components are distilled, the density of the essential oil medium will increase, making the incoming light more challenging to refract. This finding leads to a more extensive oil refractive index. According to Guenther and Ketaren [39], the index value is also influenced, one of which is the presence of water in the oil content. The bias index value decreases as the water content increases. This fact is due to the nature of the water that it is easy to refract the oncoming light.

Results of Analysis Chemical Properties of Citronella Oil

The results of the analysis of the contents of citronella oil are provided in Table 3, and the chromatogram is displayed in Fig. 6. The predominant component of the essential oil extracted from lemongrass using the MHD method is geraniol, as shown in Fig. 6.

Citronelal and geraniol experimental results for the MHD method were 5.62 and 46.61%. In a previous study by Putri, the main components of citronella oil from lemongrass leaves extraction by the MHD method are geraniol and citronellal 28.44 and 6.85%, respectively. This result does not correspond to the expected essential oil, where the components of geraniol and citronellal,

Table 3. Result of GC-MS analysis of citronella oil

Retention time (min)	% area	Compounds
1.723	0.70	3-Methyl pentane
1.767	23.41	Hexane
1.892	1.80	Methyl cyclopentane
7.873	0.36	Linalool
8.693	3.00	Citronella
8.864	0.37	Isoneral
9.136	0.67	Isocitral
9.822	2.62	Citronella
10.044	10.35	Geraniol
10.226	19.65	Geraniol
10.469	16.61	Geraniol
11.545	0.50	Butanoic acid
11.707	9.71	Eugenol
11.955	3.21	Geranyl acetate
12.610	1.69	Caryophyllene
12.933	0.83	Phenol
13.390	0.47	Germacrene
13.785	0.98	Naphthalene
14.565	0.84	Cyclodecadiena
14.685	0.95	Caryophyllene
15.327	0.52	Naphthalene
15.481	0.76	Cyclohexane
Total	100	

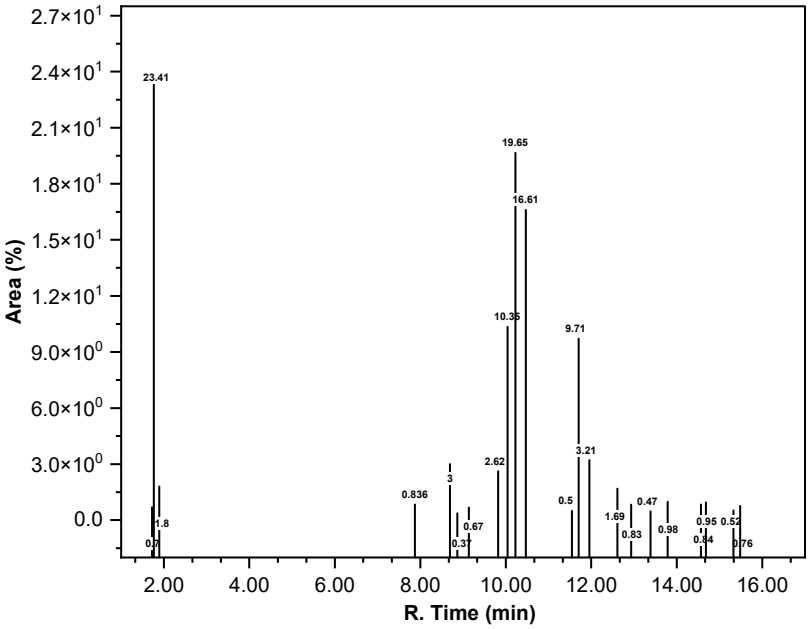

Fig 6. Gas chromatography-mass spectrometry chromatogram

according to SNI. 06-3953-1995, are respectively 85 and 35%. According to Widyastuti and Sugiarso [41], genetic and environmental factors cause variation in the levels of geraniol and citronellal in this study. The availability of nutrients in the soil results in differences in the results of plant metabolic processes [42].

CONCLUSION

The extraction of lemongrass leaves by the MHD Method shows that the smaller the material size affects, the greater the yield with an optimum size of 0.5 cm. The best value of the power of the MHD method's extraction process of lemongrass leaves is 450 W. As the ratio of solvents used increases, the yield obtained increases. The best solvent per material ratio value is F/S = 0.1, and the best solvent for the extraction process of lemongrass leaves by the MHD method is aquadest. Physical and chemical results of the analysis of citronella oil analyzed by GC-MS show that citronellal and geraniol components get results of 5.62 and 46.61%, respectively. The solubility analysis of citronella oil in alcohol is 70%, following previous research and Indonesian National Standardization results. The yield of citronella oil obtained from extraction by the MHD method using water solvents is more remarkable than using 2% NaCl, and this is because the dielectric constant of NaCl is more diminutive than water and needs to be studied further for higher NaCl concentrations.

ACKNOWLEDGMENTS

The author thanks the Directorate General of Higher Education (DIKTI) Ministry of Education and Culture of the Republic of Indonesia through Doctorate Research Scheme (PDD) with contract number No. 1401/PKS/ITS/2022.

REFERENCES

[1] Ministry of Trade Republic of Indonesia, 2011, *Indonesian Essential Oils: The Scents of Natural Life*, Trade Policy Analysis and Development Agency, Ministry of Trade Republic of Indonesia.

[2] Ali, B., Al-Wabel, N.A., Shams, S., Ahamad, A., Khan, S.A., and Anwar, F., 2015, Essential oils used in aromatherapy: A systemic review, *Asian Pac. J. Trop. Biomed.*, 5 (8), 601–611.

[3] Sharmeen, J.B., Mahomoodally, F.M., Zengin, G., and Maggi, F., 2021, Essential oils as natural sources of fragrance compounds for cosmetics and cosmeceuticals, *Molecules*, 26 (3), 666.

[4] Singh, N., Shrivastava, P., and Shah, M., 2014, Microwave-assisted extraction of lemongrass essential oil: Study of the influence of extraction method and process parameters on the extraction process, *J. Chem. Pharm. Res.*, 6 (11), 385–389.

[5] Kiani, H.S., Ali, A., Zahra, S., Hassan, Z.U., Kubra, K.T., Azam, M., and Zahid, H.F., 2022, Phytochemical composition and pharmacological potential of lemongrass (*Cymbopogon*) and impact on gut microbiota, *AppliedChem*, 2 (4), 229–246.

[6] Ma'sum, Z., Mahfud, M., and Altway, A., 2019, Parameter for scale-up of extraction *Cymbopogon nardus* dry leaf using microwave-assisted hydro-distillation, *J. Appl. Eng. Sci.*, 17 (2), 126–133.

[7] Haqqyana, H., Altway, A., and Mahfud, M., 2021, Microwave-assisted hydro-distillation of clove (*Syzgium aromaticum*) stem oil: Optimization and chemical constituents analysis, *Indones. J. Chem.*, 21 (6), 1358–1370.

[8] Tran, T.H., Nguyen, D.C., Phu, T.N.N., Ho, V.T.T., Vo, D.V.N., Bach, L.G., and Nguyen, T.D., 2019, Research on lemongrass oil extraction technology (hydro-distillation, microwave-assisted hydro-distillation), *Indones. J. Chem.*, 19 (4), 1000–1007.

[9] Kurji, B.M., Abed, K.M., Rashid, S.A., and Abdulmajeed, B.A., 2019, Kinetics and thermodynamics of peppermint oil extraction from peppermint leaves, *Iraqi J. Chem. Pet. Eng.*, 20 (4), 1–6.

[10] Sulaswatty, A., Rusli, M.S., Abimanyu, H., and Tursiloadi, S., 2019, *Quo Vadis: Minyak Serai Wangi dan Produk Turunannya*, LIPI Press, Jakarta, Indonesia.

[11] Chemat, F., Abert-Vian, M., Fabiano-Tixier, A.S., Strube, J., Uhlenbrock, L., Gunjevic, V., and Cravotto, G., 2019, Green extraction of natural products. Origins, current status, and future challenges, *TrAC, Trends Anal. Chem.*, 118, 248–263.

[12] Kusuma, H.S., Putri, D.K.Y., Triesty, I., and Mahfud, M., 2019, Comparison of microwave hydro-distillation and solvent-free microwave extraction for extraction of agarwood oil, *Chiang Mai J. Sci.*, 46 (4), 741–755.

[13] Mahfud, M., Putri, D.K.Y., Dewi, I.E.P., and Kusuma, H.S., 2017, Extraction of essential oil from cananga (*Cananga odorata*) using solvent-free microwave extraction: A preliminary study, *Rasayan J. Chem.*, 10 (1), 86–91.

[14] Routray, W., and Orsat, V., 2012, Microwave-assisted extraction of flavonoids: A review, *Food Bioprocess Technol.*, 5 (2), 409–424.

[15] Modi, P.I., Parikh, J.K., and Desai, M.A., 2021, Salt additive extraction of cinnamon oil using microwave radiation, *IOP Conf. Ser.: Mater. Sci. Eng.*, 1126, 012021.

[16] Zghaibi, N., Omar, R., Mustapa Kamal, S.M., Awang Biak, D.R., and Harun, R., 2019, Microwave-assisted brine extraction for enhancement of the quantity and quality of lipid production from *Microalgae nannochloropsis* sp., *Molecules*, 24 (19), 3581.

[17] Peng, X., Zhao, R., Yang, X., Feng, C., Gu, H., and Yang, L., 2022, Separation of essential oil from fresh leaves of *Phellodendron amurense* rupr. by solvent-free microwave-assisted distillation with the addition of lithium salts, *J. Cleaner Prod.*, 372, 133772.

[18] Sembiring, B.B., and Balai, F.M., 2015, Pengaruh pelayuan dan penyulingan terhadap rendemen dan mutu minyak serai wangi (*Cymbopogon nardus*), *Prosiding Seminar Nasional Swasembada Pangan Politeknik Negeri Lampung*, 29 April 2015, 447–451.

[19] Feriyanto, Y.E., Sipahutar, P.J., Mahfud, M., and Prihatini, P., 2013, Pengambilan minyak atsiri dari daun dan batang serai wangi (*Cymbopogon winterianus*) menggunakan metode distilasi uap dan air dengan pemanasan microwave, *Jurnal Teknik ITS*, 2 (1), 93–97.

[20] Chen, F., Zu, Y., and Yang, L., 2015, A novel approach for isolation of essential oil from fresh leaves of *Magnolia sieboldii* using microwave-assisted simultaneous distillation and extraction, *Sep. Purif. Technol.*, 154, 271–280.

[21] Beale, D.J., Morrison, P.D., Karpe, A.V., and Dunn, M.S., 2017, Chemometric analysis of lavender essential oils using targeted and untargeted GC-MS acquired data for the rapid identification and characterization of oil quality, *Molecules*, 22 (8), 1339.

[22] Mahfud, M., Chandra, K.F.A., Qadariyah, L., and Prihatini, P., 2015, Distillation assisted by microwave for extracting essential oil from Java cananga flowers, *Mod. Appl. Sci.*, 9 (7), 199–205.

[23] Ismanto, A.W., Kusuma, H.S., and Mahfud, M., 2018, Solvent-free microwave extraction of essential oil from *Melaleuca leucadendra* L., *MATEC Web Conf.*, 156, 03007.

[24] Destandau, E., and Michel, T., 2022, "Microwave-Assisted Extraction" in *Natural Product Extraction: Principles and Applications*, Eds. Rostagno, M.A., and Prado, J.M., RSC Publishing, Cambridge, UK, 144–201.

[25] Benmoussa, H., Elfalleh, W., He, S., Romdhane, M., and Benhamou, A., 2018, Microwave hydrodiffusion and gravity for rapid extraction of essential oil from Tunisian cumin (*Cuminum cyminum* L.) seeds: Optimization by response surface methodology, *Ind. Crops Prod.*, 124, 633–642.

[26] Mahfud, M., Ma'sum, Z., Bhuana, D.S., Altway, A., and Yuniati, Y., 2022, A comparison of essential oil extraction from the leaves of lemongrass (*Cymbopogon nardus* L.) using two microwave-assisted methods, *J. Eng. Appl. Sci.*, 20 (3), 881–888.

[27] Hashim, M.A., Yahya, F., and Mustapha, W.A.W., 2019, Effect of different drying methods on the morphological structure, colour profile and citral concentration of lemongrass (*Cymbopogon citratus*) powder, *Asian J. Agric., Biol.*, 7 (1), 93–102.

[28] Basit, H.M., Mohd Amin, M.C.I., Ng, S.F., Katas, H., Shah, S.U., and Khan, N.R., 2020, Formulation and evaluation of microwave-modified chitosan-curcumin nanoparticles–A promising nanomaterials platform for skin tissue regeneration applications following burn wounds, *Polymers*, 12 (11), 2608.

[29] Akhihiero, E.T., Ayodele, B.V., and Akpojotor, G.E.,

2013, Effect of particle size and temperature variation on the yield of essential oil from lemon grass using steam distillation, *Afr. J. Phys.*, 6, 105–112.

[30] Kurji, B.M., Hamid, K.J., Salih, S.M., Abed, K.M., and Mirghani, M.E.S., 2022, Extraction essential oil from *Thymus vulgaris* L. leaves using microwave reactor: Optimization and kinetic study, *Int. J. Mech. Eng.*, 7 (1), 6700–6709.

[31] Tran, T.H., Ha, L.K., Nguyen, D.C., Dao, T.P., Nhan, L.T.H., Nguyen, D.H., Nguyen, T.D., Vo, D.V.N., Tran, Q.T., and Bach, L.G., 2019, The study on extraction process and analysis of components in essential oils of black pepper (*Piper nigrum* L.) seeds harvested in Gia Lai Province, Vietnam, *Processes*, 7 (2), 56.

[32] Pérez, A.G., Romero, C., Yousfi, K., and García, J.M., 2008, Modulation of olive oil quality using NaCl as extraction coadjuvant, *J. Am. Oil Chem. Soc.*, 85 (7), 685–691.

[33] Moradi, S., Fazlali, A., and Hamedi, H., 2018, Microwave-assisted hydro-distillation of essential oil from rosemary: Comparison with traditional distillation, *Avicenna J. Med. Biotechnol.*, 10 (1), 22–28.

[34] Horikoshi, S., Sumi, T., and Serpone, N., 2012, Unusual effect of the magnetic field component of the microwave radiation on aqueous electrolyte solutions, *J. Microwave Power Electromagn. Energy*, 46 (4), 215–228.

[35] Veggi, P.C., Martínez, J., and Meireles, M.A.A., 2013, "Fundamentals of Microwave Extraction" in *Microwave-Assisted Extraction for Bioactive Compounds Theory and Practice*, Eds. Chemat, F., and Cravotto, G., Springer, US, 15–53.

[36] Metaxas, A.C., 1996, *Foundations of Electroheat: A Unified Approach*, Wiley, New York, US.

[37] Gavish, N., and Promislow, K., 2016, Dependence of the dielectric constant of electrolyte solutions on ionic concentration: A microfield approach, *Phys. Rev. E*, 94 (1), 012611.

[38] Timung, R., Barik, C.R., Purohit, S., and Goud, V.V., 2016, Composition and anti-bacterial activity analysis of citronella oil obtained by hydro-distillation: Process optimization study, *Ind. Crops Prod.*, 94, 178–188.

[39] Guenther, E., and Ketaren, S., 1987, *Minyak Atsiri Jilid I*, UI Press, Jakarta, Indonesia.

[40] Putri, S.N., 2018, Ekstraksi Minyak Atsiri dari Bunga Mawar dan Serai Wangi dengan Metode Microwave Hydrodistillation (MHD) dan Solvent-Free Microwave Extraction (SFME), *Undergradute Thesis*, Sepuluh Nopember Institute of Technology, Surabaya, Indonesia.

[41] Widyastuti, Y., and Sugiarso, S., 2003, Pengaruh beberapa tingkat dosis pupuk organik dan tiga jenis tanah pada pertumbuhan dan kandungan minyak atsisi ketumbar (*Coriandrum sativum* L.), *Jurnal Bahan Alam Indonesia*, 2 (3), 105.

[42] Zhang, H., and Hu, Q.P., 2014, Study on salting out-steam distillation extraction technology and antibacterial activities of essential oil from cumin seeds, *Aceh Int. J. Sci. Technol.*, 3 (3), 174–179.

Impregnation of Fe^{3+} into MCM-41 Pores: Effect of Fe^{3+} Concentration on the Weight Percent of Fe-Frameworks and Fe-Non-Frameworks

Suyanta Suyanta*, Agus Kuncaka, and Mudasir Mudasir

Department of Chemistry, Faculty of Mathematics and Natural Sciences, Universitas Gadjah Mada, Sekip Utara, Yogyakarta 55281, Indonesia

** Corresponding author:*

email: suyanta_mipa@ugm.ac.id

Received: November 28, 2022
Accepted: May 15, 2023

DOI: 10.22146/ijc.79468

Abstract: *Silica from rice husks (RH) has been used as a starting ingredient in the sonication synthesis of MCM-41 (RH-MCM-41). The impregnation of Fe^{3+} into RH-MCM-41 pores to produce RH-MCM-41 containing Fe_2O_3 and Fe (denoted as Fe_2O_3-Fe-RH-MCM-41) was carried out by examining the effect of various Fe^{3+} concentrations on the weight percent of Fe-frameworks (Fe^{3+} that replaces Si^{4+} in silicate frameworks) and Fe-non-frameworks, i.e., the iron oxide formed outside the silicate frameworks. Fe_2O_3-Fe-RH-MCM-41 was washed with a 0.01 M HCl solution to remove Fe-non-frameworks from the materials and give Fe-RH-MCM-41 containing Fe-frameworks. The Fe content in Fe_2O_3-Fe-RH-MCM-41 (Fe-total) and Fe-RH-MCM-41 (Fe-frameworks) for each sample was determined by an AAS (atomic absorption spectrometer), whereas the content of Fe-non-frameworks was calculated from the difference between Fe-total and Fe-frameworks. The XRD (X-ray diffraction) pattern, N_2 adsorption-desorption isotherm profile, as well as the TEM (transmission electron microscope) image clearly demonstrate that the RH-MCM-41 exhibits an ordered p6mm hexagonal mesostructure with a large specific surface area and uniform pore size. Based on the weight percents of Fe-frameworks found in each sample, it is clear that the content of Fe-non-frameworks is significantly enhanced compared to that of Fe-frameworks when the more concentrated Fe^{3+} is used.*

Keywords: *RH-MCM-41; impregnation; Fe-frameworks; Fe-non-frameworks*

INTRODUCTION

Zeolites are being used as solid acid catalysts in a growing number of refining processes, as well as in the production of petrochemicals and specialty chemicals, because of their remarkable environmental friendliness, shape selectivity, durability, and reusability [1-2]. However, this material cannot be used to catalyze processes involving big molecules due to its very tiny (± 1 nm) pore size [3]. Thankfully, the mesoporous M41S family, which was discovered in 1992, has numerous advantages over microporous materials because of its larger pore size (3-10 nm) [4].

In general, silica precursors such as tetraethyl orthosilicate (TEOS) [5-7] and sodium silicate [8-11] are used in the synthesis of MCM-41, which is relatively expensive. Iron ore tailing [12-13], siliceous sugar industry waste [14], silicon carbide sludge and granite sludge [15], bentonite [16] and rice husk ash [17-19] have all been investigated for use as a silica precursor in the manufacture of MCM-41 to minimize production costs. Rice husk ash (RH) is the most potent natural substance because it contains SiO_2 at concentrations of over 90% [20-22]. Rice is also widely grown in China, India, Pakistan, and East Asia [23]. Rice Husk-MCM-41 (RH-MCM-41) prepared from rice husk material is reported to possess some properties such as porosity, crystallinity, and hydrothermal stability that are comparable to those synthesized from commercial silicates, such as tetraethyl orthosilicate (TEOS) [24].

MCM-41 is usually produced via the hydrothermal process, which entails heating the reactants with air in a sealed container (autoclave) [25-27]. Since the hydrothermal method requires a lot of time and energy to complete the reaction, it is less efficient and does not

meet the green chemistry principle. Alternative approaches, such as the sonochemistry process, which makes use of ultrasonic waves, have been used in a number of works to synthesize MCM-41 [28-30]. Ultrasonic vibrations can initiate chemical reactions in liquids by producing tiny bubbles known as micro-cavitation. The high temperature and pressure created by the pulsation of the bubbles [31], of course, create conditions conducive for chemical reactions to occur. The sonochemistry approach requires less time and energy, making it a more cost-effective and environmentally friendly technique.

It is well known that pure siliceous Si-MCM-41 has no acidity and lacks intrinsic catalytic applicability. Therefore, it must be heterogenized with transition metals to make it suitable for catalytic applications [32]. For example, Fe has been added to the MCM-41 structure to yield Fe-MCM-41, which has a negative framework charge due to some replacement of SiO_4 by FeO_4 tetrahedrons. Counter ions, such as H^+, could balance out the internal negative charge of the structure to produce the Brønsted-acidity [33]. For this reason, iron-modified mesoporous MCM-41 silica materials, Fe-MCM-41, have received significant attention as new nanostructured and catalyst materials in the last decade [34].

So far, impregnation has become one of several approaches to incorporate transition metals into the mesoporous MCM-41 frameworks [35-38]. However, in the impregnation of Fe^{3+} into MCM-41 material, there is always evidence for isomorphic substitution of trivalent iron in the frameworks that lead to the formation of Fe-MCM-41, as well as iron oxide nanoparticles on the outer frameworks [38]. In general, transition metal oxides also have catalytic properties, so several researchers have synthesized metal oxide nanoparticles in the pores of MCM-41 [39-40] and SBA-15 [41-42], which are applied as catalysts for various reactions. In contrast, there are also some serious problems if the filling of the pores by Fe_2O_3 nanoparticles (denoted as Fe-non-frameworks) induces the blockage of the trivalent iron in the frameworks (denoted as Fe-frameworks), thereby reducing the catalytic activity as reported by Pieterse et al. [43]. Significant blockage of the pore channels apparently reduces the diffusion of the reactants. It means that the iron oxide nanoparticles outside frameworks are not preferable if their content exceeds the appropriate level. Therefore, the optimum ratio of Fe-frameworks to Fe-non-frameworks contents should be investigated to maximize the catalytic activity of the materials.

As far as we know, there are hardly any reports that focus on the investigation of the ratio of Fe-frameworks to Fe-non-frameworks in MCM-41. In fact, this information is essentially required in designing catalysts with the best performance in their catalytic activity. Based on this idea, in this study, we have synthesized MCM-41 from rice husk ash (RH-MCM-41) by the sonication method and systematically investigated the effect of Fe^{3+} impregnation at various concentrations on the weight percent ratio of Fe-frameworks to Fe-non-frameworks in the RH-MCM-41 with the purpose of maximizing the catalytic properties of the materials. The use of rice husk as starting material is very advantageous, as there is a lot of rice husk waste in our surroundings, while the choice of the sonication method reduces the energy used for heating; thus, this study meets the principle of green chemistry and is environmentally more benign.

■ EXPERIMENTAL SECTION

Materials

The materials used in this study were rice husk taken from the rice huller in the district of Bantul, Special Region of Yogyakarta, Indonesia. Merck (Germany) provided the chemicals used in this study, which included hydrochloric acid (HCl, 37%), cetyltrimethylammonium bromide (CTAB, 99%), sulfuric acid (H_2SO_4, 96%), sodium hydroxide (NaOH, 100%), ferric nitrate nonahydrate ($Fe(NO_3)_3{\cdot}9H_2O$, pro analysis), and nitric acid (HNO_3, 65%). All of these chemicals are of analytical grade and are used directly without pretreatment. All experiments utilized distilled water.

Instrumentation

The instrumentations used in this study were ultrasonic waves produced by the Bransonic 220

ultrasonic device at room temperature (25 to 32 °C) using a 48 kHz frequency and a 100 W heating capacity. On a Shimadzu model XD-3H X-ray diffractometer operating at room temperature, X-ray diffraction (XRD) patterns were produced using Cu-K_α powder that had been irradiated at = 0.154 nm. A Shimadzu FTIR-8010PC was used to carry out the Fourier-transform infrared (FTIR) spectroscopy examination. The KBr disc technique was used to get the spectra at room temperature and the transmittance mode in the 4000–400 cm^{-1} range. Using the Quantachrome Nova 1200 gas sorption analyzer, we looked at the nitrogen adsorption-desorption isotherm at the temperature of liquid nitrogen (GSA). Prior to the examination, samples were outgassed for a whole night at 250 °C. The Brunauer-Emmett-Teller (BET) surface area is determined by the multipoint BET method using adsorption data at relative pressures (P/P_0) between 0.03 and 0.1. At a relative pressure of 0.95, a mesoporous volume was calculated using isotherms. The Barrett-Joyner-Halenda (BJH) approach was used to calculate the average mesoporous diameter based on the nitrogen isotherm adsorption branch. The transmission electron microscope (TEM, JEM-3010) was used to analyze the properties of the RH-MCM-41 pores. The Atomic Absorption Spectrophotometer (AAS, Perkin Elmer 3110) was used to determine the content of Fe in the samples.

Procedure

The extraction of silica and synthesis of sodium silicate solution

The following procedure, similar to the one we previously reported [25], was used to obtain rice husk silica. First, rice husks were washed using water and dried for 12 h at 120 °C. The clean and dry rice husks (100 g) were put into a 3 M HCl solution (500 mL) and then refluxed at 80 °C for 3 h in a round-bottom flask equipped with a magnetic stirrer. The mixture was cooled, filtered, and washed with distilled water to remove residual acid. The result was again dried at a temperature of 120 °C for 12 h, then calcined at a temperature of 650 °C for 6 h at a speed of 2 °C min^{-1}. To make sodium silicate solution, rice husk silica (4.0 g) and NaOH pellets (1.25 g) were put into distilled water (35 g), then stirred to form a gel. This gel was heated to 80 °C with stirring for 2 h, then cooled in the air to room temperature.

Synthesis of RH-MCM-41

To produce a CTAB solution, CTAB (10 g) was added to distilled water (50 mL) at 60 °C and stirred for 30 min. A 15-mL solution of sodium silicate was added to the above CTAB solution to form the gel. The pH of this gel was adjusted to 11 by steadily dropping 5 M H_2SO_4. After that, the gel was placed in a sealed glass bottle and exposed to ultrasonic exposure at a frequency of 40 Hz at room temperature for 180 min. The white precipitate was collected after the ultrasonic treatment, rinsed with the necessary amount of distilled water, and dried at 110 °C for 100 min. The sample was calcined in air at a rate of 2 °C min^{-1} to 540 °C and held there for 5 h for the template to dissipate, and RH-MCM-41 was produced.

Impregnation of Fe^{3+} into RH-MCM-41 pores

Initially, RH-MCM-41 (1 g) was activated by heating at 120 °C for 3 h. The sample was then placed in a 100 mL solution of various concentrations (0.02, 0.04, 0.06, 0.08, and 0.10 M) of $Fe(NO_3)_3{\cdot}9H_2O$ solutions that had been acidified with HNO_3 until pH 2. At 40 °C, the mixture was magnetically stirred for 8 h, then left to stand for 4 h to achieve maximal impregnation. The solid phase was filtered out with Whatman 42 paper, washed three times with distilled water, dried at room temperature, heated at 110 °C for 3 h, and then calcined in air at 500 °C for 8 h. The resulting materials were labeled as Fe_2O_3(0.02)Fe-RH-MCM-41, Fe_2O_3(0.04)Fe-RH-MCM-41, Fe_2O_3(0.06)Fe-RH-MCM-41, Fe_2O_3(0.08)Fe-RH-MCM-41, and Fe_2O_3(0.10)Fe-RH-MCM-41. The Fe-total content in the five samples was determined by the AAS method.

Removing of Fe_2O_3 from Fe_2O_3-Fe-RH-MCM-41

Each 0.5 g of Fe_2O_3-Fe-RH-MCM-41 material acquired from the previous procedure was put into 50 mL of HCl 0.01 M, then magnetically stirred at ambient temperature for 2 h. The sediments were then separated by filtering with Whatman No. 42 paper, washed three times with distilled water, dried at room temperature, and then dried at 110 °C for 2 h. The new

materials were labeled as (0.02)Fe-RH-MCM-41, (0.04)Fe-RH-MCM-41, (0.06)Fe-RH-MCM-41, (0.08)Fe-RH-MCM-41, and (010)Fe-RH-MCM-41. The content of Fe-frameworks in the five samples was determined by the AAS method, while the content of Fe-non-frameworks is the difference between Fe-total and Fe-frameworks.

■ RESULTS AND DISCUSSION

X-ray Diffractogram Analysis

The X-ray diffractograms for RH-MCM-41 and Fe_2O_3-Fe-RH-MCM-41 were collected in Fig. 1(A) (small angle) and 1(B) (wide angle). The standard XRD pattern of α-Fe_2O_3 (ICDD No. 33-0664) is included in Fig. 1(B/g) for comparison. The small angle diffractogram for RH-MCM-41 (Fig. 1(A/a)) exhibits three well-resolved bands that can be indexed as 100, 110, and 200 reflections indicated with 2D p6mm hexagonal symmetry of the lattice. All samples of Fe_2O_3-Fe-RH-MCM-41, which were synthesized with Fe^{3+} concentration of less than 0.1 M (Fig. 1(A/b-e)), still had three diffraction peaks with fairly high intensity. This shows a high degree of pore symmetry even after impregnation. However, the synthesized Fe_2O_3-Fe-RH-MCM-41 sample with a 0.1 M Fe^{3+} concentration (Fig. 1(A/f)) only had two diffraction peaks with relatively low intensity. This is an indication of damage to some of the pore structures [44].

The decrease in intensity of the small angle diffractogram on all samples after the impregnation should be attributed to the incorporation of Fe_2O_3 nanoparticles in the pores. These Fe_2O_3 nanoparticles lessen the contrasting scatter of the mesoporous materials pores and frameworks. Erdem et al. [45] and Costa et al. [46] stated that, in general, the scattering intensity for Bragg reflections decreased when the scattering material

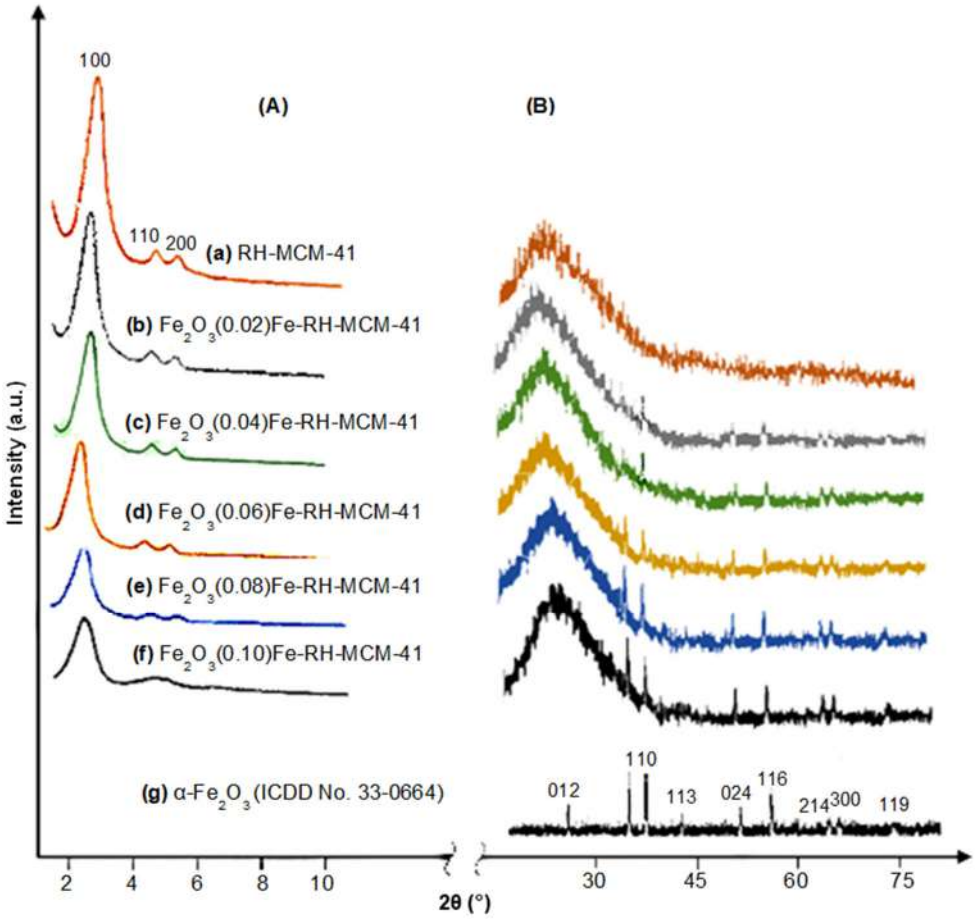

Fig 1. The X-ray diffractogram of RH-MCM-41 and Fe_2O_3-Fe-RH-MCM-41 in the small angle (A) and wide angle (B/a-f), and hematite (B/g)

was filled into the pores because it increased the phase cancellation between the scattering from the walls and the pore region.

The absorption widens with a peak at 2θ = 23° (Fig. 1(B/a-f)), characteristic of the amorphous silica forming the pore walls (ICDD 29-0085). In addition, characteristic weak peaks for hematite (α-Fe_2O_3) were observed at 2θ 30–75° (Fig. 1(B/b-f)), where the intensity increased with increasing Fe^{3+} concentration in the precursor solution. This case also indicates that the impregnation of Fe^{3+} into the pores of MCM-41 resulted in the formation of α-Fe_2O_3 particles outside the frameworks.

As illustrated in Fig. 2, iron oxide nanoparticles developing in RH-MCM-41's pores are thought to be triggered by hydrogen bonds developing between the silanol groups on the RH-MCM-41 surface and the hydrated Fe(III) cations, such as the two-core cation $Fe_2(OH)_2(H_2O)^{4+}$, which is present in large amounts in a pH-low solution of Fe(III) [47]. The concentration of $Fe_2(OH)_2(H_2O)^{4+}$ increased significantly during the filtering, washing, and calcination operations, reaching a super-saturated state and precipitating iron oxide nanoparticles.

The impregnation of Fe^{3+} also induces the reflected diffraction peaks of all samples to shift to a lower diffraction angle (2θ), indicating an increase in both basal spacing (d) and lattice parameter (a_o). The increase in these parameters can be attributed to isomorphic substitution, in which tetravalent silicon in the frameworks is replaced by trivalent iron. This increase occurs because the Pauling radius of Fe (64 pm) is larger than that of Si (42 pm). As a result, the bond length of Fe-O is larger than that of Si-O, and thus the lattice parameters are increased. Similar results have also been reported by previous researchers [48-49].

As illustrated in Fig. 3, it is believed that the isomorphic substitution mechanism of Si^{4+} in the frameworks by Fe^{3+} is initiated by the protonation of the two oxygen atoms of the siloxane bridge (O-Si-O), which causes the breaking of the two Si-O bonds, followed by the release of Si^{4+} and the entry of Fe^{3+}. There is an excess of negative charge on Fe in the product because Si with a charge of 4+ is replaced by Fe with a charge of 3+. The positive ions, primarily H^+, neutralize the negative charge, leading to the formation of Brønsted acid sites, which is very useful for catalytic activity.

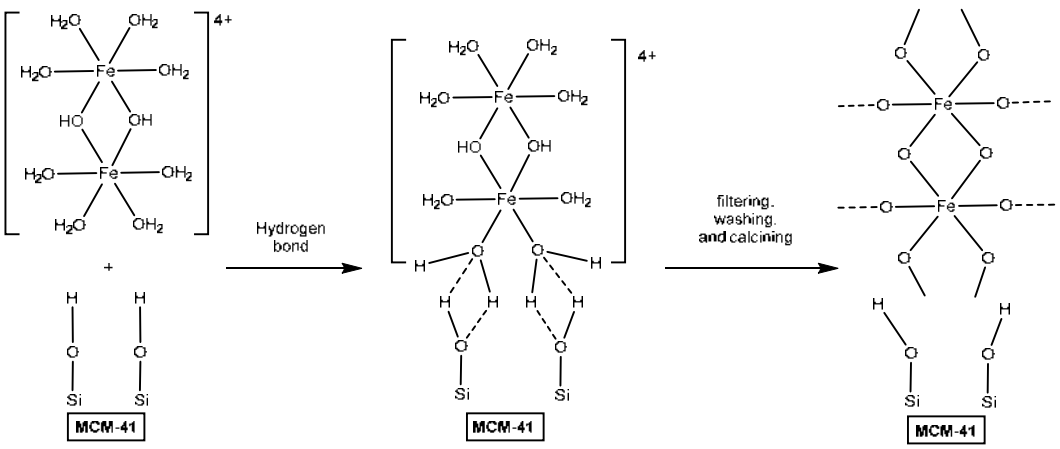

Fig 2. Mechanism estimation of the formation of iron oxide nanoparticles in the pores of RH-MCM-41

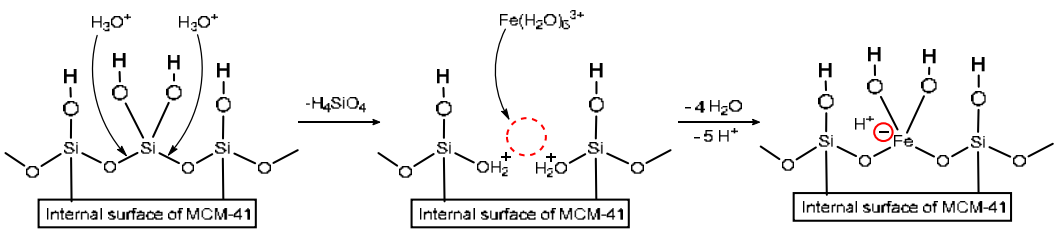

Fig 3. Estimation on the mechanism of isomorphous substitution of Si^{4+} in the MCM-41 frameworks by Fe^{3+}

FTIR Spectra Analysis

Fig. 4 shows the FTIR spectra of RH-MCM-41 and all of Fe_2O_3-Fe-RH-MCM-41. For comparison, the α-Fe_2O_3 (hematite) spectrum is also presented. The absorption of the asymmetric stretching vibration of OH silanol groups and adsorbed water molecules emerged as a widened peak of about 3400 cm^{-1} in all spectra. The peak of about 940 cm^{-1} is due to the symmetric and antisymmetric stretching of Si-O bonds within tetrahedral SiO_4 groups [50]. The symmetrical strain vibration of the Si-O-Si link of the RH-MCM-41 frameworks is represented by the absorption peak of 1084 cm^{-1}, while the bending vibration of the adsorbed water is represented by the absorption peak of 1635 cm^{-1} (remember the hydrophilic property of the OH group). A symmetric Si-O-Si stretching mode is connected with the band near 842 cm^{-1}, whereas a SiO_4 bending mode is associated with the band near 461 cm^{-1} [51].

In Fig. 4(f), Fe-O-Fe vibrations of Fe_2O_3 in the RH-MCM-41 pore cause the weak peaks at 635 and 572 cm^{-1} [52]. The intensity of these two peaks increased along with the increasing concentration of Fe^{3+} in the precursor solution. The absorption at 1084 cm^{-1}, which is typical of the Si-O-Si group's strain vibration, changed to 1076 cm^{-1}. This shows that a part of Si in the framework has been replaced by Fe, resulting in the creation of Si-O-Fe bonds with a higher reduced mass. The band at 461 cm^{-1}, which is associated with SiO_4's bending mode in RH-MCM-41, changed to 438 cm^{-1} due to the bending vibrations of Fe(III)-O-Si in the Fe_2O_3-Fe-RH-MCM-41 frameworks. At around 446 cm^{-1}, another peak linked with Fe-O bonding was found, which was

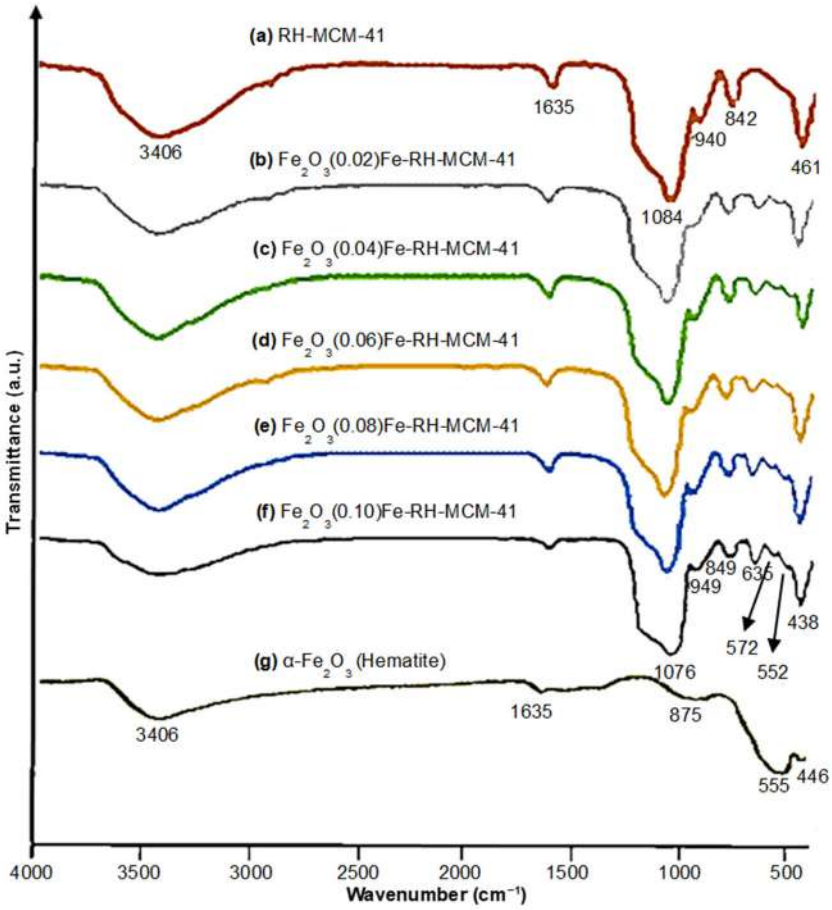

Fig 4. The FTIR Spectra of RH-MCM-41 and Fe-containing RH-MCM-41. The spectrum of α-Fe_2O_3 (hematite) is included for comparison

related to the Fe-O strain mode [53]. This peak, however, coincides with the peak bend vibrations of Fe(III)-O-Si, which are 438 cm^{-1}. Thus, the isomorphic substitution of Si^{4+} on the pore wall by Fe^{3+} and the creation of iron oxide nanoparticles in the pores of RH-MCM-41 are clearly visible in the FTIR spectral analysis. The absence of a nitrate-like peak at 1380 cm^{-1} shows that the iron(III) salt has entirely decomposed.

Gas Sorption Analysis

The N_2 adsorption-desorption isotherms of RH-MCM-41 and Fe-containing RH-MCM-41 are collected in Fig. 5. The isotherm of RH-MCM-41 showed typical IV isotherms, indicating a typical mesoporous material with hexagonal cylindrical channels [54]. The rise in the isotherm curve at low pressure ($P/P_0 < 0.3$) was attributed to the adsorption of a single layer of N_2 on the walls of the pore. The step with a steep slope of about $0.30 < P/P_0 < 0.38$ represents capillary condensation in the pores of RH-MCM-41. The homogeneity of pores and their narrow size distribution is to blame for the acuity of this isotherm's capillary condensation stage. The presence of relatively homogeneous pores with a restricted size distribution accounts for the steep slope of the curve during these isotherms' capillary condensation stage. These findings are consistent with the XRD patterns (Fig. 1(A/a)), which show well-resolved secondary and tertiary diffraction above $2\theta = 4–6°$ ([110] and [200] peaks) and indicate a very long-range order of these materials. The H1-type hysteresis loop in this range is caused by the capillary condensation that is typical for mesoporous materials. The almost flat curve at the end was attributed to the multilayer adsorption on the surface of mesopores. The H4-type hysteresis loop that appears at $P/P_0 > 0.40$ indicates the narrow pore size distribution contained in the material.

The isotherms of Fe_2O_3-(0.02)-Fe-RH-MCM-41, Fe_2O_3-(0.04)-Fe-RH-MCM-41, and Fe_2O_3-(0.06)-Fe-RH-MCM-41, which were of type IV and almost identical to the parent RH-MCM-41, indicated that the pore dimension of the host materials still remained. This case shows that the resulting Fe_2O_3-Fe-MCM-41 material still has a mesoporous structure, and iron oxide nanoparticles only fill a small part of the RH-MCM-41 pores. However,

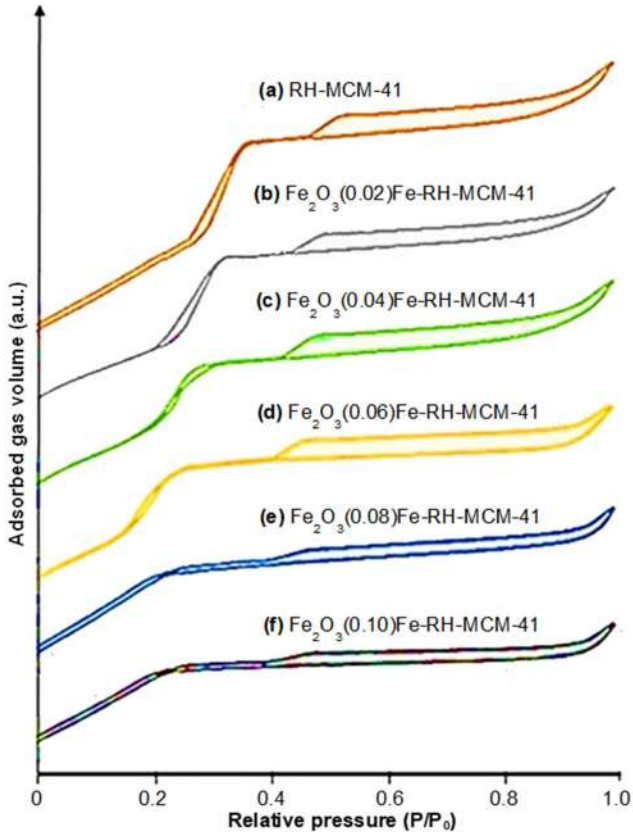

Fig 5. The N_2 adsorption-desorption isotherms of RH-MCM-41 and Fe_2O_3-Fe-RH-MCM-41

the starting point of the inflection shifts further left (toward a smaller P/P_0), which marks the reduction of pore size. Additionally, the height of the curve reduces, which indicates a reduced specific surface area. This was caused by the increasing amount of material (iron oxide) that filled the mesoporous channels as a result of the greater concentration of Fe^{3+} in the precursor solution.

In contrast, samples of Fe_2O_3-(0.08)-Fe-RH-MCM-41 and Fe_2O_3-(0.10)-Fe-RH-MCM-41 showed an isotherm that is markedly different from the parent RH-MCM-41 silica. The characteristic pore-filling step of the isotherm disappears for the two samples. This feature is thought to be due to the significant narrowing of the RH-MCM-41 pore, as it is partially blocked by iron oxide particles [55]. According to this explanation, Table 1 shows a systematic decrease in surface area, specific pore volume, and pore diameter as the impregnated Fe^{3+} concentration increases, where a significant decrease occurs in the fifth and sixth samples.

Analysis of TEM

The TEM images of RH-MCM-41 and Fe_2O_3-(0.06)-Fe-RH-MCM-41 samples are presented in Fig. 6. The TEM image of the RH-MCM-41 sample (Fig. 6(a)) shows that the pores are regularly arranged in a hexagonal shape, related to the p6mm 2D hexagonal symmetry. This is in agreement with the analytical results of the XRD data. In addition, Fig. 6(a) reveals a significant degree of pore regularity with a pore diameter of 2.9 nm. For Fe_2O_3-(0.06)-Fe-RH-MCM-41 (Fig. 6(b)), TEM images show a pore diameter of 2.5 nm. This is also close to the results obtained from GSA data, which are 2.861 nm. This result matches those found by GSA data, showing that the average pore diameter of this material was 3.241 nm.

The decrease in pore diameter can be attributed to the presence of iron oxide nanoparticles, which form and fill some of the pores. In addition, Fig. 6(b) also shows the reduced pore regularity caused by the isomorphic substitution of Si^{4+} by Fe^{3+} that occurs in the frameworks, indicated by the shift of the 100-plane peak to the left side, as discussed previously.

Table 1. The porosity of RH-MCM-41 and Fe_2O_3-Fe-RH-MCM-41 samples

Sample	S_{BET}[(a)] (m^2/g)	V_P[(b)] (mL/g)	D_{BJH}[(c)] (nm)
RH-MCM-41	934	0.759	3.241
Fe_2O_3-(0.02)-Fe-RH-MCM-41	916	0.703	3.088
Fe_2O_3-(0.04)-Fe-RH-MCM-41	897	0.668	2.965
Fe_2O_3-(0.06)-Fe-RH-MCM-41	886	0.632	2.861
Fe_2O_3-(0.08)-Fe-RH-MCM-41	567	0.421	2.398
Fe_2O_3-(0.10)-Fe-RH-MCM-41	432	0.398	2.013

Note: (a) Using adsorption data with a P/P0 range of 0.05 to 0.30, the multipoint BET technique was used to determine BET surface area; (b) The specific pore volume is calculated using P/P0 = 0.95; (c) The BJH approach was used to determine the sizes of the pores from the nitrogen isotherm's adsorption branch

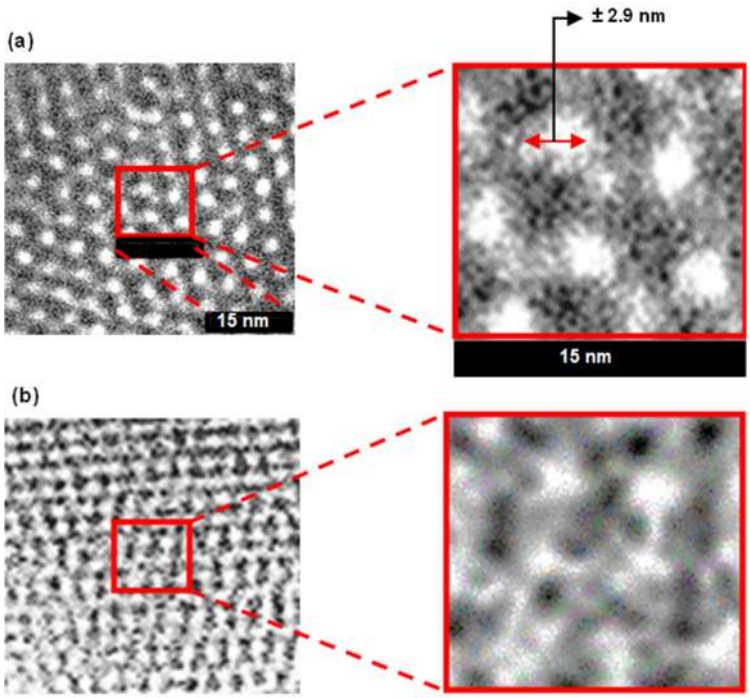

Fig 6. The TEM image of RH-MCM-41 and Fe_2O_3-(0.06)-Fe-RH-MCM-41 sample

The Content of Fe

The interpretation of the XRD diffractogram indicated that the Fe^{3+} impregnation of the MCM-41 pores led to the isomorphous substitution of Si^{4+} by Fe^{3+} as well as the formation of iron oxide at the out of frameworks. Table 2 shows the Fe content in the materials before and after the HCl treatment. The content of Fe increases with the increase in Fe^{3+} concentration in the precursor solution. The maximum Fe^{3+} concentration that can be used without causing damage to the pore structure of RH-MCM-41 is 0.08 M, which produces a material with a Fe content of 2.97%. Several researchers have previously reported comparable Fe contents. He et al. [56] reported a maximum Fe content of 1% by weight in Fe-MCM-41 material produced in situ without harming the silica host. Pasqua et al. [57] modified the process to manage the incorporation of Fe to the point where the content reaches 5% by weight without harming the silica host.

As shown in Table 2, the treatment using a solution of 0.01 M HCl caused a decrease in the amount of Fe content. The reaction associated with the decrease in Fe content is [58]:

$$Fe_2O_{3(s)} + 6HCl_{(aq)} \rightarrow 2FeCl_{3(aq)} + 3H_2O_{(l)}$$

In this case, Fe_2O_3 was iron oxide particles dispersed on the outer surface of the silica frameworks, both inside and outside of the pores (denoted as Fe-non-frameworks). The HCl treatment was assumed to dissolve all of the Fe-non-frameworks but not for Fe isomorphic substituted in the frameworks (denoted as Fe-frameworks). Based on this assumption, the composition of Fe in the initial sample (before treatment) can be deduced, as shown in Table 3.

By using the bar curve (Fig. 7), the difference in Fe content between Fe-frameworks and Fe-non-frameworks of each sample can be clearly seen. The content of Fe-frameworks in the five samples is almost the same, while that of Fe-non-frameworks is significantly increased when a higher concentration of Fe^{3+} in the precursor solution is used. This trend indicates that Fe-framework content reaches its maximum faster than Fe-non-framework content. Therefore, when a precursor with a higher concentration of Fe^{3+} is used, only a small amount of Fe^{3+} displaces Si^{4+} in the frameworks, whereas most of them form iron oxide particles outside the frameworks. This is not surprising because, based on our calculations, the isomorphic substitution of Si^{4+} by Fe^{3+} in the silica frameworks is endothermic ($\Delta H = +1{,}650$ kJ mol^{-1}), while the formation of Fe_2O_3 outside the frameworks is exothermic ($\Delta H = -16{,}484$ kJ mol^{-1}).

Table 2. The content of Fe in the sample before and after the HCl treatment

Sample	Fe content (wt.%)	
	Before HCl treatment	After HCl treatment
MCM-41	0	0
Fe_2O_3(0.02)Fe-RH-MCM-41	1.12	0.48
Fe_2O_3(0.04)Fe-RH-MCM-41	1.89	0.73
Fe_2O_3(0.06)Fe-RH-MCM-41	2.53	0.86
Fe_2O_3(0.08)Fe-RH-MCM-41	2.97	0.89
Fe_2O_3(0.10)Fe-RH-MCM-41	3.19	0.91

Table 3. Composition of Fe in samples before treatment with 0.01 M HCl

Sample	Fe total (wt.%)	Fe-frameworks (wt.%)	Fe-non-frameworks (wt.%)
RH-MCM-41	0	0	0
Fe_2O_3(0.02)Fe-RH-MCM-41	1.12	0.48	0.64
Fe_2O_3(0.04)Fe-RH-MCM-41	1.89	0.73	1.16
Fe_2O_3(0.06)Fe-RH-MCM-41	2.53	0.86	1.67
Fe_2O_3(0.08)Fe-RH-MCM-41	2.97	0.89	2.08
Fe_2O_3(0.10)Fe-RH-MCM-41	3.19	0.91	2.28

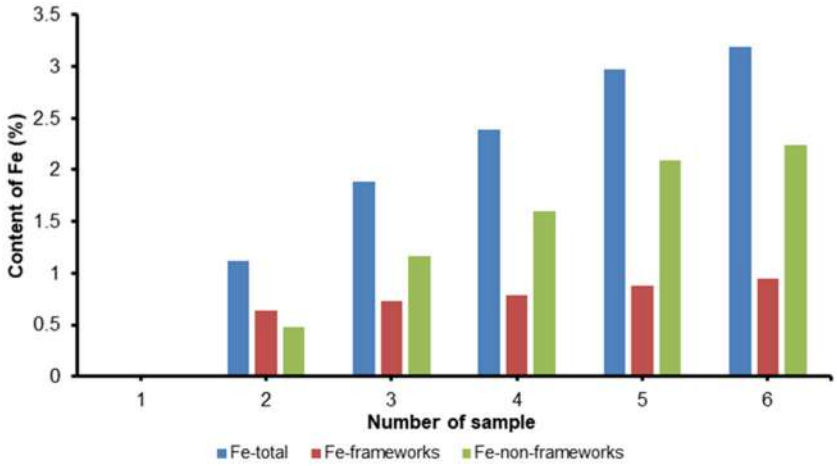

Fig 7. Content of Fe in the samples before treatment with 0.01 M HCl

CONCLUSION

According to XRD patterns, N_2 adsorption-desorption isotherms, and a TEM image, rice husk silica can be employed as the starting material for the sonication synthesis of RH-MCM-41, which displays a p6mm hexagonal mesostructure with a high specific surface area and narrow porosity size distribution. Impregnation of Fe^{3+} (0.02, 0.04, 0.06, 0.08, and 0.10 M) into the pores of RH-MCM-41 resulted in iron oxide outside the frameworks as well as isomorphic substitution in the frameworks, in which Fe^{3+} replaced Si^{4+}. The tendency of iron oxide formation is greater than the isomorphic substitution, as shown by the weight percents of Fe-non-frameworks of 0.64, 1.16, 1.67, 2.08, and 2.28% for each sample and the weight percents of Fe-frameworks of 0.48, 0.73, 0.86, 0.89, and 0.91% for each sample. This is due to the fact that isomorphic substitution of Si^{4+} by Fe^{3+} in the silica frameworks is endothermic ($\Delta H = +1{,}650$ kJ mol^{-1}), while the formation of Fe_2O_3 outside the frameworks is exothermic ($\Delta H = -16{,}484$ kJ mol^{-1}). Based on these findings, the mass percentage of Fe-non-frameworks to Fe-frameworks in RH-MCM-41 can be controlled by adjusting the concentration of Fe^{3+} used in the impregnation process. This is very important if the material is going to be applied as a catalyst, because the presence of iron oxide nanoparticles to a certain degree can increase the catalytic activity, but in contrast, excessive addition may also block the active site of Brønsted acid and therefore reduce the catalytic activity.

ACKNOWLEDGMENTS

The authors acknowledge financial support from a research grant administered by Universitas Gadjah Mada under the funding contract number 0127/J01.1.28/PL.06.02/2015 from the Directorate General of Higher Education (DGHE), Ministry of Education, Culture, Research, and Technology, The Republic of Indonesia.

REFERENCES

[1] Li, S.C., Lin, Y.C., and Li, Y.P., 2021, Understanding the catalytic activity of microporous and mesoporous zeolites in cracking by experiments and simulations, *Catalysts*, 11 (9), 1114.

[2] Ho, P.H., Yao, D., Creaser, D., and Olsson, L., 2022, Advantages of high-siliceous zeolites in the reactivity and stability of diesel oxidation catalysts, *ACS Eng. Au*, 2 (3), 219–235.

[3] Bingre, R., Louis, B., and Nguyen, P., 2018, An overview on zeolite shaping technology and solutions to overcome diffusion limitations, *Catalysts*, 8 (4), 163.

[4] Costa, J.A.S, de Jesus, R.A., Santos, D.O., Mano, J.F., Romão, L.P.C., and Paranhos, C.M., 2020, Recent progresses in the adsorption of organic, inorganic, and gas compounds by MCM-41-based mesoporous materials, *Microporous Mesoporous Mater.*, 291, 109698.

[5] Dinh Du, P., Hieu, N.T., To, T.C., Bach, L.G., Tinh, M.X., Mau, T.X., and Quang Khieu, D., 2019,

Aminopropyl functionalised MCM-41: Synthesis and application for adsorption of Pb(II) and Cd(II), *Adv. Mater. Sci. Eng.*, 2019, 8573451.

[6] Valiey, E., Dekamin, M.G., and Alirezvani, Z., 2021, Sulfamic acid pyromellitic diamide-functionalized MCM-41 as a multifunctional hybrid catalyst for melting-assisted solvent-free synthesis of bioactive 3,4-dihydropyrimidin-2-(1*H*)-ones, *Sci. Rep.*, 11 (1), 11199.

[7] Oliveira, D.M., and Andrada, A.S., 2019, Synthesis of ordered mesoporous silica MCM-41 with controlled morphology for potential application in controlled drug delivery systems, *Cerâmica*, 65 (374), 170–179.

[8] Ng, E.P., Goh, J.Y., Ling, T.C., and Mukti, R.R., 2013, Eco-friendly synthesis for MCM-41 nanoporous materials using the non-reacted reagents in mother liquor, *Nanoscale Res. Lett.*, 8 (1), 120.

[9] Parangi, T.F., Patel, R.M., and Chudasama, U.V., 2014, Synthesis and characterization of mesoporous Si-MCM-41 materials and their application as solid acid catalysts in some esterification reactions, *Bull. Mater. Sci.*, 37 (3), 609–615.

[10] Juárez-Serrano, N., Berenguer, D., Martínez-Castellanos, I., Blasco, I., Beltrán, M., and Marcilla, A., 2021, Effect of reaction time and hydrothermal treatment time on the textural properties of SBA-15 synthesized using sodium silicate as silica source and its efficiency for reducing tobacco smoke toxicity, *Catalysts*, 11 (7), 808.

[11] Fu, P., Yang, T., Feng, J., and Yang, H., 2015, Synthesis of mesoporous silica MCM-41 using sodium silicate derived from copper ore tailings with an alkaline molted-salt method, *J. Ind. Eng. Chem.*, 29, 338–343.

[12] Yang, G., Deng, Y., Ding, H., Lin, Z., Shao, Y., and Wang, Y., 2015, A facile approach to synthesize MCM-41 mesoporous materials from iron ore tailing: Influence of the synthesis conditions on the structural properties, *Appl. Clay Sci.*, 111, 61–66.

[13] Yang, G., Deng, Y., and Wang, J., 2014, Non-hydrothermal synthesis and characterization of MCM-41 mesoporous materials from iron ore tailing, *Ceram. Int.*, 40 (5), 7401–7406.

[14] Shah, B.A., Patel, A.V., Bagia, M.I., and Shah, A.V., 2017, Green approach towards the synthesis of MCM-41 from siliceous sugar industry waste, *Int. J. Appl. Chem.*, 13 (3), 497–514.

[15] Lin, Y.W., Lee, W.H., Lin, K.L., and Kuo, B.Y., 2021, Synthesis and grafted NH_2-Al/MCM-41 with amine functional groups as humidity control material from silicon carbide sludge and granite sludge, *Processes*, 9 (12), 2107.

[16] Ali-Dahmane, T., Brahmi, L., Hamacha, R., Villieras, F., and Bengueddach, A., 2016, Synthesis of MCM-41 nanomaterial from Algerian bentonite: Influence of synthesis pH, *J. Fundam. Appl. Sci.*, 9 (2), 636–649.

[17] Zhang, X., and Du, T., 2022, Study of rice husk ash derived MCM-41-type materials on pore expansion, Al incorporation, PEI impregnation, and CO_2 adsorption, *Korean J. Chem. Eng.*, 39 (3), 736–759.

[18] Abbas, S.H., Adam, F., and Muniandy, L., 2020, Green synthesis of MCM-41 from rice husk and its functionalization with nickel(II) salen complex for the rapid catalytic oxidation of benzyl alcohol, *Microporous Mesoporous Mater.*, 305, 110192.

[19] Suyanta, S., and Kuncaka, A., 2011, Utilization of rice husk as raw material in synthesis of mesoporous silicates MCM-41, *Indones. J. Chem.*, 11 (3), 279–284.

[20] Nguyen, T.T., Ma, H.T., Avti, P., Bashir, M.J.K., Ng, C.A., Wong, L.Y., Jun, H.K., Ngo, Q.M., and Tran, N.Q., 2019, Adsorptive removal of iron using SiO_2 nanoparticles extracted from rice husk ash, *J. Anal. Methods Chem.*, 2019, 6210240.

[21] Jongpradist, P., Homtragoon, W., Sukkarak, R., Kongkitkul, W., and Jamsawang, P., 2018, Efficiency of rice husk ash as cementitious material in high-strength cement-admixed clay, *Adv. Civ. Eng.*, 2018, 8346319.

[22] Xu, K., Sun, Q., Guo, Y., and Dong, S., 2013, Effects on modifiers on the hydrophobicity of SiO_2 films from nano-husk ash, *Appl. Surf. Sci.*, 276, 796–801.

[23] Nguyen, M.N., 2020, Worldwide bans of rice straw burning could increase human arsenic exposure, *Environ. Sci. Technol.*, 54 (7), 3728–3729.

[24] Cazula, B.B., Oliveira, L.G., Machado, B., and Alves, H.J., 2021, Optimization of experimental conditions for the synthesis of Si-MCM-41 molecular sieves using different methods and silica sources, *Mater. Chem. Phys.*, 266, 124553.

[25] Meléndez-Ortiz, H.I., Mercado-Silva, A., García-Cerda, L.A., Castruita, G., and Perera-Mercado, Y.A., 2013, Hydrothermal synthesis of mesoporous silica MCM-41 using commercial sodium silicate, *J. Mex. Chem. Soc.*, 57 (2), 73–79.

[26] Golezani, A.S., Fateh, A.S., and Mehrabi, H.A., 2016, Synthesis and characterization of silica mesoporous material produced by hydrothermal continues pH adjusting path way, *Prog. Nat. Sci.: Mater. Int.*, 26 (4), 411–414.

[27] Santos, E.C., Costa, L.S., Oliveira, E.S., Bessa, R.A., Freitas, A.D.L., Oliveira, C.P., Nascimento, R.F., and Loiola, A.R., 2018, Al-MCM-41 synthesized from kaolin via hydrothermal route: Structural characterization and use as an efficient adsorbent of methylene blue, *J. Braz. Chem. Soc.*, 29 (11), 2378–2386.

[28] Deka, J.R., Vetrivel, S., Wu, H.Y., Pan, Y.C., Ting, C.C., Tsai, Y.L., and Kao, H.M., 2014, Rapid sonochemical synthesis of MCM-41 type benzene-bridged periodic mesoporous organosilicas, *Ultrason. Sonochem.*, 21 (1), 387–394.

[29] Sönmez, D.M., Gudovan, D., Truşca, R. Ficai, D., Andronescu, E., and Vasile, B.S., 2015, Synthesis, characterization and testing of MCM-41/TiO_2 catalyst for organic dye degradation, *Dig. J. Nanomater. Biostruct.*, 10 (4), 1329–1341.

[30] Soltani, R., Dinari, M., and Mohammadnezhad, G., 2018, Ultrasonic-assisted synthesis of novel nanocomposite of poly (vinyl alcohol) and amino-modified MCM-41: A green adsorbent for Cd(II) removal, *Ultrason. Sonochem.*, 40, 533–542.

[31] Wang, X., Chen, W., Zhou, M., Zhang, Z., and Zhang, L., 2022, Dynamics of double bubbles under the driving of burst ultrasound, *Ultrason. Sonochem.*, 84, 105952.

[32] Yu, X., and Williams, C.T., 2022, Recent advances in the applications of mesoporous silica in heterogeneous catalysis, *Catal. Sci. Technol.*, 12 (19), 5765–5794.

[33] Srividhya, N., 2014, Synthesis characterization and catalytic evaluation of mesoporous Fe-MCM-41 and Si-MCM-41 materials, *IOSR J. Appl. Chem.*, 7 (6), 41–49.

[34] Zhang, Q., Wang, Y., Itsuki, S., Shishido, T., and Takehira, K., 2001, Fe-MCM-41 for selective epoxidation of styrene with hydrogen peroxide, *Chem. Lett.*, 30 (9), 946–947.

[35] Dhal, J.P., Dash, T., and Hota, G., 2020, Iron oxide impregnated mesoporous MCM-41: Synthesis, characterization and adsorption studies, *J. Porous Mater.*, 27 (1), 205–216.

[36] Mokhonoana, M.P., and Coville, N.J., 2009, Highly loaded Fe-MCM-41 materials: Synthesis and reducibility studies, *Materials*, 2 (4), 2337–2359.

[37] Sasieekhumar, A.R., Somanathan, T., Abilarasu, A., and Shanmugam, M., 2017, Mesoporous Fe/MCM-41 as heterogeneous photocatalyst for the photodegradation of methylene blue, *Res. J. Pharm. Technol.*, 10 (10), 3398–3400.

[38] Guo, Y., Chen, B., Zhao, Y., and Yang, T., 2021, Fabrication of the magnetic mesoporous silica Fe-MCM-41-A as efficient adsorbent: Performance, kinetics and mechanism, *Sci. Rep.*, 11 (1), 2612.

[39] Huo, C., Ouyang, J., and Yang, H., 2014, CuO nanoparticles encapsulated inside Al-MCM-41 mesoporous materials via direct synthetic route, *Sci. Rep.*, 4 (1), 3682.

[40] Yang, G., Xu, Y., Su, X., Xie, Y., Yang, C., Dong, Z., and Wang, J., 2014, MCM-41 supported CuO/Bi_2O_3 nanoparticles as potential catalyst for 1,4-butynediol synthesis, *Ceram. Int.*, 40 (3), 3969–3973.

[41] Li, X., Liu, W., Ma, J., Wen, Y., and Wu, Z., 2015, High catalytic activity of magnetic FeO_x/NiO_y/SBA-15: The role of Ni in the bimetallic oxides at the nanometer level, *Appl. Catal., B*, 179, 239–248.

[42] Hassanzadeh-Afruzi, F., Asgharnasl, S., Mehraeen, S. Amiri-Khamakani, Z., and Maleki, A., 2021, Guanidinylated SBA-15/Fe_3O_4 mesoporous nanocomposite as an efficient catalyst for the

synthesis of pyranopyrazole derivatives, *Sci. Rep.*, 11 (1), 19852.

[43] Pieterse, J.A.Z., Booneveld, S., and van den Brink, R.W., 2005, Evaluation of Fe-zeolite catalysts prepared by different methods for the decomposition of N_2O, *Appl. Catal., B*, 45, 156–172.

[44] Atchudan, R., Perumal, S., Jebakumar Immanuel Edison, T.N., and Lee, Y.R., 2015, Highly graphitic carbon nanosheets synthesized over tailored mesoporous molecular sieves using acetylene by chemical vapor deposition method, *RSC Adv.*, 5 (113), 93364–93373.

[45] Erdem, S., Erdem, B., Öksüzoglu, R.M., and Çitak, A., 2013, Bifunctional Fe-SBA-15-SO_3H mesoporous catalysts with different Si/Fe molar ratios: Synthesis, characterization and catalytic activity, *Bull. Korean Chem. Soc.*, 34 (5), 1481–1486.

[46] Costa, M.B.G., Juárez, J.M., and Anunziata, O.A., 2016, "Synthesis and Characterization of CMK Porous Carbons Modified with Metals Applied to Hydrogen Uptake and Storage" in *Microporous and Mesoporous Materials*, Eds. Dariani, R.S., IntechOpen, Rijeka, Croatia, 51–85

[47] Cotton, F.A., and Wilkinson, G., 1976, *Basic Inorganic Chemistry*, Wiley, New York, US.

[48] Qian, W., Wang, H., Chen, J., and Kong, Y., 2015, Spherical V-Fe-MCM-48: The synthesis, characterization and hydrothermal stability, *Materials*, 8 (4), 1752–1765.

[49] AlDhawi, Z.A., Alomair, N.A., Kochkar, H., and Grevathy, C.G., 2022, One pot synthesis of chromium incorporated SBA-16 under acid medium-application in the selective oxidation of benzyl alcohol derivatives, *Arabian J. Chem.*, 15 (7), 103861.

[50] Yusuf, M.O., 2023, Bond characterization in cementitious material binders using Fourier-transform infrared spectroscopy, *Appl. Sci.*, 13 (5), 3353.

[51] Casillas, P.E.G., Pérez, C.A.M., Gonzalez, C.A.R., 2012, "Infrared Spectroscopy of Functionalized Magnetic Nanoparticles" in *Infrared Spectroscopy - Materials Science, Engineering and Technology*, Eds. Theophanides, T., IntechOpen, Rijeka, Croatia, 405–420.

[52] Ulu, A., Noma, S., Koytepe, S., and Ates, B., 2018, Magnetic Fe_3O_4@MCM-41 core–shell nanoparticles functionalized with thiol silane for efficient L-asparaginase immobilization, *Artif. Cells, Nanomed., Biotechnol.*, 46, 1035–1045.

[53] Quy, D.V., Hieu, N.M., Tra, P.T., Nam, N.H., Hai, N.H., Thai Son, N., Nghia, P.T., Anh, N.T.V., Hong, T.T., and Luong, N.H., 2013, Synthesis of silica-coated magnetic nanoparticles and application in the detection of pathogenic viruses, *J. Nanomater.*, 2013, 603940.

[54] Sing, K.S.W., Everett, D.H., Haul., R.A.W., Moscou, L., Pierotti, R.A., Rouquérol, J., and Siemieniewska, T., 1985, Reporting physisorption data for gas/solid systems with special reference to the determination of surface area and porosity, *Pure Appl. Chem.*, 57 (4), 603–619.

[55] Huang, S., Fan, Y., Cheng, Z., Kong, D., Yang, P., Quan, Z., Zhang, C., and Lin, J., 2009, Magnetic mesoporous silica spheres for drug targeting and controlled release, *J. Phys. Chem. C*, 113 (5), 1775–1784.

[56] He, N.Y., Cao, J.M., Bao, S.L., and Xu, Q.H., 1997, Room-temperature synthesis of an Fe-containing mesoporous molecular sieve, *Mater. Lett.*, 31 (1-2), 133–136.

[57] Pasqua, L., Testa, F., Aiello, R., Di Renzo, F., and Fajula, F., 2001, Influence of pH and nature of the anion on the synthesis of pure and iron-containing mesoporous silica, *Microporous Mesoporous Mater.*, 44-45, 111–117.

[58] Chastukhin, A.E., Izotov, A.D., Gorichev, I.G., and Kutepov, A.M., 2004, Analysis of the kinetics of iron(II, III) oxide dissolution in hydrochloric acid using a generalized Delmon Model, *Theor. Found. Chem. Eng.*, 38 (1), 81–85.

Basis Set Effects on the Stabilities and Interaction Energies of Small Amide Molecules Adsorbed on Kaolinite Surface

Najwa-Alyani Mohd Nabil[1], Lee Sin Ang[1*], and Shukri Sulaiman[2]

[1]*Faculty of Applied Sciences, Universiti Teknologi MARA, Perlis Branch, Arau 02600, Malaysia*

[2]*School of Distance Education, Universiti Sains Malaysia, Pulau Pinang 11800, Malaysia*

* ***Corresponding author:***

email: anglee631@uitm.edu.my

Received: December 6, 2022
Accepted: May 19, 2023

DOI: 10.22146/ijc.79795

Abstract: *Adsorptions of small amide molecules, acetamide (AA) and* N*-methyl-acetamide (NMA) on the surface of kaolinite are investigated in this study. The focus is on the basis set effects towards the stabilities and the interaction energies of the molecules on the Al–O surface. With a fixed B3LYP functional, we increased the size of the basis sets for the single-point calculations, to find the converged interaction energies and obtain the relative stabilities. We found that, under the direct usage of Pople-type and Dunning's correlation consistent basis sets, it is not possible to achieve the pattern of convergence for the interaction energies and the relative stabilities. Compared to the complete basis set (CBS) extrapolation scheme, the double zeta basis sets deviated the most, in the range of 21 to 27%, while it is from 1 to 7% for the triple zeta basis sets. Based on the results, we suggest using 6-311++G(2df,2pd) or cc-pVQZ for energy-related quantities. Compared to AA, NMA attached more strongly by 0.5 eV on the surface of Al–O.*

Keywords: *adsorption; amide molecules; basis set; density functional theory; kaolinite*

INTRODUCTION

Basis sets are the wavefunctions for individual atoms. Its importance cannot be overstated as it forms the basis of quantum chemical calculations. The wavefunction of molecular systems is usually obtained under the linear combination of atomic orbitals (LCAO), especially those density-based and *ab initio* calculations. The accuracy of a wavefunction depends on the quality of the basis sets [1-2]. Consensus stated that the larger the basis set, the better the wavefunction [3]. With this notion, calculations are usually performed at the largest basis set that the computational resources can afford [4]. However, this does not guarantee that the basis set used is adequate for the work being done. The better-quality work is always the one where the calculation is supposed to be calculated with the next higher basis set, which infuses uncertainty into the results of the current work.

This brings to the topic of basis set convergence, which is an aspect of calculations that needed to be addressed [5-6]. The obtained values from calculations with increasing sizes of basis sets will be stopped only when the changes to the values are below a certain threshold. A direct way to deal with the basis set convergence is by systematically increasing the size of the basis set and adding polarization and diffusion functions [7]. However, the approach is not straightforward as it is difficult to find basis sets that are defined beyond a certain size, not to mention that the calculations to be performed will need enormous computer resources. Another approach is by using extrapolation schemes, known as complete basis set (CBS) [8-10]. Even though it is applied primarily to the wavefunction-based method, complete basis set calculations have also been used to extrapolate the structural and frequencies at the limit of the DFT at the B3LYP level [11-14]. However, the size of the systems investigated consisted only of small molecules. Conveniently, an online calculator has been set up to calculate the extrapolated values from different schemes [15]. CBS is also a well-known approach to overcome the incompleteness of basis sets.

One of the important calculations in theoretical work is to find the strength of an interaction between

components. It is also used as a check on the stability of systems. For example, the adsorption of molecules on surfaces (e.g., graphene, boron nitride, metals, and clay). Theoretical approaches used to study the interactions include the cluster and periodic calculations, under a variety of approximations, either quantum mechanical, Monte Carlo, or force fields [16-18]. The interactions between constituent molecules of a system have a few names to them. Interaction energy (also known as the adsorption energy) and binding energy have been used to show the strength of the interaction between constituents as Eq. (1). Using a supermolecular approach, the interaction energy (E_{int}) and binding energy (E_{bin}) can be calculated by:

$$E_{int} \text{ or } E_{bin} = E_{complex\ AB} - E_{monomer\ A} - E_{monomer\ B} \quad (1)$$

The difference between E_{int} and E_{bin} is the way the energies of the monomers are obtained. For E_{int}, the energies of the monomers are "calculated at the same positions of the nuclei as those in the total system", while for E_{bin}, the nuclei of the monomers are at their optimal positions [19-20]. However, some research papers do not seem to separate clearly these two quantities.

Previously, adsorption of the amide molecules has been performed [21-24]. However, the reported relative stability for formamide (FA), acetamide (AA), *N*-methylformamide (NMFA), and *N*-methylacetamide (NMA) absorbed on the kaolinite surfaces have been inconsistent with different basis sets [24], which may be rectified by considering the basis sets effects. In this project, we investigate the differences between the two systems in terms of interaction energy and relative stability. The focus is on the adsorption of amide molecules on kaolinite surfaces. Two smallest amide molecules, AA and NMA were selected for the investigations, as we would like to keep computational resources within a manageable range. Also, both molecules were investigated in a previous report [24], which enables comparisons to be made. We show that the strength of the interaction between the kaolinite surface and the amide molecules is dependent on the basis sets used and found that one should not conclude on the relative stability of an adsorption study based on the results of a single basis set. Finally, we suggested basis sets to be used for the investigation of interaction energies and relative stability in amides absorbed on the Al–O surface.

■ EXPERIMENTAL SECTION

Materials

The Al–O kaolinite surface is modeled from the crystal structure of kaolinite by Bish et al. [25]. Only the octahedral surface is used as it can form stronger interactions with adsorbates, as compared to the tetrahedral [21,26], hence easier to obtain converged structures. The final octahedral (001) surface cluster has 6 silicone atoms, 6 aluminum atoms, 36 oxygen atoms, and 23 hydrogen atoms. For the initial positions of the AA and NMA molecules, both vertical and horizontal orientations of the amide molecules on the surface of the Al–O are considered (the molecules are shown in Fig. 1).

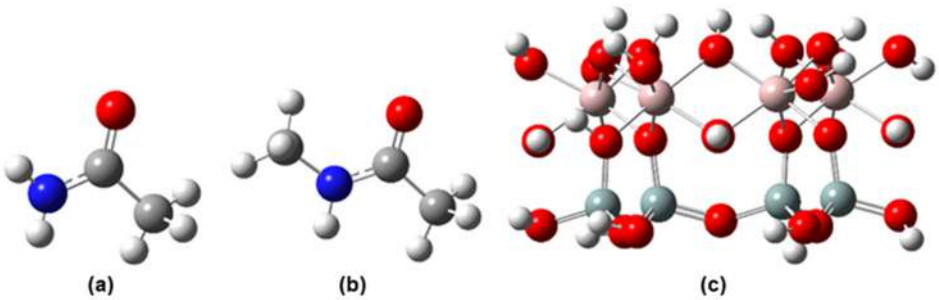

Fig 1. The structures used in this investigation: (a) acetamide (AA), (b) *N*-methyl-acetamide (NMA), (c) model of Al–O. Red sphere represents oxygen, blue represents the nitrogen, grey represents the silicon, peach represents the aluminium. For clarity, in the subsequent figures, the closest surface to the AA and NMA is the Al–O surface

Procedure

Geometry relaxations were performed at the basis 6-31G* and 6-31G**, to gauge the effects of adding polarization functions to the hydrogen atoms. Only the hydrogen and the oxygen atoms closest to the amide molecules are relaxed, together with the amide molecules. All the quantum mechanical calculations in this work were performed with the G09 suite of program [27], and the analyses on the wavefunction by Multiwfn [28]. The renderings of the figures in the work were done with GaussView [29] and UCSF ChimeraX [30]. With the geometry obtained at 6-31G*, and later re-optimized at 6-31G**, single point calculations using larger size basis sets were performed with split-valence (6-311++G** and 6-311++G(2df,2pd)) and Dunning's correlation-consistent (cc-pVDZ, cc-pVTZ, and cc-pVQZ) basis sets. The number of basis functions for the AA and NMA is shown in Table 1. With 505 and 513 electrons in the system of AA and NMA, respectively, the smallest number of the basis functions is 884, while the largest is 3863.

Using the B3LYP functional, we set out to find the changes in the interaction energies of the attachment of the amide molecules on the Al–O kaolinite surface. B3LYP is omnipresent in the molecular studies, making this level of theory a standard across many fields of study. Semi-empirical dispersion corrections of GD3BJ were included in the calculations of the interaction energies. Eq. (1) is used in the calculations of the strength of the interactions between adsorbates and Al–O surface.

Table 1. Number of basis functions in the calculations

Basis sets	System	
	AA	NMA
6-31G*	884	903
6-31G**	968	993
6-311++G**	1436	1472
6-311++G(2df,2pd)	2284	2348
cc-pVDZ	916	940
cc-pVTZ	2000	2058
cc-pVQZ	3748	3863

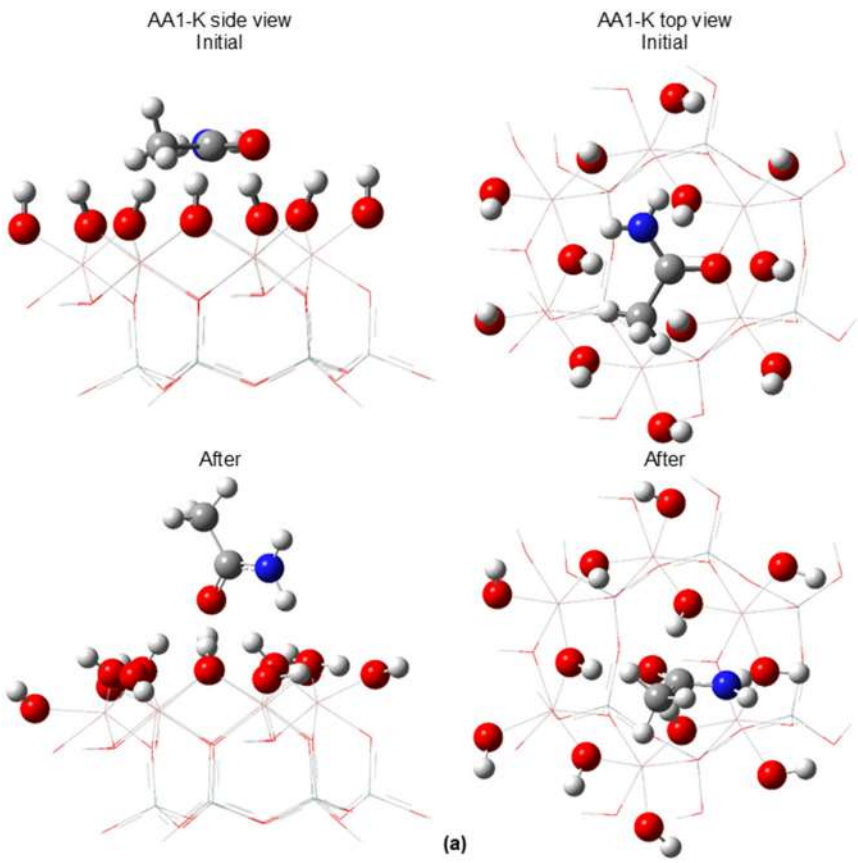

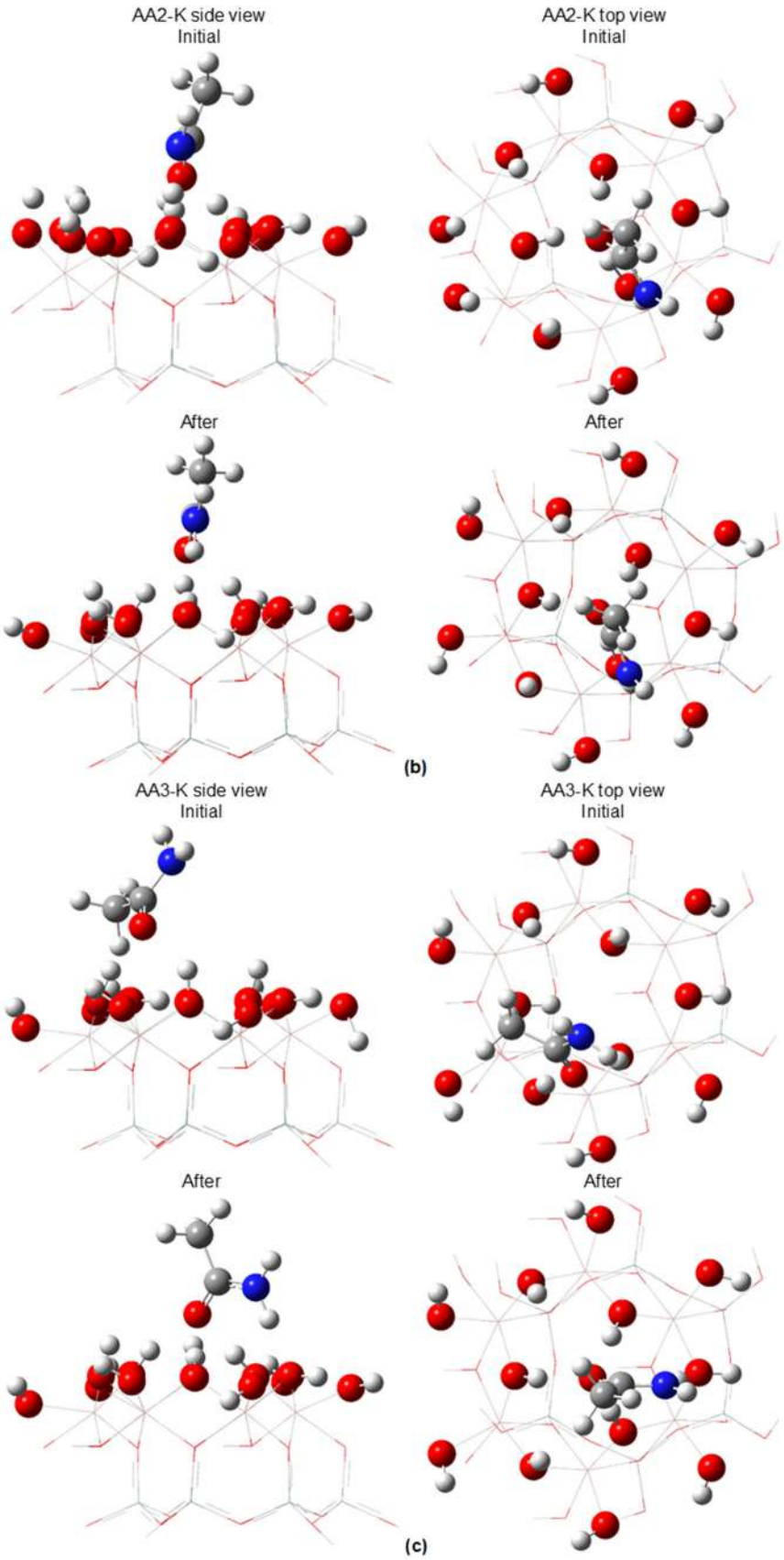
AA2-K side view
Initial
AA2-K top view
Initial
After
After
(b)
AA3-K side view
Initial
AA3-K top view
Initial
After
After
(c)

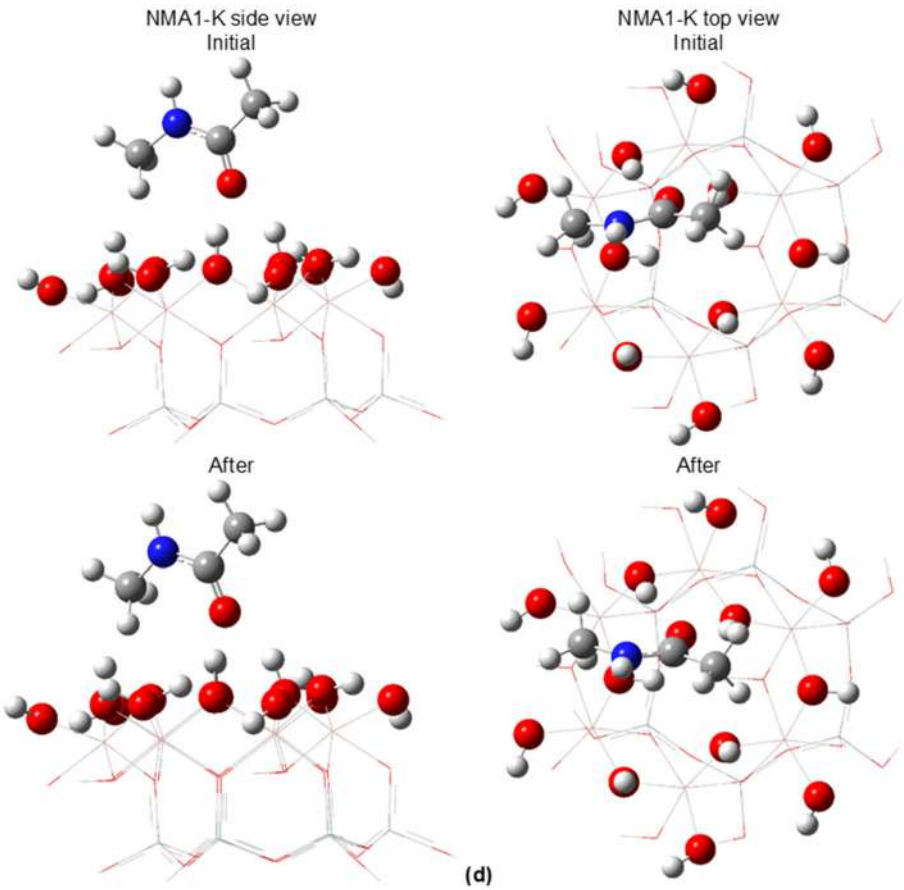
NMA1-K side view
Initial
NMA1-K top view
Initial
After
After

(d)

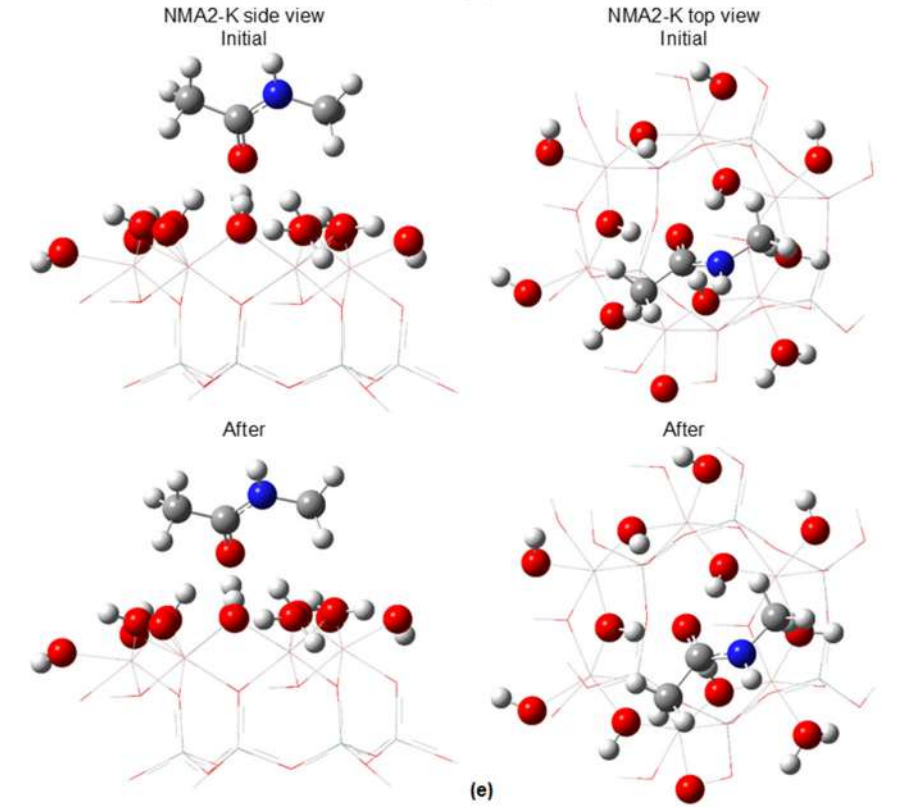
NMA2-K side view
Initial
NMA2-K top view
Initial
After
After

(e)

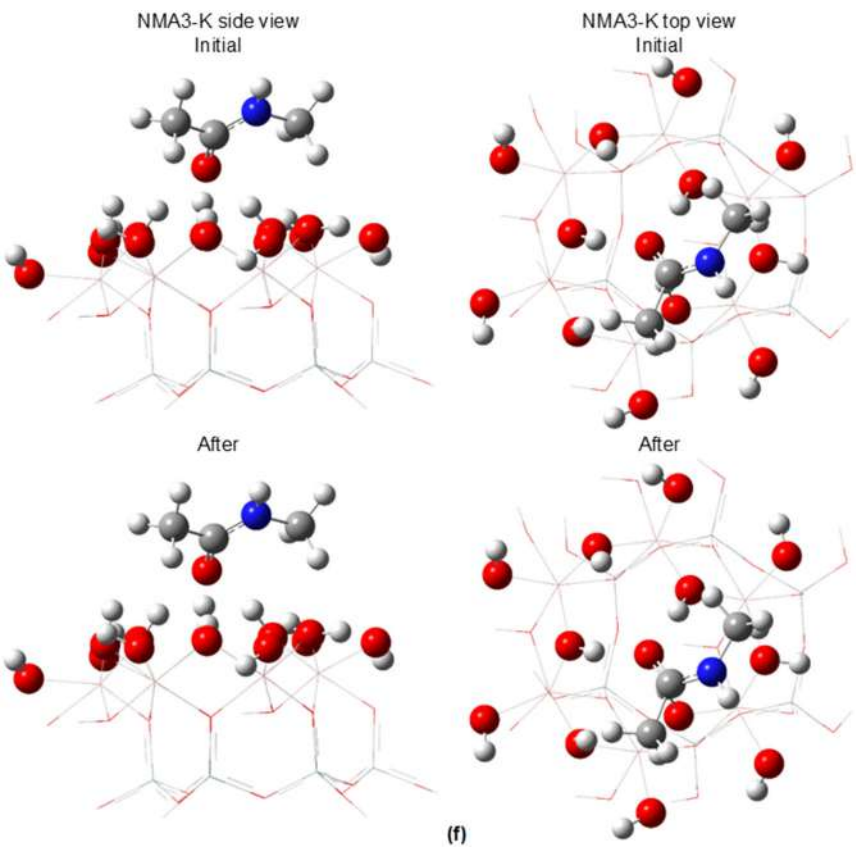

Fig 2. The initial and optimized structures of AAi-K ((a) to (c)) and NMAi-K ((d) to (f)) cluster I, where i = 1, 2, 3

■ RESULTS AND DISCUSSION

The resultant geometries as relaxed using the B3LYP/6-31G** method, which are shown in Fig. 2. The atoms shown in spheres were relaxed, while the ones in the wireframe were fixed. With the initial orientations of either planar or vertical, the AA and NMA molecules were found to always move to vertical or oblique orientations. The preferred orientation common in all cases is where the oxygen of the AA and NMA is directed toward the surface of the Al–O. This orientation is similar to the geometries obtained for water and acetic acid [26] and formamide [21], and hydrogen bondings are observed. For AA (Fig. 2(a) to (c)), the $-NH_3$ is found to be closer to the surface, and $-CH_3$ pointing up. For NMA, in Fig. 2(d), the $-NH-CH_3$ is found to be closer to the Al–O surface than the $-CH_3$ side alone. This behavior changes in Fig. 2(e) and 2(f), where there is no significant difference between the two side moieties as to which side is preferable to the Al–O surface.

The distances between the atoms in AA and NMA to Al–O are given in Tables 2 and 3. The O80 and O72 are the oxygens from AA and NMA, respectively. The other oxygens in Tables 2 and 3 are the Al–O surface oxygens, each attached to a hydrogen. These O–H are relaxed. For the AA molecule, AA3 system has the shortest and largest distances between O80 and the hydrogen on the surface of Al–O (1.770 Å with H33 and 3.066 Å with H56), while the corresponding values for AA1 and AA2 systems are in between these two extremes. For the NMA molecule, O72 has the shortest distance with hydrogen at 1.765 Å (in NMA3 system), and the longest at 3.746 Å (in NMA1 system). Within the three systems, NMA2 and NMA3 have the NMA molecule closer to the surface of Al–O (in which their average O72···H is shorter than in NMA1).

As for the O–H on the Al–O surface, the distances for the three systems are between 0.963 and 0.977 Å for AA, and between 0.961 and 0.976 Å for NMA. These values, using B3LYP/6-31G**, do not deviate much from

Table 2. The distances between atoms in the relaxed structure for AA systems

Selected atom pairs		Distances in systems (Å)		
Atom 1	Atom 2	AA1	AA2	AA3
O80	H33	1.792	1.835	**1.770**
O80	H45	1.902	1.992	1.798
O80	H56	2.976	2.848	3.066
O80	H61	2.062	1.772	1.920
O4	H14	0.975	0.973	0.976
O12	H13	0.975	0.972	0.972
O17	H18	0.972	0.965	0.969
O23	H45	0.972	0.965	0.969
O24	H33	0.977	0.970	0.972
O27	H28	0.972	0.968	0.970
O36	H37	0.974	0.971	0.970
O40	H56	0.968	0.965	0.964
O48	H49	0.974	0.970	0.968
O51	H57	0.965	0.964	0.963
O60	H61	0.971	0.976	0.967
O63	H64	0.974	0.971	0.970

Table 3. The distances between atoms in the relaxed structure for NMA systems

Selected atom pairs		Distances in systems (Å)		
Atom 1	Atom 2	NMA1	NMA2	NMA3
O72	H33	1.860	1.785	**1.765**
O72	H45	3.746	1.960	1.955
O72	H56	1.899	2.823	2.955
O72	H61	2.425	1.785	1.890
O4	H14	0.975	0.968	0.976
O12	H13	0.976	0.975	0.975
O17	H18	0.966	0.968	0.967
O23	H45	0.961	0.966	0.965
O24	H33	0.968	0.971	0.972
O27	H28	0.967	0.969	0.970
O36	H37	0.971	0.970	0.970
O40	H56	0.974	0.965	0.965
O48	H49	0.968	–	0.968
O51	H57	0.962	0.964	0.962
O60	H61	0.967	0.976	0.971
O63	H64	0.969	0.970	0.970

the O–H bond lengths reported in the adsorption of urea on kaolinite, but underestimated the experimental values from Bish [25]. This observation shows that the impact on the O–H bond length of the cluster for the adsorption of AA and NMA is similar to that of urea, possibly due to the similar fashion in AA and NMA react to the Al–O surface.

The distance of oxygen from AA to the hydrogen on the kaolinite surface, as reported by Song et al. [24] ranged from 1.906 to 2.305 Å, using B3LYP/6-31G*. In the same report, for the case of NMA, Song et al. [24] obtained 1.807 to 2.983 Å. Using a larger basis set (6-31G**) does produce a shorter and larger distance between the adsorbate and the surface. As the difference between the reported results [24] and this report in obtaining geometry is the polarization function added to hydrogen (6-31G* versus 6-31G**), it is interesting to check the effects on the larger basis sets on the geometrical relaxations. The result (Tables 2 and 3) where NMA moved closer to the kaolinite surface compared to AA, agrees with the result reported by Song et al. [24].

Further analysis of the depth of the molecules being absorbed on the Al–O surface was done by calculating the distance of O80 and O72 to the centroid of the seven aluminum atoms. This centroid was chosen because the aluminum atoms are the closest fixed atoms to the O80 or O72. It was found that AA3 and NMA2 are closest to the centroid, which means the two systems penetrated further than the other systems studied. NMA1 is displaced the furthest, compared to NMA2 and NMA3. The values are shown in Table 4.

For the stability, the relative energy (the difference in energy between the most stable to the other systems) is used. The relative energy gives insight into how strong the whole system is. While the total energy of the systems increases as the basis set increases in size (double zeta, triple zeta, quadruple zeta, and adding diffuse functions, as in Table 1), as required in the variational principle, the energies of the components also followed this trend: the

Table 4. Distance of the closest oxygen of AA (O80) and NMA (O72) to the centroid of the kaolinite cluster

System	Distance of O80 or O72 to centroid (Å)
AA1	3.024
AA2	3.038
AA3	2.913
NMA1	3.573
NMA2	2.903
NMA3	2.954

energy of kaolinite model and the amides increased with the basis sets. This observation applies to the Pople and Dunning's correlation-consistent basis sets. In Table 5, the relative energy shows that AA1 and NMA2 are the most stable systems. This observation is valid across the basis sets and the extrapolated values. Using the relative energy as a stability indicator, for acetamide, the ranking has it that AA1 is the most stable, followed by AA3 and AA2: AA1 > AA3 > AA2. For NMA, the stability has the order of NMA2 > NMA3 > NMA1. Hence, based on the relative energy, AA1 is the most stable system, while for the larger amide, NMA2 is the most stable system. As the orientation of the amides to the surface of kaolinite are all in a similar fashion (vertical or oblique), the lowest stability of AA2 and NMA1 can be attributed to the lack of penetration onto the surface of kaolinite, as mentioned in the optimized geometries.

To obtain the strength of the interaction between the components, the interaction energies are sought by using Eq. (1). The interaction energies are tabulated in Table 6. For the interaction energy of the AA-kaolinite systems, the strongest interaction is AA3 for the basis 6-31G** to cc-pVQZ, except for cc-pVDZ. However, although the total energies and the energies of the components increased as the basis sets becomes larger, the interaction energies are not always increasing accordingly. This is observed in the NMA-kaolinite systems: it increased in NMA1 and fluctuated in NMA2. But for the other systems, it decreased and is believed to converge to a constant value. The fluctuation in the interaction energy might be due to the non-uniform decrease in the total energy as the basis sets became larger.

As in the relative stability, CBS extrapolation has also been performed on the interaction energies. Referring to header CBS in Table 6, among the AA-kaolinite systems, AA3 possesses the strongest interaction, which is the same pattern observed for other basis sets (Pople's and Dunning's, except for cc-pVDZ). For AA3, the extrapolated value of –1.77 eV agrees well with the values obtained from triple-zeta and above basis sets (in Pople and Dunnings' basis sets), where the percentage difference from those values ranges from 1 to 7%. In comparison, the interaction energy for AA3, of 6-31G** and cc-pVDZ (the double zeta basis sets used in this study) deviated 21 and 27% respectively from those CBS values. Our CBS values are higher than the values

Table 5. Relative energy based on the total energy between the systems. The system with the most negative total energy is taken as the reference energy. The unit of the energy is eV

	6-31G** (geom. opt.)	6-311++G**	6-311++G(2df,2pd)	cc-pVDZ	cc-pVTZ	cc-pVQZ	CBS (exp)
AA1	0.00	0.00	0.00	0.00	0.00	0.00	0.00
AA2	0.94	1.09	1.15	1.10	1.15	1.59	1.93
AA3	0.11	0.13	0.11	0.07	0.10	0.11	0.12
NMA1	1.20	1.35	1.16	1.78	1.68	0.91	0.26
NMA2	0.00	0.00	0.00	0.00	0.00	0.00	0.00
NMA3	0.36	0.33	0.02	0.13	0.03	0.03	0.05

Table 6. Interaction energy of the AA and NMA from using Eq. (1). The unit of the energy is eV

	6-31G** (geom. opt.)	6-311++G**	6-311++G(2df,2pd)	cc-pVDZ	cc-pVTZ	cc-pVQZ	CBS (exp)
AA1	−1.93	−1.70	−1.63	−1.94	−1.66	−1.60	−1.58
AA2	−1.82	−1.59	−1.52	−2.25	−1.55	−1.07	−0.78
AA3	−2.14	−1.89	−1.81	−2.15	−1.84	−1.78	−1.77
NMA1	−1.27	−1.09	−1.02	−0.48	−0.54	−1.76	−2.76
NMA2	−2.82	−2.59	−2.27	−2.61	−1.70	−2.27	−2.73
NMA3	−1.98	−1.74	−1.67	−1.99	−1.69	−1.62	−1.60

shown by Song et al. [24] for the AA-kaolinite, in which their value is 0.39 eV. However, the magnitude of the interaction obtained here agree with the other hydrogen-bonded systems, for example, in the systems involving water molecule [31]. For the NMA-kaolinite systems, the fluctuations in the interaction energy from cc-pVDZ, cc-pVTZ, and cc-pVQZ render the CBS extrapolated values unreliable. Furthermore, the distance of O72 to the centroid for NMA1 is the furthest of the three positions, hence the interaction should not be the highest. The only trend that is acceptable is for NMA3, in which the CBS extrapolated value of –1.60 eV makes the interaction energy at 6-311++G(2df,2pd) 4% higher (–1.67 eV versus –1.60 eV). The comparison of CBS extrapolation and 6-311++G(2df,2pd) of AA2 is to be neglected, on the argument that the cc-pVDZ, cc-pVTZ and cc-pVQZ deviated too much from those of Pople basis sets. As can be seen from Table 6, the interaction energies from 6-311++G(2df,2pd) are all overestimated from the CBS extrapolated values, between 2.5 to 4.2%. Thus, the CBS extrapolated values for NMA2 should be lower by no more than 5% of –2.27 eV, making it still the highest interaction energy, agreeing with the distance of oxygen to the centroid in Table 4.

Taking CBS as the more accurate energy (with a few exceptions in the values as discussed in the preceding paragraph) in our current calculation, it is found that 6-311++G(2df,2pd) and cc-pVQZ have consistently produced interaction energies closer to CBS extrapolated values, as compared to other basis sets. For the size of the systems considered in this study, the wall time for the double-zeta basis sets completion is mostly under 2 h, while for triple zeta in the range of 8 h to 4 d, and the largest basis is roughly doubled that of triple zeta. Hence, if permissible, for future energetic calculations on amide adsorption, these two basis sets can be used, if the application of CBS scheme is not possible. Keep in mind that the interaction energy obtained will still be overestimation over the CBS extrapolated values. Larger basis sets, for example, cc-pV5Z or 6-311G++G(3df,3pd) would require larger memory requirements, rather than processing power. For geometry optimization of molecular clusters involving kaolinite, it is suggested to use triple-zeta basis sets [32]. As to the contradictory result reported before this, by comparing the strongest interaction energy of NMA- and AA-kaolinite, the CBS values shown in Table 6 generally show that NMA-kaolinite attaches more strongly to kaolinite than AA-kaolinite. Using the highest interaction energy at 6-311++G(2df,2pd) (–2.76 eV for NMA and –1.77 eV for AA), the difference in interaction energy is 0.45 eV.

Further analysis of the interactions between the amide molecules and the kaolinite surface is based on the electron density ρ at the bond critical point (BCP), as suggested by Emamian et al. [33]. The suggested formula of binding energy (BE), mentioned in Eq. (2), enables finding the contribution of hydrogen bonding to the interactions. The BCPs are calculated from the Multiwfn [28], and an example of the locations of BCPs from the Multiwfn is shown in Fig. 3. It was found that the electron densities at BCPs are insensitive to the basis sets used, whence only the hydrogen bonding energy using the largest basis sets is shown in Table 7.

$$\mathrm{BE} \approx -223.08 \times \rho(\mathrm{rBCP}) + 0.7423 \quad (2)$$

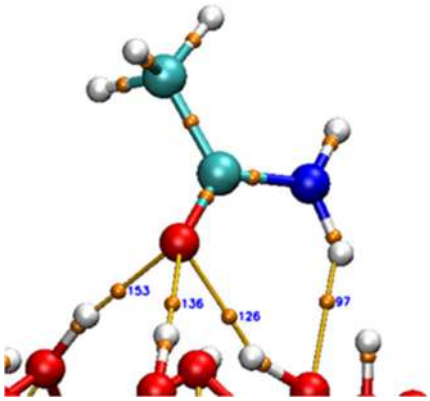

Fig 3. Locations of BCPs of hydrogen bonding between acetamide and Al–O surface. The figure is obtained using VMD [34].

Table 7. The binding energy (BE) of hydrogen bonding

System	BE (eV)
AA1	-1.14
AA2	-1.03
AA3	-1.20
NMA1	-0.66
NMA2	-1.06
NMA3	-0.96

As shown in Table 7, the hydrogen bonding to the interactions agrees with the distance to the centroid in Table 4. The shorter the distance, the higher the hydrogen bonding strength. The hydrogen bonding strengths in AA and NMA are similar (in the range –0.96 to –1.20 eV) when the distances are similar (2.90 to 3.04 Å). The lowest value at –0.66 eV is due to the large distance to the centroid. Compared to the reliable CBS values in Table 6, the hydrogen bonding is seen as a major component in the interaction energy and is important in stabilizing the system. The residue of the interaction energy might be due to the van der Waals or the dispersion energy.

CONCLUSION

The basis sets effects were studied systematically in our investigations of the adsorption of two simple amide molecules, acetamide and *N*-methyl-acetamide, on the Al–O surface of kaolinite. Although the decreasing pattern is obtained, using three basis sets in increasing size does not provide the convergence of the energies, be it with Pople or Dunning's basis sets. With the CBS extrapolation scheme, the extrapolated values are also needed to be assessed carefully, as the magnitude of increase in energy does not follow the increase in basis sets. Thus, comparison to the other basis of similar sizes is necessary to gauge the final extrapolated values. Even though the CBS value provides the limit of a functional at the basis set limit, in the case where it is not applicable, we found that the use of 6-311++G(2df,2pd) or cc-pVQZ is a good choice in studying the energetic components, with a certain degree of overestimation in magnitude. Finally, between AA and NMA, NMA is more strongly attached to the Al–O surface.

ACKNOWLEDGMENTS

The authors would like to express their sincere gratitude to Universiti Teknologi MARA (UiTM) and Universiti Sains Malaysia (USM) for their valuable support in the form of research funding and facilities.

REFERENCES

[1] Lehtola, S., 2021, Straightforward and accurate automatic auxiliary basis set generation for molecular calculations with atomic orbital basis sets, *J. Chem. Theory Comput.*, 17 (11), 6886–6900.

[2] Coşkun, M., and Ertürk, M., 2022, Double hyperbolic cosine basis sets for LCAO calculations, *Mol. Phys.*, 120 (17), e2109527.

[3] Morgante, P., and Peverati, R., 2020, The devil in the details: A tutorial review on some undervalued aspects of density functional theory calculations, *Int. J. Quantum Chem.*, 120 (18), e26332.

[4] Kirschner, K.N., Reith, D., and Heiden, W., 2020, The performance of Dunning, Jensen, and Karlsruhe basis sets on computing relative energies and geometries, *Soft Mater.*, 18 (2-3), 200–214.

[5] Akbudak, S., Uğur, G., Uğur, Ş., and Ocak, H.Y., 2019, Basis set convergence of binding energy with and without CP-correction utilizing PBEO method: A benchmark study of X_2 (X = Ge, As, Se, Sc, Ti, V, Cr, Mn, Co, Cu, Zn), *J. Theor. Comput. Chem.*, 18 (8), 1950034.

[6] Bowman, M.C., Zhang, B.Y., Morgan, W.J., and Schaefer, H.F., 2019, A remarkable case of basis set dependence: The false convergence patterns of the methyl anion, *Mol. Phys.*, 117 (9-12), 1069–1077.

[7] Myllys, N., Elm, J., and Kurtén, T., 2016, Density functional theory basis set convergence of sulfuric acid-containing molecular clusters, *Comput. Theor. Chem.*, 1098, 1–12.

[8] Jensen, F., 2023, Basis set extrapolation of vibrational frequencies, *J. Phys. Chem. A*, 127 (12), 2859–2863.

[9] Kraus, P., 2021, Extrapolating DFT toward the complete basis set limit: Lessons from the PBE family of functionals, *J. Chem. Theory Comput.*, 17 (9), 5651–5660.

[10] Pansini, F.N.N., Neto, A.C., and Varandas, A.J.C., 2016, Extrapolation of Hartree-Fock and multiconfiguration self-consistent-field energies to the complete basis set limit, *Theor. Chem. Acc.*, 135 (12), 261.

[11] Kupka, T., Buczek, A., Broda, M.A., Gajda, L., and Ignasiak, M., 2018, Convergence of nuclear magnetic shieldings and one-bond (1)J((BH)-B-11-

H-1) indirect spin-spin coupling constants in small boron molecules, *Magn. Reson. Chem.*, 56 (5), 338.

[12] Buczek, A., Kupka, T., Broda, M.A., and Żyła, A., 2016, Predicting the structure and vibrational frequencies of ethylene using harmonic and anharmonic approaches at the Kohn–Sham complete basis set limit, *J. Mol. Model.*, 22 (1), 42.

[13] Kitagawa, Y., Matsui, T., Yasuda, N., Hatake, H., Kawakami, T., Yamanaka, S., Nihei, M., Okumura, M., Oshio, H., and Yamaguchi, K., 2013, DFT calculations of effective exchange integrals at the complete basis set limit on oxo-vanadium ring complex, *Polyhedron*, 66, 97–101.

[14] Isegawa, M., Neese, F., and Pantazis, D.A., 2016, Ionization energies and aqueous redox potentials of organic molecules: Comparison of DFT, correlated ab Initio theory and pair natural orbital approaches, *J. Chem. Theory Comput.*, 12 (5), 2272–2284.

[15] Vasilyev, V., 2017, Online complete basis set limit extrapolation calculator, *Comput. Theor. Chem.*, 1115, 1–3.

[16] Sacchi, M., and Tamtögl, A., 2023, Water adsorption and dynamics on graphene and other 2D materials: Computational and experimental advances, *Adv. Phys.: X*, 8 (1), 2134051.

[17] Zhao, N., Tan, Y.X., Zhang, X., Zhen, Z.S., Song, Q.W., Ju, F., and Ling, H., 2023, Molecular insights on the adsorption of polycyclic aromatic hydrocarbons on soil clay minerals, *Environ. Eng. Sci.*, 40 (3), 105–113.

[18] Cheng, Q., Conejo, A.N., Wang, Y., Zhang, J., Zheng, A., and Liu, Z., 2023, Adsorption properties of hydrogen with iron oxides (FeO, Fe_2O_3): A ReaxFF molecular dynamics study, *Comput. Mater. Sci.*, 218, 111926.

[19] Piela, L., 2014, "Chapter 13 - Intermolecular Interactions" in *Ideas of Quantum Chemistry (Second Edition)*, Elsevier, Oxford, UK, 793–882.

[20] Grabowski, S.J., 2017, New type of halogen bond: Multivalent halogen interacting with π- and σ-electrons, *Molecules*, 22 (12), 2150.

[21] Dawley, M.M., Scott, A.M., Hill, F.C., Leszczynski, J., and Orlando, T.M., 2012, Adsorption of formamide on kaolinite surfaces: A combined infrared experimental and theoretical study, *J. Phys. Chem. C*, 116 (45), 23981–23991.

[22] Michalkova Scott, A., Dawley, M.M., Orlando, T.M., Hill, F.C., and Leszczynski, J., 2012, Theoretical study of the roles of Na^+ and water on the adsorption of formamide on kaolinite surfaces, *J. Phys. Chem. C*, 116 (45), 23992–24005.

[23] Song, K., Wang, X., Qian, P., Zhang, C., and Zhang, Q., 2013, Theoretical study of interaction of formamide with kaolinite, *Comput. Theor. Chem.*, 1020, 72–80.

[24] Song, K.H., Zhong, M.J., Wang, L., Li, Y., and Qian, P., 2014, Theoretical study of interaction of amide molecules with kaolinite, *Comput. Theor. Chem.*, 1050, 58–67.

[25] Bish, D.L., 1993, Rietveld refinement of the kaolinite structure at 1.5 K, *Clays Clay Miner.*, 41 (6), 738–744.

[26] Tunega, D., Haberhauer, G., Gerzabek, M.H., and Lischka, H., 2002, Theoretical study of adsorption sites on the (001) surfaces of 1:1 clay minerals, *Langmuir*, 18 (1), 139–147.

[27] Frisch, M.J., Trucks, G.W., Schlegel, H.B., Scuseria, G.E., Robb, M.A., Cheeseman, J.R., Scalmani, G., Barone, V., Petersson, G.A., Nakatsuji, H., Li, X., Caricato, M., Marenich, A., Bloino, J., Janesko, B.G., Gomperts, R., Mennucci, B., Hratchian, H.P., Ortiz, J.V., Izmaylov, A.F., Sonnenberg, J.L., Williams-Young, D., Ding, F., Lipparini, F., Egidi, F., Goings, J., Peng, B., Petrone, A., Henderson, T., Ranasinghe, D., Zakrzewski, V.G., Gao, J., Rega, N., Zheng, G., Liang, W., Hada, M., Ehara, M., Toyota, K., Fukuda, R., Hasegawa, J., Ishida, M., Nakajima, T., Honda, Y., Kitao, O., Nakai, H., Vreven, T., Throssell, K., Montgomery, Jr., J.A., Peralta, J.E., Ogliaro, F., Bearpark, M., Heyd, J.J., Brothers, E., Kudin, K.N., Staroverov, V.N., Keith, T., Kobayashi, R., Normand, J., Raghavachari, K., Rendell, A., Burant, J.C., Iyengar, S.S., Tomasi, J., Cossi, M., Millam, J.M., Klene, M., Adamo, C., Cammi, R., Ochterski,

J.W., Martin, R.L., Morokuma, K., Farkas, O., Foresman, J.B., and Fox, D.J., 2016, *Gaussian 09, Revision D.01*, Gaussian, Inc., Wallingford CT.

[28] Lu, T., and Chen, F., 2012, Multiwfn: A multifunctional wavefunction analyzer, *J. Comput. Chem.*, 33 (5), 580–592.

[29] Dennington, R., Keith, T.A., and Millam, J.M., 2016, *GaussView, Version 6.1*, Semichem Inc., Shawnee Mission, KS.

[30] Pettersen, E.F., Goddard, T.D., Huang, C.C., Meng, E.C., Couch, G.S., Croll, T.I., Morris, J.H., and Ferrin, T.E., 2021, UCSF ChimeraX: Structure visualization for researchers, educators, and developers, *Protein Sci.*, 30 (1), 70–82.

[31] Xiao, J., Zhao, Y.P., Fan, X., Cao, J.P., Kang, G.J., Zhao, W., and Wei, X.Y., 2017, Hydrogen bonding interactions between the organic oxygen/nitrogen monomers of lignite and water molecules: A DFT and AIM study, *Fuel Process. Technol.*, 168, 58–64.

[32] Nabil, N.N.A.M., and Ang, L.S., 2022, Selecting suitable functionals and basis sets on the study structural and adsorption of urea-kaolinite system using cluster method, *Indones. J. Chem.*, 22 (2), 361–373.

[33] Emamian, S., Lu, T., Kruse, H., and Emamian, H., 2019, Exploring nature and predicting strength of hydrogen bonds: A correlation analysis between atoms-in-molecules descriptors, binding energies, and energy components of symmetry-adapted perturbation theory, *J. Comput. Chem.*, 40 (32), 2868–2881.

[34] Humphrey, W., Dalke, A., and Schulten, K., 1996, VMD: Visual molecular dynamics, *J. Mol. Graphics*, 14 (1), 33–38.

Rapid Colorimetric Sensor Based on Gold Nanoparticles Functionalized 4-Amino-3-hydrazino-5-mercapto-1,2,4-triazole for Cortisol Detection in Saliva Sample

Hanim Istatik Badi'ah[1,2], Ni Nyoman Tri Puspaningsih[1], Ganden Supriyanto[1*], and Nasronudin Nasronudin[3]

[1]*Department of Chemistry, Faculty of Science and Technology, Airlangga University, Jl. Dr. Ir. H. Soekarno, Mulyorejo, Surabaya 60115, Indonesia*

[2]*Department of Medical Laboratory Technology, Institute of Health Science Banyuwangi, Jl. Letkol Istiqlah No. 109, Banyuwangi 68422, Indonesia*

[3]*Department of Medicine, Faculty of Medicine, Airlangga University, Jl. Dr. Ir. H. Soekarno, Mulyorejo, Surabaya 60115, Indonesia*

* ***Corresponding author:***

email: ganden-s@fst.unair.ac.id

Received: January 2, 2023
Accepted: June 13, 2023

DOI: 10.22146/ijc.80874

Abstract: *The rapid, simple, and selective colorimetric sensing method of cortisol has been successfully developed using AuNPs modified with 4-amino-3-hydrazino-5-mercapto-1,2,4-triazole (AuNPs-AHMT). The principle of this method is based on the color change from wine red to purple (redshift) when AuNPs-AHMT interacts with cortisol. The hydrogen bonding between the hydroxyl group from cortisol and the amine group from AHMT induces the aggregation of AuNPs. The modification of the AuNPs surface with AHMT aims to increase its stability. The properties of AuNPs and AuNPs-AHMT were characterized by UV-vis spectrophotometer. The interaction between AuNPs-AHMT and cortisol was studied by UV-vis and FTIR spectroscopies. The proposed method was optimized and validated. Au(III) was reduced to AuNPs at an optimum $NaBH_4$ concentration of 1.0 mM. Validation of the proposed method showed good analytical performance with linearity from 1.0–50.0 nM, accuracy 91.07–102.77%, intra-day precision < 2.22% and inter-day precision < 2.17%, detection limit 0.76 nM, quantification limit 2.54 nM, and sensitivity 0.0112 nM/mL. The proposed method also showed good selectivity with the presence of some interferences in the sample. The proposed method was successfully applied for the determination of cortisol in the saliva by the standard addition method with acceptable recovery.*

Keywords: *AHMT; colorimetric sensing; cortisol; gold nanoparticles*

■ INTRODUCTION

Cortisol is a glucocorticoid steroid hormone that is produced in the adrenal glands. The secretion of cortisol in biological fluid has a circadian rhythm where the concentration of cortisol in the morning is higher than in the night [1-2]. Cortisol is also known as a stress hormone because the secretion of cortisol can be induced by psychological and physical stress [3-5]. Besides that, the increase in cortisol concentration levels is linked to other diseases including stroke. The correlation between stroke and cortisol level shows that acute stroke mortality is related to the increase in cortisol level and is associated with the biomarker of early stroke detection and severity [6]. Cortisol is not only present in serum and urine but is also released in saliva samples. In saliva, steroidal hormones are only present in free form [7], because of their diffusion through the cells of the salivary gland [6]. It was demonstrated that salivary cortisol concentration has a correlation with free cortisol in the serum [2,6,8-9].

Some methods have been developed for cortisol detection in saliva samples, such as an immunochemical assay [10-12] and liquid chromatography-mass spectrophotometry (LCMS) [13-14]. But these methods need laboratory instruments that are relatively

expensive. These methods also require instrumentation carried out by an expert. Additionally, they are a multi-step analysis method and relatively expensive. So, the development of a new method that can be used for the early detection of cortisol that is rapid, simple, and cost-effective, such as colorimetric sensing, is very important.

In recent years, colorimetric sensors have received a lot of attention as a promising method for biological and chemical analyte detection due to their significant advantages, including the ability to be recognized with the naked eye, ease of use, quick assay times, and low cost. The principle of a colorimetric sensor is that color changes when sensing materials interact with an analyte. The color is produced by the variation in absorbance brought on by the optical characteristics of plasmonic material sensing [15-17]. Since the intensity, frequency, and location of the localized surface plasmon resonance (LSPR) bands strongly depend on the size, shape, surface modification, dielectric, and aggregation of material sensing, this optical property serves as the foundation for colorimetric sensing and can be used to detect the color change in colloid [18-19]. Specifically, gold nanoparticles (AuNPs) display an LSPR band within the visible region and have the potential as a colorimetric sensor.

AuNPs are materials or particles that have a size distribution between 1 and 100 nm and have been used in many applications such as biomedicine [20], immunochemical analysis [21], environmental monitoring [22], food safety screening [23], and colorimetric sensing for diagnostics [24]. AuNPs are interesting candidates for rapid colorimetric sensing because of their optical properties, such as their high absorption coefficients and very strong LSPR absorption band in the visible area [25]. The high surface-to-volume ratio and optical properties of AuNPs assist highly selective and sensitive detections [26]. The principle of AuNPs as a colorimetric sensor is based on color change. Colloidal AuNPs are generally red or pink and will change to another color when the aggregation of AuNPs occurs as a result of interaction with the analyte. However, AuNPs need to be stabilized to prevent self-aggregation.

Stabilization of AuNPs is carried out by using stabilizing or capping agents to increase their stability. During the chemical synthesis of AuNPs, ascorbic acid, sodium citrate, or sodium borohydride ($NaBH_4$) are normally used as capping agents. However, many capping agents are also used, such as albumin [27], γ-cyclodextrin [28], chitosan [29], and PEG [30]. In this work, 4-amino-3-hydrazino-5-mercapto-1,2,4-triazole (AHMT) was used as the capping agent to modify the AuNPs. AHMT contains mercapto, amino, hydrazine, and triazole groups and can bind with AuNPs surface via the mercapto groups. AHMT can also bind with cortisol through the hydrogen bonding interaction between the –NH group from AHMT and the –OH group from cortisol.

In this research, a novel colorimetric sensor for cortisol using AuNPs modified with AHMT was developed. The AuNPs produced, the interaction between AuNPs and AHMT, and the interaction between AuNPs-AHMT and cortisol were characterized and studied by UV-vis spectrophotometers. Fourier transform infrared (FTIR) was used to characterize the bonding between AuNPs and AHMT. The reaction between AuNPs-AHMT and cortisol was optimized, and the proposed method was validated. Finally, the proposed method was applied to the determination of cortisol in saliva samples.

■ EXPERIMENTAL SECTION

Materials

Chloroauric acid ($HAuCl_4$) was made from gold bars that dissolved in aqua regia (nitric acid and hydrochloric acid at a ratio 1:3). Sodium borohydride ($NaBH_4$, 99%) from Sigma-Aldrich with the CAS number 16940-66-2, 4-amino-3-hydrazino-5-mercapto-1,2,4-triazole (AHMT, ≥ 99%) from Sigma Aldrich with CAS number 1750-12-5), and cortisol (Hydrocortisone) from Sigma Aldrich with CAS number 50-23-7 were used in this study.

Instrumentation

The instrumentals used were a UV-visible spectrophotometer Shimadzu-1800 from Germany to measure the wavelength and absorbance of AuNPs, AuNPs-AHMT, AHMT, and AuNPs-AHMT-cortisol. Particle size analyzer (PSA) and zeta potential

measurements were performed on Zetasizer Ver. 7.01 (Malvern 1061025, Germany) to measure the size of particles and size distribution of AuNPs formed, respectively. The FTIR spectral measurements were carried out by Shimadzu IR Prestige-21, Germany.

Procedure

Synthesis of AuNPs

AuNPs were synthesized by reduction of $HAuCl_4$ with $NaBH_4$ and sodium citrate as a reduction agent, according to the literature [31], with a little modification. The procedure is as follows: 10 mL $HauCl_4$ 1 mM was stirred in a beaker glass, then added with 10 mL trisodium citrate 2 mM. While stirring, 10 mL of $NaBH_4$ 1 mM was added drop by drop into the mixture of solutions. The mixture of solutions turned into a red color after the addition of $NaBH_4$. After stirring was stopped, the stir bar was removed, and the solution was centrifuged and filtered. The result of this synthesis is a red color of AuNPs. The red colloidal AuNPs were then stored in the vial bottle at 4 °C.

Optimization of $NaBH_4$ concentration

The quantity of $NaBH_4$ as a reduction plays an important role in the production of gold nanoparticles with high stability. The concentrations of $NaBH_4$ used in this research were 0.50, 0.75, 1.00, 1.25, and 1.50 mM. The procedure is that 10.00 mL $HAuCl_4$ 1.00 mM was stirred in a beaker glass, then added to 10.00 mL of trisodium citrate 2.00 mM. While stirring, 10.00 mL of $NaBH_4$ 1.00 mM was added drop by drop into the mixture of solutions. The mixture of the solution turned a red color after the addition of $NaBH_4$. After stirring was stopped, the stir bar was removed, and the solution was centrifuged and filtered. The same procedure was carried out for the $NaBH_4$ concentrations of 0.50, 0.75, 1.25 and 1.50 mM.

Surface modification of AuNPs with AHMT

Gold nanoparticles were modified as follows: AHMT modified by 30.00 mL of AuNPs was added to 1.00 mL of AHMT at 0.05 mM. This solution was stirred for 2 h at room temperature and then centrifuged at 12000 rpm for 20 min. The AuNPs modified by AHMT were characterized by UV-vis and FTIR spectrophotometers.

The stability of AuNPs before and after modification with AHMT was observed for 2 months. The absorbance of AuNPs and AuNPs-AHMT was measured by UV-vis spectrophotometer at intervals of 15 min, 30 min, 60 min, 2 h, 3 h, 5 h, 24 h, 7 d, 30 d, and 60 d.

Colorimetric detection of cortisol using AuNPs-AHMT

The principle of AuNPs for cortisol detection is based on the color change of AuNPs-AHMT solution. As much as 2.0 mL of cortisol 10.0 nM was added into a test tube that contained 2.0 mL of AuNPs-AHMT and the 1.0 mL buffer phosphate (pH 7.0) was also added. Then the color change was observed, and the absorbance was measured by a UV-vis spectrophotometer in the range of 300–800 nm.

Method validation of AuNPs-AHMT as cortisol detection

The analytical parameter was optimized, and the proposed method was validated. The method validation was performed by analyzing some parameters such as the linearity, limit of detection (LOD), accuracy, precision, selectivity, and sensitivity. The linearity was determined with cortisol concentration ranging from 0.0 nM to 50.0 nM. LOD was evaluated from the equation $3S_b/m$, where S_b is the standard deviation of the blank and m is the slope from the calibration curve. The limit of quantification (LOQ) of an analytical method validation can be defined as 3.3 × LOD. Precision was determined from the coefficient of variance that was analyzed during the intra-day and inter-day. Accuracy was determined by the recovery of cortisol standard solutions. Recovery was determined by the standard addition method and the selectivity of this colorimetric sensor was evaluated by the addition of other substances that are normally present in the saliva, such as amylase and some hormones such as testosterone, progesterone, cortisone, and adrenal hormones.

■ RESULTS AND DISCUSSION

Synthesis of AuNPs

AuNPs were synthesized by using the chemical reduction method of the $HAuCl_4$ solution with $NaBH_4$

and sodium citrate as a reduction agent. The addition of $NaBH_4$ to the Turkevich method was established in an attempt to simplify the synthesis by eliminating the heating process [32]. The success of AuNPs colloidal formation was confirmed by the color change from yellow to wine-red colloidal solution. Then, it was characterized by a UV-vis spectrophotometer to know the surface plasmon resonance of AuNPs and by PSA to know the size distribution of AuNPs colloidal formation. The absorption spectrum of AuNPs is shown in Fig. 1(a), with the maximum surface plasmon resonance at about 540 nm, which resembles the surface plasmon resonance band of AuNPs [33]. PSA analysis shows the size distribution of AuNPs at 38.67 nm within the nanoparticle size range [34] (Fig. 1(b)).

Optimization of $NaBH_4$ Concentration

The formation of stable AuNPs colloidal is influenced by the concentration of the reducing agent. Thus, in this work, the absorption of AuNPs produced at different $NaBH_4$ concentrations was investigated. The concentrations of NaBH4 are an important factor in controlling the size of AuNPs [35]. The variations of $NaBH_4$ were 0.50, 0.75, 1.00, 1.25, and 1.50 mM. The color and size of AuNPs colloidal results were confirmed by UV-vis spectrophotometer and PSA to determine the optimum $NaBH_4$ concentration. The absorbance of UV-vis spectra with variations in $NaBH_4$ concentration is shown in Fig. 2. The highest absorbance is 0.546 at 1.0 mM of $NaBH_4$ concentration. The higher absorbance and narrower peak indicated that AuNPs formed a small

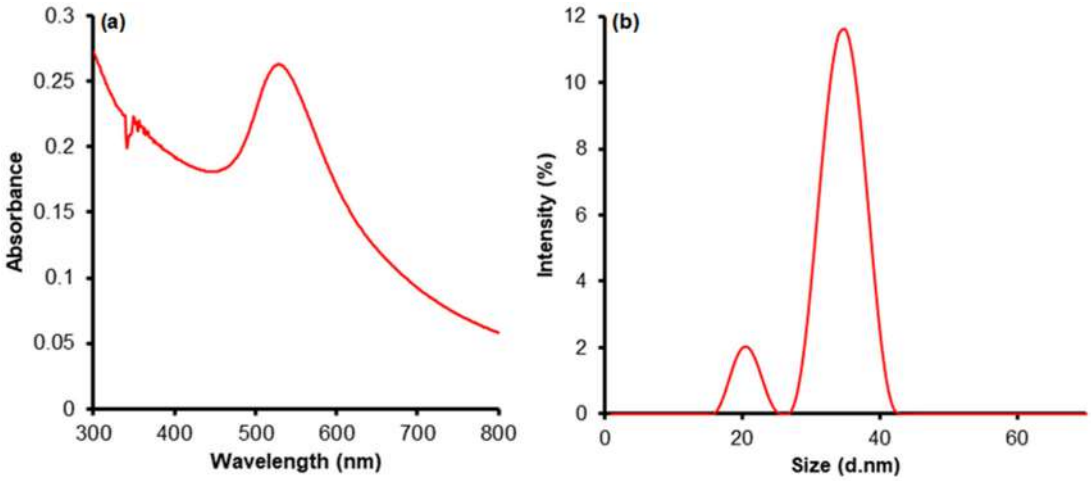

Fig 1. (a) The UV-vis spectra of AuNPs colloidal and (b) the size distribution of AuNPs colloidal

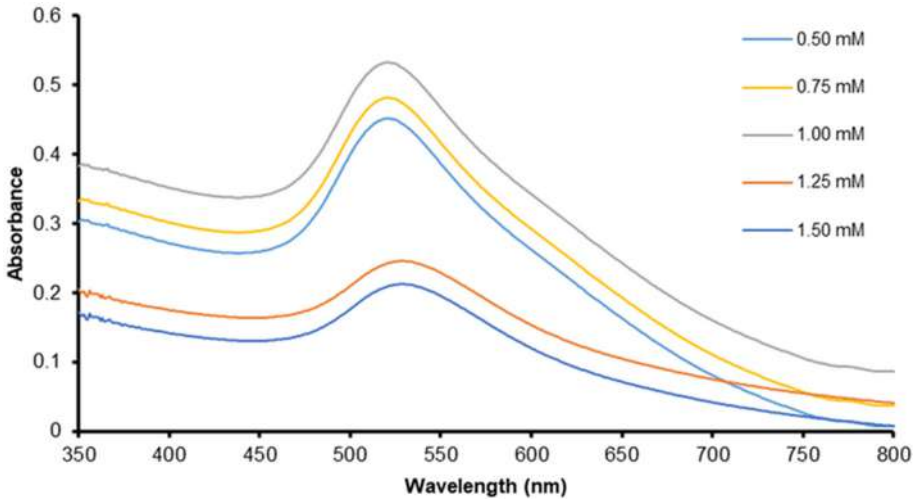

Fig 2. The UV-vis spectra of AuNPs colloidal with variation of $NaBH_4$ concentration

and homogeneous size distribution. The PSA result indicates that the smallest size distribution is 13.30 nm at a 1.00 mM concentration of $NaBH_4$, as shown in Fig. 3. The high absorbance of UV-vis spectra on 1.00 mM of $NaBH_4$ with the narrower full-width half maximum (FWHM). The FWHM criterion is potentially a very sensitive measurement for monodispersity. The narrower peak has a better signal-to-noise ratio, allowing for the detection of a smaller change in the colorimetric sensor [36].

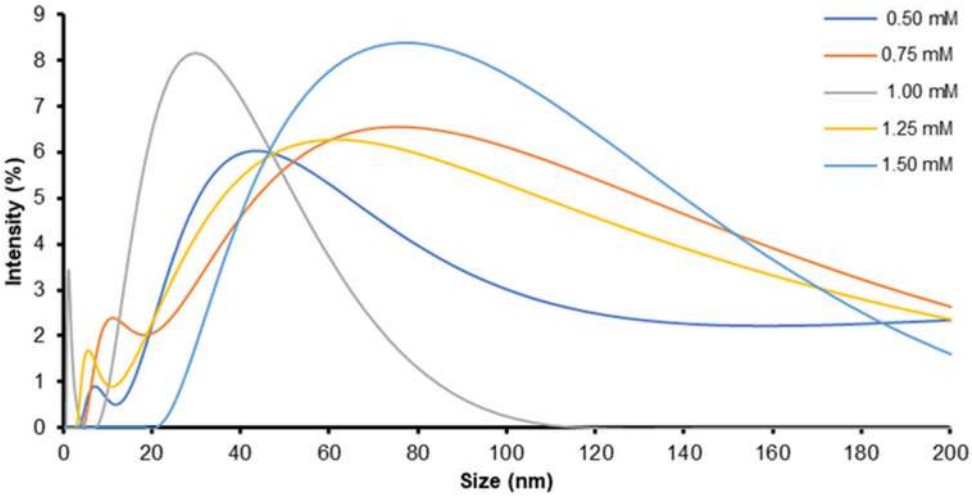

Fig 3. The PSA result of AuNPs colloidal with variation of $NaBH_4$

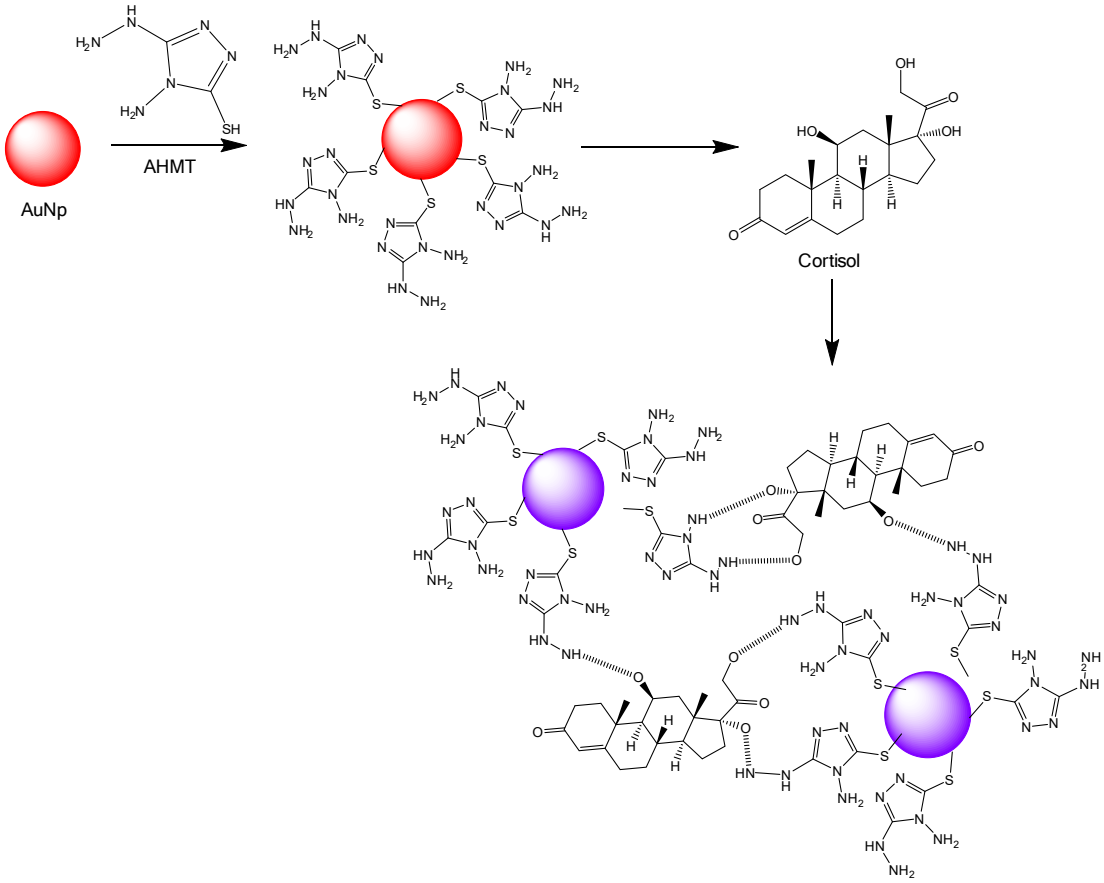

Fig 4. Illustration of reaction mechanism from colorimetric detection of cortisol using AuNPs-AHMT

Surface Modification of AuNPs with AHMT

Generally, AuNPs without modification very easy to cause aggregation and form a larger size distribution. Therefore, it is necessary to modify the surface of AuNPs with a capping agent to increase their stability. The surface attachment of mercapto groups and electron-rich nitrogen to the surface of AuNPs has been well developed [37]. One of the materials that has the ability to be a capping agent is AHMT. AHMT has one mercapto group, which can strongly coordinate with the AuNPs surface with sulfur atoms present in its assembly to protect AuNPs from aggregation [38]. In addition, AHMT also has two exocyclic amino groups and three nitrogen hybrid rings, which have a good ability to form hydrogen bonds (NH···N and OH···N) with analytes as shown in Fig. 4.

The characterization of AuNPs surface modified with AHMT was confirmed by UV-vis spectrophotometer and FTIR. Fig. 5 presents the spectra of absorption of AuNPs with and without AHMT. The surface modification of AuNPs with AHMT results in narrower peak spectra with higher absorbance compared with AuNPs without surface modification. It indicated that AHMT could lead to homogeneous size distributions and also prevent the aggregation of AuNPs.

To confirm that the surface modification of AuNPs-AHMT is successful, FTIR measurements were carried out. The FTIR spectra of AHMT with and without AuNPs are presented in Fig. 6. The characteristic peak of AHMT is 3447, 2043, and 1636 cm^{-1} which corresponds to –N–H, S–H, and N=N stretching, respectively. When

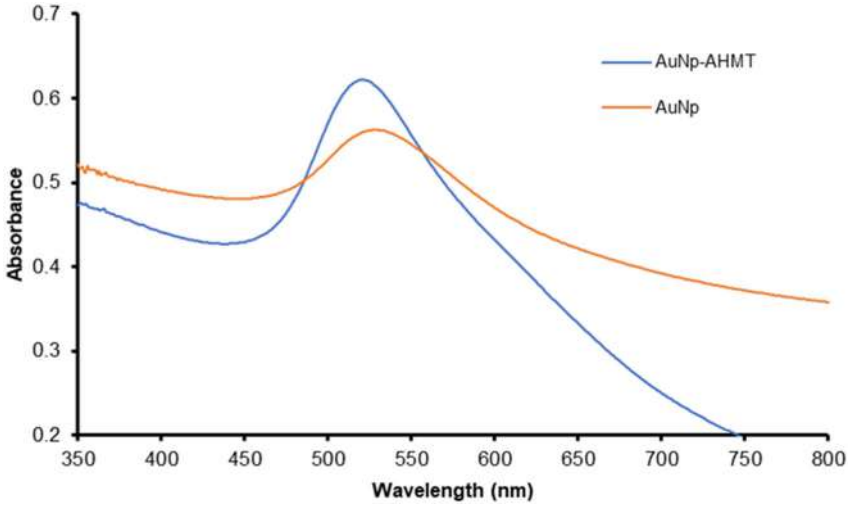

Fig 5. The UV-vis spectra absorption of AuNPs with and without modification with AHMT

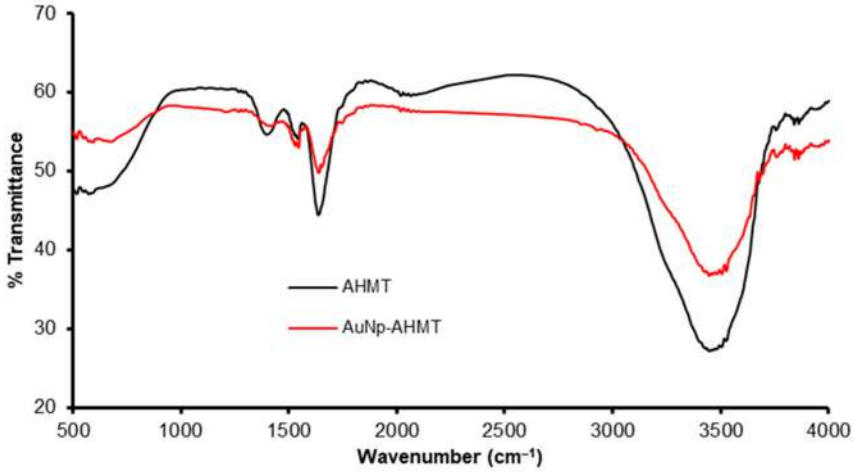

Fig 6. The FTIR spectra of AuNPs with and without modification with AHMT

AuNPs have been modified with AHMT, it causes the peak of the S–H group at 2043 cm^{-1} to disappear. This is an indication that the –SH group of AHMT coordinates with the surface of AuNPs.

The stability of AuNPs before and after modification with AHMT was evaluated during storage for 2 months and characterized with a UV-vis spectrophotometer. The UV-vis spectra in Fig. 7(a) show that AuNPs without modification with AHMT are stable for 7 d, with the highest absorbance at 0.764. The absorbance of AuNPs increases after synthesis for 7 d and decreases continuously for 2 months. This indicates that AuNPs without modification with AHMT are stable for 7 d, and after that, aggregation begins to occur on the AuNPs surface to form larger nanoparticle sizes. Whereas the AuNPs modification with AHMT is stable for up to 2 months. This is evidenced by the results of UV-vis spectra (Fig. 7(b)) that the absorbance always increased until 2 months. This indicates that the presence of AHMT will protect and prevent the aggregation on the surface of AuNPs, so the AuNPs will be more stable.

Colorimetric Detection of Cortisol Using AuNPs-AHMT

The development of AuNPs-AHMT is for the colorimetric detection of cortisol. Cortisol is a steroid hormone and is also known as a stress hormone. The level of cortisol correlates with stroke potency [6], so this compound is widely used as a biomarker of stroke. The principle of AuNPs-AHMT for cortisol detection is the hydrogen bond formation between the –OH group from cortisol and the –NH group from AHMT (Fig. 4). The cortisol structure has three hydroxyl groups that play important roles in binding with AuNPs-AHMT as a probe. Another mechanism is the aggregation of AuNPs-AHMT which causes the formation of a charge transfer complex between AHMT that is rich in electrons and electron-deficient in cortisol, which can induce the agglomeration of AuNPs and cause the color change of AuNPs-AHMT [28].

The colorimetric detection of cortisol using AuNPs-AHMT is based on the color change of AuNPs-AHMT from wine red to purple when there is an interaction

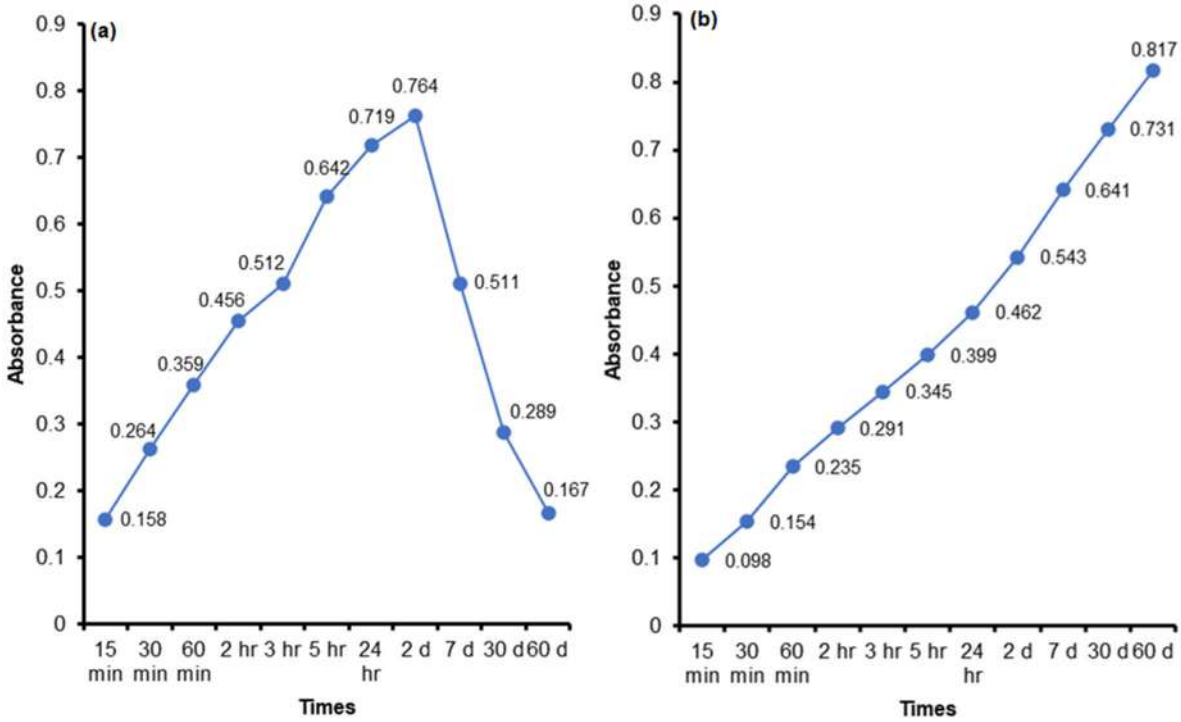

Fig 7. The stability of UV-vis spectra absorption of (a) AuNPs and (b) AuNPs-AHMT

between AuNPs-AHMT and cortisol, as shown in Fig. 8. This color can be easily visualized by the naked eye. The addition of cortisol also causes a new strong red shift at around 640 nm as shown in Fig. 9.

Fig 8. The color change from wine red (AuNPs-AHMT) to purple (AuNPs-AHMT-Cortisol)

Method Validation of AuNPs-AHMT as Cortisol Detection

The proposed method of AuNPs-AHMT for colorimetric cortisol detection was validated. The calibration curve is shown in Fig. 10. The linear response of cortisol is in the range of 1–50 nM with the correlation

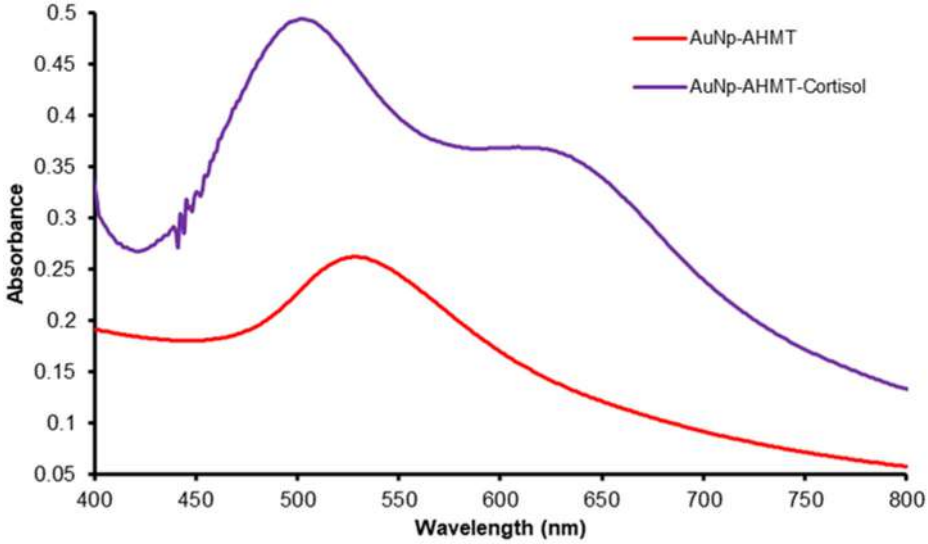

Fig 9. The UV-vis spectra absorption of cortisol colorimetric sensing using AuNPs-AHMT

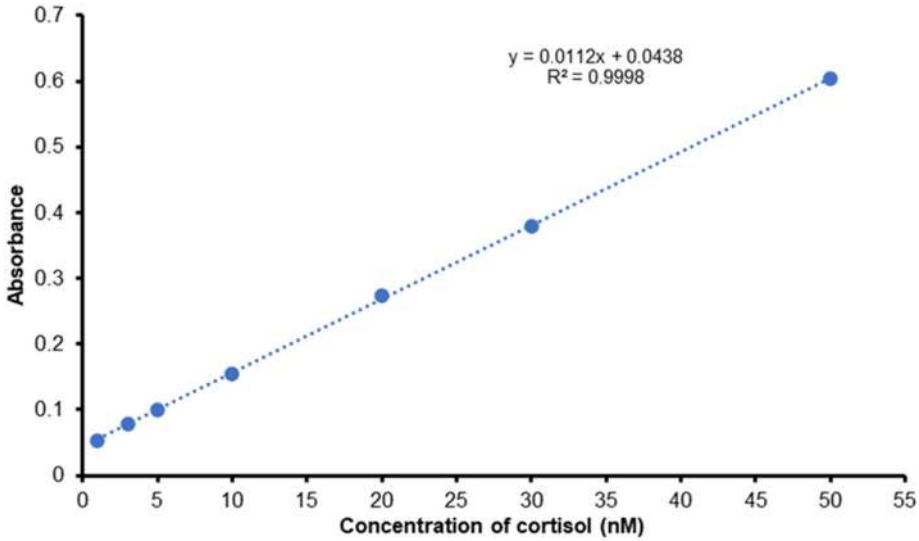

Fig 10. The linear response of cortisol with AuNp-AHMT

coefficient is 0.9998, and the sensitivity is 0.0112 nM/mL (from the slope of the curve). The LOD and LOQ values for cortisol detection using AuNPs-AHMT are 0.76 and 2.54 nM, respectively.

The precision of the developed method was determined with a standard solution of cortisol during intra-day and inter-day. The precision for intra-day and inter-day are < 2.22% and < 2.17%, respectively, as shown in Table 1. And the accuracy is 91.07–102.77%. The result of AuNPs-AHMT method validation as a cortisol colorimetric sensor are summarized in Table 2.

Selectivity of AuNPs-AHMT for Colorimetric Detection of Cortisol

The selectivity of the colorimetric sensor is very important to study as signal responses on the specific target binding-induced aggregation of AuNPs-AHMT. The probe must be insensitive to the other compound and nonspecific binding. To evaluate the selectivity of the proposed method, some interference compounds were added to the AuNPs-AHMT solution. Some potential interference compounds are testosterone, progesterone, corticosterone, and estradiol. The interference concentration added was 100.0 nM which is much higher than the cortisol concentration (10.0 nM). The result of the selectivity study is presented in Fig. 11, which

Table 1. The precision of AuNPs-AHMT as cortisol colorimetric detection

The concentration of cortisol (nM)	%Precision	
	Intra-day (%)	Inter-day (%)
1.00	1.85	2.17
3.00	2.22	1.54
5.00	1.01	1.22
10.00	1.93	0.39
20.00	0.36	0.43
30.00	0.26	0.41
50.00	0.16	0.27

Table 2. The summary of method validation

Variable	Result
Calibration equation	Absorbance = 0.0112[cortisol] + 0.0438
Correlation coefficient (R^2)	0.9998
Sensitivity (nM/mL)	0.0112
LOD (nM)	0.76
LOQ (nM)	2.54
Precision (%)	Intra-day < 2.22
	Inter-day < 2.17
Accuracy (%)	91.07–102.77

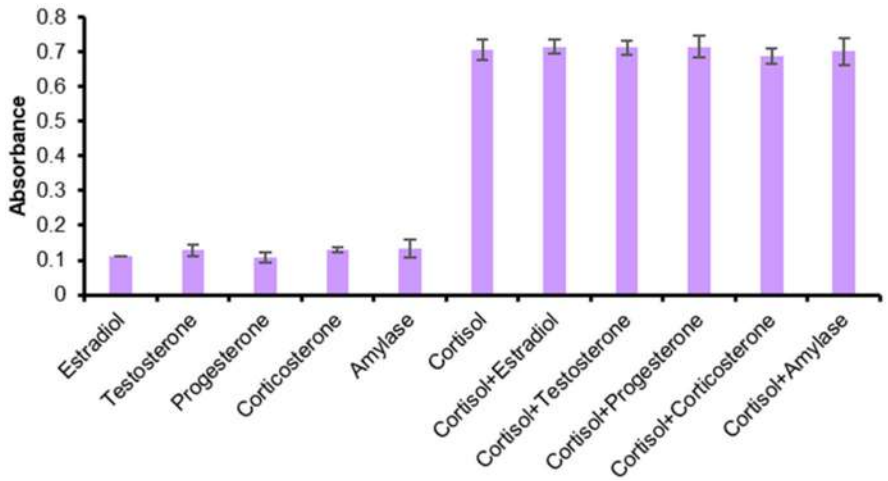

Fig 11. The selectivity of AuNPs-AHMT colorimetric sensing in some potential interferences of cortisol

Table 3. The determination of cortisol in saliva

The concentration of cortisol standard solution (nM)	Found amount (nM)	% Recovery	% RSD	ELISA assay (nM)
5.0	4.55	91.07	0.71	4.91
10.0	9.46	94.64	0.48	10.05

shows that the absorbance of cortisol (individually or mixed with another interference compound) has no obvious influence on the detection of cortisol. Accordingly, this result indicated that AuNPs-AHMT has acceptable selectivity to the cortisol.

Detection of Cortisol in Saliva

To verify the reliability of cortisol colorimetric sensing using AuNPs-AHMT, the content of cortisol in saliva samples was determined. Colorimetric sensing was applied for the detection and determination of cortisol in spiked samples by adding the standard solution of cortisol with different concentrations (5.0 and 10.0 nM) into saliva. The result is shown in Table 3 that the recovery was obtained in the range of 91.07–94.64%. This confirms the success of AuNPs-AHMT application for cortisol detection in saliva samples.

■ CONCLUSION

In this study, cortisol can be detected with a simple, rapid, and selective colorimetric assay using AuNPs modified with AHMT. The hydrogen bonding between AHMT and cortisol induces the aggregation of AuNPs-AHMT as a probe and leads to the color change from wine red to purple. The detection of cortisol was achieved by the naked eye as a colorimetric method and confirmed with UV-vis spectrophotometry which measures the absorbance change of AuNPs corresponding to the cortisol solution. No special organic or additive solvent and no complicated instruments were required in this method. From this work, good linearity, selectivity, precision, accuracy, recovery and low detection limit are obtained for cortisol detection. The rapid colorimetric method for cortisol detection using AuNPs-AHMT in saliva samples has been successfully developed and applied. In the future, it is expected to be a potential method for early detection or monitoring of stroke disease based on cortisol concentration in saliva.

■ ACKNOWLEDGMENTS

The authors thank all members of the Analytical Laboratory, Chemistry Department, Airlangga University for the use of analytical instruments.

■ REFERENCES

[1] Mohd Azmi, N.A.S., Juliana, N., Azmani, S., Mohd Effendy, N., Abu, I.F., Mohd Fahmi Teng, N.I., and Das, S., 2021, Cortisol on circadian rhythm and its effect on the cardiovascular system, *Int. J. Environ. Res. Public Health*, 18 (2), 676.

[2] Ramamoorthy, S., and Cidlowski, J.A., 2016, Corticosteroids: Mechanisms of action in health and disease, *Rheum. Dis. Clin. N. Am.*, 42 (1), 15–31.

[3] Dahlgren, A., Kecklund, G., Theorell, T., and Åkerstedt, T., 2009, Day-to-day variation in saliva cortisol–Relation with sleep, stress and self-rated health, *Biol. Psychol.*, 82 (2), 149–155.

[4] Hakamata, Y., Komi, S., Moriguchi, Y., Izawa, S., Motomura, Y., Sato, E., Mizukami, S., Kim, Y., Hanakawa, T., Inoue, Y., and Tagaya, H., 2017, Amygdala-centred functional connectivity affects daily cortisol concentrations: A putative link with anxiety, *Sci. Rep.*, 7 (1), 8313.

[5] Lee, D.Y., Kim, E., and Choi, M.H., 2015, Technical and clinical aspects of cortisol as a biochemical marker of chronic stress, *BMB Rep.*, 48 (4), 209–216.

[6] Barugh, A.J., Gray, P., Shenkin, S.D., MacLullich, A.M., and Mead, G.E., 2014, Cortisol levels and the severity and outcomes of acute stroke: A systematic review, *J. Neurol.*, 261 (3), 533–545.

[7] Aguilar Cordero, C.M., Sánchez López, A.M., Mur Villar, N., García García, I., Rodríguez López, M.A., Ortegón Piñero, A., and Cortés Castell, E., 2014, Cortisol salival como indicador de estrés fisiológico

en niños y adultos; Revisión sistemática, *Nutr. Hosp.*, 29 (5), 960–968.

[8] Perogamvros, I., Keevil, B.G., Ray, D.W., and Trainer, P.J., 2010, Salivary cortisone is a potential biomarker for serum free cortisol, *J. Clin. Endocrinol. Metab.*, 95 (11), 4951–4958.

[9] Estrada-Y-Martin, R.M., and Orlander, P.R., 2011, Salivary cortisol can replace free serum cortisol measurements in patients with septic shock, *Chest*, 140 (5), 1216–1222.

[10] Boolani, A., Channaveerappa, D., Dupree, E.J., Jayathirtha, M., Aslebagh, R., Grobe, S., Wilkinson, T., and Darie, C.C., 2019, "Trends in Analysis of Cortisol and Its Derivatives" in *Advances in Experimental Medicine and Biology*, Eds. Woods, Alisa G., and Darie, C.C., Springer International Publishing, Cham, Switzerland, 649–664.

[11] Pappachan, J.M., Hariman, C., Edavalath, M., Waldron, J., and Hanna, F.W., 2017, Cushing's syndrome: A practical approach to diagnosis and differential diagnoses, *J. Clin. Pathol.*, 70 (4), 350–359.

[12] Russell, E., Kirschbaum, C., Laudenslager, M.L., Stalder, T., de Rijke, Y., van Rossum, E.F., Van Uum, S., and Koren, G., 2015, Toward standardization of hair cortisol measurement: Results of the first international interlaboratory round robin, *Ther. Drug Monit.*, 37 (1), 71–75.

[13] Kannankeril, J., Carroll, T., Findling, J.W., Javorsky, B., Gunsolus, I.L., Phillips, J., and Raff, H., 2020, Prospective evaluation of late-night salivary cortisol and cortisone by EIA and LC-MS/MS in suspected cushing syndrome, *J. Endocr. Soc.*, 4 (10), bvaa107.

[14] Raff, H., and Phillips, J.M., 2019, Bedtime salivary cortisol and cortisone by LC-MS/MS in healthy adult subjects: Evaluation of sampling time, *J. Endocr. Soc.*, 3 (8), 1631–1640.

[15] Yang, X., Yu, Y., and Gao, Z.A., 2014, Highly sensitive plasmonic DNA assay based on triangular silver nanoprism etching, *ACS Nano*, 8, 4902–4907.

[16] Ma, X., Chen, Z., Kannan, P., Lin, Z., Qiu, B., and Guo, L., 2016, Gold nanorods as colorful chromogenic substrates for semiquantitative detection of nucleic acids, proteins, and small molecules with the naked eye, *Anal. Chem.*, 88 (6), 3227–3234.

[17] Zhang, Z., Wang, H., Chen, Z., Wang, X., Choo, J., and Chen, L., 2018, Plasmonic colorimetric sensors based on etching and growth of noble metal nanoparticles: Strategies and applications, *Biosens. Bioelectron.*, 114, 52–65.

[18] Zhou, W., Gao, X., Liu, D., and Chen, X., 2015, Gold nanoparticles for *in vitro* diagnostics, *Chem. Rev.*, 115 (19), 10575–10636.

[19] Cabuzu, D., Cirja, A., Puiu, R., and Grumezescu, A.M., 2015, Biomedical applications of gold nanoparticles, *Curr. Top. Med. Chem.*, 15 (16), 1605–1613.

[20] Tvrdonova, M., Vlcnovska, M., Vanickova, L.P., Kanicky, V., Adam, V., Ascher, L., Jakubowski, N., Vaculovicova, M., and Vaculovic, T., 2019, Gold nanoparticles as labels for immunochemical analysis using laser ablation inductively coupled plasma mass spectrometry, *Anal. Bioanal. Chem.*, 411 (3), 559–564.

[21] Sadiq, Z., Safiabadi Tali, S.H., Hajimiri, H., Al-Kassawneh, M., and Jahanshahi-Anbuhi, S., 2023, Gold nanoparticles-based colorimetric assays for environmental monitoring and food safety evaluation, *Crit. Rev. Anal. Chem.*, 1–36.

[22] Chang, K., Wang, S., Zhang, H., Guo, Q., Hu, X., Lin, Z., Sun, H., Jiang, M., and Hu, J., 2017, Colorimetric detection of melamine in milk by using gold nanoparticles-based LSPR via optical fibers, *PLoS One*, 12 (5), e0177131.

[23] Badi'ah, H.I., Seedeh, F., Supriyanto, G., and Zaidan, A.H., 2019, Synthesis of silver nanoparticles and the development in analysis method, *IOP Conf. Ser.: Earth Environ. Sci.*, 217, 012005.

[24] Mauriz, E., 2020, Clinical applications of visual plasmonic colorimetric sensing, *Sensors*, 20 (21), 6214.

[25] Saha, K., Agasti, S.S., Kim, C., Li, X., and Rotello, V.M., 2012, Gold nanoparticles in chemical and biological sensing, *Chem. Rev.*, 112 (5), 2739–2779.

[26] Bolaños, K., Kogan, M.J., and Araya, E., 2019, Capping gold nanoparticles with albumin to

improve their biomedical properties, *Int. J. Nanomed.*, 14, 6387–6406.

[27] Slavgorodska, M.V., Gurova, Y.O., and Kyrychenko, A., 2021, γ-Cyclodextrin as a capping agent for gold nanoparticles, *Comput. Theor. Chem.*, 1194, 113060.

[28] Li, F., He, T., Wu, S., Peng, Z., Qiu, P., and Tang, X., 2021, Visual and colorimetric detection of uric acid in human serum and urine using chitosan stabilized gold nanoparticles, *Microchem. J.*, 164, 105987.

[29] Thambiliyagodage, C., 2022, Ligand exchange reactions and PEG stabilization of gold nanoparticles, *Curr. Res. Green Sustainable Chem.*, 5, 100245.

[30] Bouduban, M.E.F., Burgos-Caminal, A., Ossola, R., Teuscher, J., and Moser, J.E., 2017, Energy and charge transfer cascade in methylammonium lead bromide perovskite nanoparticle aggregates, *Chem. Sci.*, 8 (6), 4371–4380.

[31] Chan, K.L., Fawcett, D., and Poinern, G.E.J., 2016, Gold nanoparticle treated textile-based materials for potential use as wearable sensors, *Int. J. Sci.*, 5 (5), 82–89.

[32] De Souza, C.D., Nogueria, B.R., and Rostelato, M.E.C.M., 2019, Review of the methodologies used in the synthesis gold nanoparticles by chemical reduction, *J. Alloys Compd.*, 798, 714–740.

[33] Kesik, M., Kanik, F.E., Hizalan, G., Kozanoglu, D., Esenturk, E.N., Timur, S., and Toppare, L., 2013, A functional immobilization matrix based on a conducting polymer and functionalized gold nanoparticles: Synthesis and its application an amperometric glucose biosensor, *Polymer*, 54 (17), 4463–4471.

[34] Mehravani, B., Ribeiro, A.I., and Zille, A., 2021, Gold nanoparticles synthesis and antimicrobial effect on fibrous materials, *Nanomaterials*, 11 (5), 1067.

[35] Radich, J.G., and Kamat, P.V., 2013, Making graphene holey gold nanoparticle mediated hydroxyl radical attack on reduced graphene oxide, *ACS Nano*, 7, 5546–5557.

[36] Oliveira, J.P., Prado, A.R., Keijok, W.J., Ribeiro, M.R.N., Pontes, M.J., Nogueira, B.V., and Guimarães, M.C.C., 2020, A helpful method for controlled synthesis of monodisperse gold nanoparticles through response surface modeling, *Arabian J. Chem.*, 13 (1), 216–226.

[37] Khezri, S., Bahram, M., and Samadi, N., 2018, Hydrogen bonding recognition and colorimetric detection of isoprenaline using 2-amino-5-mercapto-1,3,4-thiadiazol functionalized gold nanoparticles, *Spectrochim. Acta, Part A*, 189, 522–527.

[38] Qin, L., Zeng, G., Lai, C., Huang, D., Zhang, C., Xu, P., Hu, T., Liu, X., Cheng, M., Liu, Y., Hu, L., and Zhou, Y., 2017, A visual application of gold nanoparticles: Simple, reliable and sensitive detection of kanamycin based on hydrogen bonding, *Sens. Actuators, B,* 243, 946–954.

Physical Properties of Polyvinyl Alcohol/Chitosan Films with the Addition of Anthocyanin Extract from Butterfly Pea for Food Packaging Applications

Siti Khanifah, Alda Dwi Karina Legowo, Sholihun Sholihun, and Ari Dwi Nugraheni*

Department of Physics, Faculty of Mathematics and Natural Sciences, Universitas Gadjah Mada, Sekip Utara, Yogyakarta 55281, Indonesia

* ***Corresponding author:***

email: ari.dwi.n@ugm.ac.id

Received: January 4, 2023
Accepted: June 8, 2023

DOI: 10.22146/ijc.80946

Abstract: *Composites of polyvinyl alcohol (PVA) and chitosan (CH) polymers, with the addition of anthocyanin (AN) obtained from the butterfly pea flower, were prepared using drop-casting. The composites were made by adding different concentrations of 5–40% anthocyanin with 5 wt.% PVA and 2 wt.% CH solutions (weight ratio of PVA/CH is 80:20). These polymers solution was mixed at 80 °C and dried using the drop-casting method at 25 °C for 48 h. The composites were characterized using a scanning electron microscope (SEM), Fourier-transform infrared (FTIR), ultraviolet-visible (UV–vis spectroscopy), contact angle, antibacterial properties, and food packaging applications. The morphology obtained using an SEM showed that the PVA/CH surface with AN and glycerol was smoother than that of PVA/CH. The increased absorption at a wavelength of 650–700 nm from UV-vis spectroscopy confirmed the success addition of AN. The contact angles of PVA/CH/AN and PVA/CH/GS/AN films were 15°–66°, which showed that the films were hydrophilic. The simple antibacterial test with* Escherichia coli *and* Staphylococcus aureus *showed 16 mm inhibition zone by adding AN. The test results of these characteristics show the potential for using PVA/CH/AN and PVA/CH/GS/AN composite film to be used as an excellent development food packaging material.*

Keywords: *anthocyanin; butterfly pea; chitosan; food packaging; polyvinyl alcohol*

INTRODUCTION

Plastic consumption is increasing in all foods and beverage applications. Plastic has been used in various ways in everyday life, such as food preparation and household equipment. Based on the data from the Ministry of Industry of the Republic of Indonesia in 2018, the national demand for plastic products was 4.6 million tons. It increased by 5% in the last five years. Indeed, this problem could raise pollution because plastic is a substance that is difficult to degrade and is not environmentally friendly [1].

Reducing the amount of plastic usage can prevent environmental pollution [2]. In 2015, the United Nations implemented the 2030 program (Sustainable Development Goals) that applies ecological food packaging materials, which are easy to be recycled, nontoxic, and can be used long-term [3]. Some materials that are often used in the manufacture of food packaging are polyvinyl alcohol (PVA) because they have good mechanical properties and flexibility, water resistance, and high melting temperatures [4]. PVA is often used as a matrix in manufacturing food packaging with a chitosan (CH) filler. CH is a polysaccharide macromolecule mainly obtained from shells of marine animals, such as shrimp, which has biodegradability, compatibility, nontoxic, and easily renewable properties [5]. However, in a previous study, pure CH processed into food packaging materials had hydrophobic properties that reduced the flexibility of a film [6]. In recent years, the PVA/CH film has often been mixed with anthocyanin (AN) [7] to cause food spoilage, as observed in the changes in the food color based on the pH indicator [8].

The mixture of PVA and CH showed much better stability, mechanical properties, and material compatibility than the combination of pure PVA and pure CH [9]. As a result, it became a good development

as food packaging material. Several studies have been conducted by mixing PVA/CH with glycerol (GS) to increase the flexibility of films so that they cannot be easily destroyed [10]. AN was previously extracted from red cabbage [11] and purple sweet potato [12]. This work extracted AN from butterfly pea to fabricate PVA/CH film for food packaging. From the Ultraviolet–visible spectroscopy (UV-vis) characterization, it was found that as the AN concentration was increased, the absorbance increased.

■ EXPERIMENTAL SECTION

Materials

The plant used in this study is the butterfly pea flower from Kulon Progo Regency, Special Region of Yogyakarta. PVA (Sigma-Aldrich MW 85,000–150,000) with +99% hydrolyzed as a matrix, CH (Sigma-Aldrich MW medium) as a filler, and 85% GS ($C_3H_8O_3$) as a plasticizer were used in this study. Acetic acid (CH_3COOH, 100%) from PT. Brataco was used for diluting CH.

Instrumentation

The SEM used in the test was the Thermo Fisher (Nicolet iS10). The thickness was measured using a micrometer 150 mm QST-600. The FTIR spectrometer used was the Thermo Fisher (Nicolet iS10). The tests were conducted using UV–vis Ocean Optics (USB4000).

Procedure

Extraction of AN from the butterfly pea

The AN extraction process from Butterfly pea used the maceration method [11]. Maceration is a widely used method, and it was quickly applied by adding dried butterfly pea flowers to a 70% ethanol solution [12]. As much as 10 g of dried butterfly pea flowers were soaked in 50 mL of ethanol solution for 3 d at room temperature (25 °C). After 3 d, the results of the first immersion were filtered, and then a second immersion was performed on the dregs of the first immersion with 25 mL of ethanol. The soaked and dried process was conducted in the same way as the first process. The results of the first and second filtrations were mixed and then heated at 50 °C to remove ethanol from the extract. AN levels were measured using the pH differential method [13]. The AN content obtained from butterfly pea is 36 ± 1%wb.

Preparation PVA, CH, and GS

Fabrication films used several polymer materials. The first process is PVA solution, 50 mL of distilled water was put into a beaker glass, and the distilled water solution was heated at 120 °C. When the temperature of the distilled water solution reaches 80 °C, 5 g of PVA powder was added into the distilled water. PVA powder was dissolved in distilled water for 4 h at 80 °C to obtain a homogeneous solution. To make 2 w/v% CH solution, 10 mL of acetic acid was heated at 80 °C, then added by 2 g of CH powder into the solution. Stirring was carried out for 3 h to obtain a CH solution. The weight ratio of PVA/CH was 80/20. The mixed solution was carried out for 1 h at 60 °C, and then 0.1432 mL of GS was added. The mixed solution was poured into the petri dish and left at 25 °C for 24 h to obtain PVA/CH composite without AN.

Characterization SEM testing was performed by observing the film surface and observing the level homogeneity from the PVA, CH, AN or PVA/CH/AN and PVA, CH, GS, AN or PVA/CH/GS/AN films. If the surface film was smooth, then the homogeneity of the solution was good.

Film thickness measurements were carried out with the aim of knowing the resulting film thickness. The thickness of the film was measured by cutting the size film 1 × 1 cm.

The FTIR test was conducted to determine the functional groups of compounds formed during the mixture of PVA/CH/GS and AN. The test was performed by cutting a 1 mg film to form pellets for the testing film.

Changes in the color of the food packaging film greatly affected the AN levels in the film. The film color would be darker if it was given a large anthocyanin variation, such as 40% composition. UV–vis spectroscopy on the film color was performed by attaching a film to a 1 × 1 cm quartz blank and then observing the transmittance and absorbance of the film.

The film properties can be determined by measuring the contact angle of the film. The contact angle was measured by dripping a drop of water on the

surface of the 2 × 2 cm film. Then, the droplets on the surface were observed using a loop, and a photo was taken. The image result was processed using the application to determine the angle produced by the films.

Antibacterial testing of the film used two types of bacteria: *Escherichia coli* (ATCC 27922) and *Staphylococcus aureus* (ATCC 25923). Antibacterial observations were performed by inserting a 1 × 1 cm film into a 12 cm petri dish containing bacteria and then incubating it at 125 °C for 7 d.

Application of the PVA/CH/GS/AN films as active packaging for broccoli

The food packaging film in this study was applied to the broccoli vegetable wrap. The PVA/CH/AN and PVA/CH/GS/AN films were used to wrap broccoli by observing changes in broccoli's color and physical properties for 7 d. Based on the observations, the color change of the film would be known when the broccoli was put in a rotten state. Observations were made at a room temperature (25 °C) and a refrigerator temperature of 4 °C.

■ RESULTS AND DISCUSSION

Characterization of the Films

The mixture of several materials, such as PVA, CH, GS, and AN, in the PVA/CH/AN and PVA/CH/GS/AN films produced a different film surface under the level homogeneity of the solution materials. The surface film test results based on the SEM test are shown in Fig. 1.

The SEM results in Fig. 1(a) show that the film's surface morphology looks smoother than the surface film with the addition of GS and AN. Fig. 1(b) shows the presence of a few small grains, which are suspected of being CH powder. Fig. 1(c) shows black spots on the surface, which are supposed as dregs from the CH extract. Adding more AN concentration made the film darker and produced black holes of dregs on the sample surface [13]. Moreover, a smoother surface can be observed by adding GS, which could cover the spots on the film surface. In Fig. 1(d), adding GS produced the smoothest surface.

The addition of GS could cover the cracks on the film surface. When GS was mixed with a solution of CH and PVA, hydrogen bonds formed, which could inhibit the flexibility of macromolecule chains. Films showed the stiffness of the material mixture, which could improve the mechanical properties, such as tensile strength and flexibility, of thin films for food packaging [14]. Adding AN to the mixture of materials could also

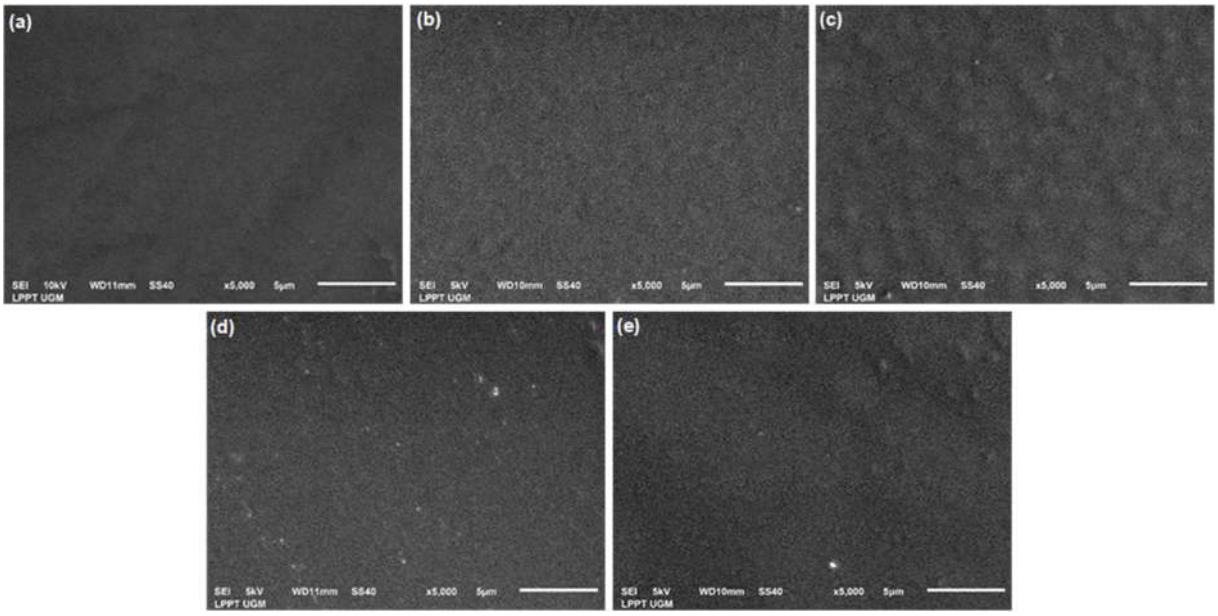

Fig 1. SEM morphology: (a) PVA/CH, (b) PVA/CH with 10% AN, (c) PVA/CH with 40% AN, (d) PVA/CH/GS with 10% AN, and (e) PVA/CH/GS with 40% AN

improve the biopolymer microstructure. This result is attributed to O–H groups in the AN structure, which interacted with H bonds in biopolymers, such as CH, resulting in the distribution and dispersion according to the biopolymer matrix [15].

With the addition of AN, PVA/CH films, with or without GS, were involved in several functional groups of PVA, CH, AN, and GS. The functional groups could be observed via FTIR spectroscopy. Fig. 2 shows the FTIR of PVA/CH, adding 5, 10, 20, and 40% AN without GS (Fig. 2(a)) and with GS (Fig. 2(b)). The presence of CH with N–H groups showed at the wavenumber of 3896 cm^{-1}, and O–H groups showed the existence of PVA and AN. With the addition of AN, the wavenumber increased drastically.

At the absorption peak of 2931 cm^{-1}, symmetrical and asymmetrical strains of C–H were produced in various layers. The absorption peak in the PVA/CH layer shows the C–O group at a wavenumber of 2331 cm^{-1}, which illustrates a deformation CH_3 absorption event [16]. The increase in peak intensity in the 1635 cm^{-1} wave indicated a rise in the amide absorption area. The aromatic ring from the 1635 cm^{-1} anthocyanin alkene bond is a C=C group that produces 1118 cm^{-1} C–N group as a mixed group of CH and AN [17].

Transparency

The PVA/CH and PVA/CH/GS films with 5, 10, 15, 20, 30, and 40% AN produced different color. Films with or without GS and AN had a blue-purple color. The addition of AN had a darker film color due to neutral quinoids and anionic quinoidal bases in equilibrium [18]. AN formed quinoidal blue due to the bathochromic displacement caused by the AN molar absorption coefficient–the transparency and UV-vis results tested on films with different AN variations.

Based on the transparency test results, different AN created darker color film. The lightest color was found in the PVA/CH and PVA/CH/GS films with an additional 5% AN variation, and the darkest color was found in the PVA/CH and PVA/CH/GS films with 40% AN with or without the addition of GS. Fig. 3 shows the transparency of PVA/CH/AN and PVA/CH/GS/AN films, where the dark color of AN can protect food from spoilage because it absorbs UV rays. Thus, avoiding UV radiation by slowing food spoilage [19].

Fig. 4(a) and 4(b) show the UV-vis films with the addition of 10–40% AN. The PVA/CH/AN and PVA/CH/GS/AN films were gradually increased at 580 and 630 nm peaks. The addition of AN produced a blue-purple color at the 550–650 nm peak. The ratio changes in the intensity of absorbance of the butterfly pea by increasing the AN at 580 and 630 nm can be attributed to the stability of the AN in the film. Mainly, the color change in the food packaging film of the butterfly pea resulted in a shift in the increase in the maximum AN absorption peak [8].

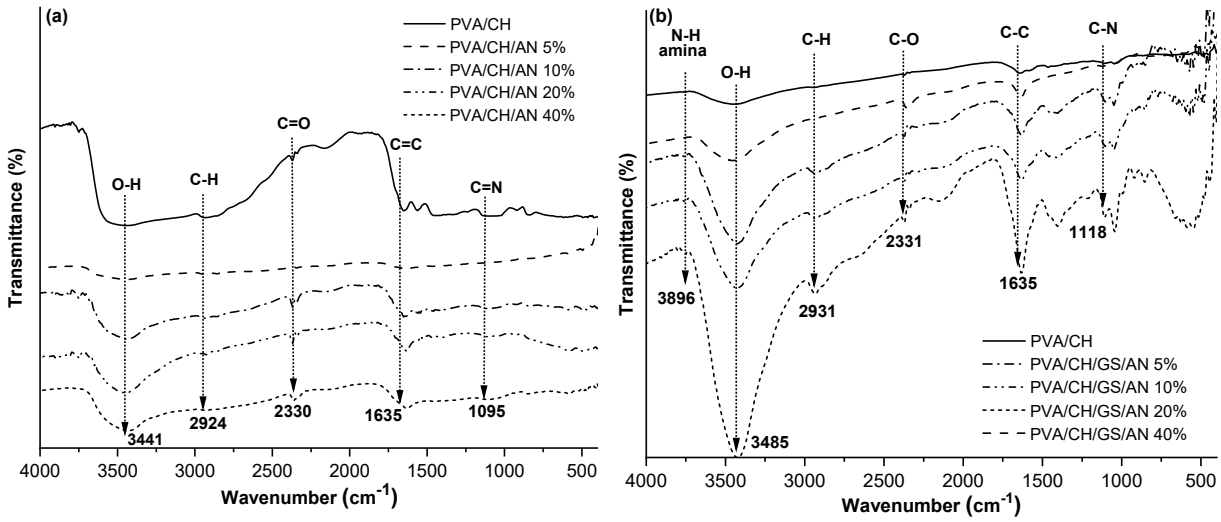

Fig 2. FTIR of PVA/CH/AN films: (a) without and (b) with glycerol

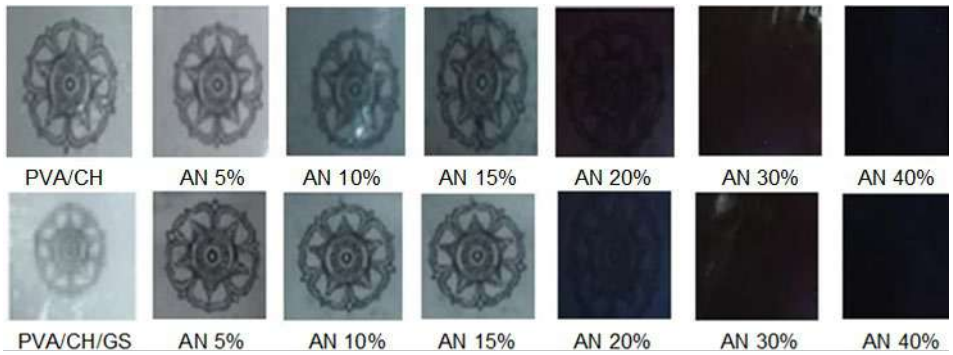

Fig 3. Transparency of PVA/CH and PVA/CH/GS with the addition of AN

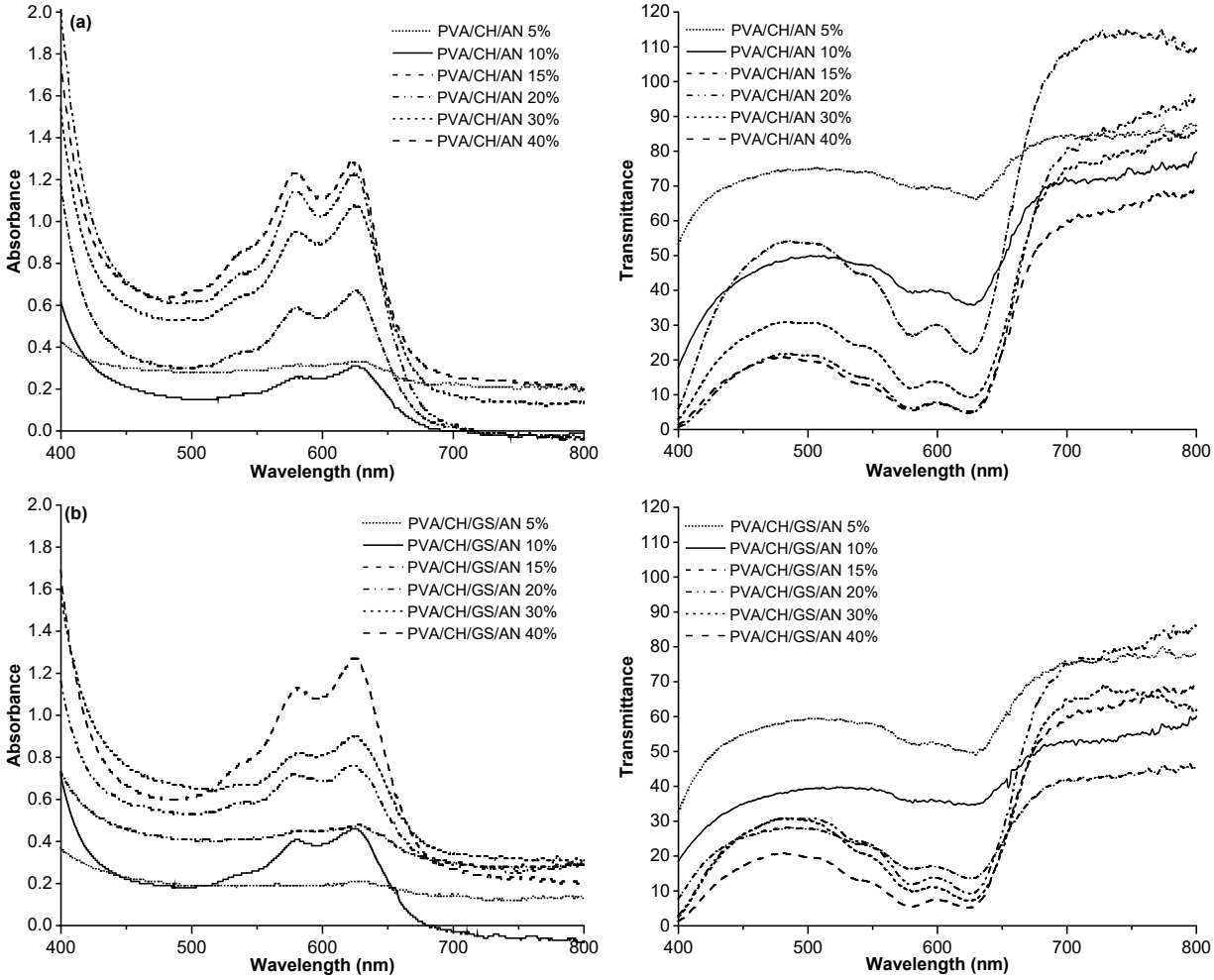

Fig 4. UV-vis film: (a) PVA/CH/AN and (b) PVA/CH/GS/AN

Meanwhile, Fig. 4(a) and 4(b) found that the transmittance gradually decreases by increasing AN composition at 200–300 nm. It is shown that there were more reflections than wave absorption. With a great reflection, the films could not block UV rays, considering the acceleration of the oxidation of food due to UV radiation. The PVA/CH/AN and PVA/CH/GS/AN films have good potential when used as food packaging. The UV-vis test data showed that the more AN added to the film, the more food oxidation would be prevented.

AN affects film contact angle with the increasing number of AN resulting in smaller contact angle values

[16]. Table 1 shows the composition of PVA/CHA/N 40% (40° ± 4°) and PVA/CH/GS/AN 40% (15° ± 1°). All the contact angles of the films with the addition of AN had a hydrophilic contact angle of < 60°. In brief, the addition of AN caused the film to absorb water.

Water absorption in the film was caused by pores on the film surface, which formed when the hydroxyl group bonded with PVA and CH. The highest contact angles were found in the PVA/CH (65° ± 1°) and PVA/CH/GS/AN 5% (66° ± 4°) films. This result can be attributed to the ionic interaction between CH and pectin, which reduced the hydrophilic groups in PVA and AN [20]. The higher the number of hydrophobic acetyl groups in CH, the higher the contact angle. The contact angle is also related to the surface roughness of the film, with a rough surface containing grains in the PVA/CH composition, as shown in the SEM results in Fig. 1.

Antibacterial Activity

Based on several characterization tests, such as the contact angle test to determine the hydrophilic nature of the film and the addition of CH polymer to films, bacterial testing was required to observe the antibacterial properties of CH and the effect of the addition of AN on the hydrophilic properties of films to inhibit bacteria when films were applied as food packaging. Mixing PVA and CH in manufacturing film food packaging can increase antibacterial activities. CH is a hydrophobic polysaccharide macromolecule, so bacteria cannot easily invade [21]. A mixture of CH and PVA was used to reduce the hydrophilic nature of PVA so that bacteria cannot easily infect the film [22]. The composition of PVA/CH/AN 5% and PVA/CH/AN 10% had an excellent absorption property because there are NH_2 and OH groups in the mixture. Accordingly, the PVA and CH materials showed film quality in inhibited antimicrobials but had poor stretching [23]. Hence, GS was added to PVA/CH/GS/AN 5% and PVA/CH/GS/AN 40%.

The addition of AN in-manufacturing food packaging films also affected their antibacterial properties. PVA/CH/AN *E. coli* (Fig. 5(a)) and PVA/CH/AN 10% *S. aureus* (Fig. 5(b)) films had clear zones of no microbial growth around 16 mm. In contrast, with the addition of GS, PVA/CH/GS/AN 5% *E. coli* (Fig. 5(e)) and PVA/CH/GS/AN 5% *S. aureus* (Fig. 5(f)) had clear zones of no microbial growth around 5 mm. Meanwhile, with the addition of more anthocyanin, PVA/CH/AN 5% *E. coli* (Fig. 5(c)), PVA/CH/AN *S. aureus* (Fig. 5(d)), PVA/CH/GS/AN 40% *E. coli* (Fig. 5(g)), and PVA/CH/GS/AN 40% *S. aureus* (Fig. 5(h)) had no clear zones of no microbial growth around. The area is decreased because the increasing levels of AN cover the function of CH as an antibacterial. Fig. 6 shows the antibacterial zone of all variants. The addition of 40% AN could inhibit the antibacterial properties of CH. Additional AN is significantly suitable for the body because they contain antioxidant properties, which can be applied to food and beverages to reduce oxidative stress [24].

Potential Test Films

After antibacterial observations, the potential of films was tested to examine the ability of the PVA/CH/AN and PVA/CH/GS/AN films to increase the shelf life of food. The test was performed on broccoli, a vegetable that quickly rots. The test was conducted by wrapping broccoli using several types of films, such as

Table 1. Contact angles of the (a) PVA/CH/AN and (b) PVA/CH/GS/AN films

(a) Materials	Contact angle (°)	**(b)** Materials	Contact angle (°)
PVA/CH	65 ± 1	PVA/CH/GS	62 ± 4
PVA/CH/AN 5%	65 ± 1	PVA/CH/GS/AN 5%	66 ± 4
PVA/CH/AN 10%	56 ± 2	PVA/CH/GS/AN 10%	51 ± 1
PVA/CH/AN 15%	62 ± 4	PVA/CH/GS/AN 15%	42 ± 6
PVA/CH/AN 20%	51 ± 2	PVA/CH/GS/AN 20%	60 ± 1
PVA/CH/AN 30%	51 ± 2	PVA/CH/GS/AN 30%	43 ± 4
PVA/CH/AN 40%	39 ± 4	PVA/CH/AN 40%	15 ± 1

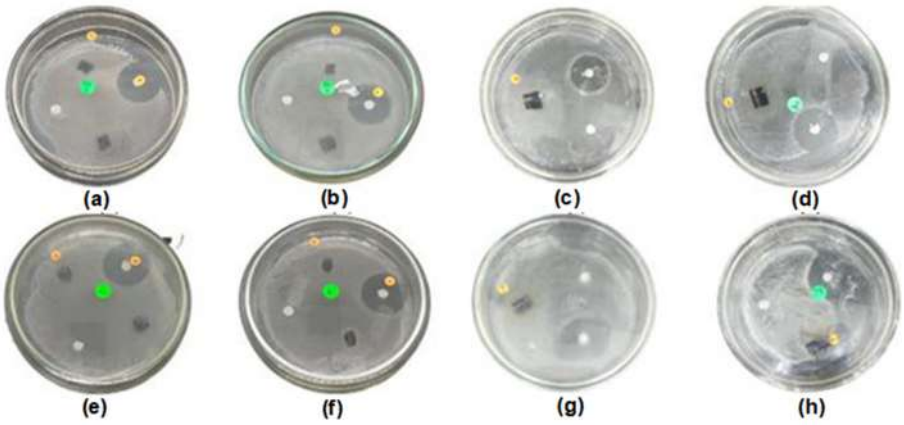

Fig 5. Bacterial test films: (a) PVA/CH/AN 10% *E. coli*, (b) PVA/CH/AN 10% *S. aureus*, (c) PVA/CH/AN 40% *E. coli*, (d) PVA/CH/AN 40% *S. aureus*, (e) PVA/CH/GS/AN 5% *E. coli*, (f)PVA/CH/GS/AN 5% *S. aureus*, (g) PVA/CH/GS/AN 40% *E. coli*, and (h) PVA/CH/GS/AN 40% *S. aureus*

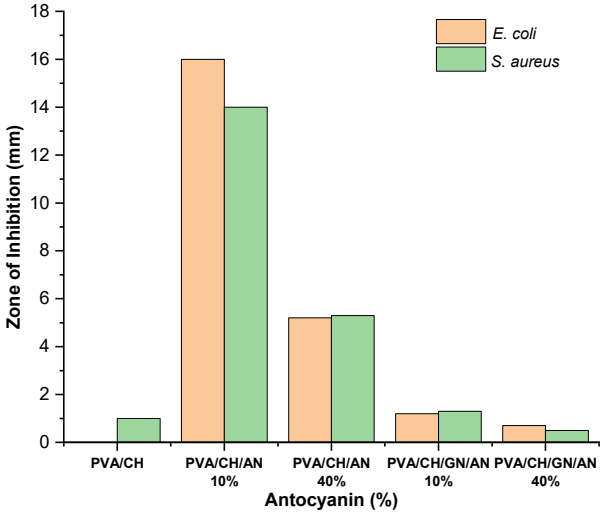

Fig 6. Zone of inhibition with different concentrations of anthocyanin

PVA/CH/AN and PVA/CH/GS/AN, with AN variation. Table 2 shows the application of the PVA/CH/AN film in the refrigerator. The test was performed by inhibiting the broccoli wrapped in films and then leaving it at refrigerator temperature. Observations were made for 7 × 24 h.

Table 3 shows the application of PVA/CH/GS/AN in the refrigerator. Based on the film observation, the first fungus in the broccoli was found in the food packaging film with the PV/CH/GS/AN composition on the fourth day at room temperature. At room temperature, bacteria multiplied, whereas, at refrigerator temperature, bacterial growth is inhibited because of the cold. The food packaging film with GS had an oilier surface than the film without GS. Hence, the addition of GS made the

Table 2. Application of the PVA/CH/AN film in a refrigerator

Sample	Day 1	Day 2	Day 3	Day 4	Day 5	Day 6	Day 7
 PVA/CH							
 PVA/CH/AN 5							

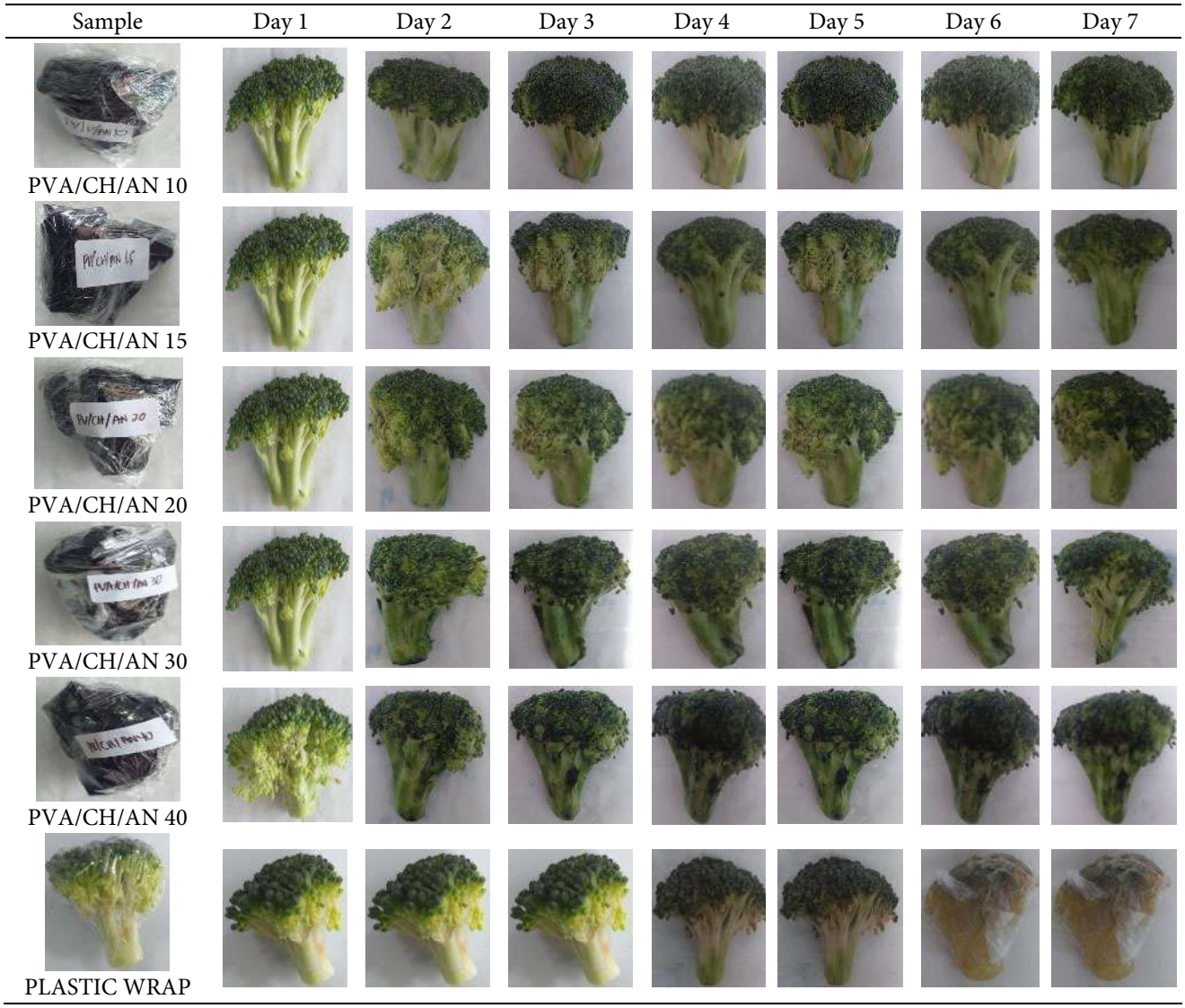

food oxidation occur quickly, such that bread wrapped using a PV/CH/GS/AN film had more moldings [13].

Furthermore, adding GS to the food packaging film resulted in the plasticization effect of GS and PVA, which can reduce the function of CH as an antibacterial. The antibacterial properties of CH bind positively charged amino groups to negatively charged sites on the bacterial wall, which binds to the cytoplasmic membrane, preventing the diffusion of nutrients into cells while destroying bacteria [25]. Adding GS also created a high level of interaction between the active groups of PVA, with the polymer leaving few free amino groups in the CH chain. This condition reduced the antibacterial activity of the mixed material when applied to food packaging.

The color of AN can changes in acid, neutral, and wet conditions. In addition, the film in the acidic condition is reddish-purple, the film in the neutral condition is blue-purple, and the film in the wet condition is blue green. The PVA/CH/AN and PVA/CH/GS/AN films with all variations provided the food information with discoloration of films when applied as food packaging. In short, AN added in PVA/CH/AN and PVA/CH/GS/AN films can be used as a pH indicator considering the color produced.

Table 3. Application of the PVA/CH/GS/AN film in a refrigerator

Sample	Day 1	Day 2	Day 3	Day 4	Day 5	Day 6	Day 7
 PVA/CH/GS							
 PVA/CH/GS/AN 5							
 PVA/CH/GS/AN 10							
 PVA/CH/GS/AN 15							
 PVA/CH/GS/AN 20							
 PVA/CH/GS/AN 30							
 PVA/CH/GS/AN 40							
 PLASTIC WRAP							

CONCLUSION

In this study, PVA/CH/AN and PVA/CH/GS/AN films with the addition of AN showed some change in physical properties. The highest contact angle film was observed in a 10% AN concentration of PVA/CH/AN composition. The film's surface looked smoother in the composition of PVA/CH/GS/AN compared to PVA/CH/AN. The FTIR test showed that the PVA/CH/AN and PVA/CH/GS/AN compositions with AN variations (5–40%) contained an AN peak. UV-vis spectroscopy shows the increase at 550–650 nm with increasing AN composition. The potential film test showed a change in the film color when the broccoli was rotting, with the fastest decay occurring at room temperature. The PVA/CH/AN composition had clear antibacterial zones of no microbial growth around 16 mm. Briefly, adding AN in small amounts, i.e., 5 and 10%, increased the antibacterial value of the films, and therefore it can be applied as a food packaging film.

ACKNOWLEDGMENTS

We would like to thank Universitas Gadjah Mada for the research facilities at the Laboratory of Instrumentation and Material Physics.

AUTHOR CONTRIBUTIONS

Siti Khanifah and Alda Dwi Karina Legowo conducted the experiment. Siti Khanifah, Ari Dwi Nugraheni, and Sholihun wrote and revised the manuscript. All authors agreed to the final version of this manuscript.

REFERENCES

[1] Ali, A., and Ahmed, S., 2018, Recent advances in edible polymer based hydrogels as a sustainable alternative to conventional polymers, *J. Agric. Food Chem.*, 66 (27), 6940–6967.

[2] Arfat, Y.A., Benjakul, S., Prodpran, T., Sumpavapol, P., and Songtipya, P., 2014, Properties and antimicrobial activity of fish protein isolate/fish skin gelatin film containing basil leaf essential oil and zinc oxide nanoparticles, *Food Hydrocolloids*, 41, 265–273.

[3] Arun Karthick, S., Ragavi, T.K., Naresh, K., and Rama Sreekanth, P.S., 2022, A study on collagen-PVA and chitosan-PVA nanofibrous matrix for wound dressing application, *Mater. Today: Proc.*, 56, 1347–1350.

[4] Bang, Y.J., Shankar, S., and Rhim, J.W., 2019, *In situ* synthesis of multi-functional gelatin/resorcinol/silver nanoparticles composite films, *Food Packag. Shelf Life*, 22, 100399.

[5] BenBettaïeb, N., Karbowiak, T., Bornaz, S., and Debeaufort, F., 2015, Spectroscopic analyses of the influence of electron beam irradiation doses on mechanical, transport properties and microstructure of chitosan-fish gelatin blend films, *Food Hydrocolloids*, 46, 37–51.

[6] Bourtoom, T., and Chinnan, M.S., 2008, Preparation and properties of rice starch–chitosan blend biodegradable film, *LWT-Food Sci. Technol.*, 41 (9), 1633–1641.

[7] Han, J.W., Ruiz-Garcia, L., Qian, J.P., and Yang, X.T., 2018, Food packaging: A comprehensive review and future trends, *Compr. Rev. Food Sci. Food Saf.*, 17 (4), 860–877.

[8] Hosseini, S.F., Rezaei, M., Zandi, M., and Farahmandghavi, F., 2016, Development of bioactive fish gelatin/chitosan nanoparticles composite films with antimicrobial properties, *Food Chem.*, 194, 1266–1274.

[9] Hu, D., and Wang, L., 2016, Fabrication of antibacterial blend film from poly (vinyl alcohol) and quaternized chitosan for packaging, *Mater. Res. Bull.*, 78, 46–52.

[10] Huang, J., Liu, J., Chen, M., Yao, Q., and Hu, Y., 2021, Immobilization of roselle anthocyanins into polyvinyl alcohol/hydroxypropyl methylcellulose film matrix: Study on the interaction behavior and mechanism for better shrimp freshness monitoring, *Int. J. Biol. Macromol.*, 184, 666–677.

[11] Kaewklin, P., Siripatrawan, U., Suwanagul, A., and Lee, Y.S., 2018, Active packaging from chitosan-titanium dioxide nanocomposite film for prolonging storage life of tomato fruit, *Int. J. Biol. Macromol.*, 112, 523–529.

[12] Liu, J., Huang, J., Ying, Y., Hu, L., and Hu, Y., 2021, pH-sensitive and antibacterial films developed by incorporating anthocyanins extracted from purple potato or roselle into chitosan/polyvinyl alcohol/nano-ZnO matrix: Comparative study, *Int. J. Biol. Macromol.*, 178, 104–112.

[13] Shojaee Kang Sofla, M., Mortazavi, S., and Seyfi, J., 2020, Preparation and characterization of polyvinyl alcohol/chitosan blends plasticized and compatibilized by glycerol/polyethylene glycol, *Carbohydr. Polym.*, 232, 115784.

[14] Mallakpour, S., and Madani, M., 2012, Transparent and thermally stable improved poly (vinyl alcohol)/Cloisite Na^+/ZnO hybrid nanocomposite films: Fabrication, morphology and surface properties, *Prog. Org. Coat.*, 74 (3), 520–525.

[15] Marpaung, A.M., Andarwulan, N., Hariyadi, P., and Nur Faridah, D., 2017, The colour degradation of anthocyanin-rich extract from butterfly pea (*Clitoria ternatea* L.) petal in various solvents at pH 7, *Nat. Prod. Res.*, 31 (19), 2273–2280.

[16] Migliorini, A.A., Piroski, C.S., Daniel, T.G., Cruz, T.M., Escher, G.B., Vieira do Carmo, M.A., Azevedo, L., Marques, M.B., Granato, D., and Rosso, N.D., 2019, Red chicory (*Cichorium intybus*) extract rich in anthocyanins: Chemical stability, antioxidant activity, and antiproliferative activity *in vitro*, *J. Food Sci.*, 84 (5), 990–1001.

[17] Ngo, T.M.P., Nguyen, T.H., Dang, T.M.Q., Tran, T.X., and Rachtanapun, P., 2020, Characteristics and antimicrobial properties of active edible films based on pectin and nanochitosan, *Int. J. Mol. Sci.*, 21 (6), 2224.

[18] Moloney, M., Robbins, R.J., Collins, T.M., Kondo, T., Yoshida, K., and Dangles, O., 2018, Red cabbage anthocyanins: The influence of D-glucose acylation by hydroxycinnamic acids on their structural transformations in acidic to mildly alkaline conditions and on the resulting color, *Dyes Pigm.*, 158, 342–352.

[19] Nuanmano, S., Prodpran, T., and Benjakul, S., 2015, Potential use of gelatin hydrolystate as plasticizer in fish myofibrillar protein film, *Food Hydrocolloids*, 47, 61–68.

[20] Pereira, V.A., de Arruda, I.N.Q., and Stefani, R., 2015, Active chitosan/PVA films with anthocyanins from *Brassica oleraceae* (red cabbage) as time–temperature indicators for application in intelligent food packaging, *Food Hydrocolloids*, 43, 180–188.

[21] Qin, C., Li, H., Xiao, Q., Liu, Y., Zhu, J., and Du, Y., 2006, Water-solubility of chitosan and its antimicrobial activity, *Carbohydr. Polym.*, 63 (3), 367–374.

[22] Ramli, M.E., Mohd Salleh, R., Tajarudin, H.A., and Zulkurnain, M., 2021, Influence of amylose content on phenolics fortification of different rice varieties with butterfly pea (*Clitoria ternatea*) flower extract through parboiling, *LWT-Food Sci. Technol.*, 147, 111493.

[23] Rana, P., Murmu, N., Padhan, S.K., and Sahu, S.N., 2020, Butterfly pea (*Clitoria ternatea*) extract as a green analytical tool for selective colorimetric detection of bisulphate (HSO_4^-) ion in aqueous medium, *Spectrochim. Acta, Part A*, 237, 118376.

[24] Shankar, S., and Rhim, J.W., 2017, Preparation and characterization of agar/lignin/silver nanoparticles composite with ultraviolet light barrier and antibacterial properties, *Food Hydrocolloids*, 71, 76–84.

[25] Wu, Z., Huang, X., Li, Y.C., Xiao, H., and Wang, X., 2018, Novel chitosan films with laponite immobilized Ag nanoparticles for active food packaging, *Carbohydr. Polym.*, 199, 210–218.

Supplementary Data

This supplementary data is a part of a paper entitled "Synthesis of Calix[4]resorcinarene Derivatives as Antimalarial Agents through Heme Polymerization Inhibition Assay".

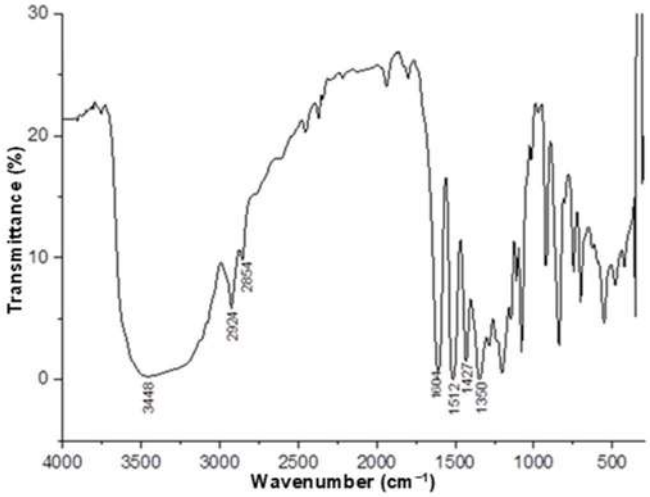

Fig S1. The FTIR spectra of calix[4]resorcinarene **1**

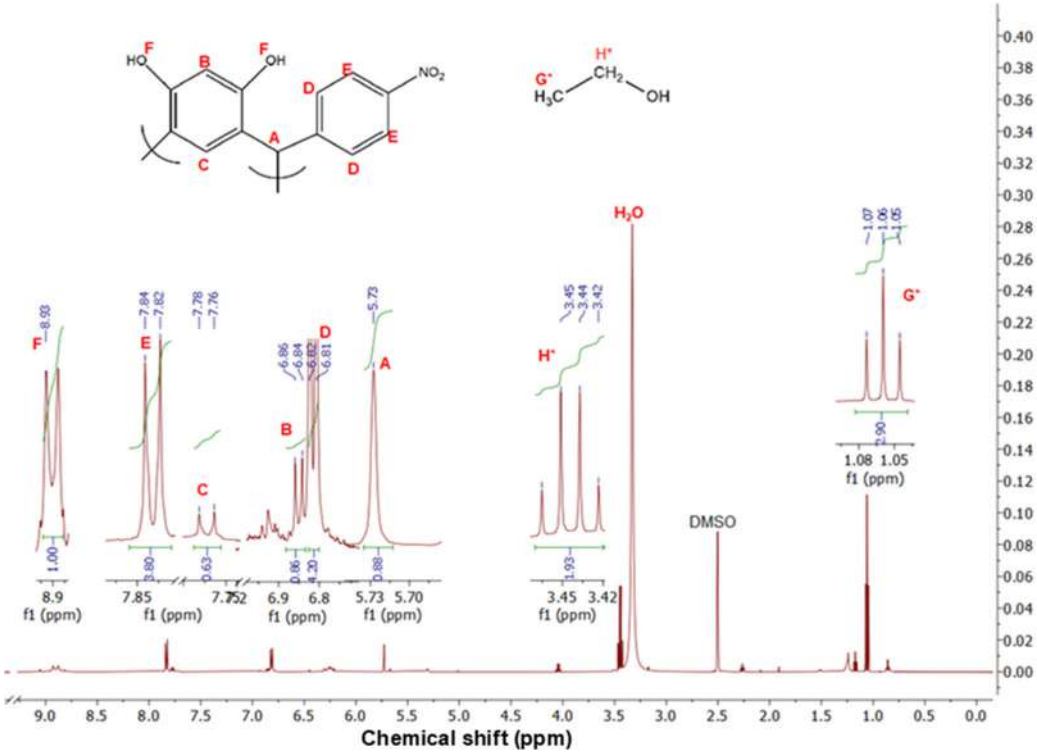

Fig S2. The ^{1}H-NMR spectra of calix[4]resorcinarene **1**

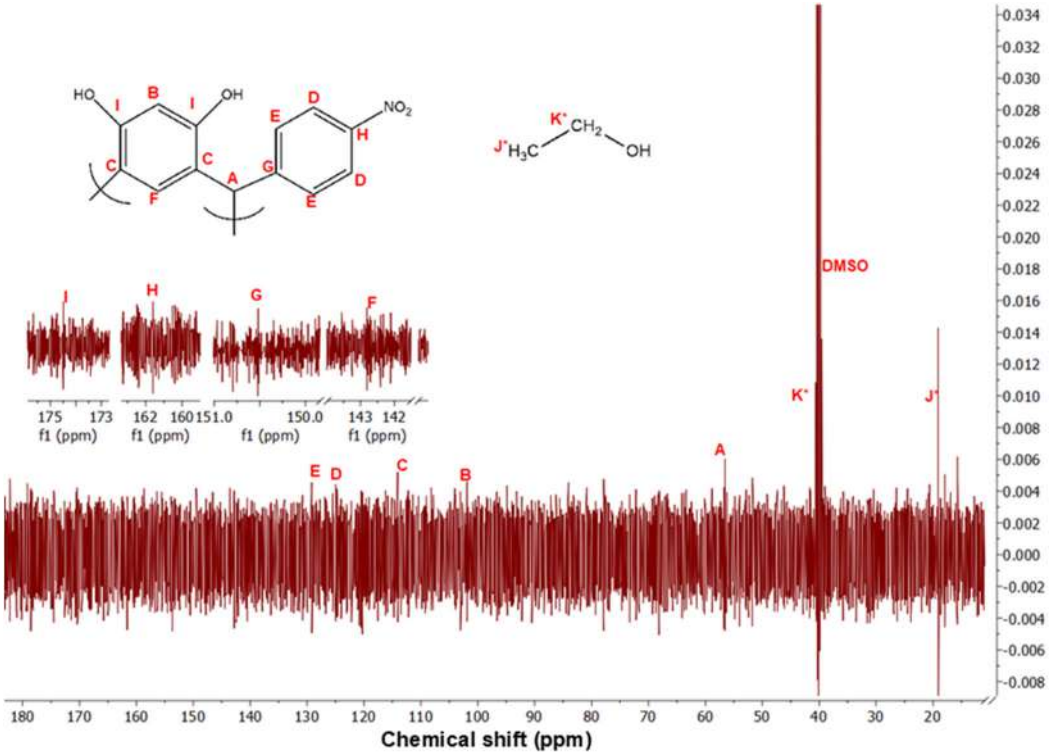

Fig S3. The ^{13}C-NMR spectra of calix[4]resorcinarene **1**

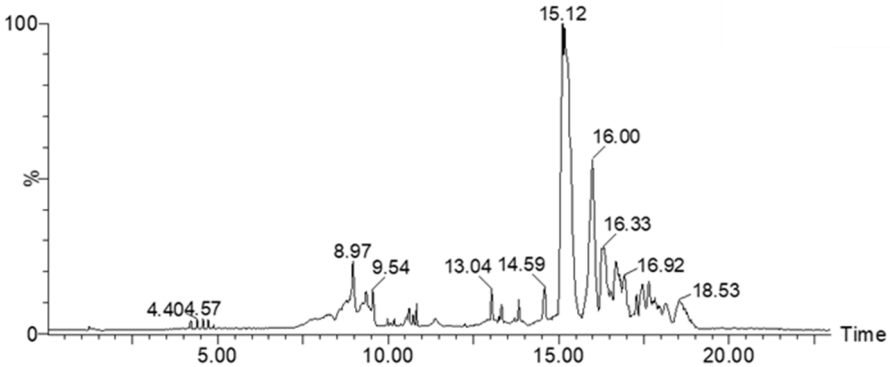

Fig S4. The LC chromatogram of calix[4]resorcinarene 1

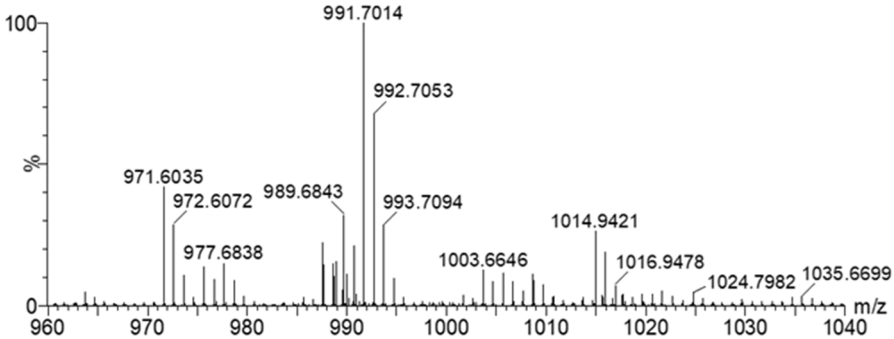

Fig S5. The MS spectra of calix[4]resorcinarene **1**

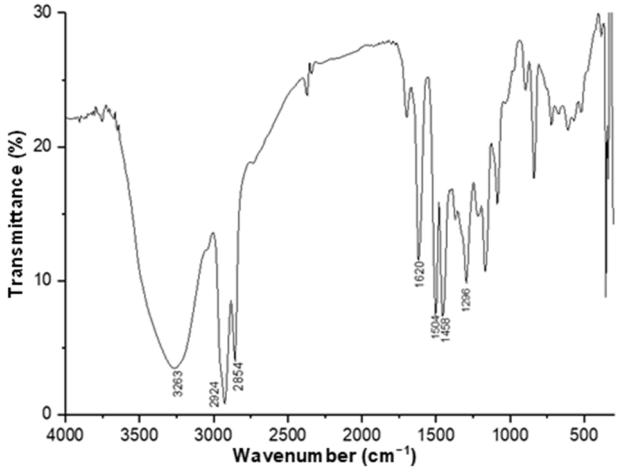

Fig S6. The FTIR spectra of calix[4]resorcinarene **2**

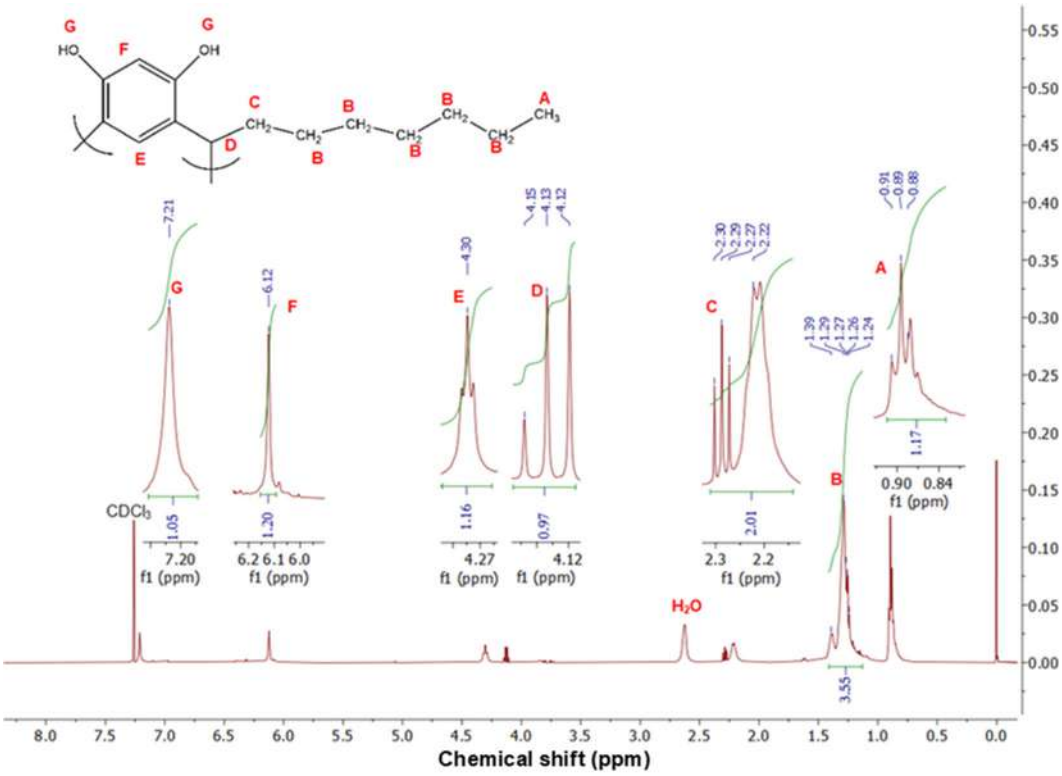

Fig S7. The ^{1}H-NMR spectra of calix[4]resorcinarene **2**

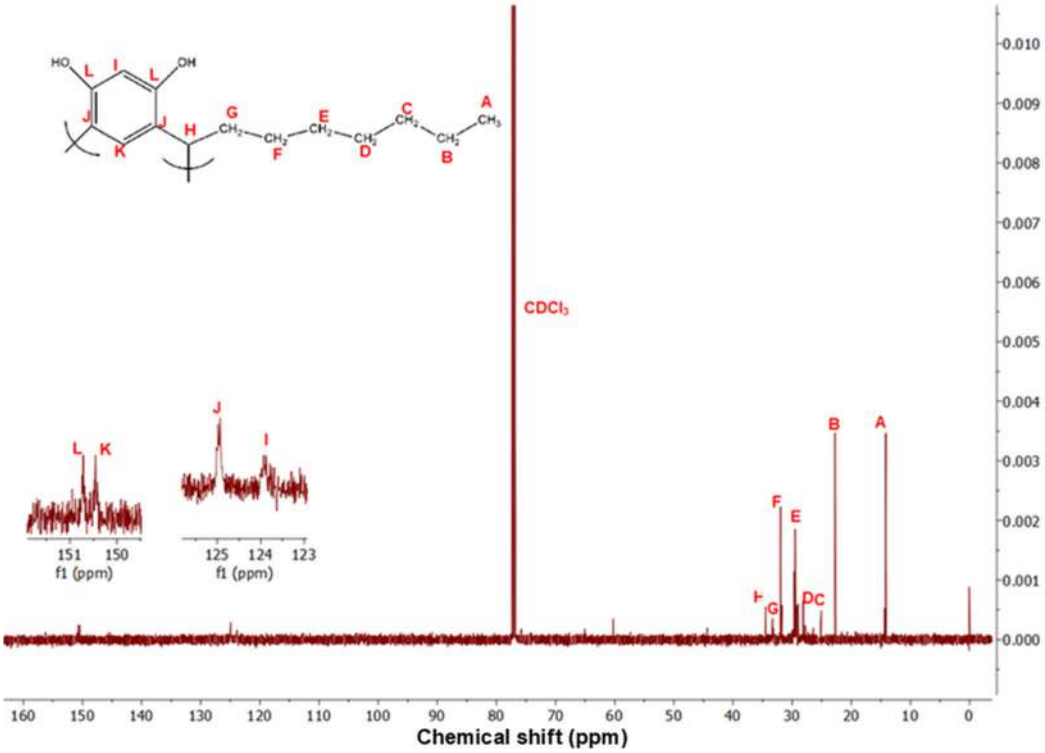

Fig S8. The ^{13}C-NMR spectra of calix[4]resorcinarene **2**

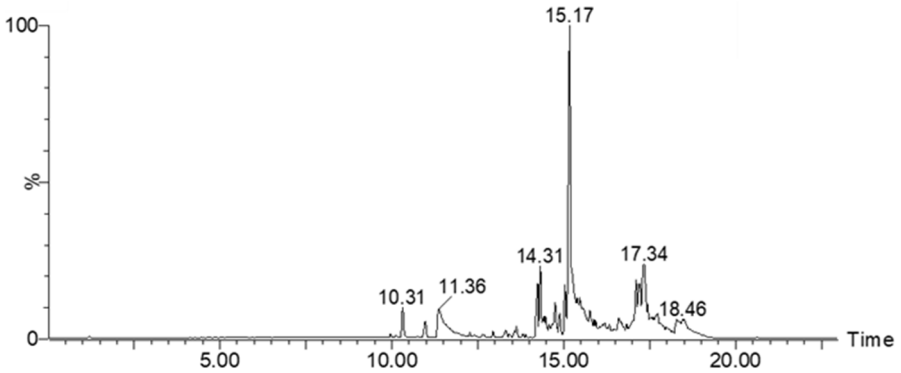

Fig S9. The LC chromatogram of calix[4]resorcinarene **2**

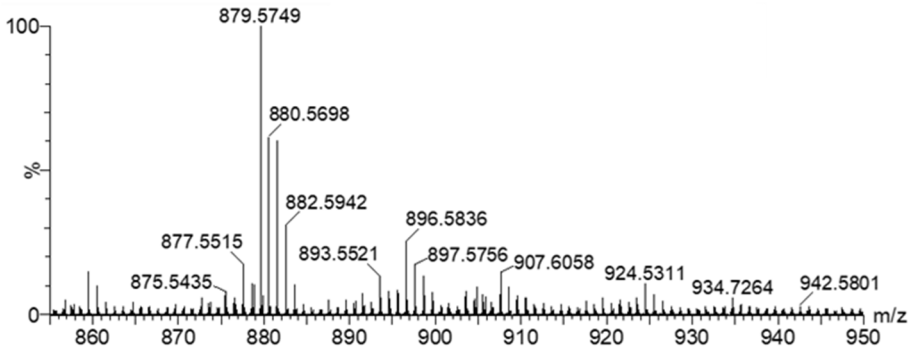

Fig S10. The MS spectra of calix[4]resorcinarene **2**

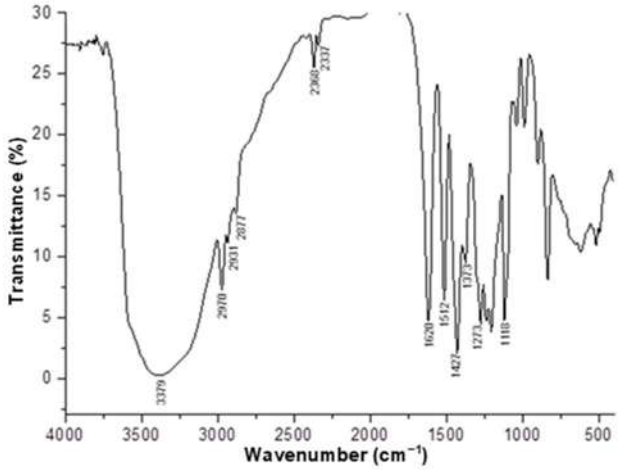

Fig S11. The FTIR spectra of calix[4]resorcinarene **3**

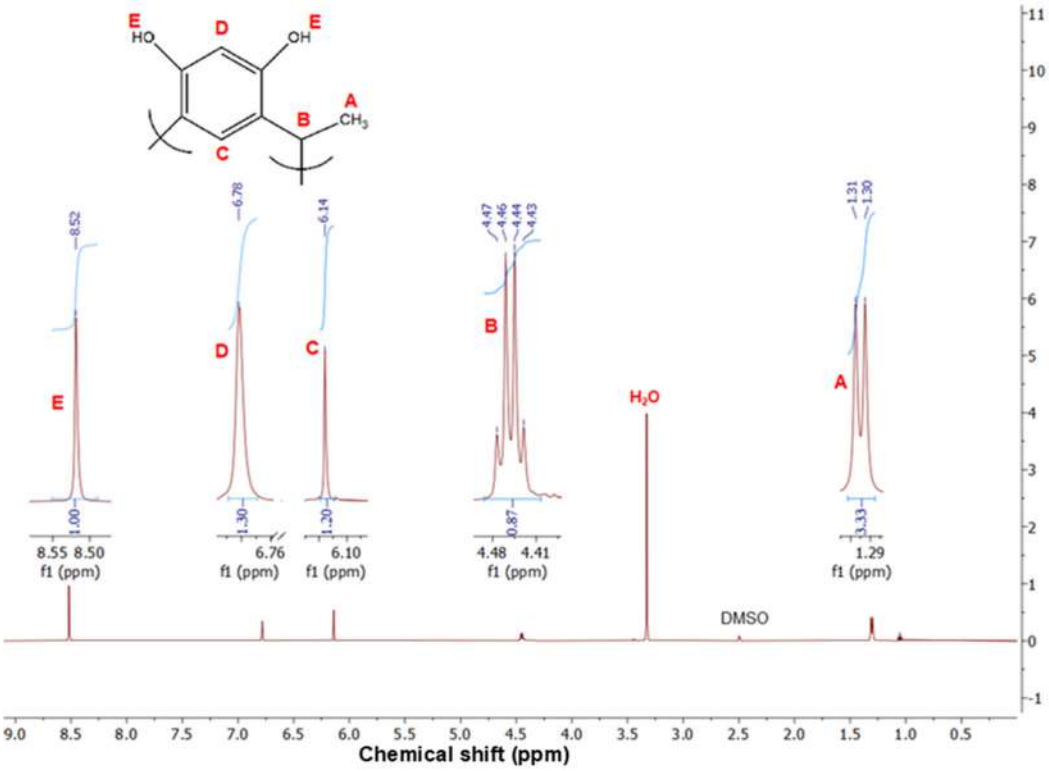

Fig S12. The ^{1}H-NMR spectra of calix[4]resorcinarene **3**

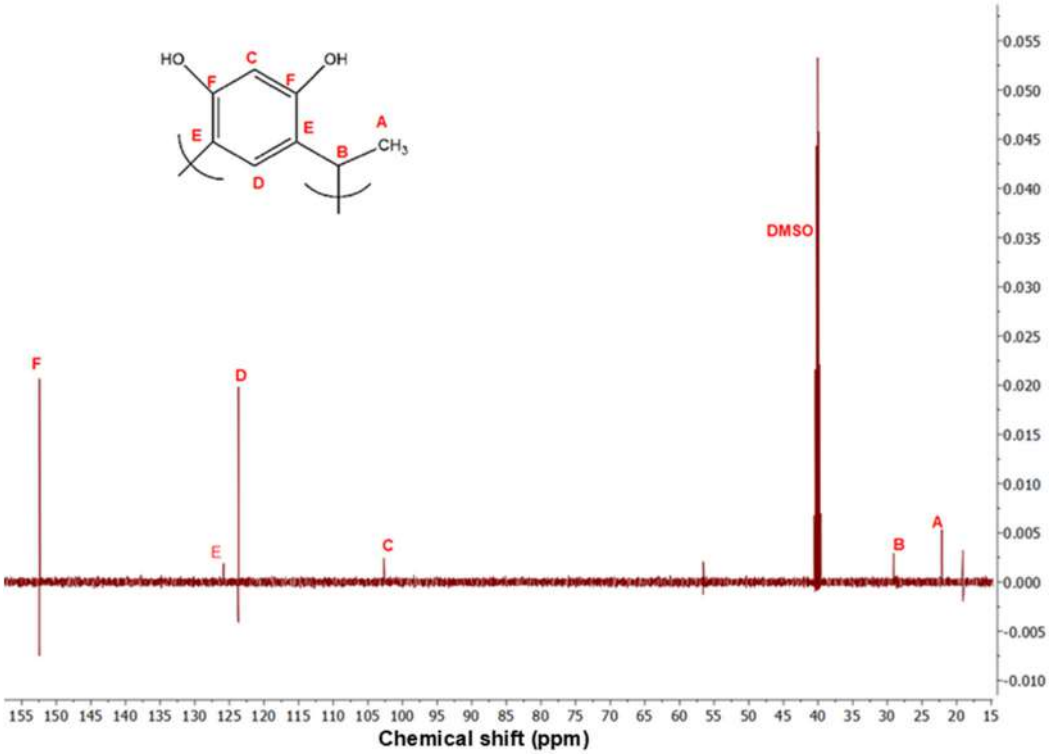

Fig S13. The ^{13}C-NMR spectra of calix[4]resorcinarene **3**

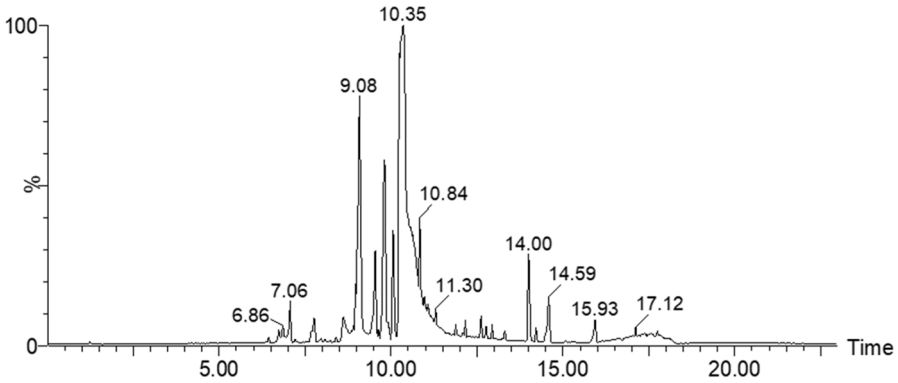

Fig S14. The LC chromatogram of calix[4]resorcinarene **3**

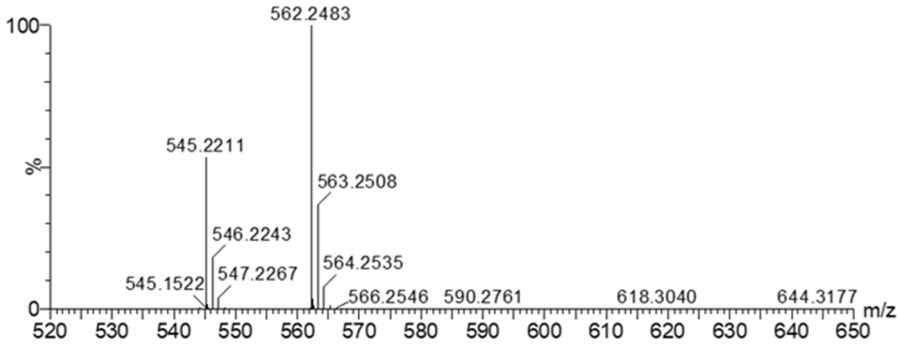

Fig S15. The MS spectra of calix[4]resorcinarene **3**

Synthesis of Calix[4]resorcinarene Derivatives as Antimalarial Agents through Heme Polymerization Inhibition Assay

Rizky Riyami Putri[1], Harno Dwi Pranowo[1], Yehezkiel Steven Kurniawan[1], Hana Anisa Fatimi[2], and Jumina Jumina[1*]

[1]*Department of Chemistry, Faculty of Mathematics and Natural Sciences, Universitas Gadjah Mada, Sekip Utara, Yogyakarta 55281, Indonesia*

[2]*Department of Pharmaceutical Technology, Faculty of Pharmacy, Universitas Gadjah Mada, Sekip Utara, Yogyakarta 55281, Indonesia*

* ***Corresponding author:***

email: jumina@ugm.ac.id

Received: January 18, 2023
Accepted: July 4, 2023

DOI: 10.22146/ijc.81452

Abstract: *Malaria is an endemic disease in tropical countries, including Indonesia, with a high annual mortality rate. Because of that, serious attention shall be given to find new antimalarial agents that are highly active for medical treatment. In this work, we designed and synthesized three calix[4]resorcinarene derivatives and evaluated them as antimalarial agents through* in vitro *heme polymerization inhibitory assay. The calix[4]resorcinarenes were prepared from resorcinol and corresponding aldehyde derivatives in ethanol media through a cyclo-condensation reaction. The calix[4]resorcinarene products were obtained in 31.1–85.1% yield. The synthesized compounds were subjected to structure elucidation using spectroscopy techniques. The antimalarial activity of calix[4]resorcinarene with aromatic substituent (IC_{50} = 0.198 mg/mL) was higher than the aliphatic ones (IC_{50} = 0.282–0.814 mg/mL). It was found that all calix[4]resorcinarenes in this work exhibited stronger antimalarial activity than chloroquine diphosphate as the positive control (IC_{50} = 1.157 mg/mL). The calix[4]resorcinarenes could interact with hydrogen bonding, thus inhibiting the heme polymerization process. These findings demonstrate that calix[4]resorcinarene derivatives are potential antimalarial agents to be developed for effective medical treatment in the near future.*

Keywords: *antimalarial; aromatic; aliphatic; calix[4]resorcinarene; heme polymerization*

■ INTRODUCTION

Malaria disease is caused by *Plasmodium* infection in humans with the aid of *Anopheles* mosquitos. In 2020, it was estimated that 70% of malaria cases were generated by *P. falciparum* while 25% of active cases were caused by *P. vivax* infection. World Health Organization (WHO) reported that global malaria cases in 2020 reached 241 million in 85 countries. Among 241 million cases, 627 thousand patients died in 2020, which was higher than in 2019. The annual death number has kept increasing over the past several years. Indonesia contributed to 95 thousand active malaria cases, which is the highest number in the Southeast Asia region [1]. Therefore, serious attention shall be given to suppress death and active malaria cases in the future.

Chloroquine diphosphate, as one of the commercial antimalarial drugs, inhibits the conversion of toxic heme to hemozoin in the vacuole of *Plasmodium* parasites [2]. However, chloroquine resistance has been reported since 1950 in Africa and resistance cases are widely found recently in many countries, including Indonesia [3-4]. This resistance leads to higher chloroquine doses required in the treatment of malaria patients [5]. Unfortunately, increasing the chloroquine dose leads to serious side effects in high doses, such as headache, insomnia, nausea, diarrhea, anemia, skin itching, muscle weakness, blurred vision, difficulty

breathing, and irregular heartbeats [6-8]. Therefore, researchers are giving their best efforts to design and discover new antimalarial agents to replace chloroquine diphosphate as the standard drug [9-10]. This issue shall be handled seriously to suppress the growth of active malaria cases in the future.

Hundreds of antimalarial agents have been designed and evaluated recently [11-16]. Natural antimalarial compounds from terrestrial and marine sources have been also reported. Herlina et al. [13] reported the isolation of natural compounds from the stem bark of *Erythrina variegate*. It was found that ethyl acetate fraction exhibited antimalarial activity with a half-maximal inhibitory concentration (IC_{50}) value of 23.8 mg/mL. Further chromatographic purification process led to a well-known isoflavonoid compound named warangalone with an IC_{50} value of 4.80 mg/mL. On the other hand, the isolation of antimalarial agents from the marine sponge *Xestospongia* sp. has been reported by Murtihapsari et al. [14]. The *n*-hexane extract of *Xestospongia* sp. gave the IC_{50} value of 7.13 mg/mL. This fraction consisted of flavonoids and triterpenoids; however, detailed structure elucidation and their antimalarial activity were not reported due to the complicated separation and purification processes.

In contrast to natural compounds, the synthetic antimalarial agent is sometimes preferable due to the high purity of a single compound; thus, the researchers could understand the relationship between the chemical structure and antimalarial activity. The antimalarial of synthetic compounds, i.e., chalcones and pyrazolines, has been also reported. Chalcone derived from 4-chlorobenzaldehyde and 4-chloroacetophenone gave antimalarial activity with an IC_{50} of 98.66 mg/mL. Further functionalization of chalcone to its *N*-phenyl pyrazoline form increased its antimalarial activity (IC_{50} = 20.83 mg/mL); however, the IC_{50} value was still higher than chloroquine diphosphate (IC_{50} = 3.54 mg/mL) [15]. Other pyrazoline compounds with formyl and aryl substituents gave the IC_{50} value of 5.68–427.33 mg/mL [16].

Among the developed synthetic antimalarial drugs, calixarene derivatives attract the attention of researchers due to their ease of synthesis, high stability, and strong bioactivities [17-19]. Shah et al. [18] reported that calix[4]arene derivatives with quinoline and pyrimidine substituents gave up to 4 times lower IC_{50} value than chloroquine. In our previous study, we investigated the antimalarial activity of calixarene derivatives, named calix[4]pyrogallolarenes, through heme polymerization inhibitory assay [19]. Heme polymerization inhibitory assay was selected because the β-hematin is identic to hemozoin and β-hematin could be easily inspected in the laboratory using spectrophotometry measurement; thus, it is widely applied as an initial screening for antimalarial agents [20]. It was found that the calix[4]pyrogallolarenes gave IC_{50} values in the range of 0.238–1.268 mg/mL, which were more active than chloroquine diphosphate, which was remarkable [19]. On the other hand, calix[4]resorcinarenes belong to the metacyclophane family together with calix[4]arenes and calix[4]pyrogallolarenes with the different numbers of hydroxyl group, i.e., 4, 12 and 8 hydroxyl groups for calix[4]arenes, calix[4]pyrogallolarenes, and calix[4]resorcinarenes, respectively [17]. These variations in the numbers of hydroxyl groups may contribute to different antimalarial activities through the heme polymerization mechanism. In continuation of our research, we evaluated the antimalarial activity of the other calixarene derivatives, named calix[4]resorcinarenes, through *in vitro* heme polymerization inhibitory assay in this study.

■ EXPERIMENTAL SECTION

Materials

The used materials in this work, i.e., resorcinol ($C_6H_6O_2$), octanaldehyde ($C_8H_{16}O$), etanaldehyde (C_2H_4O), 4-nitrobenzaldehyde ($C_7H_5NO_3$), concentrated hydrochloric acid (HCl), ethanol (C_2H_5OH), glacial acetic acid (CH_3CO_2H), dimethyl sulfoxide (C_2H_6SO), sodium hydroxide (NaOH), and acetone (C_3H_6O), were purchased from Merck in pro analytical grade. Meanwhile, hematin ($C_{34}H_{33}FeN_4O_5$) and chloroquine diphosphate ($C_{18}H_{26}ClN_3{\cdot}2H_3PO_4$) were obtained from Sigma-Aldrich in pro analytical grade.

Instrumentation

The instrumentations used for the synthesis of calix[4]resorcinarenes were hotplate (ThermoScientific) and analytical balance (Shimadzu Libror EB-330). The used instrumentations for the characterization of the synthesized products were melting point apparatus (Electrothermal 9100), Fourier transforms infrared (FTIR, Thermo Scientific Nicolet iS10), liquid chromatography-mass spectrometry (LC-MS, Thermo Fischer Scientific), and nuclear magnetic resonance (500 MHz for ^{1}H- and 125 MHz for ^{13}C-NMR, JEOL JNM-ECZ 500R). On the other hand, the used apparatus for the antimalarial assay were micropipette (ThermoScientific), microcentrifuge (Thermo Sorvall Legend Micro 17R), CO_2 incubator (Sakura), vortex mixer (Thermolyne 34600 mixer), 96-well microplate (Biochemix), and ELISA reader (Bio-Rad 660 XR).

Procedure

Synthesis of calix[4]resorcinarene derivatives

The calix[4]resorcinarene was prepared in a similar manner to the previous report [21-22]. Resorcinol (5 mmol) was dissolved in ethanol (10 mL) and then acidified with concentrated HCl (0.5 mL). Aldehyde derivative (5 mmol) was added dropwise into the mixture. The mixture was stirred and refluxed for 24 h. After the reaction was completed, the mixture was cooled to room temperature and then added to distilled water (10 mL). The resulting solids were filtered and washed with a mixture of ethanol and distilled water (1:1 v/v). The melting point of the product was measured, and the product was characterized using FTIR, NMR and LC-MS analyses.

***C*-4-nitrophenylcalix[4]resorcinarene (compound 1).** Compound **1** (1.03 g) was obtained as a yellowish solid in 85.1% yield. m.p. 300 °C (decomposed). FTIR (KBr, cm^{-1}): 3448, 2924, 2854, 1604, 1512, 1350, 1427. ^{1}H-NMR (DMSO-d_6, δ, ppm): 5.73 (*s*, 4H), 6.81 (*d*, 4H), 6.86 (*s*, 4H), 7.78 (*s*, 4H), 7.84 (*d*, 4H), 8.93 (*s*, 8H). ^{13}C-NMR (DMSO-d_6, δ, ppm): 55.9, 109.0, 120.0, 122.0, 129.0, 143.0, 151.0, 162.0, 174.0. LC: major peak at a retention time of 15.12 min. Mass spectrum (EI): m/z = 971.6035 (M$^+$).

***C*-heptylcalix[4]resorcinarene (compound 2).** Compound **2** (0.83 g) was obtained as a yellowish solid in 75.5% yield. m.p. 295 °C (decomposed). FTIR (KBr, cm^{-1}): 3263, 2924, 2854, 1620, 1458. ^{1}H-NMR (DMSO-d_6, δ, ppm): 0.90 (*t*, 12H), 1.30 (*m*, 40H), 2.30 (*q*, 8H), 4.13 (*t*, 4H), 4.30 (*s*, 8H), 6.12 (*s*, 4H), 7.21 (*s*, 4H). ^{13}C-NMR (DMSO-d_6, δ, ppm): 14.1, 22.7, 25.1, 28.1, 29.6, 31.6, 33.3, 34.0, 122.0, 124.0, 150.3, 150.6. LC: major peak at a retention time of 15.17 min. Mass spectrum (EI): m/z = 879.5749 (M$^+$).

***C*-methylcalix[4]resorcinarene (compound 3).** Compound **3** (0.22 g) was obtained as a yellowish solid in 31.1% yield. m.p. 270 °C (decomposed). FTIR (KBr, cm^{-1}): 3379, 2970, 2877, 1620, 1427. ^{1}H-NMR (DMSO-d_6, δ, ppm): 1.30 (*d*, 12H), 4.46 (*q*, 4H), 6.14 (*s*, 4H), 6.78 (*s*, 4H), 8.52 (*s*, 8H). ^{13}C-NMR (DMSO-d_6, δ, ppm): 21.5, 39.0, 102.0, 123.0, 125.0, 151.0. LC: major peak at a retention time of 10.35 min. Mass spectrum (EI): m/z = 545.2211 (M+H$^+$).

In vitro *antimalarial assay*

The *in vitro* antimalarial assay was conducted using the heme polymerization inhibitory method according to the previously published procedure [19]. The heme polymerization method was performed by the addition of 1 mM hematin (100 µL) into 0.2 M NaOH solution (50 µL). The sample (50 µL) with a series concentration of 5.00, 2.50, 1.25, 0.63, and 0.31 mg/mL and glacial acetic acid (50 µL) were added into the mixture. The mixture was incubated at 37 °C for 24 h. After that, the mixture was centrifuged at 8000 rpm for 10 min. The residue was washed with dimethyl sulfoxide (200 µL). The residue was dissolved in 0.1 M NaOH solution (200 µL). The solution (100 µL) was added into a 96-well microplate to be measured with an ELISA reader at a wavelength of 405 nm. The absorbance was further converted through probit analysis to inhibitory percentage and IC_{50} value. Chloroquine diphosphate was used as the positive control while dimethyl sulfoxide 10% was used as the negative control. Each sample was subjected to triplicate measurement.

■ RESULTS AND DISCUSSION

Synthesis of Calix[4]resorcinarene Derivatives

In this work, three calix[4]resorcinarenes have been prepared from resorcinol and aldehyde derivative

which is shown in Fig. 1. The corresponding calix[4]resorcinarenes were obtained in 31.1–85.1% yield as yellowish solid from a one-pot synthetic method with ethanol as the solvent and hydrochloric acid as the catalyst. The employed aldehyde for compounds **1**, **2**, and **3** was 4-nitrobenzaldehyde, octanaldehyde, and ethanaldehyde, respectively. Different from calix[4]resorcinarenes **1** and **2**, calix[4]resorcinarene **3** was obtained in the lowest yield (31.1% yield), probably due to less stability of carbonium ions in etanaldehyde compared to aromatic aldehyde (4-nitrobenzaldehyde) and longer chain aliphatic aldehyde (octanaldehyde). It was reported that calix[4]resorcinarene was produced from the cyclo-condensation between resorcinol and aldehyde derivative in acidic conditions. According to Eddaif et al. [23], the carbonyl of aldehyde was protonated, and electrophilic substitution started to the ortho and para position of the hydroxyl groups at the aromatic ring of resorcinol. The reaction continued by the formation of its dimer and trimer and then finished when the tetramer of resorcinol was cyclized to produce a calix[4]resorcinarene structure. The proposed reaction mechanism is shown in Fig. 2.

The spectroscopic data of the synthesized products are shown in Fig. S1-S15. Calix[4]resorcinarene **1** was decomposed at 300 °C due to strong intramolecular and intermolecular hydrogen bondings as reported in other calix[4]resorcinarene derivatives [17]. The FTIR spectra of compound **1** revealed the O–H and C=C aromatic functional groups from the resorcinol at 3448 and 1604 cm^{-1}, respectively (Fig. S1). The C–H methine group was observed as weak signals at 2924 and 2854 cm^{-1} for its Csp^3–H stretching and at 1427 cm^{-1} for its C–H bending. The C–NO_2 group from the 4-nitrobenzaldehyde was confirmed by the presence of strong absorption signals at 1512 and 1350 cm^{-1}.

The ^{1}H-NMR spectrum of compound **1** in DMSO-d_6 solvent is shown in Fig. S2. The O–H of resorcinol was observed at 8.93 ppm as a singlet signal, while the aromatic protons of resorcinol were found at 6.86 and 7.78 ppm as singlet signals due to the absence of neighboring hydrogen atoms. The C–H signal of methine was confirmed by the presence of a singlet signal at 5.73 ppm, while the aromatic protons of 4-nitrobenzaldehyde were observed at 6.81 and 7.84 ppm as doublet signals. On the other hand, the ^{13}C-NMR spectrum of compound **1** in DMSO-d_6 revealed a C–H methine signal (55.9 ppm) and eight aromatic carbon signals (109.0–174.0 ppm), as shown in Fig. S3. The mass spectrum of compound 1 showed the M^+ peak at m/z = 971.6035 (Fig. S5), suggesting that the calix[4]resorcinarene structure has been formed.

Calix[4]resorcinarene **2** was decomposed at 295 °C due to intramolecular and intermolecular hydrogen bondings. Compared to the decomposition temperature of calix[4]resorcinarene **1**, calix[4]resorcinarene **2** decomposed at a lower temperature due to smaller molecular mass. The FTIR spectra of compound **2** showed the presence of O–H and C=C aromatic functional groups from the resorcinol at 3263 and 1620 cm^{-1},

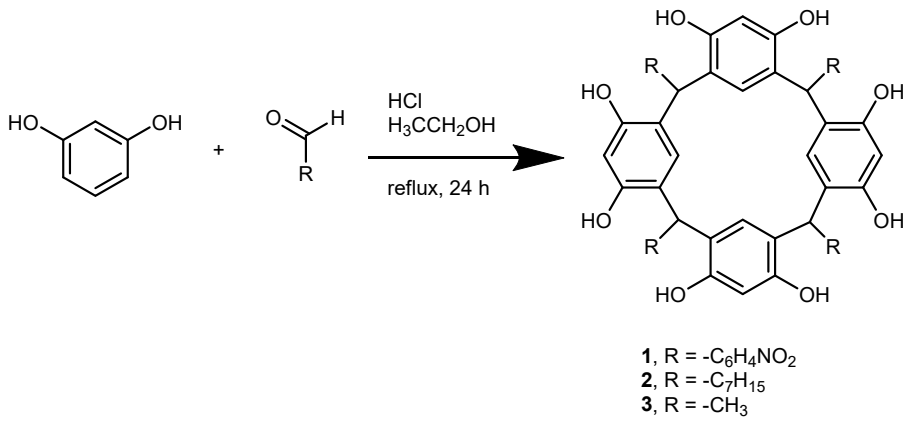

Fig 1. The synthesis scheme of calix[4]resorcinarenes

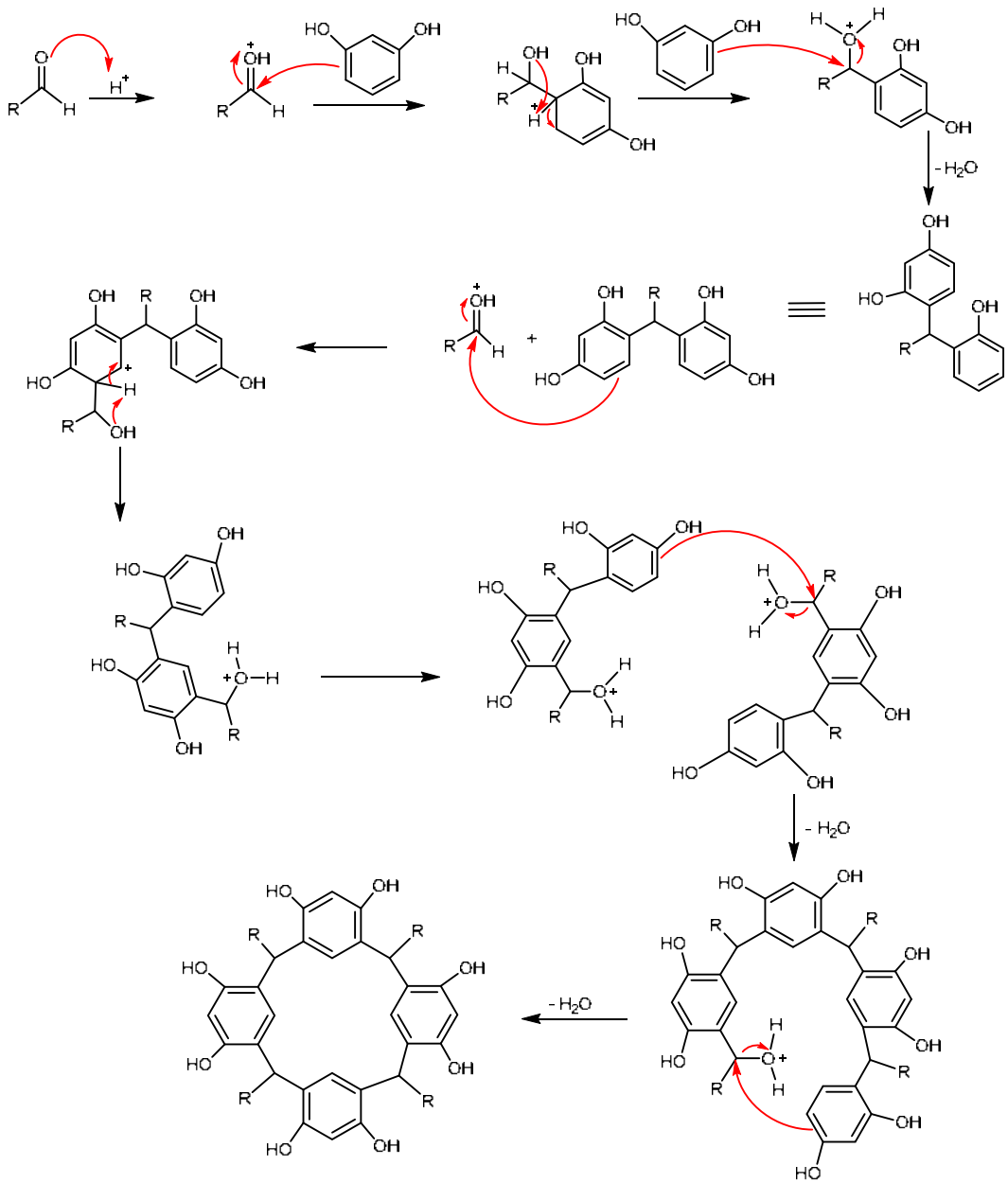

Fig 2. The proposed reaction mechanism on the synthesis of calix[4]resorcinarenes

respectively (Fig. S6). The C–H methine and *n*-heptyl groups were observed as weak signals at 2854–2924 and 1458 cm^{-1} for their bending and stretching modes, respectively.

The ^{1}H-NMR spectrum of compound **2** in deuterated DMSO solvent was displayed in Fig. S7. The O–H of resorcinol was observed at 4.30 ppm as a singlet signal, while the aromatic protons of resorcinol were found at 6.12 and 7.21 ppm as singlet signals which were similar to the spectrum of calix[4]resorcinarene **1**. The C–H signal of methine was confirmed by the presence of a triplet signal at 4.13 ppm, while the aliphatic protons of the *n*-heptyl group were found as triplet ($-CH_3$), multiplet ($-CH_2-$), and quartet ($C_{methine}-CH_2-$) signals at 0.90, 1.30 and 2.30 ppm, respectively, with a total number of 60 hydrogen atoms. On the other hand, the ^{13}C-NMR spectrum of compound **2** in DMSO-d_6 solvent confirmed the presence of a methine carbon (34.0 ppm), a methyl carbon (14.1 ppm), six methylene carbons (22.7–33.3 ppm), and four aromatic carbons (122.0–

150.6 ppm), which was matched with the total number of carbon on calix[4]resorcinarene **2** (Fig. S8). The MS spectra (Fig. S10) revealed that the M^+ signal of compound **2** was found at *m/z* = 879.5749, which was matched with its chemical formula ($C_{56}H_{80}O_8$).

On the other hand, the calix[4]resorcinarene **3** was decomposed at 270 °C, which was the lowest compared to the synthesized calix[4]resorcinarene in this work due to the smallest molecular mass as indicated by the MS spectrum (*m/z* of M^+ = 545.2211) (Fig. S15). The FTIR spectra of calix[4]resorcinarene **3** revealed the O–H and C=C aromatic functional groups from the resorcinol at 3379 and 1620 cm^{-1}, respectively (Fig. S11). The C–H of methine and methyl groups was observed as weak signals at 2970 cm^{-1} for its stretching mode and at 2877 cm^{-1} for its bending mode.

The ^{1}H-NMR spectrum of compound **3** in DMSO-d_6 as the solvent is shown in Fig. S12. The O–H of resorcinol was observed as a singlet signal at 8.52 ppm, while the aromatic protons of resorcinol were found as singlet signals at 6.14 and 6.78 ppm. The C–H proton of methine existed as a quartet signal at 4.46 ppm due to the presence of three hydrogens of methyl, which is covalently connected with the methine carbon. Meanwhile, the methyl protons were found as doublet signal at 1.30 ppm. Fig. S13 shows the ^{13}C-NMR spectrum of compound **3** in DMSO-d_6. Calix[4]resorcinarene **3** consisted of a C–H methine carbon, a methyl carbon and four aromatic carbons at 39.0, 21.5, and 102.0–151.0 ppm, respectively.

For a summary, the FTIR spectra of calix[4]resorcinarenes showed the hydroxyl functional groups at 3448–3263 cm^{-1} while C–H methine was observed at 1458–1427 cm^{-1}. The C–H methine was also observed at 4.13–5.73 and 34.0–55.9 ppm at ^{1}H- and ^{13}C-NMR, respectively. These trends were in agreement with the previous result [22]. It was reported that calix[4]resorcinarenes could be obtained in some conformations such as chair (C_4), boat (C_{2v}), chair (C_{2h}), diamond (C_s), saddle (S_4), etc., due to flexible C-C rotation on the methine bridge as reported previously [24]. The variation in the conformations of calix[4]resorcinarenes generates some peaks at the LC chromatogram (Fig. S4, S9, S14) with the same molecular ion, demonstrating that the calix[4]resorcinarenes have been successfully synthesized in the present work.

In Vitro Antimalarial Assay

Three calix[4]resorcinarenes were then evaluated as the antimalarial agent through *in vitro* heme polymerization inhibitory assay with chloroquine diphosphate as the positive control. Hematin, an artificial *Plasmodium* hemozoin, polymerizes in an acidic solution through hydrogen bonds. When this polymerization is inhibited, the heme concentration in the vacuole of the parasite will be higher, leading to the death of parasites due to the toxic properties of heme. Therefore, heme polymerization inhibitory assay is a well-established assay for rapid screening of the antimalarial activity of chemical compounds [25].

The antimalarial activity of calix[4]resorcinarenes is listed in Table 1. A series of calix[4]resorcinarene concentrations was prepared in a range of 0.31–5.00 mg/mL to obtain the average inhibition percentage for each triplicate measurement. The heme polymerization inhibition percentage was higher by increasing the used concentration of calix[4]resorcinarene. From the probit analysis, calix[4]resorcinarenes **1**, **2** and **3** gave the IC_{50} value of 0.198, 0.814, and 0.282 mg/mL, respectively.

Table 2 shows that all calix[4]resorcinarenes (IC_{50} = 0.198–0.814 mg/mL) give higher antimalarial activity than the natural extracts, i.e., *Erythrina variegate* (IC_{50} = 23.8 mg/mL), warangalone (IC_{50} = 4.80 mg/mL), and *Xestospongia* sp. (IC_{50} = 7.13 mg/mL) because natural extracts usually contain active compounds in very low concentration. Compared to the other synthetic compounds, such as chalcone (IC_{50} = 98.66 mg/mL) and pyrazolines (IC_{50} = 5.68–427.3 mg/mL), the synthesized calix[4]resorcinarenes exhibited 28.69–2158 times stronger antimalarial activity demonstrating the critical effect of calix[4]resorcinarene skeleton on the antimalarial activity.

As a family of calixarenes, the antimalarial activity of calix[4]resorcinarenes was compared with calix[4] arenes and calix[4]pyrogallolarenes. The antimalarial

Table 1. The antimalarial activity of calix[4]resorcinarenes through *in vitro* heme polymerization inhibitory assay

Calix[4]resorcinarene	Concentration	Average inhibition percentage ± SD (%)	IC_{50} (mg/mL)
1	5.00	89.28 ± 0.04	0.198
	2.50	79.56 ± 0.15	
	1.25	75.85 ± 0.25	
	0.63	69.19 ± 0.31	
	0.31	53.77 ± 0.26	
2	5.00	87.51 ± 0.18	0.814
	2.50	78.02 ± 0.39	
	1.25	65.80 ± 0.40	
	0.63	52.49 ± 0.16	
	0.31	39.47 ± 0.16	
3	5.00	85.95 ± 0.20	0.282
	2.50	80.85 ± 0.22	
	1.25	73.29 ± 0.07	
	0.63	67.35 ± 0.24	
	0.31	47.35 ± 0.15	

*SD: standard deviation

Table 2. The comparison of *in vitro* antimalarial activity of the reported antimalarial agents

Compound	IC_{50} (mg/mL)	Ref.
calix[4]resorcinarene **1**	0.198	This work
calix[4]resorcinarene **2**	0.814	
calix[4]resorcinarene **3**	0.282	
Chloroquine diphosphate	1.157	
Erythrina variegate extract	23.80	[13]
Warangalone	4.800	
Xestospongia sp. extract	7.130	[14]
chalcone	98.66	[15]
N-phenylpyrazoline	20.83	
N-formylpyrazoline	5.680	[16]
N-arylpyrazoline	427.3	
C-8-hydroxyquinolinecalix[4]arene	0.073	[18]
C-2-aminopyrimidinecalix[4]arene	0.043	
C-phenylcalix[4]pyrogallolarene	1.268	[19]
C-4-hydroxy-3-methoxyphenylcalix[4]pyrogallolarene	1.029	
C-2-chlorophenylcalix[4]pyrogallolarene	0.238	

activity of calix[4]resorcinarenes (IC_{50} = 0.198–0.814 mg/mL) was weaker than the calix[4]arenes (IC_{50} = 0.043–0.073 mg/mL). It was reported that nitrogenated functional groups such as amino, nitro, quinoline, and pyrimidine yielded stronger antimalarial activity due to stronger interactions with iron central ion in the heme framework [18]. On the other hand, the antimalarial activity of calix[4]resorcinarenes (IC_{50} = 0.198–0.814 mg/mL) was higher than calix[4]pyrogallolarenes (IC_{50} = 0.238–1.268 mg/mL) due to stronger intramolecular hydrogen bonds in calix[4]pyrogallolarenes; thus, the hydroxyl groups of calix[4]pyrogallolarenes could not strongly interact with iron cation and lowering the heme polymerization inhibitory activity [19].

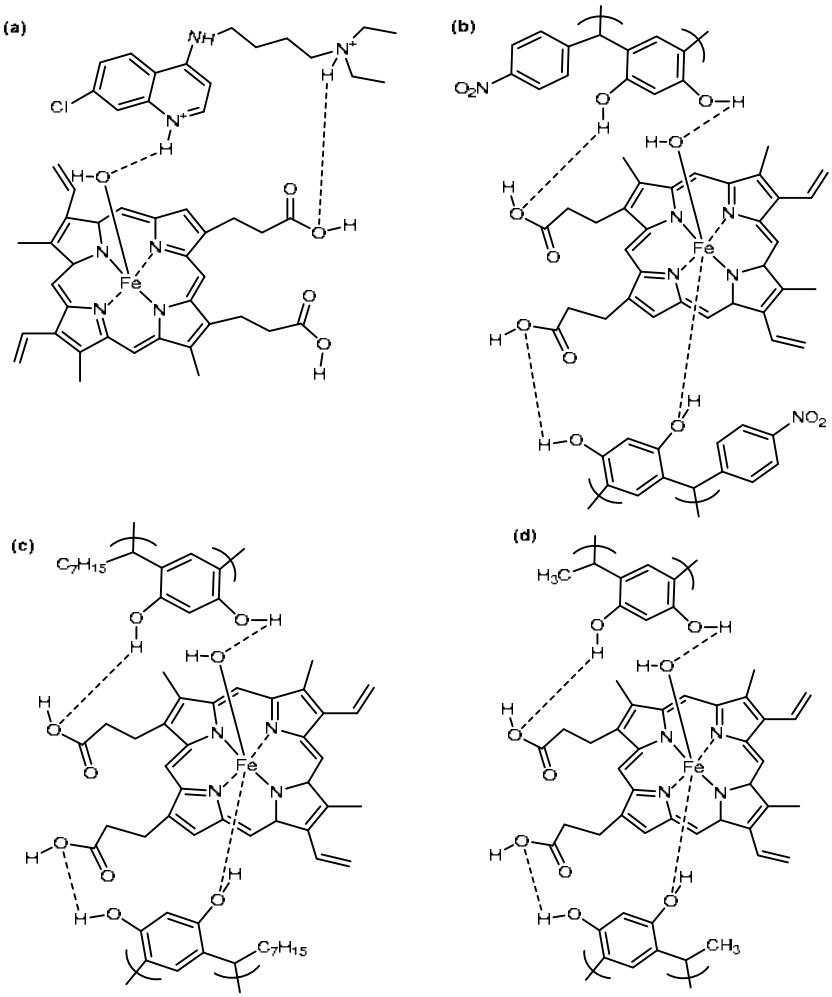

Fig 3. Plausible interactions of heme with (a) chloroquine, (b) calix[4]resorcinarene **1**, (c) calix[4]resorcinarene **2**, and (d) calix[4]resorcinarene **3**

It shall be noted that the calix[4]resorcinarenes (IC_{50} = 0.198–0.814 mg/mL) exhibited stronger antimalarial activity than chloroquine diphosphate as the positive control (IC_{50} = 1.157 mg/mL), which was remarkable. Furthermore, aromatic aldehyde moiety in compound **1** (IC_{50} = 0.198 mg/mL) exhibited stronger antimalarial activity than the aliphatic aldehyde ones (IC_{50} = 0.282–0.814 mg/mL). Meanwhile, the longer alkyl chain in compound **2** demarcated the antimalarial activity due to the non-polar nature of compound **2**. It meant that the polarity of the antimalarial agent strongly influenced its antimalarial activity. Therefore, it is reasonable that calix[4]resorcinarene **1** with nitro functional groups gave the strongest antimalarial activity in this study.

Priyangga et al. [26] reported that calix[4] resorcinarenes could form a stable chelate complex with iron metal ions through their hydroxyl groups. On the other hand, Sari et al. [19] reported that hydroxyl groups of calix[4]pyrogallolarenes interacted with iron center ion and carboxylic group of heme, thus inhibiting its polymerization process. Since calix[4]resorcinarenes' structure is similar to calix[4]pyrogallolarenes; thus, we predict that the interactions of calix[4]resorcinarenes with heme are similar to the calix[4]pyrogallolarene ones. The plausible interactions of calix[4]pyrogallolarenes and chloroquine with heme are shown in Fig. 3.

CONCLUSION

We reported the successful synthesis of three calix[4]resorcinarene derivatives in 31.1–85.1% yield. The chemical structures of all synthesized calix[4]resorcinarenes have been elucidated using FTIR, NMR, and LC-MS analyses. Besides, the *in vitro* antimalarial activity of calix[4]resorcinarenes revealed higher antimalarial activity than chloroquine diphosphate as the positive control. The type of substituent on methine carbon influenced the antimalarial activity of calix[4]resorcinarenes. Aromatic substituents gave stronger antimalarial activity than the aliphatic ones due to higher polarity. It was predicted that the calix[4]resorcinarenes interacted with heme through hydrogen bondings, thus inhibiting the heme polymerization process.

ACKNOWLEDGMENTS

The authors deeply thank to the Department of Chemistry, Faculty of Mathematics and Natural Science, Universitas Gadjah Mada, for providing financial assistance for this research through the Department Research Grant budget year 2022 with a contract number of 50/UN1/FMIPA.1.3/KP/PT.01.03/2023.

AUTHOR CONTRIBUTIONS

Conceptualization and Methodology: Jumina. Supervision: Jumina and Harno Dwi Pranowo. Resources: Jumina. Investigation: Rizky Riyami Putri. Formal analysis: Rizky Riyami Putri, Yehezkiel Steven Kurniawan and Hana Anisa Fatimi. Writing and revising the manuscript: Yehezkiel Steven Kurniawan and Hana Anisa Fatimi.

REFERENCES

[1] Oluwafemi, T., and Azuaba, E., 2022, Impact of hygiene on malaria transmission dynamics: A mathematical model, *J. Multidiscip. Appl. Nat. Sci.*, 2 (1), 1–9.

[2] Pandey, A.V., Bisht, H., Babbarwal, V.K., Srivastava, J., Pandey, K.C., and Chauhan, V.S., 2001, Mechanism of malarial haem detoxification inhibition by chloroquine, *Biochem. J.*, 355 (2), 333–338.

[3] Talapko, J., Škrlec, I., Alebić, T., Jukić, M., and Včev, A., 2019, Malaria: The past and the present, *Microorganisms*, 7 (6), 179.

[4] Pannu, A.K., 2019, Malaria today: Advances in management and control, *Trop. Doct.*, 49 (3), 160–164.

[5] Kim, J., Tan, Y.Z., Wicht, K.J., Erramilli, S.K., Dhingra, S.K., Okombo, J., Vendome, J., Hagenah, L.M., Giacometti, S.I., Warren, A.L., Nosol, K., Roepe, P.D., Potter, C.S., Carragher, B., Kossiakoff, A.A., Quick, M., Fidock, D.A., and Mancia, F., 2019, Structure and drug resistance of the *Plasmodium falciparum* transporter PfCRT, *Nature*, 576 (7786), 315–320.

[6] Veiga, M.I., Dhingra, S.K., Henrich, P.P., Straimer, J., Gnädig, N., Uhlemann, A.C., Martin, R.E., Lehane, A.M., and Fidock, D.A., 2016, Globally prevalent PfMDR1 mutations modulate *Plasmodium falciparum* susceptibility to artemisinin-based combination therapies, *Nat. Commun.*, 7 (1), 11553.

[7] Braga, C.B., Martins, A.C., Cayotopa, A.D.E., Klein, W.W., Schlosser, A.R., da Silva, A.F., de Souza, M.N., Andrade, B.W.B., Filgueira-Júnior, J.A., Pinto, W.J., and da Silva-Nunes, M., 2015, Side effects of chloroquine and primaquine and symptom reduction in malaria endemic area (Mancio Lima, Acre, Brazil), *Interdiscip. Perspect. Infect. Dis.*, 2015, 346853.

[8] Al-Bari, M.A.A., 2015, Chloroquine analogues in drug discovery: New directions of uses, mechanism of actions and toxic manifestation from malaria to multivarious diseases, *J. Antimicrob. Chemother.*, 70 (6), 1608–1621.

[9] Tse, E.G., Korsik, M., and Todd, M.H., 2019, The past, present and future of anti-malarial medicines, *Malar. J.*, 18 (1), 93.

[10] Belete, T.M., 2020, Recent progress in the development of new antimalarial drugs with novel targets, *Drug Des., Dev. Ther.*, 14, 3875–3889.

[11] Ungogo, M.A., Ebiloma, G.U., Ichoron, N., Igoli, J.O., de Koning, H.P., and Balogun, E.O., 2020, A review of the antimalarial, antitrypanosomal, and antileishmanial activities of natural compounds isolated from Nigerian flora, *Front. Chem.*, 8, 617448.

[12] Nqoro, X., Tobeka, N., and Aderibigde, B.A., 2017, Quinoline-based hybrid compounds with antimalarial activity, *Molecules*, 22 (12), 2268.

[13] Herlina, T., Supratman, U., Soedjanaatmadja, M.S., Subarnas, A., Sutardjo, S., Abdullah, N.R., and Hayashi, H., 2009, Anti-malarial compound from the stem bark of *Erythrina variegate*, *Indones. J. Chem.*, 9 (2), 308–311.

[14] Murtihapsari, M., Parubak, A.S., Mangallo, B., Ekasari, W., Asih, P.B., and Lestari, A.I., 2013, Isolation and presence of antimalarial activities of marine sponge *Xestospongia* sp., *Indones. J. Chem.*, 13 (3), 199–204.

[15] Cahyono, R.N., Andari, S.A., and Wahyuningsih, T.D., 2022, Synthesis of *N*-phenylpyrazoline derivative from 4-chlorobenzaldehyde and 4-chloroacetophenone and its activity as an antimalarial agent, *Mater. Sci. Forum*, 1061, 211–216.

[16] Wiratama, M., Waskitha, S.S.W., Haryadi, W., and Wahyuningsih, T.D., 2022, Synthesis, antimalarial activity assay and molecular docking study of *N*-substituted chloro-pyrazolines, *Trop. J. Pharm. Res.*, 21 (6), 1255–1261.

[17] Nasuhi Pur, F., 2016, Calixdrugs: Calixarene-based clusters of established therapeutic drug agents, *Mol. Diversity*, 20 (3), 781–787.

[18] Shah, R.B., Valand, N.N., Sutariya, P.G., and Menon, S.K., 2015, Design, synthesis and characterization of quinoline-pyrimidine linked calix[4]arene scaffolds as anti-malarial agents, *J. Inclusion Phenom. Macrocyclic Chem.*, 84 (1), 173–178.

[19] Sari, D.K., Hidayat, D.N.W., Fatmawati, D.R., Triono, S., Kurniawan, Y.S., and Jumina, J., 2022, Synthesis and antimalarial activity assay of *C*-arylcalix[4]pyrogallolarenes using heme polymerization inhibition activity (HPIA) method, *Mater. Sci. Forum*, 1061, 187–193.

[20] Coronado, L.M., Nadovich, C.T., and Spadafora, C., 2014, Malarial hemozoin: From target to tool, *Biochim. Biophys. Acta, Gen. Subj.*, 1840 (6), 2032–2041.

[21] Jumina, J., Priastomo, Y., Setiawan, H.R., Mutmainah, M., Kurniawan, Y.S., and Ohto, K., 2020, Simultaneous removal of lead(II), chromium(III), and copper(II) heavy metal ions through an adsorption process using *C*-phenylcalix[4]pyrogallolarene material, *J. Environ. Chem. Eng.*, 8 (4), 103971.

[22] Priyangga, K.T.A., Kurniawan, Y.S., and Yuliati, L., 2021, The role of a nitro substituent in *C*-phenylcalix[4]resorcinarenes to enhance the adsorption of gold(III) ions, *ChemistrySelect*, 6 (21), 5366–5373.

[23] Eddaif, L., Trif, L., Telegdi, J., Egyed, O., and Shaban, A., 2019, Calix[4]resorcinarene macrocycles, *J. Therm. Anal. Calorim.*, 137 (2), 529–541.

[24] Firdaus, F., Jumina, J., and Sastrohamidjojo, H., 2007, Synthesis and conformation of *p*-(amino)butoxycalix[4]arene, *Indones. J. Chem.*, 7 (1), 49–57.

[25] Basilico, N., Pagani, E., Monti, D., Olliaro, P., and Taramelii, D., 1998, A microtitre-based method for measuring haem polymerization inhibitory activity (HPIA) of antimalarial drugs, *J. Antimicrob. Chemother.*, 42 (1), 55–60.

[26] Priyangga, K.T.A., Kurniawan, Y.S., Ohto, K., and Jumina, J., 2022, A review on calixarene fluorescent chemosensor agents for various analytes, *J. Multidiscip. Appl. Nat. Sci.*, 2 (1), 23–40.

Utilization of Lignin and Lignosulfonate from Oil Palm Empty Fruit Bunches as Filler in PVDF Proton Exchange Membrane Fuel Cell

Nala Ridhwanul Mu'izzah, Pinka Zuhdiana Hapsari, Nabila Putri Aulia, Dian Wahyu Tri Wulansari, Fauziyah Azhari, and Edi Pramono*

Department of Chemistry, Faculty of Mathematics and Natural Sciences, Universitas Sebelas Maret, Jl. Ir. Sutami 36A, Kentingan, Surakarta 57126, Indonesia

*** Corresponding author:**

email: edi.pramono.uns@staff.uns.ac.id

Received: January 26, 2023
Accepted: June 19, 2023

DOI: 10.22146/ijc.81750

Abstract: *A study on the polyvinylidene fluoride (PVDF) membrane using lignin and lignosulfonate oil palm empty fruit bunch (OPEFB) fillers have been carried out. This study aims to determine the additional effect of lignin and lignosulfonate on PVDF membrane. Lignin sulfonation has a good result proven by Fourier transform infrared spectra with a peak at 1192 cm^{-1} which indicates sulfonate group. The sulfonation degree was increased by 8.9% for lignosulfonate. The membrane was prepared by the phase inversion method. Data present that all the membranes have an asymmetric structure with finger-like and sponge-like pores. Good thermal stability indicated by thermal gravimetric analysis showed degradation at 432 °C. The mechanical properties of the membrane decrease with the addition of filler. From the X-ray diffraction, peaks appeared at 18.39°, 21.35°, and 23.75° for all the membranes indicating of α and β phases. Lignin and lignosulfonate increased membrane hydrophilicity and water uptake. The presence of the sulfonate group increases the ionic exchange capacity and ionic conductivity up to 2.78 mmol/g and 9.95 × 10^{-5} S/cm, respectively, for 5% lignosulfonate addition. Thus, PVDF/lignosulfonate has the potential as a polymer electrolyte membrane.*

Keywords: *lignin; lignosulfonate; OPEFB; polymer electrolyte membrane; PVDF*

INTRODUCTION

A fuel cell is an electrochemical device in which chemical energy is directly converted into electrical energy [1]. Fuel cells are one of the alternative energy production technologies [2], where hydrogen is used as an energy source [3]. Hydrogen can produce high energy and lower calorific value than hydrocarbon-based fossil fuels, making it more efficient [4] and environmentally friendly [2]. In addition, hydrogen is ideally used for fuel cells due to its rapid electrochemical reaction kinetics and the absence of exhaust gases since the only by-product of the reaction is water [4]. The essential elements of a fuel cell are the positive electrode (cathode), the negative electrode (anode), and the electrolyte membrane [4-5].

The perfluorosulfonic acid polymer (Nafion®) has high ionic conductivity, mechanical and chemical stability at lower temperatures [6]. Nafion® also has a multiphase structure, namely the hydrophobic phase as the continuous phase and the sulfonic acid group as the hydrophilic phase. The continuous hydrophobic phase is helpful for the structural integrity of the membrane, and the hydrophilic phase acts as a reservoir of water [7]. However, Nafion® is expensive and challenging to synthesize [8], so researchers are looking for another alternative to be developed. One alternative polymer that can be used is polyvinylidene fluoride (PVDF), which has good mechanical properties, thermal stability, and chemical resistance [9]. Even so, PVDF has limitations due to its low conductivity [10], which requires to be modified.

Physical modification, such as mixing with other components, can be used to improve PVDF membrane performance [11]. Lignin has the potential to modify PVDF membranes. Lignin has some polar groups in its structure, especially the hydroxyl group [12], which can be an active modification center [13]. Lignin has

advantages, including high carbon content, good thermal stability, biodegradability, good antioxidant activity, and good mechanical properties. With modification by sulfonation reaction, lignin has hydrophilic properties [7-8] and has the potential to be used as a polymer electrolyte. The presence of a sulfonate group facilitated the transfer of protons [14], increasing the conductivity of the PVDF membrane. Lignin is also an abundant biopolymer and is a by-product of cellulose extraction [15] from various biomass such as oil palm empty fruit bunches (OPEFB). In Indonesia, around 7 million tons of OPEFB are estimated to be produced annually [16]. Previous research reports that the effect of lignin coating on PVDF membranes showed promising results on membrane surface properties with increased hydrophilicity values [17]. Lignin was also increasing the ionic exchange capacity of poly (ether ether ketone) (SPEEK) membranes [18]. However, the blending of lignin and lignosulfonate in PVDF as polymer electrolyte membranes has never been studied. This research determines the effect of lignin and lignosulfonate on morphology, matrix structure, hydrophilicity, thermal, mechanical, and electrolyte properties.

■ EXPERIMENTAL SECTION

Materials

The materials used are oil empty palm fruit bunches (OPEFB) obtained from Polytech Institute Technology Indonesia. PVDF Solef 1010 pellets were bought from Solvay. Sodium hydroxide (NaOH), sulfuric acid (H_2SO_4), hydrochloric acid (HCl), dimethylacetamide (DMAC), sodium chloride (NaCl), and sodium sulfite (Na_2SO_3) in analytical grades were purchased from Merck.

Instrumentation

The instruments used in this study are Fourier transform infrared (FTIR, Shimadzu IR Prestige-21), scanning electron microscope (SEM, Jeol JCM-7000), simultaneous thermal analyzer (STA, LINSEIS PT1600), X-ray diffractogram (XRD, D8 Advance Bruker Germany), attenuated total reflection-Fourier transform infrared (ATR-FTIR, Agilent Cary 600), and electrochemical impedance spectroscopy (EIS, EUGOL U2826).

Procedure

Lignin isolation from OPEFB

Extraction was performed by refluxing OPEFB using a 0.5 M NaOH solution in a ratio of 1:20 (w/v) for 2 h at 90–100 °C. The results were filtered so that black liquor was obtained. Black liquor was acidified using H_2SO_4 1 M to reach pH 2 and precipitated for at least 8 h. The precipitate was filtered and dried at room temperature.

Sulfonation of lignin

Sulfonation followed the procedure of previous research [19] with modifications. Lignin was mixed with Na_2SO_3 and distilled water with a ratio of 2:1:20. The mixture was stirred for 4 h at 80 °C. The mixture was evaporated in the oven at 60 °C for 6 h. The resulting lignosulfonate is grounded and sifted using a 200-size mesh before use.

Sulfonation degree

The sulfonation degree was calculated using conductometric titration based on previous research [20]. First, 0.1 g of lignin and lignosulfonate was diluted in 60 mL NaOH 0.01 M through ultra-sonification for 10 min and pH was adjusted to 2.8 by adding HCl 0.1 M to ensure all the sulfonated groups were protonated. The dispersion was purged with nitrogen for 20 min and titrated using NaOH 0.01 M. The change in conductance was observed. The value of the sulfonation degree was computed using Eq. (1).

$$SD = \frac{(V_{NaOH} \times C_{NaOH}) - (V_{HCl} \times C_{HCl})}{w} \quad (1)$$

where SD is sulfonation degree (mmol/g) and w is weight of lignin or lignosulfonate (g).

Membrane fabrication

PVDF, PVDF/Lignin (PL), and PVDF/Lignosulfonate (PLS) membranes were prepared using the phase inversion method followed by previous research [21]. The total mass of the casting solution (dope) was 12 g with a composition of lignin and lignosulfonate varied to 1, 3, and 5% by weight of PVDF. The composition of the membranes is shown in Table 1. Dope was made by dissolving lignin or lignosulfonate in DMAC and then supplemented with PVDF. The dope

Table 1. Membrane composition

Membrane	Composition*			
	PVDF (% w/w)	Lignin (% w/w)	Lignosulphonate (% w/w)	DMAC
PVDF	18	-	-	82
PL-1	18	1	-	82
PL-3	18	3	-	82
PL-5	18	5	-	82
PLS-1	18	-	1	82
PLS-3	18	-	3	82
PLS-5	18	-	5	82

*The composition of Lignin and lignosulfonate is calculated based on PVDF weight

was stirred for 24 h at 50–60 °C, cast on glass with a thickness regulator of 130 μm and directly put into a coagulant bath filled with water.

Characterization

Isolation and sulfonated lignin were characterized by FTIR. Sample scanned 48× with resolution 1 cm^{-1} at range 4000–400 cm^{-1} using KBr pellet.

Membrane surface and cross-section morphology were analyzed using SEM. The membrane was observed with a magnification of 10,000× for surface morphology and 1,000× for cross-section.

Membrane thermal analysis was conducted using the STA with an alumina crucible dish and an air atmosphere. Membranes were burned with a heating rate of 10°/min (dpm) in the temperature range of 25–900 °C. Further analysis was performed using Origin software.

The mechanical properties of the membrane were characterized using Inston MOD 1026 tensile strength tester. Membrane with the dimensions of 6 × 0.5 cm^2 tested at the speed of 80 mm/min, pinch distance of 20 mm and weight of 500 g. The mechanical properties were calculated using Eq. (2-4);

$$\sigma = \frac{F}{A} \tag{2}$$

$$\varepsilon = \frac{\Delta l}{l} \times 100\% \tag{3}$$

$$\gamma = \frac{\sigma}{\varepsilon} \tag{4}$$

where σ is tensile strength (MPa), F is force (kg/ms^2); A is surface area (cm^2), ε is elongation (%), Δl is change in length (mm), l is original length (mm), and γ is Young Modulus (MPa).

Membrane structure was characterized using XRD. The membrane was cut with dimensions of 2 × 2 cm^2 and dried at 60 °C for 24 h. The membrane was scanned at 2θ 10–90°, and the data was processed using Origin software.

ATR-FTIR was used to identify the α and β phases related to membrane hydrophilicity. The analysis is carried out at a wavelength of 4000–400 cm^{-1}, and the β fraction was computed using Eq. (5) [22].

$$F(\beta) = \frac{A\beta}{A\beta + 1.26A\alpha} \times 100\% \tag{5}$$

where Aα and Aβ were the absorbances at peaks of 762 and 840 cm^{-1} corresponding to the α and β phases, respectively.

Membrane hydrophilicity was determined by measuring the water contact angle (WCA). The measurement was carried out by calculating the angle of water drops on the membrane surface. The images were taken using a 48-megapixel HP camera lens with a magnification of 5×. Images were analyzed using ImageJ software with a contact angle plugin.

The water uptake membrane was analyzed using the gravimetric method. The wet membrane (W_w) was weighed and dried at 60 °C for 24 h. The dry membrane (W_d) was weighed again, and the water uptake was determined through Eq. (6) [18].

$$\text{Water uptake} = \frac{(W_w - W_d)}{W_d} \times 100\% \tag{6}$$

Ion exchange capacity (IEC) is characterized using acid-base titration with NaCl media. A membrane with a size of 2 × 2 cm^2 was immersed in HCl 0.1 M solution for 24 h. The membrane in the form of H^+ was converted

into Na^+ by soaking in NaCl 1 M for 24 h. Then, the removed H^+ was titrated with NaOH 0.01 M using the phenolphthalein indicator. IEC was measured using Eq. (7) [18].

$$IEC = \frac{(M \times V)_{NaOH}}{W_d} \quad (7)$$

Electrochemical impedance spectroscopy (EUGOL U2826) was used to analyze the conductivity of the membrane. The membrane was clamped using Cu electrodes and tested at room temperature in the 20 Hz–5 MHz frequency range. The value of membrane conductivity (σ) was measured using Eq. (8) [23];

$$\sigma = \frac{l}{R \times A} \quad (8)$$

where l is membrane thickness (cm), R is resistance (Ω), and A is probe area (cm^2).

RESULTS AND DISCUSSION

Isolation and Sulfonation of Lignin OPEFB

Analysis of lignin and lignosulfonate was carried out using FTIR. The shift of wavenumber and the peak of new uptake that exists in the isolation results showed in Fig. 1. Based on the spectra, it can be seen that the peak at the wavenumber 3387, 2931, and 1240 cm^{-1} indicates the presence of an O–H, C–H, and aromatic C=C bond respectively. This result aligns with the previous report [24] in Table 2. Sulfonation using sodium sulfite showed an absorption peak at 1192, 1663, and 1540 cm^{-1}, which indicates the sulfonate group, OH, and CH_3 groups following previous research [25-27]. Spectra of lignosulfonate appear in Fig. 2.

The sulfonation degree of lignin and lignosulfonate is characterized using conductometric titration. Table 3 shows the increasing sulfonate content at the material filler. The sulfonation degree increased by 8.9% in the lignosulfonate. Sulfonation occurs through the substitution of a sulfonate group on the aliphatic hydroxyl group of lignin through an addition reaction,

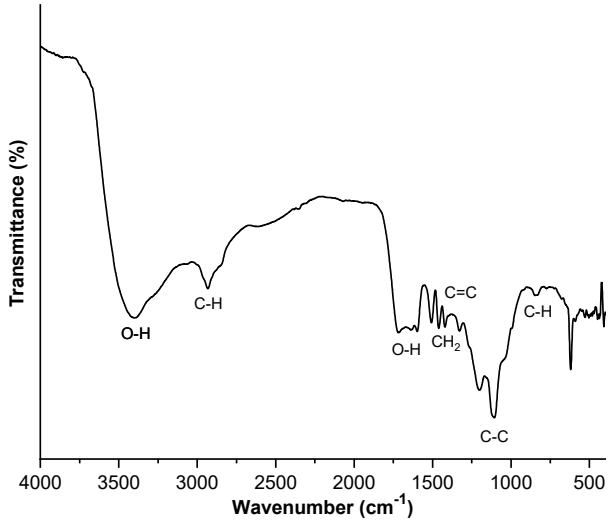

Fig 1. FTIR spectra of lignin OPEFB

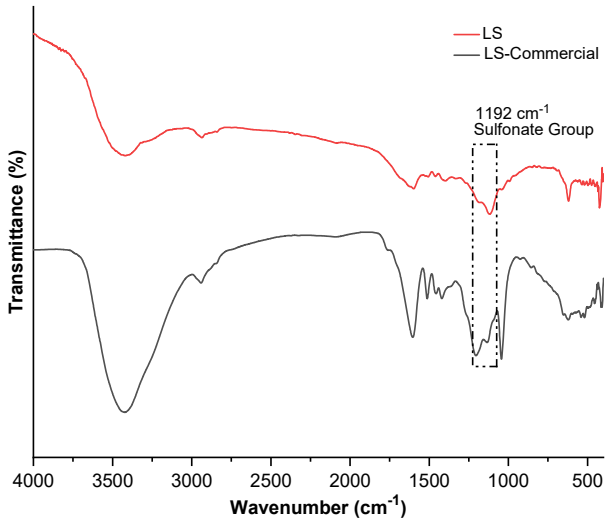

Fig 2. FTIR spectra of lignosulfonate

Table 2. Lignin FTIR uptake peaks

Absorption	Wavenumber (cm^{-1})	Wavenumber (cm^{-1}) [24]
O–H stretching	3387	3322
C–H stretching	2931	2918
O–H deformation	1597	1593
$-CH_2$ deformation	1420	1420
Aromatic C=C	1240	1238
C–C stretching	1030	1027
C–H deformation	899	895

Table 3. Sulfonation degree of lignin and lignosulfonate

Material	Sulfonation degree (mmol/g)
Lignin	1.35
Lignosulfonate	1.47

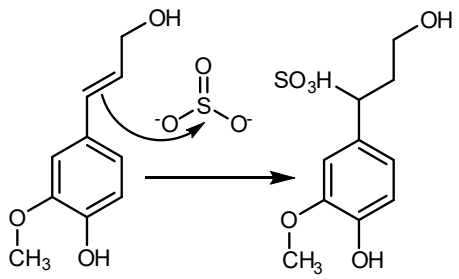

Fig 3. Lignin sulfonation mechanism [28]

as shown in Fig. 3. Sulfite reacts with the carbon double bond at the alpha position [28].

Lignin thermally decomposed in a large range of temperatures because of various functional groups that attached have different thermal stability. The differences in the structure and chemical nature of lignin from different sources could account for the diversity of its degradation behavior [29]. From Fig. 4, it can be seen that lignin begins to degrade at the temperature of 250 °C and ends at 776 °C. At this temperature, propanoid side chains such as methyl-, ethyl, vinyl guaiacol, and the main aromatic structure of lignin began to decompose [30]. While for lignosulfonate, degradation occurs in three stages at temperatures of 29, 408, and 611 °C. The first degradation below 100 °C can be mainly attributed to the loss of moisture [29]. The higher temperature of main structure degradation that occurs above 408 °C can be caused due to cross-link between lignin on sulfonate bonds that need more energy to degrade [31]. The last degradation that occurs at a temperature above 500 °C possibly related to the slow decomposition of some aromatic rings in the lignosulfonate [29]. The data indicate that lignosulfonate has higher thermal stability than lignin.

Membrane PVDF/Lignin and PVDF/Lignosulfonate

The membrane was prepared by phase inversion, and the result is presented in Fig. 5. The addition of lignin and lignosulfonate affect the color and homogeneity of the membranes. The addition of lignin gives a deeper yellow color with increasing filler concentration. In PLS

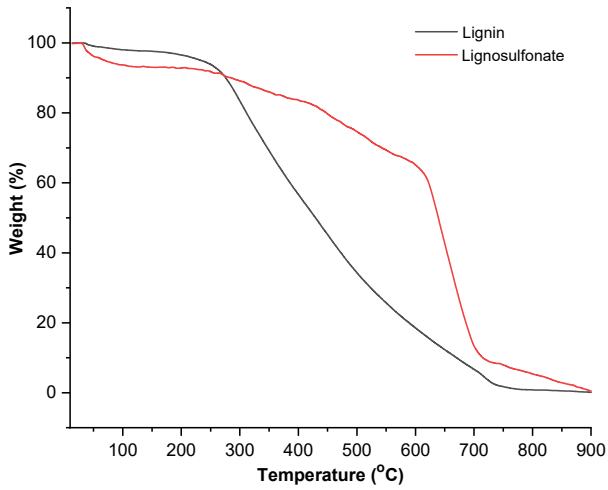

Fig 4. Diffractogram TGA of lignin and lignosulfonate

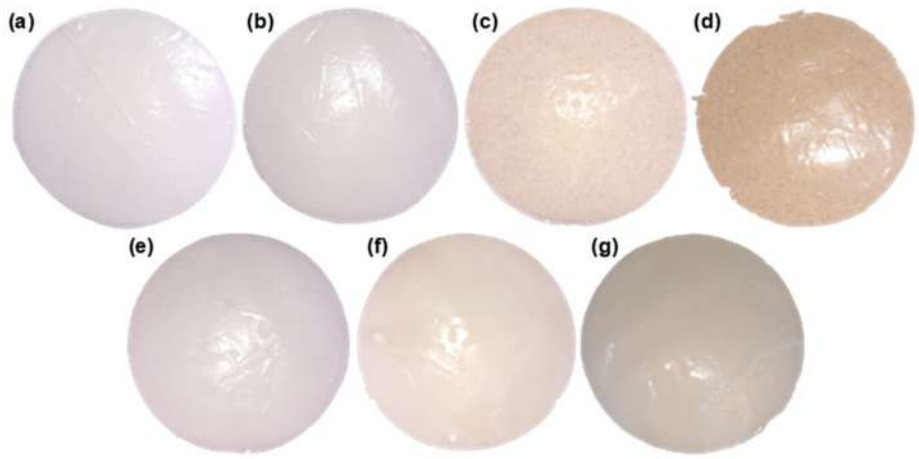

Fig 5. The photograph of membrane (a) PVDF, (b) PL-1, (c) PL-3, (d) PL-5, (e) PLS-1, (f) PLS-3, and (g) PLS-5

membranes, homogeneity is formed better, making that membrane surface more transparent than the PL membrane. The presence of cross-link in the lignosulfonate reduces hydrophilicity that makes well interact with the PVDF and solvent, resulting more homogenous membrane.

Membrane Morphology

In Fig. 6, membrane PVDF has a tight surface. The addition of lignin and lignosulfonate makes the membrane surface rougher. Fig. 6 also shows the cross-section membrane. It can be seen that all the membranes have an asymmetric structure with finger-like and sponge-like pores. PVDF membrane has a shorter finger-like and thicker sponge-like area than PL and PLS. When the phase inversion occurs, the solvent is rapidly transferred to the water, forming finger-like pores. However, solvent migration occurs slowly at the lower area and leaves a sponge-like pore structure. The hydroxyl group from lignin and lignosulfonate attracts more water at PL and PLS membranes and affects the speed of solvent migration, producing longer finger-like pores.

Membranes Thermal Analysis

Fig. 7 shows the thermogram TGA of the PVDF, PL, and PLS membranes. Degradation of the membrane occurs at temperatures of 432–760 °C with two stages of degradation. Thermal degradation of all samples was similar, caused by weak interaction between filler and PVDF matrix. This suggests that the addition of filler did not change the degradation mechanism of PVDF membrane [32]. On the membrane, the first stage of degradation occurs at 432 °C that related to the decomposition of hydrogen and fluorine from the main chain of the PVDF structure [33]. The second stage at above 480 °C indicates the degradation of PVDF backbone [34].

Mechanical Properties

The mechanical properties of polymer electrolyte membranes with the addition of lignin and lignosulfonate are shown in Table 4. At the PVDF membrane, tensile strength reaches 4.8 MPa with an elongation of 93% and

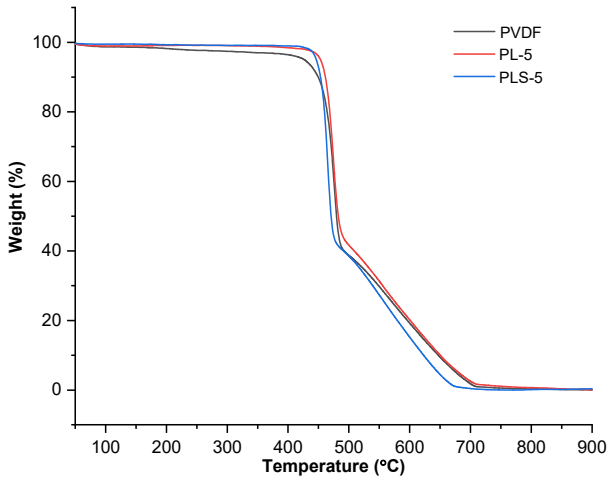

Fig 7. Thermogram TGA of PVDF, PL, and PLS membranes

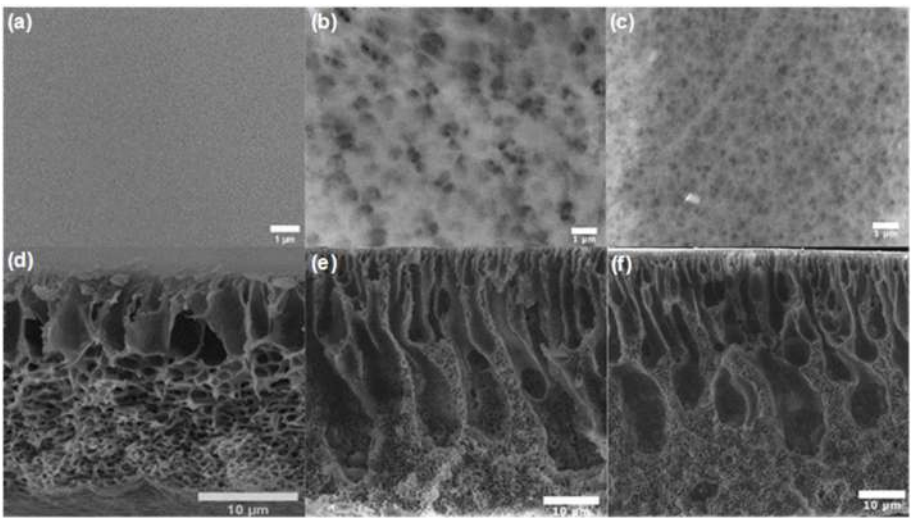

Fig 6. Surface and cross-section morphology of (a,d) PVDF, (b,e) PL-5, and (c,f) PLS-5

Table 4. Mechanical properties of the membranes

Membrane	l (mm)	σ at break (MPa)	ε at break (%)	γ (MPa)
PVDF	0.05	4.80	93.30	16.60
PL-1	0.07	2.80	60.00	17.50
PL-3	0.05	2.90	76.70	31.40
PL-5	0.05	2.50	56.70	22.20
PLS-1	0.05	4.80	86.70	60.10
PLS-3	0.07	3.40	66.70	16.60
PLS-5	0.06	3.60	80.00	37.00

a low young modulus of 16.6 MPa. In general, the addition of lignin or lignosulfonate reduces the value of tensile strength and elongation but increases the young modulus. These mechanical properties show that the membrane becomes more brittle than pure PVDF membrane. This can be caused by the presence of polar groups and aromatic rings, which make the membrane more rigid. Good dispersion also affects the mechanical properties of membranes [35]. With lignin addition, the membrane has a poor homogeneity caused by different polarities between the hydrophobic PVDF and hydrophilic side of lignin. This results in a big decrease in tensile strength and elongation by 42%. While with lignosulfonate filler, PVDF forms a homogeneous membrane and fewer pores that resulted in less decrease in mechanical strength.

Matrix Structure and Membrane Hydrophilicity

The matrix structure of membranes was observed using XRD and ATR-FTIR. Fig. 8 reveals the peaks at 2θ of 18.39°, 23.75°, and 21.35°, which correspond to α and β phases of PVDF, respectively [36-37]. At the peak of 18.39° and 23.75°, PVDF membranes have a relatively higher intensity than PL or PLS, which indicates a decrease in the α phase. The addition of lignin or lignosulfonate increases the intensity of the peak at 21.35° related to polyethylene-like structure, which indicate β phase.

ATR-FTIR spectra in Fig. 9 showed the presence of α and β phases that supported XRD data. β phase was observed at 840 cm^{-1}, which is stretching asymmetry of CF_2 [38] while the peak at 762 cm^{-1} is CF_2 bending of α phase [39]. Based on Fig. 9, it can be seen that intensity of the β phase for PL and PLS increases meanwhile the α phase is reduced. The higher β phase intensity means that

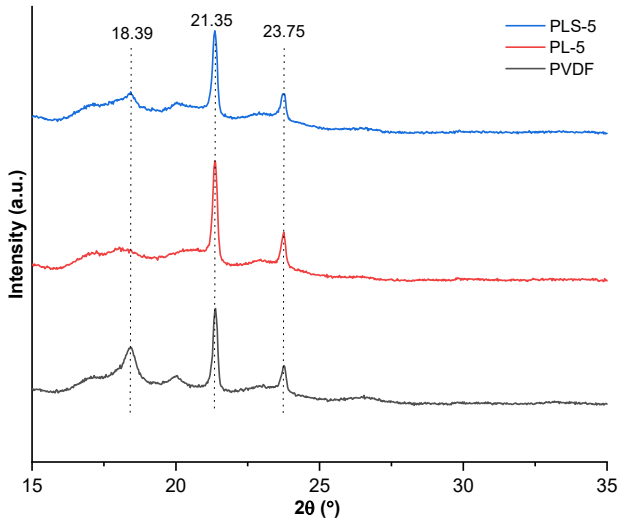

Fig 8. Diffractogram XRD of PVDF, PL-5, and PLS-5 membranes

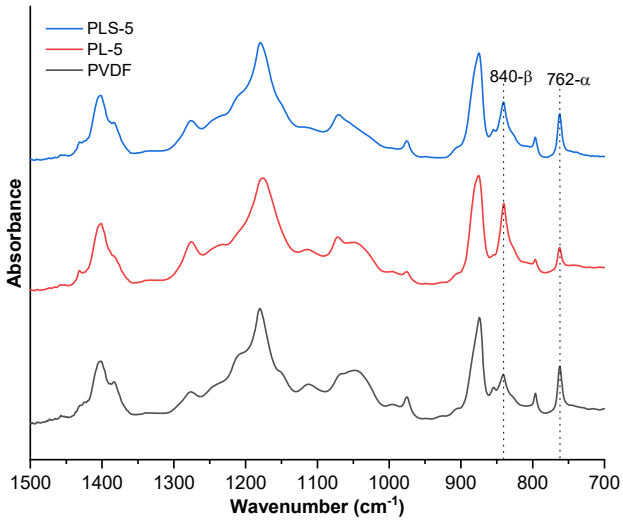

Fig 9. Membranes ATR-FTIR spectra

more hydrophilic membranes are formed [40]. β fraction of the membrane PVDF increased from 40.6 to 60.2% and 49.5% in PL and PLS, respectively. This suggests that lignin is more significant in increasing the hydrophilicity value of the membrane.

Surface hydrophilicity was also analyzed using a water contact angle and the data shown in Fig. 10. PVDF membrane has a contact angle of 74.7° while the addition of filler, the contact angle decreases, which means the hydrophilicity increased. The membrane PL-5 has the lowest water contact angle of 57.9° while for lignosulfonate addition contact angle decrease to 66.7° for PLS-1. This data is supported by the β fraction that shows PL is more hydrophilic than PLS membrane.

Water Uptake, Ion Exchange Capacity, and Conductivity of Membranes

The water uptake value indicates the membrane's ability to absorb and transport water, while the IEC represents the number of cations that can be exchanged with protons. The water uptake data are shown in Fig. 11. Water uptake increase with a higher concentration of lignin or lignosulfonate due to the hydrophile group attached to the membrane.

Fig. 12 shows the IEC value on the membrane has increased along with the high concentration of lignin and lignosulfonate. The addition of lignosulfonate resulted in a higher IEC value than the addition of lignin because the presence of sulfonate groups resulted in the

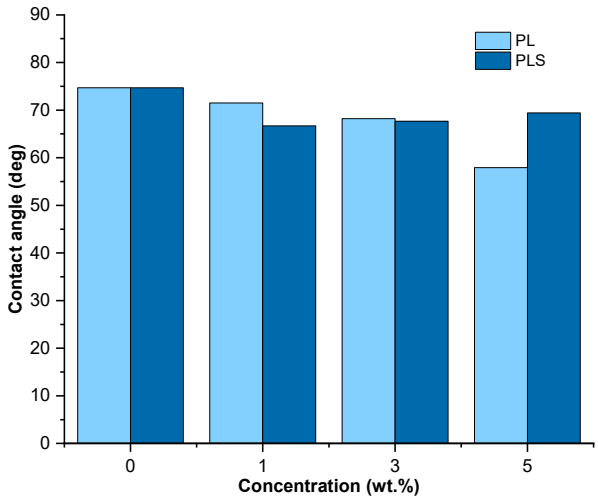

Fig 10. Membrane water contact angle

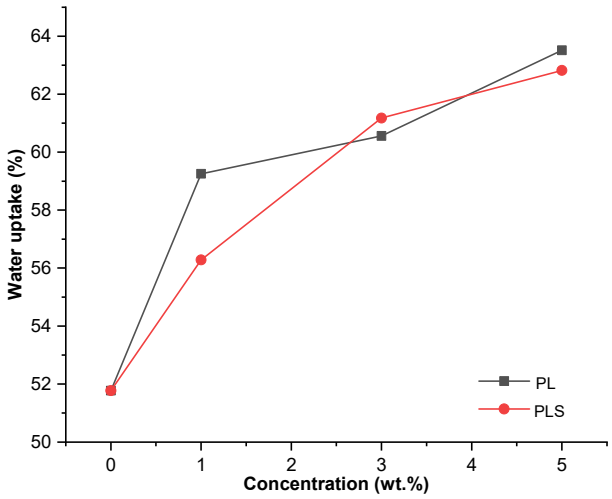

Fig 11. Membrane water uptake

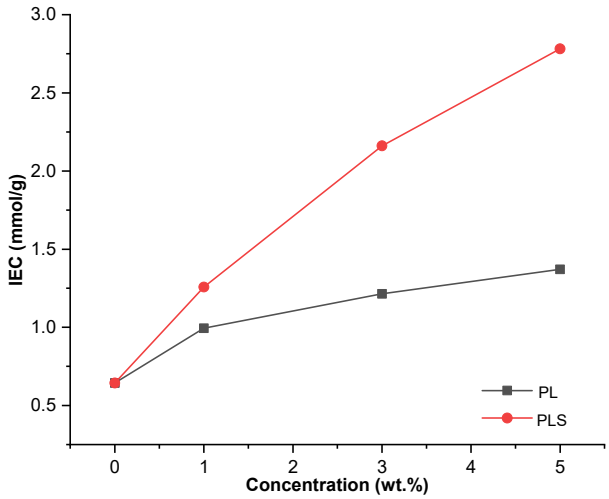

Fig 12. Membrane ion exchange capacity

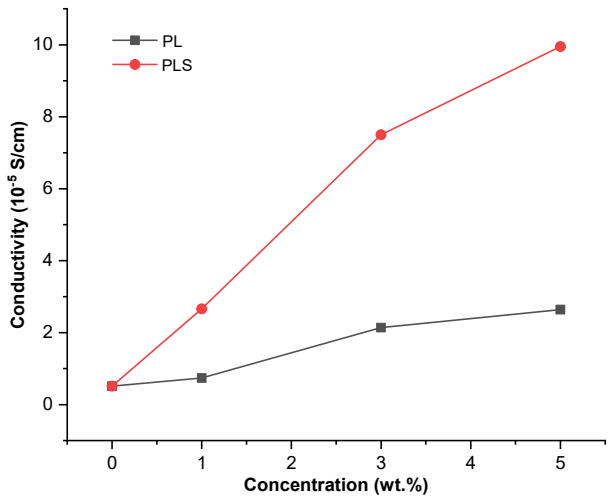

Fig 13. Membrane ionic conductivity

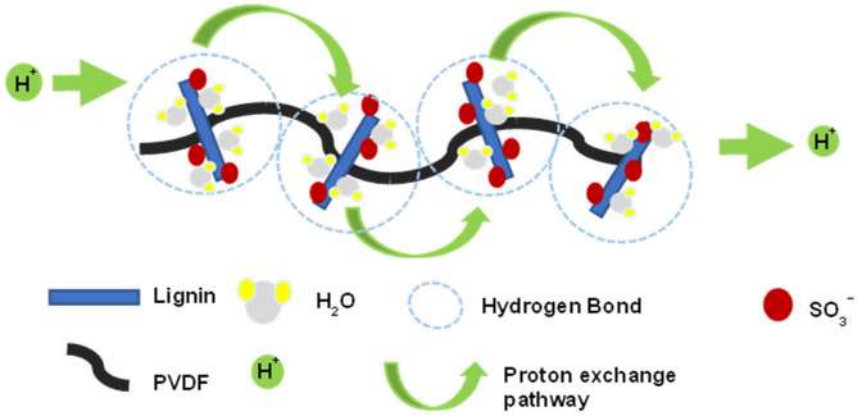

Fig 14. Proton transport mechanism

presence of sites in ion exchange. Membrane PLS-5 with an IEC of 2.78 mmol/g has a higher value than the Nafion® 117 polymer which only 0.91 mmol/g [41].

Ionic conductivity increases with increasing filler concentration as shown in Fig. 13. From the data, PVDF membrane has 0.51×10^{-5} S/cm and increase up to 9.95×10^{-5} S/cm for 5% lignosulfonate addition. This data is linear with IEC because IEC affects the ionic conductivity of the membrane [38-39]. The presence of sulfonate groups helps in the process of ion transfer. The proton transport mechanism via the Grotuss mechanism is shown in Fig. 14. Proton transportation occurs because of the protonation and deprotonation of hydrogen bonds [42]. Proton jumps between adjacent sulfonic acid groups or water molecules to achieve proton transfer [43]. In PLS-5, conductivity increases due to greater water uptake and IEC, where sulfonic facilitated proton transport from anode to cathode [44].

CONCLUSION

Isolation and sulfonation of lignin from OPEFB were successfully carried out. Adding lignin and lignosulfonate fillers affects membrane morphology, thermal, mechanical, matrix structure, hydrophilicity, and water uptake. Membranes have asymmetric structures with finger-like and sponge-like pores. All the membrane has similar degradation temperature caused by weak interaction between filler and PVDF matrix. The mechanical properties decreased with the addition of filler, while the surface hydrophilicity and water uptake increased. Membrane matrix composed of α and β phase. The β phase intensity increase with the addition of lignin and lignosulfonate. The ion exchange capacity and ionic conductivity also showed a high increase of 2.78 mmol/g and 9.95×10^{-5} S/cm, respectively. Based on the data obtained, it shows that the membrane PVDF modified with lignosulfonate has the potential as a polymer electrolyte membrane.

ACKNOWLEDGMENTS

The authors thank *Badan Pengelolaan Dana Perkebunan Kelapa Sawit* (BPDPKS) as the research funder of *Riset Sawit Mahasiswa 2022* No. PENG-2/DPKS.4/2022 and also to the Chemistry Laboratory UNS for facilitating the research to completion.

AUTHOR CONTRIBUTIONS

Nala Ridhwanul Mu'izzah and Pinka Zuhdiana Hapsari conducted the experiment and wrote the manuscript. Nabila Putri Aulia, Dian Wahyu Tri Wulansari, and Fauziyah Azhari do the analysis and reviewing. Edi Pramono supervised and review the manuscript. All authors agreed to the final version of this manuscript.

REFERENCES

[1] Abeleda Jr, J.M.A., and Espiritu, R., 2022, The status and prospects of hydrogen and fuel cell technology in the Philippines, *Energy Policy*, 162, 112781.

[2] Sokmez, E., Taymaz, I., and Kahveci, E.E., 2022, Performance evaluation of direct ethanol fuel cell using a three-dimensional CFD model, *Fuel*, 313, 123022.

[3] Nicolay, S., Karpuk, S., Liu, Y., and Elham, A., 2021, Conceptual design and optimization of a general aviation aircraft with fuel cells and hydrogen, *Int. J. Hydrogen Energy*, 46 (64), 32676–32694.

[4] Perčić, M., Vladimir, N., Jovanović, I., and Koričan, M., 2022, Application of fuel cells with zero-carbon fuels in short-sea shipping, *Appl. Energy*, 309, 118463.

[5] Ferraren-De Cagalitan, D.D.T., and Abundo, M.L.S., 2021, A review of biohydrogen production technology for application towards hydrogen fuel cells, *Renewable Sustainable Energy Rev.*, 151, 111413.

[6] Sigwadi, R., Dhlamini, M.S., Mokrani, T., Ṇemavhola, F., Nonjola, P.F., and Msomi, P.F., 2019, The proton conductivity and mechanical properties of Nafion®/ZrP nanocomposite membrane, *Heliyon*, 5 (8), e02240.

[7] Bose, S., Kuila, T., Nguyen, T.X.H., Kim, N.H., Lau, K.T., and Lee, J.H., 2011, Polymer membranes for high temperature proton exchange membrane fuel cell: Recent advances and challenges, *Prog. Polym. Sci.*, 36 (6), 813–843.

[8] Ayyubi, S.N., and Admaja, L., 2020, Pengaruh variasi konsentrasi montmorillonit terhadap sifat dan kinerja membran kitosan/PVA/MMT untuk aplikasi DMFC, *Walisongo J. Chem.*, 3 (1), 1–9.

[9] Silitonga, R.S., Widiastuti, N., Jaafar, J., Ismail, A.F., Abidin, M.N.Z., Azelee, I.W., and Naidu, M., 2018, The modification of PVDF membrane via cross-linking with chitosan and glutaraldehyde as the cross-linking agent, *Indones. J. Chem.*, 18 (1), 1–6.

[10] Dyartanti, E.R., Purwanto, A., Widiasa, I.N., and Susanto, H., 2018, Ionic conductivity and cycling stability improvement of PVDF/nano-clay using PVP as polymer electrolyte membranes for $LiFePo_4$ batteries, *Membranes*, 8 (3), 36.

[11] Abriyanto, H., 2021, Hydrophilic modification of PVDF membrane: A review, *JMM*, 1 (1), 1–9.

[12] Lu, J., Cheng, M., Zhao, C., Li, B., Peng, H., Zhang, Y., Shao, Q., and Hassan, M., 2022, Application of lignin in preparation of slow-release fertilizer: Current status and future perspectives, *Ind. Crops Prod.*, 176, 114267.

[13] Liu, Y., Mao, X., Wu, H., Wang, X., Shi, B., Fan, C., Kong, Y., and Jiang, Z., 2022, Sulfonated lignin intercalated graphene oxide membranes for efficient proton conduction, *J. Membr. Sci.*, 644, 120126.

[14] Lupatini, K.N., Schaffer, J.V., Machado, B., Silva, E.S., Ellendersen, L.S.N., Muniz, G.I.B., Ferracin, R.J., and Alves, H.J., 2018, Development of chitosan membranes as a potential PEMFC electrolyte, *J. Polym. Environ.*, 26 (7), 2964–2972.

[15] Ganguly, P., Sengupta, S., Das, P., and Bhowal, A., 2020, Valorization of food waste: Extraction of cellulose, lignin and their application in energy use and water treatment, *Fuel*, 280, 118581.

[16] Fatriasari, W., Ulwan, W., Aminingsih, T., Sari, F.P., Fitria, F., Suryanegara, L., Iswanto, A.H., Ghozali, M., Kholida, L.N., Hussin, M.H., Fudholi, A., and Hermiati, E., 2021, Optimization of maleic acid pretreatment of oil palm empty fruit bunches (OPEFB) using response surface methodology to produce reducing sugars, *Ind. Crops Prod.*, 171, 113971.

[17] Zakaria, N.A., Hazwan Hussin, M., Ahmad, A.L., Leo, C.P., Poh, P.E., Behzadian, K., Akinwumi, I.I., Moghayedi, A., and Diazsolano, J., 2021, Lignin modified PVDF membrane with antifouling properties for oil filtration, *J. Water Process Eng.*, 43, 102248.

[18] Ye, J., Cheng, Y., Sun, L., Ding, M., Wu, C., Yuan, D., Zhao, X., Xiang, C., and Jia, C., 2019, A green SPEEK/lignin composite membrane with high ion selectivity for vanadium redox flow battery, *J. Membr. Sci.*, 572, 110–118.

[19] Setiati, R., Siregar, S., and Wahyuningrum, D., 2020, "Laboratory Optimization Study of Sulfonation Reaction toward Lignin Isolated from Bagasse" in *Biotechnological Applications of Biomass*, Eds., Basso, T.P., Basso, T.O., and Basso, L.C., IntechOpen, Rijeka, Croatia.

[20] Rocha, I., Ferraz, N., Mihranyan, A., Strømme, M., and Lindh, J., 2018, Sulfonated nanocellulose beads as potential immunosorbents, *Cellulose*, 25 (3), 1899–1910.

[21] Bărdacă Urducea, C., Nechifor, A.C., Dimulescu, I.A., Oprea, O., Nechifor, G., Totu, E.E., Isildak, I., Albu, P.C., and Bungău, S.G., 2020, Control of

nanostructured polysulfone membrane preparation by phase inversion method, *Nanomaterials*, 10 (12), 2349.

[22] He, Z., Rault, F., Vishwakarma, A., Mohsenzadeh, E., and Salaün, F., 2022, High-aligned PVDF nanofibers with a high electroactive phase prepared by systematically optimizing the solution property and process parameters of electrospinning, *Coatings*, 12 (9), 1310.

[23] Grewal, M.S., Kisu, K., Orimo, S., and Yabu, H., 2022, Increasing the ionic conductivity and lithium-ion transport of photo-cross-linked polymer with hexagonal arranged porous film hybrids, *iScience*, 25 (9), 104910.

[24] Pradana, M.A., Ardhyananta, H., and Farid, M., 2017, Pemisahan selulosa dari lignin serat tandan kosong kelapa sawit dengan proses alkalisasi untuk penguat bahan komposit penyerap suara, *Jurnal Teknik ITS*, 6 (2), 413–416.

[25] Ganie, K., Manan, M.A., Ibrahim, A., and Idris, A.K., 2019, An Experimental approach to formulate lignin-based surfactant for enhanced oil recovery, *Int. J. Chem. Eng.*, 2019, 4120859.

[26] Ismiyati, I., Suryani, A., Mangunwidjaya, D., Machfud, M., and Hambali, E., 2009, Pembuatan natrium lignosulfonat berbahan dasar lignin isolat tandan kosong kelapa sawit: Identifikasi, dan uji kinerjanya sebagai bahan pendispersi, *J. Tek. Ind. Pert.*, 19 (1), 25–29.

[27] Karimov, O.K., Teptereva, G.A., Chetvertneva, I.A., Movsumzade, E.M., and Karimov, E.K., 2021, The structure of lignosulfonates for production of carbon catalyst support, *IOP Conf. Ser.: Earth Environ. Sci.*, 839, 022086.

[28] Eraghi Kazzaz, A., Hosseinpour Feizi, Z., and Fatehi, P., 2019, Grafting strategies for hydroxy groups of lignin for producing materials, *Green Chem.*, 21 (21), 5714–5752.

[29] Poletto, M., 2017, Assessment of the thermal behavior of lignins from softwood and hardwood species, *Maderas: Cienc. Tecnol.*, 19 (1), 63–74.

[30] Ramezani, N., and Sain, M., 2018, Thermal and physiochemical characterization of lignin extracted from wheat straw by organosolv process, *J. Polym. Environ.*, 26 (7), 3109–3116.

[31] Montoya-Ospina, M.C., Verhoogt, H., Ordner, M., Tan, X., and Osswald, T.A., 2022, Effect of cross-linking on the mechanical properties, degree of crystallinity and thermal stability of polyethylene vitrimers, *Polym. Eng. Sci.*, 62 (12), 4203–4213.

[32] Yi, G., Li, J., Henderson, L.C., Lei, W., Du, L., and Zhao, S., 2022, Enhancing thermal conductivity of polyvinylidene fluoride composites by carbon fiber: Length effect of the filler, *Polymers*, 14 (21), 4599.

[33] Lusiana, R.A., Indra, A., Prasetya, N.B.A., Sasongko, N.A., Siahaan, P., Azmiyawati, C., Wijayanti, N., Wijaya, A.R., and Othman, M.H.D., 2021, The effect of temperature, sulfonation, and PEG addition on physicochemical characteristics of PVDF membranes and its application on hemodialysis membrane, *Indones. J. Chem.*, 21 (4), 942–953.

[34] Li, W., Li, H., and Zhang, Y.M., 2009, Preparation and investigation of PVDF/PMMA/TiO_2 composite film, *J. Mater. Sci.*, 44 (11), 2977–2984.

[35] de Menezes, B.R.C., Ferreira, F.V., Silva, B.C., Simonetti, E.A.N., Bastos, T.M., Cividanes, L.S., and Thim, G.P., 2018, Effects of octadecylamine functionalization of carbon nanotubes on dispersion, polarity, and mechanical properties of CNT/HDPE nanocomposites, *J. Mater. Sci.*, 53 (20), 14311–14327.

[36] Gao, M., Zhu, Y., Yan, J., Wu, W., and Wang, B., 2022, Micromechanism study of molecular compatibility of PVDF/PEI blend membrane, *Membranes*, 12 (8), 809.

[37] Bai, H., Wang, X., Zhou, Y., and Zhang, L., 2012, Preparation and characterization of poly(vinylidene fluoride) composite membranes blended with nano-crystalline cellulose, *Prog. Nat. Sci.: Mater. Int.*, 22 (3), 250–257.

[38] Sui, Y., Chen, W.T., Ma, J.J., Hu, R.H., and Liu, D.S., 2016, Enhanced dielectric and ferroelectric properties in PVDF composite flexible films through doping with diisopropylammonium bromide, *RSC Adv.*, 6 (9), 7364–7369.

[39] Cai, X., Lei, T., Sun, D., and Lin, L., 2017, A critical analysis of the α, β and γ phases in poly(vinylidene fluoride) using FTIR, *RSC Adv.*, 7 (25), 15382–15389.

[40] Teoh, G.H., Ooi, B.S., Jawad, Z.A., dan Low, S.C., 2021, Impacts of PVDF polymorphism and surface printing micro-roughness on superhydrophobic membrane to desalinate high saline water, *J. Environ. Chem. Eng.*, 9 (4), 105418.

[41] Espiritu, R., Mamlouk, M., and Scott, K., 2016, Study on the effect of the degree of grafting on the performance of polyethylene-based anion exchange membrane for fuel cell application, *Int. J. Hydrogen Energy*, 41 (2), 1120–1133.

[42] Wang, M., Wang, L., Deng, N., Wang, X., Xiang, H., Cheng, B., and Kang, W., 2021, Electrospun multi-scale nanofiber network: Hierarchical proton-conducting channels in Nafion composite proton exchange membranes, *Cellulose*, 28 (10), 6567–6585.

[43] Zhai, S., Dai, W., Lin, J., He, S., Zhang, B., and Chen, L., 2019, Enhanced proton conductivity in sulfonated poly(ether ether ketone) membranes by incorporating sodium dodecyl benzene sulfonate, *Polymers*, 11 (2), 203.

[44] Lee, K.H., Chu, J.Y., Kim, A.R., and Yoo, D.J., 2019, Effect of functionalized SiO_2 toward proton conductivity of composite membranes for PEMFC application, *Int. J. Energy Res.*, 43 (10), 5333–5345.

Improved Mucoadhesive Properties of Repaglinide-Loaded Nanoparticles: Mathematical Modelling through Machine Learning-Based Approach

Nader Ibrahim Namazi*

Department of Pharmaceutics and Pharmaceutical Technology, College of Pharmacy, Taibah University, Al Madinah Al Munawarah 30001, Saudi Arabia

*** Corresponding author:**

email: nnamazi@taibahu.edu.sa

Received: February 4, 2023
Accepted: March 1, 2023

DOI: 10.22146/ijc.82031

Abstract: *This research work aims to develop a modified repaglinide-loaded chitosan-ethyl cellulose nanoparticles (RPG-ECSNPs) as a novel sustained-release dosage form with improved mucoadhesive properties using an emulsification solvent-evaporation technique. The RPG-ECSNPs with different particle sizes were prepared from various polymers containing ethyl cellulose (EC) as the internal phase and chitosan (CS) as the external phase, and the use of surfactants, including Tween 80 and poloxamer 188 as emulsifiers.* In vitro *drug release, drug loading amount, and entrapment efficiency have been influenced by changes in the concentrations of CS and EC. The mean droplet size and zeta potential of RPG-ECSNPs were 213 ± 8.5 nm and 16.4 ± 2.4 mV, respectively. The optimized formulation's entrapment efficiency was 66 ± 2.3%, and drug loading was 7.9 ± 1.65%. The release profile was significantly higher in PBS (90%) than in diluted hydrochloric acid (30%) during 24 h of the study. The mucoadhesive function of the particles was examined* in vitro *using part of rat intestines. The highest adhesive % was observed for the chitosan-coated NPs. No adhesive properties were noticed for chitosan-free NPs (P-value > 0.05). This indicated that ECSNPs can be successfully utilized for sustained and controlled drug delivery of RPG through the GIT.*

Keywords: *adhesive properties; chitosan; ethyl cellulose; nanoparticles*

INTRODUCTION

Nowadays, controlling the drug release rate is one of the interesting topics in the pharmaceutical industry. Scientists are focusing on drug release rate development and optimization through different methods. Diabetes mellitus is a worldwide health issue affecting patient quality of life [1]. Diabetes is a chronic metabolic problem that increases blood glucose because of insulin shortage. Repaglinide (RPG) is known as a fast-acting prandial glucose regulator. The action of RPG plays a role in stimulating the insulin release from pancreatic b-cells through the activation of ATP-dependent K^+ channel and can normalize the mealtime glucose excursion. The RPG is low soluble in water solution, which is about 34 μg/mL. Thus, sustained drug delivery systems have been implied to overcome many challenges associated with the adverse effects of conventional dosage forms leading to improved therapeutic outcomes. Designing a drug delivery system through synthesizing nanoparticles is a very useful method to optimize the prolonged release rate for different drugs. Surface modification of these nanocarriers through semi-synthetic polymers is able to improve drug bioavailability. Chitosan molecules (CS) are widely applied to optimize the physicochemical characteristics of the drug due to their mucoadhesive properties. They are very good candidates due to their good biocompatibility, biodegradability, and low toxicity properties [2-3]. Also, surface coating of nanocarriers using chitosan resulted in improving their stability in gastric and intestinal fluids [4]. Moreover, CS has been extensively applied in different research work to design a drug delivery system [5], artificial skin [6], artificial corneal [7], and gene therapy [8]. The role of ethyl cellulose (EC) is to control the release of RPG and gives floating characteristics. Drug release from the CS microsphere can be controlled by utilizing a naturally

existing crosslinking agent to impart a skeleton network for the pursuit of a prolonged release profile and better physiological compatibility [9]. For example, Wu and co-workers [10] reported RPG-loaded nanostructured lipid carriers with various particle sizes for enhancing oral bioavailability by solvent diffusion method.

In this study, novel nanoparticles, ethyl cellulose/chitosan (ECCS), with CS coating and EC core, was provided using the o/w emulsification procedure [11]. EC was chosen to act as a hydrophobic layer to prevent NPs from dissolving in the stomach [12]. The influence of preparation methods including CS and EC concentrations, on sustained release was studied. RPG has been chosen as the model drug that can be considered as the potential of the loaded nanoparticles in the delivery system. Further, the release profiles of RPG and mucoadhesive properties of the system were studied. Ebrahimi and co-authors [11] demonstrated the RPG drug encapsulation within solid lipid nanoparticle (SLN)-based formulations under the effect of Tween 80 and phosphatidylcholine. They discovered that the SLN formulations based on Tween 80 and phosphatidylcholine had the smallest size, the longest drug release time, and the greatest loading capacity [13]. Lokhande et al. [12] studied the encapsulation and release of RPG drug by saturated EC-ethyl acetate solution through solvent diffusion. The aim of this research work is to develop a modified repaglinide-loaded chitosan-ethyl cellulose nanoparticles (RPG-ECSNPs) as a novel sustained-release dosage form with improved mucoadhesive properties using an emulsification solvent-evaporation technique. The RPG-ECSNPs with different particle sizes were prepared from various polymers containing EC as the internal phase and CS as the external phase and the use of surfactants, including Tween 80 and poloxamer 188 as emulsifiers. *In vitro* drug release, drug loading amount, and entrapment efficiency were studied by changes in the concentrations of CS and EC.

■ EXPERIMENTAL SECTION

Materials

CS (Mw 250 kD, degree of deacetylation (DD) 90%) was provided from Aladdin Chemistry Co. Ltd. EC (200 cPa·s) was provided from Sinopharm Chemical Reagent Co. Ltd. Anhydrous ethanol, dichloromethane, sodium dihydrogen phosphate, sodium hydrogen phosphate, Tween 80, and acetic acid were obtained from Tianjin Feng Chuan Chemical Reagent. The provided materials and solvents were analytical grade. RPG was provided by Shanghai purple reagent factory. A dialysis bag was provided by Spectrum Chemical MFG.

Instrumentation

A transmission electron microscope (TEM, Tecnai G2–12–Spirit Biotwin-120 kV from FEI) has been used to characterize the morphology of nanoparticles. The particle size distribution (PSD) of the microsphere was measured using photon correlation spectroscopy. A vibrating incubator (HZQ-F160, Harbin Donglian Electronic & Technology Development, China) was used to extract the entrapped RPG.

Procedure

Preparation of microspheres

As much as 1 g EC was dissolved in 10 mL of a mixture of dichloromethane (DCM) and ethanol (3:1, v/v). RPG was added in EC solution at a concentration of 2% w/v, which constitutes the oil phase. Then 0.2 g CS was dissolved in 40 mL acetic aqueous solution (1%, v/v) at 25 °C, which constitutes the aqueous phase. Tween 80 (1%, v/v) was added into the CS solution under stirring [14]. The EC solution was poured into the CS solution dropwise under vigorous stirring at 2000 rpm/min for 60 min to form the primary o/w emulsified solution [15-16]. The obtained emulsified solution was put under moderate stirring for another three hours to allow the removal of the organic solvent. In the end, the obtained nanoparticles were filtered and dried at room temperature.

Characterization of nanoparticles

Particle size and zeta potential determination. The sample was diluted 100 times with pure nano water and all measurements were performed at 25 °C at a fixed scattering angle of 90 utilizing a He–Ne laser at 633 nm using PSD. The same instrument was applied to measure the surface charge of the microsphere diluted sample. All measurements were done in triplicate.

Surface morphology. TEM has been used to characterize the morphology of nanoparticles. First, nanoparticles were freeze-dried under a vacuum at −40 °C utilizing a ScanVac CoolSafe freeze dryer (LaboGene ApS, Denmark). In the next step, 1 mg of the dried nanoparticles was loaded on the copper sample stub utilizing a double-sided carbon adhesive, and the extra number of particles were deleted. In order to analyze the images, image software "Soft-Imaging Software GmbH CM-Prof 2.11.002" has been used.

Determination of loading amount and entrapment efficiency. An amount of 50 mg of the lyophilized nanoparticles were triturated until a fine powder was obtained. A mixture of 50 mL of acetone and distilled water (1:3, v/v) was added to get a homogeneous dispersion. The obtained suspension was stirred continuously at 150 rpm/min in a vibrating incubator at 37.5 °C (HZQ-F160, Harbin Donglian Electronic & Technology Development, China) to extract the entrapped RPG. After filtrating the suspension, the filtrate was collected to analyze the content of RPG spectrophotometrically at 243 nm. The drug loading (DL) was measured through Eq. (1):

$$DL\% = \frac{Wt_{dl}}{Wt_{td}} \times 100 \quad (1)$$

where Wt_{td} denotes the total value of the drug included and Wt_{dl} denotes the value of drug in the microspheres. Then the entrapment efficiency (EE) was calculated from Eq. (2):

$$EE\% = \frac{Wt_{dl}}{Wt_{tm}} \times 100 \quad (2)$$

where Wt_{tm} denotes the total amount of microspheres.

Release kinetics

The release kinetic of RPG from the microsphere was studied by fitting the release data within gastric and intestinal fluids using the following mathematical models. Zero-order release method was described in Eq. (3) [18-19]:

$$Q_t = k_0 t \quad (3)$$

where Q_t denotes the percentage of drug release rate at time t, k_0 is the release rate constant, and k_1 denotes the release rate constant for the first-order kinetics. First order release model was described in Eq. (4) as follows [18-19]:

$$\ln(100 - Q_t) = \ln 100 k_1 t \quad (4)$$

while Higuchi's equation (Eq. (5)) is as follows:

$$Q_t = k_H t^{0.5} \quad (5)$$

where k_H denotes the Higuchi release rate constant [20].

HPLC analysis

The mobile phase contains acetonitrile (40%), and phosphate buffer (60%, pH 2.5, 10 mM) was delivered at a flow rate of 1.0 mL/min. In order to characterize the results, a UV detector was used at a wavelength of 245 nm. The NPs were diluted using a chloroform:methanol (1:1, v/v) mixture, and the drug content was determined by the HPLC.

Physical stability of NPs

The storage stability of optimized NPs was analyzed at three various temperatures, i.e., 4, 25, and 45 °C for 2 months. Then, the changes in particle size, ZP, entrapment efficiency, and drug content are measured as well. In order to investigate the stability of NEs at pH 1.2 at a range of time including 0, 0.5, 1, 2, 5, 12, and 24 h, then the NEs samples were studied for mean droplet size, polydispersity index, and zeta potential.

Mucoadhesive properties

To evaluate the mucoadhesive function of the NPs *in vitro*, a particle counting method (Coulter counter) was used after confirming the relationship between the NPs concentration (mg/mL) and the number of NPs measured. This test was carried out using an intestinal tube (10 cm) isolated from a Wistar rat. After washing the intestine tube with saline solution, the tube was filled with the NPs solution and diluted 100 times with a phosphate buffer solution (pH 7.4), and then sealed with closers. The tube was then incubated in water at 37 °C for 2 h. The number of NPs was measured before and after incubation and the mucoadhesive % was calculated by the following equation (Eq. (6)):

$$Mucoadhesive\% = \frac{N_0 - N_s}{N_0} \times 100 \quad (6)$$

where N_0 and N_s are the number of NPs before and after incubation, respectively.

In vitro *release study*

"Dialysis sac" procedure was applied consisting of a dialysis membrane (cut-off 12 kDa) collected as a closed sac, including 3 mL of RPG-NPs or Cs-RPG-NE, in 100 mL of dissolution test medium with stirring at 70 rpm for 60 min at 37 °C. As much as 0.5 mL of the samples were withdrawn after 12 h, and the amount of RPG was determined by HPLC. In order to illustrate the influence of pH on the drug release rate, the test was carried out at different pH (1.2 and 7.4) as gastric and intestinal fluids, respectively.

Statistical analysis

All analyses were repeated three times. Statistical analyses were carried out utilizing some statistical software such as Prism-5 (GraphPad Software Inc., San Diego, CA).

■ RESULTS AND DISCUSSION

Preparation and Characterization of NPs

Size characterization of ECSNPs in different buffer media shows the stability of the formulation. From the TEM micrographs, it is shown that the nanoparticles prepared by emulsification solvent-evaporation are generally with uniform particle size distribution and spherical in shape. TEM micrograph of ECSNPs illustrated that the range of dimensions was about 150–250 nm in length and 7–10 nm in width (Fig. 1), while RPG-loaded ECSNPs had size ranges from 50 to 100 nm in length and 4–6 nm in width (Fig. 2). The outputs are in good agreement with DLS results. González et al. [17] have shown the morphology of CS NPs through low molecular weight by TEM analysis that has the size of individual particles was 5 to 10 nm.

Table 1 indicates the results of RPG-ECSNPs with different particle sizes, which are prepared from EC, Tween 80, poloxamer 188, and CS using an emulsification solvent-evaporation technique. Table 1 illustrates that all five formulations were stable and showed changes in particle size growth when the ratio of CS in comparison with EC increased from 117 ± 5.09 to

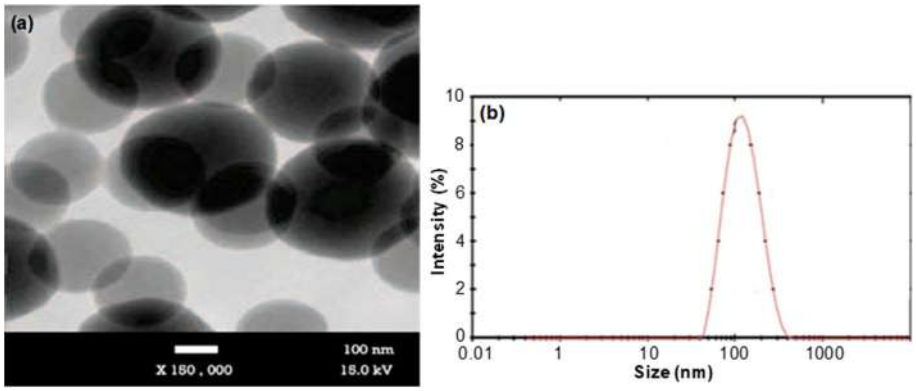

Fig 1. (a) TEM monographs and (b) DLS techniques of the ECSNPs nano-formulation

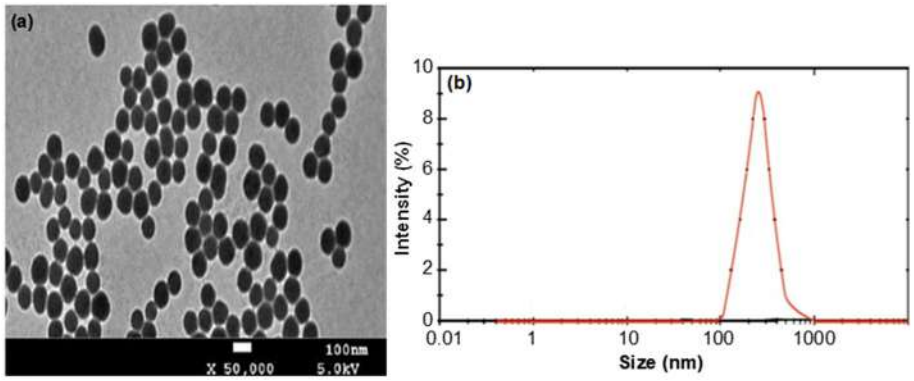

Fig 2. (a) TEM monographs and (b) DLS techniques of the RPG-ECSNPs nano-formulation

Table 1. Results of optimized formulations

Batch	EC/CS Ratio	PDI (Mean ±SD), n = 3	*In vitro* drug release (%) (Mean ±SD), n = 3	Particle size (nm) (Mean ±SD), n = 3	Zeta potential (mV) (Mean ±SD), n = 3
A	1:1	0.510 ± 0.12	2.88 ± 0.98	117.00 ± 5.09	−22.90 ± 0.48
B	1:2	0.267 ± 0.06	44.69 ± 1.21	213.50 ± 8.68	16.40 ± 2.43
C	1:3	0.248 ± 0.04	52.71 ± 1.29	386.70 ± 10.88	15.69 ± 0.89
D	1:4	0.355 ± 0.05	59.64 ± 1.10	443.70 ± 7.56	29.40 ± 1.00
E	1:5	0.478 ± 0.07	78.26 ± 2.08	509.40 ± 11.56	28.00 ± 2.56

509.4 ± 11.56 in batches A-E. The PDI values with a higher amount of CS for all batches reduced from 0.510 ± 0.12 to 0.248 ± 0.04, while the percent drug release is increased from 2.88 ± 0.98% to 78.26 ± 2.08%. Therefore, the addition of CS caused an enhancement in drug release. Vaghani et al. [21] showed the network of CS and polyvinyl pyrrolidone hydrogels improved the loading of RPG by up to 95%. The RPG-NPs had various zeta potentials and particle sizes with corresponding blank NPs, indicating that the participation of RPG had an influence on the zeta potential and particle size. However, the RPG-ECSNPs with the different batches had variant zeta potential values, indicating various surface charges between batch A and other batches. For example, Wu et al. [8] reported the RPG-loaded nanostructured lipid carriers (RPG-NLCs) had similar zeta potential and particle size compared to NLCs, showing that the taking part of REP had no significant influence on the zeta potential and particle size.

Drug Loading and Entrapment Efficiency

Poovi et al. [22] illustrated the alteration of the polymer and RPG ratios could affect the drug loading and entrapment efficiency. In this work, RPG was loaded onto polymeric nanoparticles by emulsification solvent-evaporation technique. Drug loading, particularly in the case of polymeric nanoparticles (PCENs), is based on adsorption and calculated using Eq. (1) [23]. The DL% and EE% values in order were 6.5 and 51.7% in batch A and 7.9 and 66.0% in batch B. The highest DL found in batch B may be because of the larger surface area and pore volume than that of batch A. It could be noticed that the drug loading amount was enhanced with an increase in the EC concentration in the formulation. This is attributed to the drug adsorption onto EC due to its non-ionic cellulose properties (binding properties). The more EC amount used, the more RPG loading amount. Increasing the ratio of CS/EC produced less or unpredictable results of drug content inside the nanoparticle (Table 2).

In Vitro Drug Release

Different mathematical models have been utilized to explain the kinetics of the drug release from the ECSNPs. In this study, the drug release rate has been analyzed at different pH, which is responsible for the ionization of the existing functional group [18-19]. It has been shown that the structure of the polymer does not change in acidic media, and the release rate can be controlled through diffusion. In less acidic media, the release is increased due to the relaxing of the polymers' chain owing to their swelling properties. It has been found that the drug release rate was increased through the loading of the drug in the ECSNPs. The designed formulation (B) has been applied to analyze the influence of various media pH. An appropriate model has been chosen to illustrate drug-release behavior. The kinetic rate constant (k) and the correlation coefficient (R^2) are illustrated in Table 3. The release behavior from this formulation (B) did not follow the Higuchi model, indicating high drug content and related to drug content.

Table 2. The amount of drug loading efficiency (DL) and entrapment efficiency (EE) of RPG-ECSNPs

Batch	CS (w/v%)	EC (w/v%)	DL (%)	EE (%)
A	1.0	1.0	6.5	51.7
B	1.0	2.0	7.9	66.0
C	2.0	1.0	5.3	54.7
D	3.0	1.0	4.4	52.4
E	4.0	1.0	4.1	50.4

Table 3. Parameters of *in vitro* release evaluation through different pH

Fitting Model	pH	Equation	Relative parameters	
			k value	R^2
Zero-order	2.0	1	0.339	0.958
	6.8		0.230	0.942
First-order	2.0	2	0.002	0.973
	6.8		0.007	0.990
Higuchi	2.0	3	4.309	0.978
	6.8		3.155	0.983

The release data of all examined models illustrated proper fitting to the Higuchi model, which is shown through the higher R^2 values (0.968–1.000) in comparison with the other applied models such as zero-order and first-order kinetics equations. Hence, the drug release kinetics illustrate a correlation between concentration and drug release rate.

Mucoadhesive Properties

The polymer layer on the platform was shown using the zeta potential. The mucoadhesive function of the ECSNPs was examined *in vitro* using part of rat intestines. The number of particles was adopted to evaluate the adhesive % of the ECSNPs. The highest adhesive % was observed for the (CS-Poloxamer)-coated NPs. No adhesive properties were noticed for CS-free NPs. The amount of CS polymer in the coating layer described the mucoadhesion function. It could be concluded that the more effective coating leads to higher adhesiveness [20].

■ CONCLUSION

The aim of this research work is to develop a modified RPG-ECSNPs as a novel sustained-release dosage form with improved mucoadhesive properties using an emulsification solvent-evaporation technique. The results demonstrated that the alteration in the concentrations of CS and EC has a great impact on drug loading amount, entrapment efficiency, and drug release. The drug release from ECSNPs was remarkably higher in PBS (90%) than in diluted 30% HCl during 24 h of the study. The highest adhesive % was observed for the chitosan-coated NPs. The output of this study illustrated that the saturated EC-ethyl acetate solution enhanced the efficiency of RPG encapsulation at 0.5% PVA. The RPG-EC nanoparticle's effect on control of the drug release rate prolongs it with no chemical interaction between them.

■ ACKNOWLEDGMENTS

The authors extend their appreciation to the Deputyship for Research & Innovation, Ministry of Education in Saudi Arabia, for funding this research work through project number 442-170. Also, the author would like to extend his appreciation to Taibah University for its supervision support.

■ REFERENCES

[1] Cho, N.H., Shaw, J.E., Karuranga, S., Huang, Y., da Rocha Fernandes, J.D., Ohlrogge, A.W., and Malanda, B., 2018, IDF Diabetes atlas: Global estimates of diabetes prevalence for 2017 and projections for 2045, *Diabetes Res. Clin. Pract.*, 138, 271–281.

[2] Röder, P.V., Wu, B., Liu, Y., and Han, W., 2016, Pancreatic regulation of glucose homeostasis, *Exp. Mol. Med.*, 48 (3), e219.

[3] Liu, W.F., Kang, C.Z., Kong, M., Li, Y., Su, J., Yi, A., Cheng, X.J., and Chen, X.G., 2012, Controlled release behaviors of chitosan/α,β-glycerophosphate thermo-sensitive hydrogels, *Front. Mater. Sci.*, 6 (3), 250–258.

[4] Liu, Y., Ma, L., and Gao, C., 2012, Facile fabrication of the glutaraldehyde cross-linked collagen/chitosan porous scaffold for skin tissue engineering, *Mater. Sci. Eng., C*, 32 (8), 2361–2366.

[5] Young, T.H., Wang, I.J., Hu, F.R., and Tsung, J.W., 2014, Fabrication of a bioengineered corneal endothelial cell sheet using chitosan/polycaprolactone blend membranes, *Colloids Surf., B*, 116, 403–410.

[6] Hu, H., Tang, C., and Yin, C., 2014, Folate conjugated trimethyl chitosan/graphene oxide nanocomplexes as potential carriers for drug and gene delivery, *Mater. Lett.*, 125, 82–85.

[7] Larbi-Bouamrane, O., Bal, Y., Aliouche, D., Cote, G., and Chagnes, A., 2016, Preparation and characterization of cross-linked chitosan microcapsules for controlled delivery of

oxytetracycline, *Indian J. Pharm. Sci.*, 78 (6), 715–724.

[8] Wu, L., Zhao, L., Su, X., Zhang, P., and Ling, G., 2020, Repaglinide-loaded nanostructured lipid carriers with different particle sizes for improving oral absorption: Preparation, characterization, pharmacokinetics, and *in situ* intestinal perfusion, *Drug Delivery*, 27 (1), 400–409.

[9] Lee, Y.S., Johnson, P.J., Robbins, P.T., and Bridson, R.H., 2013, Production of nanoparticles-in-microparticles by a double emulsion method: A comprehensive study, *Eur. J. Pharm. Biopharm.*, 83 (2), 168–173.

[10] El-Habashy, S.E., Allam, A.N., and El-Kamel, A.H., 2016, Ethyl cellulose nanoparticles as a platform to decrease ulcerogenic potential of piroxicam: Formulation and *in vitro*/*in vivo* evaluation, *Int. J. Nanomed.*, 11, 2369–2380.

[11] Ebrahimi, H.A., Javadzadeh, Y., Hamidi, M., and Jalali, M.B., 2015, Repaglinide-loaded solid lipid nanoparticles: Effect of using different surfactants/stabilizers on physicochemical properties of nanoparticles, *Daru, J. Pharm. Sci.*, 23, 46.

[12] Lokhande, A.B., Mishra, S., Kulkarni, R.D., and Naik, J.B., 2013, Preparation and characterization of repaglinide loaded ethylcellulose nanoparticles by solvent diffusion technique using high pressure homogenizer, *J. Pharm. Res.*, 7 (5), 421–426.

[13] Aghaei, M., Erfani-Moghadam, V., Daneshmandi, L., Soltani, A., Abdolahi, N., Cordani, M., Yahyazadeh, A., Rad, S.M., Tavassoli, S., and Balakheyli, H., 2021, Non-ionic surfactant vesicles as novel delivery systems for sulfasalazine: Evaluation of the physicochemical and cytotoxic properties, *J. Mol. Struct.*, 1230, 129874.

[14] Ansari, M.J., Aldawsari, M.F., Zafar, A., Soltani, A., Yasir, M., Jahangir, M.A., Taleuzzaman, M., Erfani-Moghadam, V., Daneshmandi, L., Mahmoodi, N.O., Yahyazadeh, A., Rahman, M.L., and Sarjadi, M.S., 2022, *In vitro* release and cytotoxicity study of encapsulated sulfasalazine within LTSP micellar/liposomal and TSP micellar/niosomal nano-formulations, *Alexandria Eng. J.*, 61 (12), 9749–9756.

[15] El-Say, K.M., 2016, Maximizing the encapsulation efficiency and the bioavailability of controlled-release cetirizine microspheres using Draper–Lin small composite design, *Drug Des., Dev. Ther.*, 10, 825–839.

[16] Laracuente, M.L., Yu, M.H., and McHugh, K.J., 2020, Zero-order drug delivery: State of the art and future prospects, *J. Controlled Release*, 327, 834–856.

[17] González, C., Reyes, L.H., Muñoz-Camargo, C., and Cruz, J.C., 2021, Synthesis, characterization, and functionalization of chitosan and gelatin type B nanoparticles to develop novel highly biocompatible cell-penetrating agents, *Mater. Proc.*, 4 (1), 30.

[18] Ghauri, Z.H., Islam, A., Qadir, M.A., Gull, N., Haider, B., Ullah-Khan, R., and Riaz, T., 2021, Development and evaluation of pH-sensitive biodegradable ternary blended hydrogel films (chitosan/guar gum/PVP) for drug delivery application, *Sci. Rep.*, 11, 21255.

[19] Suhail, M., Wu, P.C., and Usman-Minhas, M., 2021, Development and characterization of pH-sensitive chondroitin sulfate-co-poly(acrylic acid) hydrogels for controlled release of diclofenac sodium, *J. Saudi Chem. Soc.*, 25 (4), 101212.

[20] Ways, T.M., Man-Lau, W., and Khutoryanskiy, V.V., 2018, Chitosan and its derivatives for application in mucoadhesive drug delivery systems, *Polymers*, 10 (3), 267.

[21] Vaghani, S.S., and Patel, M.M., 2011, Hydrogels based on interpenetrating network of chitosan and polyvinyl pyrrolidone for pH-sensitive delivery of repaglinide, *Curr. Drug Discovery Technol.*, 8 (2), 126–135.

[22] Poovi, G., Dhana-Lekshmi, M., Narayanan, N., and Reddy, N., 2011, Preparation and characterization of repaglinide loaded chitosan polymeric nanoparticles, *Res. J. Nanosci. Nanotechnol.*, 1 (1), 12–24.

[23] Zhou, H.Y., Cao, P.P., Zhao, J., Wang, Z.Y., Li, J.B., and Zhang, F.L., 2014, Release behavior and kinetic evaluation of berberine hydrochloride from ethyl cellulose/chitosan microspheres, *Front. Mater. Sci.*, 8 (4), 373–382.

Synthesis and Antidiabetic Evaluation of *N'*-Benzylidenebenzohydrazide Derivatives by *In Silico* Studies

Yusuf Syaril Alam[1], Pratiwi Pudjiastuti[2*], Saipul Malulana[3], Nur Rahmayanti Affifah[1], Fahimah Martak[1], Arif Fadlan[1], Tutik Sri Wahyuni[3], and Syukri Arief[4]

[1]*Department of Chemistry, Faculty of Science and Data Analytics, Institut Teknologi Sepuluh Nopember, Jl. Arif Rahman Hakim, Surabaya 60115, Indonesia*

[2]*Department of Chemistry, Faculty of Science and Technology, Airlangga University, Surabaya 60115, Indonesia*

[3]*Department of Pharmaceutical Science, Faculty of Pharmacy, Airlangga University, Surabaya 60115, Indonesia*

[4]*Department of Chemistry, Faculty of Mathematics and Natural Sciences, Andalas University, Limau Manis Campus, Padang 25163, Indonesia*

**** Corresponding author:***

email: pratiwi-p@fst.unair.ac.id

Received: February 6, 2023
Accepted: June 7, 2023

DOI: 10.22146/ijc.82073

Abstract: *Three new* N'*-benzylidenebenzohydrazide (NBB) derivatives were successfully synthesized and yielded 50–58%. FTIR, ESI-MS, ^{1}H- and ^{13}C-NMR were used to investigate the characteristic of NBB derivates. The structure and relationship of NBB derivatives into α-glucosidase and α-amylase as good targets for diabetes treatment were evaluated using* in silico *screening. Molecular mechanics-Poisson Boltzmann/generalized born surface area (MM-PB/GBSA) was used to calculate the free binding energy ($\Delta G_{bind\ (MM\text{-}GBSA)}$) of NBB to α-glucosidase and α-amylase receptors showed that the results of −0.45 and −20.79 kcal/mol, respectively. In the* ortho *position, NBB derivatives exhibited electron donating groups (EDG like -OCH_3, -OH and -Cl with binding free energies of −21.94, −6.71, and 21.94, respectively, and acarbose, a native ligand energy of −32.62 kcal/mol. In addition, the binding free energy of N-2-(-OCH_3, -OH and -Cl)-NBB to the α-amylase receptor showed the number of −39.33, −43.96, −42.81, respectively and −46.51 kcal/mol in comparing with a native ligand. As a result, it was found that all the NBB derivatives were able to interact with several amino acids in the α-glucosidase cavity as well as the native ones, including Ala281, Asp282, and Asp616. NBB and native ligand showed similar interaction between α-amylase with Gly110 amino acid residue.*

Keywords: N'*-benzylidenebenzohydrazide; α-amylase; derivatives; antidiabetic;* in silico

INTRODUCTION

Diabetes, in general, is a chronic metabolic disease characterized by elevated levels of blood glucose, which is divided into several types. Specifically, type-2 diabetes is a metabolic disorder distinguished by chronic hyperglycemia and either complete or partial deficiencies of insulin secretion [1]. Over the past few decades, there has been a rise in the prevalence of type-2 diabetes in many countries of the world from a wide range of income levels. An alternative therapeutic approach for controlling hyperglycemia associated with type-2 diabetes is to target α-glucosidase and α-amylase enzymes that catalyze starch hydrolysis in the intestine. Inhibition of α-glucosidase and α-amylase can decrease hyperglycemia in non-insulin-dependent diabetes mellitus (NIDDM) and retard the absorption of glucose [2]. Acarbose, miglitol, and voglibose are the three α-glucosidase inhibitors that have been approved for use in clinical trials at this time [3]. Voglibose comes from a microbial origin, whereas miglitol is synthetically derived

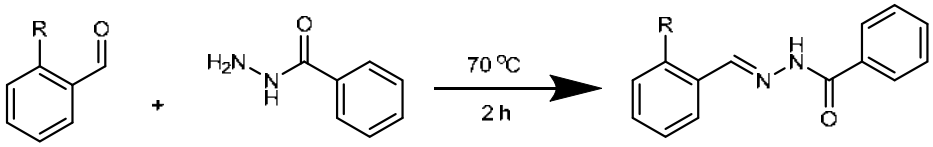

Fig 1. Synthesis of NBB and derivatives

from 1-deoxynojirimycin [4]. The α-amylase is a calcium metalloenzyme that helps in the digestion of polysaccharide molecules into small saccharides. As same as α-glucosidase, the α-amylase enzyme causes postprandial hyperglycaemia and increased blood glucose levels. With these characteristics, α-amylase is a well-known therapeutic target for the treatment and maintenance of elevated postprandial blood glucose [5].

N'-benzylidenebenzohydrazide (NBB) and its derivatives are important to the development of a significant class of new drugs [6]. Taha et al. [7] recently reported benzothiazole NBB derivatives containing benzohydrazide as α-glucosidase inhibitor with a wide range of IC_{50} values. Ullah et al. [8] also reported that benzohydrazide-based imine and thiazolidine-4-one inhibit α-glucosidase and α-amylase enzymes. According to Fan et al. [9] chromone-based NBB derivatives may have the potential to perform as α-glucosidase inhibitors. The core of benzohydrazide is crucial to the inhibition of their enzymes. Therefore, the research aims to synthesize and evaluate NBB-derived with electron-donating groups (-OCH_3, -OH and -Cl) (Fig. 1) as antidiabetic to target α-glucosidase and α-amylase enzymes by using molecular docking.

■ EXPERIMENTAL SECTION

Materials

Analytical grades of benzohydrazide, benzaldehyde, salicylaldehyde, *o*-anisaldehyde, and *o*-chlorobenzaldehyde were purchased from Sigma Aldrich. Analytical grades of hexane, dimethylformamide, dimethyl sulfoxide, dichloromethane, sodium acetate and glacial acid were purchased from Merck. The pure solvents of ethanol 99.9%, methanol 99.8%, chloroform, and ethyl acetate were prepared from Fulltime.

Instrumentation

NMR measurement was used TMS as an internal reference, NMR spectra were recorded on a JEOL Resonance 400 MHz spectrometer, and the chemical shifts were reported in δ (ppm). TLC was performed using silica gel 60 F254 aluminium sheet, while ESI-MS data were obtained using water mass spectrometer Q-TOF XEVO. At last, functional groups were analyzed using FTIR Bruker Opus with KBr pellet preparation. Software for docking analysis**:** the computing study in this research was performed under a Dell WorkStation Personal Computer, Linux Ubuntu 20.04.3 LTS OS, Intel® Xeon(R) W-2223 CPU @3.60 GHz octa-core; RAM 16 GB and GPU NVIDIA Quadro P2200. Meanwhile, molecular docking was conducted with Maestro Schrödinger 2022-1 software (Schrödinger, New York, NY, USA).

Procedure

Synthesis of NBB derivatives

NBB synthesis was conducted by using the reflux process and several modified procedures from Jubie et al. [10]. The ligands were prepared by adding 6 mmol (0.8169 g) of benzohydrazide in 30 mL of ethanol. Then, 6 mmol of the *o*-benzaldehyde derivative and 30 mL of ethanol were added to the flask with a small amount of acetic acid. The mixture was refluxed for 2 h at 70 °C temperature. After that, the product was cooled overnight at 4 °C and separated by using a funnel. As the last step, an aluminium sheet with TLC gel 60 F_{254} was used for product tracing. This procedure was repeated for the synthesis of the other four derivates, such as *N*-2-(-Cl, -OH, and -OMe)benzohydrazide.

***N'*-(2-chlorobenzylidene)-benzohydrazide 1.** Yield: 53.40%. FTIR (KBr, cm^{-1}): 3181 (-C_{sp2}H aromatic); 1643 (-C=O); 1555 (-N=N-). ^{1}H-NMR (DMSO-d_6): 12.05 (*s*, 1H, -NH); 8.84 (*s*, 1H, -CH=N); 8.00 (*m*, 1H); 7.91 (*d*, 2H); 7.57 (*t*, 1H); 7.50 (*dd*, 3H); 7.42 (*m*, 2H). ^{13}C-NMR (DMSO-d_6): 163.8 (-C=O); 144.2 (-CH=N); 133.8; 133.7; 132.5; 132.1; 132.1; 130.5; 129.1; 128.2; 128.2; 127.4. ESI-MS: 259.0636 (100%) $[L+H]^+$; 281.0360 (100%) $[L+Na]^+$.

***N'*-(2-hydroxybenzylidene)-benzohydrazide 2.** Yield: 50.12%. FTIR (KBr, cm^{-1}): 3268 (-NH); 3268 (-OH); 3057 (-C_{sp2}H aromatic); 1672 (-C=O); 1538 (-N=N); 1271 (-C-O). ^{1}H-NMR (DMSO-d_6): 12.1 (*s*, 1H, -NH); 11.37 (*s*, 1H, -CH=N); 8.61 (*s*, 1H); 7.90 (*m*, 2H); 7.58 (*t*, 1H); 7.51 (*ddd*, 3H); 7.27 (*td*, 1H); 6.90 (*m*, 2H). ^{13}C-NMR (DMSO-d_6): 163.4 (-C=O); 158.0 (-C-OH); 148.9 (-CH=N)-; 133.4; 132.5; 132.1 130.1; 129.1; 128.2; 119.9; 119.2; 117.0. ESI-MS: 241.0979 (100%) $[L+H]^+$.

***N'*-(2-methoxybenzylidene)-benzohydrazide 3.** Yield: 57.93%. FTIR (KBr, cm^{-1}) 3184 (-C_{sp2}H aromatic); 2988 (-C_{sp3}H of methyl); 1640 (C=O); 1556 (-N=N); 1251 (-C-O). ^{1}H-NMR (DMSO-d_6): 11.81 (*s*, 1H, -NH); 8.79 (*s*, 1H, -CH=N); 7.89 (*m*, 2H); 7.85 (*dd*, 1H); 7.55 (*dd*, 1H); 7.48 (*t*, 2H), 7.38 (*m*, 1H); 7.07 (*d*, 1H); 6.99 (*t*, 1H); 3.83 (*s*, 3H, -OCH_3). ^{13}C-NMR (DMSO-d_6): 163.5 (-C=O); 158.3 (-C=OCH_3); 143.8 (-CH=N); 133.9; 132.3; 132.1; 129.0; 128.2; 126.1; 122.9; 121.3; 112.4; 56.2 (-OCH_3). ESI-MS: 255.1136 (100%) $[L+H]^+$.

Ligands and receptor preparation

ChemDraw was used to generate the ligand structures, which were then converted into a 3D model using LigPrep [11] module in Schrodinger 2022-1 as well as protonated at pH 7.4 with Epik [12] and OPLS4 forcefield [13]. These processes aim to restore improper or missing bonds, assign protonation, possible ionization, and tautomeric states [14-16]. Moreover, α-glucosidase (PDB ID: 5NN8) protein was prepared by removing the residual solvent, optimizing the hydrogen bond, and protonating using ProtAssign [17] and PROPKA [18]. At the same time, in the "protein preparation wizard" that is incorporated into Maestro Schrodinger 2022-1 [19-20], the partial charge was also added using OPLS4 forcefield.

Molecular docking

The docking study was performed using Glide [21] Maestro Schrodinger's 2022-1 to predict the binding affinities and molecular interactions of synthesized compounds against two receptor targets: α-glucosidase (PDB ID: 5NN8) and α-amylase (PDB ID: 6GXV). Acarbose, an inhibitor that acts as the native ligand, was used for comparing to compounds. A grid box was placed at the center of acarbose position with similar dimensions for both receptors (20 × 20 × 20 Å) for setting the docking region. The docking grid box for α-glucosidase and α-amylase were assigned based on the coordinates of the native ligand at (x = −13.92, y = −38.29, z = 95.23) and (x = 44.03, y = 22.72, and z = −11.87), respectively. Redocking the native ligand was conducted to validate docking protocols and calculated their root mean square deviation (RMSD) with 100 conformations limit numbers. The docking protocol was deemed valid if the RMSD value was < 2 Å [22]. The docking process was carried out with Glide in extra precision (XP) mode under rigid receptors and flexible ligand conditions. The molecular mechanics-generalized Born surface area (MM-GBSA) was calculated to assess the docking pose of the ligands and determine the potency of each compound [23-26]. The "ligand interactions panel" on Maestro Schrodinger was used to visualize the molecular interactions. The results provide valuable insights into the binding modes and mechanisms of these receptors. It could help to guide the design of new compounds with improved efficacy and specificity.

■ RESULTS AND DISCUSSION

Computer-Aided Drug Discovery

Computer-aided drug discovery is the most important tool to predict drug activity through computational structure-based drug discovery. The relationship between sites of protein action and compounds acting as ligands can be explained using a variety of software. In point of fact, a physics-based equation is used to determine the binding free energy [27]. The α-glucosidase is an essential enzyme that is found on the luminal surface of enterocytes that functions to regulate blood glucose by converting complex carbohydrates into absorbable glucose, which is required for energy metabolism [28-29]. The removal of the anomeric carbon from the glucosyl group and the glycosidic oxygen (C_1–O) is the first step in the hydrolysis reactions carried out by α-glucosidases. Then, the glucosyl group is replaced by a proton from water resulting in the process of hydrolysis and transglycosylation exchange process between glucosyl residues and the protons [30]. Acarbose (Fig. 2) inhibits

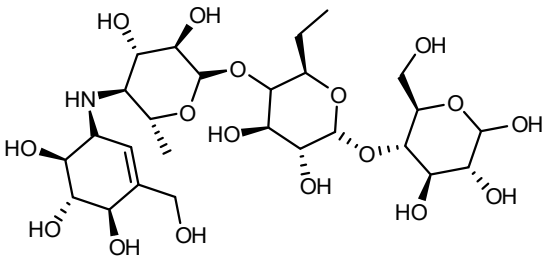

Fig 2. Acarbose

intestinal α-glucosidases, the enzymes responsible for the metabolism of complex carbohydrates into absorbable monosaccharide units in a reversible manner. This mechanism might be used to identify and develop new diabetic medications that are useful for showing diabetes progression [31-34].

Molecular Docking

Molecular docking is an important and helpful tool to predict the binding affinity of molecules to proteins [6]. In this study, the docking protocol was validated by internal validation after redocking the native ligand in its original positions resulting in RMSD values of 1.812 and 1.165 Å for α-glucosidase and α-amylase receptors. Based on these findings, it is possible to determine the test compound's activity against α-glucosidase as well as α-amylase receptors using either docking protocol [22]. Prior to docking the molecule, RMSD was used to determine the native acarbose ligand's docking position, as depicted in Fig. 3.

Compounds NBB **1**, **2**, and **3** with aromatic parts in their structures were evaluated for the protein-ligand complexes in the structure-activity relationship. It was discovered that a more negative score of binding affinity indicated a stronger binding. This ligand-protein binding process is correlated with this score which is also known as the change of the free energy. The measurement of how strong the interaction between the ligand and the protein is often directly related to the potential for ligand activity [35-36]. NBB without substituents resulted in an MMGBSA score of −0.45 on the binding affinity of complexes ligand-receptors. The *ortho* positions of the NBB derivatives with EDG (-Cl, -OH and -OMe) were −18.28, −6.71, and −21.94 kcal/mol, respectively. As can be seen in Table 1 and Fig. 4, the results of the ligand-receptor binding indicated that these compounds were bound to the same residues (Ala284, Asp282 and Asp616) in the entry area of the α-glucosidase active site.

The native acarbose inhibitor was validated by a redocking process on α-amylase in its original positions, which resulted in an RMSD value of 1.165 Å. In Table 2, the docking result between NBB derivatives and the α-amylase receptors showed that the value of MMGBSA as a binding affinity score for the ligand-receptors complex had a nearly equal range between −43.09 to −39.42, with native ligand acarbose −46.51 kcal/mol. Similar to α-glucosidase, the NBB grid score, −20.78 kcal/mol, was found to be greater than the NBB derivatives. Through the use of a hydrogen bond, NBB derivatives were able to interact with the same amino acids in the cavity of α-amylase Gly110 in a strong π-π interaction [37]. It should

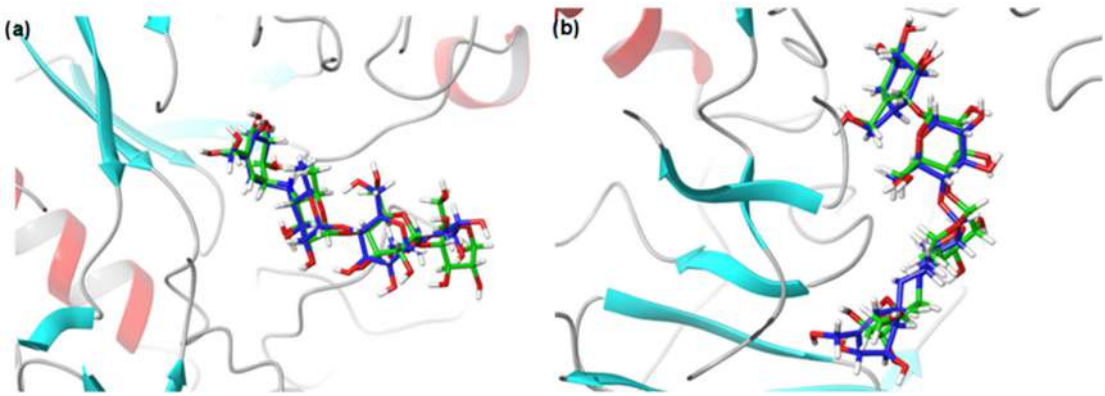

Fig 3. The acarbose native ligand on (a) α-glucosidase and (b) α-amylase receptors (Blue = original position and green = native ligand after redocking)

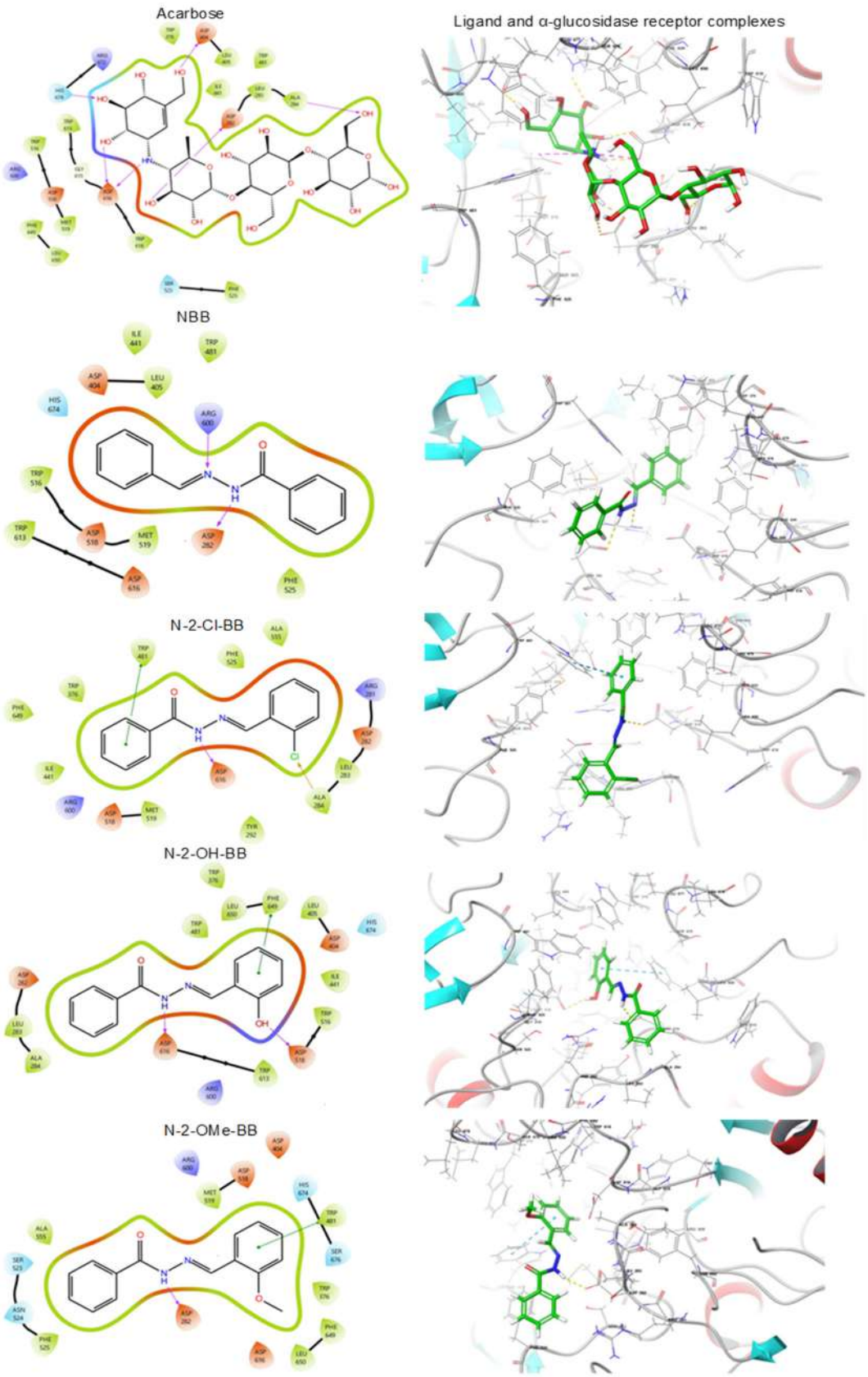

Fig 4. The binding of NBB derivatives and α-glucosidase

Table 1. Molecular docking result against α-glucosidase receptor

No.	Compound	MMGBSA (kcal/mol)	Amino acid interaction
1	*N'*-benzylidenebenzohydrazide	−0.45479	**Asp282**, Arg600
2	*N'*-(2-chlorobenzylidene)benzohydrazide, **1**	−17.2886	**Ala284**, Trp481, **Asp616**
3	*N'*-(2-hydroxybenzylidene)benzohydrazide, **2**	−6.71190	Asp518, **Asp616**, Phe649
4	*N'*-(2-methoxybenzylidene)benzohydrazide, **3**	−21.9442	**Asp282**, Trp481
5	Acarbose (Native ligand)	−32.6238	**Asp 282**, **Ala284**, Asp404, **Asp616**, His674

Table 2. Molecular docking results against α-amylase receptor

No.	Compound	MMGBSA (kcal/mol)	Amino acids interaction
1	Acarbose (Native ligand)	−46.5148	**Gly110**, Asp166, Asp234, Arg232, Asp332
2	*N'*-benzylidenebenzohydrazide	−20.7892	Tyr58, Tyr196
3	*N'*-(2-chlorobenzylidene)benzohydrazide, **1**	−42.8137	**Gly110**, Ala111
4	*N'*-(2-hydroxybenzylidene)benzohydrazide, **2**	−43.0944	**Gly110**, Gln51
5	*N'*-(2-methoxybenzylidene)benzohydrazide, **3**	−39.3278	**Gly110**, Ala111

be noted that NBB was not involved in binding interactions with Gly110 and other amino acid residues that include the native ligand (Table 2).

Through a variety of hydrophobic and hydrogen bonds, the active site of residue α-amylase receptor with NBB and its derivates can be followed in Fig. 5.

The compounds synthesized exhibit affinity energy values that are suboptimal compared to native ligands. However, some of the synthesized compounds show interactions with the catalytic site of the α-glucosidase receptor, specifically *N'*-(2-chlorobenzylidene)benzo hydrazide, *N'*-(2-hydroxybenzylidene)benzohydrazide,

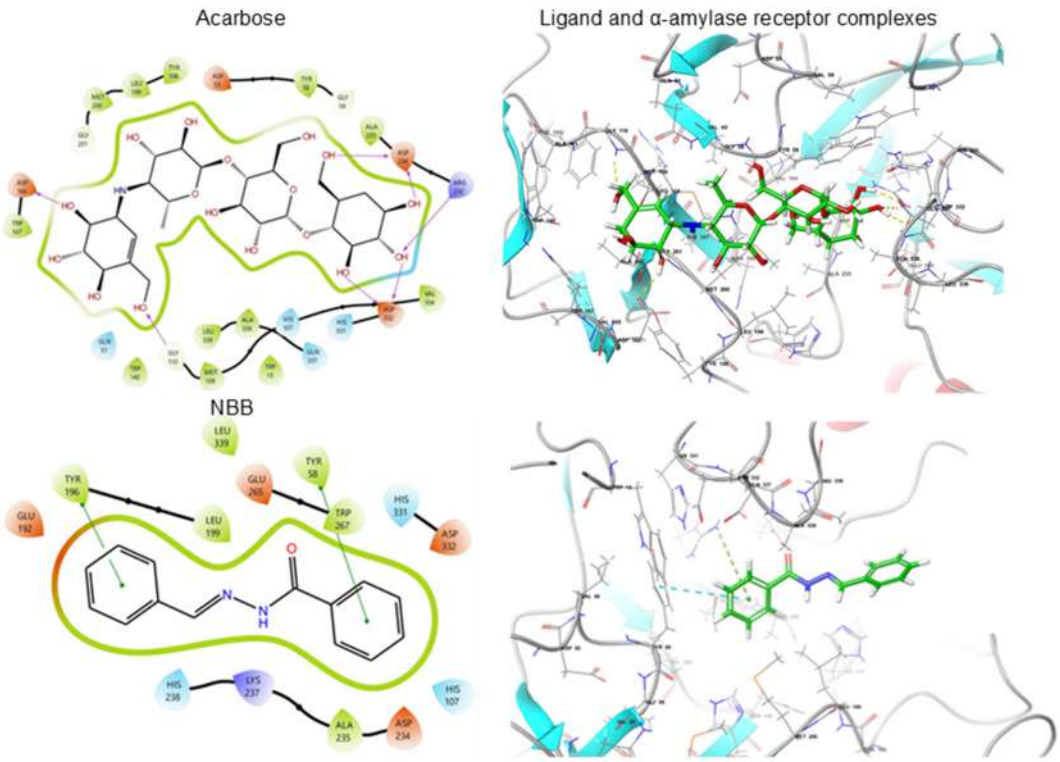

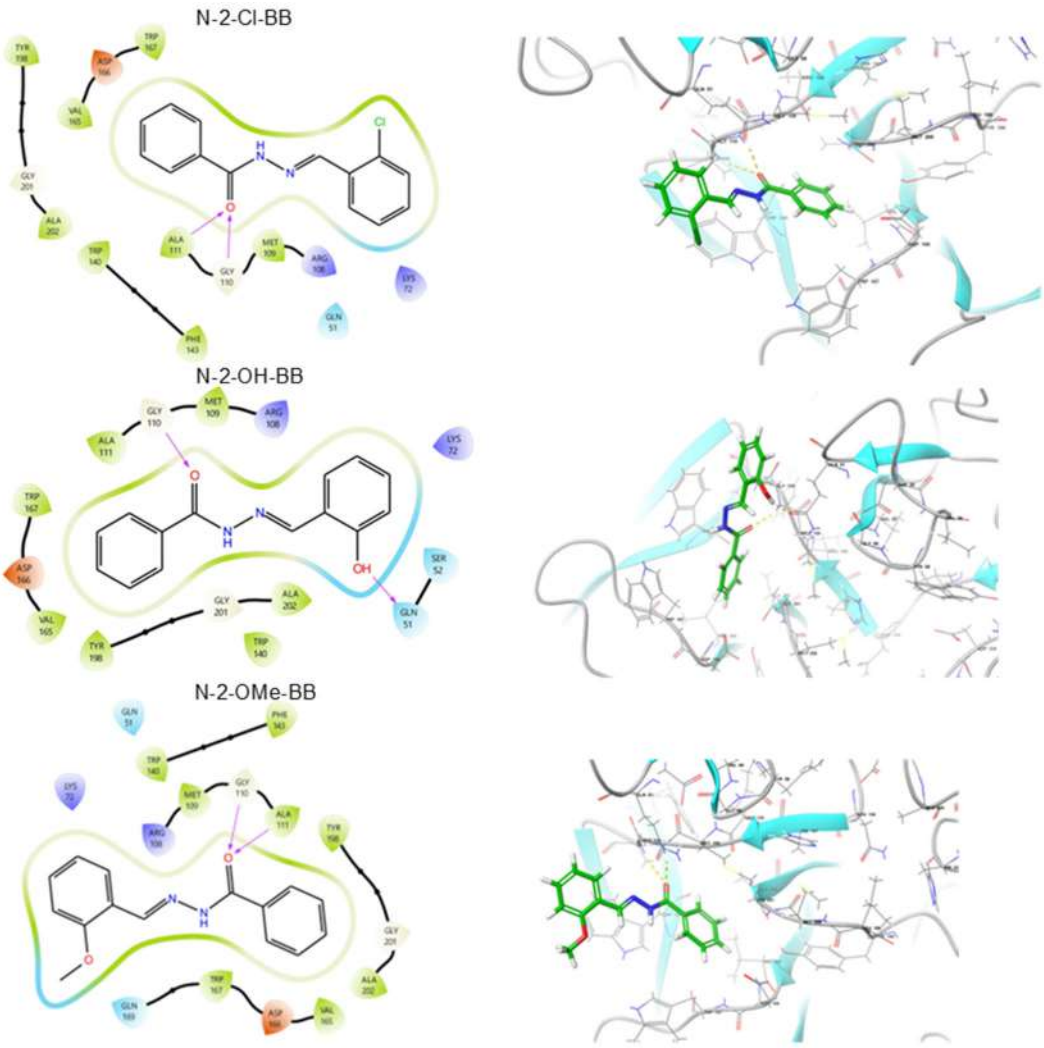

Fig 5. The binding of NBB and derivatives toward α-amylase receptor

and *N'*-(3-nitrobenzylidene)benzohydrazide on amino acids Asp518 and Asp616. Although these interactions can inhibit the activity of the α-glucosidase enzyme, they do not perform as well as the native ligand due to the lack of other molecular interactions that could enhance the affinity of the interaction. Despite this limitation, these three compounds hold the potential for further development as α-glucosidase inhibitor agents [38].

CONCLUSION

In drug design, the molecular docking technique has been used extensively to predict the ligands-receptor interactions. Substituents on the benzene ring play a role in antidiabetic activity. NBB derivatives ligand with electron-donating groups at the *ortho* position has the potential to increase the activity of antidiabetic target receptors for both α-glucosidase and α-amylase. Numerous functional groups and para positions will be performed in the subsequent experiment.

ACKNOWLEDGMENTS

The authors would like to thank Research, Innovation and Community Development and LPPM, Airlangga University for funding this research number 1076/UN3.15/PT/2022 through the "*Riset Kolaborasi Indonesia*" Research Grant organized by Ministry of Education, Culture, Research and Technology, Republic Indonesia in FY 2022.

AUTHOR CONTRIBUTIONS

Yusuf Syarif Alam, Nur Rahmayanti Afifah, Arif Fadlan conducted the synthesis experiment, Tutik Sri Wahyuni and Saipul Maulana performed docking analysis. Pratiwi Pudjiastuti, Fahimah Martak and Arif Syukri wrote and revised the manuscript. All authors agreed to the final version of this manuscript.

REFERENCES

[1] Ramadhan, R., and Phuwapraisirisan, P., 2015, Arylalkanones from *Horsfieldia macrobotrys* are effective antidiabetic agents achieved by α-glucosidase inhibition and radical scavenging, *Nat. Prod. Commun.*, 10 (2), 325–328.

[2] Poovitha, S., and Parani, M., 2016, *In vitro* and *in vivo* α-amylase and α-glucosidase inhibiting activities of the protein extracts from two varieties of bitter gourd (*Momordica charantia* L.), *BMC Complementary Altern. Med.*, 16 (1), 185.

[3] Dirir, A.M., Daou, M., Yousef, A.F., and Yousef, L.F., 2022, A review of alpha-glucosidase inhibitors from plants as potential candidates for the treatment of type-2 diabetes, *Phytochem. Rev.*, 21 (4), 1049–1079.

[4] Tan, K., Tesar, C., Wilton, R., Jedrzejczak, R.P., and Joachimiak, A., 2018, Interaction of antidiabetic a-glucosidase inhibitors and gut bacteria α-glucosidase, *Protein Sci.*, 27 (8), 1498–1508.

[5] Bashary, R., Vyas, M., Nayak, S.K., Suttee, A., Verma, S., Narang, R., and Khatik, G.L., 2020, An Insight of alpha-amylase inhibitors as a valuable tool in the management of type 2 diabetes mellitus, *Curr. Diabetes Rev.*, 16 (2), 117–136.

[6] Kaur, N., Kumar, V., Nayak, S.K., Wadhwa, P., Kaur, P., and Sahu, S.K., 2021, Alpha-amylase as molecular target for treatment of diabetes mellitus: A comprehensive review, *Chem. Biol. Drug Des.*, 98 (4), 539–560.

[7] Taha, M., Ismail, N.H., Lalani, S., Fatmi, M.Q., tul-Wahab, A., Siddiqui, S., Khan, K.M., Imran, S., and Choudary, M.I., 2015, Synthesis of novel inhibitors of α-glucosidase based on the benzothiazole skeleton containing benzohydrazide moiety and their molecular docking studies, *Eur. J. Med. Chem.*, 92, 387–400.

[8] Ullah, H., Uddin, I, Rahim, F., Khan, F., Sobia, S., Taha, S.M., Khan, M.U., Hayat, S., Ullah, M., Gul, Z., Ullah, S., Zada, H., and Hussain, J., 2022, *In vitro* α-glucosidase and α-amylase inhibitory potential and molecular docking studies of benzohydrazide based imines and thiazolidine-4-one derivatives, *J. Mol. Struct.*, 1251, 132058.

[9] Fan, M., Yang, W., Peng, Z., He, Y., and Wang, G., 2023, Chromone-based benzohydrazide derivatives as potential α-glucosidase inhibitor: Synthesis, biological evaluation and molecular docking study, *Bioorg. Chem.*, 131, 106276.

[10] Jubie, S., Ashish, W., Sabaritha, K., Nishanthini, P., Thomas, A., and Antony, J., 2016, Synthesis and *in-vitro* anti-cancer screening of N^1 [(substituted phenyl)benzylidene]benzohydrazides, *J. Pharm. Sci. Res.*, 8 (7), 582–585.

[11] Lanka, G., Bathula, R., Bhargavi, M., and Potlapally, S.R., 2019, Homology modeling and molecular docking studies for the identification of novel potential therapeutics against human PHD3 as a drug target for type 2 diabetes mellitus, *J. Drug Delivery Ther.*, 9 (4), 265–273.

[12] Johnston, R.C., Yao, K., Kaplan, Z., Chelliah, M., Leswing, K., Seekins, S., Watts, S., Calkins, D., Chief Elk, J., Jerome, S.V., Repasky, M.P., and Shelley, J.C., 2023, Epik: pK_a and protonation state prediction through machine learning, *J. Chem. Theory Comput.*, 19 (8), 2380–2388.

[13] Lu, C., Wu, C., Ghoreishi, D., Chen, W., Wang, L., Damm, W., Ross, G.A., Dahlgren, M.K., Russell, E., Von Bargen, C.D., Abel, R., Friesner, R.A., and Harder, E.D., 2021, OPLS4: Improving force field accuracy on challenging regimes of chemical space, *J. Chem. Theory Comput.*, 17 (7), 4291–4300.

[14] Choudhary, M.I., Shaikh, M., tul-Wahab, A., and ur-Rahman, A., 2020, *In silico* identification of potential inhibitors of key SARS-CoV-2 3CL hydrolase (Mpro) *via* molecular docking, MMGBSA predictive binding energy calculations,

and molecular dynamics simulation, *PLoS One*, 15 (7), e0235030.

[15] Khairul Ikram, N.K., Durrant, J.D., Muchtaridi, M., Zalaludin, A.S., Purwitasari, N., Mohamed, N., Abdul Rahim, A.S., Lam, C.K., Normi, Y.M., Abd Rahman, N., Amaro, R.E., and Wahab, H.A., 2015, A virtual screening approach for identifying plants with anti H5N1 neuraminidase activity, *J. Chem. Inf. Model.*, 55 (2), 308–316.

[16] Schrödinger Release 2022-1, 2021, *Desmond Molecular Dynamics System*, D.E. Shaw Research, New York.

[17] Fusani, L., Palmer, D.S., Somers, D.O., and Wall, I.D., 2020, Exploring ligand stability in protein crystal structures using binding pose metadynamics, *J. Chem. Inf. Model.*, 60 (3), 1528–1539.

[18] Rostkowski, M., Olsson, M.H.M., Søndergaard, C.R., and Jensen, J.H., 2011, Graphical analysis of pH-dependent properties of proteins predicted using PROPKA, *BMC Struct. Biol.*, 11 (1), 6.

[19] Schrödinger Release 2022-1, 2022, *Protein Preparation Wizard*, Epik, Schrödinger, LLC, New York.

[20] Jokinen, E.M., Niemeläinen, M., Kurkinen, S.T., Lehtonen, J.V., Lätti, S., Postila, P.A., Pentikäinen, O.T., and Niinivehmas, S.P., 2023, Virtual screening strategy to identify retinoic acid-related orphan receptor γt modulators, *Molecules*, 28 (8), 3420.

[21] Friesner, R.A., Banks, J.L., Murphy, R.B., Halgren, T.A., Klicic, J.J., Mainz, D.T., Repasky, M.P., Knoll, E.H., Shelley, M., Perry, J.K., Shaw, D.E., Francis, P., and Shenkin, P.S., 2004, Glide: A new approach for rapid, accurate docking and scoring. 1. Method and assessment of docking accuracy, *J. Med. Chem.*, 47 (7), 1739–1749.

[22] Hevener, K.E., Zhao, W., Ball, D.M., Babaoglu, K., Qi, J., White, S., and Lee, R.E., 2009, Validation of molecular docking programs for virtual screening against dihydropteroate synthase, *J. Chem. Inf. Model.*, 49 (2), 444–460.

[23] Schrödinger Release 2022-1, 2022, *Glide*, Schrödinger, LLC, New York.

[24] Genheden, S., and Ryde, U., 2015, The MM/PBSA and MM/GBSA methods to estimate ligand-binding affinities, *Expert Opin. Drug Discovery*, 10 (5), 449–461.

[25] Friesner, R.A., Murphy, R.B., Repasky, M.P., Frye, L.L., Greenwood, J.R., Halgren, T.A., Sanschagrin, P.C., and Mainz, D.T., 2006, Extra precision glide: Docking and scoring incorporating a model of hydrophobic enclosure for protein–ligand complexes, *J. Med. Chem.*, 49 (21), 6177–6196.

[26] Schrödinger Release 2022-1, 2022, *Prime*, Schrödinger, LLC, New York.

[27] Al-Karmalawy, A.A., Dahab, M.A., Metwaly, A.M., Elhady, S.S., Elkaeed, E.B., Eissa, I.H., and Darwish, K.M., 2021, Molecular docking and dynamics simulation revealed the potential inhibitory activity of ACEIs against SARS-CoV-2 targeting the *h*ACE2 receptor, *Front. Chem.*, 9, 661230.

[28] Kumar, S., Narwal, S., Kumar, V., and Prakash, O., 2011, α-Glucosidase inhibitors from plants: A natural approach to treat diabetes, *Pharmacogn. Rev.*, 5 (9), 19–29.

[29] Kazmi, M., Zaib, S., Ibrar, A., Amjad, S.T., Shafique, Z., Mehsud, S., Saeed, A., Iqbal, J., and Khan, I., 2018, A new entry into the portfolio of α-glucosidase inhibitors as potent therapeutics for type 2 diabetes: Design, bioevaluation and one-pot multi-component synthesis of diamine-bridged coumarinyl oxadiazole conjugates, *Bioorg. Chem.*, 77, 190–202.

[30] Feng, Y., Nan, H., Zhou, H., Xi, P., and Li, B., 2022, Mechanism of inhibition of α-glucosidase activity by bavachalcone, *Food Sci. Technol.*, 42, e123421.

[31] Hakim, R.W., Fadilah, F., Tarigan, T.J.E., Jusman, S.W.A., and Purwaningsih, E.H., 2021, Molecular study of *Acalypha indica* to leptin, alpha glucosidase, and its antihyperglycemic effect on alpha alucosidase, *Pharmacogn. J.*, 13 (6s), 1639–1647.

[32] Li, D.Q., Qian, Z.M., and Li, S.P., 2010, Inhibition of three selected beverage extracts on α-glucosidase and rapid identification of their active compounds using HPLC-DAD-MS/MS and biochemical detection, *J. Agric. Food Chem.*, 58 (11), 6608–6613.

[33] Kim, K.T., Rioux, L.E., and Turgeon, S.L., 2014, Alpha-amylase and alpha-glucosidase inhibition is

differentially modulated by fucoidan obtained from *Fucus vesiculosus* and *Ascophyllum nodosum*, *Phytochemistry*, 98, 27–33.

[34] Papoutsis, K., Zhang, J., Bowyer, M.C., Brunton, N., Gibney, E.R., and Lyng, J., 2021, Fruit, vegetables, and mushrooms for the preparation of extracts with α-amylase and α-glucosidase inhibition properties: A review, *Food Chem*., 338, 128119.

[35] Lahlou, M., 2007, Screening of natural products for drug discovery, *Expert Opin. Drug Discovery*, 2 (5), 697–705.

[36] Xue, Q., Liu, X., Russell, P., Li, J., Pan, W., Fu, J., and Zhang, A., 2022, Evaluation of the binding performance of flavonoids to estrogen receptor alpha by Autodock, Autodock Vina and Surflex-Dock, *Ecotoxicol. Environ. Saf.*, 233, 113323.

[37] Peng, W., Shen, H., Lin, B., Han, P., Li, C., Zhang, Q., Ye, B., Rahman, K., Xin, H., Qin, L., and Han, T., 2018, Docking study and antiosteoporosis effects of a dibenzybutane ligan isolated from *Litsea cubeba* targeting Capthepsin K and MEK1, *Med. Chem. Res.*, 27 (9), 2062–2070.

[38] Roig-Zamboni, V., Cobucci-Ponzano, B., Iacono, R., Ferrara, M.C., Germany, S., Bourne, Y., Parenti, G., Morraci, M., and Sulzenbacher, G., 2017, Structure of human lysosomal acid α-glucosidase–a guide for the treatment of Pompe disease, *Nat. Commun.*, 8 (1), 1111.

Synthesis of ZnO Nanoparticle and Utilized as a Drug Carrier to Treat Leukemia

Areej Ali Jarullah[1*], Nidhal Meteab Khamees[1], and Taghreed Mohy Al-Deen Musa[2]

[1]*Department of Chemistry, College of Science, University of Diyala, Baquba, Diyala, Iraq*

[2]*Department of Chemistry, College of Science, Mustansiriyah University, Baghdad 10052, Iraq*

* ***Corresponding author:***

email: Aroo977@gmail.com

Received: February 10, 2023
Accepted: March 11, 2023

DOI: 10.22146/ijc.82208

Abstract: *This study includes two parts, and the first was the preparation of the Zn(II)complex by reacting* N-*[4-(5-{(Z)-[(5-oxo-2-sulfanyl-4,5-dihydro-1*H*-imidazol-1-yl)imino]methyl}furan-2-yl)phenyl]acetamide with* $ZnCl_2$*. The complex was characterized by using microscopic analysis such as UV-Vis spectrum, LC-MS, FTIR spectrophotometer, measurements of conductivity, magnetic susceptibility, and atomic absorption. The second part was the preparation of the ZnO nanoparticles by dissolving the Zn(II) complex in* HNO_3 *and HCl and its use as a drug transporter to treat leukemia. FSEM, TEM, and XRD were examined for the characterization of ZnO nanoparticles that will be used in the synthesis of most medicines and drugs in the future.*

Keywords: *zinc(II)complex; ZnO nanoparticles; carrier for anti-cancer drugs; leukemia; microscopic analysis*

INTRODUCTION

During the past decades, new trends have emerged widely known as nanotechnology, where they include the ability to manufacture new or improved properties, which are controlled by nanotechnology, which may include these characteristics, electrical delivery thermal, visual response, flexibility, corrosion resistance as well in the vital and medical fields with special treatment properties against cancer cells [1]. Where the focus of scientists in various fields has become a deep influence on all specialists in all scientific fields, such as engineering, physics, and medical biology. Because of the new properties of nanomaterials that have been discovered, nanoparticles can be used in catalysts, functional coatings, medicine, and vital medicine [2].

Nanomaterials play an important role in medicine and pharmaceutical sciences, where nanomaterials affect levels of cytotoxicity in living systems. Therefore, nanomaterials have been used in biological applications because it was discovered that they have potential in the future in the future in bio-diagnostics (bio-characterization devices), treatments, and drug delivery [3]. It was used as a drug delivery compound because it controls drug release for a prolonged period. It also has the ability to deliver proteins, peptides, and DNA transporters in gene therapy to its potential in recruiting disabled members [4-6].

Nano-oxide is used in various medical and industrial sectors, for example, in pharmaceuticals and cosmetics usages [7]. Also, it has different types of usages to treat various skin diseases besides its ability to absorb the light of ultraviolet rays. All previous studies gave us evidence that ZnO nanoparticles exhibit anticancer and antibacterial activities. Besides ZnO nanoparticles, leukemia cells were investigated to show that compounds can be drugs besides gene delivery, biosensing, and cancer treatment [8-9]. ZnO is a hopeful and multiple functional inorganic material for a great area implementation. Moreover, it has bio-safe properties which own photo-oxidizing besides photocatalysis effects on chemicals and biological compounds [10-11]. ZnO is a non-toxic substance that has biological and therapeutic importance, so it has been used in the synthesis of most medicines and drugs.

Leukemia is a kind of blood cancer that can be classified depending on the type of mutated precursor cell for example lymphoid or myeloid, and how quickly the disease progresses either acute or chronic.

Accordingly, leukemia can include acute lymphocytic leukemia (ALL), chronic lymphocytic leukemia (CLL), acute myeloid leukemia (AML) and chronic myeloid leukemia (CML) [12]. Human Leukemia 60 (HL60) is a hematopoietic model system *in-vitro* that has been utilized for a long time to study normal myeloid differentiation and leukemia biology [13]. The aim of this research is to synthesis of nano-carriers that serve as carriers for the transport of leukemia drugs.

■ EXPERIMENTAL SECTION

Materials

The materials used in this study were zinc chloride anhydrous ($ZnCl_2$, 99% purity, Sigma-Aldrich, USA), high-quality absolute ethanol and trimethylamine (99% purity, Fluka), hydrochloric acid (HCl, 37%, Sigma-Aldrich, USA), and the ligand used was synthesized with the same procedure used in the reference [14].

Instrumentation

The instrumentations used in this study were FTIR spectroscopy (Shimadzu FTIR 8400S), LC-MS (SCIEX 3200 QTRAP), X-ray diffraction spectroscopy (Phillips PANalytical X'Pert), filed emission scanning electron microscopy (FESEM Tescan Mira3), transmission electron microscopy (TEM Philips em208s 100 kV), and atomic absorption flame (Analytik Jena NovAA 350).

Procedure

Synthesis of the complex $[Zn(C_{16}H_{14}N_4O_3S)Cl_2]\cdot H_2O$ and ZnO nanoparticles

A ligand (0.068 g, 0.000201 mol) was dissolved in ethanol (25 mL) while $ZnCl_2$ (0.0273 g, 0.000201 mol) was dissolved in ethanol. The solution of $ZnCl_2$ and one drop of trimethylamine were added to the solution of ligand. The mixture was refluxed for 1 h and then cooled the produce of reaction at standard circumstances of 25 °C. The gained precipitate was collected before it filtered and then dried, Yield: 80.64%, m.p decomposition above 350 °C, metal percentage % Calc. (Found). For $C_{16}H_{16}Cl_2N_4O_4SZn$:Zn, 13.16 (12.95). After that, the 0.05 g from the complex $[Zn(C_{16}H_{14}N_4O_3S)Cl_2]\cdot H_2O$ has been dissolved in HCl and HNO_3 mixture [15]. The solution was heated at 150 °C for 15 min to completely dissolve the chemicals. The mixture was transferred to a 25 mL volumetric vial and diluted with deionized water. The solution was filtered prior to measurement.

Treatment of leukemia cell line

The HL-60 cells were grown in 96 flat well micro-titer plates, in a final volume of 200 mL for complete culture medium per each well. The microplate was covered by sterile parafilm with shacked slowly. The plates were incubated at 37 °C in a 5% CO_2 atmosphere for 24 h. After incubation, the medium was removed and various concentrations of azacytidine drug (12.5, 25, 50, 100, and 200 mg/mL) in loaded ZnO nanoparticles were added to the wells. Plates were incubated at 37 °C in a 5% CO_2 atmosphere for 24 h as the exposure time. After that, 10 mL of the MTT solution was added to each well. Plates were further incubated at 37 °C in a 5% CO_2 atmosphere for 4 h. The media were carefully removed and then 100 mL of solubilization solution was added per each well for 5 min.

■ RESULTS AND DISCUSSION

Characterization of the Complex $[Zn(C_{16}H_{14}N_4O_3S)Cl_2]\cdot H_2O$

The FTIR spectrum complex exhibited an occurrence of shifting in the vibration of stretching for C=O from 1667 cm^{-1} in ligand to 1617 cm^{-1} in complex and azomethine group from 1596 cm^{-1} in ligand to 1600 cm^{-1} in complex, which was a good proof on the coordination of ligand and the metal ion from the nitrogen atom of an azomethine group and oxygen atom of the carbonyl. On the other hand, a new band appeared with a weak intensity at 533 cm^{-1} refers to M–N stretching vibration, and M–O appeared at 462 cm^{-1} [16-17]. While the band at 325 cm^{-1} refers to the M–Cl [18].

UV-Visible spectrum for Zn(II) complex was characterized and displayed two peaks around 287 and 339 nm, which resulted from π to π* and appeared as the third peak at 358 nm, referring to the n to π* transition. Also displayed a new peak at 421 nm, referring to charge transfer, but some shifting besides turning in the form of the bands were contrasted with bands for the free ligand that appeared at 284 and 363 nm, resulting from π to π*

and n to π* transition, respectively. These results became proof of the coordination link between the active site atom for the ligand and the transition metal ion. The spectrum of Zn(II) complex was illustrated by not finding the visible absorption band because of the absence of d to d, which can be referred to as the full saturation of d shell (d^{10}). For the same reason, the prepared Zn(II) complex has diamagnetic properties and conductivity data for dissolved samples in DMSO solvent at room temperature displayed that it was not an ionic compound [19-20].

The liquid-chromatography mass spectrum of the complex, Fig. 1 showed a peak, *m/z* = 496.1 g/mol assigned to the molecular of the complex that confirms the suggested structure $[Zn(C_{16}H_{14}N_4O_3S)Cl_2]\cdot H_2O$, where conformable approximately with the theoretical calculation that equal 496.7 g/mol.

Investigation of the ZnO Nanoparticles

X-ray diffraction

X-ray diffraction (XRD) is a technique that aims to describe crystalline materials and provide information about the structure and characteristic appearance such as average grain size, crystallinity, defects of crystals as well as identifying the different chemical phases that may be present in the sample. The diffractogram was compared with the standards in the database of the International Center for Diffraction Information.

By analyzing the XRD of the prepared nanoparticles of zinc metal, the sharply appearing peaks were determined (Fig. 2), as it was noted that 6 distinct and different. Diffraction peaks appeared at the 2θ angles, with the match card reference card in the international database (JCDPS Card No:1451). The MDI Jade is sacrificed at the (tops) and collected, which is viewed in Table 1. We focused on each hkl as described to identify the structure of ZnO nanoparticles. The XRD results of prepared ZnO nanoparticles showed a hexagonal crystal structure of type (Wurtzite) belonging to the space group P36 mc with the next trellis constants: a = b = 3.2498 Å, c = 5.2066 Å, also α = β = 90° and γ = 120°.

The nanoparticle scanning electron microscope (FESEM) and transmission electron microscope (TEM)

FESEM's purpose is to analyze the constitutional morphological qualities of the surface of the prepared

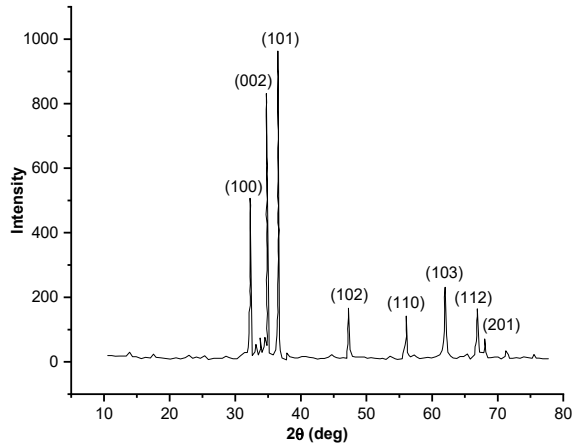

Fig 2. The spectrum of XRD for the ZnO nanoparticles

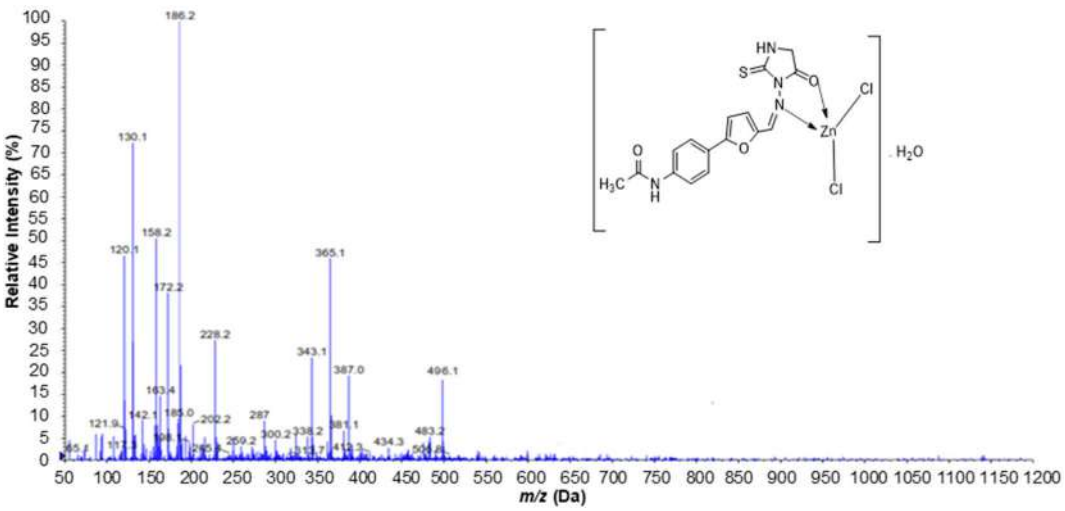

Fig 1. LC-MS of $[Zn(C_{16}H_{14}N_4O_3S)Cl_2]\cdot H_2O$

Table 1. The angle 2θ and crystalline levels for ZnO nanoparticles

Angles (2θ)	31.99	34.84	36.20	47.14	55.97	61.95	66.94	67.96
Crystal levels (hkI)	100	002	101	102	110	103	112	201

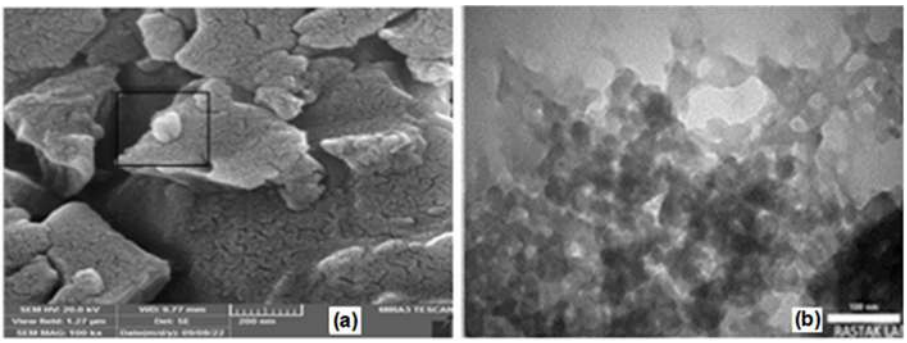

Fig 3. (a) The FESEM images and (b) TEM image of ZnO nanoparticles

nanoparticles after being installed on glass slides and imaging. There is 100 nm in size of ZnO nanoparticles. The microimage did not show them as a clear in high magnification image, however, we saw there were composed nanoparticles thus we referred to it by a small text box on the FESEM original picture for the ZnO nanoparticles which it referred to it in Fig. 3(a).

The TEM technology gives a clear, high-resolution, magnified and three-dimensional image of the surfaces of nanoparticles that was examined by a TEM, where an image of the prepared ZnO nanoparticles with a size of 100 nm was shown in Fig. 3(b).

The Route Treatment of Leukemia Cell Line Using ZnO Nanoparticles as a Drug Transporter: Rules for Guiding Treatment

To direct the drug to cancer cells using nanotechnology accurately, the study concluded that this is achieved through 3 main rules, the first of which is that the dose of chemotherapy is placed in nano-carriers, which are nanomaterials that are used as a drug transport unit to direct it to cancer cells only [9,21]. The second is that there are so-called "chemical ligands" on the surface of these vectors, and their function is to identify the third element in the process, which is the "receptors" that are present in a large amount on the surface of cancerous cells, but it is not present on healthy ones. When the ligands and receptors unite together, the drug is emptied into the cancer cells with extreme precision, without reaching the healthy cells [22]. In this research, the ZnO nanoparticles have been used as a drug transport unit against leukemia as shown in Table 2. Where it gave clear effectiveness and effect as the concentration of drug-loaded on ZnO nanoparticles increased, as shown

Table 2. Mean value of the HL-60 concentration

Drug concentration	HL-60	
	Mean	SD
200.00	44.98	6.45
100.00	49.42	4.48
50.00	66.09	1.97
25.00	78.67	1.58
12.50	87.62	2.95

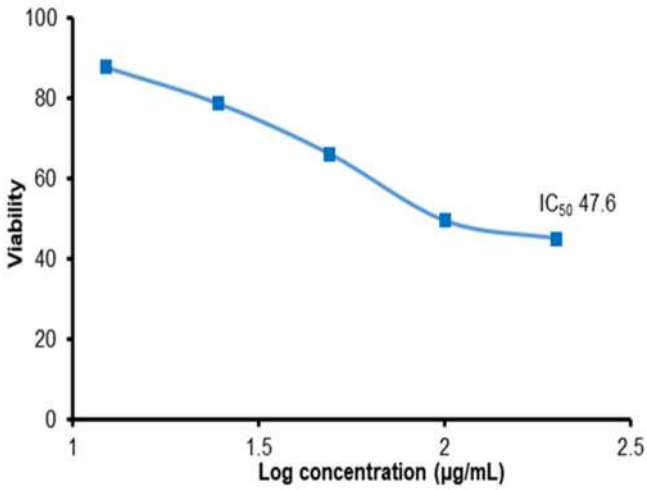

Fig 4. The curve measurement of effectiveness against HL-60

in Fig. 4. The curve was drawn between the log of concentration on the x-axis and the survival rate of cancer cells on the y-axis, where the line of leukemia represented the HL-60 cell line. The test was conducted on cancer cells, and the result was a decrease in the percentage of cancer cells with an increase in the concentrations of the drug, where the results obtained, which is the highest table, show that the ratio has been reduced to 50%.

CONCLUSION

The ZnO nanoparticles were synthesized from Zn(II) tetrahedral complex with HCl and HNO_3 and characterized. The ZnO nanoparticles were found in 100 nm size and they can be used as a drug carrier to treat leukemia after combining it with drugs, where the ratio has been reduced to 50%.

ACKNOWLEDGMENTS

The researchers thank the Chemistry Department at the University of Diyala, College of Science, Chemistry Department at Mustansiriyah University. Thin films laboratory of the physics, Department at the Faculty of Science, University of Mustansiriyah, CAC (Chemistry Analysis Center), and the company for mining industries Ibn-Sina factory to help us with this work.

REFERENCES

[1] Iqbal, A., Iqbal, K., Qin, W., and Mateen, M., 2019, Recent revolutions in nanoscience and nanotechnology with its application's, *Adv. Nanosci. Nanotechnol.*, 3 (3), 1–6.

[2] Huang, C., Chen, X., Xue, Z., and Wang, T., 2020, Effect of structure: A new insight into nanoparticle assemblies from inanimate to animate, *Sci. Adv.*, 6 (20), eaba1321.

[3] Nazeruddin, G.M., Prasad, S.R., Shaikh, Y.I., and Prasad, N.R., 2015, A brief review: Science at nanoscale, *Int. J. Nanomater. Nanostruct.*, 1 (1), 16–32.

[4] Richards, D.A., Maruani, A., and Chudasama, V., 2017, Antibody fragments as nanoparticle targeting ligands: A step in the light direction, *Chem. Sci.*, 8 (1), 63–77.

[5] Pudlarz, A., and Szemraj, J., 2018, Nanoparticles as carriers of proteins, peptides and other therapeutic molecules, *Open Life Sci.*, 13, 285–298.

[6] Lee, M., and Kim, S., 2005, Polyethylene glycol-conjugated copolymers for plasmid DNA delivery, *Pharm. Res.*, 22 (1), 1–10.

[7] Hahn, Y.B., 2011, Zinc oxide nanostructures and their applications, *Korean J. Chem. Eng.*, 28 (9), 1797–1813.

[8] Mirzaei, H., and Darroudi, M., 2017, Zinc oxide nanoparticles: Biological synthesis and biomedical applications, *Ceram. Int.*, 43 (1, Part B), 907–914.

[9] Zhang, Y., Nayak, T.R., Hong, H., and Cai, W., 2013, Biomedical applications of zinc oxide nanomaterials, *Curr. Mol. Med.*, 13 (10), 1633–1645.

[10] Mohd Yusof, H., Mohamad, R., Zaidan, U.H., and Abdul Rahman, N.A., 2019, Microbial synthesis of zinc oxide nanoparticles and their potential application as an antimicrobial agent and a feed supplement in animal industry: A review, *J. Anim. Sci. Biotechnol.*, 10 (1), 57.

[11] Sirelkhatim, A., Mahmud, S., Seeni, A., Mohamad Kaus, N.H., Ann, L.C., Mohd Bakhori, S.K., Hasan, H., and Mohamad, D., 2015, Review on zinc oxide nanoparticles: Antibacterial activity and toxicity mechanism, *Nano-Micro Lett.*, 7 (3), 219–242.

[12] Dozzo, A., Galvin, A., Shin, J.W., Scalia, S., O'Driscoll, C.M., and Ryan, K.B., 2023, Modelling acute myeloid leukemia (AML): What's new? A transition from the classical to the modern, *Drug Delivery Transl. Res.*, 13 (8), 2110–2141.

[13] Basu, J., Madhulika, S., Murmu, K.C., Mohanty, S., Samal, P., Das, A., Mahapatra, S., Saha, S., Sinha, I., and Prasad, P., 2023, Molecular and epigenetic alterations in normal and malignant myelopoiesis in human leukemia 60 (HL60) promyelocytic cell line model, *Front. Cell Dev. Biol.*, 11, 1060537.

[14] Ward, H.A., Musa, T.M., and Nasif, Z.N., 2022, Synthesis and Characterization of some transition metals complexes with new ligand azo imidazole derivative, *Al-Mustansiriyah J. Sci.*, 33 (2), 31–38.

[15] Budavari, S., 1996, *The Merck Index: An Encyclopedia of Chemicals, Drugs, and Biologicals*, 12th Ed., Merck, Whitehouse Station, New Jersey.

[16] Numan, A.T., Sanak, K.A., Atiyah, E.M., and Sadiq, S.A., 2015, Synthesis and characterization of new bidentate chalcone ligand type (NO) and its Mn^{II}, Co^{II}, Ni^{II} and Cu^{II} complexes with study of their antibacterial activity, *Diyala J. Pure Sci.*, 11 (3), 25–42.

[17] Al-Shemary, R.K.R., 2017, Microwave preparation, spectral studies and antimicrobial activities evaluation of $Mn^{(II)}$, $Ni^{(II)}$, $Hg^{(II)}$, $Co^{(II)}$ and $Cu^{(II)}$ complexes with Schiff base ligand, *Ibn Al-Haitham J. Pure Appl. Sci.*, 30 (3), 58–67.

[18] Bader, A.T., Al-Abdaly, B.I., and Jassim I.K., 2019, Synthesis and characterization new metal complexes of heterocyclic units and study antibacterial and antifungal, *J. Pharm. Sci. Res.*, 11 (5), 2062–2073

[19] Alias, M.F., and Seewan, A.N., 2013, Synthesis, spectral study, theoretical treatment and biological activity of some transition metal complexes with 2-amino acetic acid-6-chloro benzothiazole, *Diyala J. Pure Sci.*, 9 (4), 93–103.

[20] Lateef, H.S., Jarullah, A.A., and Faraj, F.L., 2019, Cytotoxicity effecting of new ligand (LCl) and it's complexes on a breast cancer, *Int. J. Pharm. Res.*, 11 (4), 1–10.

[21] Krug, H.F., and Wick, P., 2011, Nano toxicology: An interdisciplinary challenge, *Angew. Chem., Int. Ed.*, 50 (6), 1260–1278.

[22] Kaur, G., Kaur, P., and Kaur, R., 2019, Quinoline: Its synthesis and pharmacological activities, *Pramana Res. J.*, 9 (6), 1718–1748.

Performance Assessment: Influence of Sorbate-Sorbent Interphase Using Magnetite Modified Graphene Oxide to Improve Wastewater Treatment

Olayinka Oluwaseun Oluwasina[1,2], Mochamad Zakki Fahmi[1*], and Olugbenga Oludayo Oluwasina[3]

[1]*Department of Chemistry, Universitas Airlangga, Kampus C Mulyorejo, Surabaya 60115, Indonesia*

[2]*Department of Marine Science and Technology, The Federal University of Technology, P.M.B 704, Akure 340110, Nigeria*

[3]*Department of Chemistry, The Federal University of Technology, P.M.B 704, Akure 340110, Nigeria*

* ***Corresponding author:***

email: m.zakki.fahmi@fst.unair.ac.id

Received: February 20, 2023
Accepted: May 20, 2023

DOI: 10.22146/ijc.82454

Abstract: *The adsorption of brilliant green onto magnetite-graphene oxide nanoparticles (MGONPs) from an aqueous solution was explored via batch experiments. The adsorption properties of MGONPs were carried out under various experimental conditions related to pH, contact time, adsorbent dose, temperature, and initial adsorbate concentration. The adsorption capacity of MGONPs and optimum pH were 54.57 mg g^{-1} and 6, respectively. Equilibrium was attained after 30 min, and the adsorption kinetics data best fitted the pseudo-second-order. The Freundlich isotherm best fits the equilibrium. Acetone was able to desorb the dye from the loaded adsorbent. Additionally, the newly developed adsorption attributes effective surface area (eS_{BET}) and dimensionless preferential adsorption (q_p) were more accurate than the conventional specific surface area (S_{BET}). The adsorption capacity provides information about the sorbate-sorbent interface (q). The relevance and accuracy of the new parameters for future adsorption system design by correlation analysis were validated. This study confirms the successful modification of MGONPs for the sorption of the cationic dye brilliant green.*

Keywords: *magnetite-graphene oxide nanoparticles; preferential adsorption; specific surface area; effective surface area; brilliant green*

■ INTRODUCTION

The use and discharge of dye in waterbody have created toxicity risks for humans and aquatic creatures. The dye's color prevents sunlight penetration into the water body, resulting in a loss of primary productivity. Dye molecules can be classed based on their ionic charge, which can be zwitterionic, anionic, non-ionic, or cationic [1]. It has been reported over the years that there are more than 100,000 different synthetic dyes that are commercially available, with a yearly production of more than 700,000 metric tons [2]. It was revealed that about half of the applied dye was present in the effluent after analyzing the chemical composition of textile dye effluents. The high concentration of colors in wastewater from textile manufacturing has been connected to the low absorption properties of fibers of dyes [1]. The complex molecules that make up synthetic dyes are typically composed of azo, triphenylmethane, or heterocyclic/polymeric structures, and due to their stability, they can last for a very long time in the natural ecosystem without changing or being discolored. The excessive use of these dyestuffs has become a growing source of environmental concern. During production and use, more than 10 to 15% of dyes are released into the environment [3]. A million tons of azo dyes are estimated to be produced annually on a global scale. For a healthy ecology, a sustainable economy, and excellent health, there must be access to high-quality water. Lack of access to clean water is a severe issue in both industrialized and developing nations. Water that contains trace levels of color (less than 1 mg/L) is visibly unpleasant and inappropriate for irrigation, domestic use, or human eating [4].

Brilliant green (BG) is a cationic triaryl methane dye that comes in a yellowish-green powder. Because its

color change from green to yellow at pH 2, BG can also be used as an indicator, a biological stain in veterinary medicine, and a stabilizer in poultry feed to limit fungi attacks [5-6]. Exposure to this dye may cause gastrointestinal and respiratory tract issues and systemic dermatitis in humans, resulting in nausea, vomiting, diarrhea, cough, trouble breathing, and jaundice [7]. In addition, BG is toxic to aquatic life with long-term consequences. Brilliant green has been used as an antiseptic on the skin, but it is harmful when it comes into contact with the eyes.

Sedimentation, filtration, oxidation, electrochemical techniques, adsorption, and ion exchange have all been employed to remove dye from aqueous solutions [8-9]. Among the different methods utilized, adsorption has several advantages, including simplicity, high adsorption capacity, low cost, and environmental friendliness [10]. The use of nanoparticles for dye removal from wastewater has been investigated by various researchers [11-13]. Magnetite nanoparticles have recently received a lot of interest because they are inexpensive, environmentally acceptable, and easy to produce. These particles also exhibit excellent optical, chemical, and electrical properties and significant superparamagnetic capabilities. However, these particles agglomerate easily and oxidize quickly [14]. The aqueous dispersion of iron nanoparticles is improved by embedding them on sheets of carbonaceous materials, and graphene-based materials are kind of promising carbonaceous substances for such purposes [15].

Graphene oxide (GO)-based nanomaterial synthesized with iron nanoparticles exhibited improved dispersion behavior in water [16]. When graphite is oxidized, oxygen functional groups are introduced into the structure, making it hydrophilic and allowing it to form a stable suspension in aqueous conditions. GO is made by sonicating graphite oxide in water to exfoliate it. The high surface area of GO enables the incorporation of a wide range of functionalization groups into the sheets [17-18]. Graphene-based composites are formed by incorporating various functional groups, thereby improving the materials' photocatalytic, biocidal, electroactive, and capability [19-21]. Chemical modification of graphene-based materials has been used to develop nanocomposites with improved dispersion and compatibility in aqueous conditions. The integration of magnetite with graphene or GO may be a promising method for the removal of pollutants. Synthesis of magnetite-GO has recently been produced and utilized for drug delivery [22], magnetic-based imaging [23], and pollutant treatment from wastewater [24-27]. Magnetite-GO was synthesized for pollutant removal because of its stability and performance high.

However, there is no integrative report on the adsorption efficiency of brilliant green upon nanocomposite of magnetite-GO. Thus, in the present research, we focused on studying the design of magnetite-based nanocomposite material that can effectively remove emerging contaminants even when they are present in low concentrations (Scheme 1). The adsorption properties were examined by studying the effect of pH, the adsorption kinetics, and the adsorption isotherms to identify the adsorption mechanism. The study gives a novel assessment of the adsorbents' performance by computation of newly developed physical features, which shed light on the effect of the sorbents' physical and chemical properties and sorbates on the separation process. As a result, the statistical estimations used to assess the sorbents' efficiency are also presented. The interaction between the sorbent and sorbate is also carefully considered in relation to the contaminant's sorption.

■ EXPERIMENTAL SECTION

Materials

Chemicals such as graphite powder (20 μm, synthetic), sulfuric acid (98%, H_2SO_4), hydrochloric acid (30%, HCl), hydrogen peroxide (30%, H_2O_2), potassium permanganate ($KMnO_4$), ferrous ammonium sulfate, ammonium ferric sulfate, aqueous ammonia, sodium hydroxide pellets and brilliant green (BG, $C_{27}H_{33}N_2{\cdot}HO_4S$) were purchased from Sigma-Aldrich and used without further purification.

Instrumentation

UV-Visible absorption spectra of the sample obtained by UV-Vis-NIR spectrophotometer UV-3600 (Shimadzu, Japan). The morphology of MGONPs was determined by Ultra PLUS Field Emission Scanning Electron Microscopy instrument (Zeiss, Germany), and functional group data of the nanomaterial provided by Fourier transform infrared spectrometry Spectrum 100 spectrometer (PerkinElmer, USA). The textural properties, surface area and porosity of the material were measured with a Tristar II 3020 analyzer (Micromeritics, USA).

Procedure

Synthesis of graphene oxide

The synthesis of modified GO was prepared using the method reported by Oluwasina et al. [28]. About 4 g of graphite, 2 g of sodium nitrate, and 92 mL of concentrated H_2SO_4 were mixed with magnetic stirring in an ice bath to give a black slurry. $KMnO_4$ (12 g) was added slowly to keep the temperature below 5 °C. The suspension was removed from the ice bath and heated to 35–40 °C for 90 min. A 190 mL of deionized water was then added, and the temperature was adjusted to 98 °C for 20 min. A 40 mL of 30% H_2O_2 was added to the mixture (the mixture turned bright yellow). The mixture was diluted with 200 mL of deionized water and stirred for 30 min. The reaction product was centrifuged and washed with Milli-Q water and 10% HCl solution until the pH was neutral. The product was vacuum dried at 60 °C for 48 h and stored for further characterization and application.

Synthesis of magnetite-graphene oxide nanoparticles

Magnetite-graphene oxide nanoparticles (MGONPs) were prepared by co-precipitating iron oxide magnetic nanoparticles decorated on GO. Briefly, GO (1 g) was dispersed in deionized water (100 mL) and sonicated. Next, about 10.7 g ammonium ferric sulfate and 58 g ferrous ammonium sulfate were dissolved in 100 mL of deionized water under oxygen-free conditions. After that, 10 mL aqueous ammonia was added into the solution to give iron oxide nanoparticles, with the addition of GO. The reaction was stirred for 45 min at 85 °C and cooled at room temperature. The resulting MGONPs were collected by a magnet and washed with water and anhydrous ethanol, dried at 70 °C for 12 h in a vacuum oven.

Adsorption study

To obtain the concentrations required, working solutions of BG were produced from the stock solution, which is prepared by dissolution of BG (1 g) on deionized water (up to 1 mg dm^{-3}). Batch adsorption was performed by agitating 25 cm^3 of BG solutions of known concentration at a given temperature with a sorbent dosage of 10 mg, and the pH was changed by

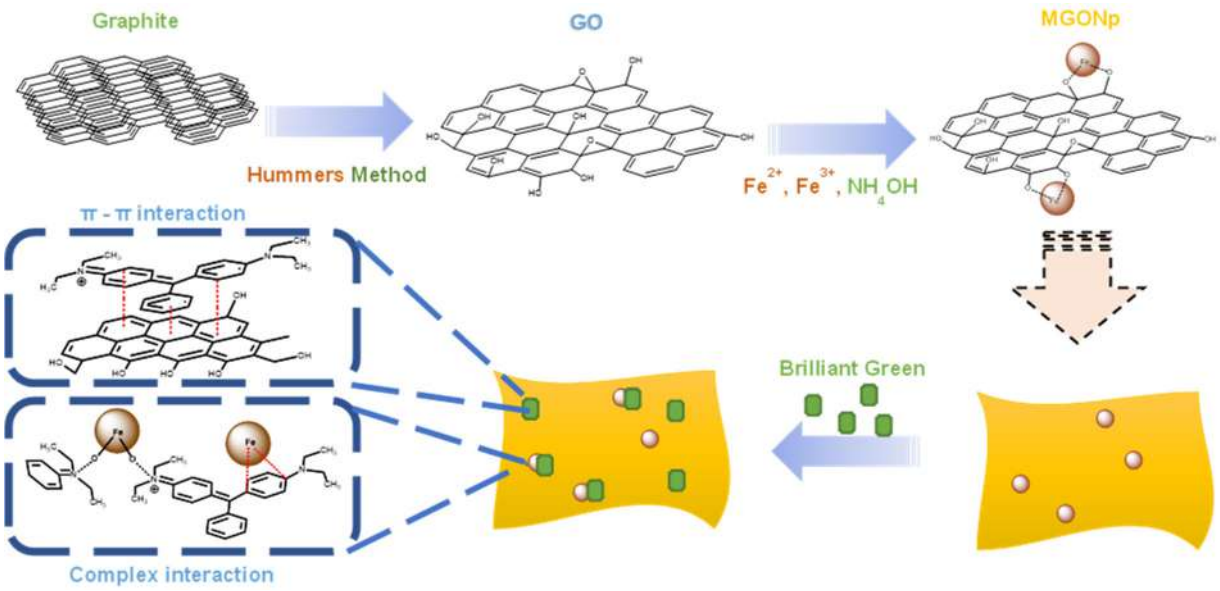

Scheme 1. Schematic illustration of MGONPs and the adsorption process of BG

Table 1. Adsorption isotherm models investigated for the sorption of BG onto MGONPs

Isotherm model	Equation*	Parameters	Reference
Langmuir	$q_{eq} = \frac{q_m b C_{eq}}{1 + b C_{eq}}$	q_m, b	[29]
Freundlich	$q_{eq} = K_F C_{eq}^{1/n}$	K_F, n	[30]
Sips	$q_{eq} = \frac{q_m b C_{eq}^{1/n}}{1 + b C_{eq}^{1/n}}$	q_m, b, n	[31]
Temkin	$q_{eq} = \frac{RT}{b_T} \ln(A_T C_{eq})$	b_T, A_T	[32]
Dubinin-Radushkevich	$\varepsilon = RT \ln\left(1 + \frac{1}{C_{eq}}\right)$	q_m, β	[33]
Redlich-Peterson	$q_{eq} = \frac{K_{RP} C_{eq}}{1 + a_{RP} C_{eq}^{g}}$	K_{RP}, a_{RP}, g	[34]
Khan	$q_{eq} = \frac{q_m b_K C_{eq}}{(1 + b_K C_{eq})^{a_K}}$	q_m, a_k, b_k	[35]

*q_{eq} is the adsorption capacity (mg g^{-1}); C_{eq} is the adsorbate equilibrium concentration in solution (mg dm^{-3}); q_m is the maximum monolayer capacity (mg g^{-1}); b is the Langmuir isotherm constant (dm^3 mg^{-1}); K_F is the Freundlich isotherm constant (mg g^{-1})(dm^3 mg^{-1}); n is the intensity of adsorption intensity; A_T, Temkin isotherm equilibrium binding constant (dm^3 g^{-1}); b_T, Temkin isotherm constant; β, Dubinin-Radushkevich isotherm constant (mol^2 kJ^{-2}); K_T, Redlich-Peterson isotherm constant (dm^3 g^{-1}); g, Redlich-Peterson isotherm exponent; a_{RP}, Redlich-Peterson isotherm constant; a_k, Khan isotherm exponent; b_k, Khan isotherm constant

adding either 0.1 M NaOH or HCl. The final concentration of the dye after filtering was determined at 624 nm by ultraviolet-visible (UV-Vis) spectrophotometry. The effects of pH, adsorbent dosage, temperature, and initial BG concentrations were investigated to identify the best adsorption conditions. The adsorption capacity was calculated by the Freundlich, Langmuir, and Sips models, respectively, presented in Table 1.

Eq. (1) and (2) were used to calculate the adsorption capacity (q_e) and efficiency, respectively.

$$(\%)\text{adsorbed} = \left(\frac{C_i - C_{eq}}{C_i}\right) \times 100\% \quad (1)$$

$$q_{eq} = \frac{V}{m} \times \left(C_i - C_{eq}\right) \quad (2)$$

where C_i represents the initial adsorbate concentration (mg dm^{-3}), q_e is the adsorption capacity (mg g^{-1}), C_{eq} is the equilibrium concentration of adsorbate (mg dm^{-3}), V is the adsorbate volume (dm^3), and m is the mass of adsorbent (mg).

Adsorption isotherms

The adsorption isotherms were investigated with BG concentrations ranging from 10 to 100 mg dm^{-3}. Aliquots of 25 cm^3 of varied concentration were introduced to 40 mg of adsorbents and shaken for 4 h in a thermostated shaking water bath at 298 K. The equilibrium concentration of BG in the suspensions was determined using UV-Vis spectrophotometry after 4 h. To analyze the equilibrium data, the isotherm models in Table 1 were used.

Adsorption kinetics

Adsorption kinetics was investigated by mixing a 25 cm^3 aliquot of a 20 mg dm^{-3} BG solution with a 40 mg adsorbent dosage. The time intervals for contacting the solutions were in the range of 5–300 min. UV-Vis spectrophotometry was used to determine the final concentration of BG after filtering. The experimental adsorption data attained through the batch studies were applied to the pseudo-first-order, pseudo-second-order, Elovich kinetics, and intraparticle diffusion models given in Table 2.

Desorption experiment

The desorption experiment was carried out by mixing 30 mg of the adsorbent with 25 cm^3 aliquots of 20 mg dm^{-3} BG solution for 3 h. After that, the mixture was filtered through a Whatman No. 1 filter paper, and

Table 2. Adsorption kinetics model explored for the removal of BG onto MGONPs

Kinetic model	Equation*	Parameters	Reference
Pseudo-first-order	$q_t = q_{eq}(1 - e^{-k_1 t})$	q_{eq}, k_1	[36-38]
Pseudo-second-order	$q_t = \frac{k_2 q_{eq}^2 t}{1 + k_2 q_{eq} t}$	k_2, q_{eq}	[36-37]
Intraparticle diffusion	$q_t = k_{id}(t)^{1/2} + c$	k_{id}, c	[39]
Elovich	$q_t = \frac{1}{\beta}\ln(1 + \alpha\beta t)$	α, β	[40]

*q_{eq} is the amount adsorbed at equilibrium (mg g^{-1}), q_t is the amount adsorbed at adjusted times (mg g^{-1}), k_1 is the pseudo-first-order rate constant (min^{-1}), k_2 is the pseudo-second-order rate constant (g mg^{-1} min^{-1}), k_{id} is the intraparticle diffusion rate constant (mg g^{-1} $min^{0.5}$), β is the Elovich parameter defined as the desorption constant (g mg^{-1}), α is the Elovich parameter defined as the initial adsorption rate (mg g^{-1} min^{-1})

the filtrate was analyzed for BG. The adsorbent that was filtered off was dried at 60 °C. After that, 20 mg of the BG loaded-adsorbent was added to a 25 cm^3 acetone and shaken for 12 h. The filtrate was analyzed using UV-Vis spectrophotometry after the mixture was filtered. SEM-EDX and FTIR were used to examine the loaded and desorbed adsorbent to evaluate if the dye had desorbed from the adsorbent surface. There was a significant change as the dye was desorbed on the surface of the adsorbent.

Data analysis

Using routine nls in the R statistical computing environment, the adsorption data were fitted into the adsorption isotherms and kinetics models. The model's effectiveness was determined by looking at the sum of squared residuals (SSR) and residual squared errors (RSE). The SSR of the model with the lowest SSR was chosen.

■ RESULTS AND DISCUSSION

Characterization of the Synthesized Material

The textural features of MGONPs were determined using N_2 adsorption-desorption isotherms. This provides information on the sample's pore volume size distribution and specific surface area. The pore volume determined according to nitrogen adsorption by the specified method applies only to mesopores and does not consider macropores (> 50 nm). Therefore, the pores could be grouped into micropores (< 2 nm), mesopores (2–50 nm), and macropores (> 50 nm). The result indicates that MGONPs are mesoporous, having an average pore diameter of 14.13 nm. The pore volume determined according to nitrogen adsorption by the specified method applies only to mesopores and does not take into account macropores (> 50 nm). In addition, the adsorbents exhibited type IV isotherms and

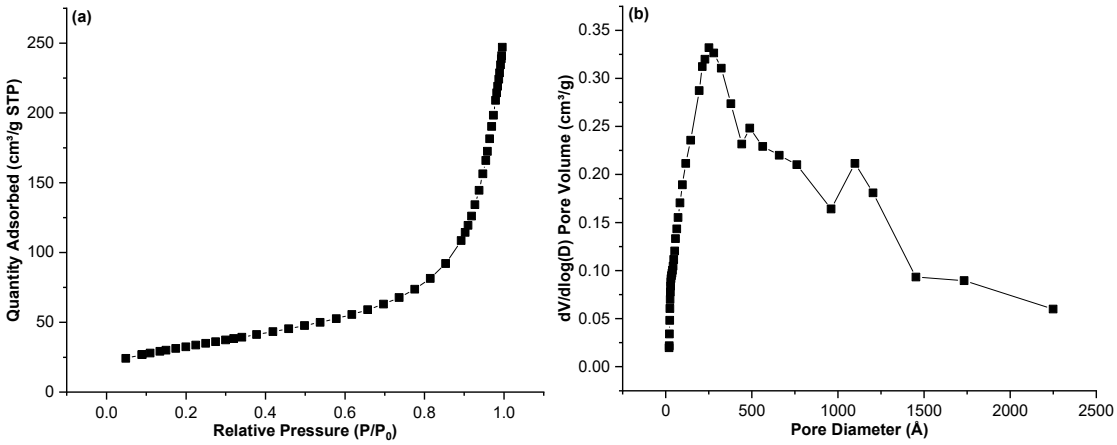

Fig 1. (a) BET Nitrogen adsorption-desorption isotherms and (b) BHJ pore volumes of MGONPs

H3-Type hysteresis loops, indicating that the nanomaterial is mesoporous [41]. Type IV represents an adsorption isotherm with hysteresis related to capillary condensation in mesopores. MGONPs showed a large surface area of 116.81 $m^2 g^{-1}$, having a Barrett–Halenda–Joyner (BHJ) based pore volume of 0.3763 $cm^3 g^{-1}$ (Fig. 1).

The FTIR spectrum displayed in Fig. 2 appears the functional groups on the surface of MGONPs. The absorption peak at around 598 cm^{-1} can be referred to as the Fe–O vibrational mode of Fe_3O_4 nanoparticles. The absorption peaks at 3604 and 1692 cm^{-1} correspond to the extending vibration of –OH and –FeOO, respectively [42]. This finding demonstrates that Fe_3O_4 successfully decorated the GO surface, as confirmed by SEM examination. In addition, the FTIR spectrum shows three broad peaks at 1749, 1565, and 1031 cm^{-1}, which correspond to the aromatic C=O stretch, C=C, and C-H stretching, respectively [43]. The peaks around 1938, 2091, and 2331 cm^{-1} correspond to the peaks of the dye molecules on the adsorbent.

The morphology of MGONPs was investigated using SEM, as shown in Fig. 3. The MGONPs have a

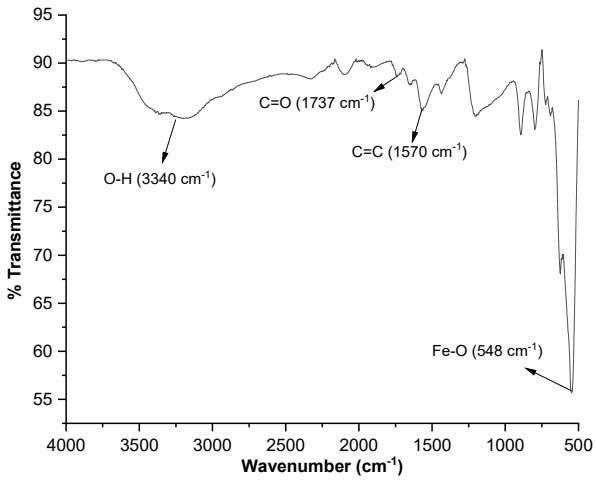

Fig 2. FTIR spectra of MGONPs before adsorption

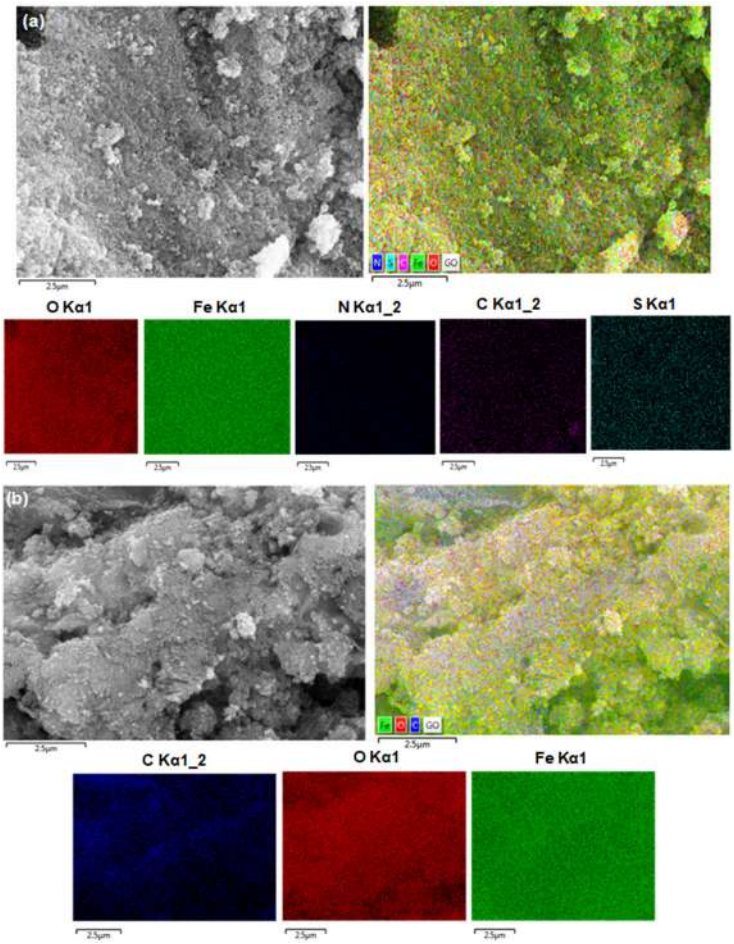

Fig 3. SEM and EDX images of MGONPs (a) after adsorption, 2.5 μm scale and (b) desorption of BG, 2.5 μm scale

crumpled surface. This might be the effect of the quick drying of the liquid phase from the MGONPs during the preparation process. Also, small granular particles were observed on its surface, where Fe_3O_4 deposits. The SEM-EDX images revealed that the dye molecules were adsorbed on the surface of the adsorbent during adsorption.

Sorption Characteristics

Batch adsorption tests for BG adsorption onto MGONPs were carried out to investigate the adsorbent's adsorption characteristics and efficiency in removing BG. pH, adsorbent dosage, contact time, temperature, and initial adsorbate concentration were all investigated as sorption parameters. The experimental data were also used to investigate adsorption isotherms and kinetics. Desorption tests for the dye were carried out to see if the adsorbents could be regenerated and reused.

Effect of pH

A solution's pH influences the dye structure and the adsorbent nature due to the ionization behavior and changes in surface charge, respectively [44]. The experiment pH was studied by varying the pH from 3 to 10 (using 0.1 g of adsorbent and 10 mg dm^{-3} BG concentration for 300 min contact time at 180 rpm) because at pH ≤ 2, the BG dye solution became colorless. The disparity of color concentration could result from its extended conjugated system of alternate double and single bonds. The reaction between OH^- ions and BG molecules occurs with conjugation interruption at higher pH values. The reduced color following increased pH may happen due to the central carbon atom of BG acting as an electrophilic center, and the OH^- is favored. The dye's rate of color change was faster in alkaline media, which could be attributed to its high nucleophilic nature. Decolorization of the dye could also occur through nucleophilic attack by H_3O^+, but the color fades more slowly in an acidic medium. A colorless compound is formed at low pH because H_3O^+ destroys the conjugation between the aromatic rings [45]. Fig. 4 depicts the outcome. The removal of BG was increased by increasing the pH to a maximum pH of 6 (46%) and then decreased to reach a minimum removal percentage at pH 9 (41%). It

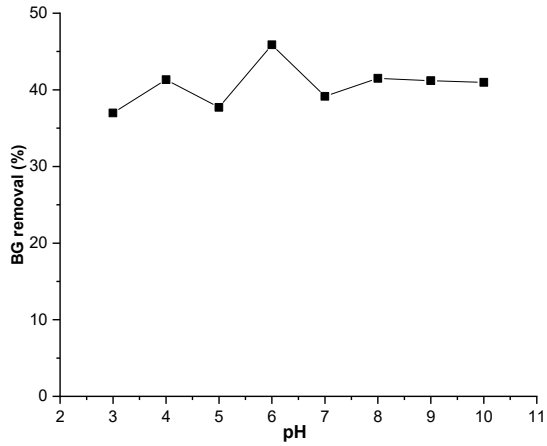

Fig 4. Effect of pH on the adsorption of BG (conditions: 25 cm^3 of 10 mg dm^{-3} BG, 5 h equilibration time, 10 mg sorbent dose, agitation speed of 180 rpm, temperature 298 K)

was discovered that the removal percentage in acidic environments is lower than in neutral environments. This could be due to the partial dissociation of surface functional groups in an acidic BG solution, resulting in electrostatic repulsion between the BG and MGONPs [46]. The reduction in the alkaline environments related to the neutral and acidic environment could be attributed to the higher electrostatic repulsion between the MGONPs and the dye molecules [47].

Given the structures of graphene's sp^2-bonded carbon particle, it is anticipated that a π–π interaction may play a critical part in the adsorption of natural fragrant compounds on MGONPs. There are a parcel more oxygen-containing useful bunches on the surface of MGONPs, and these bunches can work as electron-withdrawing bunches, localizing electrons from the π framework of graphene and interferometer with the π–π scattering strengths between the fragrant ring and graphene. The oxygen-containing functional groups repressed the adsorption of natural chemicals on carbon materials by means of water adsorption, dispersive-repulsive intelligence, and hydrogen holding, in this way driving the lower adsorption capacity of MGONPs [46].

Effect of dosage

By varying the mass of MGONPs from 10 to 120 mg, the effect of dosage on BG removal from aqueous solution was examined (Fig. 5). The result showed that the

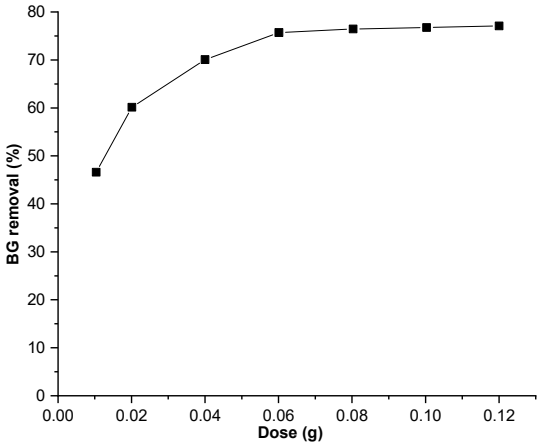

Fig 5. Effect of adsorbent dose on the sorption of BG (conditions: 25 cm^3 of 20 mg dm^{-3} BG, 4 h equilibration time, pH 6, agitation speed of 180 rpm, temperature 298 K)

percentage adsorbed increases as the adsorbent dose increases. For example, using 10 mg of MGONPs, a removal percentage of 46% was initially attained and then rose to 70% when the dosage was increased to 40 mg. After then, it increased to 75%, with no discernible increase in the percentage adsorbed. This could be because the nanocomposite agglomerated, reducing the surface area accessible for adsorption [48]. Furthermore, as the MGONPs dosage was increased from 10 to 40 mg, the BG percentage removal increased remarkably. This can be attributed to an increase in the number of unoccupied adsorption sites and functional groups on the adsorbent surface. This indicates that 40 mg has the necessary number of active sites to achieve maximal uptake.

Kinetics study

The removal of BG from MGONPs was investigated to establish the equilibrium sorption time, with time intervals ranging from 5 to 300 min. Fig. 6 shows the percentage of BG adsorbed onto the sorbent as a function of time. The percentage adsorbed onto MGONPs increases as the contact time increases, from the results obtained. After 30 min, the equilibrium was reached, with a maximum removal of 60%. After that, there was no discernible change in the BG concentration, indicating that the adsorption sites had been saturated [49].

The adsorption kinetics of BG using MGONPs were studied using four kinetics models: pseudo-first-order, pseudo-second-order, intraparticle diffusion, and Elovich models. The linear findings for the four kinetic models are shown in Fig. 7, and the kinetic parameters of the fitted models are listed in Table 3. Pseudo-second-order model better explained the adsorption of BG onto MGONPs. The experimental q_e values obtained are near the calculated values for both pseudo-first-order and pseudo-second-order models. The results of these models revealed that BG adsorption on MGONPs occurred via a biomolecular interaction involving the exchange or sharing of electrons between the adsorbent and the dye. As a result, the sorbent's adsorption capacity is related to its surface's number of active sites [51]. The following steps are involved in explaining the diffusion mechanism of adsorption processes: a) transfer

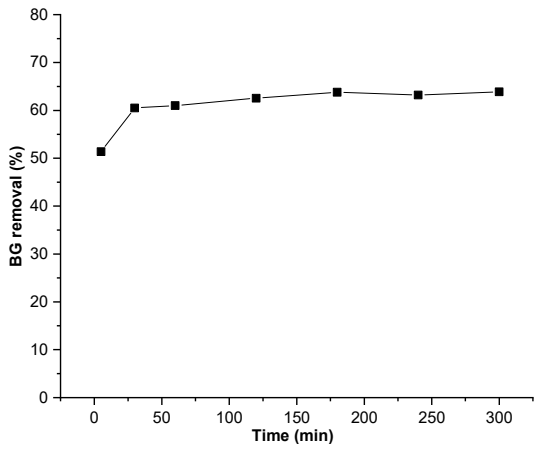

Fig 6. Effect of contact time on the sorption of BG (conditions: 25 cm^3 of 20 mg dm^{-3} BG, 40 mg sorbent dose, speed of 180 rpm, pH 6, temperature 298 K)

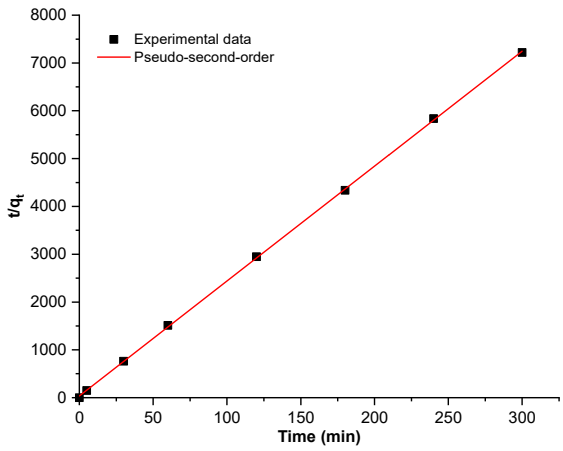

Fig 7. Pseudo-second-order kinetic model

Table 3. The calculated parameters for the four kinetics models tested for the sorption of BG onto MGONPs at different time intervals

Model	Parameters	BG
Experimental	q_{eq}/mg g^{-1}	0.053
Pseudo-first-order	$q_{eq.cal}$/mg g^{-1}	0.051
	$k_1/10^{-2}$/min	-0.001
	R^2	0.112
Pseudo-second-order	q_{eq}/mg g^{-1}	0.0410
	$k_2/10^{-3}$/g mg^{-1} min^{-1}	17.050
	R^2	0.999
Intraparticle diffusion	k_{id}/mg g^{-1} min$^{-0.5}$	0.002
	R^2	0.406
Elovich	α/mg g^{-1} min^{-1}	529.100
	β/g mg^{-1}	16.650
	R^2	0.887

Conditions: 25 cm^3 of 20 mg dm^{-3} BG, pH 6, 40 mg adsorbent, agitation speed 180 rpm, temperature 25 °C

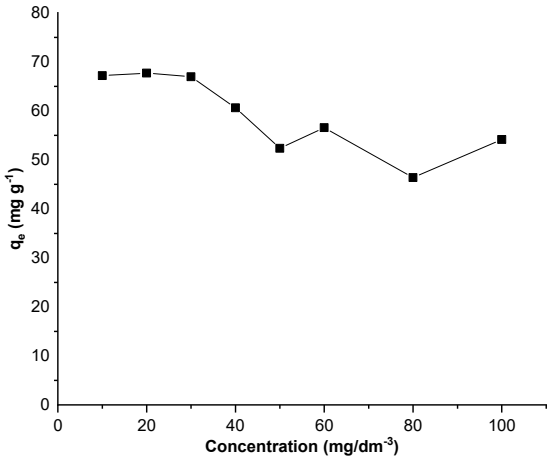

Fig 8. Effect of initial concentration on the adsorption of BG onto MGONPs (conditions: 25 cm^3 of 10 to 100 mg dm^{-3} BG solution, 40 mg adsorbent dose 4 h equilibration time, pH 6, agitation speed of 150 rpm, the temperature of 298 K)

of the adsorbate from the bulk solution to the surface of the solid phase; b) passage through the liquid film attached to the solid surface (film diffusion); c) internal mobility by pore dispersion from the surface of the solid phase to the inner surface of the permeable structure (intraparticle diffusion); and d) diffusion of the solute on the adsorption sites of the solid phase bringing about physisorption and chemisorption on the surface of the solid phase [52]. The intraparticle diffusion show was utilized to decide the rate-limiting step of the method. In the event that a direct plot that passes through the origin is gotten, adsorption is said to happen as it were by intraparticle diffusion [52]. It is presumed that two or more stages regulate the process if a linear plot that does not pass through the origin is obtained. The linear graphs obtained in this investigation passed through all the dots for pseudo-second-order, which indicates that the model is suitable for the experimental data.

Adsorption isotherms

Over a concentration range of 10 to 100 mg dm^{-3}, the influence of initial BG concentration on adsorption onto MGONPs was examined. As the dye concentration increased, the percentage of dye removed decreased (Fig. 8). This could be owing to the fixed number of active sites available for BG molecules on the adsorbent. At higher dye concentrations, the active sites of the adsorbent become saturated, and the adsorption capacity is thus determined by the initial concentration [50].

The equilibrium adsorption isotherm is required to determine the interacting behavior between the adsorbent and the adsorbent. It is also essential for the adsorption system's strategy. The Langmuir adsorption isotherm assumes that the binding sites are evenly distributed across the sorbent surface and have a similar affinity for single molecular layer sorption. The bonding to the sorption sites might be chemical or physical, but it must be sufficiently strong to prevent the adsorbed molecules from being displaced [53-54]. According to the Freundlich adsorption isotherm, sorption occurs on a heterogeneous surface, implying multilayer adsorption. This means that as the starting concentration of the solution is increased, the adsorbate concentration will rise [55-56]. The Langmuir and Freundlich models were used to fit the experimental equilibrium data. The slope and intercept of each equilibrium graph were used to calculate the Langmuir and Freundlich parameters (Fig. 9).

Table 4 appear the adsorption isotherm parameters for models that fitted the test balance information for BG adsorption. The Freundlich isotherm best fits the

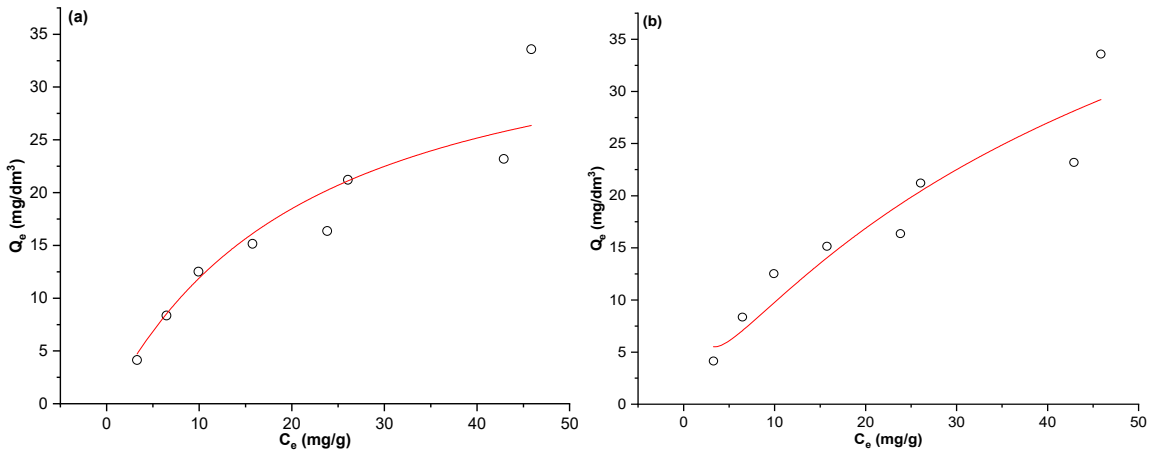

Fig 9. The Langmuir (a) and Freundlich (b) adsorption isotherms fitted the experimental data for the sorption of BG onto MGONPs

Table 4. Isotherm models' parameters

Isotherms	Parameters	Value
Freundlich	k_F/mg g^{-1}	2.412
	n	1.567
	SSR*	16.640
	RSE*	3.024
Langmuir	q_m/mg g^{-1}	54.572
	b/dm^3 mg^{-1}	0.024
	SSR	16.867
	RSE	3.228
Sips	q_m	5.932
	b	6.994
	n	1.606
	SSR	66.621
	RSE	5.176
Temkin	K	0.389
	b	282.010
	SSR	17.830
Dubinin-Radushkevich	q_m	25.220
	e	207.33
	SSR	28.690
Redlich-Peterson	K	0.3896
	a	0.0126
	g	1.7025
Klan	q_m	5.9320
	a	1.2607
	b	6.994
	SSR	586.24

*SSR: sum of squared residuals; *RSE: residual squared error

information based on the whole of SSR gotten. The Freundlich isotherm demonstration is based on the wonders of heterogeneous surfaces with a few adsorption components included, where K_F and n are the Freundlich constants related to the adsorption capacity and adsorption concentrated, respectively. The Freundlich parameter, n, shows the adsorption favorability. When the adsorption intensity, $n < 1$, it shows the favorability of the adsorption intensity over all the concentration ranges studied, but if $n > 1$, it shows that the adsorption intensity is favorable at high concentrations but less at lower concentrations [57]. The experimental data obtained for MGONPs shows an n value greater than 1, indicating that adsorption is favorable at higher concentrations but less at lower concentrations. According to the Langmuir model, q_m was 54.57 mg g^{-1}. On the other hand, the Freundlich model yielded an adsorption intensity value of 1.57, indicating a successful adsorption process [58].

The Langmuir adsorption capacities (q_m) of MGONPs were stacking up with various reported adsorbents for the removal of BG. Table 5 shows that the removal (q_m) by MGONPs used in this study compares favorably with other adsorbents.

The Langmuir model results in some parameters that can be used to estimate the favorability of the adsorption process. The separation factor (R_L), was calculated by using Eq. (3) [64]:

$$R_L = \frac{1}{1 + bC_i} \quad (1)$$

where C_i denotes the initial BG concentrations (mg dm^{-3}),

Table 5. Comparison of adsorption capacity of various reported adsorbents

Adsorbent	Temperature/K	q_m/mg g^{-1}	Reference
Hydroxyapatite/chitosan composite	-	49.10	[59]
Luffa cylindrical sponge	303	18.52	[60]
Corncob biochar	-	16.53	[61]
Areca nut husk	298	18.21	[62]
Poly(AN-coVP)/Zeolite composite	303	19.61	[63]
MGONPs	298	54.57	This study

and b denotes the Langmuir constant (dm^3 mg^{-1}). The value of R_L can be used to calculate the sequestration process's favorability. If $0 < R_L < 1$, adsorption is assumed to be favorable, unfavorable if $R_L > 1$, irreversible if $R_L = 0$, and linear if $R_L = 1$ [64]. All R_L values obtained in this study were found to fall between $0 < R_L < 1$; hence, the removal of BG onto MGONPs showed favorable adsorption. The procedure is more favorable when R_L values are minimal (Fig. 10).

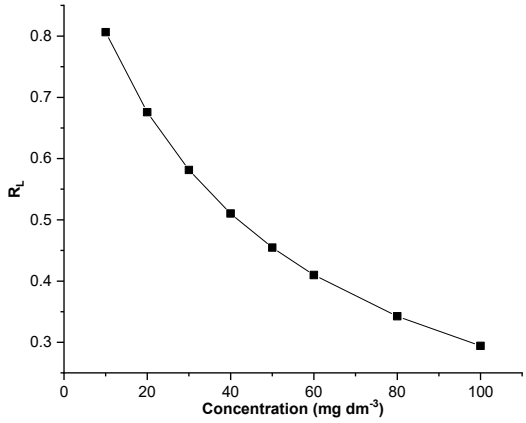

Fig 10. Separation factor R_L of BG onto MGONPs

Preferential adsorption

The special sorbate adsorption (q_P) and viable surface region (eS_{BET}) are the novel adsorption properties calculated for the performance evaluations. The found eS_{BET} is noteworthy since, notwithstanding the general S_{BET} of the adsorbent, chemical species adsorption pivots on the number of germane dynamic locales with a great fondness for the sorptive. The determination of eS_{BET} gives data on the importance of the dynamic locales to the q and, more essentially, the q_P esteem. Most of the considerations inspected within the current work did not allow data with respect to the sorts or sums of chemical functionalities on the sorbents. As a result, it is expected that the eS_{BET} will rise directly as long as the pertinent chemical surface usefulness is shown on the S_{BET}, either normally or misleadingly, through chemical impregnation. Table 6 appears the calculated adsorption parameters and highlights from the literature.

The adsorbent's mass adsorption capacity (q, mg g^{-1}) for a particular dye serves as the primary indicator for determining the extent of the sorbate-sorbent interphase. Only 2 of the 22 studies (Table 6) showed q_P values greater than 1, indicating that the sorbates preferred the sorbent to remain in the solution. The highest values were reported by Li et al. [76] (SN = 18; q_P = 49, ZnO nanoparticles on Congo red) and Lv et al. [77] (SN = 19; q_P = 336, sodium alginate/graphite based on malachite green), respectively. Fig. 11 shows a plot revealing the trend in the reported and derived adsorption properties for the selected adsorbents and pollutants.

The dataset's correlation data are shown in Table 7. After looking into the analyses, we found that the correlations increased noticeably. The q for brilliant green and the other adsorbates showed a similar trend with eS_{BET} (35.61 and 81.19%) than with S_{BET} (18.88 and 71.58%), respectively. The negative correlations between S_{BET} and eS_{BET} demonstrate that an adsorbent's adsorption capability is not always correlated with its S_{BET}. Inclusive, the derived adsorption properties (q_P and eS_{BET}) are much more consistent for equitable comparison between studies with various experimental settings and research goals.

The moles of the sorbent and q_P value of the adsorbate over solubility performed a positive relationship. Therefore, the more the sorbate's mass transfers onto the adsorbent, the higher the sorbent mass

Table 6. Estimated adsorption features of the various experiments

S/N	Dye	Sorbent mass (g)	q (mol g^{-1})	Surface area (m^2 g^{-1})	Effective Surf. Area (mol m^{-2})	Moles of sorbent (mol)	Volume (L)	Solubility (mol L^{-1})	Moles in solution (mol)	qp (Sorbent/Sol)	Ref
1	BG	0.01	4.75×10^{-4}	84.25	5.63×10^{-6}	4.75×10^{-6}	0.01	8.29×10^{-4}	8.29×10^{-4}	0.060	[65]
2	BG	0.01	3.11×10^{-4}	2.94	1.06×10^{-4}	3.11×10^{-6}	0.01	8.29×10^{-4}	8.29×10^{-4}	0.038	[65]
3	BG	0.01	1.71×10^{-3}	495.54	3.45×10^{-6}	1.71×10^{-5}	0.01	8.29×10^{-4}	8.29×10^{-4}	0.021	[65]
4	BG	0.80	1.86×10^{-4}	310	6.01×10^{-7}	1.49×10^{-4}	0.05	8.29×10^{-4}	4.14×10^{-3}	0.036	[66]
5	BG	1.00	3.43×10^{-5}	770.69	4.44×10^{-8}	3.43×10^{-5}	0.10	8.29×10^{-4}	8.29×10^{-3}	0.004	[61]
6	BG	1.20	1.15×10^{-3}	3.07	3.75×10^{-4}	1.38×10^{-3}	0.025	8.29×10^{-4}	2.07×10^{-3}	0.666	[67]
7	BG	0.04	4.93×10^{-4}	5.60	8.81×10^{-5}	1.97×10^{-5}	0.05	8.29×10^{-4}	4.14×10^{-3}	0.005	[68]
8	BG	0.005	2.03×10^{-6}	92	2.21×10^{-08}	1.01×10^{-8}	0.005	8.29×10^{-4}	4.14×10^{-3}	2.45×10^{-5}	[69]
9	BG	0.10	2.01×10^{-5}	19.64	1.02×10^{-6}	2.01×10^{-6}	0.05	8.29×10^{-4}	4.14×10^{-3}	4.85×10^{-4}	[63]
10	BG	0.03	3.48×10^{-4}	110	3.16×10^{-6}	1.04×10^{-5}	0.01	8.29×10^{-4}	8.29×10^{-4}	0.013	[70]
11	BG	0.75	2.30×10^{-4}	232.31	9.91×10^{-7}	1.73×10^{-4}	0.10	8.29×10^{-4}	8.29×10^{-3}	0.021	[71]
12	BG	0.40	2.59×10^{-4}	100.28	2.58×10^{-6}	1.03×10^{-4}	0.10	8.29×10^{-4}	8.29×10^{-3}	0.013	[72]
13	BG	0.10	5.93×10^{-4}	2304	2.57×10^{-7}	5.93×10^{-5}	0.05	8.29×10^{-4}	4.14×10^{-3}	0.014	[73]
14	BG	0.05	5.68×10^{-4}	1035	5.48×10^{-07}	2.84×10^{-5}	0.02	8.29×10^{-4}	1.66×10^{-3}	0.017	[74]
15	BG	0.05	6.96×10^{-4}	1425	4.88×10^{-7}	3.48×10^{-5}	0.02	8.29×10^{-4}	1.66×10^{-3}	0.021	[74]
16	BG	0.05	9.28×10^{-4}	424	2.19×10^{-6}	4.64×10^{-5}	0.01	8.29×10^{-4}	8.29×10^{-4}	0.056	[75]
17	BG	0.04	1.13×10^{-4}	116.81	9.68×10^{-7}	4.52×10^{-6}	0.025	8.29×10^{-4}	2.07×10^{-3}	0.002	This study
18	Congo red	0.04	1.02×10^{-4}	5.60	1.83×10^{-5}	4.09×10^{-6}	0.05	1.66×10^{-6}	8.32×10^{-8}	49.241	[76]
19	Malachite green	0.005	7.36×10^{-3}	237.42	3.10×10^{-5}	3.68×10^{-5}	0.01	1.10×10^{-5}	1.10×10^{-7}	335.945	[77]
20	Methylene blue	0.005	4.75×10^{-4}	85.60	5.55×10^{-6}	2.37×10^{-6}	0.01	0.14	1.36×10^{-3}	1.74×10^{-3}	[78]
21	Neutral red	0.005	1.06×10^{-3}	68.20	1.55×10^{-5}	5.30×10^{-6}	0.015	0.17	2.59×10^{-3}	2.04×10^{-3}	[79]
22	Methyl orange	0.15	8.53×10^{-5}	186	4.58×10^{-7}	1.27×10^{-5}	0.05	0.02	7.64×10^{-4}	1.67×10^{-2}	[80]

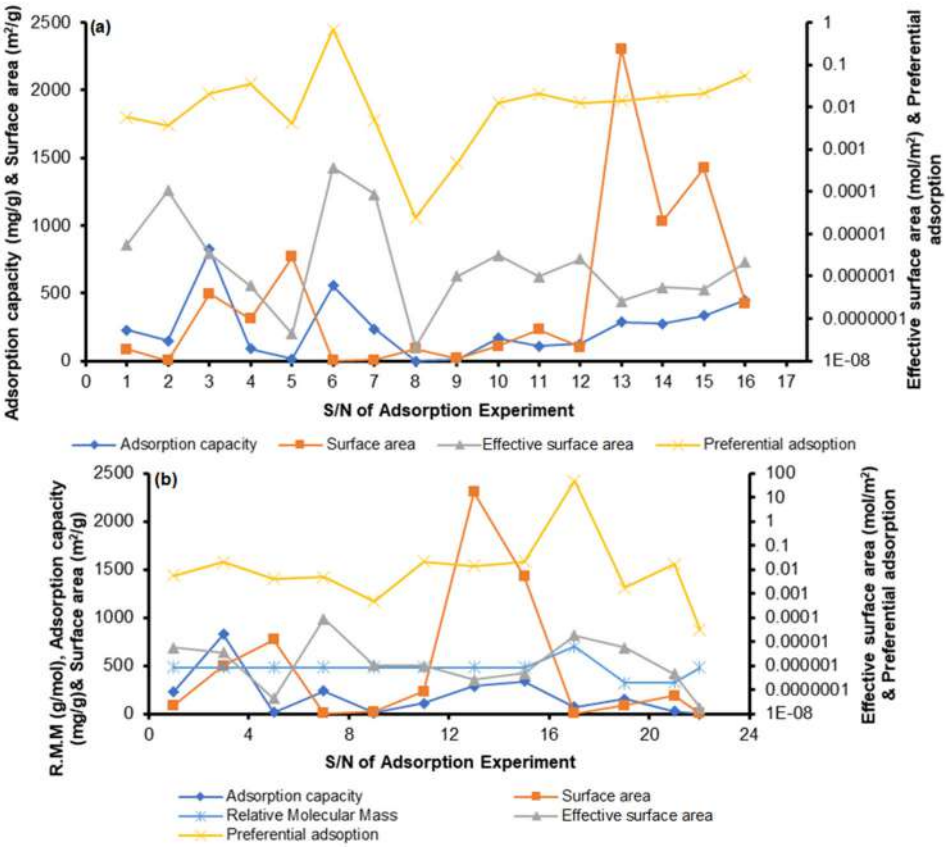

Fig 11. The several properties of (a) different adsorbents towards brilliant green, and (b) various adsorbents towards brilliant green and other dyes of different relative molecular mass, (S/N 1-16, and 17-22) in Table 6, respectively

Table 7. Correlation data of reported and derived adsorption properties of sorbate and sorbents

Adsorption properties	Sorbent mass vs. Moles in solution	q vs. S_{BET}	eS_{BET} vs. q_p	Moles of sorbent vs. q_p	S_{BET} vs. eS_{BET}	Sorbent mass vs. eS_{BET}	q vs. eS_{BET}
All	0.6088	0.0137	0.0037	-0.0506	-0.2188	0.5017	0.1037
Brilliant green	0.5795	0.1883	0.9283	0.9903	-0.2710	0.4955	0.3561
Others	-0.2262	0.7158	0.8315	0.9344	0.3736	-0.5728	0.8119

in the solution. For brilliant green (99%) and other dyes (93.45%), the relationship between the moles of sorbent and q_p is significant, demonstrating the agreement between the sorptive and the sorbents in this adsorption relationship [81-82].

CONCLUSION

This study revealed the successful modification of MGONPs for the adsorption of the cationic brilliant green dye from an aqueous solution. The following are the conclusions achieved from the study; the removal of BG was increased by increasing the pH to a maximum pH of 6, then decreased to reach a minimum removal percentage at pH 9. The pseudo-second-order model best described the experimental adsorption data fitted into the kinetic models. The adsorption isotherms study revealed that the Freundlich model best-fitted MGONPs. The maximum adsorption capacity (q_m) for MGONPs was 54.57 mg g^{-1}. A desorption study was carried out, and the SEM-EDX revealed that the dye molecules were desorbed after using acetone as the desorbing agent. The FTIR analysis showed the disappearance of the characteristic BG dye peaks after the desorption study. This showed that acetone is an excellent desorbing agent for BG, and the adsorbents can be recovered and recycled for reuse. Thus, this study indicates that MGONPs is a better adsorbent with higher adsorption capacity for the uptake of BG, and its application in the industry could be further explored. Additionally, dimensionless preferential adsorption (q_p) and effective surface area (eS_{BET}) performed more accurately than the conventional adsorption capacity and specific surface area (S_{BET}) in providing information about the sorbate-sorbent interface (q). We also validated the relevance and accuracy of the new parameters for future adsorption system design by correlation analysis. Adsorption is, therefore, an excellent method for reducing brilliant green pollutants in an aqueous medium.

ACKNOWLEDGMENTS

The authors thank the Universitas Airlangga Postdoctoral Fellowship, Indonesia, for the financial support of this work. This work was supported by the Universitas Airlangga Postdoctoral Fellowship, Indonesia (Ref No: 2480/UN3.22/KS/2022).

AUTHOR CONTRIBUTIONS

Olayinka Oluwaseun Oluwasina contributed in Conceptualization, Visualization, Investigation; Olayinka Oluwaseun Oluwasina contributed in Data curation, Writing- Original draft preparation; Mochamad Zakki Fahmi contributed in Supervision, Methodology, Writing- Reviewing and Editing.

REFERENCES

[1] Jadhav, I., Vasniwal, R., Shrivastava, D., and Jadhav, K., 2016, Microorganism-based treatment of azo dyes, *J. Environ. Sci. Technol.*, 9 (2), 188–197.

[2] Rani, B., Kumar, V., Singh, J., Bisht, S., Teotia, P., Sharma, S., and Kela, R., 2014, Bioremediation of dyes by fungi isolated from contaminated dye effluent sites for bio-usability, *Braz. J. Microbiol.*, 45 (3), 1055–1063.

[3] Alabdraba, W.M.S., and Albayati, M.B.A., 2014, Biodegradation of Azo Dyes—A Review, *Int. J. Environ. Sci. Nat. Resour.*, 4, 179–189.

[4] Zaman, A., Das, P., and Banerjee, P., 2016, "Biosorption of Dye Molecules" in *Toxicity and Waste Management Using Bioremediation*, Eds. Rathoure, A.K., and Dhatwalia, V.K., Global IGI, New York, US, 51–74.

[5] Vaid, V., and Jindal, R., 2022, An efficient pH-responsive kappa-carrageenan/tamarind kernel powder hydrogel for the removal of brilliant green and rose Bengal from aqueous solution, *J. Appl. Polym. Sci.*, 21, 139–151.

[6] Pandey, S., Do, J.Y., Kim, J., and Kang, M., 2020, Fast and highly efficient removal of dye from aqueous solution using natural locust bean gum based hydrogels as adsorbent, *Int. J. Biol. Macromol.*, 143, 60–75.

[7] Manickam, P., and Vijay, D., 2021, "Chemical Hazards in Textiles" in *Chemical Management in Textiles and Fashion*, Eds. Muthu, S.S., Woodhead Publishing, Cambridge, US, 19–52.

[8] Song, W., Li, J., Wang, Z., and Zhang, X., 2019, A mini review of activated methods to persulfate-based advanced oxidation process, *Water Sci. Technol.*, 79 (3), 573–579.

[9] Oguntimein, G., 2015, Biosorption of dye from textile wastewater effluent onto alkali treated dried sunflower seed hull and design of a batch adsorber, *J. Environ. Chem. Eng.*, 3 (4, Part A), 2647–2661.

[10] Chaari, I., Fakhfakh, E., Medhioub, M., and Jamoussi, F., 2019, Comparative study on adsorption of cationic and anionic dyes by smectite rich natural clays, *J. Mol. Struct.*, 1179, 672–677.

[11] Mahmoud, H.R., Ibrahim, S.M., and El-Molla, S.A., 2016, Textile dye removal from aqueous solutions using cheap MgO nanomaterials: Adsorption kinetics, isotherm studies and thermodynamics, *Adv. Powder Technol.*, 27 (1), 223–231.

[12] Fan, Y.H., Zhang, S.W., Qin, S.B., Li, X.S., and Qi, S.H., 2018, An enhanced adsorption of organic dyes onto NH_2 functionalization titanium-based metal-organic frameworks and the mechanism investigation, *Microporous Mesoporous Mater.*, 263, 120–127.

[13] Sirajudheen, P., Manuvel, R., Perumal, K., and Sankaran, M., 2020, Perceptive removal of toxic azo dyes from water using magnetic Fe_3O_4 reinforced graphene oxide–carboxymethyl cellulose recyclable composite: Adsorption investigation of parametric studies and their mechanisms, *Surf. Interfaces*, 21, 100648.

[14] Stefaniuk, M., Oleszczuk, P., and Ok, Y.S., 2016, Review on nano zerovalent iron (nZVI): From synthesis to environmental applications, *Chem. Eng. J.*, 287, 618–632.

[15] Mortazavian, S., An, H., Chun, D., and Moon, J., 2018, Activated carbon impregnated by zero-valent iron nanoparticles (AC/nZVI) optimized for simultaneous adsorption and reduction of aqueous hexavalent chromium: Material characterizations and kinetic studies, *Chem. Eng. J.*, 353, 781–795.

[16] Yoon, Y., Park, W.K., Hwang, T.M., Yoon, D.H., Yang, W.S., and Kang, J.W., 2016, Comparative evaluation of magnetite-graphene oxide and magnetite-reduced graphene oxide composite for As(III) and As(V) removal, *J. Hazard. Mater.*, 304, 196–204.

[17] Fahmi, M.Z., Wathoniyyah, M., Khasanah, M., Rahardjo, Y., and Wafiroh, S., 2018, Incorporation of graphene oxide in polyethersulfone mixed matrix membranes to enhance hemodialysis membrane performance, *RSC Adv.*, 8 (2), 931–937.

[18] Fahmi, M.Z., Andriyani, V., Dzikri, M.F., Armedya, T.P., Wathoniyyah, M., Wibowo, D.L.N., and Permana, A.J., 2019, *In situ* synthesis process of nanographene and its characteristic, *IOP Conf. Ser.: Earth Environ. Sci.*, 245, 012045.

[19] Kemp, K.C., Seema, H., Saleh, M., Le, N.H., Mahesh, K., Chandra, V., and Kim, K.S., 2013, Environmental applications using graphene composites: Water remediation and gas adsorption, *Nanoscale*, 5 (8), 3149–3171.

[20] Purnamasari, W., Budiastanti, T.A., Aminatun, A., Rahmah, U., Sumarsih, S., Chang, J.Y., and Fahmi, M.Z., 2022, Naproxen release behaviour from graphene oxide/cellulose acetate composite nanofibers, *RSC Adv.*, 12 (13), 8019–8029.

[21] Ramalingam, G., Perumal, N., Priya, A.K., and Rajendran, S., 2022, A review of graphene-based semiconductors for photocatalytic degradation of pollutants in wastewater, *Chemosphere*, 300, 134391.

[22] Fahmi, M.Z., Prasetya, R.A., Dzikri, M.F., Sakti, S.C.W., and Yuliarto, B., 2020, $MnFe_2O_4$ nanoparticles/cellulose acetate composite nanofiber for controllable release of naproxen, *Mater. Chem. Phys.*, 250, 123055.

[23] Torkashvand, N., and Sarlak, N., 2019, Synthesis of completely dispersed water soluble functionalized graphene/γ-Fe_2O_3 nanocomposite and its application as an MRI contrast agent, *J. Mol. Liq.*, 291, 111286.

[24] Liu, M., Chen, C., Hu, J., Wu, X., and Wang, X., 2011, Synthesis of magnetite/graphene oxide composite and application for cobalt(II) removal, *J. Phys. Chem. C*, 115 (51), 25234–25240.

[25] Weng, X., Lin, Z., Xiao, X., Li, C., and Chen, Z., 2018, One-step biosynthesis of hybrid reduced graphene oxide/iron-based nanoparticles by eucalyptus extract and its removal of dye, *J. Cleaner Prod.*, 203, 22–29.

[26] Rodríguez-García, S., Santiago, R., López-Díaz, D., Merchán, M.D., Velázquez, M.M., Fierro, J.L.G., and Palomar, J., 2019, Role of the structure of graphene oxide sheets on the CO_2 adsorption properties of nanocomposites based on graphene oxide and polyaniline or Fe_3O_4-nanoparticles, *ACS Sustainable Chem. Eng.*, 7 (14), 12464–12473.

[27] Kazemi, A., Bahramifar, N., Heydari, A., and Olsen, S.I., 2019, Synthesis and sustainable assessment of thiol-functionalization of magnetic graphene oxide and superparamagnetic Fe_3O_4@SiO_2 for Hg(II) removal from aqueous solution and petrochemical wastewater, *J. Taiwan Inst. Chem. Eng.*, 95, 78–93.

[28] Oluwasina, O.O., Ranu, S., Jonnalagadda, S.B., and Martincigh, B.S., 2021, Synthesis and characterization of graphene oxide under different conditions, and a preliminary study on its efficacy to adsorb Cu^{2+}, *Adv. Sci. Technol. Eng Syst. J.*, 6, 10–16.

[29] Langmuir, I., 1918, The adsorption of gases on plane surfaces of glass, mica and platinum, *J. Am. Chem. Soc.*, 40 (9), 1361–1403.

[30] Freundlich, H., 1906, Über die adsorption in lösungen, *Z. Phys. Chem.*, 57, 385–471.

[31] Sips, R., 1948, On the structure of a catalyst surface, *J. Chem. Phys.,* 16, 490–495.

[32] Temkin, M.I., and Pyzhev, V., 1940, Kinetics of ammonia synthesis on promoted iron catalyst, *Acta Physicochim. URSS*, 12, 327–356.

[33] Dubinin, M.M., 1947, The equation of the characteristic curve of activated charcoal, *Dokl. Akad. Nauk SSSR*, 55, 327–329.

[34] Redlich, O., and Peterson, D., 1959, A useful adsorption isotherm, *J. Phys. Chem.*, 63 (6), 1024.

[35] Yadav, A., Bagotia, N., Sharma, A.K., and Kumar, S., 2021, Simultaneous adsorptive removal of conventional and emerging contaminants in multi-component systems for wastewater remediation: A critical review, *Sci. Total Environ.*, 799, 149500.

[36] Ho, Y.S., 2003, Removal of copper ions from aqueous solution by tree fern, *Water Res.*, 37 (10), 2323–2330.

[37] Ho, Y.S., 2004, Comment on "Cadmium removal from aqueous solutions by chitin: Kinetic and equilibrium studies", *Water Res.*, 38 (12), 2962–2964.

[38] Somsesta, N., Sricharoenchaikul, V., and Aht-Ong, D., 2020, Adsorption removal of methylene blue onto activated carbon/cellulose biocomposite films: Equilibrium and kinetic studies, *Mater. Chem. Phys.*, 240, 122221–122231.

[39] Demirbas, E., Kobya, M., Senturk, E., and Ozkan, T., 2004, Adsorption kinetics for the removal of chromium(VI) from aqueous solutions on the activated carbons prepared from agricultural wastes, *Water SA*, 30, 533–539.

[40] Chien, S.H., and Clayton, W.R., 1980, Application of Elovich equation to the kinetics of phosphate release and sorption in soils, *Soil Sci. Soc. Am. J.*, 44 (2), 265–268.

[41] Ball, P.C., and Evans, R., 1989, Temperature dependence of gas adsorption on a mesoporous solid: Capillary criticality and hysteresis, *Langmuir*, 5 (3), 714–723.

[42] Wang, Y., Wei, X., Qi, Y., and Huang, H., 2021, Efficient removal of bisphenol-A from water and wastewater by Fe_2O_3-modified graphene oxide, *Chemosphere*, 263, 127563.

[43] Permadi, A., Fahmi, M.Z., Chen, J.K., Chang, J.Y., Cheng, C.Y., Wang, G.Q., and Ou, K.L., 2012, Preparation of poly(ethylene glycol) methacrylate coated $CuInS_2$/ZnS quantum dots and their use in cell staining, *RSC Adv.*, 2 (14), 6018–6022.

[44] Hu, Z.P., Gao, Z.M., Liu, X., and Yuan, Z.Y., 2018, High-surface-area activated red mud for efficient removal of methylene blue from wastewater, *Adsorpt. Sci. Technol.*, 36 (1-2), 62–79.

[45] Rao, C.V., Giri, A.S., Goud, V.V., and Golder, A.K., 2016, Studies on pH-dependent colour variation and decomposition mechanism of Brilliant Green dye in Fenton reaction, *Int. J. Ind. Chem.*, 7 (1), 71–80.

[46] Xu, H., Jia, W., Ren, S., and Wang, J., 2019, Magnetically responsive multi-wall carbon nanotubes as recyclable demulsifier for oil removal from crude oil-in-water emulsion with different pH levels, *Carbon*, 145, 229–239.

[47] Xu, H., Jia, W., Ren, S., and Wang, J., 2018, Novel and recyclable demulsifier of expanded perlite grafted by magnetic nanoparticles for oil separation from emulsified oil wastewaters, *Chem. Eng. J.*, 337, 10–18.

[48] Lin, C.C., and Lee, C.Y., 2020, Adsorption of ciprofloxacin in water using Fe_3O_4 nanoparticles formed at low temperature and high reactant concentrations in a rotating packed bed with co-precipitation, *Mater. Chem. Phys.*, 240, 122049.

[49] Shahnaz, T., Patra, C., Sharma, V., and Selvaraju, N., 2020, A comparative study of raw, acid-modified and EDTA-complexed *Acacia auriculiformis* biomass for the removal of hexavalent chromium, *Chem. Ecol.*, 36 (4), 360–381.

[50] Liu, J., Wang, N., Zhang, H., and Baeyens, J., 2019, Adsorption of Congo red dye on $Fe_xCo_{3-x}O_4$ nanoparticles, *J. Environ. Manage.*, 238, 473–483.

[51] Sitko, R., Turek, E., Zawisza, B., Malicka, E., Talik, E., Heimann, J., Gagor, A., Feist, B., and Wrzalik, R., 2013, Adsorption of divalent metal ions from aqueous solutions using graphene oxide, *Dalton Trans.*, 42 (16), 5682–5689.

[52] Eeshwarasinghe, D., Loganathan, P., Kalaruban, M., Sounthararajah, D.P., Kandasamy, J., and Vigneswaran, S., 2018, Removing polycyclic aromatic hydrocarbons from water using granular activated carbon: Kinetic and equilibrium adsorption studies, *Environ. Sci. Pollut. Res.*, 25 (14), 13511–13524.

[53] Travlou, N.A., Kyzas, G.Z., Lazaridis, N.K., and Deliyanni, E.A., 2013, Graphite oxide/chitosan composite for reactive dye removal, *Chem. Eng. J.*, 217, 256–265.

[54] Al-Asheh, S., Banat, F., Al-Omari, R., and Duvnjak, Z., 2000, Predictions of binary sorption isotherms for the sorption of heavy metals by pine bark using single isotherm data, *Chemosphere*, 41 (5), 659–665.

[55] Shirsath, S.R., Patil, A.P., Patil, R., Naik, J.B., Gogate, P.R., and Sonawane, S.H., 2013, Removal of brilliant green from wastewater using conventional and ultrasonically prepared poly(acrylic acid) hydrogel loaded with kaolin clay: A comparative study, *Ultrason. Sonochem.*, 20 (3), 914–923.

[56] Maebana, M.O., Mishra, S.B., Mamba, B.B., and Mishra, A.K., 2013, Study on the efficiency of ethylene vinyl acetate–fly ash composites for the uptake of phenols from synthetic waste water, *J. Appl. Polym. Sci.*, 128 (3), 2073–2080.

[57] El-Bindary, A.A., Hussien, M.A., Diab, M.A., and Eessa, A.M., 2014, Adsorption of Acid Yellow 99 by polyacrylonitrile/activated carbon composite: Kinetics, thermodynamics and isotherm studies, *J. Mol. Liq.*, 197, 236–242.

[58] Ooi, J., Lee, L.Y., Hiew, B.Y.Z., Thangalazhy-Gopakumar, S., Lim, S.S., and Gan, S., 2017, Assessment of fish scales waste as a low cost and eco-friendly adsorbent for removal of an azo dye: Equilibrium, kinetic and thermodynamic studies, *Bioresour. Technol.*, 245, 656–664.

[59] Ragab, A., Ahmed, I., and Bader, D., 2019, The removal of brilliant green dye from aqueous solution using nano hydroxyapatite/chitosan composite as a sorbent, *Molecules*, 24 (5), 847.

[60] Segun Esan, O., Nurudeen Abiola, O., Owoyomi, O., Olumuyiwa Aboluwoye, C., and Olubunmi Osundiya, M., 2014, Adsorption of brilliant green onto Luffa cylindrical sponge: Equilibrium, kinetics, and thermodynamic studies, *ISRN Phys. Chem.*, 2014, 743532.

[61] Giri, B.S., Gun, S., Pandey, S., Trivedi, A., Kapoor, R.T., Singh, R.P., Abdeldayem, O.M., Rene, E.R., Yadav, S., Chaturvedi, P., Sharma, N., and Singh, R.S., 2020, Reusability of brilliant green dye contaminated wastewater using corncob biochar and *Brevibacillus parabrevis*: Hybrid treatment and kinetic studies, *Bioengineered*, 11 (1), 743–758.

[62] Sukla Baidya, K., and Kumar, U., 2021, Adsorption of brilliant green dye from aqueous solution onto

chemically modified areca nut husk, *S. Afr. J. Chem. Eng.*, 35, 33–43.

[63] Tanyol, M., Kavak, N., and Torğut, G., 2019, Synthesis of poly(AN-co-VP)/zeolite composite and its application for the removal of brilliant green by adsorption process: Kinetics, isotherms, and experimental design, *Adv. Polym. Technol.*, 2019, 8482975.

[64] Doke, K.M., and Khan, E.M., 2013, Adsorption thermodynamics to clean up wastewater; Critical review, *Rev. Environ. Sci. Bio/Technol.*, 12 (1), 25–44.

[65] Aichour, A., and Zaghouane-Boudiaf, H., 2019, Highly brilliant green removal from wastewater by mesoporous adsorbents: Kinetics, thermodynamics and equilibrium isotherm studies, *Microchem. J.*, 146, 1255–1262.

[66] Mansour, R.A., El Shahawy, A., Attia, A., and Beheary, M.S., 2020, Brilliant green dye biosorption using activated carbon derived from guava tree wood, *Int. J. Chem. Eng.*, 2020, 8053828.

[67] Coşkun, Y.I., Aksuner, N., and Yanik, J., 2019, Sandpaper wastes as adsorbent for the removal of brilliant green and malachite green dye, *Acta Chim. Slov.*, 66 (2), 402–413.

[68] Kataria, N., and Garg, V.K., 2019, Application of EDTA modified Fe_3O_4/sawdust carbon nanocomposites to ameliorate methylene blue and brilliant green dye laden water, *Environ. Res.*, 172, 43–54.

[69] Thakur, S., Singh, S., and Pal, B., 2021, Superior adsorptive removal of brilliant green and phenol red dyes mixture by CaO nanoparticles extracted from egg shells, *J. Nanostruct. Chem.*, 12 (2), 207–221.

[70] Romzi, A.A., Lim, L.B.L., Chan, C.M., and Priyantha, N., 2020, Application of *Dimocarpus longan* ssp. *malesianus* leaves in the sequestration of toxic brilliant green dye, *Desalin. Water Treat.*, 189, 428–439.

[71] Zolgharnein, J., Bagtash, M., and Shariatmanesh, T., 2015, Simultaneous removal of binary mixture of brilliant green and crystal violet using derivative spectrophotometric determination, multivariate optimization and adsorption characterization of dyes on surfactant modified nano-γ-alumina, *Spectrochim. Acta, Part A,* 137, 1016–1028.

[72] Saif Ur Rehman, M., Kim, I., Rashid, N., Adeel Umer, M., Sajid, M., and Han, J.I., 2016, Adsorption of brilliant green dye on biochar prepared from lignocellulosic bioethanol plant waste, *Clean: Soil, Air, Water*, 44 (1), 55–62.

[73] Ur Rehman, M.S., Munir, M., Ashfaq, M, Rashid, N., Nazar, M., Danish, M., and Han, J.I., 2013, Adsorption of brilliant green dye from aqueous solution onto red clay, *Chem. Eng. J.*, 228, 54–62.

[74] Asadullah, M., Asaduzzaman, M., Kabir, M.S., Mostofa, M.G., and Miyazawa, T., 2010, Chemical and structural evaluations of activated carbon prepared from jute sticks for brilliant green dye removal from aqueous solution, *J. Hazard. Mater.*, 174 (1-3), 437–443.

[75] Mansour, R.A.E.G., Simeda, M.G., and Zaatout, A.A., 2021, Removal of brilliant green dye from synthetic wastewater under batch mode using chemically activated date pit carbon, *RSC Adv.*, 11, 14, 7851–7861.

[76] Li, Z., Hanafy, H., Zhang, L., Sellaoui, L., Netto, M.S., Oliveira, M.L., Seliem, M.K., Datto, G.L., Petriciolet, A.B., and Li, Q., 2020, Adsorption of Congo red and methylene blue dyes on an ashitaba waste and a walnut shell-based activated carbon from aqueous solutions: Experiments, characterization and physical interpretations, *Chem. Eng. J.*, 388, 124263.

[77] Lv, M., Yan, L., Liu, C., Su, C., Zhou, Q., Zhang, X., Lan, Y., Zheng, Y., Lai, L., Liu, X., and Ye, Z., 2018, Non-covalent functionalized graphene oxide (GO) adsorbent with an organic gelator for co-adsorption of dye, endocrine-disruptor, pharmaceutical and metal ion, *Chem. Eng. J.*, 349 (1), 791–799.

[78] Verma, A., Thakur, S., Mamba, G., Prateek, P., Gupta, R.K., Thakur, P., and Thakur, V.K., 2020, Graphite modified sodium alginate hydrogel composite for efficient removal of malachite green dye, *Int. J. Biol. Macromol.,* 148, 1130–1139.

[79] Wang, X., Zhang, Y., Shan, R., and Hu, H., 2020, Polydopamine interface encapsulating graphene

and immobilizing ultra-small, active Fe_3O_4 nanoparticles for organic dye adsorption, *Ceram. Int.*, 47 (3), 3219–3231.

[80] Wang, S., Wei, J., Lv, S., Guo, Z., and Jiang, F., 2013, Removal of organic dyes in environmental water onto magnetic-sulfonic graphene nanocomposite, *Clean: Soil, Air, Water*, 41 (10), 992–1001.

[81] Ighalo, J.O., Adeniyi, A.G., and Adelodun, A.A., 2021, Recent advances on the adsorption of herbicides and pesticides from polluted waters: Performance evaluation via physical attributes, *J. Ind. Eng. Chem.*, 93, 117–137.

[82] Raharjo, Y., Fahmi, Z., Wafiroh, W., Widati, A.A., Amanda, E.R., Ismail, A.F., Othman M.H.D., and Santoso, D., 2019, Incorporation of imprinted-zeolite to polyethersulfone/cellulose acetate membrane for creatinine removal in hemodialysis treatment, *Jurnal Teknologi*, 81 (3), 137–144.

Supplementary Data

This supplementary data is a part of a paper entitled "Simple Microfluidic Paper-Based Analytical Device (μ-PAD) Coupled with Smartphone for Mn(II) Detection Using Tannin as a Green Reagent".

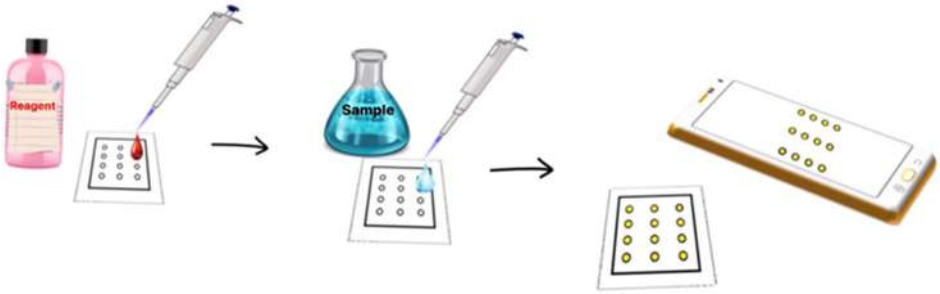

Fig S1. Schematic representation of the optimization procedure of μ-PAD and the determination of Mn(II) using μ-PAD

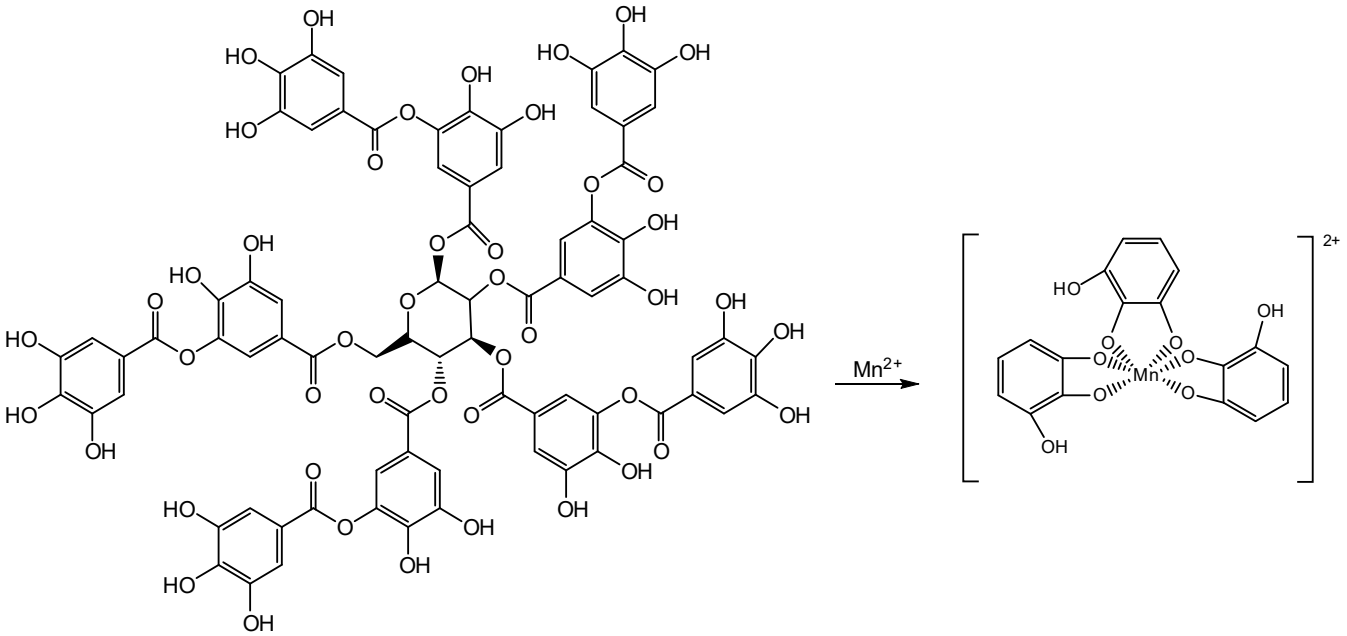

Fig S2. Schematic representation of reaction between tannin reagent and Mn(II)

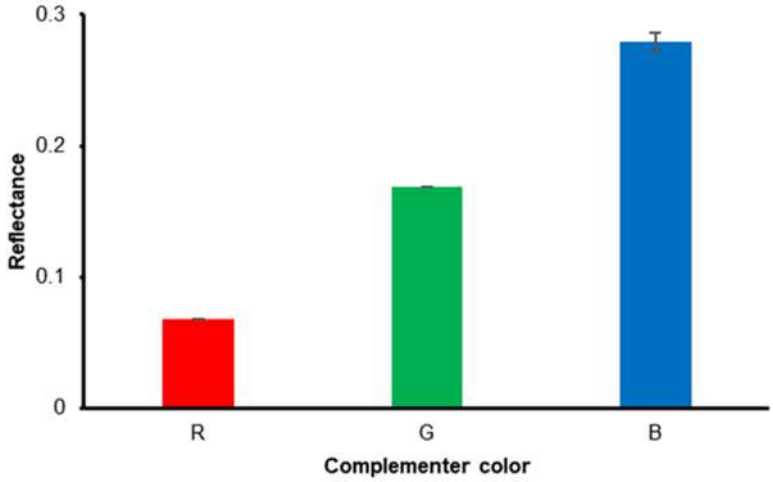

Fig S3. The reflectance after the addition of Mn(II) standard in the μ-PADs calculated using R, G and B intensity

Simple Microfluidic Paper-Based Analytical Device (μ-PAD) Coupled with Smartphone for Mn(II) Detection Using Tannin as a Green Reagent

Fidelis Nitti[1*], Wendelina Archangela Ati[1], Philiphi de Rozari[1], Pius Dore Ola[1], David Tambaru[1,2], and Luther Kadang[1]

[1]*Department of Chemistry, University of Nusa Cendana, Jl. Adi Sucipto, Penfui, Kupang 85001, Indonesia*

[2]*School of Chemistry, The University of Melbourne, Masson Road, Parkville 3052, Australia*

* ***Corresponding author:***

email: fnitti@staf.undana.ac.id

Received: February 22, 2023
Accepted: July 14, 2023

DOI: 10.22146/ijc.82511

Abstract: *The development of a simple yet greener microfluidic paper-based analytical device (μ-PAD) for on-site detection of Mn(II) in various types of waters using tannin as a natural reagent was described. The μ-PAD consists of twelve detection zones, created on a Whatman Number 1 filter paper by a simple drawing technique using an acrylic watercolor. The detection of Mn(II) was based on the color change on the reaction zone due to the reaction between Mn(II) and the pre-deposited tannin. The μ-PAD image was captured by a portable smartphone detector, and the blue intensity was digitized using a color picker application to generate the reflectance as the analytical response. The proposed method was characterized by a linear dynamic range of 0.05–0.25 mg L^{-1} with the limit of detection (LOD) for the determination of Mn(II) of 0.026 mg L^{-1}. The other analytical merits of the proposed method, such as precision (RSD, 1.107%), accuracy (E, 6.697%), and recovery (104–112%), were all comparable to the existing spectrophotometric methods. The method's successful application to natural water samples from manganese mining sites aligns with the reference spectrophotometric method, indicating its good selectivity and accuracy without significant influence of commonly associated interfering ions.*

Keywords: *microfluidic paper based analytical device (μ-PAD); Mn(II) detection; tannin; green reagent*

INTRODUCTION

As an essential trace element in humans, manganese (Mn) is required in small quantities for both growth and development as well as the maintenance of human health. Manganese has been identified as part of the chemical composition of several essential enzymes (i.e., arginase, pyruvate carboxylase, superoxide dismutase, and glycosyltransferase), which directly involves in several important processes in the human body, including bone system development, carbohydrate and lipid metabolism, immunity, nervous system, and reproductive hormone function [1]. Despite its significant roles, long-term excessive exposure to manganese in larger quantities may be detrimental to human health. It has been reported that excessive exposure to manganese can primarily lead to the disruption in neurological function and trigger the development of manganism, an occupational disease resembling Parkinson's disease [2-3]. In addition, excessive exposure to manganese has also been associated with several early chronic symptoms such as pneumonitis, cough and bronchitis, metal fume fever, decrease in lung function and chronic obstructive lung disease [4-5].

As the 12th most abundant element in the earth's crust, manganese can be naturally found not only in rocks and soil but also in water and a variety of food. While manganese can exist in natural waters in several oxidation states, it is most frequently found as its ionic Mn(II) in water with a pH lower than 7 and/or low dissolved oxygen content [6-7]. Mn(II) contamination could occur through natural processes, anthropogenic activities, and agricultural or household products.

Natural processes such as volcanic eruptions, rock weathering and erosion of the earth's crust are among the main sources of Mn(II) in aquatic systems. An elevated Mn(II) concentration in water could also be the result of anthropogenic activities such as from iron and steel plants, production of matches, fireworks, dry-cell batteries, and porcelain and other manganese compounds. Moreover, many agricultural and household products, including fertilizers, pesticides, fungicides, livestock supplements, antialgal agents, disinfectants, metal cleaners, tanning, and bleaching agents containing either manganese sulfate or potassium permanganate that also contribute to the high level of Mn(II) contamination in water systems. Due to its wide range of use and its high solubility characteristics in water, manganese can ubiquitously be present in environmental water because of the release or discharge from industrial and domestic waste or as leachate from landfills and agricultural runoff. Thus, considering its abundance along with its adverse health effects, a regular determination of Mn(II) ions in a variety of environmental waters, wastewater, and industrial effluents is of great significance, especially in ensuring a sustainable public health system.

To date, numerous analytical techniques have been commonly applied for the regular measurement of Mn(II) ions in various environmental waters. These include graphite furnace atomic absorption spectroscopy (GF-AAS), atomic absorption spectroscopy (AAS), and inductively coupled plasma mass spectrometry (ICP-MS) [8-11]. Despite their high accuracy, precision, and sensitivity; these techniques require the use of sophisticated instrumentations and involve laborious operational procedures, which contributes to the high analytical cost and hampers their use for the regular on-site analysis of Mn(II) ions. In order to comply with the standards established by the national and international environmental agencies and by considering the need for regular on-site monitoring of Mn(II) concentration, it is therefore vital to develop a simple yet cost-effective technique for the detection of the Mn(II) ions which can be easily applied for regular on-site monitoring in a variety of environmental samples.

Over the past decade, microfluidic paper-based analytical devices (μ-PADs) have garnered significant attention as a powerful analytical platform due to several attractive features, including portability, cost-effectiveness, user-friendliness, and less reagent consumption [12]. The main advantage of using the paper sheet as the support is that it is cheap, readily available, and easy to handle and streamline the chemical reaction through the capillary channel without external energy sources [13]. There has been a variety of fabrication techniques for creating the hydrophobic barrier and hydrophilic zone on μ-PADs, including screen printing, inkjet printing, flexography printing, wax printing, photolithography, inkjet etching, drawing, and plasma treatment [14]. Of all the fabrication techniques, the drawing technique is preferable due to its simplicity, and cost-effectiveness, as it needs only a permanent marker, a wax pen or an acrylic watercolor to manually hand draw the hydrophobic barrier on a filter paper [15].

Since the first report by the Whitesides group from Harvard University [16], there has been a vast development of μ-PADs as analytical tools for applications in food safety [17], health care [18-19] and environmental science [20-21], with some μ-PADs particularly devoted to the detection of Mn(II) in water samples [22-24]. Meredith et al. [22] reported the development of paper-based microfluidics for the selective determination of Mn(II) in the presence of other cations using 4-(2-pyridylazo)resorcinol (PAR) as the non-specific colorimetric ligand. It was reported that when using triethylenetetramine hydrate (0.1 M) and dimercaptosuccinic acid (0.1 M) in borate buffer (0.125 M) pH 10 as the masking agent, Mn(II) could be selectively detected with 87% masking of all interfering metals including Cu, Zn, Cd, Pb, Co, Ni, and Fe [22]. Lee et al. [24] developed a colorimetric chemosensor filter paper to distinguish between Mn(III) and Mn(II) in the aqueous solution. The research undertaken indicated that the differentiation between Mn(II) and Mn(III) was based on the reaction time of each ion with a colorimetric chemosensor which was synthesized from the combination of 2-(aminomethyl) aniline and

4-(diethylamino)-2-hydroxybenzaldehyde. It was revealed that Mn(II) could be detected via the complex formation with a colorimetric chemosensor with a shorter reaction time in comparison to that of the Mn(III) ion [24]. In a more recent study, Kamnoet et al. [23] proposed a μ-PAD for the selective and simultaneous detection of Cu(II), Co(II), Ni(II), Hg(II), and Mn(II) in water samples. They reported that Mn(II) could be selectively detected by using a μ-PAD containing a 2.5 μL pre-deposited reagent containing 5 mM PAR and 5% w/w poly(diallyldimethylammonium chloride) in a 0.1 M borate buffer pH 9.3. Under the optimum conditions, it was revealed that a linear range of 0.0020–0.0100 mM Mn(II) with a limit of detection (LOD) of 0.0020 mM could be achieved. Thiourea (1 M) and ethylenediamine (8 M) were previously added to the pre-treatment zone to obtain a selective detection of Mn(II) by masking other interfering ions such as Co(II), Cu(II), Ni(II), Zn(II), Cd(II), and Pb(II) [23].

While the above-mentioned μ-PADs have been successful for the detection of Mn(II) in a variety of water samples, their continuous use in the regular detection of Mn(II) is not in line with green chemistry due to the use of synthetic reagents which are expensive and mostly toxic [22-25]. Moreover, the existing μ-PADs for Mn(II) detection were not fully suitable for on-site applications to monitor environmental Mn(II) pollution due to the use of desktop equipment such as the scanner and the use of laptop-based application in processing and digitizing the response image such as image J [22-23]. Therefore, to further extend the greenness, simplicity, and portability of the current μ-PAD technique, herein we report the development of a simple μ-PAD technique coupled with a smartphone for on-site detection of Mn(II) in water using a natural reagent, tannin. Tannin is a high molecular weight phenolic compound that can be easily extracted from a variety of plant tissues using a variety of solvents. Due to its abundant presence in plant tissues and low toxicity, tannin is an excellent greener alternative compound for a variety of applications, including coagulants, food additives, flotation agents, antioxidants, dyeing agents, and adsorbents [26-28]. Additionally, its numerous hydroxyl group content provides tannin with high-water solubility and excellent metal chelating properties, which is promising for other analytical and environmental applications [29-30]. Thus, the present research explores the use of tannin as the complexing agent for Mn(II) in μ-PAD for the analytical determination of Mn(II) in water. The μ-PAD was fabricated using a simple drawing technique [31-33] using the commercially available acrylic watercolor, and the resulting color on μ-PAD due to the reaction between Mn(II) and tannin was captured using a smartphone as a portable detector [34-36]. A free-download "color picker" application which has been successfully utilized and reported elsewhere [37] as an alternative method to the existing desktop computer-based application (i.e., image J) was used for digitizing the color change of the μ-PAD which was further used as the analytical response.

■ EXPERIMENTAL SECTION

Materials

All chemicals used in this research were of analytical grade and were used as received without any further purification. $MnSO_4$ was obtained from Merck and was used in the preparation of Mn(II) solutions. Other chemicals used in this research, such as CH_3COOH, CH_3COONa, H_2SO_4, $NaIO_4$, and CH_3OH were also obtained from Merck and used as received. Tannin powder was commercially available and was bought from Kempan®. The μ-PADs were fabricated using Whatman No.1 filter paper (Whatman/GE Healthcare) using commercially available acrylic color set (Hepi Iop1), crayon (Heppi pop 1), and acrylic spray paint (Nippon paint) as the hydrophobization agents. All the aqueous solutions were prepared in deionized water obtained from OneMed. Mn(II) standard solutions used throughout the experiment were prepared in acetic acid buffer pH 3.

Instrumentation

A laminating machine (GK-Tech) was used in the fabrication of the μ-PADs to prevent the evaporation of the reagent and avoid any possible contamination. The image of the μ-PADs was captured using a smartphone

Iphone 6S Plus (camera resolution of 12 megapixels). Spectrophotometer UV-vis 100DA-X (B-one) was used as the reference method in the μ-PADs validity test.

Procedure

Fabrication of the μ-PADs

The proposed μ-PAD (Fig. 1) consisted of 12 reaction zones (0.5 cm internal diameter) with the size of a credit card (9 cm × 8 cm). Several commercial products were assessed for their use as hydrophobization agents to create the hydrophobic barrier on the μ-PAD, including an acrylic color set, crayon, and acrylic spray. When an acrylic color set or crayon was used as the hydrophobization agent, the hydrophobic barrier was manually drawn on the filter paper to create a hydrophilic reaction zone using a paintbrush. When the acrylic spray was used as the hydrophobization agent, the manual spraying technique was used to create the hydrophobic barrier. In both cases, the hydrophobization agents were only applied on one side of the filter paper and a plastic film as the template was used to create the circular hydrophobic barrier. The resulting filter paper was then ironed from the other side to facilitate the penetration of the hydrophobization agent into the cellulose fiber of the filter paper. After that, the μ-PAD was laminated using an ID-card size laminating plastic to prevent the evaporation of the sample and tannin solutions during the detection process. Prior to the laminating, a screw punch was used to punch a sample insertion hole of 2 mm in diameter in the laminating plastic over the center of each sampling zone which will be used for introducing the reagent and sample.

The resulting μ-PADs produced using the above-mentioned hydrophobization agents were assessed for the ability of the fabricated hydrophobic zone to contain an aqueous solution (25 μL of deionized water), which was deposited on the created reaction zone (hydrophilic zone) [14]. For the optimization and the analysis, the selected hydrophobization agent was used to fabricate the hydrophobic barrier and the preparation of μ-PAD involves the addition of the pre-optimized tannin solution as the reagent. In each case, the μ-PAD with pre-deposited tannin reagent was air-dried for 1–2 min prior to the addition of the water sample.

Analytical procedures and optimization of the μ-PADs

As shown in Fig. S1, the measurement of Mn(II) using the μ-PAD was carried out by initially depositing a certain volume of tannin solution as the chromogenic natural reagent to the hydrophilic zones. The μ-PAD was air-dried for several minutes before a certain volume of Mn(II) standard solution or real sample solution containing Mn(II) was dropped onto each detection zone. The μ-PAD was further kept for a pre-optimized reaction time at room temperature. Immediately after the optimum reaction time was achieved, the μ-PAD was

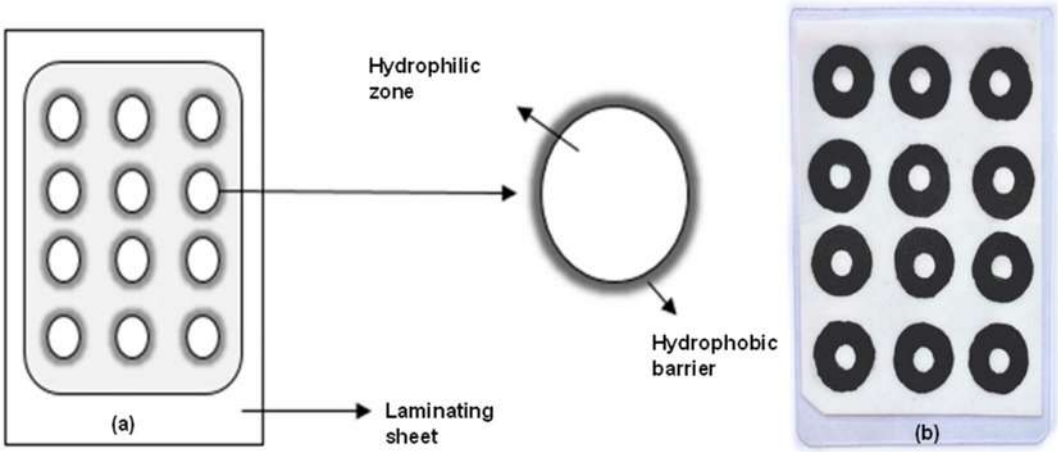

Fig 1. (a) Schematic representation of the proposed μ-PAD. The diameter of the hydrophilic zone was 0.5 cm (b) photographic of the fabricated μ-PAD

placed in a homemade box before the μ-PAD image was captured using the smartphone. In this way, the effect of external radiation by the laboratory lighting conditions could be minimized. Finally, the RGB intensity of each detection zone was determined using the free download software "color picker" from the center of each zone. The optimum RGB intensity was then used to calculate the reflectance of each detection zone using the Birch and Stickle method (Eq. 1) [38].

$$R = -\log \frac{I}{I_0} \quad (1)$$

The R variable indicates the reflectance of each detection zone, I is the mean blue color intensity of each standard or real sample solution, and I_0 shows the mean blue color intensity for the blank. The blank intensity was obtained by performing the measurement using the μ-PAD using deionized water as the replacement.

Prior to the application of the μ-PAD, several important parameters were optimized to obtain the optimum conditions of the measurement using the μ-PAD. The parameters include reagent volume, reaction time, and sample volume. The optimization process was carried out using the univariate technique, where one variable was varied when all the others were kept constant. The highest reflectance obtained for each optimized parameter value was chosen as the optimum combination for further analysis of Mn(II) in real water samples.

The analytical performance of the μ-PAD was assessed by evaluating the analytical figures of merit of the proposed method, including the precision, accuracy, % recovery, LOD and limit of quantitation (LOQ). The precision, accuracy and % recovery of the μ-PAD based method were characterized by measuring the reflectance for 0.02 mg L^{-1} Mn(II) standards (n = 6). The precision of the μ-PAD based method, characterized as the repeatability of the measurement, was described as the relative standard deviation (RSD) and was determined using Eq. (2):

$$\%RSD = \frac{SD}{\bar{x}} \times 100\% \quad (2)$$

where SD is the standard deviation of the measurement and $\bar{x}$ is the average concentration of Mn(II) determined using μ-PAD based method.

The accuracy of the μ-PAD based method was characterized as the % error of the measurement and was determined using Eq. (3):

$$\%E = \left(\frac{\bar{x} - \mu}{\mu} \right) \times 100\% \quad (3)$$

The recovery of the μ-PAD based method was determined using Eq. (4):

$$\%R = \frac{\bar{x}}{\mu} \times 100\% \quad (4)$$

where $\bar{x}$ is the average concentration of Mn(II) determined using μ-PAD based method, and μ is the true concentration of Mn(II).

The LOD was defined as the minimum analyte concentration that can be detected with confidence using the proposed method. It was determined by using Eq. (5).

$$LOD = \frac{3S_Y}{S} \quad (5)$$

The LOQ was characterized as the lowest concentration of the analyte that can be reliably quantified using the proposed method. It was determined by applying Eq. (6):

$$LOQ = \frac{10S_Y}{S} \quad (6)$$

where S_Y is the standard error of the intercept, and S is the slope of the calibration curve of the proposed method.

Selectivity of the μ-PADs

The effect of several interfering cations on the determination of Mn(II) using the proposed μ-PADs was investigated individually by introducing different amounts of each interfering cation in the determination of a 0.2 mg L^{-1} Mn(II). These include the most encountered cations in environmental waters, such as Na(I), K(I), Ca(II), Mg(II), and Fe(III). The response of the μ-PADs indicated as reflectance was measured both in the presence and absence of the interfering ions. The tolerable limit was defined as the amount of interfering ions causing ±5% error in the determination of 0.2 mg L^{-1} Mn(II).

Validation of the μ-PADs

The applicability of the proposed μ-PAD was demonstrated by the measurement of Mn(II) concentration in environmental samples. The natural

water samples used in this research were collected from the surrounding manganese mining sites in Kupang Regency (East Nusa Tenggara Province, Indonesia). Validation was performed by comparing the measurement results using the μ-PAD to the corresponding measurement results obtained using the standard spectrophotometric UV-Vis. The standard spectrophotometric UV-Vis was based on the measurement of colored permanganate absorbance due to the oxidation of Mn(II) ions in the natural water samples by $NaIO_4$ [39]. The quantification of Mn(II) in the natural water samples was performed by comparing the absorbance of the unknown signal with the pre-constructed standard calibration curve. Each sample was measured in triplicates, and the average concentration of Mn(II) was determined.

Stability of the μ-PADs

The stability of the optimized μ-PAD was assessed under two different storage conditions. First, the μ-PAD was stored under laboratory conditions and was kept in an open air at room temperature; second, the μ-PAD was vacuum sealed in a vacuum sealing bag. In both conditions, the μ-PADs were stored in the dark to avoid the degradation of the tannin reagent due to the light effect. The stability of μ-PAD under both storage conditions was studied by measuring the reflectance of their detection zones after the addition of a pre-optimized volume of the Mn(II) standard containing 1 mg L^{-1} Mn(II). For the determination of Mn(II), the devices were removed from storage bags, and left them at room temperature for at least 15 min prior to the addition of the standard solution.

■ RESULTS AND DISCUSSION

Selection of the Commercial Hydrophobic Products

A preliminary study was conducted to assess the suitability of using several commercial products in the fabrication of the hydrophobic barrier on the μ-PADs, including crayons, acrylic spray paint, and acrylic watercolor. The successful μ-PAD was indicated by the ability to contain the aqueous solution within the hydrophobic barrier. The results indicated that hydrophobic barriers produced using acrylic spray paint were unevenly distributed, and the resulting μ-PAD was softened when compared to the original filter paper, which made it tear easily when handling. Moreover, the hydrophobicity test indicated that water dropped into the hydrophilic zone and seeped through the hydrophobic barrier. When a crayon was used as the hydrophobization agent, it was found that the hydrophobic barrier was able to contain the water inside the hydrophilic zone and no water seepage through the hydrophobic barrier was observed. However, the hydrophobic surface of the μ-PADs was found to peel off after the drawing and heating process, and the solidified crayon was clumped on the surface of the paper substrate. On the contrary, the hydrophobic barrier on the μ-PADs created using the acrylic color set results in an evenly distributed hydrophobic barrier which could contain the aqueous solution within the hydrophobic barrier. Based on these results, it was decided that the acrylic color set was selected to create the hydrophobic barrier on the μ-PADs for the further optimization process.

Optimization Results

An initial analysis was performed on the successfully produced μ-PADs using the acrylic color set to select the highest analytical response among the red, green, and blue intensity. The analysis was based on the reaction between the pre-deposited tannin solution with Mn(II) present in the standards/samples. Tannins can form coordination complexes with Mn(II) ions due to their phenolic groups, which can act as ligands. The phenolic groups within tannin molecules can coordinate with the Mn(II) ions through oxygen atoms, forming chelates. This coordination gives rise to the formation of stable complexes Mn(II)-tannin complex with distinctive structures and properties, as shown in Fig. S2. The resulting color change of the tannin indicator on the μ-PADs was captured and then converted to the reflectance based on Eq. (1). Fig. S3 presents the individual reflectance calculated using the red, green, or blue intensity. As seen, the highest analytical response expressed as the reflectance was obtained when calculated using the blue intensity. Therefore, the blue intensity was then chosen and applied as the analytical response for further analytical experiments.

The effect of reagent volume on the reflectance of the μ-PADs was examined within the range of 10–50 μL. It was shown that the reflectance increased following the increase in the volume of the reagent which could be attributed to the increase in the total amount of tannin present in the reagent solution (Fig. 2). However, the reflectance tends to significantly decrease when the volume of the reagent used exceeds 40 μL. This could be due to the excessive volume of water, which fades off the color of the complex formed between tannin and Mn(II). Thus, 40 μL reagent was considered optimum and was used for further experiments.

As an analytical device intended for field analysis, the time required to conduct a measurement is considered a crucial factor. It is expected that the time required per analysis is faster or at least within the range of 5–30 min, which is equal to that of the commercially available Mn(II) test kits. Thus, the interval time required for the analysis was examined within the interval of 10–50 min. The color development time was determined after the introduction of a known volume of Mn(II) standard solution into the hydrophilic zone containing a pre-deposited tannin reagent. The results presented in Fig. 3 indicated that a gradual increase in the color development time was achieved from 10–30 min, after which the reflectance leveled between 30 to 40 min. After 40 min of reaction, a significant decrease in the reflectance was observed, which could be attributed to the degradation of the complex initially formed between Mn(II) and the tannin reagent. Consequently, 30 min of reaction was selected as the optimum color development time for further analytical experiments.

The effect of sample volume on the reflectance was examined between 10–30 μL. The results, presented in Fig. 4. indicated that the reflectance was gradually decreased as the volume of sample was increased from 10 to 30 μL. This was due to the excessive volume of water, which may fade the pre-formed color developed due to the reaction between tannin and Mn(II). Consequently, based on the presented results, a sample volume of 10 μL was selected for further experiment as it yielded the highest reflectance within the range of sample volume examined.

Analytical Figures of Merit

The analytical performance of the μ-PAD for the determination of Mn(II) was evaluated under the pre-optimized conditions, and the corresponding analytical figures of merit are summarized in Table 1. The analytical

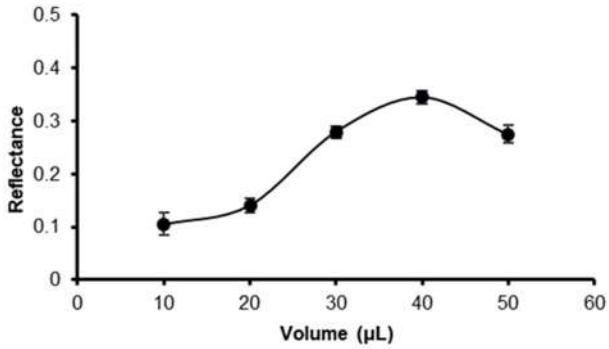

Fig 2. The effect of tannin reagent volume on the reflectance of the μ-PADs

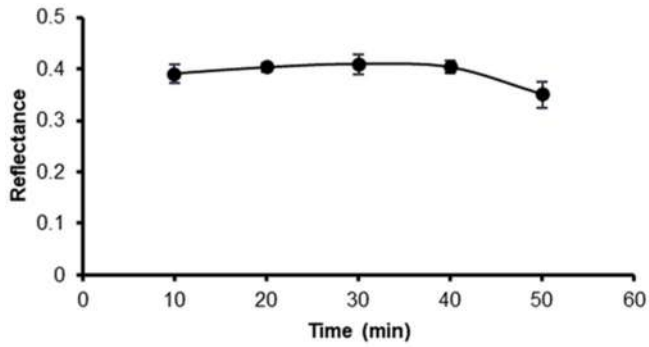

Fig 3. The effect of reaction time on the reflectance of the μ-PADs

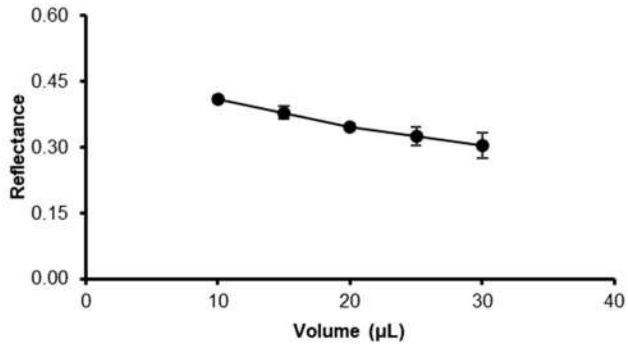

Fig 4. The effect of sample volume on the reflectance of the μ-PADs

Table 1. Analytical figures of merit of the newly developed μ-PAD method for the determination of Mn(II) and the standard reference spectrophotometric UV-vis method

Parameters	Methods	
	Spectrophotometer UV-vis	μ-PAD
Linear range (mg L^{-1})	0–0.25	0.05–0.25
Accuracy (%E)	1.509%	6.697%
Precision (%RSD)	0.311%	1.107%
Recovery (%)	97–105 %	104–112%
Limit of detection (LOD)	0.0068 mg L^{-1}	0.0260 mg L^{-1}
Limit of quantification (LOQ)	0.0227 mg L^{-1}	0.0860 mg L^{-1}

merits of the μ-PAD for the determination of Mn(II), such as linear dynamic range, calibration curve equation, correlation coefficient, accuracy, precision and limit of detection, were studied and compared to that of the standard reference method of spectrophotometric UV-Vis based on the use of $NaIO_4$ reagent. The proposed method offered a relatively satisfied linear dynamic range of 0.05–0.25 mg L^{-1} (Fig. 5) with the regression coefficients for Mn(II) determination described by Eq. (7) where Y is the reflectance and X is the concentration of Mn(II) in mg L^{-1}, respectively. The linear relationship between the reflectance and the concentration of Mn(II) is expressed by coefficient correlation (R^2) of 0.9912, which confirms that the proposed method complied with the Lambert-Beer law of an applicable method (Eq. (7)).

$$Y = 0.360X - 0.0059 \quad (7)$$

The data presented in Table 1 indicated that the accuracy (%E), precision (%RSD) and recovery (%) were 6.697, 1.107, and 104–112 and were all comparable to the corresponding analytical merits obtained using the standard reference spectrophotometric method. The LOD and LOQ of the proposed method, determined by the linear regression method of Miller and Miller, for the determination of Mn(II) were 0.026 and 0.086 mg L^{-1}, respectively [40]. These values are four times higher than the LOD and LOQ of the standard reference method, which are 0.0068 and 0.0227 μg L^{-1}, respectively. However, the LOD and LOQ of the proposed μ-PAD method are lower than the tolerable concentration of Mn(II) in drinking water and clean water specified by the Indonesian Ministry of Health Regulation Number 492/MENKES/PER/IV/2010 of 0.4 mg L^{-1}. These results indicated that the newly developed μ-PAD is suitable for the determination of Mn(II) concentration in drinking water and clean water.

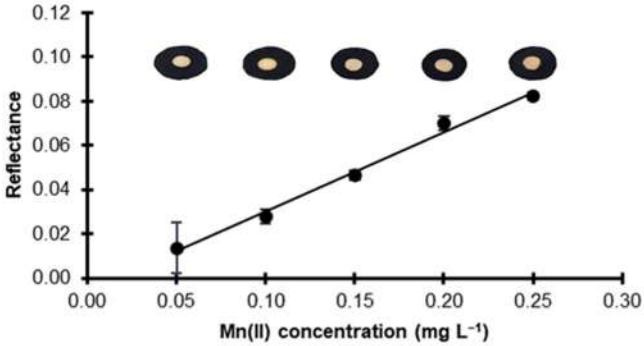

Fig 5. The calibration curve of the μ-PADs for the determination of Mn(II) concentration in water

The Effect of Interfering Cations

Selectivity is obviously one of the most important characteristics of the μ-PAD based method. This property signifies the preference response of the proposed μ-PAD method to the Mn(II) ions with respect to the potential interference effects caused by various interferents. In this research, the primary focus was on the effect of the competing cations such as Na(I), K(I), Ca(II), Mg(II), and Fe(III), as these are the most common cations present in environmental waters and can form complexes with tannin and can thus affect the accurate determination of Mn(II). Under the optimum conditions, each of the interfering cations was added individually to a solution containing 0.2 mg L^{-1} of Mn(II). The introduction of increasing amounts of the interfering ion continued until a tolerable ±5% error in the relative reflectance was observed. Table 2 summarizes the influence of these cations on the relative reflectance of the tannin-Mn(II) complex. The results

Table 2. The tolerable interference effects of Na(I), K(I), Ca(II), Mg(II), and Fe(III) ions on the determination of 0.2 mg L^{-1} Mn(II) using the proposed μ-PAD method

Interfering cations (salt)	Tolerable ratio
Na(I) (NaCl)	50
K(I) (KCl)	50
Ca(II) ($CaCl_2$)	12.5
Mg(II) ($MgSO_4$)	25
Fe(III) ($FeCl_3$)	2.5

revealed that Fe(III) ions had the most severe interference effect when compared to the other investigated interfering cations. However, the co-existence of Fe(III) with Mn(II) in the sample was tolerable up to a ratio of 2.5. The interfering effect of Fe^{3+} indicated a potential cross-sensitivity of the proposed μ-PAD method when determining Mn(II) concentration in a sample containing also Fe(III) ions. However, this unwanted cross-sensitivity caused by the presence of Fe(III) could be eliminated by the addition of 0.5 M orthophosphate as a suitable masking agent, which has been proposed by Zhang et al. [41]. Under this condition, Fe(III) could be precipitated as $Fe_3(PO_4)_2$ prior to the determination of Mn(II) using the proposed method leaving Mn(II) ions to complex with tannin.

While the effect of the other interfering cations was observed at higher ratios compared to that of the Fe(III), these ratios are not sufficiently significant for the determination of Mn(II) in water with high matrix complexity. Thereby, it is anticipated that the use of the proposed method for an accurate determination of Mn(II) was limited in water samples with less complex matrices.

Analysis of Environmental Water Samples

The applicability of the proposed μ-PAD method to measure Mn(II) in water was examined by the determination of Mn(II) in several natural water samples. The results of Mn(II) concentration obtained using the μ-PAD method were compared to those obtained using the standard reference spectrophotometric method and presented in Table 3. A 2-tail Student's t-test was performed to assess the difference in the concentration of Mn(II) determined using the μ-PAD method and the standard reference method. The null hypothesis was accepted (i.e., no statistically significant difference between Mn(II) concentration determined by using both methods) if the calculated t-value was lower than the critical t-value at the selected confidence level (95%). It can be seen from the table that below the LOD of the μ-PAD (i.e., samples 1 and 2), a high deviation of the concentration of Mn(II) determined using μ-PAD method from those determined using the standard reference method was observed. The t-value calculated for both samples were respectively 181.26 and 39.60, while the critical t-value was 2.77 at the 95% confidence level (df = 4). The significantly higher calculated t-value compared to the critical t-value showed the presence of a statistically significant difference between the results of Mn(II) concentration determined by using the μ-PAD method and the standard reference method. Thus, this indicated the limitation of the proposed μ-PAD method to measure Mn(II) concentration in water below its limit of detection.

Above the limit of detection of the proposed μ-PAD method (Sample 3 and 4), the concentration of Mn(II) determined using the μ-PAD method were respectively 0.104 and 0.101 mg L^{-1} while the corresponding Mn(II) concentration determined using standard reference method were 0.105 and 0.097 mg L^{-1}. The t-value calculated for samples 3 and 4 were respectively 0.40 and 1.03, while the critical t-value was 2.77 at the 95% confidence level (df = 4), which indicated

Table 3. Mn(II) concentration in natural water samples collected from the surrounding manganese mining sites (n = 3 per sample) was determined using μ-PAD method and the standard reference method (Spectrophotometric UV-vis)

Sample	Mn(II) concentration (mg L^{-1})		Calculate t-value	Critical t-value (% confidence)
	Spectrophotometric UV-vis	μ-PAD		
1	0.014	0.029	181.26	
2	0.086	0.186	39.60	2.77
3	0.105	0.104	0.40	(95%)
4	0.097	0.101	1.03	

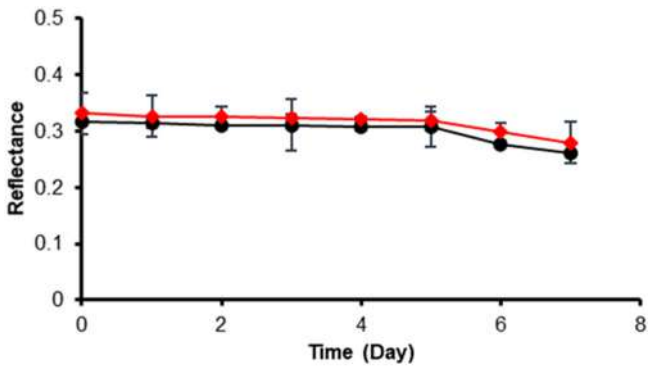

Fig 6. The stability of the μ-PADs for the determination of Mn(II) concentration in water over 7 day examination with the μ-PAD stored in vacuum sealed in a vacuum sealing bag (♦) and in open air at room temperature (•)

that there were no statistically significant differences in the average concentration of Mn(II) determined using the proposed μ-PAD method and the standard reference method. This specified a good agreement between the concentration of Mn(II) determined using the proposed μ-PAD method and the standard reference method, with %Error range from −0.952–4.124. The comparable concentration of Mn(II) in similar samples determined by using both the proposed method and the spectrophotometric method indicated that the proposed method was applicable for the measurement of Mn(II) in the contaminated environmental water. It was important to note that a good agreement between the proposed μ-PAD method and the standard reference method in terms of Mn(II) concentration also indicated no significant effect of interfering cations or anions. These results demonstrated the suitability of the proposed μ-PAD method for the measurement of Mn(II) concentration not only in drinking water or clean water with low interference species but also in natural environmental waters with relatively complex matrix.

Stability Study

One of the most important advantages of the proposed μ-PAD method is its portability for the direct measurement of Mn(II) concentration in the field in remote areas, which requires longer transport time [20]. Therefore, it was an immense important to assess the stability of the μ-PAD as to meet the required transport time to the point of measurement. For this purpose, the μ-PAD was prepared with pre-deposited tannin solution as the green reagent and the stability expressed as reflectance was assessed using a known concentration of Mn(II) solution over a 7-day period under two different storage conditions. Fig. 6 indicated that the in both storage conditions, the reflectance of μ-PAD was stable up to day 5th when assessed using a known concentration of Mn(II). However, after 5 d, the reflectance of μ-PAD under both conditions tends to decrease significantly. These results indicated that, under both storage conditions, the maximum storage time of the μ-PAD prior to the field analysis was 5 d.

■ CONCLUSION

In summary, a new, simple and greener μ-PAD method for the determination of Mn(II) in water has been successfully developed based on the use of tannin as a natural reagent. The proposed μ-PADs were created on a Whatman Number 1 filter paper (9 cm × 8 cm) by a simple drawing technique using a commercially available acrylic watercolor. The detection of Mn(II) was based on the color change observed in the reaction zone of the μ-PAD due to the reaction between Mn(II) and the pre-deposited tannin in the detection zone. The red-green-blue intensity of the complex was captured by a smartphone that functioned as a portable detector, and the blue intensity of the complex digitized using a free-download color picker application was used to calculate the reflectance as the analytical response. It has been demonstrated that the analytical merits of the proposed μ-PAD method, including the accuracy (%E), precision (%RSD) and recovery (%), were 6.697, 1.107, and 104–112 and were all comparable to the corresponding analytical merits obtained using the standard reference spectrophotometric method. The proposed method offered a relatively satisfied linear dynamic range of 0.05–0.25 mg L^{-1} with the limit of detection (LOD), and limit of quantification (LOQ) for the determination of Mn(II) were 0.026 and 0.086 mg L^{-1}, respectively. It was also demonstrated that the μ-PAD was stable for at least 5 days when stored under vacuum-sealed bags. These findings demonstrated that the μ-PAD prepared using a

simple drawing technique using a commercially available acrylic watercolor as the hydrophobization agent and tannin as green reagent could potentially be used as an alternative to the corresponding spectrophotometric method for the on-site determination of Mn(II) in environmental and drinking water samples.

■ ACKNOWLEDGMENTS

This work was financially funded by a DIPA PNBP research grant 2023 No. 15/UN15.15.3.PPK/SPP/FST/IV/2023 of the Faculty of Science and Engineering, University of Nusa Cendana, Kupang, Indonesia. The authors thank Maria F.D. Noe and Yohana F. Dhema for their assistance in the examination of the selectivity of the μ-PAD.

■ AUTHOR CONTRIBUTIONS

Fidelis Nitti formulated the idea, secured funding, performed the experiments and data analysis, supervised the project, wrote the original draft, and revised the manuscript. Wendelina Archangela Ati performed the experiment and data analysis, wrote the original draft, and revised the manuscript. Fidelis Nitti and Wendelina Archangela Ati contributed equally to this work. Philiphi de Rozari, Pius Dore Ola, Luther Kadang formulated the idea, secured funding, supervised the project, and revised the manuscript. David Tambaru wrote the original draft and revised the manuscript. All authors agreed to the final version of this manuscript.

■ REFERENCES

[1] O'Neal, S.L., and Zheng, W., 2015, Manganese toxicity upon overexposure: A decade in review, *Curr. Environ. Health Rep.*, 2 (3), 315–328.

[2] Li, L., and Yang, X., 2018, The essential element manganese, oxidative stress, and metabolic diseases: Links and interactions, *Oxid. Med. Cell. Longevity*, 2018, 7580707.

[3] Iyare, P.U., 2019, The effects of manganese exposure from drinking water on school-age children: A systematic review, *NeuroToxicology*, 73, 1–7.

[4] Bouchard, M.F., Surette, C., Cormier, P., and Foucher, D., 2018, Low level exposure to manganese from drinking water and cognition in school-age children, *NeuroToxicology*, 64, 110–117.

[5] Pfalzer, A.C., and Bowman, A.B., 2017, Relationships between essential manganese biology and manganese toxicity in neurological disease, *Curr. Environ. Health Rep.*, 4 (2), 223–228.

[6] Nádaská, G., Lesny, J., and Michalík, I., 2010, Environmental aspect of manganese chemistry, *HEJ,* ENV-100702-A.

[7] Huang, H.H., 2016, The Eh-pH diagram and its advances, *Metals*, 6 (1), 23.

[8] Andreas, R., and Zhang, J., 2016, Fractionation and environmental risk of trace metals in surface sediment of the East China Sea by modified BCR sequential extraction method, *Molekul*, 11 (1), 42–52.

[9] Kohl, P.M., and Medlar, S.J., 2006, *Occurrence of Manganese in Drinking Water and Manganese Control*, American Water Works Association, Denver, US.

[10] Xu, X., Yang, S., Wang, Y., and Qian, K., 2022, Nanomaterial-based sensors and strategies for heavy metal ion detection, *Green Anal. Chem.*, 2, 100020.

[11] Kumar, K., Saion, E., Yap, C.K., Balu, P., Cheng, W.H., and Chong, M.Y., 2022, Distribution of heavy metals in sediments and soft tissues of the *Cerithidea obtusa* from Sepang River, Malaysia, *Indones. J. Chem.*, 22 (4), 1070–1080.

[12] Noviana, E., Ozer, T., Carrell, C.S., Link, J.S., McMahon, C., Jang, I., and Henry, C.S., 2021, Microfluidic paper-based analytical devices: From design to applications, *Chem. Rev.*, 121 (19), 11835–11885.

[13] Almeida, M.I.G.S., Jayawardane, B.M., Kolev, S.D., and McKelvie, I.D., 2018, Developments of microfluidic paper-based analytical devices (μPADs) for water analysis: A review, *Talanta*, 177, 176–190.

[14] Phansi, P., Janthama, S., Cerdà, V., and Nacapricha, D., 2022, Determination of phosphorus in water and chemical fertilizer samples using a simple

drawing microfluidic paper-based analytical device, *Anal. Sci.*, 38 (10), 1323–1332.

[15] Xia, Y., Si, J., and Li, Z., 2016, Fabrication techniques for microfluidic paper-based analytical devices and their applications for biological testing: A review, *Biosens. Bioelectron.*, 77, 774–789.

[16] Martinez, A.W., Phillips, S.T., Butte, M.J., and Whitesides, G.M., 2007, Patterned paper as a platform for inexpensive, low-volume, portable bioassays, *Angew. Chem., Int. Ed.*, 46 (8), 1318–1320.

[17] Rakkhun, W., Jantra, J., Cheubong, C., and Teepoo, S., 2022, Colorimetric test strip cassette readout with a smartphone for on-site and rapid screening test of carbamate pesticides in vegetables, *Microchem. J.*, 181, 107837.

[18] Tambaru, D., Rupilu, R.H., Nitti, F., Gauru, I., and Suwari, S., 2017, Development of paper-based sensor coupled with smartphone detector for simple creatinine determination, *AIP Conf. Proc.*, 1823 (1), 020095.

[19] Yurike, F., Iswantini, D., Purwaningsih, H., and Achmadi, S.S., 2022, Tyrosinase-based paper biosensor for phenolics measurement, *Indones. J. Chem.*, 22 (5), 1454–1468.

[20] Firdaus, M.L., Aprian, A., Meileza, N., Hitsmi, M., Elvia, R., Rahmidar, L., and Khaydarov, R., 2019, Smartphone coupled with a paper-based colorimetric device for sensitive and portable mercury ion sensing, *Chemosensors*, 7 (2), 25.

[21] Mufidah Sari, P., Daud, A., Sulistyarti, H., Sabarudin, A., and Nacapricha, D., 2022, An application study of membraneless-gas separation microfluidic paper-based analytical device for monitoring total ammonia in fish pond water using natural reagent, *Anal. Sci.*, 38 (5), 759–767.

[22] Meredith, N.A., Volckens, J., and Henry, C.S., 2017, Paper-based microfluidics for experimental design: Screening masking agents for simultaneous determination of Mn(II) and Co(II), *Anal. Methods*, 9 (3), 534–540.

[23] Kamnoet, P., Aeungmaitrepirom, W., Menger, R.F., and Henry, C.S., 2021, Highly selective simultaneous determination of Cu(II), Co(II), Ni(II), Hg(II), and Mn(II) in water samples using microfluidic paper-based analytical devices, *Analyst*, 146 (7), 2229–2239.

[24] Lee, S.A., Lee, J.J., You, G.R., Choi, Y.W., and Kim, C., 2015, Distinction between Mn(III) and Mn(II) by using a colorimetric chemosensor in aqueous solution, *RSC Adv.*, 5 (116), 95618–95630.

[25] Yue, J., Lv, Q., Wang, W., and Zhang, Q., 2022, Quantum-dot-functionalized paper-based device for simultaneous visual detection of Cu(II), Mn(II), and Hg(II), *Talanta Open*, 5, 100099.

[26] Das, A.K., Islam, M.N., Faruk, M.O., Ashaduzzaman, M., and Dungani, R., 2020, Review on tannins: Extraction processes, applications and possibilities, *S. Afr. J. Bot.*, 135, 58–70.

[27] Fraga-Corral, M., García-Oliveira, P., Pereira, A.G., Lourenço-Lopes, C., Jimenez-Lopez, C., Prieto, M.A., and Simal-Gandara, J., 2020, Technological application of tannin-based extracts, *Molecules*, 25 (3), 614.

[28] Shirmohammadli, Y., Efhamisisi, D., and Pizzi, A., 2018, Tannins as a sustainable raw material for green chemistry: A review, *Ind. Crops Prod.*, 126, 316–332.

[29] Üçer, A., Uyanik, A., and Aygün, Ş.F., 2006, Adsorption of Cu(II), Cd(II), Zn(II), Mn(II) and Fe(III) ions by tannic acid immobilised activated carbon, *Sep. Purif. Technol.*, 47 (3), 113–118.

[30] Bacelo, H.A.M., Santos, S.C.R., and Botelho, C.M.S., 2016, Tannin-based biosorbents for environmental applications – A review, *Chem. Eng. J.*, 303, 575–587.

[31] Das, S., and Bhatia, R., 2022, Paper-based microfluidic devices: Fabrication, detection, and significant applications in various fields, *Rev. Anal. Chem.*, 41 (1), 112–136.

[32] Dhavamani, J., Mujawar, L.H., and El-Shahawi, M.S., 2018, Hand drawn paper-based optical assay plate for rapid and trace level determination of Ag^+ in water, *Sens. Actuators, B*, 258, 321–330.

[33] Anushka, A., Bandopadhyay, A., and Das, P.K., 2022, Paper based microfluidic devices: A review of fabrication techniques and applications, *Eur. Phys. J.: Spec. Top.*, 232 (6), 781–815.

[34] Grudpan, K., Kolev, S.D., Lapanantnopakhun, S., McKelvie, I.D., and Wongwilai, W., 2015, Applications of everyday IT and communications devices in modern analytical chemistry: A review, *Talanta*, 136, 84–94.

[35] Jain, B., Jain, R., Jha, R.R., Bajaj, A., and Sharma, S., 2022, A green analytical approach based on smartphone digital image colorimetry for aspirin and salicylic acid analysis, *Green Anal. Chem.*, 3, 100033.

[36] Schlesner, S.K., Voss, M., Helfer, G.A., Costa, A.B., Cichoski, A.J., Wagner, R., and Barin, J.S., 2022, Smartphone-based miniaturized, green and rapid methods for the colorimetric determination of sugar in soft drinks, *Green Anal. Chem.*, 1, 100003.

[37] David, T., Grandivoriana, N.A., and Fidelis, N., 2018, Digital-based image detection system in simple silver nanoparticles-based cyanide assays, *Res. J. Chem. Environ*, 22, 10–14.

[38] Birch, N.C., and Stickle, D.F., 2003, Example of use of a desktop scanner for data acquisition in a colorimetric assay, *Clin. Chim. Acta*, 333 (1), 95–96.

[39] Huang, C.N., Lum, B., and Liu, Y., 2018, Smartphone-assisted colorimetric analysis of manganese in steel samples, *Curr. Anal. Chem.*, 14 (6), 548–553.

[40] Miller, J.C., and Miller, J.N., 1988, *Statistics for Analytical Chemistry*, 2nd Ed., Ellis Horwood Ltd., Chichester.

[41] Zhang, L.L., Cattrall, R.W., and Kolev, S.D., 2011, The use of a polymer inclusion membrane in flow injection analysis for the on-line separation and determination of zinc, *Talanta*, 84 (5), 1278–1283.

Synthesis, Structural Determination and Antibacterial Properties of Zinc(II) Complexes Containing 4-Aminopyridine Ligands

I Wayan Dasna[1,2*], Dewi Mariyam[1], Husni Wahyu Wijaya[1,2], Ubed Sonai Fahruddin Arrozi[1], and Sugiarto Sugiarto[3]

[1]*Department of Chemistry, Faculty of Mathematics and Natural Sciences, Universitas Negeri Malang, Jl. Semarang No. 5, Malang 65145, Indonesia*

[2]*Center of Advanced Material for Renewable Energy, Universitas Negeri Malang, Jl. Semarang No. 5, Malang 65145, Indonesia*

[3]*Department of Applied Chemistry, Graduate School of Advanced Science and Engineering, Hiroshima University, 1-4-1 Kagamiyama, Higashi-Hiroshima 7398527, Japan*

* ***Corresponding author:***

email: idasna@um.ac.id

Received: March 5, 2023
Accepted: May 30, 2023

DOI: 10.22146/ijc.82801

Abstract: *Three zinc(II) complexes containing 4-aminopyridine (4-NH_2py) [Zn(4-NH_2py)$_2$(NCS)$_2$] (**1**), [Zn(4-NH_2py)$_2$Cl$_2$] (**2**), and [Zn(4-NH_2py)$_2$(NCS)Cl] (**3**) were synthesized and characterized by FTIR and single crystal X-ray diffraction. All complexes adopt a slightly distorted tetrahedral geometry with different crystal packing. Complex **1** crystallizes in the orthorhombic Pmmn space group, complex **2** in the monoclinic C2/c space group, and complex **3** in the orthorhombic Pbca space group. Non-covalent interactions such as NC-S···H, -Cl···H, and μ-μ stacking interaction between 4-NH_2py and other ligands (NCS^- and Cl^-) are observed in the crystals packing.* In vitro, *antibacterial screening of all complexes was evaluated against two bacteria (*Escherichia coli *and* Staphylococcus aureus*). The results show that **1** has the highest antibacterial activity than **2** and **3**. This difference is due to differences in the interactions elicited by the anion ligands.*

Keywords: *zinc(II) complexes; 4-NH_2py; thiocyanato; chloro ligand; antibacterial activity*

INTRODUCTION

Transition metal complexes of nitrogen heterocyclic ligands, such as pyridine and its derivatives, have garnered a lot of interest due to their interesting properties, such as catalysts, developing photographic images, antimicrobial agents, and thermal reaction batteries [1]. Moreover, complexes with aminopyridine have been studied due to their potential as antibacterial agents [2-4]. Complexes with aminopyridine ligand such as poli-[Cu(NCS)$_2$(x-NH_2py)$_2$] [2], [Cd(μ-L)$_2$(NH_2py)$_2$] (L = SCN^-, dca, N_3^-) [5-7], [Mn(L)$_2$(3-NH_2py)$_2$] (L = dca, SCN^-) [5-6,8] and [Co(dca)$_2$(2-NH_2py)$_2$] [3] have shown to form a polymeric structure through bidentate ligands such as dicyanamide ion (dca), nitride ion (N_3^-) and ambidentate ligand such as SCN^-. The polymeric complexes can be obtained as long as octahedral coordination of the metal center is preserved, whereas complex compounds with tetrahedral geometry such as [Zn(NCS)$_2$(x-NH_2py)$_2$] (x = 2 and 3) [9-10], [Zn(CN)$_2$(x-NH_2py)$_2$] [11], [MCl$_2$(x-NH_2py)$_2$] (M = Zn(II), Co(II) [4,12] tend to form monomeric complexes [9,13-14]. In addition, the aminopyridine ligands prefer to act as monodentate ligands, with amino groups acting as potential H-bond donors or acceptor sites [8-9,15] Meanwhile, the bidentate anion-ligands such as thiocyanate, dicyanamide, and acetate are potential ligands to form coordination polymer. This indicates that ligands and metal ions affect the structure of aminopyridine-based complexes.

The structure of the complexes also affects their antibacterial activity. Some ligands can increase the lipophilicity of complexes. The increase in lipophilicity allows it to penetrate the lipid layer of the bacterial

membrane [16]. Functional groups on pyridines such as $-NH_2$, −OR, −CN, and −Br might increase antibacterial activity through the formation of bonding with lipopolysaccharides in the cell walls and change its spatial structure [17]. Complex $[CdL^I(SCN)_2]$ showed higher antibacterial activity against *Escherichia coli* and *Bacillus subtilis* than $[CdL^II]I$ (L^I = 3,10-*C*-*meso*-3,5,7,7,10,12,14,14-octamethy1-1,4,8,11-tetraazacy clotetradeca-4,11-diene) [18]. These results show that the combination of ligands is an important factor in designing effective antimicrobial agents.

In this work, we have synthesized three complexes of zinc(II) and 4-NH_2py with different anionic ligands, i.e., $[Zn(NCS)_2(4\text{-}NH_2py)_2]$ (**1**), $[ZnCl_2(4\text{-}NH_2py)_2]$ (**2**), and $[ZnCl(NCS)(4\text{-}NH_2py)_2]$ (**3**). Thiocyanate is one of the favored substrates for lactoperoxidase (LPO)-driven catalytic reduction of hydrogen peroxide (H_2O_2) to generate hypothiocyanous acid (HOSCN), a potent antimicrobial agent and better tolerated by host tissue [19-20]. Moreover, chloride (Cl^-) is one of the substrates that can generate hypochlorite (OCl^-) in myeloperoxidase (MPO) defensive peroxidase systems [21]. Chloride in the form of salt (NaCl) also inhibits microbial growth through an osmotic process. It draws water out of the bacterial cells causing the bacterial cells to shrink and die [22-23]. Therefore, chloride and thiocyanate anions were used in this study. *In vitro*, the antibacterial activity of the three complexes was also evaluated against *Staphylococus aureus* and *Escherichia coli*.

■ EXPERIMENTAL SECTION

Materials

The materials used in this study, zinc(II) chloride anhydrous ($ZnCl_2$, Merck, p.a. 98%), potassium thiocyanate (KSCN, Emsure, p.a. 99%), 4-aminopyridine (4-NH_2py, Sigma Aldrich, p.a. 98%), methanol (CH_3OH, Emsure p.a. 99%), and aquadest, were used without further purification.

Instrumentation

The instrumentations used in this study were Fourier-transform spectrophotometer (IRPrestige21, Shimadzu, Japan), conductivity meter (Cyberscan CON 11/110, Eutech Instruments, USA), X-ray single crystal diffraction spectroscopy (Bruker SMART APEX 2, USA), and melting point apparatus (Fisher-John 48061, Thermo Scientific, USA).

Procedure

Synthesis of complex $[Zn(NCS)_2(4\text{-}NH_2py)_2]$

A $ZnCl_2$ (0.1363 g, 1 mmol) in 5 mL CH_3OH was mixed into a 5 mL solution of 4-NH_2py (0.1882 g, 2 mmol) and stirred continuously for 2 h. Then, KSCN (0.1944 g, 2 mmol) was added slowly. Heating under reflux and stirring was continued for up to 4 h. The needle-shaped crystals were obtained after several days. Yield: 76.30%, melting point: 220–223 °C.

Synthesis of complex $[ZnCl_2(4\text{-}NH_2py)_2]$

A $[ZnCl_2(4\text{-}NH_2py)_2]$ was synthesized according to a previous report [10]. A $ZnCl_2$ (0.1363 g, 1 mmol) that had been dissolved in 5 mL CH_3OH was mixed with 4-NH_2py (0.1882 g, 2 mmol). The mixture was heated at 64 °C under reflux for 6 h while being continuously stirred. The final solution was chilled to room temperature. Colorless crystals were formed after several days. Yield: 61.23%, melting point: 245–248 °C.

Synthesis of complex $[ZnCl(NCS)(4\text{-}NH_2py)_2]$

A $ZnCl_2$ (0.1363 g, 1 mmol) in 5 mL CH_3OH was mixed into 5 mL solution of 4-NH_2py (0.1882 g, 2 mmol) and stirred continuously for 2 h. Then, KSCN (0.0927 g, 1 mmol) was added slowly. Heating under reflux and stirring was continued for up to 4 h. After a week, colorless crystals were obtained. Yield: 53.79%, melting point: 214–215 °C.

Characterization technique

Melting point temperature was measured in the range of 30–300 °C using a Fisher-John melting point apparatus. The electrical conductivity of complex solutions was measured using Cyberscan CON 11/110 conductivity meter. The infrared spectra were recorded using Shimadzu spectrophotometer type IRPrestige21 on KBr pellets in the range 4000–400 cm^{-1}.

Single crystal X-ray structure determination

Intensity data were gathered at 123 K using Bruker SMART APEX2 diffractometer equipped with a CCD area detector and Mo Kα source (λ = 0.71073 Å)

monochromated by layered confocal mirrors. Data reduction and scaling were performed using Bruker APEX3 suite, and absorption correction was performed using SADABS. SHELXT was used to solve the initial structure, revealing non-hydrogen atoms' positions, which were refined using the SHELXL program on a ShelXle user interface. Anisotropic refinement was performed on non-hydrogen atoms. Hydrogen atoms were placed in the calculated positions using a riding model.

Antibacterial tests

The antibacterial tests were conducted in the Laboratory of Microbiology, Universitas Negeri Malang. The tests were done on different types of pathogen bacteria, gram-positive- *S. aureus* and gram-negative- *E. coli*. The reference antibacterial drug chloramphenicol was evaluated for its antibacterial activity, and the results were compared with those of the free ligands and the complexes. Samples were dissolved in the DMSO 10% to obtain a 5 mg/mL solution. The method used is the disc diffusion method [13,16]. The disc containing antimicrobial agents or compounds was applied to the MHA plate within 20 min after inoculating it with the bacteria. Three discs were coated per petri dish. The plates were inverted and incubated at 37 °C for 24 h. After that, the zones of complete inhibition were measured.

■ RESULTS AND DISCUSSION

Synthesis of Complexes $[Zn(NCS)_2(4\text{-}NH_2py)_2]$ (1), $[ZnCl_2(4\text{-}NH_2py)_2]$ (2), $[ZnCl(NCS)(4\text{-}NH_2py)_2]$ (3)

Three complexes **1**, **2**, and **3** were reacted directly in CH_3OH as a solvent with the mol ratio Zn(II): 4-NH_2py: KSCN of 1:2:0 (complex **1**), 1:2:1 (complex **2**), and 1:2:2 (complex **3**). The results gave colorless crystals with several shapes like needle and beam-shaped, as shown in Fig. 1. The reaction of complex formation is presented in Fig. 2. The reaction of $ZnCl_2$ with 4-NH_2py produced complex $[ZnCl_2(4\text{-}NH_2py)_2]$, then the addition of NCS^- ion substituted the Cl^- ligand to form complexes $[ZnCl(NCS)(4\text{-}NH_2py)_2]$ and $[Zn(NCS)_2(4\text{-}NH_2py)_2]$. Based on the spectrochemical series (Fajans-Tsuchida), the NCS^- ion is stronger than the chloride anion ligand; thus NCS^- can replace Cl^- ligand to form complexes **1** and **3** [24].

Physical Properties of Zinc(II) Complexes 1, 2, 3

All complexes **1**, **2**, and **3** were obtained as colorless crystals (Fig. 1). Complex **1** is needle-shaped crystal (Fig. 1(a)), while complexes **2** (Fig. 1(b)), and **3** (Fig. 1(c)) were block-shaped crystals. The three complexes are air-stable and have sharp melting points around > 200 °C. The melting point data of the three complexes are higher

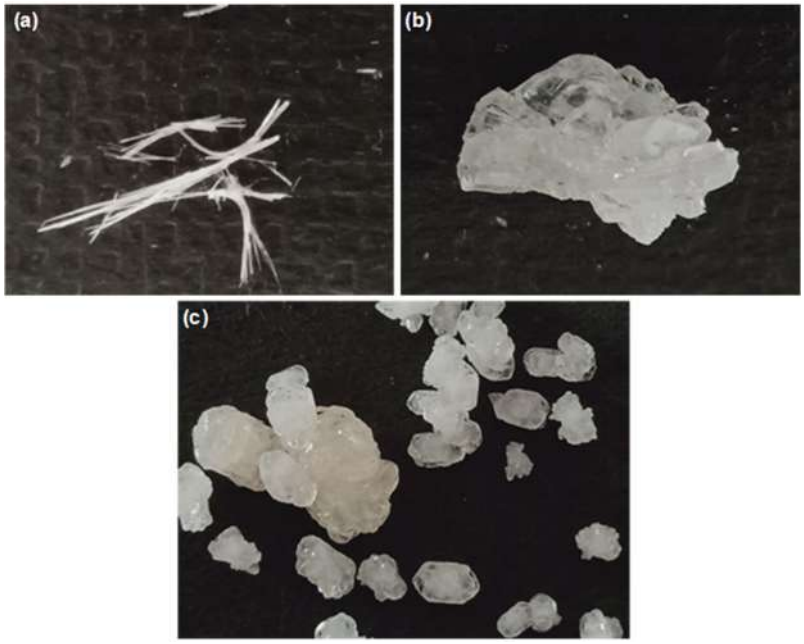

Fig 1. Crystal images of (a) $[Zn(4\text{-}NH_2py)_2(SCN)_2]$ (**1**); (b) $[ZnCl_2(4\text{-}NH_2py)_2]$ (**2**); (c) $[ZnCl(NCS)(4\text{-}NH_2py)_2]$ (**3**)

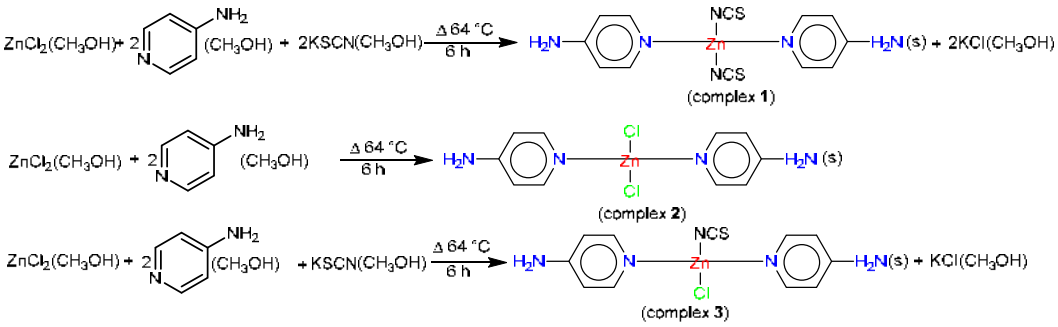

Fig 2. Reaction of the formation Zn(II) complexes **1**, **2**, and **3**

than complex $[Zn(NCS)_2(2\text{-}NH_2py)_2]$ [10] and $[Co(NCS)_2(2\text{-}NH_2py)_2]$ [25]. This could be due to the stronger intermolecular interactions of complexes **1**, **2**, and **3** compared to the two complexes. All complex solutions have been measured for their electrical conductivity in 1 mg/mL using CH_3OH solvent and showed the results: 101.5 μS (complex **1**), 96.3 μS (complex B2), 54.7 μS (complex **3**). These results show that complex solutions are non-electrolytes [26].

Structural Determination of Complexes 1, 2, 3

The reaction between $ZnCl_2$, KSCN, and 4-NH_2py leading to the formation of complexes $[Zn(NCS)_2(4\text{-}NH_2py)_2]$ (**1**), $[ZnCl_2(4\text{-}NH_2py)_2]$ (**2**), and $[ZnCl(NCS)(4\text{-}NH_2py)_2]$ (**3**). The structural determination of all complexes was carried out using single-crystal XRD. The crystallographic data of complexes are shown in Table 1.

Table 1. Crystallographic data

Compound	1	2	3
No. CCDC	2224923	2224925	2224924
Empirical formula	$C_{12}H_{12}N_6S_2Zn$	$C_{10}H_{12}Cl_2N_4Zn$	$C_{11}H_{12}ClN_5SZn$
Empirical mass	369.79	324.53	347.16
System	Orthorombic	Monoclinic	Orthorombic
Space group	Pmmn	C2/c	Pbca
a (Å)	12.9473	8.8309(7)	10.2571(11)
b (Å)	14.3833	9.8240(7)	16.1744(17)
c (Å)	4.1770(8)	14.9961(11)	17.2842(18)
α (°)	90	90	90
β (°)	90	102.3360(10)	90
γ (°)	90	90	90
V (Å^3)	777.827	1268.40(16)	2867.5(5)
Z	2	4	8
T (K)	123	123	123
λ Mo Kα (Å)	0.71073	0.71073	0.71073
F_{000}	376	656	1408
μ (mm^{-1})	1.848	2.339	2.037
D_{calc} (mg/m^3)	1.579	1.699	1.608
θ_{min} (°)	2.116	3.143	2.357
θ_{max} (°)	27.472	27.495	27.574
Goodness of fit	1.129	1.092	1.051
R1 (1 > 2σ(I))	0.0188	0.0209	0.0258
wR2	0.0492	0.0554	0.0611

The structure of complex molecules is shown in Fig. 3. According to Fig. 3, the central ion of all complexes is bonded with two N atoms from two 4-NH_2py molecules and two anions as the ligands to form distorted tetrahedral geometry [8,27-29]. While the bond length of Zn–N pyridine in all complexes has a similar bond length, the angle between N–Zn–N has different distortion depending on ligands [30] (Fig. 4). The bond length of Zn–N2 (2.104 Å) is longer than that of Zn–N1 (1.970 Å) due to the different size of the two ligands. A 4-NH_2py ligand is larger than the NCS^-, and the larger molecular size causes a stronger steric effect; as a result, the distance between Zn and 4-NH_2py is farther apart to reduce the repulsion effect. The steric effect of the ligand also affects the angle of N2–Zn–N2^i, which is larger than that of N1–Zn–N1^i. The angle between N1–Zn–N2 is smaller than the N2–Zn–N2^i bond angle because the position of 4-NH_2py gives minimal repulsion. Complex **1** also shows a larger N2–Zn–N2 angle distortion compared to complexes **2** and **3**. This may be due to the electronegativity of the N atom of NCS^- (X N = 3.06) being higher than Cl^- (X = 3.16) [31]; the more electronegative the atom, the more it will pull, the more electron density to itself. This decreases the electron pair repulsion between bonded electron pairs on the central atom. Cl^- ligand will pull the bonded electron pair towards itself and away from the central atom. Bond angles between the groups should be reduced when the core atom's electron pair repulsion decreases, so the bond angle between Cl–Zn–Cl will decrease. In addition, the Zn–NCS bonds lengths are shorter compared to Zn–Cl, shorter bond length permits electron-density to be displaced towards zinc to a smaller extent than in Zn–Cl, thus more electron density remains and electron repulsion between the bonded pairs in complex **1** increases and bond angles of complex **1** increases compared to that complex **2** and **3**.

Complex **2** shows that the Zn–Cl bond is longer than that for Zn–N1 (Table 2). This is related to the covalent radius of Cl, which is much longer than the covalent radius N. The angle formed between N1–Zn–N1 and Cl1–Zn–Cl1 in the complex is also smaller than the angle in complex **1**. This is related to the more electronegative of Cl^- ions. The Cl atom will attract the

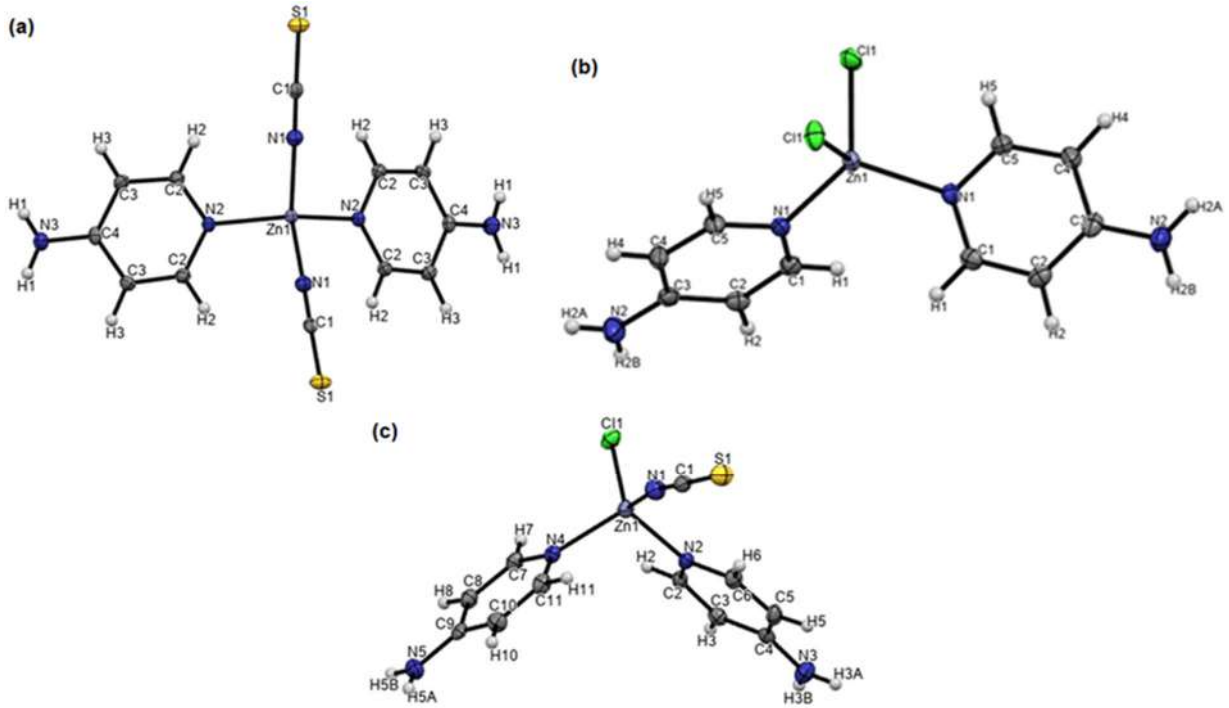

Fig 3. ORTEP view of the structures of (a) [Zn(NCS)$_2$(4-NH_2py)$_2$] (**1**); (b) [$ZnCl_2$(4-NH_2py)$_2$] (**2**); (c) [ZnCl(NCS)(4-NH_2py)$_2$] (**3**), showing the atom-labelling scheme. Displacement ellipsoids are drawn at the 50% probability level

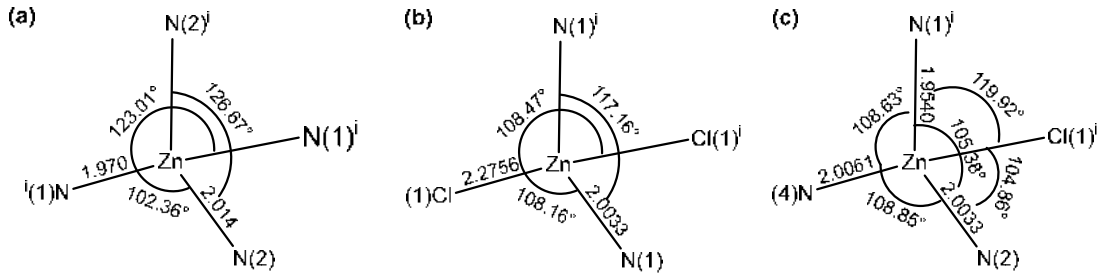

Fig 4. Chemical structures of complexes (a) $[Zn(NCS)_2(4\text{-}NH_2py)_2]$ (**1**); (b) $[ZnCl_2(4\text{-}NH_2py)_2]$ (**2**); (c) $[ZnCl(NCS)(4\text{-}NH_2py)_2]$ (**3**)

Table 2. Selected bond lengths (Å) and angles (°) of **1**–**3**

Complex **1**			
Zn1–N1^i	1.9698(16)	N1^i–Zn1–N1	123.01(10)
Zn1–N1	1.9698(16)	N1^i–Zn1–N2^i	102.36(3)
Zn1–N2^i	2.0140(15)	N1–Zn1–N2^i	102.36(3)
Zn1–N2	2.0141(15)	N1^i–Zn1–N2	102.36(3)
		N1–Zn1–N2	102.36(3)
		N2^i–Zn1–N2	126.67(9)
Complex **2**			
Zn1–N1	2.0033(13)	N1–Zn1–N1^i	117.61(7)
Zn1–N1^i	2.0033(13)	N1–Zn1–Cl1	107.09(4)
Zn1–Cl1	2.2756(4)	N1^i–Zn1–Cl1	108.16(4)
Zn1–Cl1^i	2.2756(4)	N1–Zn1–Cl1^i	108.16(4)
		N1^i–Zn1–Cl1^i	107.09(4)
		Cl1–Zn1–Cl1^i	108.47(2)
Complex **3**			
Zn1–N1	1.9540(16)	N1–Zn1–N4	108.63(7)
Zn1–N4	2.0061(15)	N1–Zn1–N2	105.38(6)
Zn1–N2	2.0192(15)	N4–Zn1–N2	108.85(6)
Zn1–Cl1	2.2575(5)	N1–Zn1–Cl1	119.92(5)
		N4–Zn1–Cl1	108.72(4)
		N2–Zn1–Cl1	104.86 (5)

bonding electrons in its own direction, thereby reducing the bonding electron repulsion on the central atom. In addition, the presence of lone pair electrons in the Cl ligand also reduces the angle of Cl1–Zn–Cl1, N1–Zn–N1, and N1–Zn–Cl1 in complex **2**. This is because the high electrical charge of lone pair electrons causes a strong repulsion, the bond becomes longer, and the angle becomes smaller.

The three complexes have the same geometry; however, they crystallize in different space groups. Complex **1** is isostructural with $[Co(NCS)_2(4\text{-}NH_2py)_2]$ [27], it crystallizes in an orthorhombic space group Pmmn, and there are complex **2** molecules of $[Zn(NCS)_2(4\text{-}NH_2py)_2]$ in 1 unit cell (Fig. 5(a)). The Zn(II) ion in complex **1** is in the special mm2 position, and the asymmetric unit only contains a quarter of the molecule. Weak interaction was also observed between the H from the NH_2 group and the S of SCN (N-H···S-CN) (2.715 Å). Complex **2** showed an isostructural result with complex $[CoCl_2(4\text{-}NH_2py)_2]$ that was reported by Sanchez Montilva et al. [12]. Complex from $ZnCl_2$ and 4-NH_2py have been synthesized by Moustafa et al. [4], but the obtained complex had a different structure from the complex we reported. As-synthesized complex **2** crystallizes in monoclinic with the C2/c space group and 4 complex molecules in each unit cell (see Fig. 5(b)). The central atom is located on 2 folding axes, and the asymmetric unit only contains half of the molecule. Non-covalent interactions such as N-H···Cl (2.8336 Å) and weak μ···μ stacking interactions between C atoms of two 4-NH_2py (C4···C5 3.371 Å) and (C4···C4 3.172 Å) are observed in complex **2**. The non-covalent interaction of N-H···Cl enables the formation of unlimited chains through the ac plane. Meanwhile, asymmetric complex **3** crystallizes in the Pbca group with 8 molecules in each unit cell (see Fig. 5(c)). Weak interaction between Cl···H-NH (2.554 Å) and S···H-NH (2.843 Å) are also observed in the packing crystal system of complex **3**.

FTIR Spectroscopy

Although it is commonly accepted that for N-bound thiocyanate complexes, ν_{SC} exhibits higher frequency values and ν_{CN} shows lower frequency values, these principles must be applied with caution because a variety of other factors can affect the locations of these bands.

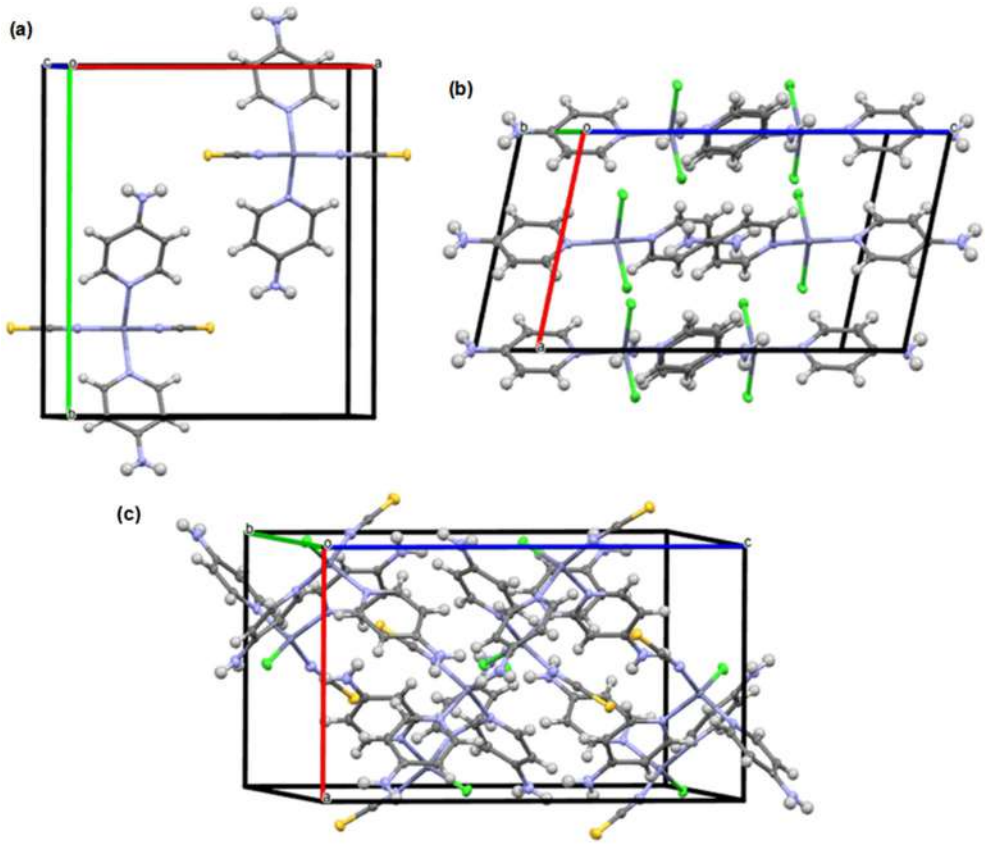

Fig 5. Packing diagrams of (a) $[Zn(NCS)_2(4\text{-}NH_2py)_2]$ (**1**); (b) $[ZnCl_2(4\text{-}NH_2py)_2]$ (**2**); (c) $[ZnCl(NCS)(4\text{-}NH_2py)_2]$ (**3**)

Table 3. Selected wavenumbers (cm^{-1}) of ligands in the tree complexes

Assignment	4-NH_2py	KSCN	**1**	**2**	**3**
$\nu_{as}(NH_2)$	3439s		3443s	3443s	3470s
$\nu_s(NH_2)$	3305s		3341s	3341s	3346s
ν_{ring}	1682s, 1584s, 1337s		1655s, 1633s, 1362m	1659s, 1634s, 1352s	1643s, 1634s, 1352s
$\nu(C\text{-}NH_2)$	1217s		1219s	1223s	1211s
ν_{CN}		2170s	2056m		2050m
ν_{SC}		743s	817s		829s

We already know, based on the crystal structure, that all metal ions of complexes **1**-**3** are bonded to the thiocyanate ions through the N atom. This is also proved by the appearance of ν_{CN} bands around 2050 cm^{-1} (Table 3) [2,32]. The ν_{SC} in complexes **1** and **3** were observed around 820–850 cm^{-1}. These bands are in accordance with N–bonding behavior (ν_{SC} 760–860 cm^{-1}) compared to S–bonding behavior (ν_{SC} 690–720 cm^{-1}) (Fig. 6). Meanwhile, according to structure crystals data, it appears that 4-NH_2py ligands bind to the Zn(II) ions through the nitrogen atom of the pyridine ring. The $\nu(NH_2)$ (symmetric and asymmetric) bands do not show a significant shift in wavenumber (see Table 3), and it is generally known that the NH_2 stretching vibrations undergo a significant red shift when $-NH_2$ in 2-aminopyridine forms a coordination bond with metal ions (Δ = 150–200 cm^{-1}) [33]. Therefore, it is proved that the NH_2 group is not directly involved in the formation of coordination bonds.

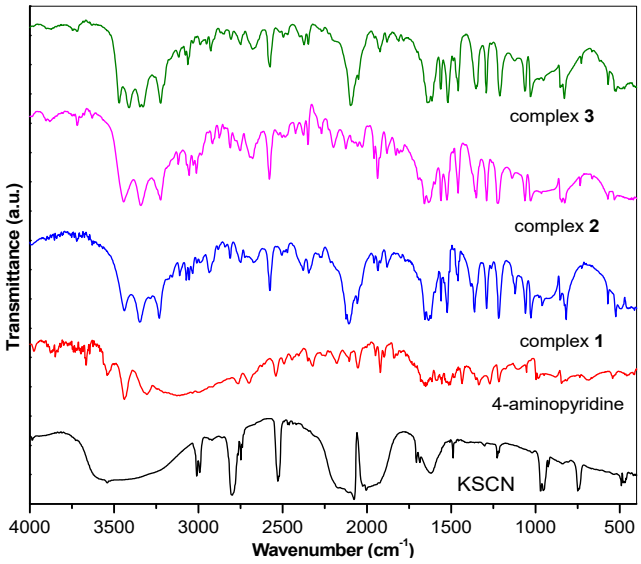

Fig 6. FTIR spectra of complexes and ligands

Antibacterial Activity

Fig. 7 and 8 show the results of the antibacterial test of complexes **1**, **2** and **3** against *E. coli* and *S. aureus*. The test results in the form of the diameter of the inhibition zones (mm) are presented in Table 4. Fig. 4 and 5 show that complexes **1** and **2** give a better antibacterial activity than their metal salt and free ligands. We observed that the antibacterial activity of complexes and 4-NH_2py is through the formation of hydrogen bonds between the cell membrane and N atom from 4-NH_2py and blocking the way for nutrients to enter the cell [17]. The antibacterial activity of complexes increase in order [Zn(4-NH_2py)$_2$Cl$_2$] (**2**) < [Zn(4-NH_2py)$_2$(NCS)Cl] (**3**) < [Zn(4-NH_2py)$_2$(NCS)$_2$] (**1**). This indicates that co-ligands also play an important role in increasing their antimicrobial activity. Complexes with thiocyanate exhibit better antibacterial activity than that with chloride ions. The

Table 4. Diameter of inhibition zones of the ligands, metal salt and complexes

Compounds	Inhibition zones (mm)	
	S. aureus	*E. coli*
4-NH_2py	6.7	6.3
KSCN	10.0	6.7
$ZnCl_2$	7.5	11.9
[Zn(4-NH_2py)$_2$(NCS)$_2$] (**1**)	11.6	12.1
[Zn(4-NH_2py)$_2$Cl$_2$] (**2**)	6.8	6.0
[Zn(4-NH_2py)$_2$(NCS)Cl] (**3**)	11.1	10.8
Chloramphenicol	31.5	34.0

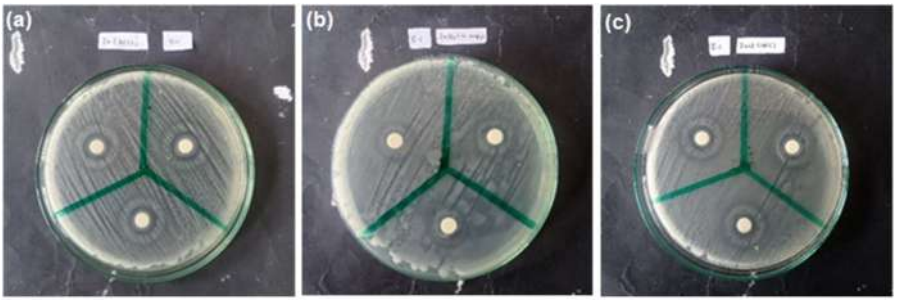

Fig 7. Zone inhibition against *E. coli* with complexes (a) **1**; (b) **2**, and (c) **3**

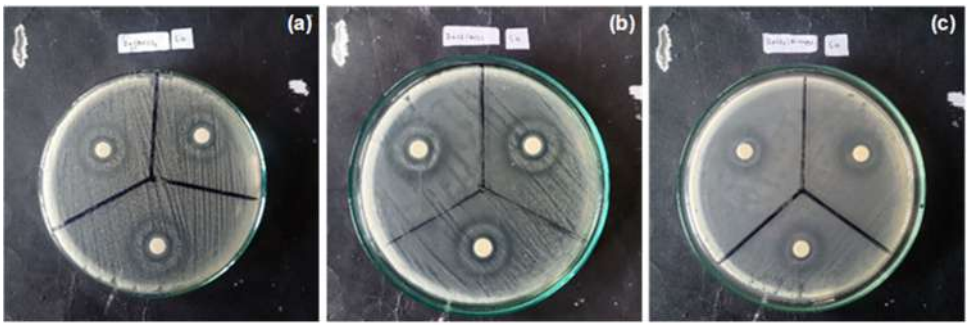

Fig 8. Zone inhibition against *S. aureus* with complexes (a) **1**; (b) **2**, and (c) **3**

antibacterial activity of a complex is affected by its structure and stability, acid-base properties, donor atoms, lipophilicity and the most preferred binding site for biomolecules [34]. We hypothesize that increasing antibacterial activity in these complexes was influenced by several factors. First, based on the spectrochemical series (Fajans-Tsuchida), NCS^- is a stronger ligand than Cl^- [31], leading to the interaction NCS^- with Zn(II) is stronger than Zn(II) and Cl^-. This interaction will decrease the polarity of the metal ion due to the partial sharing of positive charge with the donor atom, resulting in the delocalization of electrons within metal complexes [3,16,25]. This may increase the lipophilic character of the metal complex, thus allowing it to penetrate the lipid layer of the bacterial membrane more easily [3,16,25]. Secondly, the slow release of Zn(II) in bacteria cells could lead to an interaction formation of the metal ion with nucleic acids and deactivate the enzymes of the respiratory system [35]. Lastly, the substituent group, such as $-NH_2$ interacts with a polar site of bacteria cell wall and disrupt the passage of solutes between the cell and the outer environment [36-39]; the metal ions also could bind to SH (sulfhydryl group) of the cell enzyme and breakdown the cell membrane [40]. Several other complexes, such as $[Zn(NCS)_2(2\text{-}NH_2py)_2]$ [10], $[Co(L)_2(2\text{-}NH_2py)_2]$ (L = $[N(CN)_2]$, NCS^-) [3,25], have been reported to exhibit a low to moderate antibacterial activity. The complex **1** has similar inhibition zones with $[Zn(NCS)_2(2\text{-}NH_2py)_2]$ [10] around 11 mm, while $[Co(L)_2(2\text{-}NH_2py)_2]$ (L = $[N(CN)_2]$, NCS^-) [3,25], and $[Mn(dca)_2(2\text{-}NH_2py)_2]$ [7] have higher antibacterial activity than the three complexes.

CONCLUSION

Three complexes $[Zn(4\text{-}NH_2py)_2(NCS)_2]$ **1**, $[Zn(4\text{-}NH_2py)_2Cl_2]$ **2**, and $[Zn(4\text{-}NH_2py)_2(NCS)Cl]$ **3** have been successfully synthesized, and the yields obtained were 76.30%, 61.23%, and 53.79%, respectively. The Zn(II) in all complexes bind two N atoms of two $4\text{-}NH_2py$ rings and 2 anionic ligands to form distorted tetrahedral geometry. The three complexes crystallize in different crystal lattices such as Pmmn (**1**), C2/c (**2**), and Pbca (**3**). Non-covalent interactions between $4\text{-}NH_2py$ and anionic ligands are observed to play a role in the crystal packing of all complexes. The preliminary antimicrobial screening against *S. aureus* and *E. coli* bacteria indicates that the complexes are moderately active. In this study, the complexes with thiocyanate ion exhibit greater antibacterial activity than with chloride ion due to stronger interaction with the central ion that leads to the increasing the lipophilic character of the metal complex.

SUPPORTING INFORMATION

Crystallographic data for the structural information have been put on deposit in the Cambridge Crystallographic Data Centre, CCDC no. 2224923-2224925. Copies of this information may be obtained from The Director, CCDC, 12 Union Road, Cambridge, CB2 1EZ, UK (fax: +44-1233-336033; e-mail: deposit@ccdc.cam.ac.uk or www: http://www.ccdc.cam.ac.uk).

ACKNOWLEDGMENTS

Universitas Negeri Malang, Indonesia, is gratefully acknowledged for funding this research through Internal funds in 2022 (contract number: 19.5.909/UN32.20.1/LT/2022). We also thank the Department of Applied Chemistry at Hiroshima University for using XRD single crystal.

AUTHOR CONTRIBUTIONS

I Wayan Dasna and Dewi Mariyam conducted the experiment. I Wayan Dasna, Husni Wahyu Wijaya and Dewi Mariyam concept the methodology. Sugiarto conducted the structure crystal determination, and I Wayan Dasna, Husni Wahyu Wijaya, Ubed Sonai Fahruddin Arrozi, Sugiarto and Dewi Mariyam wrote and revised the manuscript. All authors agreed to the final version of this manuscript.

REFERENCES

[1] Pal, S., 2018, "Pyridine: A Useful Ligand in Transition Metal Complexes" in *Pyridine*, Eds. Pandey, P.P., IntechOpen, Rijeka, Croatia, 57–74.

[2] Handy, J.V., Ayala, G., and Pike, R.D., 2017, Structural comparison of copper(II) thiocyanate pyridine complexes, *Inorg. Chim. Acta*, 456, 64–75.

[3] Yuoh, A.C.B., Agwara, M.O., Yufanyi, D.M., Conde, M.A., Jagan, R., and Oben Eyong, K., 2015, Synthesis, crystal structure, and antimicrobial properties of a novel 1-D cobalt coordination polymer with dicyanamide and 2-aminopyridine, *Int. J. Inorg. Chem.*, 2015, 106838.

[4] Moustafa, M.E., Meshal, N.M., Ayad, M.I., and Goda, O.A., 2020, Aminopyridine transition metals complexes; Characterization, application and molecular orbital calculation, *Benha J. Appl. Sci.*, 5 (7), 231–243.

[5] Mautner, F.A., Jantscher, P., Fischer, R.C., Torvisco, A., Vicente, R., Karsili, T.N.V., and Massoud, S.S., 2019, Synthesis and characterization of 1D coordination polymers of metal(II)-dicyanamido complexes, *Polyhedron*, 166, 36–43.

[6] Suckert, S., Terraschke, H., Reinsch, H., and Näther, C., 2017, Synthesis, crystal structures, thermal, magnetic and luminescence properties of Mn(II) and Cd(II) thiocyanate coordination compounds with 4-(Boc-amino)pyridine as co-ligand, *Inorg. Chim. Acta*, 461, 290–297.

[7] Mbani, A.L.O., Yufanyi, D.M., Tabong, C.D., Hubert, N.J., Yuoh, A.C.B., Paboudam, A.G., and Ondoh, A.M., 2022, Synthesis, crystal structure, DFT studies and Hirshfeld surface analysis of manganese(II) and cadmium(II) coordination polymers of 2-aminopyridine and dicyanamide, *J. Mol. Struct.*, 1261, 132956.

[8] Mautner, F.A., Jantscher, P.V., Fischer, R.C., Torvisco, A., Reichmann, K., and Massoud, S.S., 2021, Syntheses, structural characterization, and thermal behaviour of metal complexes with 3-aminopyridine as co-ligands, *Transition Met. Chem.*, 46 (3), 191–200.

[9] Yufanyi, D.M., Nono, H.J., Yuoh, A.C.B., Tabong, C.D., Judith, W., and Ondoh, A.M., 2021, Crystal packing studies, thermal properties and hirshfeld surface analysis in the Zn(II) complex of 3-aminopyridine with thiocyanate as co-ligand, *Open J. Inorg. Chem.*, 11 (3), 63–84.

[10] Mariyam, D., Farida, N., Wijaya, H.W., and Dasna, I.W., 2022, Studi karakterisasi dan aktivitas antibakteri senyawa kompleks dari zink(II) klorida, kaliumtiosianat dan 2-aminopiridina, *J. Ris. Kim.*, 13 (1), 100–110.

[11] Kartal, Z., and Şahin, O., 2021, The synthesis of heteroleptic cyanometallate aminopyridine complexes and an investigation into their structural properties with various spectroscopic methods, *J. Mol. Struct.*, 1227, 129514.

[12] Sanchez Montilva, O.C., Movilla, F., Rodriguez, M.G., and Di Salvo, F., 2017, Synthesis, crystal structure and study of the crystal packing in the complex bis(4-aminopyridine-κN1)dichloridocobalt(II), *Acta Crystallogr., Sect. C: Struct. Chem.*, 73 (5), 399–406.

[13] Wöhlert, S., Jess, I., Englert, U., and Näther, C., 2013, Synthesis and crystal structures of Zn(II) and Co(II) coordination compounds with *ortho* substituted pyridine ligands: Two structure types and polymorphism in the region of their coexistence, *CrystEngComm*, 15 (26), 5326–5336.

[14] Jochim, A., Radulovic, R., Jess, I., and Näther, C., 2020, Crystal structure of bis(tetramethylthiourea-κS)bis(thiocyanato-κN)cobalt(II), *Acta Crystallogr., Sect. E: Crystallogr. Commun.*, 76 (8), 1373–1377.

[15] Jafari, M., Salehi, M., Kubicki, M., Arab, A., and Khaleghian, A., 2017, DFT studies and antioxidant activity of Schiff base metal complexes of 2-aminopyridine. Crystal structures of cobalt(II) and zinc(II) complexes, *Inorg. Chim. Acta*, 462, 329–335.

[16] Tsague Chimaine, F., Yufanyi, D.M., Colette Benedicta Yuoh, A., Eni, D.B., and Agwara, M.O., 2016, Synthesis, crystal structure, photoluminescent and antimicrobial properties of a thiocyanato-bridged copper(II) coordination polymer, *Cogent Chem.*, 2 (1), 1253905.

[17] Setifi, Z., Geiger, D., Jelsch, C., Maris, T., Glidewell, C., Mirzaei, M., Arefian, M., and Setifi, F., 2018, The first Fe(II) complex bearing end-to-end dicyanamide as a double bridging ligand: Crystallography study and Hirshfeld surface analysis; completed with a CSD survey, *J. Mol. Struct.*, 1173, 697–706.

[18] Nath, R.K., Roy, T.G., and Sutradhar, R.K., 2017, Synthesis of some Cd(II) and Zn(II) complexes of a tetraazamacrocyclic ligand and their antimicrobial activities, *Asian-Australas. J. Biosci. Biotechnol.*, 2 (2), 136–144.

[19] Day, B.J., 2019, The science of licking your wounds: Function of oxidants in the innate immune system, *Biochem. Pharmacol.*, 163, 451–457.

[20] Magacz, M., Kędziora, K., Sapa, J., and Krzyściak, W., 2019, The significance of lactoperoxidase system in oral health: Application and efficacy in oral hygiene products, *Int. J. Mol. Sci.*, 20 (6), 1443.

[21] Prasch, J., Bernhart, E., Reicher, H., Kollroser, M., Rechberger, G.N., Koyani, C.N., Trummer, C., Rech, L., Rainer, P.P., Hammer, A., Malle, E., and Sattler, W., 2020, Myeloperoxidase-derived 2-chlorohexadecanal is generated in mouse heart during endotoxemia and induces modification of distinct cardiomyocyte protein subsets *in vitro*, *Int. J. Mol. Sci.*, 21 (23), 9235.

[22] Mishra, O.P., Popov, A.V., Pietrofesa, R.A., Nakamaru-Ogiso, E., Andrake, M., and Christofidou-Solomidou, M., 2018, Synthetic secoisolariciresinol diglucoside (LGM2605) inhibits myeloperoxidase activity in inflammatory cells, *Biochim. Biophys. Acta, Gen. Subj.*, 1862 (6), 1364–1375.

[23] Li, F., Xiong, X.S., Yang, Y.Y., Wang, J.J., Wang, M.M., Tang, J.W., Liu, Q.H., Wang, L., and Gu, B., 2021, Effects of NaCl concentrations on growth patterns, phenotypes associated with virulence, and energy metabolism in *Escherichia coli* BW25113, *Front. Microbiol.*, 12, 705326.

[24] Effendy, E., 2007, *Perspektif Baru Kimia Koordinasi Jilid 1*, Bayumedia Publishing, Malang.

[25] Munadhiroh, A., Wijaya, H.W., Farida, N., Golhen, S., and Dasna, I.W., 2022, Synthesis, characterization, and preliminary study of [Co(2-aminopyridine)$_2$(NCS)$_2$] or bis(2-aminopyridine)dithiocyanato cobalt(II) as an antibacterial, *J. Kim. Valensi*, 8 (1), 23–29.

[26] Svirchuk, Y.S., 2006, Electrical Conductivity, *A-to-Z Guide to Thermodynamics, Heat & Mass Transfer, and Fluids Engineering*, e (l), 1–13.

[27] Sugiyama, H., Sekine, A., and Uekusa, H., 2015, Crystal structure of bis(4-aminopyridine)bis(isothiocyanato)cobalt(II), *X-Ray Struct. Anal. Online*, 31, 2014–2015.

[28] Makhlouf, J., Valkonen, A., and Smirani, W., 2022, Transition metal precursor impact on thiocyanate complexes crystallization: Isomorphous cobalt and nickel properties, *Polyhedron*, 213, 115625.

[29] Moustafa, I.M.I., Mohamed, N.M., and Ibrahim, S.M., 2022, Molecular modeling and antimicrobial screening studies on some 3-aminopyridine transition metal complexes, *Open J. Inorg. Chem.*, 12 (3), 39–56.

[30] Linker, G.J., van Duijnen, P.T., and Broer, R., 2020, Understanding trends in molecular bond angles, *J. Phys. Chem. A*, 124 (7), 1306–1311.

[31] Effendy, E., 2017, *Molekul, Struktur dan Sifat-Sifatnya*, Indonesian Academic Publishing, Malang, Indonesia.

[32] Nakamoto, K., 2006, "Infrared and Raman Spectra of Inorganic and Coordination Compounds" in *Handbook of Vibrational Spectroscopy*, Eds. Chalmers, J.M., and Griffiths, P.R., Wiley, Hoboken, US.

[33] Buyukmurat, Y., and Akyuz, S., 2003, Theoretical and experimental studies of IR spectra of 4-aminopyridine metal(II) complexes, *J. Mol. Struct.*, 651-653, 533–539.

[34] Ramotowska, S., Wysocka, M., Brzeski, J., Chylewska, A., and Makowski, M., 2020, A comprehensive approach to the analysis of antibiotic-metal complexes, *TrAC, Trends Anal. Chem.*, 123, 115771.

[35] Claudel, M., Schwarte, J.V., and Fromm, K.M., 2020, New antimicrobial strategies based on metal complexes, *Chemistry*, 2 (4), 849–899.

[36] Tevyashova, A.N., and Tevyashova, A.N., 2021, Recent trends in synthesis of chloramphenicol new derivatives, *Antibiotics*, 10 (4), 370.

[37] Dinos, G.P., Athanassopoulos, C.M., Missiri, D.A., Giannopoulou, P.C., Vlachogiannis, I.A., Papadopoulos, G.E., Papaioannou, D., and Kalpaxis, D.L., 2016, Chloramphenicol derivatives

as antibacterial and anticancer agents: Historic problems and current solutions, *Antibiotics*, 5 (2), 20.

[38] Tsirogianni, A., Kournoutou, G.G., Bougas, A., Poulou-Sidiropoulou, E., Dinos, G., and Athanassopoulos, C.M., 2021, New chloramphenicol derivatives with a modified dichloroacetyl tail as potential antimicrobial agents, *Antibiotics*, 10 (4), 394.

[39] Kostopoulou, O.N., Magoulas, G.E., Papadopoulos, G.E., Mouzaki, A., Dinos, G.P., Papaioannou, D., and Kalpaxis, D.L., 2015, Synthesis and evaluation of chloramphenicol homodimers: Molecular target, antimicrobial activity, and toxicity against human cells, *PLoS One*, 10 (8), e0134526.

[40] Al–Shaheen, A.J., 2010, Study on synthesis and antibacterial activity of Co(II) and Ni(II) complexes including isopropylacetone thiosemicarbozone and cresol, *Iraqi Natl. J. Chem.*, 37, 111–127.

Activated Charcoal from Coffee Dregs Waste as an Alternative Biosorbent of Cu(II) and Ag(I)

Susy Yunita Prabawati*, Priyagung Dhemi Widiakongko, and Mohammad Ahsani Taqwim

Chemistry Program Study, Faculty of Science and Technology, UIN Sunan Kalijaga, Jl. Laksda Adisucipto, Yogyakarta 55281, Indonesia

** Corresponding author:*

email: susy.prabawati@uin-suka.ac.id

Received: March 19, 2023
Accepted: July 23, 2023

DOI: 10.22146/ijc.83269

Abstract: *This study examines the use of coffee dregs waste as biosorbents of Cu(II) and Ag(I). Coffee dregs waste still contains a high level of carbon and cellulose for biosorbents production. The production process was started with charcoal activation using H_3PO_4. The batch method was applied by variations of contact time, the mass of the biosorbent, and the initial concentration of metal ions. The results showed that Cu(II) and Ag(I) were optimally adsorbed at pH 6 and 4, respectively. The amount of adsorbed metal ions increased with adsorption contact time. The adsorption process of both metal ions reaches stability within 60 min and the optimum biosorbent mass is 1 g. Isothermal adsorption studies show that Cu(II) adsorption tends to follow Langmuir isotherm with an adsorption energy of 31.42 kJ/mol and Ag(I) adsorption follows Freundlich isotherms with an adsorption energy of 27.74 kJ/mol. Based on the results, the interaction between metal ions and adsorbents is a chemical adsorption process and coffee dregs charcoal has the potential to adsorb Cu(II) and Ag(I) metal ions.*

Keywords: *Ag(I); biosorbent; coffee dregs; Cu(II); isothermal adsorption*

INTRODUCTION

Nowadays, the silver industry is one of the small industrial centers that continues to grow. Silver handicraft production's gilding, coating, and rinsing release heavy metals waste, including copper (Cu) and silver (Ag) [1]. In addition, Cu and Ag are heavy metals that are commonly used in many industries [2]. The toxic Cu and Ag ions are difficult to be identified because of their presence in cations in the water. Direct discharging of wastewater containing heavy metals into the infiltration channels, soil, or into the surrounding environment causes ecological damage because of metal degradation difficulties [3]. Also, these two metal ions pose a significant risk if contaminated in animals and humans because of their high toxicity at low concentrations [4].

The regulation of the Republic of Indonesia Minister of Environment Number 5 of 2014 concerning Wastewater Quality Standards states Cu and Ag in wastewater should not be more than 0.5 mg/L [5]. Therefore, proper handling is needed to prevent environmental pollution due to industrial wastewater disposal into the surrounding environment.

Several methods have been applied in handling metal wastewater, such as adsorption [6-8], membranes [9], photoreduction [10], precipitation [11], ion exchange [12], and solvent extraction [13]. Adsorption is a well-known method with advantages because of simplicity, low cost, good performance at low concentrations, and recyclability [14].

Materials commonly used as biosorbents are activated charcoal, alumina, silica, chitosan, and zeolite [15-17]. Among them, activated charcoal is the most accessible material to obtain and provides the largest surface area [18], so its ability as an adsorbent is also greater compared to mesoporous silica [17]. Activated charcoal is a porous solid containing 85–95% carbon produced from materials containing carbon by heating at high temperatures.

One material that is potentially to be further used is coffee dreg waste. Coffee dregs can be considered new waste because they create an unpleasant odor, especially

during the rainy season. Coffee dregs still have a moisture content of around 75–80%, which easily for spoilage microbes to grow [19]. Caetano et al. [20] reported that coffee grounds provided 47.8–58.9% carbon, 1.9–2.3% nitrogen, 0.4–1.6% ash, and 8.6% cellulose. Therefore, coffee grounds have the potential to become activated charcoal. So far, the use of coffee grounds has not been widely developed.

The adsorption process is affected by several factors, such as temperature, contact time, surface area of the adsorbent, pore structure of the adsorbent, and the pH of the solution. The interaction between the adsorbent and the adsorbate under different conditions provides different adsorption results. Therefore, the optimum condition investigation of each treatment is essential for the adsorption effectiveness [21]. In this study, the utilization of waste from coffee dregs as a biosorbent activated by H_3PO_4 to Cu(II) and Ag(I) was investigated, which are the main pollutant materials in Indonesian waters on variations in biosorbent mass and adsorption contact time. In addition, an isothermal adsorption study and an adsorption test for Ag(I) and Cu(II) in a binary solution system were carried out simultaneously. The activation process was carried out under acidic or alkaline conditions. In this study, the H_3PO_4 activator was used, which is a relatively good degrading agent because H_3PO_4 provides three H^+, which is necessary to degrade residual impurities left on the pore surface of the adsorbent.

■ EXPERIMENTAL SECTION

Materials

The materials used are coffee dregs obtained from coffee shops around Yogyakarta. Other materials include phosphate acid (H_3PO_4), copper(II) sulfate pentahydrate ($CuSO_4{\cdot}5H_2O$), nitric acid (HNO_3), sodium hydroxide (NaOH), silver(I) sulfate (Ag_2SO_4), and other chemicals used in this study were the highest purity available from Merck and were used without further purification.

Instrumentation

A set of laboratory glassware, analytical balance (OHAUS), spatula, volumetric flask, hot plate, magnetic stirrer, oven, filter paper, Fourier transform infra-red (FTIR, Shimadzu Prestige-21), X-ray diffraction (XRD, Philips XRD X'Pert MS), scanning electron microscope (SEM, JSM-6510LA), and atomic absorption spectrophotometer (AAS, GBC Australia, at UGM Analytical Chemistry Laboratory) were used in this study.

Procedure

Preparation of H_3PO_4-activated coffee dregs charcoal

The coffee dregs were ground to increase the surface area, washed using distilled water to obtain a neutral pH, dried in an oven at 110 °C for 2 h, and carried out in a furnace at 400 °C for 3 h. The charcoal from the coffee dregs is then cooled, and the yield is calculated.

As much as 30 g of coffee dregs charcoal was immersed in 200 mL of H_3PO_4 1 M for 48 h. Then, it was filtered and washed using distilled water until neutral, dried at 110 °C for 90 min, and cooled in a desiccator for 30 min. Characterization by FTIR was applied before and after activation.

Contact time effect

As much as 10 mL of Cu(II) 10 mg/L was put into an Erlenmeyer, and 0.5 g of the developed biosorbent was added. Adjustment of pH 6 was applied to Cu(II) solution. The sample was stirred at room temperature for 30, 60, 90, and 120 min and then left for 5 min. The sample was then filtered using filter paper and analyzed using AAS. The same procedure was applied for Ag(I) adsorption using 50 mL of Ag_2SO_4 20 mg/L solution at pH 4.

Effect of mass variation of biosorbent

At pH 6, Cu(II) 10 mg/L were put into an Erlenmeyer and added H_3PO_4 1 M activated coffee dregs biosorbent in the amount of 0.5, 1.0, 2.0, and 3.0 g. The sample was stirred for 60 min at room temperature and then left for 5 min. Then, the sample was filtered using filter paper and analyzed employing AAS. The procedure was also applied for the adsorption of Ag(I) using 10 mL of Ag_2SO_4 20 mg/L solution at pH 4 in variations of the coffee dregs biosorbent, 0.25, 0.50, 0.75, and 1.00 g.

Metal ion concentration effect

A series of metal solutions were prepared, i.e., 4, 8, 12, 16, and 20 mg/L. Then, 0.5 g of the biosorbent was added to 50 mL of each solution and stirred at the optimum time. A blank experiment was also carried out under similar conditions. SSA analyzed the concentration of adsorbed metal.

Simultaneous adsorption study of Ag(I) and Cu(II) metals with coffee dregs biosorbent

As much as 0.5 mg of activated biosorbent H_3PO_4 1 M interacted with a mixed solution of Ag(I):Cu(II) (mol ratio of 1:1). The sample was stirred for 60 min at room temperature and left for 5 min. The sample was then filtered using filter paper and analyzed using AAS.

■ RESULTS AND DISCUSSION

Characterization of Coffee Dregs Activated Charcoal

Synthesis of activated charcoal started with the preparation of coffee dregs, then the furnace process or charcoal manufacture, and the charcoal activation using acid. Carbonization from coffee dregs was carried out at a temperature of 400 °C for 3 h, aiming to decompose the material and produce a material with absorption and a neat structure [22]. The next step was the activation of the coffee dregs charcoal using the H_3PO_4 as an activator to open the carbon pores covered by impurities trapped in the pores. Fig. 1 shows the mechanism of the activation reaction of charcoal with H_3PO_4. Fig. 1 shows that the H_3PO_4 as activator reacts with the available charcoal and then forms micropores on the surface, serving as a host of adsorption processes. The opening of the pores and increasing the surface area of activated charcoal can increase the ability of activated charcoal to adsorb [24].

The characterization of acid-activated coffee dregs and coffee dregs was carried out using an FTIR spectrophotometer. Fig. 2 shows the spectra of coffee dregs before and after activation with H_3PO_4, and Table 1 shows the interpretation of the spectra.

Table 1 shows that the two FTIR spectra have almost the same absorption of functional groups. A few shifting occurred at 1570 to 1573 cm^{-1} for the absorption of aromatic C=C groups. Also, the absorption of the C–H

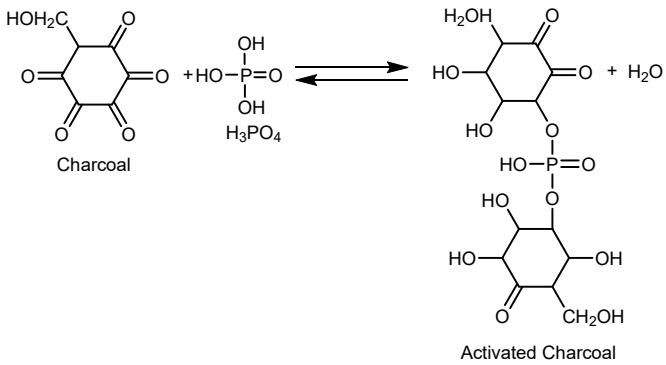

Fig 1. Charcoal activation reaction with H_3PO_4 [23]

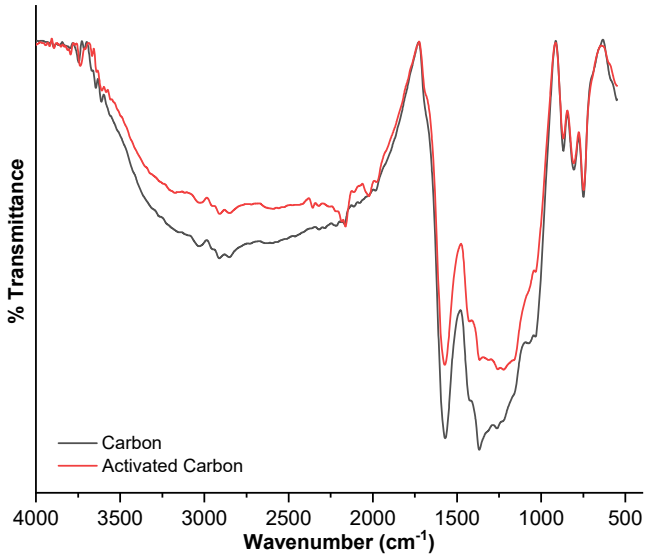

Fig 2. FTIR spectra of coffee dregs charcoal

functional group at wave number 2911 shifted to 2909 cm^{-1}. The shifting occurred because the pores in the coffee dregs charcoal became more open due to the loss of impurities after the activation process with acid. The spectra of H_3PO_4-activated coffee dregs activated charcoal showed a characteristic absorption at 1223 cm^{-1} as P=O absorption of H_3PO_4 [25].

Fig. 3 shows the morphology of H_3PO_4-activated coffee dregs charcoal using SEM. The morphology of H_3PO_4-activated coffee dregs charcoal becomes more open, so it is expected to be more effective in adsorbing heavy metal ions. In line with a study conducted by Purwiandono et al. [26], which showed that the ability of an acid-activated zalacca peel biosorbent to adsorb Cu(II) was much better than biosorbents without activation. The results of this study are also in line with

Table 1. FTIR spectra interpretation results of coffee dregs charcoal

Wavenumber (cm^{-1})		Functional group interpretation
Coffee dreds	Activated coffee dregs by H_3PO_4	
2911	2909	C-H (Csp^3)
1570	1573	C=C aromatic
-	1223	P=O of H_3PO_4

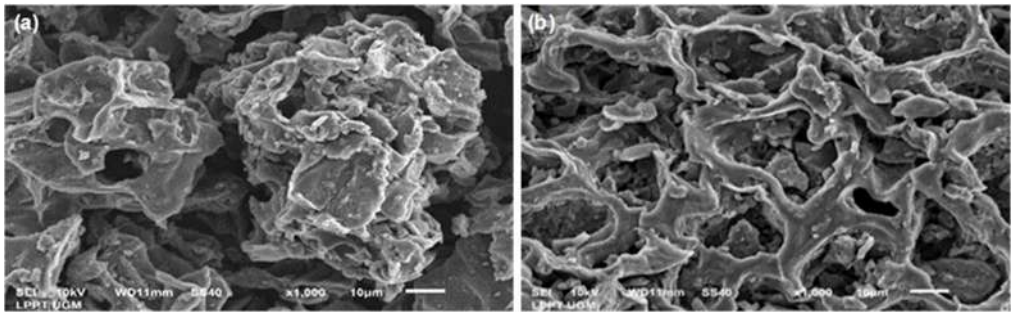

Fig 3. SEM photo of coffee dregs charcoal (a) before and (b) after activation process at magnification 1000×

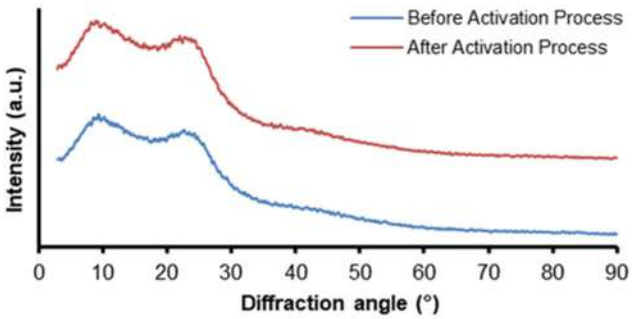

Fig 4. Diffractogram (XRD) of coffee dregs charcoal before and after activation with H_3PO_4

the results obtained by previous researchers [22]. It is because the activation treatment was able to release impurities that partially cover the biosorbent's pores, so the pores become larger to adsorb metal ions.

Further characterization was carried out using XRD. The diffractogram of coffee dregs charcoal before and after activation with acid is shown in Fig. 4. The diffractogram of coffee dregs charcoal before and after activation performed insignificant differences in intensity and diffraction patterns. It proves that the activation process did not change the charcoal structure, which has an amorphous structure. This result is in line with previous research [27]. The charcoal peaks at an angle of 2θ around 20° and 40° show typical graphite characteristics identified as basal spacing d_{002} and d_{100}, respectively [18]. A shift of the peak to a smaller angle from 23.32° to 22.88° was identified in activated charcoal with basal spacing values of 0.38 and 0.39 nm, respectively. It indicates that the charcoal structure after activation is more open than before activation, which is in line with the results of SEM and FTIR analysis. Peaks at an angle of 2θ around 9° on both diffractograms indicate the presence of an amorphous cellulose structure in the activated charcoal [18].

Adsorption of Cu(II) and Ag(I)

Effect of contact time

Metal adsorption by coffee dregs biosorbent was carried out isothermally at a constant temperature of 25 °C. Fig. 5 shows that the increased contact time helped the amount of adsorbed metal ions, and the adsorption process reached an equilibrium. After 60 min of stirring,

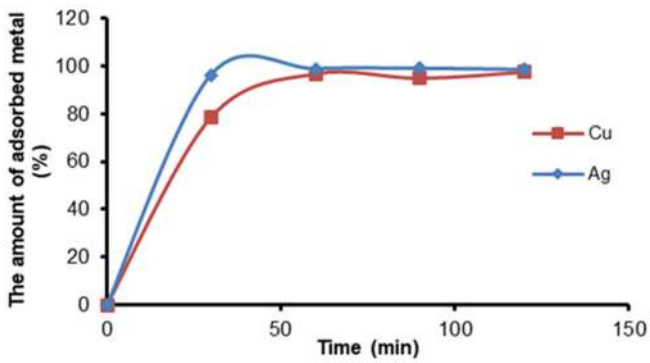

Fig 5. Effect of contact time on Cu(II) and Ag(I) adsorption

the amount of adsorbed metal ions relatively did not increase. It can be concluded that the equilibrium occurred after a stirring time of 60 min.

Effect of mass variation of biosorbent

The adsorption process on the mass variation of the biosorbent was carried out at room temperature with an adsorption contact time of 60 min, as the results indicated that the adsorption equilibrium occurred after a stirring time of 60 min. Fig. 6 shows the results on the mass variation of this biosorbent.

Fig. 6 shows that the increase in adsorbed metal ions is directly proportional to the amount of biosorbent used. The more biosorbent used, the more pores available and the wider surface area, affecting higher interaction between the active side of the pores of the coffee dregs activated charcoal and metal ions. Thus, the number of adsorbed metal ions increases [28]. The results show that the maximum absorption of Cu(II) and Ag(I) occurred using 1 g of coffee dregs biosorbent. After reaching equilibrium, the ability of the adsorbate to bind to the adsorbent decreases. Fig. 6 shows a decrease in metal ions adsorbed on biosorbents above 1 g. Because the amount of metal ions in solution is not proportional to the number of biosorbent particles available, the surface of the biosorbent has reached its saturation point and the absorption efficiency has decreased.

Adsorption Isotherms of Cu(II) and Ag(I)

This research investigated the adsorption isotherms by calculating for each treatment according to both Langmuir and Freundlich adsorption isotherms. The Langmuir isothermal adsorption equation is $1/q_e = 1/(X_m.K.C_e) + 1/X_m$ and the Freundlich equation is $\log q_e = \log k + 1/n \log C_e$ with q_e as the concentration of the adsorbate at equilibrium (mol/g), C_e is the adsorbate concentration in the aqueous phase (mol/L), X_m is the maximum adsorption capacity (μmol/g), and k is the equilibrium constant. Parameters obtained from Langmuir and Freundlich isothermal analysis are presented in Table 2.

Table 2 shows that Cu(II) provided a higher level of isothermal graphic linearity than the Langmuir model compared to the Freundlich model. The opposite occurred for Ag(I). The adsorption process for Cu(II) metal ions tends to follow the Langmuir isothermal model. The adsorption process occurred in a monolayer, assuming that maximum adsorption occurred when the adsorbate fills all the active sites of the adsorbent to form a monolayer layer. Meanwhile, the Ag(I) metal ion tends to follow the Freundlich isothermal model. The adsorption process occurred in the multilayer sheet.

The adsorption energy equation can be written as $E_{ads} = -\Delta G°$. The value of ΔG can be measured in the standard state, while for any other state, the value of the Gibbs free energy (ΔG) is: $\Delta G = \Delta G° + RT \ln K$, as R is the general gas constant (8.314 J/K mol), T is the temperature (K), and K is the adsorption equilibrium value. Huang et al. [29] state that the minimum limit for chemical adsorption energy is 5 kcal/mol or 20 kJ/mol.

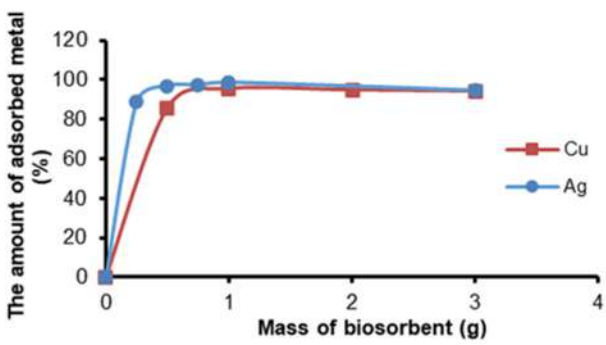

Fig 6. The effect of the mass of the biosorbent on the adsorption of Cu(II) and Ag(I)

Table 2. Adsorption isothermal parameters determined from the Langmuir and Freundlich equations

Ion	Adsorption parameter						
	Langmuir				Freundlich		
	X_m (mg/g)	$K \times 10^6$ (L/mol)	ΔG (kJ/mol)	R^2	ΔG (kJ/mol)	K (L/mol)	R^2
Cu(II)	0.4136	1.0270	31.420	0.9720			0.9007
Ag(I)		0.1949		0.0901	27.740	3.3962	0.9219

The adsorption energy value of the two metal ions is above 20 kJ/mol, so the interaction between the metal ion and the coffee dregs biosorbent can be seen as a chemical adsorption process. Coffee dregs provide active sites in the form of hydroxy groups (–OH) from cellulose. These active sites can interact with metal ions. It is understood that these OH groups can donate electron pairs to metal ions, forming coordination. This can be enhanced by activating the coffee dregs charcoal so that the pores of the charcoal become more open, making it possible to trap more metal ions effectively. An illustration of the interaction model between metals and biosorbents is shown in Fig. 7 [30].

This study shows the amount of adsorbed metal increased with the increasing number of biosorbents used and the results of adsorption investigation in a solution consisting of both metal ions. It was seen that the coffee dreg biosorbent tended to absorb more Ag(I) compared to Cu(II). The ability of biosorbents to adsorb multi-metals is also essential to determine the level of interference from the presence of co-cations in wastewater and the efficiency of biosorbents in removing these ions from wastewater [31].

This study also investigated the adsorption of Ag(I) and Cu(II) simultaneously in the binary solution system, detailed in Fig. 8. Fig. 8 shows that more Ag(I) was adsorbed by the coffee dregs biosorbent than Cu(II) even though the adsorption process was carried out simultaneously. It means that metal ions interact with each other synergistically. The interaction between metal ions and biosorbents from coffee dregs also occurred physically, where metal ions were trapped in the pores of the activated charcoal. Thus, this adsorbent does not show a high selectivity towards Ag and Cu ions compared to the composite adsorbents reported in previous studies [32]. The suitability of the size of the metal ion with the pore size of the biosorbent is one of the factors affecting the adsorption process [33]. The Ag(I) size is more suitable with the pore size of the coffee dregs charcoal, affecting more abundant ions Ag(I) could be absorbed.

This study shows that the H_3PO_4-activated coffee grounds biosorbent can potentially adsorb Cu(II) and Ag(I) metal ions. Compared to previous studies using

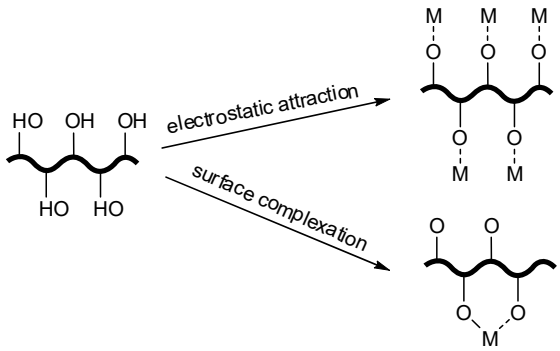

Fig 7. Model of interaction between metals and active groups from biosorbents

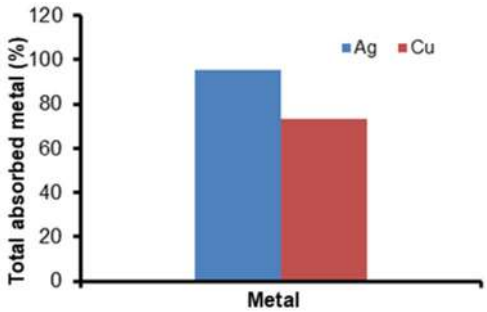

Fig 8. Amount of adsorbed metal in binary solution system

biosorbent from cassava peel [34], coffee dregs biosorbent can absorb Cu(II) metal ions at lower concentrations. Compared to research conducted by Mariana et al. [22], the adsorption process of this study requires a shorter adsorption time. The results of this study are also in line with the results obtained by previous researchers [35].

■ CONCLUSION

The study showed that coffee dregs charcoal activated with H_3PO_4 could be applied as a biosorbent for Cu(II) and Ag(I). The optimal adsorption contact time was 60 min. Adsorption isothermal investigation shows that Cu(II) tends to follow the Langmuir isotherm with adsorption energies of 31.42 kJ/mol. In contrast, Ag(I) tends to follow the Freundlich isotherm with adsorption energies of 27.74 kJ/mol. The adsorption energy of coffee dregs charcoal biosorbent is more than 20 kJ/mol. This means that the interaction between metal ions and the biosorbent can be viewed as a chemical adsorption process. It was observed that coffee

dregs charcoal was a more effective biosorbent for the removal of Ag(I) than Cu(II). The functional groups of cellulose charcoal play an important role in adsorption abilities. In general, coffee dregs charcoal biosorbent can be regarded as a potential biosorbent in heavy metal wastewater treatment applications.

■ ACKNOWLEDGMENTS

Thanks to LPPM UIN Sunan Kalijaga Yogyakarta for the research funding grant through the 2022 BOPTN Research Grant (No.116.9/2022).

■ AUTHOR CONTRIBUTIONS

Susy Yunita Prabawati: Conceptualization, methodology, resources, formal analysis, writing–original draft, writing–review & editing, supervision, project administration, funding acquisition. Priyagung Dhemi Widiakongko: Formal analysis and editing. Mohammad Ahsani Taqwim: Methodology, formal analysis, investigation, visualization, and editing.

■ REFERENCES

[1] Hernawati, T., and Ilcham, A., 2022, Heavy Metal Reducing from Kotagede Silver Handicraft Waste Using Natural Zeolite and Synthetic Zeolite, *The 1st International Conference on Engineering Optimization and Management in Industrial Applications*, Yogyakarta, Indonesia, October 29th, 2022.

[2] Aprilita, N.H., Luqman, M., and Suratman, A., 2022, Dithizone-immobilized nickel slag for the adsorption of silver(I) ion, *Rasayan J. Chem.*, 15 (2), 1071–1079.

[3] Siddiquee, S., Rovina, K., Al Azad, S., Naher, L., Suryani, S., and Chaikaew, P., 2015, Heavy metal contaminants removal from wastewater using the potential filamentous fungi biomass: A review, *J. Microb. Biochem. Technol.*, 7 (6), 384–393.

[4] Al-Senani, G.M., and Al-Fawzan, F.F., 2018, Adsorption study of heavy metal ions from aqueous solution by nanoparticle of wild herbs, *Egypt. J. Aquat. Res.*, 44 (3), 187–194

[5] Ministry of Environment and Forestry Republic of Indonesia, 2014, *Peraturan Menteri Lingkungan Hidup tentang Baku Mutu Air Limbah*, https://jdih.maritim.go.id/cfind/source/files/permen-lhk/mlh-p.5.pdf.

[6] Prabawati, S.Y., Jumina, J., Santosa, S.J., Mustofa, M., and Keisuke, O., 2012, Study on the adsorption properties of novel calix[6]arene polymers for heavy metal cations, *Indones. J. Chem.*, 12 (1), 28–34.

[7] Sellaoui, L., Ali, J., Badawi, M., Bonilla-Petriciolet, A., and Chen, Z., 2020, Understanding the adsorption mechanism of Ag^{+} and Hg^{2+} on functionalized layered double hydroxide via statistical physics modeling, *Appl. Clay Sci.*, 198, 105828.

[8] Feng, X., Long, R., Wang, L., Liu, C., Bai, Z., and Liu, X., 2022, A review on heavy metal ions adsorption from water by layered double hydroxide and its composites, *Sep. Purif. Technol.*, 284, 120099.

[9] Nádaždy, V., Gmucová, K., Poturnayová, A., Šnejdárková, M., Karpišová, I., Lányi, Š., and Hianik, T., 2012, Detection of cytochrome c with calixarenes incorporated into supported lipid membranes via charge transient measurements, *Procedia Chem.*, 6, 60–68.

[10] Bhati, A., Anand, S.R., Saini, D., Gunture, G., and Sonkar, S.K., 2019, Sunlight-induced photoreduction of Cr(VI) to Cr(III) in wastewater by nitrogen-phosphorus-doped carbon dots, *npj Clean Water*, 2 (1), 12.

[11] Bugajski, P., Nowobilska-Majewska, E., and Majewski, M., 2021, The impact of atmospheric precipitation on wastewater volume flowing into the wastewater treatment plant in Nowy Targ (Poland) in terms of treatment costs, *Energies*, 14 (13), 3806.

[12] Vecino, X., and Reig, M., 2022, Wastewater treatment by adsorption and/or ion-exchange processes for resource recovery, *Water*, 14 (6), 911.

[13] Manousi, N., Giannakoudakis, D.A., Rosenberg, E., and Zachariadis, G.A., 2019, Extraction of metal ions with metal-organic frameworks, *Molecules*, 24 (24), 4605.

[14] Aprilita, N.H., Luqman, M., and Suratman, A., 2023, Removal of cobalt(II) by dithizone-immobilized nickel slag, *Results Chem.*, 5, 100698.

[15] Kubra, K.T., Hasan, M.M., Hasan, M.N., Salman, M.S., Khaleque, M.A., Sheikh, M.C., Rehan, A.I., Rasee, A.I., Waliullah, R.M., Awual., M.E., Hossain, M.S., Alsukaibi, A.K.D., Alshammari, H.M., and Awual, M.R., 2023, The heavy lanthanide of thulium(III) separation and recovery using specific ligand-based facial composite adsorbent, *Colloids Surf., A*, 667, 131415.

[16] Awual, M.R., Hasan, M.N., Hasan, M.M., Salman, M.S., Sheikh, M.C., Kubra, K.T., Islam, M.S., Marwani, H.M., Islam, A., Khaleque, M.A., Waliullah, R.M., Hossain, M.S., Rasee, A.I., Rehan, A.I., and Awual, E., 2023, Green and robust adsorption and recovery of europium(III) with a mechanism using hybrid donor conjugate materials, *Sep. Purif. Technol.*, 319, 124088.

[17] Salman, M.S., Sheikh, M.C., Hasan, M.M., Hasan, M.N., Kubra, K.T., Rehan, A.I., Awual, M.E., Rasee, A.I., Waliullah, R.M., Hossain, M.S., Khaleque, M.A., Alsukaibi, A.K.D., Alshammari, H.M., and Awual, M.R., 2023, Chitosan-coated cotton fiber composite for efficient toxic dye encapsulation from aqueous media, *Appl. Surf. Sci.*, 622, 157008.

[18] Figueroa Campos, G.A., Perez, J.P.H., Block, I., Sagu, S.T., Saravia Celis, P., Taubert, A., and Rawel, H.M., 2021, Preparation of activated carbons from spent coffee grounds and coffee parchment and assessment of their adsorbent efficiency, *Processes*, 9, 1396.

[19] Forcina, A., Petrillo, A., Travaglioni, M., di Chiara, S., and De Felice, F., 2023, A comparative life cycle assessment of different spent coffee ground reuse strategies and a sensitivity analysis for verifying the environmental convenience based on the location of sites, *J. Cleaner Prod.*, 385, 135727.

[20] Caetano, N.S., Silva, V.F.M., and Mata, T.M., 2012, Valorization of coffee dregs for biodiesel production, *Chem. Eng. Trans.*, 26, 267–272.

[21] Nipa, S.T., Shefa, N.R., Parfin, S., Khatun, M.A., Alam, M.J., Chodhury, S., Khan, M.A., Shawon, S., Biswas, B.K., and Rahman, M.W., 2023, Adsorption of methylene blue on papaya bark fiber: Equilibrium, isotherm and kinetic perspectives, *Results Eng.*, 17, 100857.

[22] Mariana, M., Marwan, M., Mulana, F., Yunardi, Y., Ismail, T.A., and Hafdiansyah, M.F., 2018, Activation and characterization of waste coffee grounds as bio-sorbent, *IOP Conf. Ser.: Mater. Sci. Eng.*, 334, 012029.

[23] Esterlita, M.O., and Herlina, N., 2015, Pengaruh penambahan aktivator $ZnCl_2$, KOH dan H_3PO_4 dalam pembuatan karbon aktif dari pelepah aren (*Arenga pinnata*), *Jurnal Teknik Kimia USU*, 4 (1), 47–52.

[24] Rampe, M.J., and Tiwow, V.A., 2018, Fabrication and characterization of activated carbon from charcoal coconut shell Minahasa, Indonesia, *J. Phys.: Conf. Ser.*, 1028, 012033.

[25] Skoog, D.A., Holler, F.J., and Crouch, S.R., 2017, *Principles of Instrumental Analysis*, 7th Ed., Cengage Learning, Boston, US.

[26] Purwiandono, G., and Ibrahim, S., 2022, Adsorpsi logam Cu(II) menggunakan adsorben kulit buah salak teraktivasi HNO_3, *IJCR*, 7 (1), 1–7.

[27] Mukhlis, M., Salim, I., and Krimadi, L.N., 2022, Karakteristik Karbon aktif ampas kopi dan kemampuannya terhadap perbaikan parameter kimia air sumur Koya Barat, *AVOGADRO Jurnal Kimia*, 6 (1), 28–39.

[28] El-Wakil, A.M., Abou El-Maaty, W.M., and Awad, F.S., 2014, Removal of lead from aqueous solution on activated carbon and modified activated carbon prepared from dried water hyacinth plant, *J. Anal. Bioanal. Tech.*, 5 (2), 000187.

[29] Huang, Y., Li, S., Chen, J., Zhang, X., and Chen, Y., 2014, Adsorption of Pb(II) on mesoporous activated carbons fabricated from water hyacinth using H_3PO_4 activation: Adsorption capacity, kinetic and isotherm studies, *Appl. Surf. Sci.*, 293, 160–168.

[30] Iftekhar, S., Ramasamy, D.K., Srivastava, V., Asif, M.B., and Sillanpää, M., 2018, Understanding the factors affecting the adsorption of lanthanum using different adsorbents: A critical review, *Chemosphere,* 204, 413–430.

[31] Sudiarta, I.W., Suarya, P., and Widya, C.M.P., 2018, Adsorpsi multi logam berat krom(III), timbal(II)

dan tembaga(II) dalam sistem larutan binary oleh silika gel terimobilisasi difenilkarbazida, *Jurnal Kimia*, 12 (2), 159–164.

[32] Awual, M.R., 2019, Novel ligand functionalized composite material for efficient copper(II) capturing from wastewater sample, *Composites, Part B*, 172, 387–396.

[33] Kim, M.S., and Kim, J.G., 2020, Adsorption characteristics of spent coffee dregs as an alternative adsorbent for cadmium in solution, *Environments*, 7 (4), 24.

[34] Kosim, M.E., Siskayanti, R., Prambudi, D., and Rusanti, W.D., 2022, Perbandingan kapasitas adsorpsi karbon aktif dari kulit singkong dengan karbon aktif komersil terhadap logam tembaga dalam limbah cair electroplating, *Jurnal Redoks*, 7 (1), 36–47.

[35] Wang, M., Li, G., Huang, L., Xue, J., Liu, Q., Bao, N., and Huang, J., 2017, Study of ciprofloxacin adsorption and regeneration of activated carbon prepared from *Enteromorpha prolifera* impregnated with H_3PO_4 and sodium benzenesulfonate, *Ecotoxicol. Environ. Saf.*, 139, 36–42.

New Design Valve in Flow Injection System for the Determination of Pb(II) in Biological and Environmental Samples

Thekrayat Joodi Jassim* **and Raisan Kadhim Taresh**

Department of Pathological Analysis, College of Science, University of Sumer Al-Refaee, Thi-Qar 64001, Iraq

* ***Corresponding author:***

email: asaljood3@gmail.com

Received: March 24, 2023
Accepted: May 1, 2023

DOI: 10.22146/ijc.83367

Abstract: *A strategy to design an injection valve for a streamlined flow injection technique is described as speed and low-cost materials available in the environment for the determination of Pb(II) ion using the organic reagent 4-((4-methoxyphenyl)diazenyl)benzene-1,3-diol at a wavelength of 498 nm. The scope of the study is to find the optimal conditions, including the flow rate of the carrier, the dispersion coefficient, the length of the reaction coil, and the calibration drawing. The results showed that the optimum length of the reaction coil is 20 cm, and the optimum flow rate is 9.1 mL/min, which is equivalent to the pumping rate of 70 F/min. The range of linearity of the study was revealed by a calibration curve of 0.5–27 mg/L, slope = 1.507, correlation coefficient = 0.9995, the limit of quantitative (LOQ) = 0.088 mg/L, and limit of detection (LOD) = 0.026 mg/L. The system under study has a characteristic efficiency. The dispersion coefficient was calculated for concentrations of 10–15 mg/L Pb(II) ion. Furthermore, the accuracy of the flow injection technique in the estimation process was studied and compared with the Flame Atomic Absorption Spectroscopy (FAAS) technique.*

Keywords: *flow injection analysis; 4-((4-methoxy phenyl)diazenyl)benzene-1,3-diol reagent; lead ion; environmental samples; homemade valve*

■ INTRODUCTION

The ancient Romans used lead (Pb) in the manufacture of water pipes, as it was a mixture of Pb soldered with tin. Pb ion (Pb(II)) is considered an important element because of its high level of contamination in different forms, including water, soil and vegetables, which directly affects human and animal health [1]. Pb is a flexible metal and has a bluish-white color that is resistant to corrosion 207.19 g/m^2 d and belongs to group IVA. The elements IVA are characterized by the external quantitative level that has a level of d^{10}, and the s level is saturated. In addition, the two electrons are in the p level, and the change in the ionization energies of Pb to a gradual change of the elements of this group, as Pb turns into an amphoteric element [2]. The Pb(II) contains three non-radioactive and stable forms, which include Pb_2O_6, Pb_2O_7, and Pb_2O_8 [3]. Among its most important compounds, it contains three oxides: Pb_3O_4 and PbO (called red Pb), and PbO_2 [4]. Pb(II) is classified as a highly toxic heavy metal [5], and one of its most important uses is to reduce nuclear radiation and is used as a radiation insulator in the form of thick Pb sheets because of its high density and corrosion resistance [6]. It is used in the manufacturing of colors, dyes and paints, where it is called white Pb and red Pb. It is used in painting bridges and steel buildings in order to prevent corrosion [7]. It has an important role in environmental pollution. Also, radiant nature is considered a hazardous element that is sometimes transmitted from plants to the consumer body of humans and animals through the food chain [8-9]. It is considered a toxic metal regardless of whether it is ingested or inhaled. It has a great effect on the nervous system, both in children and adults. When exposed to Pb for a long time, Pb causes a decrease in performance in some functions of the nervous system, and it is absorbed by the soft tissues so that Pb has no known function inside the body and its concentration is higher overall [10-11]. It has been evaluated in several ways, including ICP-AES (Inductively Coupled Plasma- Atomic

Emission Spectroscopy) [12], ETAAS (Electrothermal Atomic Absorption Spectrometry) [13], FIA (Flow Injection Analysis) [14], SWASV (Square Wave Anodic Stripping Voltammetry), and DPSV (Differential Pulse Stripping voltammetry) [15].

Azo compounds are among the important compounds that are used for the determination and extraction of elements from environmental and health pollutants. They are characterized by many properties, including their molecules that contain functional groups or atoms that have electronic doublets capable of linking with metal ions with coordination bonds to form coordination complexes. The most prominent of these reagents are azo derivatives. In the analytical aspects, azo derivatives were used in the spectroscopic and quantitative methods for estimation the metal ions present in very few concentrations in different analytical models. It has a large molecular weight, and the aromatic azo derivatives are more stable than the aliphatic azo compounds because of the resonance in them [16-17]. Azo heterogeneous dyes have been extensively studied in thermal, optical and medical applications such as antiviral, antifungal and antioxidant properties [18]. Azo compound 4-(methoxyphenyl)diazenyl)benzene-1,3-diol (4-MDD) has a maximum wavelength of 387 nm and has high stability and behaves like a dual-clutch ligand. The FTIR study of the compound showed medium intensity bands at a frequency of 1473 cm^{-1} because of the absorption of the N=N bond. It was noted that a wide band appeared at a frequency of 3269 cm^{-1}, belonging to the hydroxyl group [19].

The technique of FIA is one of the most important analytical techniques in estimating the ions of elements in different models as it depends on the principle of chemical and physical treatments of the dispersed model area according to a continuous carrier current, and then a suitable reagent is used to detect the interaction, where the technique occupied an important and prominent position within the analytical techniques [20]. Since 1975 it has had a significant impact in many areas of application, including the pharmaceutical [21], agricultural [22], environmental [23], and life fields [24]. It has several advantages, including the transformation of open-system interactions into a closed system. Inexpensive and small in volume with a very fast response, where the time is between 5–20 s and therefore, more than one model can be analyzed within 60 s. It can reduce the analysis time by replacing mechanical processes instead of manual processes such as separation and blending and is able to rate the modeling speed at an average rate of 120 samples per h. The volume of the injected sample is between 10–20 µL, and this does not require more than 0.5 µL of reagent solution at each analysis. Individual errors are minimal when compared with other techniques [25].

This study aims to use organic reagent for the determination of Pb(II) ion in different samples by FIA technique to estimate the Pb(II) ion, which is one of the most important pollutants in the environment and human health in different models, including water and soil in different places and life models. Then, knowing the accuracy and efficiency of the technique used to estimate the Pb(II) ions under study after finding the optimum conditions of complexity. Finally, we calculated the percentage of Pb(II) ion recovery under study in different models and compared the results with the FAAS technique.

■ EXPERIMENTAL SECTION

Materials

The materials used in this study were 4-MDD organic reagent, CH_3CH_2OH with a purity of 96% GT. Becker, HCl 36.50–38.00% from BGG, Na_2HPO_4 99% from M&B, Na_2CO_3 99% from Merck, and $PbCl_2$ 99% from BDH Azo. The chemicals and reagents used were of analytical grade, and the water used in the study was distilled water.

Instrumentation

The instrumentations used in this study were homemade valves Manual injection valve made of acrylic and plastic three-way dispenser Shimadzu UV-1700 spectrophotometer, the spectrophotometer was Labomed in Single beam G, USA connected to a Siemens (Germany) Kompensograph C1032 recorder to acquire data as a peak altitude, peristaltic pump Germany,

reaction coils with 0.5 mm radius, pH meter, Denver sensitive instrument, analytical balance, Teflon tubing load, and electronic digital caliper, China.

Procedure

Prepare stock solutions

Solution of Pb(II) ion 500 mg/L: A stock solution was prepared through dissolving 0.0671 g of $PbCl_2$ in 100 mL of distilled water and by using the law of dilution, the solutions were prepared less concentrated. Solution of Na_2CO_3 500 mg/L: A stock solution was prepared through dissolving 0.0883 g of Na_2CO_3 in 100 mL of distilled water, and by the law of dilution, the solutions were prepared less concentrated. Preparation of the solutions of masking agents: 100 mg/L of the solutions of the blocking agents, each containing potassium chloride and aqueous potassium sodium tartrate, were prepared with a weight of 0.01 g and each of them dissolved in a 25 mL volumetric flask and then transferred to a 100 mL volumetric flask filled to the mark after setting the pH to 9. Reagent solution 1×10^{-3} mg/L: A stock solution prepared by dissolving a 0.0244 g of 4-MDD in 100 mL of distilled water and by using the law of dilution, the solutions were prepared less concentrated.

Design valve for injection model

The most important thing in the FIA work is the injection valve which has been designed in the laboratory from cheap and eco-friendly materials that can be recycled to give more identical results where the valve contains four secondary valves for loading chemicals. Linked on the one hand to a peristaltic pump with 8 rollers to eliminate the pump speed pulsations of 70 r/min and connected on the one hand. On the other hand, the reaction coil of 20 cm in a coiled manner is used to get rid of the dilution of the mixed materials and then connected to the injection cell that contains two input and output ports of the spectral cell, then the detector is connected to a cording device to give a record of the analytical signal by a record based on the height of the peak as in Fig. 1. We concluded that through our study, an innovative valve made of high-efficiency and cost-effective raw materials, and the injection and loading control process can be implemented by three-way sub-valves, which are fixed outside the chip.

■ RESULTS AND DISCUSSION

Absorption Spectrum Maximum for Complex Pb(II) and Compare It with λ_{max} of the Reagent

In a test tube 2 mL of a solution of Pb(II) ion was mixed in it at a concentration of 10 mg/L at pH = 9 and 2 mL of a reagent solution at a concentration of 1×10^{-4} M. Then a spectroscopic scan of the solution of the above-prepared compound was carried out in the region confined between 190–800 nm, where the λ_{max} values of the complex were determined in this region with the highest absorption value at 498 nm. Then, it was compared with the wavelength of the pre-equipped reagent of 387 nm, where we conclude the complex shift towards a longer wavelength and lower energy of 111 nm.

Flow Injection System

Chemical parameters

The effect of pH on the determination of the Pb(II) ion. Different media of pH levels 2–11 were prepared under the conditions of reagent volume 157.0 µL, Pb(II) ion volume 157.0 µL, metal ion concentration 15 mg/L,

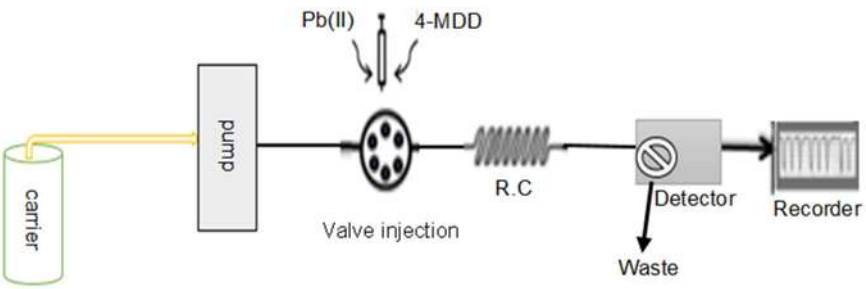

Fig 1. New design of FIA unit [4-MDD: 4-((4-methoxy phenyl)diazenyl)benzene-1,3-diol, R.C: Reaction coil, carrier: water]

reagent concentration = 1×10^{-4} M, reaction coil length = 15 cm, cell flow rate = 3.600 mL/min, optimal pH = 9. This is all shown in Fig. 2, gave the highest and best height, an ideal buffer solution was prepared tetrasodium ($Na_2B_4O_7 \cdot 10H_2O$) and boric acid (H_3BO_3)] because our study in the flow injection technique depends on the pick height and not the absorbance.

Optimum reagent concentration. Different concentrations of the reagent were prepared, ranging from 1×10^{-6} to 1×10^{-4} molar, to study the effect of the concentration of the organic reagent and through the work, we can conclude that the optimal concentration was 8×10^{-5} M, which gave the highest pick, and therefore, it is the best pick. Then, it started to decline due to the increase in the dilution of the reagent and the experiment was conducted under the following conditions: reagent volume 157.0 µL, Pb(II) ion volume 157.0 µL, metal ion concentration = 15 mg/L, pH = 9, and reaction coil length = 15 cm, cell flow rate is 3.600 mL/min. The results are shown in Fig. 3.

Physical parameters

Flow rate. After studying the optimal conditions for the chemical variables, the optimum flow velocity of the Pb(II) ion estimation process was studied in the conditions the reagent volume is 157.0 µL, and the Pb(II) ion volume is 157.0 µL, the metal ion concentration = 15 mg/L, pH = 9, reaction coil length = 15 cm, and reagent concentration 8×10^{-5} M, we obtained the highest, best height and uniform peak shape at 9.100 mL/min for mobile stage. The selection is due to the effect of increasing the dispersion, which leads to a complex concentration dilution, as shown in Fig. 4

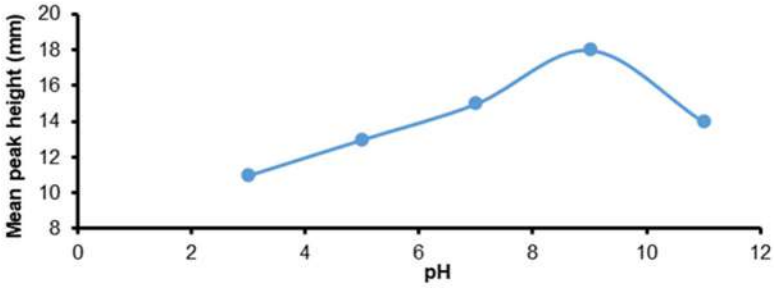

Fig 2. The effect of the pH on mean peak height

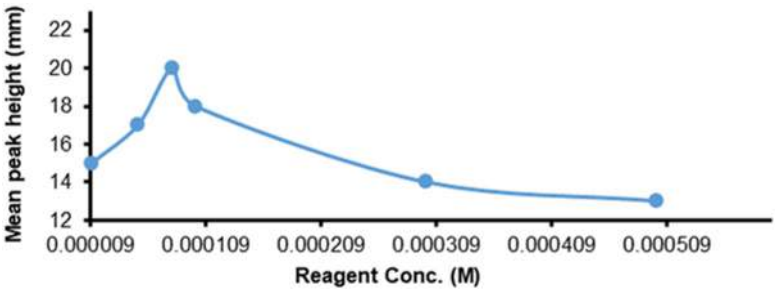

Fig 3. The effect of reagent concentration on mean peak height

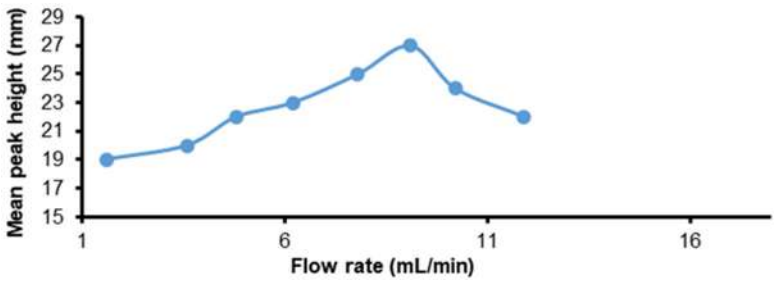

Fig 4. The effect of flow rate on mean peak height

selected because the response was sharp and dependable. Authors found that low flow rates cause double, distorted, and wide peaks, while fast flow rates decrease the response.

Reaction coil length effect. Different lengths of the reaction coil and a radius tube of 0.05 cm, which ranged between 15–35 cm, were used to know the effect of the length of the reaction coil in the estimation of the Pb(II) ion 157.0 µL, Pb(II) ion concentration = 15 mg/L, pH = 9, flow rate = 9.100 mL/min, and reagent concentration 8×10^{-5} M. At this length, we obtained a high sensitivity peak and then reduced the height to increase dispersion and attenuation [26] as shown in Fig. 5.

The effect of the volume of the organic reagent

Prepare a series of volumes for the organic reagent under study, 235.5–78.50 µL, junction length changes of 157.0 µL, Pb(II) ion concentration = 15 mg/L, flow rate = 9.100 mL/min, reagent concentration 8 × 10–5 M and reaction coil length 157.0 µL. It turns out that the optimal volume of the detector is 117.8 µL corresponding to the best peak height equivalent to a tube with a length of 15 cm, as shown in Fig. 6. An increase in the volume of the detector leads to a decrease in the response and the appearance of the double peak because the excess volume of the detector is confined between two regions that form the product of this interaction [27].

The volume of the metal ion

Different volumes of Pb(II) metal ions were used in preparing the complex to find out the ideal metal ion volume for the estimation process. It was found that the best volume of metal ion, which gives the best sensitivity and the best peak height, is 117.8 µL, which is equivalent to a tube length of 15 cm and a radius of 0.05 cm, which gives the best peak height as shown in Fig. 7, and this

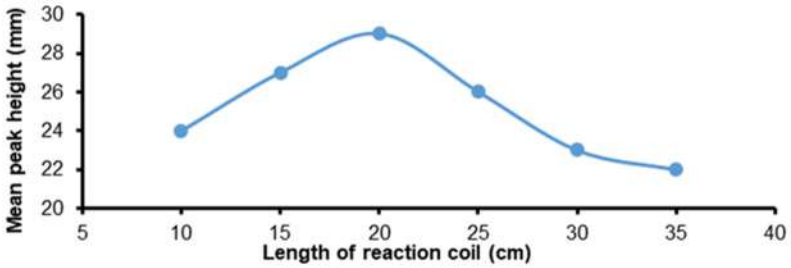

Fig 5. Effect of coil length effect on mean peak height

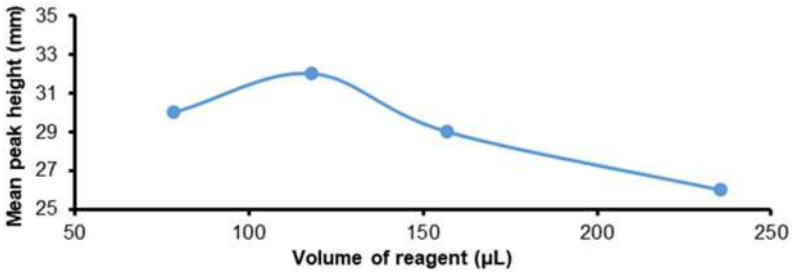

Fig 6. Effect of reagent volume on mean peak height

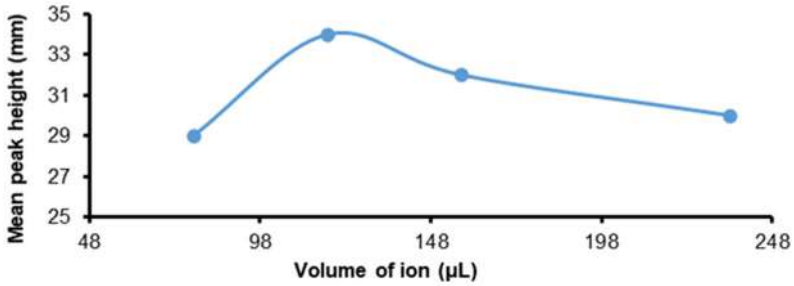

Fig 7. Effect of volume of the Pb(II) ions on mean peak height

experiment was conducted under the best conditions. The volume of the organic reagent is 117.8 µL, the concentration of the Pb(II) metal ion = 15 mg/L, pH = 9, the flow rate = 9.100 mL/min, the concentration of the reagent 8×10^{-5} M and the reaction coil length is 157.0 µL.

Dead volume study

The aim of this study is to clarify the fact that the complex is formed within the flow injection system, where two experiments were conducted. First, the reagent was injected into the first ring and in the second ring, H_2O was injected, instead of injecting the Pb(II) ion, as there was a response of 8.91 mm. In the second experiment H_2O was injected into the first ring instead of the reagent and in the ring second there is Pb(II) ion where we found that there is no response where the smaller the dead volume, means the results are better, then the Pb(II) ion and the reagent were injected for complex formation and measured the height of the peak where the result is as shown in the Table 1 and Fig. 8.

Calibration curve at optimum conditions

A calibration curve study after preparing the optimal conditions for the determination of the Pb(II) ion in different environmental and life models was used, after preparing a series of ion concentrations under study between 0.05–30 mg/L, where we get the correlation coefficient = 0.9995, the limit of detection (LOD) = 0.026 mg/L, the limit of quantification (LOQ) = 0.088 mg/L, linearity = 0.5–27 mg/L as shown in Fig. 9. The method under study was validated as the calibration curve indicated the linearity of Beer's law.

Applications to different biological and environmental samples

The purpose of this experiment was to design an injection valve for the determination of Pb(II) ions in environmental and biological models. The prepared samples were taken and analyzed using the flow injection technique. Table 2 shows satisfactory results for different samples, including agricultural and non-agricultural soils in the district of Rifai Al-Fajr, Nahr Al-Fajr, celery, cauliflower, and cabbage 100.4–96.67%. It was a comparison of the technique under study with the FAAS flame atomic absorption technique.

Table 1. Study of dead volume

No.	Test type	The height of the peak (mm)
1	Pb(II) + H_2O	0.000
2	H_2O + reagent	8.910
3	Pb(II) + reagent	25.00

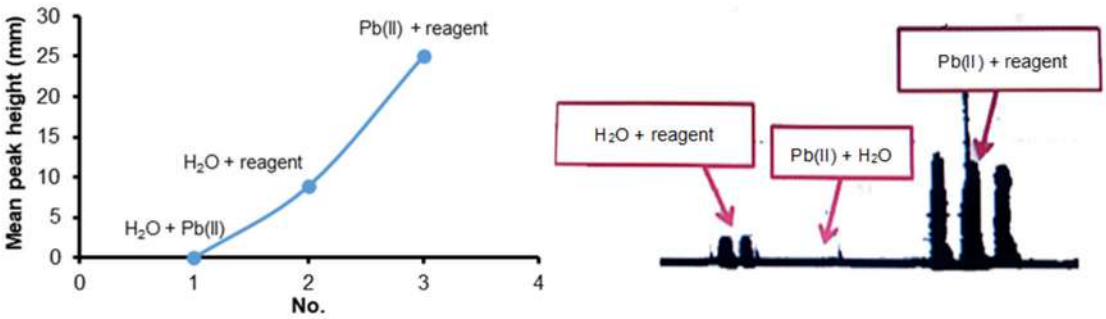

Fig 8. Study of the dead volume in FIA

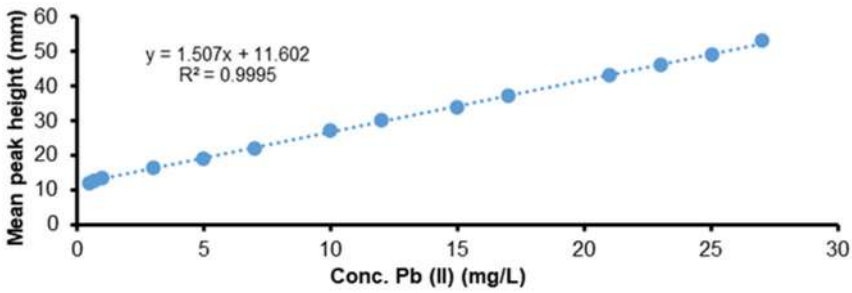

Fig 9. Calibration curve study at optimum conditions

Table 2. Determination of Pb(II) ion by FIA and FAAS technique in different samples

Sample	Value take (mg/L)	Value round mg/L FIA:FAAS	Er FIA: FAAS %	Rec FIA:FAAS %
Rifai River	0.700	0.701:0.703	0.1429:0.429	100.1:100.4
Soil agricultural land in Al-Fajr	6.000	6.025 :6.060	0.416:1.000	100.4:101.0
Soil non-agricultural land in Al-Fajr	6.000	6.015:6.018	0.250:0.300	100.3:100.3
Dirt close to the industrial neighborhood in Al-Fajr	6.000	6.130 : 5.080	-3.330:2.166	96.67:102.2
Soil agricultural land in Rifai				
Soil non-agricultural land in Rifai	6.000	6.023:6.020	0.383:0.330	100.4:100.3
The dust of the wall of Al-Nibras gas station	6.000	6.008:5.700	0.133:-5.000	100.1:95.00
Water from the car wash station	6.000	6.010:6.007	0.160:0.110	100.2:100.1
Dirt from a car wash station	6.000	6.000:6.003	0.000:0.050	100.0:100.1
Fish	6.000	6.013:6.010	0.210:0.166	100.2:100.2
Celery	7.000	7.004:7.012	0.057:0.170	7.012:100.2
Cauliflower	7.000	7.014:7.010	0.200:0.143	100.2:100.1
Cabbage	7.000	7.014:7.000	0.000:0.200	100.0:100.2
Bean	7.000	7.025:7:007	0.357:0.100	100.4:100.1
	7.000	6.890:7.032	-1.570:0.457	98.43:100.5

CONCLUSION

Through this study, the investigated system was able to estimate the aforementioned (Pb(II)) ion using the organic azo reagent with high efficiency and accuracy using the confluent areas' flow injection technique. We can dispense with other classical methods of analysis because they are stressful and use expensive chemicals. Our system is simple and eco-friendly because it is possible to be manufactured in a laboratory-designed system from environmentally available and recycled materials. The flow injection system in the confluent regions showed higher sensitivity compared to the FAAS method.

ACKNOWLEDGMENTS

The authors would like to thank the College of Science, University of Sumer, for providing the place and facilitating the completion of the scientific paper.

AUTHOR CONTRIBUTIONS

Thekrayat Joodi Jassim conducted the experiment, Raisan Kadhim Taresh did the calculations, and Thekrayat Joodi Jassim and Raisan Kadhim Taresh wrote and reviewed the manuscript. All authors approved the final version of this manuscript.

REFERENCES

[1] Alkherraz, A.M., Ali, A.K., and Elsherif, K.M., 2020, Removal of Pb(II), Zn(II), Cu(II) and Cd(II) from aqueous solutions by adsorption onto olive branches activated carbon: Equilibrium and thermodynamic studies, *Chem. Int.*, 6 (1), 11–20.

[2] Alnawmasi, J.S., 2023, Construction of amino-thiol functionalized ion-imprinted chitosan for lead (II) ion removal, *Carbohydr. Polym.*, 308, 120596.

[3] Nur, Y., Rohaeti, E., and Darusman, L.K., 2017, Optical sensor for the Determination of Pb^{2+} based on immobilization of dithizone onto chitosan-silica membrane, *Indones. J. Chem.*, 17 (1), 7–14.

[4] Pavlov, D., 2017, "Invention and Development of the Lead–Acid Battery" in *Lead-Acid Batteries: Science and Technology*, Elsevier, Amsterdam, 3–32.

[5] Kurniawan, Y.S., Ryu, M., Sathuluri, R.R., Iwasaki, W., Morisada, S., Kawakita, H., Ohto, K., Maeki, M., Miyasaki, M., and Jumina, J., 2019, Separation of Pb(II) ion with tetraacetic acid derivative of calix[4]arene by using droplet-based microreactor system, *Indones. J. Chem.*, 19 (2), 368–375.

[6] Hashim, A., and Hadi, A., 2017, Novel lead oxide polymer nanocomposites for nuclear radiation shielding applications, *Ukr. J. Phys.*, 62 (11), 978–983.

[7] Gusain, R., Kumar, N., Fosso-Kankeu, E., and Ray, S.S., 2019, Efficient removal of Pb(II) and Cd(II) from industrial mine water by a hierarchical

MoS_2/SH-MWCNT nanocomposite, *ACS Omega*, 4 (9), 13922–13935.

[8] Gao, P., Xiao, B., Liu, W., Zhang, X., Dong, J., and Xue, P., 2020, Analysis and health risk assessment of heavy metal in lotus root, *Environ. Chem.*, 39 (2), 362–370.

[9] Tong, J., Jiang, Q., Ferguson, A.J., Palmstrom, A.F., Wang, X., Hao, J., Dunfield, S.P., Louks, A.E., Harvey, S.P., Li, C., Lu, H., France, R.M., Johnson, S.A., Zhang, F., Yang, M., Geisz, J.F., McGehee, M.D., Beard, M.C., Yan, Y., Kuciauskas, D., Berry, J.J., and Zhu, K., 2022, Carrier control in Sn–Pb perovskites via 2D cation engineering for all-perovskite tandem solar cells with improved efficiency and stability, *Nat. Energy*, 7 (7), 642–651.

[10] Qu, J., Lin, X., Ziyang, L., Liu, Z., Liu, Y., Wang, Z., Liu, S., Meng, Q., Tao, Y., Hu, Q., and Zhang, Y., 2022, One-pot synthesis of Ca-based magnetic hydrochar derived from consecutive hydrothermal and pyrolysis processing of bamboo for high-performance scavenging of Pb(II) and tetracycline from water, *Bioresour. Technol.*, 343, 126046.

[11] Chlaib, H.K., and Jassim, T.J., 2022, Study the monthly changes in the physical and chemical properties of Al-Garraf river water in Qalat Suker city, Dec. 2019-April, 2020, a sustainable study, *Univ. Thi-Qar J. Agric. Res.*, 11 (1), 1–19.

[12] Shanshal, M., Faris, S.S., and Shihab, O.H., 2020, Assessment of heavy metal contamination in the soil of Fellujah city, *J. Univ. Anbar Pure Sci.*, 14 (2), 32–37.

[13] Chilian, A., Tanase, N.M., Popescu, I.V., Radulescu, C., Bancuta, O.R., and Bancuta, I., 2022, Long-term monitoring of the heavy metals content (Cu, Ni, Zn, Cd, Pb) in wastewater before and after the treatment process by spectrometric methods of atomic absorption (FAAS and ETAAS), *Rom. J. Phys.*, 67, 804.

[14] Suprun, E.V., Daboss, E.V., Pleshakov, V.M., Vokhmyanina, D.V., Radko, S.P., Karyakin, A.A., Kozin, S.A., Makarov, A.A., and Mitkevich, V.A., 2022, Application of Prussian Blue modified carbon electrodes for amperometric detection of amyloid-β peptides by flow injection analysis, *Electrochim. Acta*, 406 (20), 139829.

[15] Wang, Y., Ge, H., Wu, Y., Ye, G., Chen, H., and Hu, X., 2014, Construction of an electrochemical sensor based on amino-functionalized metal-organic frameworks for differential pulse anodic stripping voltammetric determination of lead, *Talanta*, 129, 100–105.

[16] Jassim, T.J., Hesson, H.M., and Karam, F.F., 2023, Preparation and characterization of new hetrocyclic azo thiozal dye ligand and its use as a reagent for determination of Zn^{+2} ion in drug by new analytical method, *J. Med. Chem. Sci.*, 6 (4), 857–867.

[17] Karimi-Maleh, H., Darabi, R., Shabani-Nooshabadi, M., Baghayeri, M., Karimi, F., Rouhi, J., Alizadeh, M., Karaman, O., Vasseghian, Y., and Karaman, C., 2022, Determination of D&C Red 33 and Patent Blue V Azo dyes using an impressive electrochemical sensor based on carbon paste electrode modified with ZIF-8/g-C_3N_4/Co and ionic liquid in mouthwash and toothpaste as real samples, *Food Chem. Toxicol.*, 162, 112907.

[18] Karimi-Maleh, H., Beitollahi, H., Senthil Kumar, P., Tajik, S., Mohammadzadeh Jahani, P., Karimi, F., Karaman, C., Vasseghian, Y., Baghayeri, M., Rouhi, J., Show, P.L., Rajendran, S., Fu, L., and Zare, N., 2022, Recent advances in carbon nanomaterials-based electrochemical sensors for food azo dyes detection, *Food Chem. Toxicol.*, 164, 112961.

[19] Afaq, J.K., 2021, Preparation and characterization of some complexes of transition elements with heterocyclic ligand mixture, *Thesis*, University of Kufa.

[20] Budinski, V., and Donlagic, D., 2021, All Silica Micro-fluidic flow injection sensor system for colorimetric chemical sensing, *Sensors*, 21 (12), 4082.

[21] Campmajó, G., Saurina, J., and Núñez, O., 2022, FIA–HRMS fingerprinting subjected to chemometrics as a valuable tool to address food classification and authentication: Application to red wine, paprika, and vegetable oil samples, *Food Chem.*, 373, 131491.

[22] Demir, V., and Ergin, S., 2013, Occurrence and assessment of chemical contaminants in drinking water in Tunceli, Turkey, *J. Chem.*, 2013, 238374.

[23] Wang, T., Xie, T., Liu, Z., and Li, S., 2022, An 84dB-SNDR Low-OSR 4th-order noise-shaping SAR with an FIA-assisted EF-CRFF structure and noise-mitigated push-pull buffer-in-loop technique, *2022 IEEE International Solid- State Circuits Conference (ISSCC)*, San Francisco, CA, USA, 418–420.

[24] Pagliarini, E., Spinelli, S., Proserpio, C., Monteleone, E., Fia, G., Laureati, M., Gallina Toschi, T., and Dinnella, C., 2022, Sensory perception and food neophobia drive liking of functional plant-based food enriched with winemaking by-products, *J. Sens. Stud.*, 37 (1), e12710.

[25] Sofiia, T., Barek, J., and Bohdan, J., 2023, High-performance amperometric biosensor for flow injection analysis consisting of a replaceable lactate oxidase-based mini-reactor and a silver amalgam screen-printed electrode, *Electrochim. Acta*, 445, 142033.

[26] Manousi, N., Kabir, A., Furton, K.G., Zachariadis, G.A., and Anthemidis, A., 2021, Automated solid phase extraction of Cd(II), Co(II), Cu(II) and Pb(II) coupled with flame atomic absorption spectrometry utilizing a new sol-gel functionalized silica sorbent, *Separations*, 8 (7), 100.

[27] Klamtet, J., Sanguthai, S., and Sriprang, S., 2007, Determination of lead in aqueous samples using a flow injection analysis system with on-line preconcentration and spectrophotometric detection, *NU Sci. J.*, 4 (2), 122–131.

A Sustainable Synthesis, Eco-Safe Approach Efficiency and DFT Study of Novel 5,6,7,8-Tetrahyroquinazolin-2(1*H*)-one Derivatives as Antioxidant Reagents

Mohammed Abed Kadhim[1], Amin Farouk Mohamed Fahmy[2], Emad Khelil Mohammed Zangana[3*], Aya Ibrahim Hassaballah[2], and Sameh Ahmed Rizk[2]**

[1]*Department of Chemistry, College of Sciences, University of Anbar, Ramadi 55431, Iraq*

[2]*Department of Chemistry, Faculty of Science, Ain Shams University, Cairo 11566, Egypt*

[3]*Department of Chemistry, Faculty of Science and Health, Koya University, Koya KOY45, Iraq*

* ***Corresponding author:***

email:
Emad.Zangana@koyauniversity.org;*
*samehrizk@sci.asu.edu.eg***

Received: April 2, 2023
Accepted: May 11, 2023

DOI: 10.22146/ijc.83583

Abstract: *5,6,7,8-Tetrahydroquinazolin-2-(thio)-ones (THQ) fits the class of* N-*heterocycles as a structural core in numerous bioactive compounds. They promptly extended previous decades. They were significantly recognized in combinatorial chemistry and materials science to determine the drug discovery, antioxidants, and pharmaceuticals fields. In the present work, one-pot multicomponent sustainable synthesis of THQ with easily accessible starting materials, i.e., cyclohexanone, different aromatic aldehydes and (thio)urea, has been performed to determine the proposed Biginelli mechanism that is supported by DFT. It is found that the THQs are synthesized by a mechano-chemical (grinding) tool to achieve a yield of 85.2% within 3.5 min, i.e., YE (% yield/time) 24.34 differs from the conventional method in which lower % yield (YE = 0.72) of THQ was achieved. This confirmed that in the green chemistry principle, the determination of % yield according to saving reaction time must be considered. Moreover, DFT-based antioxidant properties of the THQ were also studied in which the most potent antioxidant compounds were* ***7b*** *>* ***6d*** *>* ***2f****. Softness (σ, eV^{-1}) and hardness (η, eV mol^{-1}) can approve the soft molecule that stays more reactive as a result of decreasing the energy gap along heterocyclic with values 0.1491 > 0.1300 > 0.1168 eV^{-1} one-to-one with the efficiency of antioxidant.*

Keywords: *green chemistry; eco-safe approach efficiency; DFT; antioxidant reagents; 5,6,7,8-tetrahyroquinazolin-2(1*H*)-one*

■ INTRODUCTION

It has been 40 years since Biginelli's initial report was published. The first mechanism for the synthesis of dihydropyrimidinone was conducted by Folkers and Johnson [1], who based their deduction on the reaction yields. Bimolecular condensation of benzaldehyde and urea was suggested as an intermediate in the reaction product. In 1973, a second mechanistic proposal was suggested by Sweet and Fissekis [2], which involved an aldol condensation between benzaldehyde and ethyl acetoacetate to form a stabilized carbonium ion as a primary step. Kappe et al. [3] reinvestigated the mechanism using ^{1}H and ^{13}C-NMR spectroscopy. He established that the acid-catalyzed condensation between aldehyde and urea generated iminium ion **1**. Interception of this iminium ion by ethyl acetoacetate, possibly through its enol tautomer, produces an open chain ureide **2**, which subsequently cyclizes to dihydropyrimidine DHPMs **3** by the removal of H_2O (Scheme 1). Biginelli protocol had a problem with low to moderate yields, mainly when substituted aromatic and aliphatic aldehydes are hired. As a result of various adverse effects, further severe conditions and long reaction times have occurred [4-6].

Recently, expose improved reaction protocols for the synthesis *via* a one-pot approach [7-9] or using novel or complex multistep strategies [10-11]. The efficiency of chemical reactions is determined by atom economy

(AE), which shows the atoms in a reaction's starting components that are incorporated (reaction steps) to obtain the intended output, (i.e., how effectively the reactant atoms are used in a certain reaction. The conversion efficiency is measured by AE and yield economy (YE), which also determine the yield (%) of the desired product at reaction time (yield (%)/reaction time (min)) [12-13].

Based on green chemistry published papers, the authors have shown the significance of the density functional theory (DFT) with multicomponent reactions (MCR) method (YE, AE and RME) in approaching the sustainability of the newly heterocyclic synthesis. It has been reported that 2,2′-azino-bis-(3-ethylbenzothiazoline-6-sulphonic acid) diammonium salt (ABTS) was used to measure the antioxidant activity of pure substances in the presence of hydrogen peroxide (H_2O_2). That method is also appropriate for investigating the water and lipid-soluble antioxidants as well as studying pure substances as reducing antioxidants**.** Adding the antioxidants to the new compound (pre-formed radical cation) decreases its ABTS to a certain level over time, depending on the antioxidant activity, the concentration of the antioxidant, and reaction durations. Thus, the amount of decolorization is assessed as a percentage inhibition of the $ABTS^{\bullet+}$ radical cation, and as a function of concentration and duration, then it is computed relative to the reactivity of ascorbic acid as a standard, under the same circumstances [14-15].

In the present work, we synthesized a new series of 5,6,7,8-tetrahydroquinazolin-2-(thio)-ones, which is supported by DFT, using readily available starting materials such as cyclohexanone, various aromatic aldehydes, and (thio)urea. It has been discovered that the THQs are synthesized using a mechano-chemical (grinding) tool, which results in a yield of 85.2% in 3.5 min, or YE (% yield/time) = 24.34, as opposed to the conventional approach, which produced a lower yield (YE = 0.72) of THQ. Moreover, the most effective antioxidant molecules were **7b** > **6d** > **2f** according to investigations of the THQ's DFT-based antioxidant capabilities, the schematic diagram for this investigation is shown in Fig. 1.

■ EXPERIMENTAL SECTION

Materials

All the chemicals and solvents utilized without additional purification were from Merck, Darmstadt, Germany. These reagents included urea (CH_4N_2O, 99.0%), thiourea (CH_4N_2S, +99%), *N*-phenylurea ($C_7H_8N_2O$, 97%), potassium hydroxide anhydrous (KOH, 99.99%), cyclohexanone ($C_6H_{10}O$, 99.8%), benzaldehyde (C_7H_6, 99.5%), 4-chlorobenzaldehyde (C_7H_5ClO, 97%), 4-nitrobenzaldehyde ($C_7H_5NO_3$, 97%), 4-methoxybenzaldehyde ($C_8H_8O_2$, 98%), 4-(dimethylamino)benzaldehyde ($C_9H_{11}NO$, 98%), hydrochloric acid solution (HCl, 37%), ethanol (99.9%), benzene (99.8%), petroleum ether 60/80, sodium bisulfate ($NaHSO_4$, 99.0%), and hydrogen peroxide (H_2O_2).

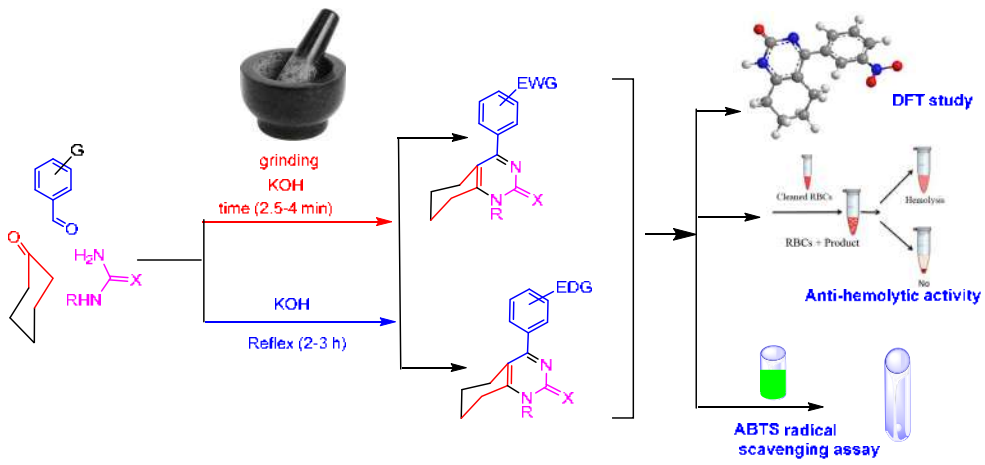

Fig 1. Schematic diagram of this study

Instrumentation

Melting point of the synthesized compounds was measured with Gallen Kamp apparatus (London, UK), and microanalytical data can be seen in Table 1. IR spectra can be verified on a Perkin Elmer RXIFTIR spectrometer (Waltham, USA). A Varian Gemini 300 MHz spectrometer was used to measure the ^{1}H-NMR spectra (Palo Alto, CA, USA) and recorded in DMSO-d_6. The chemical shifts were recorded in δ (ppm) and TMS was used as an internal standard. For the purpose of determining mass, a Tokyo, Japan-based Shimadzu GC-MS spectrophotometry QP 1000 EX system that operates at 70 eV was used. All the reactions were monitored by TLC.

Procedure

*Synthesis of 5,6,7,8-tetrahyroquinazolin-2(1*H*)-ones (THQs)* via *mechanochemical technique*

The mixture of the aromatic aldehydes (3 mmol), cyclohexanone (3 mmol) with binucleophile (3 mmol) as urea, thiourea and phenyl urea in the presence of the catalytic amount of KOH was grained together at the same time, see Table 1. Once the grinding was completed, as monitored by TLC, the mixture of the reaction has been transformed into a colored solid mass that was acidified with cold H_2O/HCl (4:1). The solid product was recovered, filtered out, and recrystallized from the appropriate solvent.

Table 1. Outline physical characterization of the synthesized compounds and the differences in both grinding times and concentrations

Prod.	Time (min.)		M.p. °C	M.F	Elemental Analysis (%)	
No.	G.	Ref.	(solvent recy.)	(M.W.)	Req.	Found
1a	3.5	120	>300 (ethanol)	$C_{14}H_{13}N_2OCl$	C:64.50 H:5.03 N:10.74	C:64.19 H:4.72 N:10.80
1b	3.5	135	180-182 (benzene)	$C_{14}H_{13}N_3O_3$	C:61.99 H:4.83 N:15.49	C:61.52 H:4.56 N:15.27
2a	4.0	150	>300 (ethanol)	$C_{14}H_{14}N_2O$	C:74.31 H:6.24 N:12.38	C:73.90 H:7.12 N:12.40
2b	4.0	150	140–142 (petroleum 60/80)	$C_{15}H_{16}N_2O_2$	C:70.29 H:6.29 N:10.93	C:69.90 H:6.80 N:10.57
2c	4.0	150	234–237 (Ethanol)	$C_{16}H_{19}N_3O$	C:71.35 H:7.11 N:15.60	C:71.12 H:7.59 N15.32
3a	3.5	180	160–162 (Benzene)	$C_{14}H_{13}N_2SCl$	C:60.75 H:4.73 N:10.12	C:60.55 H:5.91 N:10.35
3b	3.5	180	140–142 (Benzene)	$C_{14}H_{13}N_3SO_2$	C:58.52 H:4.56 N:14.62	C:58.78 H:4.77 N:14.52
4a	3.5	180	280–282 (Benzene)	$C_{14}H_{14}N_2S$	C:69.39 H:5.82 N:11.56	C:69.14 H:5.67 N:11.28
4b	3.5	180	136–138 (Benzene)	$C_{15}H_{16}N_2SO$	C:66.15 H:5.92 N:10.29	C:66.39 H:6.13 N:10.25
4c	2.5	120	170–173 (Pet/Benzene)	$C_{16}H_{19}N_3S$	C:67.33 H:6.71 N:14.72	C:66.89 H:7.25 N:14.54

Prod. No.	Time (min.) G.	Time (min.) Ref.	M.p. °C (solvent recy.)	M.F (M.W.)	Elemental Analysis (%) Req.	Elemental Analysis (%) Found
5a	3.0	120	158–160 (Ethanol)	$C_{20}H_{17}N_2OCl$	C:71.32 H:5.09 N:8.32	C:71.49 H:5.12 N:8.48
5b	3.0	120	134-136 (Ethanol)	$C_{20}H_{17}N_3O_3$	C:69.15 H:4.93 N:12.10	C:68.92 H:5.04 N:12.47
6a	3.0	120	215-217 (Ethanol)	$C_{20}H_{18}N_2O$	C:79.44 H:6.00 N:9.26	C:79.36 H:6.42 N:9.05
6b	3.0	120	224-226 (Benzene)	$C_{21}H_{20}N_2O_2$	C:75.88 H:6.06 N:8.43	C:75.36 H:6.37 H:8.27

Synthesis of 5,6,7,8-tetrahyroquinazolin-2(1*H*)-ones (THQs)* via *conventional technique

Aromatic aldehydes (3 mmol) dissolved in absolute ethanol (30 mL) and the solution was then refluxed with (3 mmol) of cyclohexanone and (3 mmol) of binucleophile for instance, urea, thiourea and phenyl urea with catalytic amount of KOH for 2–3 h (the reaction was monitored by TLC (ethyl acetate:toluene (2:1)). The reaction mixture was vacuum distilled to half of its volume, and after that, it was acidified with diluted hydrochloric acid (4:1). The identical chemicals were produced by obtaining a solid product, which was filtered and recrystallizing from appropriate solvents.

4-(4-Chlorophenyl)-5,6,7,8-tetrahydroquinazolin-2(1*H*)-one (1a). White crystal, IR (ν, cm^{-1}): 3223 (NH), 3034 (ArC–H), 2966 (AliC–H), 1700 (C=O) and 1646 (C=N), MS (*m/z*) [M+2; 55%] 264, [M^+, 100%], 262, 172, 159, 143, 120. ^{1}H-NMR (400 MHz, DMSO-d_6) δ: 1.74–2.06 (*dt*, 4H, $2CH_2$, *J* = 8.8, 4.9 Hz), 4.07–4.14 (*dt*, 4H, $2CH_2$, *J* = 8.8, 4.9 Hz), 6.37–6.68 (*m*, 4H, ArH), 10.14 (*s*, 1H, NH, exchangeable D_2O), ^{13}C-NMR (100 MHz, DMSO) δ: 22.28, 43.29, 52.82, 67.78, 128.40, 128.94 (2), 129.14, 129.41 (2), 130.72, 131.37, 132.57 (2), 139.65, 141.42, 153.54, 154.46, 155.96, 169.6., Anal. Calc. for $C_{14}H_{13}N_2OCl$ (260.072), %C:64.50; %H:5.03; %N:10.74 found, %C:64.19; %H:4.72; %N:10.80.

4-(3-Nitrophenyl)-5,6,7,8-tetrahydroquinazolin-2(1*H*)-one (1b). White crystal, IR (ν, cm^{-1}): 3432 (NH), 3002 (Arom C–H), 2991 (Aliph C–H), 1679 (C=O), MS (*m/z*) [$M^{+\cdot}$] 272, 265, 253, 240, 212. ^{1}H-NMR (400 MHz, DMSO) δ: 1.82–1.96 (*dt*, 4H, $2CH_2$, *J* = 8.8, 4.9 Hz), 2.95–2.99 (*dt*, 4H, $2CH_2$, *J* = 8.8, 4.9 Hz), 7.38–7.79 (*m*, 4H, ArH), 9.92 (*s*, 1H, NH, exchangeable D_2O), ^{13}C-NMR (100 MHz, DMSO) δ: 22.28, 43.29, 52.82, 67.78, 128.40, 128.94 (2), 129.14, 129.41 (2), 130.72, 131.37, 132.57 (2), 139.65, 141.42, 153.54, 154.46, 155.96, 168.3, Anal. Calc. for $C_{14}H_{13}N_3O_3$ (271.096), %C:61.99; %H:4.83; %N:15.49 found, %C:61.52; %H:4.56; %N:15.27.

4-Phenyl-5,6,7,8-tetrahydroquinazolin-2(1*H*)-one (2a). White crystal, IR (ν, cm^{-1}): 3324, (NH), 3062 (ArC–H), 2981 (AliC–H), 1714 (C=O), MS (*m/z*) [$M^{+\cdot}$] 228, 216, 190, 165, 95. ^{1}H-NMR (400 MHz, DMSO) δ: 1.23-1.91 (*m*, 4H, $2CH_2$, *J* = 8.8, 4.9 Hz), 2.95–2.99 (*dt*, 4H, $2CH_2$, *J* = 8.8, 4.9 Hz), 7.22–7.50 (*m*, 5H, ArH), 9.51 (*s*, 1H, NH, exchangeable D_2O). Anal. Calc. for $C_{14}H_{14}N_2O$ (226.111), %C:74.31; %H:6.24; %N:12.38 found, %C:73.90; %H:7.12; %N:12.40.

4-(4-Methoxyphenyl)-5,6,7,8-tetrahydroquinazolin-2(1*H*)-one (2b). White crystal, IR (ν, cm^{-1}): 3379 (NH), 3032 (ArC–H), 2907 (AliC–H), 1674 (C=O), MS (*m/z*) [$M^{+\cdot}$] 256, 238, 228, 203, 163, 114, 92. ^{1}H-NMR (400 MHz, DMSO) δ: 2.08–2.49 (*dt*, 4H, $2CH_2$, *J* = 8.8, 4.9 Hz), 2.95–2.99 (*dt*, 4H, $2CH_2$, *J* = 8.8, 4.9 Hz), 3.82 (*s*, 3H, OCH_3), 7.02–7.62 (*m*, 4H, ArH), 10.32 (*s*, 1H, NH, exchangeable D_2O). Anal. Calc. for $C_{15}H_{16}N_2O_2$ (256.121), %C:70.29; %H:6.29; %N:10.93 found, %C:69.90; %H:6.80; %N:10.57.

4-(4-(Dimethylamino)phenyl)-5,6,7,8-tetrahydroquinazolin-2(1*H*)-one (2c). White crystal, IR (ν, cm^{-1}): 3222 (NH), 3079 (Ar C–H), 2981 (Ali C–H), 1708 (C=O), ^{1}H-NMR (400 MHz, DMSO) δ: 1.01–1.71 (*dt*, 4H, $2CH_2$, *J* = 8.8, 4.9 Hz), 2.49–2.52 (*dt*, 4H,

$2CH_2$, *J* = 8.8, 4.9 Hz), 2.95 (*s*, 6H, $N(CH_3)_2$), 6.88–7.29 (*m*, 4H, ArH). Anal. Calc. for $C_{16}H_{19}N_3O$ (269.153), %C:71.35; %H:7.11; %N:15.60 found, %C:71.12; %H:7.59; %N15.32.

4-(4-Chlorophenyl)-5,6,7,8-tetrahydroquinazolin-2(1*H*)-thione (3a). White crystal, IR (ν, cm^{-1}): 3077 (ArC–H), 2979 (AliC–H), MS (*m/z*) [$M^{+\cdot}$+2; 55%] 280, [$M^{+\cdot}$, 100%], 278, 263, 159, 146, 120. ^{1}H-NMR (400 MHz, DMSO) δ: 1.03–1.39 (*dt*, 4H, $2CH_2$, *J* = 8.8, 4.9 Hz), 7.38–7.79 (*m*, 4H, ArH), Anal. Calc. for $C_{14}H_{13}N_2SCl$ (276.049), %C:60.75; %H:4.73; %N:10.12 found, %C:60.55; %H:5.91; %N:10.35.

4-(3-Nitrophenyl)-5,6,7,8-tetrahydroquinazolin-2(1*H*)-thione (3b). White crystal, IR (ν, cm^{-1}): 3304 N-H, 2836 (SH), 3088 (ArC–H), 2976 (AliC–H). MS (*m/z*) [$M^{+\cdot}$] 289, 284, 255, 240, 221. ^{1}H-NMR (400 MHz, DMSO) δ: 1.01–1.09 (*dt*, 4H, $2CH_2$, *J* = 8.8, 4.9 Hz), 2.22–2.30 (*dt*, 4H, $2CH_2$, *J* = 8.8, 4.9 Hz), 7.38–7.79 (*m*, 4H, ArH), 9.92 (*s*, 1H, NH, exchangeable D_2O), ^{13}C-NMR (100 MHz, DMSO) δ: 22.28, 43.29, 52.82, 67.78, 128.40, 128.94 (2), 129.14, 129.41 (2), 130.72, 131.37, 132.57 (2), 139.65, 141.42, 153.54, 154.46, 165.96. Anal. Calc. for $C_{14}H_{13}N_3SO_2$ (287.073), %C:58.52; %H:4.56; %N:14.62 found, %C:58.78; %H:4.77; %N:14.52.

4-Phenyl-5,6,7,8-tetrahydroquinazoline-2(1*H*)-thione (4a). White crystal, IR (ν, cm^{-1}): 3320 (NH), 3065 (ArC–H), 2956 (AliphC–H), 1614 (C=S), MS (*m/z*) [$M^{+\cdot}$] 239, 224, 209, 190, 165, 95. ^{1}H-NMR (400 MHz, DMSO) δ: 1.33–1.91 (*m*, 4H, $2CH_2$, *J* = 8.8, 4.9 Hz), 2.95–2.99 (*dt*, 4H, $2CH_2$, *J* = 8.8, 4.9 Hz), 7.38–7.79 (*m*, 5H, ArH), 8.06 (*s*, 1H, NH, exchangeable D_2O), 8.42 (*s*, 1H, NH, exchangeable D_2O). Anal. Calc. for $C_{14}H_{14}N_2S$ (242.088), %C:69.39; %H:5.82; %N:11.56 found, %C:69.14; %H:5.67; %N:11.28.

4-(4-methoxyphenyl)-5,6,7,8-tetrahydroquinazoline-2(1*H*)-thione (4b). White crystal, IR (ν, cm^{-1}): 3266 (NH), 3039 (ArC–H), 2920 (AliC–H), 1407 (C=S), MS (*m/z*) [$M^{+\cdot}$-NH] 260, 251, 224, 210, 142, 112, 90. ^{1}H-NMR (400 MHz, DMSO) δ: 1.91–1.95 (*dt*, 4H, $2CH_2$, *J* = 8.8, 4.9 Hz), 2.61–2.57 (*dt*, 4H, $2CH_2$, *J* = 8.8, 4.9 Hz), 3.43 (*s*, 3H, OCH_3), 7.32–7.45 (*m*, 4H, ArH), 9.27 (*s*, 1H, NH, exchangeable D_2O). Anal. Calc. for $C_{15}H_{16}N_2SO$ (272.098), %C:66.15; %H:5.92; %N:10.29 found, %C:66.39; %H:6.13; %N:10.25.

4-(4-(Dimethylamino)phenyl)-5,6,7,8-tetrahydroquinazoline-2(1*H*)-thione (4c). White crystal, IR (ν, cm^{-1}): 3327 (NH), 3082 (ArC–H), 2930, 2861 (AliC–H), 1395 (C=S), MS (*m/z*) [$M^{+\cdot}$] 282, 280, 217, 185, 151, 144, 110, 96. ^{1}H-NMR (400 MHz, DMSO) δ: 1.07–1.25 (*dt*, 4H, $2CH_2$, *J* = 8.8, 4.9 Hz), 2.95–2.95 (*dt*, 4H, $2CH_2$, *J* = 8.8, 4.9 Hz), 6.63–7.57 (*m*, 4H, ArH), 9.56 (*s*, 1H, NH, exchangeable D_2O). Anal. Calc. for $C_{16}H_{19}N_3S$ (285.13), %C:67.33; %H:6.71; %N:14.72 found, %C:66.89; %H:7.25; %N:14.54.

4-(4-Chlorophenyl)-5,6,7,8-tetrahydro-1-phenylquinazolin-2(1*H*)-one (5a). White crystal, IR (ν, cm^{-1}): 3077 (ArC–H), 2918 (AliC–H), 1664 (C=O), MS (*m/z*) [$M^{+\cdot}$+2; 55%] 338, [$M^{+\cdot}$, 100%] 336, 276, 165, 138, 111. ^{1}H-NMR (400 MHz, DMSO) δ: 1.74–2.06 (*d*, 4H, $2CH_2$, *J* = 8.8, 4.9 Hz), 44.55–4.57 (*d*, 4H, $2CH_2$, *J* = 8.8, 4.9 Hz), 7.38–7.79 (*m*, 9H, ArH), ^{13}C-NMR (100 MHz, DMSO) δ: 22.28, 43.29, 52.82, 67.78, 128.40, 128.94 (2), 129.14, 129.41 (2), 130.72, 131.37, 132.57 (2), 139.65, 141.42, 153.54, 154.46, 155.96, 169.6. Anal. Calc. for $C_{20}H_{17}N_2OCl$ (336.103), %C:71.32; %H:5.09; %N:8.32 found, %C:71.49; %H:5.12; %N:8.48.

4-(3-Nitrophenyl)-5,6,7,8-tetrahydro-1-phenylquinazolin-2(1*H*)-one (5b). White crystal, IR (ν, cm^{-1}): 3088 (ArC–H), 2956 (AliC–H), 1680 (C=O), MS (*m/z*) [$M^{+\cdot}$] 348, 331, 256, 149, 134. ^{1}H-NMR (400 MHz, DMSO) δ: 1.22–1.49 (*dt*, 4H, $2CH_2$, *J* = 8.8, 4.9 Hz), 2.95–2.99 (*dt*, 4H, $2CH_2$, *J* = 8.8, 4.9 Hz), 7.39–7.90 (*m*, 9H, ArH). Anal. Calc. for $C_{20}H_{17}N_3O_3$ (347.127), %C:69.15; %H:4.93; %N:12.10 found, %C:68.92; %H:5.04; %N:12.47.

1,4-Diphenyl-5,6,7,8-tetrahydroquinazolin-2(1*H*)-one (6a). White crystal, IR (ν, cm^{-1}): 3062 (ArC–H), 2956 (AliC–H), 1688 (C=O), MS (*m/z*) [$M^{+\cdot}$] 302, 294, 264, 206, 76. ^{1}H-NMR (400 MHz, DMSO) δ: 1.33–1.91 (*m*, 4H, $2CH_2$, *J* = 8.8, 4.9 Hz), 2.95–2.99 (*dt*, 4H, $2CH_2$, *J* = 8.8, 4.9 Hz), 7.38–7.79 (*m*, 9H, ArH). Anal. Calc. for $C_{20}H_{18}N_2O$ (302.142), %C:79.44; %H:6.00; %N:9.26 found, %C:79.36; %H:6.42; %N:9.05.

4-(4-Methoxyphenyl)-1-phenyl-5,6,7,8-tetrahydroquinazolin-2(1*H*)-one (6b). White crystal, IR (ν, cm^{-1}): 3059 (ArC–H), 2933 (AliC–H), 1674 (C=O), MS (*m/z*) [$M^{+\cdot}$] 335, 281, 129, 119, 91. ^{1}H-NMR

(400 MHz, DMSO) δ: 1.03–1.21 (*dt*, 4H, $2CH_2$, *J* = 8.8, 4.9 Hz), 2.27–2.49 (*dt*, 4H, $2CH_2$, *J* = 8.8, 4.9 Hz), 3.33 (*s*, 3H, OCH_3), 7.13–7.37 (*m*, 9H, ArH). Anal. Calc. for $C_{21}H_{20}N_2O_2$ (332.152), %C:75.88; %H:6.06; %N:8.43 found, %C:75.36; %H:6.37; %N:8.27.

Quantum mechanical calculations

Geometrically optimized using hybrid DFT with Becke 3-parameters exchange potential and L-Y-P correlation functional (B3LYP) theory [16-17] with 6-31 G. Frontier orbitals (FO) indices were calculated in electron volt (eV) for the ligands using Jaguar module of Schrödinger interface [12-13]. For this purpose, the favorable binding poses of the ligand molecules obtained after the docking protocol were subjected to DFT analysis. It was analyzed using frontier molecular orbitals, namely highest occupied molecular orbitals (HOMOs), lowest unoccupied molecular orbitals (LUMOs), and their energy gap difference (HLG). When HOMO energy values show the ability of a ligand molecule to donate electrons, LUMO energies propose the capability of a ligand molecule to accept electrons from the protein. Additionally, the global descriptors for reactivity, such as chemical potential, hardness, electrophilicity, and softness, were analyzed in order to understand the mechanistic aspects of the hits in their ground states.

Antioxidant experiment

Antihemolytic activity. The anti-hemolytic potential of extract/fraction was inspected by a spectrophotometric procedure as described previously [13]. Five milliliters of blood from a healthy person was collected in EDTA vials and centrifuged for 5 min at 1000 × g. The supernatant was removed and the pellet was washed thrice with PBS (0.2 M, pH 7.4) before re-suspending in saline solution (0.5%). A 0.5 mL of the extract/fraction (100–1000 µg/mL in PBS) was dispensed to 1 mL of erythrocyte suspension and incubated at room temperature for 20 min. Next, 0.5 mL of H_2O_2 solution made in buffered saline was added to the reaction mixture to provoke oxidative degradation of the membrane lipids. Subsequently, the samples were centrifuged at 1000 × g for 10 min and the absorbance of supernatant was noted spectrophotometrically at 540 nm. The relative hemolysis was assessed in comparison with the hemolysis in the H_2O_2 treated (negative control), which was set as 100%. For positive control, phosphate buffer saline was used. Each set of experiments was performed in triplicate and the inhibitory activity of different fractions was calculated and expressed as percent inhibition of hemolysis.

ABTS test. The ABTS test has been used to evaluate the antioxidant perspective of all the synthesised compounds. ABTS (7 mM) interacts, in the dark, with potassium persulfate (2.45 mM) for 12 h at room temperature to obtain ABTS radical cations. ABTS solution was then diluted with methanol (50%) to have an absorbance at 745 nm $ABTS^{\bullet+}$ blue/green chromophores [10-12]. Percentage inhibition was calculated by Eq. (1).

$$\text{Quenching ability (\%)} = \frac{\text{control}_{abs} - \text{sample}_{abs}}{\text{control}_{abs}} \times 100 \quad (1)$$

Ascorbic acid was utilized as a standard control.

■ RESULTS AND DISCUSSION

Chemistry

Design and green synthesis

Substituting the *N*-amino group is one of the methods to increase the MCR's adaptability with urea and thiourea moieties which means using semi-carbazide and thiosemicarbazide. Quantum chemical computations explained the efficient one-pot synthesis of 5-aryl-1,3,4-triazaspiro[5.5]undecane-2,7-dione (**1a**, **b**), 3-aryl-2,3,4,5,6,7-hexahydro-1*H*-indazole-1-carboxamide (**2a-e**), through treatment aromatic aldehydes, cyclohexanone and carbazides. The proposed mechanism (Scheme 1) has been registered by DFT. The electron-deficient group in the aromatic aldehydes (high electrophilicity index) first attracted the carbazide and then reacted with cyclohexanone to get 1,3,4-triazaspiro[5,5]undecane-2,7-dione (**1**). Lower reactivity of the substituted benzaldehyde carrying electron donated group (higher LUMO) can be preferred to couple with cyclohexanone (soft-soft attack to afford C–C bond formation) for producing the corresponding chalcone which undergoes nucleophilic attacks *via* semi- and thiosemicarbazide followed by cyclization to afford the hexahydro-1*H*-indazole-1-carboxamide derivatives (**2a-e**).

THQ has a phenyl ring condensed with pyrimidin-4-one nucleus (Scheme 1). Most of the THQ derivatives are substituted on the carbon 4 chiral center. Therefore, the present article is aimed to apply mechano-chemical MCR *via* grinding for the synthesis of such heterocycles. MCR is a crucial step in the synthesis that helps to confirm the prevalence of this strategy in the target, THQ derivatives **1**, **2**, **3** and **4** (Scheme 1). The reaction of arylidene cyclohexanone *via* Michael reaction sites (N1, C3) is intended to prepare the target compounds (Scheme 2).

Using a variety of nitrogen nucleophiles, both electron-rich and electron-deficient aldehydes were accepted e.g., urea, thiourea, and phenyl urea in the presence of cyclohexanone (Scheme 3).

Measuring and process efficiency

MCRs are broadly defined as "one-pot" processes that connect at least three components simultaneously to enable fast production, such as heterocyclic in a single operation with sufficient chemical diversity from readily available reagents and thus respect the demanding

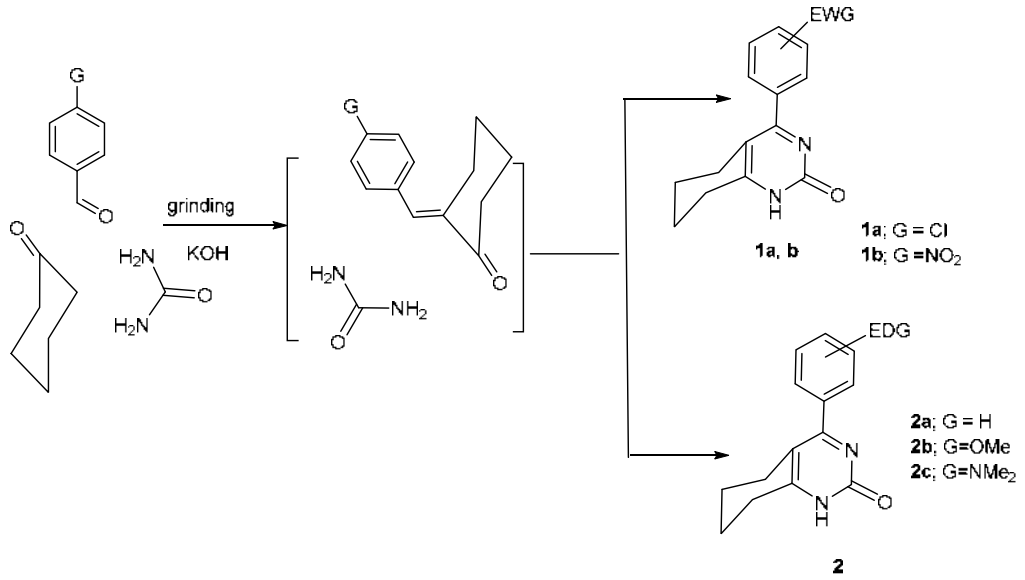

Scheme 1. Outline MCR of aromatic aldehyde, cyclohexanone and urea *via* mechanochemical method

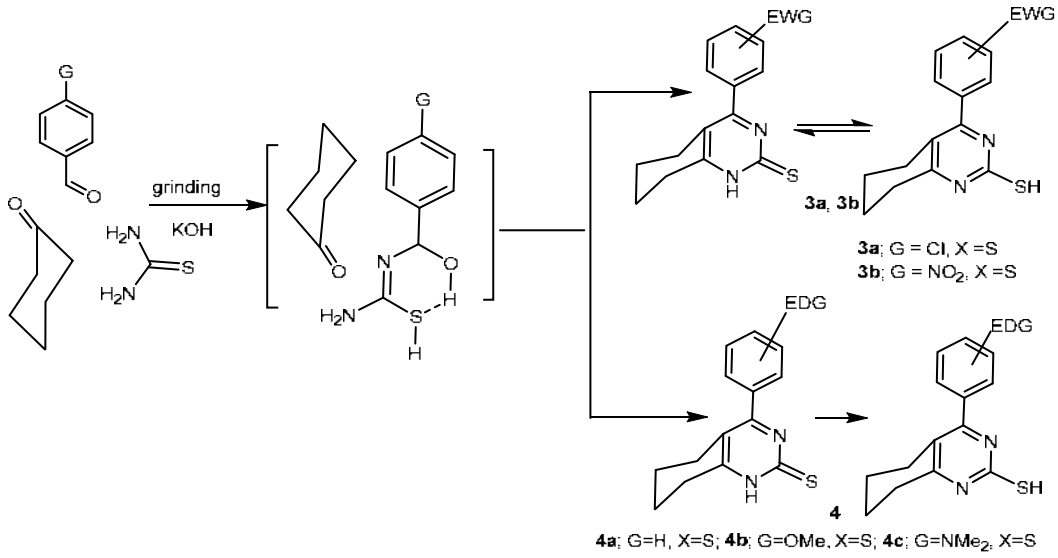

Scheme 2. Outline MCR of aromatic aldehyde, cyclohexanone and thiourea *via* the mechanochemical method

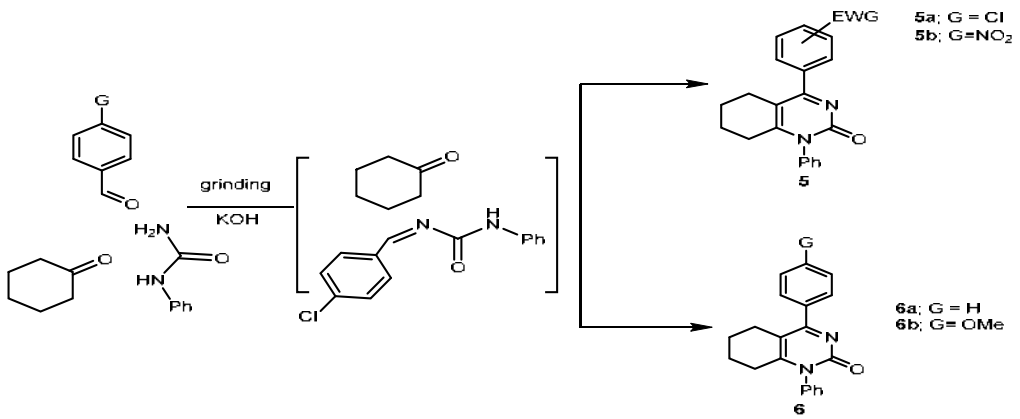

Scheme 3. Outline MCR of aromatic aldehyde, cyclohexanone and phenyl urea *via* the mechanochemical method

eco-compatibility principle like step efficiency and atom economy [15]. In addition, facile automation, simplicity, higher product yields and minimal waste generation reduce the cost, time, and energy [18]. Because of this, a greater YE suggests a higher degree of conversion, a chemical process that is considerably more effective, and the most cost-effective reaction, as previously said in Table 2. It is found that THQ **1** is synthesized by the mechanochemical (grinding) tool has % yield 85.2 at 3.5 min i.e., YE = 24.34 which differ from the conventional method YE = 0.72. In contrast, the % yield of pyrimidine **1** *via* conventional was greater (see more in Table 2).

Our MCR is used for the synthesis of THQ through a traditional method with regard to their AE [19] to yield identical target substances. As a result, we provided the YE to estimate the percentage yield (%) of the target product. An advanced level of conversion, an effective chemical process, and a cost-effective reaction are all revealed by a greater YE. Hence, 4.86 and 0.08 were the values of YE in the mechanochemical processes, respectively, disclosing the larger status of the former approach and providing conventional conditions and great yield assessment. This confirmed that in the green chemistry principle the determination of % yield according to saving reaction time must be considered.

DFT Study

High E_{HOMO} shows a strong molecule tendency to donate electrons and low values of the energy gap ($\Delta E=E_{LUMO}-E_{HOMO}$), which will render good inhibition efficiencies [16-17]. The structural optimization of the 2-benzylidenecyclohexane-1-one when reacting with urea

Table 2. Outline and description e some physical characteristics. AE (Atom economy), YE (yield economy), and RME (reaction mass efficiency) of the produced compounds

Prod.	Time (min)		Yield (%)		YE (%/min)		AE	RME		O.E (RME/AE)	
No.	Gri.	Refl.	Gri.	Refl.	Gri.	Refl.		Gri.	Refl.	Gri.	Refl.
1a	3.5	120	85.20	86.92	24.34	0.72	87.93	74.83	76.31	86.78	86.78
1b	3.5	135	81.57	82.90	23.30	0.61	87.70	71.42	72.38	81.43	82.53
2a	4.0	150	83.47	81.01	20.86	0.32	86.36	72.11	69.51	83.49	80.48
2b	4.0	150	76.59	78.04	19.14	0.013	87.41	67.22	68.64	76.90	78.52
2c	4.0	150	83.46	81.29	20.86	0.54	87.62	73.16	70.92	83.49	80.94
3a	3.5	180	86.21	86.00	28.73	0.47	90.12	61.53	77.42	68.27	85.90
3b	3.5	180	83.80	82.90	23.94	0.46	90.12	74.74	74.01	82.93	82.12
4a	3.5	180	73.70	75.99	21.05	0.42	91.51	65.31	67.63	71.36	73.90
4b	3.5	180	83.75	81.40	23.92	0.45	90.27	73.40	75.53	81.31	83.67

to produce the desire product is planned by using quantum chemical calculations. In the presence of KOH, the HOMO energy (−9.60 eV) of the cyclohexanone anion was rather than HOMO (−12.61 eV) urea nucleophile and so good matching to LUMO energy (−5.62 eV) of the electrophilic carbonyl site of benzaldehyde to form the corresponding chalcone *via* aldol reaction followed by nucleophilic addition of urea precursor (Fig. 2 and 3). While employing thiourea (Fig. 4), it is preferable to use (HOMO −8.96 eV) rather than HOMO of cyclohexanone anion (−9.60 eV). The presence of benzylidene thiourea intermediate is created by KOH using the technique in Scheme 2.

DFT simulation was assisted to know that MCRs do not occur simultaneously, meaning two components reacted first and combined with a third. The structures have been supported by full spectral analysis and micro-analytical data. Fig. 3 and 4 show the outline reaction steps of the urea cyclohexanone and 3-nitrobenzaldehyde.

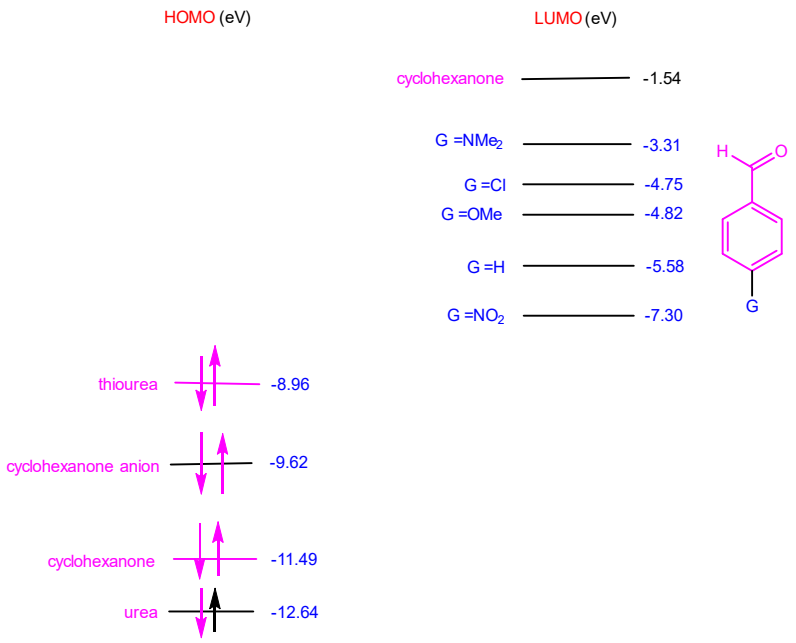

Fig 2. Outline ternary HOMO-LUMO interaction

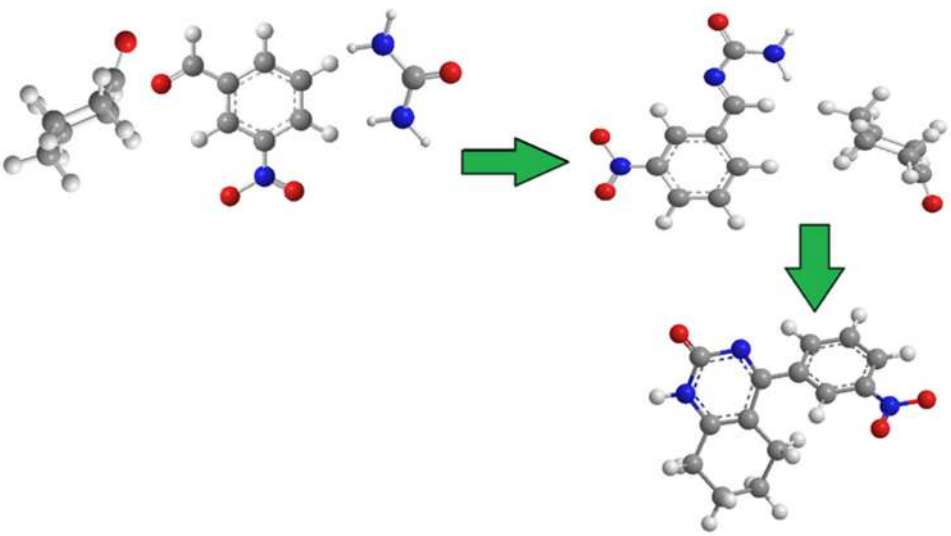

Fig 3. Outline the reaction steps of the urea cyclohexanone and 3-nitrobenzaldehyde

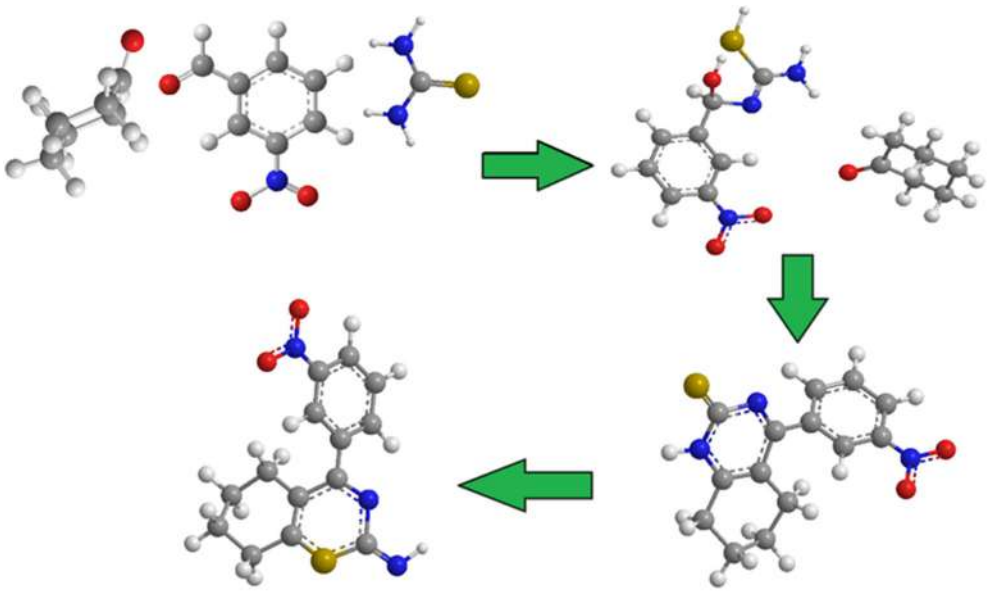

Fig 4. Outline the reaction steps of the thiourea cyclohexanone and 3-nitrobenzaldehyde

On the other hand, the HOMO energy (−10.0 eV) of phenyl urea was in a good overlap with the LUMO energy of benzaldehyde moiety in the absence of KOH because cyclohexanone has HOMO (−11.50 eV) and LUMO (−1.55 eV) besides, the lower basicity of phenyl urea is not sufficient to afford active methylene of cyclohexanone intermediate.

The authentic reaction of the (*Z*)-1-(4-chlorobenzylidene)-3-phenylurea (HOMO −8.25 eV) with LUMO (−1.55 eV) of cyclohexanone afforded the same product **5a**. The presence of KOH in the latter reaction will occur in the same mechanism as Scheme 1 because the HOMO of cyclohexanone anion become higher than the HOMO of phenyl urea. Electron-withdrawing groups of the aromatic aldehydes play an important role in aromatization, orientation and isomerization of the THQ products, see Fig 5.

Quantum chemical computations using DFT method for synthetic chemicals are also well-aligned with the antioxidant efficiency according to calculations (Table 3). The findings show that the gap energy (ΔE) values are quantum chemical computations using DFT method for synthetic chemicals are also well-aligned with the antioxidant efficiency according to calculations (Table 3). The findings show that ΔE values are within the range, where $\Delta E = E_{LUMO} - E_{HOMO}$, following the order: heterocyclic

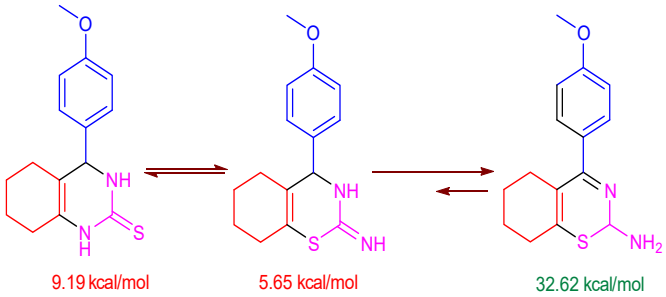

Fig 5. Outline aromatization, orientation and isomerization of the 5,6,7,8-tetrahydroquinazolin-2-one (THQ) derivatives

Table 3. Quantum chemical parameters for the most potent THQ

Compound	E_{HOMO} (eV)	E_{LUMO} (eV)	ΔE (eV)	I (eV)	A (eV)	χ (eV)	H (eV)	σ (eV^{-1})	ΔN	μ (Debye)	A_{molec} (nm^2)
2b	−8.57	−5.52	3.01	9.09	0.38	4.74	4.65	0.1068	0.26	8.790	297.443
3b	−8.13	−7.52	0.59	8.88	0.83	4.86	4.03	0.1300	0.34	11.558	542.608
4a	−5.57	−5.20	0.33	8.66	0.66	4.66	4.00	0.1491	0.38	12.139	590.401
Ascorbic acid	−3.47	−2.72	0.75	8.13	1.23	4.69	3.45	0.1281	0.31	9.395	519.866

Table 4. Outline the erythrocyte hemolysis of the synthesized compounds

Entry	Compounds	Erythrocyte hemolysis (A/B × 100)	
		Absorbance of samples (A)	% hemolysis
Absorbance of H_2O (B)		0.850	---
Vit – C		0.031	3.64
1	**1a**	0.043	5.05
2	**1b**	0.043	4.98
3	**2a**	0.048	5.64
4	**2b**	0.026	2.41
5	**2c**	0.042	4.94
6	**3a**	0.044	5.14
7	**3b**	0.037	3.88
8	**4a**	0.018	1.64
9	**4b**	0.044	4.17
10	**4c**	0.051	5.60

Table 5. Outline and an explanation of the synthetic compounds' ability to scavenge ABTS

Entry	Method	ABTS ($Abs_{control}$-Abs_{test}/$Abs_{control}$) × 100	
	Compounds	Absorbance of samples	% inhibition
	Control of ABTS	0.525	0
	Ascorbic-acid	0.061	88.4
1	**1a**	0.404	23.0
2	**1b**	0.409	22.1
3	**2a**	0.102	80.1
4	**2b**	0.047	91.5
5	**2c**	0.412	21.5
6	**3a**	0.406	22.7
7	**3b**	0.408	22.3
8	**4a**	0.035	97.8
9	**4b**	0.163	71.7
10	**4c**	0.410	21.9

derivatives **3b** < **4a** < ascorbic acid < **2b**. When a chemical has a low ΔE value, it is more reactive to surface interactions with radicals i.e., easy electron donation to the surface of a hole [20-21]. Furthermore, the great correlation, including the number and type of heteroatoms, dipole moment, electron distributions, softness (σ, eV^{-1}), and surface area (nm^2), between oxidation inhibition effectiveness and THQ-carrying hydrophobic groups were approved. Ionization potential is another factor (I, eV), and charge density distribution (ΔN) shows the greatest amount of electron transport and, hence, a stronger propensity to scavenge the radicals.

Antioxidant Assays

Anti-hemolytic activity

It was hoped to synthesize THQ derivatives which incorporate a hydrophobic group would have improved properties, such as the inhibitory activity of the opioid receptor and antioxidant characteristics. The fully optimized minimum energy geometrical configuration of the most potent antioxidant compounds **2b**, **3b** and **4a** have been approved. The significant antioxidant

activity of such compounds was corroborated by the findings of DFT-based anti-hemolytic and radical scavenger experimental tests. The results indicated that compounds **1b**, **2a**, **2b**, **3b**, **4a**, **4b**, and **4c** exhibited potent anti-hemolytic action (Table 4). It has been demonstrated that when extract or fraction concentration increases, erythrocyte lysis decreases [22]. The findings from this investigation indicate that primary antioxidants exist and have an antihemolytic effect. percentage of hemolysis is increased along heterocyclic compounds **1b** < **2a** < **4b** < **3b** < ascorbic acid (3.64%) < **2b** < **4a** that matched with the DFT study.

ABTS radical scavenging assay

The attained result nominated THQ **2b** and **4a** to scavenge the ABTS radicals. THQ **2b** (98.0 ± 0.1 μg/mL) has the lowest EC-50 values for radical ABTS scavenging while compound **4a** (> 500 ± 0.26 μg/mL) was the highest EC-50 values as shown in Table 5. % Inhibition decreases in order to these synthetic heterocyclic derivatives **4a** > **2b** > ascorbic acid (61 ± 0.2 μg/mL) > **2a** > **4b** that roughly corroborated the findings of antihemolytic and their DFT investigation.

■ CONCLUSION

The current work examines the synthesis and antioxidant properties of novel 5,6,7,8-tetrahyroquinazolin-2(1*H*)-one derivative for the first time. The two-step, straightforward, innovative, and environmentally friendly synthetic methods were used to create the novel 5,6,7,8-tetrahyroquinazolin-2(1*H*)-one derivative. Grinding and reflux techniques were compared in terms of time, yields, and reactions. All synthetic compounds' complete structural elucidations were based on spectroscopic and elemental investigations, including FTIR, mass, and ^{1}H-NMR. All products underwent insecticidal assessments. When using the ABTS test to evaluate the antioxidant perspective, compounds **2a**, **2b**, **4a**, and **4b** in particular, have shown much stronger inhibition than the other examined compounds. By using these new molecules, antioxidants are able to recognize and scavenge free radicals *in vivo* as well as *in vitro*. They will be promising as a therapeutic candidate for avoiding the onset and spread of several illnesses. This will pave the way for the synthesis of quinazolinone derivatives with maximum hydrophobicity and antioxidant activity in the near future through employing pyrimidine derivatives. The outcomes of DFT-based anti-hemolytic and radical scavenger experimental testing confirmed the considerable antioxidant activity of such substances. Compounds **1b**, **2a**, **2b**, **3b**, **4a**, **4b**, and **4c** were shown to have significant anti-hemolytic activity. Moreover, DFT-based bioassay of such compounds that had higher introduction of where $E=E_{LUMO}-E_{HOMO}$, follows the order: heterocyclic derivatives **3b** < **4a** < ascorbic acid < **2b** than the other examined compounds.

■ ACKNOWLEDGMENTS

The authors would like to extend their sincere appreciation to the organic laboratory, Department of Chemistry, Faculty of Science of Ain Shams University and STDF under call number 37139. Also, appreciation for both Departments of Chemistry in Collage of Sciences, University of Anbar, and Faculty of Science and Health, Koya University.

■ REFERENCES

[1] Folkers, K., and Johnson, T.B., 1933, Researches on pyrimidines. CXXXVI. The mechanism of formation of tetrahydropyrimidines by the Biginelli reaction[1], *J. Am. Chem. Soc.*, 55 (9), 3784–3791.

[2] Sweet, F., and Fissekis, J.D., 1973, Synthesis of 3,4-dihydro-2(1*H*)-pyrimidinones and the mechanism of the Biginelli reaction, *J. Am. Chem. Soc.*, 95 (26), 8741–8749.

[3] Kappe, C.O., Fabian, W.M.F., and Semones, M.A., 1997, Conformational analysis of 4-aryl-dihydropyrimidine calcium channel modulators. A comparison of ab initio, semiempirical and X-ray crystallographic studies, *Tetrahedron*, 53 (8), 2803–2816.

[4] Chen, R., Singh, P., Su, S., Kocalar, S., Wang, X., Mandava, N., Venkatesan, S., Ferguson, A., Rao, A., Le, E., Rojas, C., and Njoo, E., 2022, Benchtop ^{19}F nuclear magnetic resonance (NMR) spectroscopy provides mechanistic insight into the Biginelli

condensation towards the chemical synthesis of novel trifluorinated dihydro- and tetrahydropyrimidines as antiproliferative agents, *ACS Omega*, 8 (11), 10545–10554.

[5] Balraj, G., Rammohan, K., Anilkumar, A., Sharath Babu, M., and Ayodhya, D., 2023, An improved eco-friendly and solvent-free method for the one-pot synthesis of tetrahydropyrimidine derivatives *via* Biginelli condensation reaction using ZrO_2/La_2O_3 catalysts, *Results Chem.*, 5, 100691.

[6] Fu, R., Yang, Y., Lai, W., Ma, Y., Chen, Z., Zhou, J., Chai, W., Wang, Q., and Yuan, R., 2015, Efficient and green microwave-assisted multicomponent Biginelli reaction for the synthesis of dihydropyrimidinones catalyzed by heteropolyanion-based ionic liquids under solvent-free conditions, *Synth. Commun.*, 45 (4), 467–477.

[7] Fiorito, S., Genovese, S., Curini, M., Preziuso, F., Taddeo, V.A., and Epifano, F., 2017, Ytterbium triflate promoted solvent-free synthesis of 2-amino-4*H*-pyranes, *Tetrahedron Lett.*, 58 (16), 1659–1661.

[8] Bochevarov, A.D., Harder, E., Hughes, T.F., Greenwood, J.R., Braden, D.A., Philipp, D.M., Rinaldo, D., Halls, M.D., Zhang, J., and Friesner, R.A., 2013, Jaguar: A high-performance quantum chemistry software program with strengths in life and materials sciences, *Int. J. Quantum Chem.*, 113 (18), 2110–2142.

[9] Cao, M., Wang, S., Gao, Y., Pan, X., Wang, X., Deng, R., and Liu, P., 2020, Study on physicochemical properties and antioxidant activity of polysaccharides from *Desmodesmus armatus*, *J. Food Biochem.*, 44 (7), e13243.

[10] EL-Hashash, M., Rizk, S.A., El-Bassiouny, F., Guirguis, D., Khairy, S., and Guirguis, L., 2017, Facile synthesis and structural characterization of some phthalazin-1(2*H*)-one derivatives as antimicrobial nucleosides and reactive dye, *Egypt. J. Chem.*, 60 (3), 407–420.

[11] Shutalev, A.D., Kishko, E.A., Sivova, N.V., and Kuznetsov, A.Y., 1998, A new convenient synthesis of 5-acyl-1,2,3,4-tetrahydropyrimidine-2-thiones/ones, *Molecules*, 3 (3), 100–106.

[12] Abdalrazaq, E., Jbarah, A.A.Q., Al-Noor, T.H., Shinain, G.T., and Jawad, M.M., 2022, Synthesis, DFT calculations, DNA interaction, and antimicrobial studies of some mixed ligand complexes of oxalic acid and Schiff base trimethoprim with various metal ions, *Indones. J. Chem.*, 22 (5), 1348–1364.

[13] Fahmy, A.F.M., El-Sayed, A.A., and Hemdan, M.M., 2016, Multicomponent synthesis of 4-arylidene-2-phenyl-5(4*H*)-oxazolones (azlactones) using a mechanochemical approach, *Chem. Cent. J.*, 10 (1), 59.

[14] Al-Atbi, H.S., Al-Assadi, I.J., Al-Salami, B.K., and Badr, S.Q., 2020, Study of new azo-azomethine derivatives of sulfanilamide: Synthesis, characterization, spectroscopic, antimicrobial, antioxidant and anticancer activity, *Biochem. Cell. Arch.*, 20 (2), 4161–4174.

[15] Al-Khazragie, Z.K., Al-Salami, B.K., and Al-Fartosy, A.J.M., 2022, Synthesis, antimicrobial, antioxidant, toxicity and anticancer activity of a new azetidinone, thiazolidinone and selenazolidinone derivatives based on sulfonamide, *Indones. J. Chem.*, 22 (4), 979–1001.

[16] Bursavich, M.G., Parker, D.P., Willardsen, J.A., Gao, Z.H., Davis, T., Ostanin, K., Robinson, R., Peterson, A., Cimbora, D.M., Zhu, J.F., and Richards, B., 2010, 2-Anilino-4-aryl-1,3-thiazole inhibitors of valosin-containing protein (VCP or p97), *Bioorg. Med. Chem. Lett.*, 20 (5), 1677–1679.

[17] Imai, S., Kikui, H., Moriyama, K., and Togo, H., 2015, One-pot preparation of 2,5-disubstituted and 2,4,5-trisubstituted oxazoles from aromatic ketones with molecular iodine, oxone, and trifluoromethanesulfonic acid in nitriles, *Tetrahedron*, 71 (33), 5267–5274.

[18] Rizk, S.A., and Shaban, S., 2019, A facile one-pot synthesis and anticancer evaluation of interesting pyrazole and pyrimidinthione *via* heterocyclic interconversion, *J. Heterocycl. Chem.*, 56 (9), 2379–2388.

[19] El-Hashash, M.A., and Rizk, S.A., 2016, Regioselective diastereomeric Michael adducts as

building blocks in heterocyclic synthesis, *J. Heterocycl. Chem.*, 53 (4), 1236–1240.

[20] Akanni, O.O., Owumi, S.E., and Adaramoye, O.A., 2014, *In vitro* studies to assess the antioxidative, radical scavenging and arginase inhibitory potentials of extracts from *Artocarpus altilis*, *Ficus exasperate* and *Kigelia africana*, *Asian Pac. J. Trop. Biomed.*, 4, S492–S499.

[21] Yahyazadeh, A., Nafei-Kohi, M., Abbaspour-Gilandeh, E., and Aghaei-Hashjin, M., 2022, A new procedure for the preparation of 3,4-dihydropyrimidin-2(1*H*)-one and octahydroquinazolinone derivatives catalyzed by SCMNPs@CA-EASO_3H under solvent-free conditions, *Lett. Org. Chem.*, 19 (10), 867–883.

[22] Puripat, M., Ramozzi, R., Hatanaka, M., Parasuk, W., Parasuk, V., and Morokuma, K., 2015, The Biginelli reaction is a urea-catalyzed organocatalytic multicomponent reaction, *J. Org. Chem.*, 80 (14), 6959–6967.

Short Communication:

Synthesis, Characterization, and Magnetic Properties of Iron(II) Complex with 2,6-Bis(pyrazol-3-yl)pyridine Ligand and Tetracyanonickelate Anion

Fitriani Fitriani[1], Irma Mulyani[1*], Djulia Onggo[1], Kristian Handoyo Sugiyarto[2], Ashis Bhattacharjee[3], Hiroki Akutsu[4], and Anas Santria[4,5]

[1]*Inorganic and Physical Chemistry Research Group, Faculty of Mathematics and Natural Sciences, Institut Teknologi Bandung, Jl. Ganesha 10, Bandung 40132, Indonesia*

[2]*Department of Chemistry Education, Universitas Negeri Yogyakarta, Jl. Colombo No. 1, Yogyakarta 55281, Indonesia*

[3]*Department of Physics, Visva-Bharati University, Santiniketan 731204, India*

[4]*Graduate School of Science, Osaka University, 1-1 Machikaneyama, Toyonaka, Osaka 560-0043, Japan*

[5]*Research Center for Chemistry, National Research and Innovation Agency, Kawasan PUSPITEK, Serpong, Tangerang Selatan, Banten 15314, Indonesia*

* ***Corresponding author:***

email: imulyani@itb.ac.id

Received: January 24, 2023
Accepted: March 3, 2023

DOI: 10.22146/ijc.81625

Abstract: *The complex containing iron(II), 2,6-bis(pyrazol-3-yl)pyridine (3-bpp) as ligand, and tetracyanonickelate as counter anion has been synthesized and characterized. The characterization data suggest the corresponding formula of $[Fe(3\text{-}bpp)_2][Ni(CN)_4]\cdot 4H_2O$. Meanwhile, the SEM–EDX analysis image confirms the existence of all elements contained in the complex except the hydrogen atom. The infrared spectra exhibit vibration bands of the functional groups of 3-bpp ligand and $[Ni(CN)_4]^{-1}$ anion. From magnetic property measurement, the complex's molar magnetic susceptibility (X_MT) value is 2.65 emu mol^{-1} K at 300 K, which contains about 75% high-spin state of the Fe(II) complex. Upon lowering the temperature, the X_MT value gradually decreases around 1.37 emu mol^{-1} K at 13 K. It decreases sharply to about 0.73 emu mol^{-1} K at 2 K. These values reveal that Fe(II) complex is in the low-spin (LS) state. As a result, the complex exhibited spin-crossover characteristics of gradual transition without thermal hysteresis, and the transition temperature occurred below room temperature with a transition temperature ($T_{1/2}$) close to 140 K. The spin crossover property of the complex is supported by a thermochromic reversible color change from red-brown at room temperature to dark brown on cooling in liquid nitrogen associated with the high-spin to low-spin transition.*

Keywords: *iron(II); spin crossover; tetracyanonickelate; 2,6-bis(pyrazol-3-yl)pyridine*

■ INTRODUCTION

The spin-crossover (SCO) or spin transition phenomenon exhibits the interchange of two spin states from the paramagnetic high-spin (HS) to the diamagnetic low-spin (LS) and *vice versa* under the external stimulation effect of temperature changes [1], pressure [2], and irradiation of light [3]. Cambi and coworkers discovered the first SCO phenomenon in a Fe(III) dithiocarbamate mononuclear complex in 1931 [4]. Since then, many SCO materials containing the metal ions of $3d^n$ with n = 4–7 have been synthesized and extensively investigated [5].

Materials exhibiting the SCO phenomenon continue to be intensively studied because of the numerous potential applications for information storage [6], sensors [7], molecular switches [8], etc. Among the SCO materials, many research groups have widely investigated

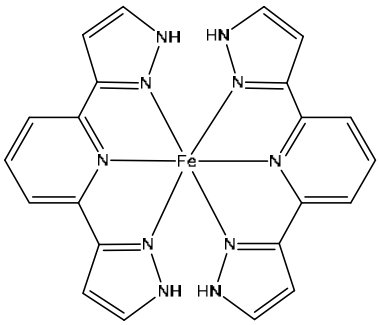

Fig 1. The mononuclear complex of $[Fe(3\text{-}bpp)_2]^{2+}$

the mononuclear complex of $[Fe(3\text{-}bpp)_2]^{2+}$ (Fig. 1) formed by the tridentate of 3-bpp ligand [9]. These complexes are particularly interesting because they can be modified by various counter anions where the difference of counter anions determines the type of spin transition and transition temperature ($T_{1/2}$). Quite recently, the presence of Fe(II) complex in the HS and LS states has been demonstrated by a single crystal of $[Fe(3\text{-}bpp)_2](CF_3COO)_2$ complex in the SCO system [10]. There are several types of spin transition commonly observed in SCO materials such as: gradual, abrupt, hysteretic, stepwise, and incomplete [11], where the $T_{1/2}$ is described as transition temperature which reveals the ratio of HS and LS states in the compound is 50:50.

The spin transition and the transition temperature in SCO materials are affected by the coordination number of metal ions and the nature of ligands and the counter anions type or even solvent molecules [12]. In the complex of $[Fe(3\text{-}bpp)_2]^{2+}$, the 3-bpp ligand is one of the intermediate ligands with the pyrazolyl ring with one nitrogen linked to an H atom free to form hydrogen bonds with the anions. While many oxides and halogenate anions have been investigated, complex anions containing transition metal ions have also been reported in many Fe(II) SCO systems. For example, the $[Fe(3\text{-}bpp)_2][Fe(CN)_5(NO)]$ complex has been synthesized from $[Fe(3\text{-}bpp)_2]^{2+}$ complex with nitroprusside $[Fe(CN)5(NO)]^{2+}$ anion containing Fe(III) metal ion. The complex showed abrupt transition, and the transition temperature occurred below room temperature with small hysteresis ($T_{1/2}\downarrow = 181$ K; $T_{1/2}\uparrow = 184$ K) [13]. Moreover, the complex of $[Fe(3\text{-}bpp)_2]^{2+}$ is also conducted using complex cyanide anion $[Au(CN)_2]^-$ containing Au(I) metal ion. The complex of $[Fe(3\text{-}bpp)_2][Au(CN)_2]_2{\cdot}2H_2O$ showed incomplete and very gradual transitions without hysteresis where the $T_{1/2}$ value of the complex can be estimated at 291 K [14]. Meanwhile, the $[Fe(3\text{-}bpp)_2][Au(CN)_2]_2$ complex showed two steps of thermal hysteresis, and the abrupt transition occurred above room temperature, showing $T_{1/2}\downarrow = 370$ K and $T_{1/2}\uparrow = 415$ K for the large hysteresis, while the $T_{1/2}\downarrow = 420$ K and $T_{1/2}\uparrow = 430$ K for the small one [15]. In this case, the difference in SCO properties from those complexes may be affected by the absence or existence of solvent molecules in the structure of the complex. The existence of solvent molecules in the complex is due to the interaction of hydrogen bonds between the hydrogen atom in the 3-bpp ligand and the oxygen atom in water molecules, with a high electronegative atom. In general, the solvent should be avoided to ensure the short contacts between the 3-bpp ligand and the anions to enhance more cooperative transitions.

The use of metal cyanide complexes as a counter anion, $[M(CN)_2]^-$ with M is Ag or Au, has been reported in the $[Fe(3\text{-}bpp)_2]^{2+}$ complex with various SCO properties [14]. Therefore, in the present study, we describe here the synthesis of $[Fe(3\text{-}bpp)_2][M(CN)_4]$ complex. Since the nitrogen atom of the cyanide (CN^-) ligand has the potential to form hydrogen bonds with a hydrogen atom of the 3-bpp ligand, the strategy synthesis of the complex needs to be elaborated. In addition to that, it is also necessary to study the magnetic property of this complex as an SCO material. In this study, the resulting complex of $[Fe(3\text{-}bpp)_2][Ni(CN)_4]{\cdot}4H_2O$ was characterized by the CHN elemental analysis, thermogravimetric analysis, and AAS measurement to determine its chemical formula. The data of SEM–EDX was evaluated to identify the surface morphology and the composition of elements in the complex. Meanwhile, coordination bonds in the complex were also analyzed from the infrared spectra. The SCO property was studied by measuring the magnetic susceptibility at various temperatures.

■ EXPERIMENTAL SECTION

Materials

The main chemicals of 2,6-(diacethyl)pyridine ($C_9H_9NO_2$), *N,N*-dimethylformamide dimethylacetal ($C_5H_{13}NO_2$), hydrazine hydrate (N_2H_4), activated charcoal, iron(II) sulfate heptahydrate ($Fe(SO_4)_2{\cdot}7H_2O$), barium chloride dihydrate ($BaCl_2{\cdot}2H_2O$), and potassium tetracyano nickelate(II) ($K_2[Ni(CN)_4]$). The solvents consist of *n*-hexane (C_6H_{14}), chloroform ($CHCl_3$), ethanol (C_2H_5OH), and methanol (CH_3OH). All chemicals and solvents were used with no further purifications, and they were respectively purchased from Sigma Aldrich and Merck.

Instrumentation

The CHN elemental analysis was measured using the ThermoFisher Scientific FlashSmart CHNS Elemental Analyzer. The metal content of the complex was estimated based on the data recorded using an Atomic Absorption Spectrophotometer (AAS) model of GBC Avanta V2. Thermal decomposition of the $[Fe(3\text{-}bpp)_2][Ni(CN)_4]{\cdot}4H_2O$ complex was performed up to 600 °C under nitrogen and used to confirm the amount of hydrate and the decomposition products of the complex. This analysis was obtained using TG/DTA Hitachi STA7300 thermal analyzer model with a heating rate of 10 °C/min. The infrared spectra of the ligand and the complex were collected using KBr pellets on a ThermoFisher Scientific Model of Nicolet IS5 in the range of 4000–400 cm^{-1}. The SEM image of the complex was recorded in SEM-EDX (Scanning Electron Microscopy with Energy Dispersive X-ray) JEOL JSM 6510 LA model to confirm the mass percentages and the content of the main elements in the sample. The temperature variation from magnetic susceptibility measurement was conducted using a Quantum Design MPMS-XL7A SQUID (Superconducting Quantum Interference Device) magnetometer in the temperature range of 2–300 K under an external 5000 Oe magnetic field.

Procedure

The synthesis procedures of 3-bpp ligand and $[Fe(3\text{-}bpp)_2][Ni(CN)_4]{\cdot}4H_2O$ complex

The 3-bpp ligand or 2,6-bis(pyrazol-3-yl)pyridine was prepared according to the previously published method by Lin and Lang [16]. A mixture containing 2,6-diacetyl-pyridine (5 g, 30.64 mmol) and *N,N'*-dimethylformamide dimethyl acetal (10 mL, 75.28 mmol) was refluxed under an atmosphere of nitrogen for 3–4 h. The reaction mixture was cooled and removed until an orange precipitate formed. Then it was dissolved in chloroform, and the solution was treated with activated charcoal, filtered off, and then concentrated. The yellow precipitate as starting material was crystallized on dilution with *n*-hexane. A suspension of the appropriate starting material (2.5 g) in ethanol (12.5 mL) and hydrazine hydrate (2.5 mL) was stirred for 3–4 h at room temperature. Dilution of the saturated solution with water until a white precipitate formed (3-bpp ligand). Then it was filtered, and the synthesis product was dried in a desiccator over silica gel. The yield was 48–50%. (m.p. 258–260 °C, literature 257–259 °C).

Meanwhile, the $[Fe(3\text{-}bpp)_2][Ni(CN)_4]{\cdot}4H_2O$ complex was synthesized using the following procedure. In 3 mL H_2O containing $FeSO_4{\cdot}7H_2O$ (0.28 g; 1 mmol) with a little addition of ascorbic acid to prevent oxidation of the Fe(II) ion, it was added in 2 mL H_2O solution of $BaCl_2{\cdot}2H_2O$ (0.27 g; 1.1 mmol). The reaction mixture was stirred in a centrifuge for about 45 min. A clear solution containing $FeCl_2$ was separated from the white precipitate of $BaSO_4$ with a syringe. The $FeCl_2$ solution was added dropwise to the solution of 3-bpp ligand (0.5 g; 2.4 mmol) in 30 mL methanol. While the mixture was stirred under an atmosphere of nitrogen, the saturated aqueous solution of $K_2[Ni(CN)_4]$ in excess (4.2 mmol, 3 mL) was then added to the mixture. The red-brown precipitate formed upon the addition. After the reaction mixture was vigorously stirred for about 1–2 h, it was filtered and washed with a small amount of water. The synthesis product was dried over silica gel in a desiccator (Yield: 58–60% w/w).

■ RESULTS AND DISCUSSION

Synthesis and Characterization of $[Fe(3\text{-}bpp)_2][Ni(CN)_4]{\cdot}4H_2O$

The preparation of $[Fe(3\text{-}bpp)_2][Ni(CN)_4]{\cdot}4H_2O$ complex was adopted by a modification of the literature

procedure [11] using the reaction of $FeSO_4$ with $BaCl_2$ in an aqueous solution produced the white precipitate of $BaSO_4$ and a clear solution of $FeCl_2$. Then the $FeCl_2$ solution was added dropwise to the methanolic solution of 3-bpp ligand, resulting in a mixture of red-brown color solution. The red-brown precipitate was formed when an excess of $K_2[Ni(CN)_4]$ salt was added to the mixture solution. Based on the solubility test, the product of red-brown powder was hardly soluble in various commonly known solvents such as water, methanol, ethanol, chloroform, acetone, acetonitrile, and diethyl ether. Therefore, attempts to produce the single crystal of the expected $[Fe(3\text{-bpp})_2][Ni(CN)_4]\cdot 4H_2O$ complex could not be attained.

Table 1 shows the result of CHN elemental analysis and AAS measurement on the elemental composition contained in the synthesized complex. The chemical formula of the complex obtained from the analysis results is $[Fe(C_{11}H_9N_5)_2][Ni(CN)_4]\cdot 4H_2O$, in agreement with the expected chemical formula.

Infrared spectra of [Fe(3-bpp)2][Ni(CN)4]·4H2O complex and 3-bpp ligand recorded at 291 K are shown in Fig. 2. The typical vibration of 3-bpp ligands such as $\nu_{(N\text{-}H)}$ stretching, $\nu_{(C=C)}$ stretching, $\nu_{(C=C\text{-}N)}$ stretching of pyridine, $\nu_{(N\text{-}H)}$ bending, and $\nu_{(C\text{-}H)}$ stretching bands were observed at around 3202, 1595, 1565, 1471, and 806 cm^{-1}, respectively, as previously reported by Gamez et al. [17]. In the infrared spectrum of the $[Fe(3\text{-bpp})_2][Ni(CN)_4]\cdot 4H_2O$ complex, the $\nu_{(C=C\text{-}N)}$ band appeared at 1575 cm^{-1}, which was higher than in the infrared spectrum of 3-bpp ligand (1565 cm^{-1}). The shift of the $\nu_{(C=C\text{-}N)}$ band indicated that the Fe(II) ion is coordinated with the nitrogen atom of the pyridine ring of the 3-bpp ligand. Moreover, the spectrum of the complex exhibited a broad and a medium intense new band at 3435 cm^{-1} due to $\nu_{(OH)}$ of water molecules [18]. The presence of H_2O molecules as a hydrate in the spectrum of the complex was also confirmed by thermogravimetric analysis. Meanwhile, the $\nu_{(C\equiv N)}$ stretching vibration band belonging to the tetracyanonickelate group in the complex was observed at 2131 cm^{-1}. This vibration band usually appears in the 2000–2200 cm^{-1} range with a sharp and strong band. Thus it can be easily identified in the vibration spectrum of

Table 1. The composition of C, H, N, and Fe

Complex	%			
	C	H	N	Fe
Found	43.65	3.39	26.95	7.76
Calculated	43.76	3.65	27.49	7.85

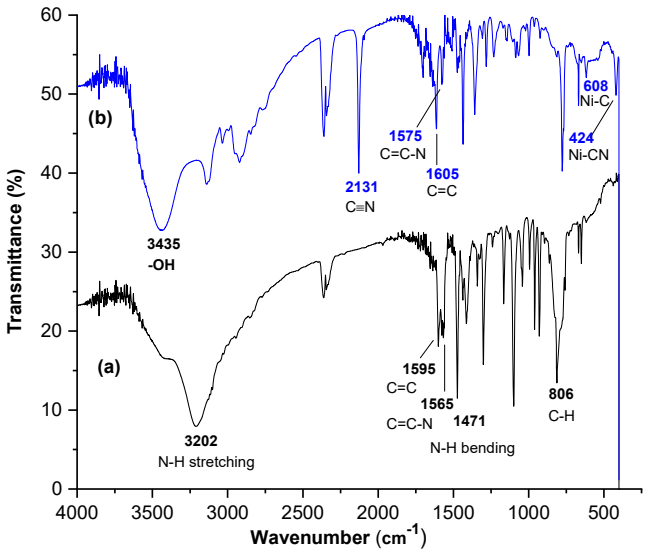

Fig 2. Infrared spectra of (a) 3-bpp ligand and (b) $[Fe(3\text{-bpp})_2][Ni(CN)_4]\cdot 4H_2O$ complex at 291 K

the complex [19]. In addition, the vibration bands of the tetracyanonickelate group in the complexes exhibit M–C stretching and M–C–N bending bands in the range of 400–600 cm^{-1} [20]. These bands were observed at 608 and 424 cm^{-1} in the complex spectrum and might be assigned to the stretching of Ni–C and bending of Ni–CN vibration bands, respectively.

Thermogravimetry analysis of the $[Fe(3\text{-bpp})_2][Ni(CN)_4]\cdot 4H_2O$ complex was performed to confirm the number of hydrates of the chemical formula and decomposition of the complex as well as the temperature range of the stability of the complex. As shown in Fig. 3, the thermal decomposition in the first and the second steps are due to the dehydration process of the complex. The thermogram displays weight losses at around 8.07 and 2.71% in the temperature range of 30–85 °C and 85–135 °C, respectively, corresponding to the total decomposition of four uncoordinated water molecules (calculated as 10.10%, found 10.78%). These results show a good agreement with the composition determined from the elemental analysis data. The loss of

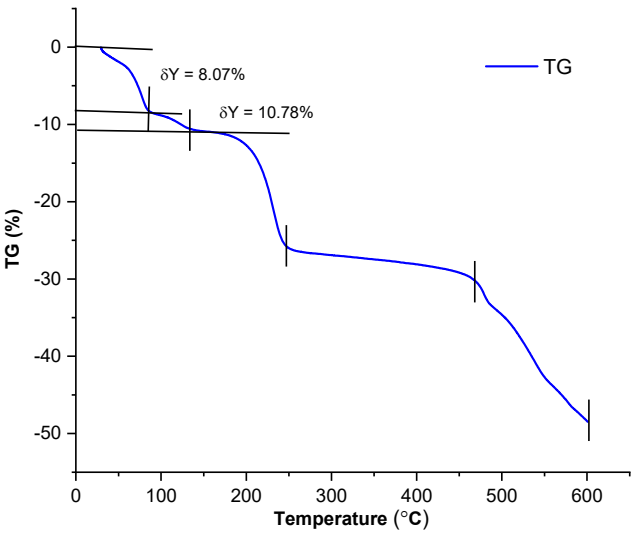

Fig 3. Thermogravimetry (TG) profile of $[Fe(3\text{-}bpp)_2][Ni(CN)_4]\cdot 4H_2O$ complex

uncoordinated water molecules usually occurs below 200 °C. As reported previously, the $[Fe(3\text{-}bpp)_2](C_6H_4NO_2)_2\cdot 4H_2O$ complex started to decompose with three water molecules and one water molecule at 54 °C and 170–220 °C temperature range, respectively [21]. While the next weight loss of about 14.26% (calculated as 14.59%) in the temperature range of 135–240 °C could be attributed to the loss of CN groups. Cordoba et al. [22] suggested that the loss of CN groups in the $SrNH_4[Fe(CN)_6]\cdot 3H_2O$ compound occurred at 150–290 °C. The continuous weight loss appears in the temperature range of 240–470 °C and 470–600 °C, which could be associated with the loss of 3-bpp ligand and the residue of the complex, respectively. The final decomposition product could be identified as FeO and NiO (calculated as 20.62%, found at 19.88%) within 470–600 °C. Thermal decomposition products have also been observed by Karaağaç and Kürkçüoğlu [23] in the cyano metal complexes with the loss of metal oxides (CuO, ZnO, and NiO) appearing by the thermogram below 700 °C.

The surface morphology and elemental content in the $[Fe(3\text{-}bpp)_2][Ni(CN)_4]\cdot 4H_2O$ complex were also determined by SEM–EDX. The selected surface of the SEM image of the complex exhibits cubic shapes on the scale of 20 µm, as depicted in Fig. 4(a). Meanwhile, the existence of the corresponding elemental content in the complex, except the hydrogen atom, was displayed in Fig. 4(b). This study used the EDX analysis to determine the mass percentages of Fe and Ni in the state of a complex compound (Table 2). Based on the EDX analysis result, the obtained Fe and Ni mass percentages were respectively 6.29 and 8.61%. These percentages were almost equal to the calculated Fe and Ni mass percentages

Table 2. The mass percentage of Fe and Ni atoms in the $[Fe(3\text{-}bpp)_2][Ni(CN)_4]\cdot 4H_2O$ complex

Atom	% Mass
C	47.80
N	36.67
O	0.63
Fe	6.29
Ni	8.61

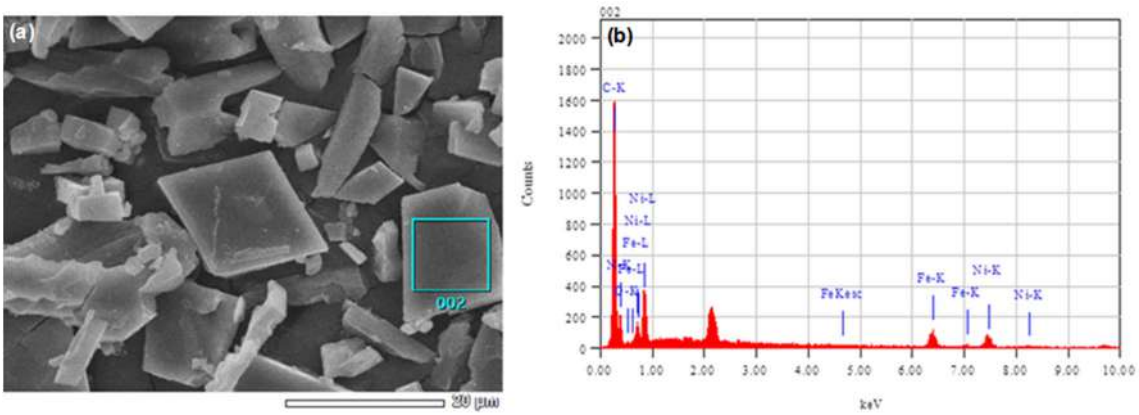

Fig 4. The image of (a) the selected surface of $[Fe(3\text{-}bpp)_2][Ni(CN)_4]\cdot 4H_2O$ complex and its (b) EDX analysis result showing the content of elements, Fe-C-N-O-Ni

of 7.85 and 8.27%, respectively. The results indicate a good agreement with the amount of Fe in the metal content (AAS). The result was 7.76%, which concluded that the chemical formula of the complex being $[Fe(3\text{-}bpp)_2][Ni(CN)_4]\cdot 4H_2O$.

Magnetic Susceptibility

Magnetic susceptibility data of $[Fe(3\text{-}bpp)_2][Ni(CN)_4]\cdot 4H_2O$ complex was collected in the temperature range of 2–300 K at cooling and heating modes. Fig. 5 displays the temperature dependence of the X_MT for $[Fe(3\text{-}bpp)_2][Ni(CN)_4]\cdot 4H_2O$ complex with the molar magnetic susceptibility is X_M, and the temperature is T. At first, the X_MT was measured from 300 K down to 2 K. After the cooling process, the X_MT was measured from 2 K up to 300 K within the heating process. At 300 K, the X_MT value is 2.65 emu mol^{-1} K, suggesting that about 75% of Fe(II) complex is in the HS state at this temperature since the HS of $[Fe(3\text{-}bpp)2]^{2+}$ shows the X_MT value is 3.5 ± 0.1 emu mol^{-1} K [24-25]. On decreasing the temperature from 300 K, the X_MT value of the complex gradually decreases around 1.37 emu mol^{-1} K at 13 K. Below 13 K. The X_MT value was abruptly decreased due to weak anti-ferromagnetic exchange interactions between the Fe^{2+} ion and/or by the zero-field splitting (ZFS) effect associated with the Fe^{2+} ion in the HS state. The final X_MT value reaches about 0.73 emu mol^{-1} K at 2 K, indicative of the complex being in the LS state. Compared to the previously described by King et al. [14], the $[Fe(3\text{-}bpp)_2][Au(CN)_2]_2\cdot 2H_2O$ complex showed a very gradual transition, and the partial conversion was incomplete. The X_MT value of the complex was 1.9 emu mol^{-1} K at 300 K, implying that the Fe(II) complex was 55–60% HS state at room temperature. On cooling, the X_MT value of the complex decreased to 0.6 emu mol^{-1} K at 150 K. The $T_{1/2}$ value can be estimated at 291 K, where the complex's HS and LS fractions equal 50%.

In this study, the plot of high-spin fraction (γ_{HS}) versus temperature in Fig. 5(b) for the $[Fe(3\text{-}bpp)_2][Ni(CN)_4]\cdot 4H_2O$ complex was measured during cooling and heating modes with the estimated of transition temperature ($T_{1/2}$) is halfway, $\gamma_{HS} = \gamma_{LS} = 0.5$. Therefore, this complex shows a gradual spin transition with an estimated $T_{1/2}$ value close to 140 K at $\gamma_{HS} = 0.5$ and no evidence of hysteretic behavior upon cooling and heating modes. Based on the result, the difference in transition temperature occurred from the $[Fe(3\text{-}bpp)_2]^{2+}$ complex cation with different metal cyanide anions, as previously described. Even with the same ligand, the nature of metal cyanide anions with varying amounts of oxidation and solvent molecules in the complexes significantly affects the spin transition and the transition temperature based on the magnetic data.

In addition, the change in magnetism due to the temperature change is supported by an apparent and reversible color change from red-brown at room temperature to dark brown on cooling in liquid nitrogen.

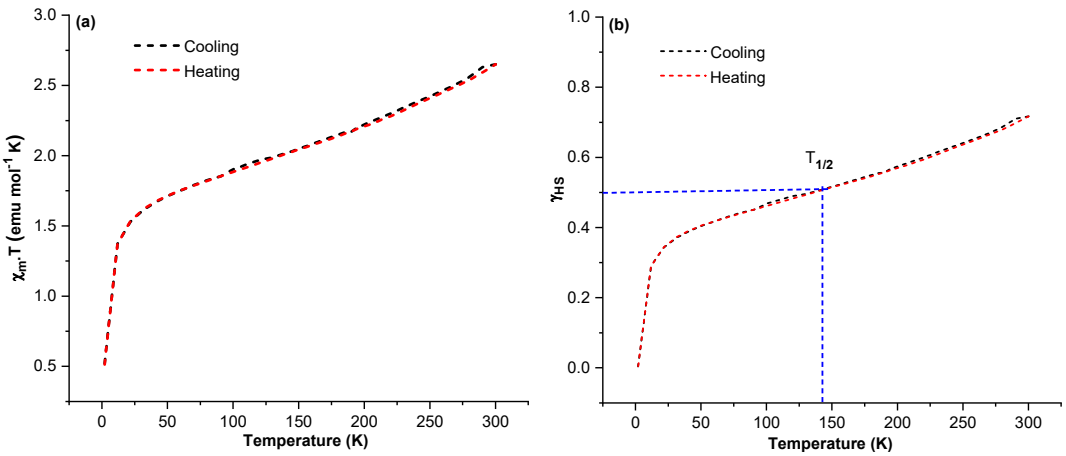

Fig 5. Magnetic susceptibility of (a) $[Fe(3\text{-}bpp)_2][Ni(CN)_4]\cdot 4H_2O$ complex and (b) its variation of high-spin fraction (γ_{HS}) with temperature during cooling and heating modes

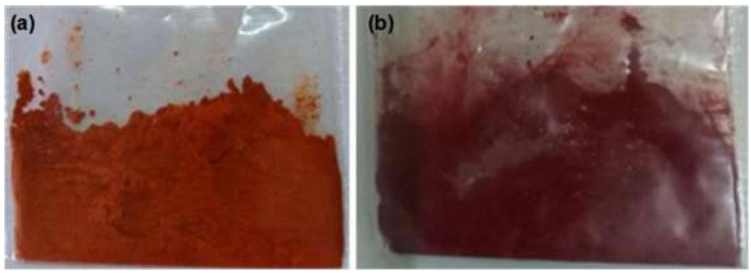

Fig 6. Color of $[Fe(3\text{-bpp})_2][Ni(CN)_4]\cdot 4H_2O$ complex (a) at 298 K and (b) in liquid nitrogen

Thus, the thermochromic nature of the $[Fe(3\text{-bpp})_2][Ni(CN)_4]\cdot 4H_2O$ complex suggests the occurrence of spin crossover property, as shown in Fig. 6.

CONCLUSION

The complex containing $[Fe(3\text{-bpp})_2]^{2+}$ cation and $[Ni(CN)_4]^{2-}$ anion has been successfully synthesized and characterized. The chemical formula of $[Fe(3\text{-bpp})_2][Ni(CN)_4]\cdot 4H_2O$ complex was estimated by AAS, while the existence of water molecules in the complex was also determined using thermal analysis. The presence of elemental content in the complex, except for the hydrogen atom, was confirmed by SEM–EDX analysis. The infrared spectra show the typical vibration bands of functional groups for the 3-bpp ligand as well as the $[Ni(CN)4]^{2-}$ anion. Moreover, the temperature dependence of the complex finds that the X_MT value at 300 K is 2.65 emu mol^{-1} K, where about 75% of the Fe(II) complex is in the HS state. Upon cooling, the X_MT value gradually decreases around 1.37 emu mol^{-1} K at 13 K. Then it decreases abruptly on cooling down to 2 K, where the X_MT value is 0.73 emu mol^{-1} K, indicating that Fe(II) complex is almost entirely in the LS state. The gradual spin transition has a $T_{1/2}$ value close to 140 K, and hysteretic behavior was not observed at cooling and heating modes. The SCO property of this complex was also supported by a reversible change of color from red-brown (HS) to dark brown (LS).

ACKNOWLEDGMENTS

The authors thank the World Class Research (WRC) Grant under contract No. 122L/IT1.C02/TA.00/2021 and 5D/IT1.C02/TA.002022. Fitriani is grateful to the LPDP Kementerian Keuangan RI (Indonesia Endowment Fund for Education Ministry of Finance Republic Indonesia) for financial support and Doctoral scholarship.

AUTHOR CONTRIBUTIONS

Fitriani, Djulia Onggo, and Irma Mulyani conducted the synthesis of complex and TG/DTA analysis; Kristian Handoyo Sugiyarto, Ashis Bhattacharjee, Hiroki Akutsu, and Anas Santria conducted the magnetic susceptibility analysis; Fitriani, Djulia Onggo, Irma Mulyani, Kristian Handoyo Sugiyarto, Ashis Bhattacharjee, Hiroki Akutsu, and Anas Santria wrote and corrected the manuscript. All authors approved the final version of this manuscript.

REFERENCES

[1] Brooker, S., 2015, Spin crossover with thermal hysteresis: Practicalities and lessons learnt, *Chem. Soc. Rev.*, 44 (10), 2880–2892.

[2] Gaspar, A.B., Molnár, G., Rotaru, A., and Shepherd, H.J., 2018, Pressure effect investigations on spin-crossover coordination compounds, *C.R. Chim.*, 21 (12), 1095–1120.

[3] Chastanet, G., Desplanches, C., Baldé, C., Rosa, P., Marchivie, M., and Guionneau, P., 2018, A critical review of the T(LIESST) temperature in spin crossover materials – What it is and what it is not, *Chem. Sq.*, 2, 21–18.

[4] Cambi, L., and Szego, L., 1931, Uber die magnetische susceptibilitat der komplexen verbindungen, *Ber. Dtsch. Chem. Ges. B*, 64 (10), 2591–2598.

[5] Gütlich, P., Gaspar, A.B., and Garcia, Y., 2013, Spin state switching in iron coordination compound, *Beilstein J. Org. Chem.*, 9, 342–391.

[6] Kumar, K.S., and Ruben, M., 2017, Emerging trends in spin crossover (SCO) based functional materials and devices, *Coord. Chem. Rev.*, 346, 176–205.

[7] Jureschi, C.M., Linares, J., Boulmaali, A., Dahoo, P.R., Rotaru, A., and Garcia, Y., 2016, Pressure and temperature sensors using two spin crossover materials, *Sensors*, 16 (2), 187.

[8] Hayami, S., Holmes, S.M., and Halcrow, M.A., 2015, Spin-state switches in molecular materials chemistry, *J. Mater. Chem. C*, 3 (30), 7775–7778.

[9] Halcrow, M.A., 2014, Recent advances in the synthesis and applications of 2,6-dipyrazolylpyridine derivatives and their complexes, *New J. Chem.*, 38 (5), 1868–1882.

[10] Sugiyarto, K.H., Onggo, D., Akutsu, H., Reddy, V.R., Sutrisno, H., Nakazawa, Y., and Bhattacharjee, A., 2021, Structural, magnetic and Mössbauer spectroscopic studies of the $[Fe(3\text{-}bpp)_2](CF_3COO)_2$ complex: role of crystal packing leading to an incomplete Fe(II) high spin ⇋ low spin transition, *CrystEngComm*, 23 (15), 2854–2861.

[11] Gutlich, P., and Goodwin, H.A., 2014, Spin crossover an overall perspective, *Top. Curr. Chem.*, 233, 1–47.

[12] Milin, E., Benaicha, B., El Hajj, F., Patinec, V., Triki, S., Marchivie, M., Gomez-Garcia, C.J., and Pillet, S., 2016, Magnetic bistability in macrocycle-based Fe(II) spin-crossover complexes: Counter ion and solvent effects, *Eur. J. Inorg. Chem.*, 2016 (34), 5305–5314.

[13] Sugiyarto, K.H., McHale, W.A., Craig, D.C., Rae, A.D., Scudder, M.L., and Goodwin, H.A., 2003, Spin transition centres linked by the nitroprusside ion. The cooperative transition in bis(2,6-bis(pyrazol-3-yl)-pyridine)iron(II) nitroprusside, *Dalton Trans.*, 12, 2443–2448.

[14] King, P., Henkelis, J.J., Kilner, C.A., and Halcrow, M.A., 2013, Four new spin-crossover salts of $[Fe(3\text{-}bpp)_2]^{2+}$ (3-bpp=2,6-bis[1H-pyrazol-3-yl]pyridine), *Polyhedron*, 52, 1449–1456.

[15] Djemel, A., Stefanczyk, O., Marchivie, M., Trzop, E., Collet, E., Desplanches, C., Delimi, R., and Chastanet, G., 2018, Solvatomorphism-induced 45 K hysteresis width in a spin crossover mononuclear compound, *Chem. - Eur. J.*, 24 (55), 14760–14767.

[16] Lin, Y., and Lang, S.A., 1977, Novel two step synthesis of pyrazoles and isoxazoles from aryl methyl ketones, *J. Heterocycl. Chem.*, 14 (2), 345–347.

[17] Gamez, P., Steensma, R.H., Driessen, W.L., and Reedijk, J., 2002, Copper(II) compounds of the planar-tridentate ligand 2,6-bis(pyrazol-3-yl)pyridine, *Inorg. Chim. Acta*, 333 (1), 51–56.

[18] Tobon, Y.A., Kabalan, L., Bonhommeau, S., Daro, N., Grosjean, A., Guionneau, P., Matar, S., Létard, J.F., and Guillaume, F., 2013, Spin crossover complexes $[Fe(NH_2trz)_3](X)_2{\cdot}nH_2O$ investigated by means of Raman scattering and DFT calculations, *Phys. Chem. Chem. Phys.*, 15 (41), 18128–18137.

[19] Karaağaç, D., and Kürkçüoğlu, G.S., 2015, Syntheses, spectroscopic and thermal analyses of the Hofmann-type metal(II) tetracyanonickelate(II) pyridazine complexes: $\{[M(pdz)Ni(CN)_4]{\cdot}H_2O\}n$ (M = Zn(II) or Cd(II)), *Bull. Chem. Soc. Ethiop.*, 29 (3), 415–422.

[20] Karaağaç, D., and Kürkçüoglu, G.S., 2015, Syntheses, spectroscopic and thermal analyses of cyanide bridged heteronuclear polymeric complexes: $[M(L)_2Ni(CN)_4]_n$(L=*N*-methylethylenediamine or *N*-ethylethylenediamine; M]Ni(II), Cu(II), Zn(II) or Cd(II)), *J. Mol. Struct.*, 1105, 263–272.

[21] Jornet-Mollá, V., Giménez-Saiz, C., and Romero, F.M., 2018, synthesis, structure, and photomagnetic properties of a hydrogen-bonded lattice of $[Fe(bpp)_2]^{2+}$ spin-crossover complexes and nicotinate anions, *Crystals*, 8 (11), 439.

[22] Córdoba, L.M., Gómez, M.I., Morán, J.A., and Aymonino, P.J., 2008, Synthesis of the $SrFeO_{2.5}$ and $BaFeO_{3-x}$ perovskites by thermal decomposition of $SrNH_4[Fe(CN)_6]3H_2O$ and $BaNH_4[Fe(CN)_6]$, *J. Argent. Chem. Soc.*, 96 (1-2), 1–12.

[23] Karaağaç, D., and Kürkçüoğlu, G.S., 2016, Syntheses and characterizations of the cyanide-bridged heteronuclear polymeric complexes with 2-ethylimidazole, *Bull. Chem. Soc. Ethiop.*, 30 (2), 263–272.

[24] Roberts, T.D., Little, M.A., Cook, L.J.K., and Halcrow, M.A., 2014, Iron(II) complexes of 2,6-

di(1*H*-pyrazol-3-yl)-pyridine derivatives with hydrogen bonding and sterically bulky substituents, *Dalton Trans.*, 43 (20), 7577–7588.

[25] Djemel, A., Stefanczyk, O., Desplanches, C., Kumar, K., Delimi, R., Benaceur, F., Ohkoshi, S.I., and Chastanet, G., 2021, Switching on thermal and light-induced spin crossover by desolvation of $[Fe(3\text{-bpp})_2](XO_4)_2\cdot$solvent (X = Cl, Re) compounds, *Inorg. Chem. Front.*, 8 (13), 3210–3221.

Review:

Modifications of Poly(lactic Acid) with Blends and Plasticization for Tenacity and Toughness Improvement

Mohd Bijarimi Mat Piah[1*], Mohammad Norazmi Ahmad[2], Erna Normaya Abdullah[2], and Muhammad Zakir Muzakkar[3]

[1]*Faculty of Chemical and Process Engineering Technology, Universiti Malaysia Pahang, Lebuh Persiaran Tun Khalil Yaakob, Kuantan 26300, Malaysia*

[2]*Experimental and Theoretical Research Laboratory, Department of Chemistry, Kulliyyah of Science, International Islamic University Malaysia, Kuantan 25200, Malaysia*

[3]*Department of Chemistry, Faculty of Mathematics and Natural Sciences, Universitas Halu Oleo, Jl. Kampus Hijau Bumi Tridharma, Anduonou, Kendari 93132, Indonesia*

* ***Corresponding author:***

email: bijarimi@ump.edu.my

Received: December 31, 2022
Accepted: May 31, 2023

DOI: 10.22146/ijc.80830

Abstract: *This review focuses on the modification of the inherent brittleness of biodegradable poly(lactic acid) (PLA) to increase its toughness, as well as recent advances in this field. The most often utilized toughening methods are melt blending, plasticization, and rubber toughening. The process of selecting a toughening scheme is still difficult, although it directly affects the blend's mechanical properties. There has been a lot of development, but there is still a long way to go before we get easily processable, totally bio-based, 100% biodegradable PLA. The blends of PLA with other polymers, such as plasticizers or rubber, are often incompatible with one another, which causes the blend's individual components to behave in a manner consistent with phase separation. Polymer blending has been shown to be particularly effective in attaining high-impact strength. This review addresses the recent progress in improving the toughened PLA to gain properties necessary for the material's future engineering applications. As 3D and 4D printing becomes more accessible, PLA characteristics may be modified and treated utilizing more sophisticated production techniques.*

Keywords: *PLA; blend; rubber; plasticization; toughness*

■ INTRODUCTION

In our modern lives, polymer materials are commonplace and can be seen almost everywhere. Due to their low cost, lightweight, and high processability, commodity plastics may be used in a wide variety of products, from consumer items to technical applications. Two issues are associated with petroleum-based plastics, i.e., the rising production cost and the non-degradability of plastic products. Lately, oil prices have been increasing steadily annually, significantly affecting synthetic plastics' production costs. This development has driven the efforts to find a possible solution that does not rely on synthetic plastics. The need for replacement has become imperative as there is mounting concern over the accumulation of petroleum-based disposal wastes worldwide. After the end of the life of plastic products, massive waste that is not biodegradable needs to be handled. Many initiatives have been launched to reduce the quantity of trash that ends up in landfills, and one clear target is plastic packaging. Despite implementing recycling and incineration efforts, this is insufficient, as we are dealing with mass disposal.

Poly(lactic acid) (PLA) and other biodegradable polymers have been developed, providing promise for a new waste management strategy. PLA, a biodegradable polyester manufactured from regenerative materials as

shown in Fig. 1-2, is pivotal in the bioplastic industry [1-5]. PLA has a limited crystallization rate, making it brittle and modest amounts of ductility, making it less than ideal for use in applications that need durability or engineering [6-10]. Prior to the last decade, PLA was only used in specialized biomedical applications such as resorbable sutures [11-12]. Due to its good biocompatibility, the PLA was used as sutures and dental, orthopedic, and drug delivery [13-15]. There is a lot of research and development going into plastics right now, and a lot of it is focused on finding ways to include biodegradable elements. Food packaging, bag and sack manufacture, loose-fill packaging, agricultural film, and a few specialized uses are only a few of the places where it has been widely adopted, contributing to its rising profile.

PLA has the potential to replace traditional polymers, including polyethylene (PE), polypropylene (PP), and polystyrene (PS). However, PLA is too brittle to be used commercially, limiting the potential applications that require high-impact toughness [15,17-18]. As a result, several efforts have been made to alleviate the problem of toughness, particularly by melt mixing in the literatures [19-21]. However, this review focuses on PLA toughening mainly through melt mixing, plasticization, and toughening. In addition, it will bridge the brittleness gap in PLA by modifying its properties, particularly plasticization and rubber/elastomer toughening.

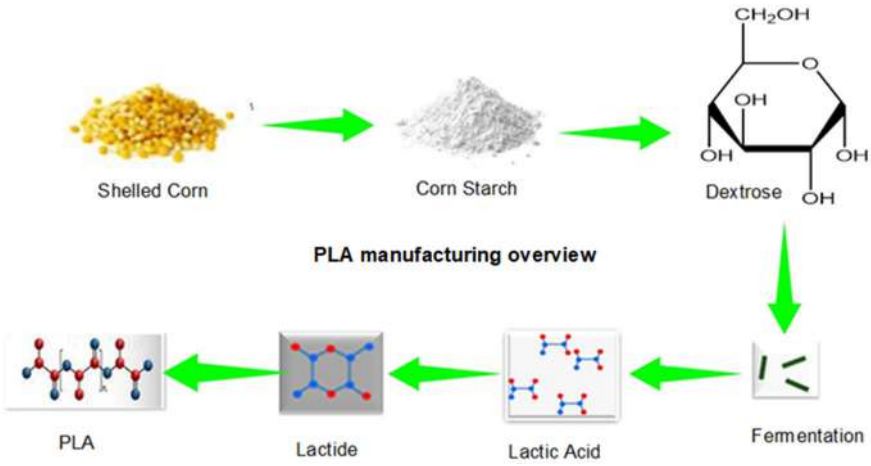

Fig 1. Overview of the production of PLA

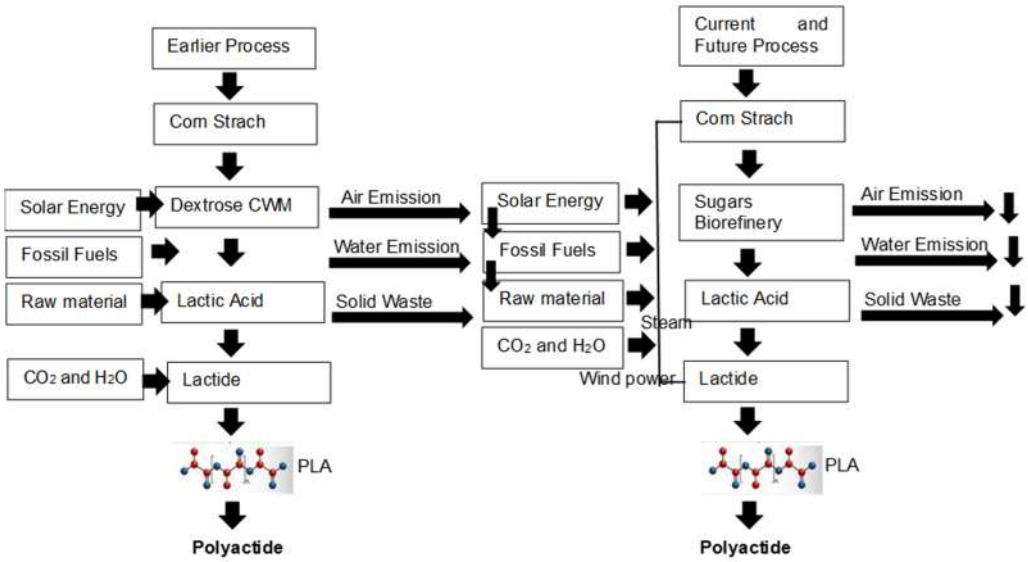

Fig 2. Current and future PLA production technology. Adapted with permission from reference [16]

Properties of PLA

The stereochemistry of the PLA chain and crystallinity significantly affect the mechanical properties. In the chemistry of PLA, the two optical isomers are denoted by the letters D and L. In contrast to its naturally occurring isomer, D-lactide, the synthetic blend of D- and L-lactide is called L-lactide. Polarized light allows us to differentiate between the L and D forms [22]. Due to its random distribution of the two isomers of lactic acid, PDLA is an amorphous polymer that cannot crystallize. This material has weak tensile strength, poor elongation, and a short degradation time. PLLA is around 37% crystalline, with a melting point between 170 and 183 °C and a glass transition temperature between 55 and 65 °C [23]. Typical physical property values of PLA are given in Table 1.

Application of PLA

Resorbable sutures and other medical supplies are only two examples of how PLA is being put to use in specialized markets. Cups, bottles, and films are just a few of the many packaging uses for PLA. Typical product applications made from PLA are given in Table 2.

In the automotive sector, PLA has been mixed with kenaf fibers for car doors and dashboards due to its biodegradability compared to traditional plastics. For example, Toyota Motor Co. reported that a spare tire cover

Table 1. Physical properties of PLA [24]

Property	Units	Typical value
Density	g cm^{-3}	1.25
Melting temperature, T_m	°C	130–215
Glass transition temperature, T_g	°C	55–70
Degree of crystallinity, X_c	%	10–40
Melt flow rate	g/10 min	2–20
Tensile strength	MPa	44–66
Yield strength	MPa	53–70
Elongation at break	%	4–7
Tensile modulus	GPa	1.9–4.1
Notched Izod impact strength	J m^{-1}	18–66
Heat deflection temperature	°C	55
Flexural strength	MPa	88–119

Table 2. Typical product application made from PLA

Business division	Applications that are commercially accessible
Rigid thermoforms	• Clear clamshells for fresh fruits and vegetables
	• Trays of deli meat
	• Opaque dairy containers
	• Packaging and advertising for consumer electronics
	• Cold drink containers and other disposable items
Films with a biaxial orientation	• Wrap candy with a twirl and a flow
	• Display carton and envelope see-through panels
	• Film for lamination
	• Gift-basket exterior wrapping
	• Holding the fort
Bottles	• Low-storage milk
	• Food oils
	• Mineral water in bottles

Adapted with permission from reference [16]

using 100% plant-derived kenaf/PLA composites was developed to replace kenaf/PP [25].

■ POLYMER BLENDS

Polymer blends have piqued the curiosity of polymer scientists for many years. *Trans* and *cis*-1,4-polyisoprene with gutta-percha (GP) blends were originally developed by Parkes in 1846. By varying the composition or adding fillers, the blends were formed into various rigid articles [26]. It has long been acknowledged that blending is the most flexible and cost-effective way to create novel materials that match the unique needs of polymer applications [27]. Many polymer resins are modified either by blending with other polymers or filling with fillers. It has been recognized that blending offers many advantages, such as improving the specific properties, e.g. toughening of brittle materials, and better procedure-friendliness thanks to a glass transition temperature-lowering miscible resin (T_g) or immiscible low viscosity resin. In addition, at the processing plant level, blending is more favorable as it increases the plant flexibility by reducing a number of grades, recycling and high productivity.

PLA Blends and Toughening

Materials made from polymer blends are anticipated to have improved characteristics compared to individual pure polymers [28-30]. It is, therefore, not surprising that PLA has been blended with several synthetics and biopolymers to enhance the properties of PLA and obtain novel materials. PLA has been blended with collagen, poly(butylenes succinate adipate), polyethylene glycol [31-42], poly(methyl methacrylate), polyethylene, poly(ethylene oxide) and poly(butylenes adipate-*co*-terephthalate) to produce materials with superior properties like as toughness, modulus, and impact strength, as well as thermal stability as compared to pure polymers [30].

The blending of PLA with other aliphatic polyesters is widely studied due to its biodegradable properties. Zhang et al. [43] developed new biodegradable materials by blending some available polyester. They investigated the property of multiphase containing poly(D, L-lactide) (PDLA), poly(ε-caprolactone) (PCL), poly(D,L-lactide-*co*-poly(ethylene glycol) (PELA), poly(ε-caprolactone)-*co*-poly(ethylene glycol) (PECL), and poly(β-hydroxybutyrate) (PHB), PLA/PCL, PELA/PECL, PHB/PLA, PHB/PELA, PHB/PCL, and PHB/PECL blends. The composition of blends was found to determine the morphology and hydrolytic behavior of immiscible PLA/PCL, PHB, and PHB/PLA and PHB/PCL blends. However, the addition of poly(ethylene glycol) (PEG) as a compatibilizer and PELA or PECL block copolymers have improved the miscibility of PELA/PECL, PHB/PELA, and PHB/PECL blends [43].

Surfactants made from a copolymer of ethylene oxide and propylene oxide might significantly improve the miscibility of PLLA and PDLLA. Chen et al. investigated the blends of biodegradable PLLA and poly-DL-lactic acid (PDLLA) or PCL, in addition to a third component, the surfactant - a copolymer of ethylene oxide and propylene oxide. They found that PLLA/PDLLA blends without surfactant had two T_g values, but with a surfactant, a linear shift of the single T_g as a function of composition occurred, with lower percentages of PLLA yielding lower glass transition temperatures, suggesting higher miscibility. The blend ratio of 40/60 PLLA/PDLLA is harder and tougher than PLLA but adding 2% surfactant increased the miscibility. Compared to PLLA/PDLLA blends, they found that PLLA/PCL blends had greater elongation and worse mechanical characteristics [44].

As discussed above, toughening of PLA remains the focus of researchers to enable PLA to be used in wider applications. Toughness is a measure of a sample's ability to absorb mechanical energy without breaking, typically defined as the area under a stress–strain curve. A tough material has a low brittleness but a high elongation to break and tensile strength. It is usually measured as the energy per unit volume to break material, proportional to the region covered by the stress-strain diagram. Nevertheless, the impact resistance test, such as Izod (ASTM D256), can be determined with a tensile test for toughness.

Plastic deformation at greater stresses is required for many uses, but its low toughness makes that impractical [45]. PLA has the processing properties of

polystyrene and the tensile strength and stiffness of polyethylene terephthalate (PET) [46]; it suffers low impact resistance [48]. It has been well established that plastics can be blended with elastomer in order to improve their toughness and impact resistance, as shown by previous researchers [22,48-51]. As a technique of enhancing mechanical characteristics and processability, blends are gaining prominence in the industrial sector. Modulus, yield stress, impact strength, and tensile strength are just some of the properties that may be enhanced by using the right polymer components in the right proportions.

Few researchers have addressed the problem of the poor toughness of PLA by blending it with other polymers to modify its properties [52-62]. Melt blending is the most common method for creating polymer blends, which are intimate mixes of polymers that are commercially accessible but do not share covalent connections. Properties of the resulting materials can be designed to meet application requirements and materials cost. In contrast to a single polymer, each component polymer in the polymer blends contributes to the final property of the material.

The combination of PLA with poly(butylene adipate-co-terephthalate) (PBAT) or another biodegradable polymer seems promising thus far, since both can be considered biodegradable. The toughening of PLA and PBAT by means of melt blending has been investigated by Jiang et al. In this immiscible blend, they found that PBAT was responsible for speeding up the PLA crystallization rate and little affected the ultimate crystallinity level. This approach obtained improved impact strength for blends containing 10% or higher PBAT. Furthermore, they concluded that the debonding-initiated shear yielding was responsible for the toughening mechanism in these PLA/PBAT blends. As for the failure mode, it has been shown that the PLA change from brittle to ductile fracture [63].

Schreck and Hillmyer [59] showed that *oligo*Nodax-*b*-poly(L-lactide) diblock copolymers might be added to a melted mix of poly(L-lactide) and NodaxH6 [poly(3-hydroxybutyrate-*co*-3hydroxyhexanoate)] to create a biodegradable composite. The notched impact resistance of the binary blends was found to be higher than that of the PLLA homopolymer after Nodax was added. However, in the ternary blends of *oligo*Nodax-*b*-poly(L-lactide) block copolymers, no additional improvement in the notched Izod impact resistance was observed. It was hypothesized that the brittleness of NodaxH6 particles and the reduced interfacial adhesion between particles and matrix may be responsible for this phenomenon [59].

Li and Shimizu [64] blended PLLA with acrylonitrile-butadiene-styrene copolymer (ABS) to increase its impact strength and elongation at the break, but they discovered that the melt mixture was immiscible and had poor mechanical qualities. PLLA/ABS was compatible when the reactive styrene/acrylonitrile/glycidyl methacrylate copolymer (SAN-GMA) was used together with ethyl triphenyl phosphonium bromide (ETPB) as a compatibilizer. As a result, the impact strength and elongation at break properties improve but with a slight loss in the modulus [64].

McDonald and co-workers [65] prepared a blend of poly(DL-lactide), poly(L-lactide-glycolide) and PCL by means of compression molding and solvent casting technique. The blend of PDLLA/PLGA was found to be miscible based on DSC analysis. However, an immiscible blend was obtained for the blend of PCL with PLGA or PDLLA; hence a strength reduction was noted. They have concluded that the blend of PCL with PLGA or PDLLA influenced the percentage of crystallinity [65].

Odent et al. [66] investigated the potential use of random aliphatic copolyesters as an impact modifier for PLA. Ring-opening polymerization synthesis between -valerolactone (VL) and -caprolactone (CL) yields amorphous poly(CL-*co*-VL) random aliphatic copolyesters (P[CL-*co*-VL]) (CL). Melt blending of PLA and random copolyesters (10 wt.%) was carried out using a DSM twin screw micro compounder at 200 °C at 60 rpm for 1 min. Injection molding and compression molding were then used to examine the impact of the copolyesters' composition and molar mass. They have found that using a higher molar mass with a molar composition of 45/55 mol% (CL/VL) improved the impact strength from neat PLA of 2.5 to 7.1 kJ m^{-2}. The

toughness improvement can be explained by the rubbery character of the dispersed phase and the blend morphology; amorphous or slightly crystalline microdomains give more impact strength as compared to high crystalline microdomains. Moreover, the samples prepared by compressing molding exhibited morphologies with larger microdomain sizes as compared to the injection molding [66].

Theryo et al. [67] prepared a rubber-toughened PLA hybrid synthesized using a polylactide graft copolymer. In this approach, a hybrid material containing 5 wt.% of rubber showed a remarkable improvement in tensile ductility and potential for optically transparent and impact-resistant PLA [67]. Meanwhile, Hashima et al. [68] developed a super-tough PLA by blending hydrogenated styrene-butadiene-styrene block copolymer (SEBS) with poly(ethylene-*co*-glycidyl methacrylate) reactive compatibilizer. A binary (PLA/SEBS) and ternary (PLA/PC/SEBS/EGMA) system were designed in this melt blend. It was found that Izod impact strength improved from 3 to 16 kJ m^{-2} for the system containing 70/30 PLA/SEBS. However, a super tough blend was obtained when ethylene-co-glycidyl methacrylate was added at 10% for the 70/20 PLA/SEBS system. In this system, they have successfully increased the impact strength to 92 kJ m^{-2} [68].

In another work, Ma et al. [69] reported the toughening of PLA by blending ethylene-*co*-vinyl acetate copolymer (EVA) with different vinyl acetate contents. It was found that the ratio of vinyl acetate and ethylene in random copolymers seems to control the compatibility and phase morphology. The optimum toughening, i.e., up to a factor of 30, was found at vinyl acetate content of approximately 50 wt.%. They concluded that there were no visible crazes following deformation and that the major toughening process for the PLA/EVA blend was internal rubber cavitation associated with matrix yielding [69].

A more comprehensive review of PLA toughening by other approaches can be found in the review by Anderson et al. [70] and Liu et al. [71]. Liu and Zhang [71] have also reviewed the progress of PLA toughening by focusing on plasticization, technology for copolymerization and more commercially viable melt-blending [71]. The focus on PLA blending for toughening has been reviewed until to date [5,72-77].

PLA/Thermoplastic Elastomer Blends

PLA is one of the sustainable thermoplastics that can be chemically synthesized from renewable material and is an ideal candidate for biodegradable plastics in the market. Blending biodegradable PLA with natural rubber (NR)/epoxidized natural rubber (ENR) to obtain the desired properties at a lower cost and environmentally friendly would be seen as a potential option. Both PLA and NR are made from naturally occurring substances and may be processed using standard polymer processing equipment. In contrast to the ductile NR, the brittle thermoplastic PLA has high strength and modulus. Blending PLA with NR is an excellent option because of the materials' complimentary properties, which allow for the enhancement of PLA attributes like toughness and elongation at the break without compromising its biodegradability. It is expected that through the introduction of a rubbery component in the blend system, additional energy dissipation can be provided during the deformation process. Thus, this supplementary energy dissipation improves toughness. Natural rubber that has been epoxidized is a chemically modified version of *cis*-1,4-polyisoprene. By introducing epoxide groups into the polymer at various points, part of the unsaturation is eliminated. It is useful in processing since it helps make incompatible mixtures work together. ENR-50's addition to rubber blends enhances their ability to be processed, stiffness, resilience, oil resistance, air permeability reduction, superior damping, and wet grip performance [78]. It has been found that higher levels of polarity in ENR lead to greater compatibility with other polymers [51].

Rubber and plastic are combined to create thermoplastic elastomer (TPE), which is rapidly becoming the most lucrative segment of the polymer industry [79]. The primary benefits of these materials are the ease with which scrap and rejects may be recycled using thermoplastic technology, which eliminates the need for a factory or vulcanization. Impact strength and

ductility are both enhanced by the rubber component in rubber-modified thermoplastics. The combination of thermoplastic with NR results in a material known as thermoplastic natural rubber (TPNR). The processing additives have a role in determining whether or not the NR and thermoplastic pair are compatible. Impact characteristics are affected by phase size, the cohesive strength of the rubber phase, and adhesion between phases, whereas dynamic mechanical properties are dependent on mutual solubility.

TPNR combines the properties of hard and brittle plastic, and soft rubber offers a wide variety of applications where flexibility and softness are required. Compared to rubber, the processing of TPNR could be employed using conventional equipment such as injection molding, compression molding, and blow molding and extrusion process. A compatibilized blend will exhibit a single T_g between the two T_g values of the components, which may be used as an indicator of the blend's degree of homogeneity [80-81]. When the T_g is lower than the two-component T_g values, the extra component has a plasticizing effect. However, in NR-polyolefin blends, NR glass transition temperatures are lower(~ −67 °C) and polyolefin (~ −60 °C) are close together; separation is less than 10 °C, and as such the movement of T_g in the blends will not be very indicative of the phase distribution [51].

Zhang et al. [82] investigated the mechanical properties of PLA, and biodegradable polyamide elastomer (PAE) blends to toughen the PLA. It was discovered that PAE, and PLA blends acquired a fair level of compatibility with one another. The tensile strength of the blend was comparable to that of clean PLA at 10% PAE concentration, but the elongation improved significantly [82].

Toughness was improved by the addition of other materials when PLA was mixed with ethylene-propylene copolymer, ethylene-acrylic rubber, acrylonitrile-butadiene rubber (NBR), and isoprene rubber by Ishida et al. According to the results of the Izod impact test, mixing PLA and NBR may result in a toughening effect because of the smaller particle size of the mixes. The morphology analysis also confirmed that interfacial tension between PLA phase and NBR was the lowest; hence according to them; rubber with high polarity is more suitable for PLA toughening. NBR and isoprene rubber (IR), on the other hand, were able to produce plastic deformation and contribute to the material's high elongation capabilities when subjected to tensile stress. They also theorized that the rubber's inherent mobility plays a crucial role in the energy dissipation process during breaking [56].

Super toughened by melt blending at 240 °C, ternary blends of PLA, an epoxy-containing elastomer, and a zinc ionomer are reported by Liu et al. to exhibit intermediate strength and stiffness. It was shown that zinc ions might hasten the cross-linking of an epoxy-containing elastomer and cause reactive compatibilization between PLA and the elastomer's interface. It was hypothesized that the large boost in notched impact strength at high blending was due to the compatibilization effect [53].

PLA/natural rubber blend containing nucleating agents such as cyclodextrin, talc and calcium carbonate has been prepared by Suskut and Deeprasertkul [83] in an effort to enhance the toughness. Talc and calcium carbonate, but not cyclodextrin, were shown to boost the PLA crystallinity in the PLA/NR blends. The use of nucleating chemicals has greatly increased PLA's tensile and impact toughness [83]. In order to counter PLA's brittleness and poor crystallization, Bitinis et al. [84] created an NR/PLA blends by mixing the two materials together in a melt. By introducing 10 wt.% of NR, they were able to increase the elongation at break from 5% for plain PLA to 200%. The addition of NR was believed to increase the rate of crystallization as well as the crystallization ability of PLA [84].

Similar to Bitinis works, Jaratrotkamjorn et al. [85] prepared a rubber-toughened PLA via extrusion melt blending to investigate the effect of rubber polarity and viscosity and molecular weight on the mechanical properties of blends. In this study, they compared the toughening effects of NR, epoxidized natural rubber (ENR25 and ENR50), and natural rubber grafted with poly(methyl methacrylate) (NR-*g*-PMMA), concluding that NR had the greatest impact. Interestingly, they have found that the viscosity and molecular weight of NR decreased with increasing mastication, increasing the

impact strength of PLA/NR blends. This work indicated that the particle diameter was very important and probably more important than the rubber polarity. As such, the smaller particles of ENR and NR-*g*-PMMA were ineffective in promoting toughness compared to NR [85].

A study by Kowalczyk and Piorkowska [86] revealed that the immiscible blend of PLA/poly(1,4-*cis*-isoprene) was successfully prepared by melt blending in the Brabender batch mixer. The strain at the break of compression-molded film during uniaxial drawing was found to rise by as much as 80% when rubber at a weight fraction of 5 wt.% was included [86].

Petchwattana et al. [87] investigated the use of ultrafine acrylate particles as a toughening agent for PLA. With the addition of 10% of acrylate rubber, the tensile elongation at break increased from 3.5 to 200% or 50 times higher as compared to the neat PLA. Similar improvement was also observed for impact strength, where they recorded a fourfold improvement. The remarkable improvement was revealed to be related to the ultrafine acrylate rubber particle contribution in inducing crazes. The degree of crystallinity was increased at only 5% of acrylate rubber [87].

Liu et al. [88] reported in another investigation that PLA was toughened using a ternary blend of ethylene/*n*-butyl acrylate/glycidyl methacrylate terpolymer elastomer (EBA-GMA) and ethylene/methacrylate acid copolymer (EMAA-Zn). In this reactive blending approach, they noted that by increasing the reactive blending temperature, it favored the interfacial wetting and increasing the crosslinking of the EBA-GMA rubber phase and hence unfavorably enhanced its cavitation's resistance [88].

Bijarimi et al. explored the use of natural rubber to toughen the PLA via melt blending [3,28,89]. Using a range of rubber concentrations, they discovered that liquid natural rubber (LNR) and liquid epoxidized natural rubber (LENR) successfully toughened the brittle PLA. The summary of mechanical properties of PLA/rubber or elastomer based are given in Table 3.

Toughening Mechanism

The ductile development of all solid polymers belies their innate brittleness [90]. Combining stiff particles that may debond before plastic flow with rubbery particles that can cavitate. Massive crazing and shear yielding are two toughening processes of polymers that are well-recognized and understood. Commodities plastics such as polyamides, polystyrene and polypropylene have been toughened by the incorporation of the rubber phase [91].

Understanding the toughening mechanism associated with the polymer blend morphology in any blend systems is imperative. There exist few literature reports on the toughening mechanism of the toughened PLA. Whitening of a tensile specimen's elongated region has been linked to crazing development in certain investigations, suggesting that toughening improvements may be linked to crazing formation [92]. Multiple craze production at the fracture tip area, with elongated fibrils and voids constructing the crazes, was shown by Todo et al. [93] in PLLA/PCL blends. Furthermore, at the high tensile stress conditions present in the crack tip area, elongated PCL spherulites developed, giving rise to the stretched fibrils structure. They have concluded that the damage formations were the principal energy dissipation mechanisms for improving fracture energy.

Table 3. Mechanical properties of PLA/rubber or elastomer based

Blend Component	Composition	Stress at break (MPa)	Elongation at break (%)	Modulus (GPa)	Ref.
PLA/NR	90/10	40.10	200	2.00	[84]
PLA/NR	90/10	32.16	7.26	1.31	[85]
PLA/ENR25	90/10	19.30	2.31	1.38	[85]
PLA/ENR50	90/10	17.80	2.25	1.36	[85]
PLA/Acrylate rubber	90/10	48.98	198	2.00	[87]

Void development due to inadequate interfacial adhesion blending component was discovered to generate cavitation inside the rubber particles and debonding between the rubber particles and matrix in rubber-toughened polymers. It was found that good adhesion between components PLA/poly(1,4-*cis*-isoprene) was obtained, hence cavitation occurred inside the rubber particle. Accordingly, it was concluded that there were three fundamental processes at work: first, the rubbery particles induced crazing, and then cavitation inside the rubber particles boosted the shear yielding of PLA [86].

In another study, the blend of PLA/ultrafine acrylate induced a large number of crazes as the mechanism for energy absorption. Microdamage, void, and craze development, together with other fracture characteristics, including pull-out and scission of polymer fibrils, were proposed as the mechanisms responsible for energy dissipation at the crack tip area. It was concluded that the ultrafine acrylate rubber particles were dispersed and adhered well with the PLA, and hence crazing mechanism was responsible for major toughening [87].

It has also been found that crazing in PLA/EVA blends causes the formation of craze fibrils, which leads to significant dispersion along the tensile axis. However, cavitation happens first during deformation, and then the cavities and rubber particles stretch out. Some of the spaces even had a fibrillar structure, which helps with bridging and slows the voids from spreading. An essential part of the rubber phase's ability to absorb energy is its fibrillation. According to their findings, the PLA/EVA blend's primary toughening process is postulated to be internal rubber cavitation in conjunction with the matrix yielding [69].

Many studies have recently been done on PLA rubber/elastomer blends to change the characteristics of PLA for numerous technical applications that need demanding applications [9,15,27,94-99]. As for FDM 3D printing, PLA and NR were mixed with increasing toughness and investigated by Fekete et al. [100]. On the other hand, Musa et al. [101] have recently analyzed the potential of 3D fused deposition modeling employing filaments made of PLA-based thermoplastic elastomer. An understanding of the toughening mechanism that governs the toughness of PLA is crucial.

■ PLA/PLASTICIZATION

In the plastics and rubber sectors, plasticizers such as phthalates, benzoates, adipates, synthetic acid, and mineral oils are the most prevalent additions. However, it has always been challenging to determine which plasticizer is best for a specific use. Cost-benefit analysis is often used to determine which plasticizer is best for a certain application. The primary function of a plasticizer is to lower T_g, melting temperature (T_m), and modulus of a polymer without altering the chemical structure of the polymer, hence increasing the plasticity and flow of the polymer.

PEG plasticizers have been added to PLA-PEG blends to improve the toughness of PLA. PLA-PEG blends are more durable, flexible, and processable than PLA alone. PEG plasticizers increase the amorphous content and decrease the crystallinity of PLA, improving its toughness. Furthermore, PEG plasticizers reduce the viscosity of PLA in its molten state, increasing its processability. Furthermore, the addition of PEG plasticizers to PLA raises the glass transition temperature, making the blends more stable over a wider temperature range. The composition and chemical structure of PEG affects the characteristics in a major way of PLA-PEG blends. In general, higher PEG content and lower molecular weight PEGs improve toughness and flexibility while lowering the melting temperature and mechanical properties of the blends. In conclusion, PLA-PEG blends are a promising alternative to PLA in a variety of applications due to their increased toughness and flexibility. The properties of the blends can be altered by adjusting the PEG concentration and chemical structure of the PEG. This section reviews the usage of several types of plasticizers in an attempt to minimize PLA brittleness and thereby boost toughness.

The brittleness of PLA is a fundamental drawback to its usage in many applications. Therefore, plasticizers must be added to lower the glass transition temperature and increase toughness and processability, as commonly used in plastic industries for glassy polymer. Commonly, plasticizers being a non-volatile solvent and low molar mass added to the polymer for processability improvement by acting as a spacer at the molecular level

so that less energy is required to allow substantial rotation about the C–C bonds, and thus T_g is lowered [102]. An efficient plasticizer should reduce the glass transition temperature of the amorphous domains; if the T_g is near or lower than the ambient temperature, flexibility is achieved [103]. Therefore, a lot of attention is being given to improving the toughness of PLA by adding plasticizers.

Murariu et al. [14] investigated the toughening of PLA- Calcium sulfate anhydrite ($CaSO_4$) -anhydrite II composites utilizing bio-sourced tributyl citrate (TBC). With as low as 10% plasticizer, plasticized composites offer higher tensile and impact toughness. They found the PLA-β-anhydrite II (AII)-10%TBC sample under consideration for future development demonstrated fascinating properties such as tensile strength of 22–26 MPa, elongation at break of 160%, and high impact resistance (5.6 kJ/m^2). Mechanical tests of composites with higher TBC concentrations (15–20%) revealed typical elastomeric behavior, despite plasticizer migration, even after a short period of age [14].

Besides being eco-friendly and biocompatible, PLA also has better thermal processability compared to other biopolymers such as poly(hydroxyl alkanoates) (PHAs), PEG, and PCL. Despite all the advantages, PLA is a very brittle material with less than 10% elongation at break [45,55]. This limitation has been overcome by introducing low molecular weight plasticizers such as glycerol, sorbitol and triethyl citrate.

The plasticization of PLA can be extensively found in the research literature. Plasticizers such as PEG, glucose monoesters, triethyl citrate (TC), acetyl triethyl citrate (ATC), fatty acid esters, oligomeric lactic acid and glycerol were used to improve the flexibility of PLA [104-106].

Labrecque and co-workers [106] investigated citrate esters plasticizer at 10, 20 and 30% by weight and found reduced T_g and improved elongation at break. Another researcher claimed that the increase of triacetin and tributyl citrate contents linearly reduces the glass transition temperature of PLA. At 25% of plasticizer content, miscibility with PLA was noted. Nevertheless, when the samples were heated at 35, 50 and 80 °C, phase separation was observed due to increased crystallinity during heat treatment. Phase separation occurs in samples heated to 35, 50, and 80 °C, probably due to the crystallization of the substance [107].

The addition of different plasticizers with low molecular weights, like PEG and glycerol, has been studied by Martin and Averous [105]. The lowest glass temperature was achieved using PEG 400 plasticizer. However, glycerol was shown to be the least effective. T_g variation and mechanical characteristics were used for the analysis. Nevertheless, for the PLA melt-blended with thermoplastic starch, two different T_gs were observed in the blends, indicating limited compatibility [105].

Baiardo et al. investigated the acetyl tri-*n*-butyl citrate (ATBC) and PEGs plasticization of PLLA. The mechanical characteristics of plasticized PLA were discovered to vary as the plasticizer concentration increased; that is when the blend T_g was brought closer to room temperature, a gradual shift in the mechanical properties of the system was seen. Even though the tensile strength and modulus are both reduced, the elongation at break rises dramatically [108]. Incorporating monomeric plasticizers such tributyl citrate and bishydroxymethyl malonate has led to a reduction in PLA's T_g. Morphology stability and enhanced flexibility were found in the oligomeric plasticizer because of stronger polar interactions with PLA and a larger molecular weight [107].

Pillin et al. [109] analyzed the thermal and mechanical properties of PLA with PEG, poly(1,3-butanediol) (PBOH), acetyl glycerol monolaurate (AGM), and dibutyl sebacate (DBS) in an effort to enhance the material's mechanical properties for packaging applications. All plasticizers were melt blended with plasticizers at 10–30% w/w concentrations. PEGs were shown to be the most effective plasticizer, resulting in a change of the glass transition temperature T_g to a lower zone for all blends. But the modulus and stress at break were both lower in the PLA/PEG blends, principally because of the reduced cohesion induction, which was mirrored in the low stress at break. On the other hand, in this study, they have shown that the PBOH, AGM and DBS exhibited mechanical properties consistent with soft packaging applications [109].

Calcium sulfate derived from lactic acid production was blended with PLA and low molecular weight plasticizers (bis(2-ethylhexyl) adipate, glyceryl triacetate, and polymeric adipates) by Murariu et al. [110]. The works aimed at reducing the brittle behaviour of PLA-calcium sulfate composite. They have reported that adding up to 10 wt.%. of plasticizer increased the composition's impact strength by a factor of four without any modifier. Furthermore, the ternary blends were observed to have better processing and good filler dispersion [110].

Similarly to polyolefins and other thermoplastics, PLA can be treated, albeit its thermal stability may be improved [111-112]. Plasticizers are required to enhance the elongation and impact characteristics of PLA polymers, which are otherwise rigid and brittle. The processability of polymers is often enhanced by adding plasticizers such as partial fatty acid esters, glycerol esters, citrates, citrate oligoesters, and dicarboxylic esters [104]. Resistance to volatility, diffusion, extraction, and/or weathering, larger molecular weight plasticizers like PEG and poly(propylene glycol) and polyester plasticizers have also been studied for PLA plasticization [113-114].

Okammoto et al. [115] investigated the effect of molecular structures of polyester-diols (PED) such as poly(ethylene adipate) (PEA), poly(diethylene adipate) (PDEA) and poly(hexamethylene) (PHA) on miscibility, mechanical and thermal properties of plasticized PLA. In this work, they prepared various compositions of PLA/PED through melt blending and solvent casting. It was found that the blends of 80PLA/20PEA and 80PLA/20PDEA are miscible blends but only partially miscible for the 80PLA/20PHA blend. The large configurationally entropy caused by the chain flexibility of PDEA with the ether bond is responsible for the good miscibility between PLA/PDEA [115].

With the goal of creating biodegradable packaging made from PLA, Lemmouchi et al. [116] plasticized the PLA with blends of tributyl citrate (TBC) and low molecular (PLA-*b*-PEG) copolymers via a melt blending. In this study, the copolymer has been synthesized using potassium-based catalyst. The thermal and mechanical properties were investigated as a function of blend composition and copolymer structure/topology. They have found that for compositions containing 80 wt.%. PLA and 20 wt.%. Blend of plasticizers showed a T_g below 30 °C, high nominal strain at break and tensile strength. It was also found that this TBC and PLA-b-PEG blend has increased the impact strength of neat PLA. In terms of biodegradation, the test conducted in compost conditions showed that this plasticizer enhanced the degradation of PLA matrix [116].

Using a solvent casting method, Hughes et al. investigated the efficacy of methylene chloride/acetonitrile mixed solvent solutions with 10% plasticizer in increasing the flexibility of PLA films. In this approach, the compound with a solvent ratio of 70% methylene chloride and 30% acetonitrile was found to have less crystallinity and the highest flexibility, i.e., at 49.36% elongation. In addition, this compound had the same thermal behavior as the more crystalline films [117].

Hassouna et al. [118] introduced a novel technique for plasticizing PLA. Here, we use a co-rotating intermeshing twin-screw extruder to combine anhydride-grafted PLA (MAG-PLA) copolymer with PEG at 181 °C and 80 rpm. Melt blending compatibility between PLA and PEG was enhanced by grafting a small amount of PEG onto the anhydride-functionalized PLA chains. It was found that the molecular weight did not drop dramatically as a result of this melt blending and extrusion process. Furthermore, the glass transition temperature decreased as compared to the blends without grafting i.e., neat PLA blended with PEG. They have also concluded the addition of MAG-PLA did not significantly influence the behavior of this blend [118].

Another study by Bijarimi et al. [4] showed that PEG has the ability to strengthen PLA. It took 15 min to melt the blend PEG/PLA in an internal mixer heated to 180 °C with the speed set at 50 rpm. The blends were tested to determine their mechanical, thermal, and morphological characteristics. When PEG was added to the PLA matrix at concentrations between 2.5 and 10%, the tensile and flexural strength, stiffness, and notched Izod impact strength all reduced dramatically. As the PEG concentration increased, the glass transition and

melting temperatures (T_g and T_m) fell. In addition, the PLA/PEG mixes exhibited lower initial and peak degradation temperatures but greater final degradation temperatures than PLA alone. Morphological investigation revealed that the PEG was disseminated as droplets in the PLA matrix, with a clear demarcation between the PLA matrix and PEG phases [4].

Kim et al. explored plasticizing effect in poly(vinyl alcohol) blown film (butylene adipate-*co*-terephthalate). PLA/poly(butylene adipate-*co*-terephthalate (PBAT) mechanical characteristics and tear resistance were tested utilizing a blown film extrusion technique. Extreme brittleness, poor stiffness, and incompatibility restrict the utilization of PLA and PBAT packaging. Adipate, adipic acid, glycerol ester, and adipic acid ester were investigated for their effects on PLA plasticization and PLA/PBAT blown film manufacturing. Adipic acid ester improves PLA's flexibility and compatibility with PBAT. Plasticizer enhanced PLA matrix chain mobility. The plasticized PLA domain's adherence to the PBAT matrix was also improved. Plasticized PLA/PBAT blown film enhanced tear resistance in the machine direction from 4.63 to 8.67 N mm^{-1} and in the transverse direction from 13.19 to 16.16 N mm^{-1} [119].

The increased flexibility of biodegradable PLA/starch blends using epoxidized palm oil as a plasticizer was examined by Awale et al. [120], epoxidized palm oil (EPO) increased the PLA/PSt combination's flexibility. PLA/starch/EPO (PSE) combinations with a constant percentage of starch and a variable quantity of EPO were created via solution casting. EPO increases chain mobility by lowering the glass transition, melting, and crystallization temperatures of PSt. According to TGA, PSE is more heat-resistant than PSt. Mechanical testing showed that EPO at all concentrations enhanced impact strength and elongation-at-break. They demonstrated the greater adaptability of PLA-EPO combinations [120].

Ghari and Nazockdast [17] compared the morphological and mechanical properties of PLA/plasticized thermoplastic starches (TPS) blends and PLA/TPS+EVA blends. Combining PLA with thermoplastic starch was studied for its potential toughening effects. Similar studies were undertaken on molten ternary mixtures of PLA, dynamically cross-linked TPS, and EVA. In a viscoelastic melt study, citric acid (CA) reduced TPS viscosity and flexibility. They hypothesized that a dynamically cross-linked EVA produced the dispersed phase percolated network. Due to their unique construction, ternary blends are far more robust than binary blends [17].

Gzyra-Jagiela et al. [121] studied PLA modification through high-molecular compounds such as ethoxylated lauryl alcohol, ethylene oxide, and propylene oxide block copolymers combined with low-molecular substances such as di-2-ethylhexyl adipate, di-2-ethylhexyl sebacate, and triethyl citrate. Depending on the plasticizer employed, all of the adjusted samples showed lower glass transition temperatures than the untreated polymer. The most successful treatments were di-2-ethylhexyl adipate (ADO) and di-2-ethylhexyl sebacate (SDO). The elongation at the fracture site increased significantly with ADO, reaching around 21%. Despite having a higher glass temperature, SDO achieved the largest elongation (approximately 35%) [121].

Several factors, including nucleating agents, plasticizers, and molding conditions, were studied by Tabi et al. to see how they affected the qualities of injection-molded PLA products. Results showed that PLA treated with nucleating agents outperformed ABS in terms of heat deflection temperature, tensile strength, and Young's modulus. Even after being annealed or subjected to simultaneous nucleation and plasticization, the PLA compounds' elongation at break was much lower than ABS's. However, the brittleness of PLA was not alleviated by using plasticizers, nucleating agents, or varying the mold temperature. There was nevertheless a significant drop in PLA's elongation at break, which hovered between 1.7 and 2.5% throughout their studies [122]. A summary of the mechanical properties of plasticized PLA found in the literatures are given in Table 4.

In the realm of plastics manufacture, PLA blends are commonly utilized as a safe and environmentally acceptable alternative to standard synthetic polymers.

Table 4. Mechanical properties of plasticized PLA

Blend component	Weight %	Stress at break (MPa)	Elongation at break (%)	Modulus (GPa)	Ref.
PLA/PEG200	10	30.0	2.00	1.70	[109]
PLA/PEG400	10	-	26.0	1.49	[105]
PLA/PEG400	20	-	160	0.98	[105]
PLA/PEG400	10	39.0	2.40	1.92	[109]
PLA/PEG400	20	16.0	21.2	0.63	[109]
PLA/PEG1000	10	39.6	2.70	1.97	[109]
PLA/PEG1000	20	21.6	200	0.29	[109]
PLA/Oligomeric lactic acid	10	-	32.0	1.49	[105]
PLA/Oligomeric lactic acid	20	-	200	0.74	[105]
PLA/PEA	20	24.8	8.15	0.37	[115]
PLA/PBA	20	42.6	4.28	0.67	[115]
PLA/PHA	20	36.8	0.19	0.71	[115]
PLA/PDEA	20	17.7	7.05	0.26	[115]

The addition of plasticizers or low-molecular-weight polymers, both of which are polymers, can enhance the physical properties of PLA, such as its flexibility, tenacity, and heat stability. Glycerol is the most common type of plasticizer used in PLA, and it gives PLA a greater degree of flexibility. The inclusion of low-molecular-weight polymers, such as polyethylene glycol and polyvinyl alcohol, can increase the heat stability and brittleness of PLA. Additionally, the brittleness of PLA can be diminished. In addition, PLA blends containing these additives have the potential to improve the material's overall processability. In general, combining PLA with plasticizers or low molecular weight polymers can enhance the material's physical qualities, making it suitable for a broader range of applications. In addition, these mixes are harmless to humans and environmentally friendly, making them a good choice for a range of industries.

■ FUTURE OUTLOOK OF PLA

The immense potential uses of biodegradable polymers provide new avenues for lessening reliance on petroleum-based polymers. Despite the rise of PLA-based goods, there remains a poor view of product performance when compared to traditional plastics. Furthermore, the high cost of biobased polymers is a factor leading to inefficiency in the industrial sectors.

Despite significant drawbacks in characteristics, particularly brittleness and limited elongation, the future prospect for PLA is highly promising. It is not surprising, however, that much research is being conducted in an attempt to make PLA more suited for a wide variety of applications via property change. As previously discussed, mixing with other polymers and plasticization might address the intrinsic brittleness issue. However, greater efforts must be made to design a material with balanced stiffness and toughness qualities. All attempts so far have shown considerable promise, indicating that the future of PLA-based materials as a possible alternative for replacing commodity plastics is unquestionably bright. With updated technology in polymer processing, such as 3D and 4D printing, it is envisaged that PLA processing would be as efficient as processing mature commodities' plastics. As such, it serves as a catalyst for the commercialization of biodegradable polymers, especially for items with short life cycles and single-use applications.

■ CONCLUSION

PLA is utilized for a wide number of tasks across many different industries, including the packaging industry, engineering, and medicine. PLA is undergoing research and development to improve its toughness, property modification, and plasticizing capabilities,

which bode well for the material's future. Research has been focused on finding ways to make PLA materials more durable. One such method involves adding a very small amount of a compound similar to rubber that is compatible with PLA. This component, similar to rubber, is referred to as a rubber modifier, and it works to improve the tenacity of PLA. Modifications to the properties of PLA, such as the inclusion of UV stabilizers and antioxidants, are being investigated in other research with the intention of making the material more weatherproof and resistant to the effects of ultraviolet light. Plasticizing PLA is another option for those interested in increasing the material's flexibility. In order to produce plasticization in PLA, a low molecular weight plasticizer is added to the PLA. Because of this, the material becomes less rigid while simultaneously increasing its softness and flexibility. Plasticized PLA is frequently used in medical applications such as implants and prostheses. Examples of these uses include: In addition, PLA can be utilized in a wide variety of engineering applications. It is possible to generate prototypes as well as final things through the use of 3D printing. Both the construction and car industries use many components, such as interior panels and gaskets.

In conclusion, it is no doubt that PLA has a positive outlook. Through continued research and development, PLA can be improved to the point that it can meet the requirements of a variety of different applications. Because of its toughness, property modification capabilities, plasticizing capabilities, and engineering applications, this biodegradable thermoplastic material has a promising future.

■ ACKNOWLEDGMENTS

The authors wish to acknowledge the Universiti Malaysia Pahang (UMP) for the financial assistance provided under the internal research grant RDU 223022 and FRGS/1/2019/TK05/UMP/02/1.

■ REFERENCES

[1] Trinh, B.M., Tadele, D.T., and Mekonnen, T.H., 2022, Robust and high barrier thermoplastic starch – PLA blend films using starch-*graft*-poly(lactic acid) as a compatibilizer, *Mater. Adv.*, 3 (15), 6208–6221.

[2] Moshiul Alam, A.K.M., Beg, M.D.H., Yunus, R.M., Bijarimi, M., Mina, M.F., Maria, K.H., and Mieno, T., 2018, Modification of structure and properties of well-dispersed dendrimer coated multi-walled carbon nanotube reinforced polyester nanocomposites, *Polym. Test.*, 68, 116–125.

[3] Bijarimi, M., Ahmad, S., and Moshiul Alam, A.K.M., 2017, Toughening effect of liquid natural rubber on the morphology and thermo-mechanical properties of the poly(lactic acid) ternary blend, *Polym. Bull.*, 74 (8), 3301–3317.

[4] Bijarimi, M., Ahmad, S., Rasid, R., Khushairi, M.A., and Zakir, M., 2016, Poly(lactic acid)/poly(ethylene glycol) blends: Mechanical, thermal and morphological properties, *AIP Conf. Proc.*, 1727, 020002.

[5] Fu, Y., Liu, L., Zhang, J., and Hiscox, W.C., 2014, Functionalized graphenes with polymer toughener as novel interface modifier for property-tailored polylactic acid/graphene nanocomposites, *Polymer*, 55 (24), 6381–6389.

[6] Hafidzah, F., Bijarimi, M., Alhadadi, W., Salleh, S., Norazmi, M., and Normaya, E., 2020, Statistical study on the interaction factors of polypropylene-graft-maleic anhydride (PP-g-MA) with graphene nanoplatelet (GNP) at various poly(lactic acid)/polypropylene (PLA/PP) blends ratio, *Indones. J. Chem.*, 21 (1), 234–242.

[7] Bijarimi, M., Syuhada, A., Zulaini, N., Shahadah, N., Alhadadi, W., Ahmad, M.N., Ramli, A., and Normaya, E., 2020, Poly(lactic acid)/acrylonitrile butadiene styrene nanocomposites with hybrid graphene nanoplatelet/organomontmorillonite: Effect of processing temperatures, *Int. Polym. Process.*, 35 (4), 355–366.

[8] Bijarimi, M., Shahadah, N., Ramli, A., Nurdin, S., Alhadadi, W., Muzakkar, M.Z., and Jaafar, J., 2020, Poly(lactic acid) (PLA)/acrylonitrile butadiene styrene (ABS) with graphene nanoplatelet (GNP) nanocomposites, *Indones. J. Chem.*, 20 (2), 276–281.

[9] Harris, M., Mohsin, H., Potgieter, J., Ishfaq, K., Archer, R., Chen, Q., De Silva, K., Guen, M.J.L., Wilson, R., and Arif, K.M., 2022, Partial

biodegradable blend with high stability against biodegradation for fused deposition modeling, *Polymers*, 14 (8), 1541.

[10] Bijarimi, M., Abdulsalam, Y., Norazmi, M., Normaya, E., Alhadadi, W., and Desa, M.S.Z., 2023, Preparation and characterization of poly(lactic acid)/linear low density polyethylene/recycled tire waste/graphene nanocomposites, *Mater. Today: Proc.*, In Press, Corrected Proof.

[11] Grijpma, D.W., Altpeter, H., Bevis, M.J., and Feijen, J., 2002, Improvement of the mechanical properties of poly(D,L-lactide) by orientation, *Polym. Int.*, 51 (10), 845–851.

[12] Jansen, J., Koopmans, S.A., Los, L.I., van der Worp, R.J., Podt, J.G., Hooymans, J.M.M., Feijen, J., and Grijpma, D.W., 2011, Intraocular degradation behavior of crosslinked and linear poly(trimethylene carbonate) and poly(D,L-lactic acid), *Biomaterials*, 32 (22), 4994–5002.

[13] Mark, J.E., 1999, *Polymer Data Handbook*, Oxford University Press, New York, US.

[14] Murariu, M., Paint, Y., Murariu, O., Laoutid, F., and Dubois, P., 2022, Tailoring and long-term preservation of the properties of PLA composites with "green" plasticizers, *Polymers*, 14 (22), 4836.

[15] Murariu, M., Arzoumanian, T., Paint, Y., Murariu, O., Raquez, J.M., and Dubois, P., 2022, Engineered polylactide (PLA)–polyamide (PA) blends for durable applications: 1. PLA with high crystallization ability to tune up the properties of PLA/PA12 blends, *Eur. J. Mater.*, 1–36.

[16] Vink, E.T.H., Rábago, K.R., Glassner, D.A., Springs, B., O'Connor, R.P., Kolstad, J., and Gruber, P.R., 2004, The sustainability of NatureWorks™ polylactide polymers and Ingeo™ polylactide fibers: An update of the future, *Macromol. Biosci.*, 4 (6), 551–564.

[17] Ghari, H.S., and Nazockdast, H., 2022, Morphology development and mechanical properties of PLA/differently plasticized starch (TPS) binary blends in comparison with PLA/dynamically crosslinked "TPS+EVA" ternary blends, *Polymer*, 245, 124729.

[18] Nofar, M., Mohammadi, M., and Carreau, P.J., 2021, Super enhancement of rheological properties of amorphous PLA through generation of a fiberlike oriented crystal network, *J. Rheol.*, 65 (4), 493–505.

[19] Ranakoti, L., Gangil, B., Mishra, S.K., Singh, T., Sharma, S., Ilyas, R.A., and El-Khatib, S., 2022, Critical review on polylactic acid: Properties, structure, processing, biocomposites, and nanocomposites, *Materials*, 15 (12), 4312.

[20] Zhao, X., Hu, H., Wang, X., Yu, X., Zhou, W., and Peng, S., 2020, Super tough poly(lactic acid) blends: A comprehensive review, *RSC Adv.*, 10 (22), 13316–13368.

[21] Abdelrazek, S.G., Abou Taleb, E.M.A., Mahmoud, A.S., and Hamouda, T., 2022, Utilization of polylactic acid (PLA) in textile food packaging: A review, *Egypt. J. Chem.*, 65 (3), 725–738.

[22] Lunt, J., 1998, Large-scale production, properties and commercial applications of polylactic acid polymers, *Polym. Degrad. Stab.*, 59 (1-3), 145–152.

[23] Gupta, A.P., and Kumar, V., 2007, New emerging trends in synthetic biodegradable polymers - Polylactide: A critique, *Eur. Polym. J.*, 43 (10), 4053–4074.

[24] Sinha Ray, S., Yamada, K., Okamoto, M., and Ueda, K., 2002, New polylactide-layered silicate nanocomposites. 2. Concurrent improvements of material properties, biodegradability and melt rheology, *Polymer*, 44 (3), 857–866.

[25] Toyota-Boshoku, 2013, *Novel bio-based plastic with top-level impact strength*, Toyota Central R&D Labs., Inc., https://www.toyota-boshoku.com/asia/news/release/detail.php?id=1954.

[26] Utracki, L.A., 2002, Compatibilization of polymer blends, *Can. J. Chem. Eng.*, 80 (6), 1008–1016.

[27] Mukherji, D., de Oliveira, T.E., Ruscher, C., and Rottler, J., 2022, Thermodynamics, morphology, mechanics, and thermal transport of PMMA-PLA blends, *Phys. Rev. Mater.*, 6 (2), 025606.

[28] Bijarimi, M., Ahmad, S., and Rasid, R., 2014, Mechanical, thermal and morphological properties

of poly(lactic acid)/epoxidized natural rubber blends, *J. Elastomers Plast.*, 46 (4), 338–354.

[29] Bijarimi, M., Ahmad, S., and Rasid, R., 2013, Mechanical, thermal and morphological properties of poly(lactic acid)/natural rubber nanocomposites, *J. Reinf. Plast. Compos.*, 32 (21), 1656–1667.

[30] Reddy, N., Nama, D., and Yang, Y., 2008, Polylactic acid/polypropylene polyblend fibers for better resistance to degradation, *Polym. Degrad. Stab.*, 93 (1), 233–241.

[31] Kanzawa, T., and Tokumitsu, K., 2009, A study for graft-reaction of PEG onto PLA chains by reactive processing, *J. Soc. Mater. Sci., Jpn.*, 21 (8), 469–473.

[32] Sun, R., Du, J., Pan, G.F., Zhang, S., Zhang, Z.P., and Xiong, C.D., 2004, Development and *in vitro* characterization of PDLLA/Î²-TCP/PLA-PEG composite scaffolds, *Transactions, 7th World Biomaterials Congress*, 17-21 May 2004, Sydney Convention & Exhibition Centre, Darling Harbour, Sydney, Australia, 869.

[33] Brown, C.D., Tae, G., Stayton, P.S., and Hoffman, A.S., 2004, Controlled delivery of growth factors from PEG/PLA degradable matrices and heparin-PEG affinity hydrogels, *Transactions, 7th World Biomaterials Congress,* 17-21 May 2004, Sydney Convention & Exhibition Centre, Darling Harbour, Sydney, Australia, 186.

[34] Ren, J., Hong, H., Ren, T., and Teng, X., 2006, Preparation and characterization of magnetic PLA-PEG composite nanoparticles for drug targeting, *React. Funct. Polym.*, 66 (9), 944–951.

[35] Ren, J., Hong, H.Y., Ren, T.B., and Teng, X.R., 2005, Preparation and characterization of magnetic PLA-PEG composite particles, *Mater. Lett.*, 59 (21), 2655–2658.

[36] Zhang, H., Xia, H., Wang, J., and Li, Y., 2009, High intensity focused ultrasound-responsive release behavior of PLA-b-PEG copolymer micelles, *J. Controlled Release*, 139 (1), 31–39.

[37] Vila, A., Gill, H., McCallion, O., and Alonso, M.J., 2004, Transport of PLA-PEG particles across the nasal mucosa: Effect of particle size and PEG coating density, *J. Controlled Release*, 98 (2), 231–244.

[38] Sasatsu, M., Onishi, H., and Machida, Y., 2005, Preparation of a PLA-PEG block copolymer using a PLA derivative with a formyl terminal group and its application to nanoparticulate formulation, *Int. J. Pharm.*, 294 (1-2), 233–245.

[39] He, G., Ma, L.L., Pan, J., and Venkatraman, S., 2007, ABA and BAB type triblock copolymers of PEG and PLA: A comparative study of drug release properties and "stealth" particle characteristics, *Int. J. Pharm.*, 334 (1-2), 48–55.

[40] Govender, T., Riley, T., Ehtezazi, T., Garnett, M.C., Stolnik, S., Illum, L., and Davis, S.S., 2000, Defining the drug incorporation properties of PLA-PEG nanoparticles, *Int. J. Pharm.*, 199 (1), 95–110.

[41] Heald, C.R., Stolnik, S., De Matteis, C., Garnett, M.C., Illum, L., Davis, S.S., and Leermakers, F.A.M., 2003, Characterisation of poly(lactic acid): Poly(ethyleneoxide) (PLA:PEG) nanoparticles using the self-consistent theory modelling approach, *Colloids Surf., A*, 212 (1), 57–64.

[42] Heald, C.R., Stolnik, S., De Matteis, C., Garnett, M.C., Illum, L., Davis, S.S., and Leermakers, F.A.M., 2001, Self-consistent field modelling of poly(lactic acid)-poly(ethylene glycol) particles, *Colloids Surf., A*, 179 (1), 79–91.

[43] Zhang, L., Xiong, C., and Deng, X., 1995, Biodegradable polyester blends for biomedical application, *J. Appl. Polym. Sci.*, 56 (1), 103–112.

[44] Chen, C.C., Chueh, J.Y., Tseng, H., Huang, H.M., and Lee, S.Y., 2003, Preparation and characterization of biodegradable PLA polymeric blends, *Biomaterials*, 24 (7), 1167–1173.

[45] Rasal, R.M., Janorkar, A.V., and Hirt, D.E., 2010, Poly(lactic acid) modifications, *Prog. Polym. Sci.*, 35 (3), 338–356.

[46] Tullo, A.H., 2002, Breaking the bank with new polymers, *Chem Eng. News*, 80 (20), 13–19.

[47] Hiljanen-Vainio, M., Varpomaa, P., Seppälä, J., and Törmälä, P., 1996, Modification of poly-(L-lactides) by blending: Mechanical and hydrolytic behavior, *Macromol. Chem. Phys.*, 197 (4), 1503–1523.

[48] Ismail, H., and Suryadiansyah, S., 2002, Thermoplastic elastomers based on

polypropylene/natural rubber and polypropylene/ recycle rubber blends, *Polym. Test.*, 21 (4), 389–395.

[49] Asaletha, R., Kumaran, M.G., and Thomas, S., 1999, Thermoplastic elastomers from blends of polystyrene and natural rubber: Morphology and mechanical properties, *Eur. Polym. J.*, 35 (2), 253–271.

[50] Pospísil, J., Horák, Z., Kruliš, Z., Nešpůrek, S., and Kuroda, S.I., 1999, Degradation and aging of polymer blends I. Thermomechanical and thermal degradation, *Polym. Degrad. Stab.*, 65 (3), 405–414.

[51] Ibrahim, A., and Dahlan, M., 1998, Thermoplastic natural rubber blends, *Prog. Polym. Sci.*, 23 (4), 665–706.

[52] Jing, F., and Hillmyer, M.A., 2008, A bifunctional monomer derived from lactide for toughening polylactide, *J. Am. Chem. Soc.*, 130 (42), 13826–13827.

[53] Liu, H., Chen, F., Liu, B., Estep, G., and Zhang, J., 2010, Super toughened poly(lactic acid) ternary blends by simultaneous dynamic vulcanization and interfacial compatibilization, *Macromolecules*, 43 (14), 6058–6066.

[54] Anderson, K.S., Lim, S.H., and Hillmyer, M.A., 2003, Toughening of polylactide by melt blending with linear low-density polyethylene, *J. Appl. Polym. Sci.*, 89 (14), 3757–3768.

[55] Rasal, R.M., and Hirt, D.E., 2009, Toughness decrease of PLA-PHBHHx blend films upon surface-confined photopolymerization, *J. Biomed. Mater. Res., Part A*, 88 (4), 1079–1086.

[56] Ishida, S., Nagasaki, R., Chino, K., Dong, T., and Inoue, Y., 2009, Toughening of poly(L-lactide) by melt blending with rubbers, *J. Appl. Polym. Sci.*, 113 (1), 558–566.

[57] Okamoto, H., Nakano, M., and Usuki, A., 2006, "Toughening of polylactide by melt blending with natural rubber(2)-effect of PLA crystallization" in *Polymer Preprints, Japan*, Vol. 55, Society of Polymer Science, Japan, 2256.

[58] Su, S.I., Jin, L.Q., Gu, Y.A., and Yang, B., 2008, Toughening PLA with E-MA-GMA, *Polym. Mater. Sci. Eng.*, 24 (4), 53–57.

[59] Schreck, K.M., and Hillmyer, M.A., 2007, Block copolymers and melt blends of polylactide with Nodax™ microbial polyesters: Preparation and mechanical properties, *J. Biotechnol.*, 132 (3), 287–295.

[60] Balakrishnan, H., Hassan, A., Wahit, M.U., Yussuf, A.A., and Abdul Razak, S.B., 2010, Novel toughened polylactic acid nanocomposite: Mechanical, thermal and morphological properties, *Mater. Des.*, 31 (7), 3289–3298.

[61] Balakrishnan, H., Hassan, A., and Wahit, M.U., 2010, Mechanical, thermal, and morphological properties of polylactic acid/linear low density polyethylene blends, *J. Elastomers Plast.*, 42 (3), 223–239.

[62] Balakrishnan, H., Hassan, A., Imran, M., and Wahit, M.U., 2012, Toughening of polylactic acid nanocomposites: A short review, *Polym.-Plast. Technol. Eng.*, 51 (2), 175–192.

[63] Jiang, L., Wolcott, M.P., and Zhang, J., 2005, Study of biodegradable polylactide/poly(butylene adipate-*co*-terephthalate) blends, *Biomacromolecules*, 7 (1), 199–207.

[64] Li, Y., and Shimizu, H., 2009, Improvement in toughness of poly(L-lactide) (PLLA) through reactive blending with acrylonitrile-butadiene-styrene copolymer (ABS): Morphology and properties, *Eur. Polym. J.*, 45 (3), 738–746.

[65] McDonald, P.F., Geever, L.M., Lyons, J.G., and Higginbotham, C.L., 2010, Physical and mechanical properties of blends based on poly (DL-lactide), poly (L-lactide-glycolide) and poly (ϵ-caprolactone), *Polym.-Plast. Technol. Eng.*, 49 (7), 678–687.

[66] Odent, J., Raquez, J.M., Duquesne, E., and Dubois, P., 2012, Random aliphatic copolyesters as new biodegradable impact modifiers for polylactide materials, *Eur. Polym. J.*, 48 (2), 331–340.

[67] Theryo, G., Jing, F., Pitet, L.M., and Hillmyer, M.A., 2010, Tough polylactide graft copolymers, *Macromolecules*, 43 (18), 7394–7397.

[68] Hashima, K., Nishitsuji, S., and Inoue, T., 2010, Structure-properties of super-tough PLA alloy with excellent heat resistance, *Polymer*, 51 (17), 3934–3939.

[69] Ma, P., Hristova-Bogaerds, D.G., Goossens, J.G.P., Spoelstra, A.B., Zhang, Y., and Lemstra, P.J., 2012, Toughening of poly(lactic acid) by ethylene-*co*-vinyl acetate copolymer with different vinyl acetate contents, *Eur. Polym. J.*, 48 (1), 146–154.

[70] Anderson, K.S., Schreck, K.M., and Hillmyer, M.A., 2008, Toughening polylactide, *Polym. Rev.*, 48 (1), 85–108.

[71] Liu, H., and Zhang, J., 2011, Research progress in toughening modification of poly(lactic acid), *J. Polym. Sci., Part B: Polym. Phys.*, 49 (15), 1051–1083.

[72] Xu, K., Yan, C., Du, C., Xu, Y., Li, B., and Liu, L., 2023, Preparation and mechanism of toughened and flame-retardant bio-based polylactic acid composites, *Polymers*, 15 (2), 300.

[73] Trivedi, A.K., Gupta, M., and Singh, H., 2023, PLA based biocomposites for sustainable products: A review, *Adv. Ind. Eng. Polym. Res.*, In Press, Corrected Proof.

[74] Ramezani Dana, H., and Ebrahimi, F., 2023, Synthesis, properties, and applications of polylactic acid-based polymers, *Polym. Eng. Sci.*, 63 (1), 22–43.

[75] Li, X., Lin, Y., Liu, M., Meng, L., and Li, C., 2023, A review of research and application of polylactic acid composites, *J. Appl. Polym. Sci.*, 140 (7), e53477.

[76] Bikiaris, N.D., Koumentakou, I., Samiotaki, C., Meimaroglou, D., Varytimidou, D., Karatza, A., Kalantzis, Z., Roussou, M., Bikiaris, R.D., and Papageorgiou, G.Z., 2023, Recent advances in the investigation of poly(lactic acid) (PLA) nanocomposites: Incorporation of various nanofillers and their properties and applications, *Polymers*, 15 (5), 1196.

[77] Aliotta, L., Gigante, V., Geerinck, R., Coltelli, M.B., and Lazzeri, A., 2023, Micromechanical analysis and fracture mechanics of poly(lactic acid) (PLA)/polycaprolactone (PCL) binary blends, *Polym. Test.*, 121, 107984.

[78] Baker, C.S.L., Gelling, I.R., and Newell, R., 1985, Epoxidized natural rubber, *Rubber Chem. Technol.*, 58 (1), 67–85.

[79] Carreau, P.J., Bousmina, M., and Ajji, A., 1993, "Rheological Properties of Blends: Facts and Challenges" in *Progress in Pacific Polymer Science 3*, Springer, Berlin Heidelberg.

[80] Aubin, M., and Prud'Homme, R.E., 1988, T_g-Composition analysis of miscible polymer blends, *Polym. Eng. Sci.*, 28 (21), 1355–1361.

[81] Campbell, J.A., Goodwin, A.A., Mercer, F.W., and Reddy, V., 1997, Studies on a miscible polyimide blend, *High Perform. Polym.*, 9 (3), 263–279.

[82] Zhang, W., Chen, L., and Zhang, Y., 2009, Surprising shape-memory effect of polylactide resulted from toughening by polyamide elastomer, *Polymer*, 50 (5), 1311–1315.

[83] Suksut, B., and Deeprasertkul, C., 2011, Effect of nucleating agents on physical properties of poly(lactic acid) and its blend with natural rubber, *J. Polym. Environ.*, 19 (1), 288–296.

[84] Bitinis, N., Verdejo, R., Cassagnau, P., and Lopez-Manchado, M.A., 2011, Structure and properties of polylactide/natural rubber blends, *Mater. Chem. Phys.*, 129 (3), 823–831.

[85] Jaratrotkamjorn, R., Khaokong, C., and Tanrattanakul, V., 2011, Toughness enhancement of poly(lactic acid) by melt blending with natural rubber, *J. Appl. Polym. Sci.*, 124 (6), 5027–5036.

[86] Kowalczyk, M., and Piorkowska, E., 2012, Mechanisms of plastic deformation in biodegradable polylactide/poly(1,4-*cis*-isoprene) blends, *J. Appl. Polym. Sci.*, 124 (6), 4579–4589.

[87] Petchwattana, N., Covavisaruch, S., and Euapanthasate, N., 2012, Utilization of ultrafine acrylate rubber particles as a toughening agent for poly(lactic acid), *Mater. Sci. Eng., A*, 532, 64–70.

[88] Liu, H., Guo, L., Guo, X., and Zhang, J., 2012, Effects of reactive blending temperature on impact toughness of poly(lactic acid) ternary blends, *Polymer*, 53 (2), 272–276.

[89] Bijarimi, M., Ahmad, S., and Rasid, R., 2014, Melt blends of poly (lactic acid)/natural rubber and liquid epoxidised natural rubber, *J. Rubber Res.*, 17 (2), 57–68.

[90] Argon, A.S., and Cohen, R.E., 2003, Toughenability of polymers, *Polymer*, 44 (19), 6013–6032.

[91] Borggreve, R.J.M., Gaymans, R.J., and Eichenwald,

H.M., 1989, Impact behaviour of nylon-rubber blends: 6. Influence of structure on voiding processes; toughening mechanism, *Polymer*, 30 (1), 78–83.

[92] Noda, I., Satkowski, M.M., Dowrey, A.E., and Marcott, C., 2004, Polymer alloys of Nodax copolymers and poly(lactic acid), *Macromol. Biosci.*, 4 (3), 269–275.

[93] Todo, M., Park, S.D., Takayama, T., and Arakawa, K., 2007, Fracture micromechanisms of bioabsorbable PLLA/PCL polymer blends, *Eng. Fract. Mech.*, 74 (12), 1872–1883.

[94] Candau, N., Albiter, N.L., Coll, P.R., and Maspoch, M.L., 2022, Dynamically vulcanized polylactic acid/natural rubber/waste rubber blends: Effect of the crosslinking agent on the morphology and tensile properties, *J. Appl. Polym. Sci.*, 139 (41), e53001.

[95] Chanthot, P., Kerddonfag, N., and Pattamaprom, C., 2022, The influence of peroxide on bubble stability and rheological properties of biobased poly(lactic acid)/natural rubber blown films, *Chin. J. Polym. Sci.*, 40 (2), 197–207.

[96] Fang, H., Zhang, L., Chen, A., and Wu, F., 2022, Improvement of mechanical property for PLA/TPU blend by adding PLA-TPU copolymers prepared via in situ ring-opening polymerization, *Polymers*, 14 (8), 1530.

[97] Terzopoulou, Z., Zamboulis, A., Papadopoulos, L., Grigora, M.E., Tsongas, K., Tzetzis, D., Bikiaris, D.N., and Papageorgiou, G.Z., 2022, Blending PLA with polyesters based on 2,5-furan dicarboxylic acid: Evaluation of physicochemical and nanomechanical properties, *Polymers*, 14 (21), 4725.

[98] Wongwat, S., Yoksan, R., and Hedenqvist, M.S., 2022, Bio-based thermoplastic natural rubber based on poly(lactic acid)/thermoplastic starch/calcium carbonate nanocomposites, *Int. J. Biol. Macromol.*, 208, 973–982.

[99] Zhang, X., Lu, X., Huang, D., Ding, Y., Li, J., Dai, Z., Sun, L., Li, J., Wei, X., Wei, J., Li, Y., and Zhang, K., 2022, Ultra-tough polylactide/bromobutyl rubber-based ionomer blends *via* reactive blending strategy, *Front. Chem.*, 10, 923174.

[100] Fekete, I., Ronkay, F., and Lendvai, L., 2021, Highly toughened blends of poly(lactic acid) (PLA) and natural rubber (NR) for FDM-based 3D printing applications: The effect of composition and infill pattern, *Polym. Test.*, 99, 107205.

[101] Musa, L., Krishna Kumar, N., Abd Rahim, S.Z., Mohamad Rasidi, M.S., Watson Rennie, A.E., Rahman, R., Yousefi Kanani, A., and Azmi, A.A., 2022, A review on the potential of polylactic acid based thermoplastic elastomer as filament material for fused deposition modelling, *J. Mater. Res. Technol.*, 20, 2841–2858.

[102] Nicholson, J.W., 2006, *The Chemistry of Polymers*, 3rd Ed., The Royal Society of Chemistry, Cambridge, UK.

[103] Zhang, J.F., and Sun, X., 2005, "Poly(lactic acid)-based bioplastics" in *Biodegradable Polymers for Industrial Applications*, Ed. Smith, R., Woodhead Publishing, Boca Raton, US, 251–288.

[104] Jacobsen, S., and Fritz, H.G., 1999, Plasticizing polylactide - the effect of different plasticizers on the mechanical properties, *Polym. Eng. Sci.*, 39 (7), 1303–1310.

[105] Martin, O., and Avérous, L., 2001, Poly(lactic acid): Plasticization and properties of biodegradable multiphase systems, *Polymer*, 42 (14), 6209–6219.

[106] Labrecque, L.V., Kumar, R.A., Davé, V., Gross, R.A., and McCarthy, S.P., 1997, Citrate esters as plasticizers for poly(lactic acid), *J. Appl. Polym. Sci.*, 66 (8), 1507–1513.

[107] Ljungberg, N., and Wesslén, B., 2002, The effects of plasticizers on the dynamic mechanical and thermal properties of poly(lactic acid), *J. Appl. Polym. Sci.*, 86 (5), 1227–1234.

[108] Baiardo, M., Frisoni, G., Scandola, M., Rimelen, M., Lips, D., Ruffieux, K., and Wintermantel, E., 2003, Thermal and mechanical properties of plasticized poly(L-lactic acid), *J. Appl. Polym. Sci.*, 90 (7), 1731–1738.

[109] Pillin, I., Montrelay, N., and Grohens, Y., 2006, Thermo-mechanical characterization of plasticized PLA: Is the miscibility the only significant factor?, *Polymer*, 47 (13), 4676–4682.

[110] Murariu, M., Da Silva Ferreira, A., Pluta, M., Bonnaud, L., Alexandre, M., and Dubois, P., 2008,

Polylactide (PLA)–$CaSO_4$ composites toughened with low molecular weight and polymeric ester-like plasticizers and related performances, *Eur. Polym. J.*, 44 (11), 3842–3852.

[111] Oksman, K., Skrifvars, M., and Selin, J.F., 2003, Natural fibres as reinforcement in polylactic acid (PLA) composites, *Compos. Sci. Technol.*, 63 (9), 1317–1324.

[112] Oksman, K., Mathew, A.P., Bondeson, D., and Kvien, I., 2006, Manufacturing process of cellulose whiskers/polylactic acid nanocomposites, *Compos. Sci. Technol.*, 66 (15), 2776–2784.

[113] Hu, Y., Hu, Y.S., Topolkaraev, V., Hiltner, A., and Baer, E., 2003, Crystallization and phase separation in blends of high stereoregular poly(lactide) with poly(ethylene glycol), *Polymer*, 44 (19), 5681–5689.

[114] Martino, V.P., Ruseckaite, R.A., and Jiménez, A., 2009, Ageing of poly(lactic acid) films plasticized with commercial polyadipates, *Polym. Int.*, 58 (4), 437–444.

[115] Okamoto, K., Ichikawa, T., Yokohara, T., and Yamaguchi, M., 2009, Miscibility, mechanical and thermal properties of poly(lactic acid)/polyester-diol blends, *Eur. Polym. J.*, 45 (8), 2304–2312.

[116] Lemmouchi, Y., Murariu, M., Dos Santos, A.M., Amass, A.J., Schacht, E., and Dubois, P., 2009, Plasticization of poly(lactide) with blends of tributyl citrate and low molecular weight poly(D,L-lactide)-*b*-poly(ethylene glycol) copolymers, *Eur. Polym. J.*, 45 (10), 2839–2848.

[117] Hughes, J., Thomas, R., Byun, Y., and Whiteside, S., 2012, Improved flexibility of thermally stable poly-lactic acid (PLA), *Carbohydr. Polym.*, 88 (1), 165–172.

[118] Hassouna, F., Raquez, J.M., Addiego, F., Dubois, P., Toniazzo, V., and Ruch, D., 2011, New approach on the development of plasticized polylactide (PLA): Grafting of poly(ethylene glycol) (PEG) via reactive extrusion, *Eur. Polym. J.*, 47 (11), 2134–2144.

[119] Kim, D.Y., Lee, J.B., Lee, D.Y., and Seo, K.H., 2020, Plasticization effect of poly(lactic acid) in the poly(butylene adipate–*co*–terephthalate) blown film for tear resistance improvement, *Polymers*, 12 (9), 1904.

[120] Awale, R.J., Ali, F.B., Azmi, A.S., Puad, N.I.M., Anuar, H., and Hassan, A., 2018, Enhanced flexibility of biodegradable polylactic acid/starch blends using epoxidized palm oil as plasticizer, *Polymers*, 10 (9), 977.

[121] Gzyra-Jagieła, K., Sulak, K., Draczyński, Z., Podzimek, S., Gałecki, S., Jagodzińska, S., Borkowski, D., 2021, Modification of poly(lactic acid) by the plasticization for application in the packaging industry, *Polymers,* 13 (21),3651

[122] Tábi, T., Ageyeva, T., and Kovács, J.G., 2022, The influence of nucleating agents, plasticizers, and molding conditions on the properties of injection molded PLA products, *Mater. Today Commun.*, 32, 103936.

Review:

Magnetic Solid Phase Extraction for Determination of Dyes in Food and Water Samples

Ruba Fahmi Abbas*, Mohammed Jasim Mohammed Hassan, and Ahmed Mahdi Rheima

Department of Chemistry, College of Science, Mustansiriyah University, Baghdad 14022, Iraq

* ***Corresponding author:***

email: rubaf1983@uomustansiriyah.edu.iq

Received: January 3, 2023
Accepted: May 13, 2023

DOI: 10.22146/ijc.80885

Abstract: *Recently, magnetic solid-phase extraction (MSPE) is an important technology due to its use in analytical chemistry, biotechnology, and medicinal fields. MSPE shows rapid isolation of target analyte from large volume samples, the huge surface area of magnetic nanoparticles (MNPs), and simplicity in application due to using an external magnetic field instead of using packing column, centrifuge, and filter papers. The aim of this review is to evaluate the extraction and determination of dyes in food and water samples by using the MSPE technique.*

Keywords: *adsorption; desorption; magnetic solid phase extraction; separation*

■ INTRODUCTION

There are more than a thousand different types of dye that can be commercially and frequently used in the textile, food, photography, cosmetics, plastics, and pharmaceutical industries. Dyes are at the forefront of the pollutant due to being hard to remove from clean water [1]. Dyes have a complex chemical structure that makes them more resistant to fading on exposure to water, light, and chemical materials. Because of that, many dyes are hard to remove or decolorize from wastewater; so, dyes are an effective risk to water, soil, fauna, plant, cattle, and human. For example, the highest toxicity was found in the diazo direct and basic dyes [2].

Due to mentioned reasons, dyes should be determined in different environmental samples by using suitable extraction methods, such as the liquid-liquid extraction (LLE) from aqueous solutions followed by UV–visible spectrophotometer for methylene blue dye [3], liquid-liquid microextraction (LLME) coupled with HPLC-DAD for Sudan dyes from tomato chili sauces [4], dispersive liquid-liquid microextraction (DLLME) based on the salting-out phenomenon followed by HPLC for Sudan dyes in turmeric powder, chili sauce, and water samples [5], solid-phase extraction (SPE) coupled with LC-ESI-MS/MS of disperse dyes in water samples [6], solid-phase microextraction (SPME) coupled with UPLC-MS for Sudan dyes in tomato sauce and hot-pot samples [7], microextraction by packed sorbent (MEPS) coupled with gas chromatography-mass spectrometry (GC–MS) of azo dyes in textiles [8], matrix solid-phase dispersion (MSPD) followed by HPLC–DAD of Sudan dyes in condiments and sauces [9], and stir-bar sorptive extraction (SBSE) coupled with HPLC of Sudan dyes in fruit juice and lake water samples [10]. Extraction methods require a long time, filter papers, centrifuge, slow packing of sorbent into the column, and a large volume of sample or solvent. To overcome these limitations, magnetic solid-phase extraction (MSPE) offers a quick extraction method that has ease of preparation with large-scale production, ease of operation by applying an external magnetic, and ease of surface modification due to many hydroxyl (–OH) groups on the surface of iron oxide. Moreover, it is considered a green chemistry method because of the ease of recoverability of magnetic particles that can be reused after rinsing a few times. It requires a small volume of sample and solvent without using filter papers and a centrifuge [11]. The aim of this review is to present the MSPE technique used for the extraction of dyes in food and water samples.

■ CLASSIFICATION OF DYES

There are many structural classifications of dyes, such as disperse, base, acidic, anthraquinone-based, diazo, azo, and metal complex dyes. Dyes are classified

in Table 1 according to their solubility in water, chemical constitution, and application in the industry [12-18] while the chemical structure of some dyes examples are listed in Table 2.

Table 1. Classification of dyes

Type of dye	Solubility	Functional group or constituent	Application
Acid dyes (anionic dyes)	Soluble in water	Sulphonic, carboxylic acid, azo, anthraquinones, triarylmethane, iminoacetone, nitro, nitrous, and/or quinoline	Nylon, silk, modified acrylic, wool, paper, food, and cosmetics
Direct dyes (anionic dyes)	Soluble in water when in the presence of salts and electrolytes	Azo compounds with thiazoles, phthalocyanines, and oxazines	Cotton and regenerated cellulose, paper, leather, and nylon
Reactive dyes (anionic dyes)	Soluble in water with the sodium salt of sulphonic acid groups	Azo, anthraquinone, and phthalocyanine	Fiber (cotton, wool, or nylon)
Basic dyes (cationic dyes)	Soluble in water as chloride, sulfate, or nitrate salts	Azo, anthraquinone, triarylmethane, methane, thiazine, oxazine, acridine, and quinoline	Modified acrylic, modified nylon, modified polyesters, and papers, and some of them have biological activity and are used in medicine as antiseptics
Dispersive dyes (non-ionic dye)	Insoluble in water	Azo dyes	Dyeing of nylon, polyamide, and polyester
Vat dyes (non-ionic dye)	Insoluble in water	Anthraquinone and indigo	Dyeing cellulosic fibers, such as leuco-soluble salts, after reduction in an alkaline bath (sodium hydrosulfite)
Sulfurous dyes	Insoluble in water but can be made soluble in water by treating them with reducing agents	Contain sulfur linkage within their molecules	Applied to cotton, linen, cotton, and jute after alkaline reduction bath, with sodium sulfite as reducing agent
Fluorescent dyes (group of the xanthenes)	Soluble in water	Fluorescent carbonyl dyes (coumarins, naphthalimides, perylenes, benzanthrone derivatives, benzoxanthones, and benzothioxanthones), rhodamines, and methine fluorescent dyes	Fluorescent dyes for textiles, daylight fluorescent pigments, dyes for lasers, solar collectors, electroluminescence, analytical, biological, and medical applications
Dye precursors	Insoluble in water	Acid Yellow 23 (pyrazole), Acid Orange 7 (monoazo), Acid Red 92 (xanthene), Acid Violet 43 (anthraquinone), 4-hydroxypropylamino-3-nitrophenol (nitro aniline), HC Yellow No. 2 (nitro aniline), *p*-phenylenediamine, *p*-aminophenol, 4-amino-2-hydroxytoluene (aromatic substituted)	Commercial hair dying systems can be divided into two main categories, oxidative or non-oxidative

Table 2. Examples of dyes

Type of dye	Functional group or constituent	Molecular formula	Structure	Ref.
Acid dyes	Anthraquinone	$C_{32}H_{28}N_2Na_2O_8S_2$	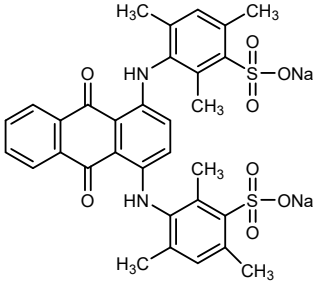	[19]
Direct dyes	Direct red 243	$C_{38}H_{28}N_{10}Na_4O_{17}S_4$	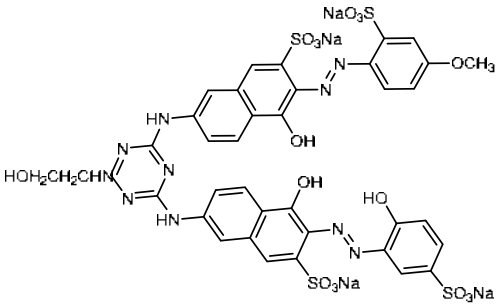	[20]
Reactive dyes	Reactive blue 109	$C_{25}H_{12}Cl_2N_9Na_5O_{16}S_5$	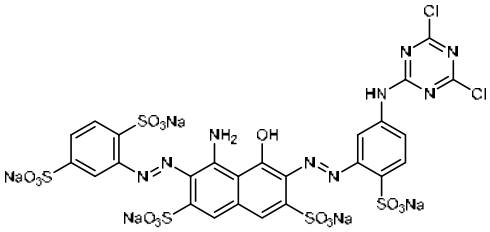	[21]
Basic dyes	Methylene blue (Basic Blue 9)	$C_{16}H_{18}ClN_3S$	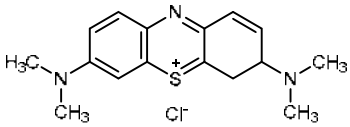	[22]
Dispersive dyes	Dispersive red 60	$C_{20}H_{13}NO_4$	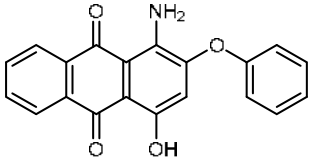	[23]
Vat dyes	Vat blue 5	$C_{16}H_6Br_4N_2O_2$	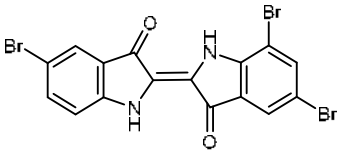	[24]
Sulfurous dyes	Sulphur blue 7	$C_{13}H_{14}N_2O$	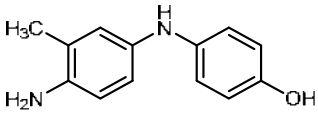	[25]
Fluorescent dyes	Disperse yellow 186	$C_{21}H_{19}N_3O$	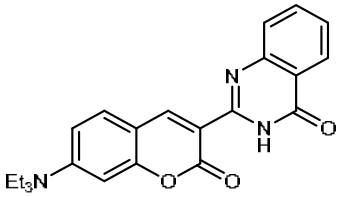	[26]

Type of dye	Functional group or constituent	Molecular formula	Structure	Ref.
Dye precursors	Acid yellow 23	$C_{16}H_9N_4Na_3O_9S_2$	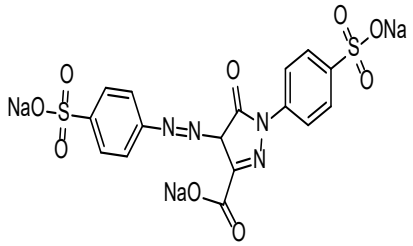	[27]

■ CLASSIFICATION OF MAGNETIC MATERIALS

There are four types of classification of magnetic materials depending on how they react with the magnetic field as described in Fig. 1 [28-30].

Ferromagnetic or superparamagnetic materials have been used widely in the MSPE technique as sorbent magnetic nanoparticle forms due to their high magnetic moments, ease of preparation, biocompatibility, and small size particles. Chemical, biological, and physical methods have been used for synthesizing iron oxides like magnetite (Fe_2O_3), spinel ferrites (MFe_2O_4), and maghemite (γ-Fe_3O_4).

■ HISTORY AND PRINCIPLES OF MSPE

The first authors to publish on MSPE were Safarik et al. [31]. It depends on adding a magnetic sorbent into an aqueous sample to adsorb the target analyte. Then, the sorbent target analyte is separated by using an external magnetic field. After that, the addition of solvent to the analyte with used external magnetic again to collect the liquid analyte, which is determined by different analytical techniques [32]. The mechanism separation of MSPE is based on the interaction between the surface functional groups of the sorbent with the analyte. The types of interactions are dispersion, ionic, hydrogen

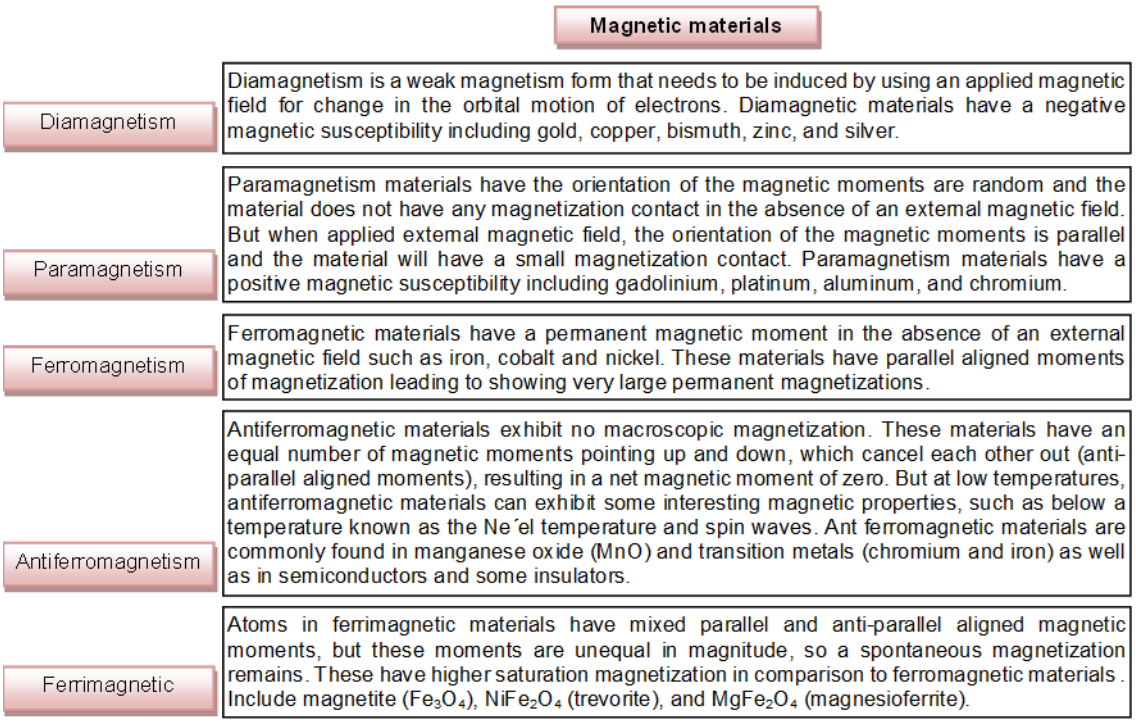

Fig 1. Classification of magnetic materials

bonding, dipole-induced dipole, and dipole-dipole forces. The dipole-dipole interactions, hydrogen bonding, and π-π interactions are the base of the analyte retention mechanism, but chemical bonding interactions are not used in the separation and retention of analyte because of their irreversibility. Other properties affect the interaction of the sorbent with the analyte, such as solubility, concentration, and polarity of the analyte with the choice of the right sorbent and solvent [33].

MSPE principles include three steps: first, the analyte was captured or adsorbed by the addition of MNPs into the sample solution (MNPs are dispersing in the sample solution). Then, the separation step uses the external magnet to separate the target analyte from the solution. The last is the desorption step, which is analyte desorption from the surface of MNPs using an appropriate solvent. Acidic solutions are used as a good solvent for the inorganic analyte and an organic solvent is used for the organic analyte. Then, HPLC coupled to MS or UV-Vis is often preferred for the separation and determination of the analyte (Fig. 2) [34-35].

■ PREPARATION OF MAGNETIC NANOPARTICLES

The magnetite of Fe_3O_4 and γ-Fe_2O_3 are widely used in the preparation of the magnetic core for the MSPE method [36]. Many methods have been used for the preparation of Fe_3O_4, such as thermal decomposition, microemulsion, high-energy ball mill, hydrothermal synthesis, sonochemical synthesis, and co-precipitation. The advantage of a thermal decomposition method to obtaining a narrow particle size distribution of MNPs, size control, and a high degree of crystalline. This method is based on the decomposition of $Fe(acac)_3$ with oleylamine, an 1,2-alkanediol and oleic acid in a high boiling point ether [37]. Microemulsion method based on microemulsion route above room temperature (65 °C). The microemulsion solution consists of forming the ternary system cyclohexane (organic phase)/Brij-97 (a non-ionic surfactant)/aqueous solution of $FeSO_4{\cdot}7H_2O/FeCl_3{\cdot}6H_2O$ in the different mole ratio. MNPs obtain from this method are higher in saturation magnetization and smaller in size [38]. A high-energy ball mill is a simple and low-cost technique. Ball milling in a hardened steel vial was used for prepared the sample (Fe^{2+}/Fe^{3+}), the molar ratio of Fe^{2+}/Fe^{3+} was 20:1, and the sample was milled to 96 h with a rotation speed of 200 rpm to obtain a 12 nm size of the magnetite particles [39]. In the hydrothermal synthesis method, the average diameters were 25 or 14 nm for α-Fe_2O_3 or Fe_3O_4, respectively. Hydrothermal reaction $FeSO_4$ solution was heated at 473 K and using *n*-decanoic acid ($CH_3(CH_2)_9COOH$) or *n*-decylamine ($CH_3(CH_2)_9NH_2$) as a surface modifier. At a higher temperature over room

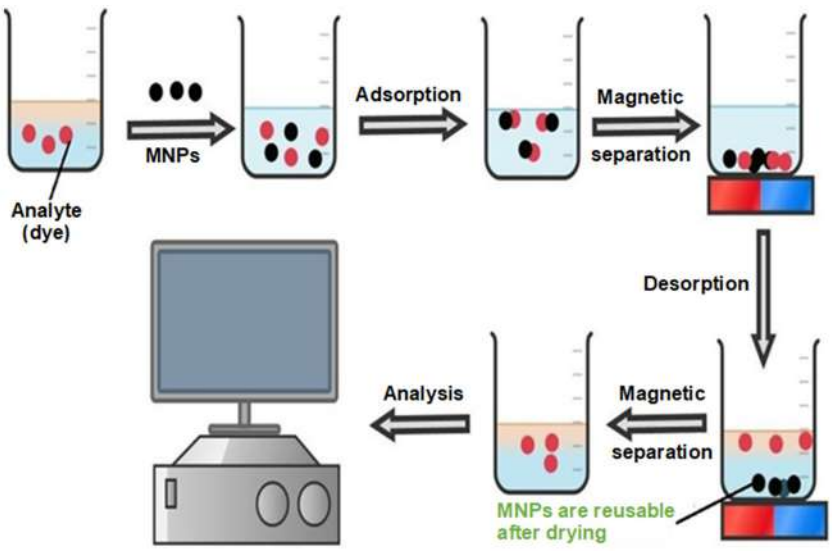

Fig 2. Steps of dye determination with MSPE

temperature, the solubility of surface modifier increased in water, but the dielectric constant of water decreased and reacted with the surface of the nanoparticles. This method is environmentally economical and without the use of organic solvents [40]. Sonochemical synthesis of $Fe(acac)_3$ in water under an argon atmosphere with tetraglyme as a solvent. Water amount had allowed control of the surface area and size of MNPs to obtain surface-modified ultra-small (1–2 nm) [41]. Co-precipitation is the simplest method used to prepare magnetite MNPs from aqueous $FeCl_2{\cdot}4H_2O/FeCl_3{\cdot}6H_2O$ solutions with a concentration ratio of 2:1 by the addition of ammonia in a vacuum or nitrogen at 80 °C or less. This method was used to obtain magnetite MNPs with diameters of 2–4 nm [42]. The morphology and microstructure of the MNPs were characterized by IR, XRD, TEM, and SEM.

■ MODIFICATION OF MAGNETIC NANOPARTICLES

Surface modification of MNP was used to ensure sensitivity and selectivity for the target analyte and to avoid weakened magnetism due to agglomerate and oxidation. Surface modification with Fe_3O_4 MNPs is commonly used to functionalize the surface of the particles and improve their selectivity for specific analytes. Fe_3O_4 MNPs have similar properties to Fe_2O_3 MNPs or FeO MNPs, but they are typically more stable, high magnetization, high surface area, and large surface-to-volume ratio. Fe_3O_4 MNPs is that they have a higher surface area than FeO MNPs, which can improve their binding capacity for target analytes [43-44].

Fe_3O_4 has been intensively investigated for the modification of MNPs because of its superparamagnetic, non-toxic, low Curie temperature, high coactivity, and biocompatible. Physical modification methods include plasma radiation, ultraviolet, adsorption, and deposition of the surfaces. In the chemical modification, the surface of MNPs was changed by chemical reactions. The external layer of MNPs was modified by three main materials: inorganic substances, organic substances, and metal-organic frameworks (MOFs) (Fig. 3).

■ MODIFICATION OF INORGANIC SUBSTANCES

One of the well-coated is SiO_2, which is prepared by the sol-gel method. This method's advantage is to obtain a spherical particle's shape, a size-controlled and it is considered a simple method for synthesizing MNPs [45]. Metallic oxides such as ZrO_2, $CoFe_2O_4$, CoO, NiO, TiO_2, and Al_2O_3 are usually used to modify MNPs. Coating using metallic oxide provides several advantages, such as the prevention of agglomeration and increased stability biocompatibility, and hydrophilicity of MNPs. For example, $Fe_3O_4@Al_2O_3$ core-shell NPs were more air-stable than the naked Fe_3O_4 NPs, Fe_3O_4@ZnO core-shell NPs were antioxidation and $Fe_3O_4@CoFe_2O_4$ have more magnetic properties than Fe_3O_4 NPs [46]. Composite materials were used in MSPE methods, such as $Fe_3O_4@ZrO_2@$*N*-cetylpyridinium and

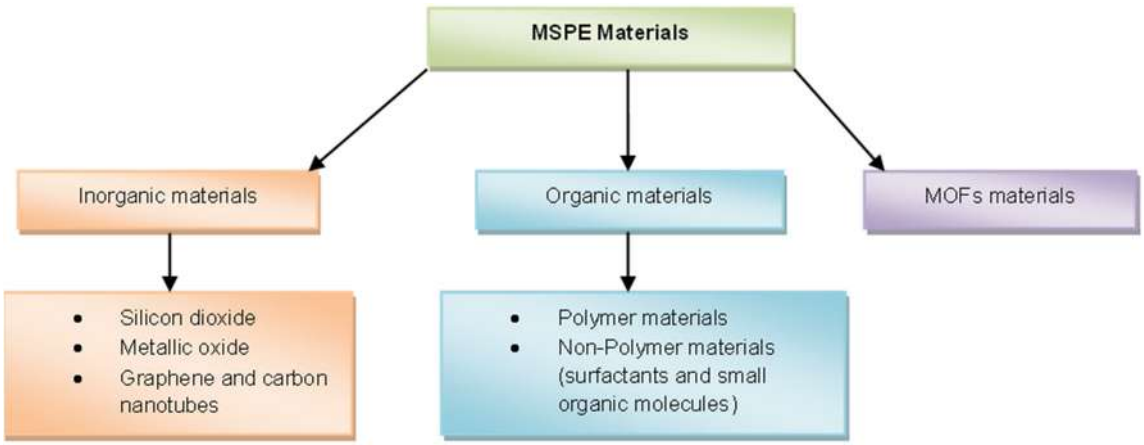

Fig 3. Materials used for modification of the MSPE method

alumina-coated Fe_3O_4 MNP modified by dithizone and sodium dodecyl sulfate (SDS) in acidic media [47-48]. Ring-structured compounds and carbon-based have been adsorbed by graphene and carbon nanotubes from different samples. For example, Fe_3O_4@SiO_2@G@PIL was magnetite graphene modified with ionic liquids and through electrostatic interactions; graphene oxide was modified with the amino-functional silica-coated Fe_3O_4spheres [49].

■ MODIFICATION OF ORGANIC SUBSTANCES

There are many advantages of polymer modification. It can effectively prevent MNPs oxidation, reduce agglomeration, and dipole-dipole interaction to become weakened between MNPs. 3D network polymer types with stability and adsorption capabilities are molecularly imprinted polymers (MIPs). Covalent organic frameworks (COFs) modification allows through van der Waals forces, hydrogen bonding, and the size-exclusion effect to adsorb target analyte [50]. Non-polymer materials include two types; the first type is surfactants, which include octadecyl trimethyl ammonium chloride (OTAB), cetyltrimethylammonium bromide (CTAB), and SDS, which have a good extraction ability, high chemical stability, and large specific surface area. The second type of non-polymer material is small organic molecules, including oleic acid and fatty acid, which improve the stability and dispersion of MNPs [51].

■ MODIFICATION OF METAL-ORGANIC FRAMEWORKS (MOFs) SUBSTANCES

Metal-organic frameworks (MOFs) are crystalline inorganic-organic hybrid materials that give rise to new materials which have an internal surface area, porous, tunable pore size, and hollow structure. Magnetic MOFs materials were used in MSPE, such as MOF-5 ($Zn_4O(BDC)_3$) (BDC=1,4-benzenedicarboxylate) with a cubic 3D porous structure, ZIF-8([$Zn(MeIM)_2$]) and ZIF-67 ([$Co(MeIM)_2$]) (MeIM=2-methylimidazole). The advantages of MOFs are large pore volume, mechanical and chemical stability, superparamagnetism, and working at a high temperature, making MOFs more useful for the MSPE [52-54]. Overall, the choice of inorganic, organic, or MOF modification will depend on the specific application and the properties required for the MNPs. Organic modifications are often preferred for biological applications, where biocompatibility and dispersibility in solution are critical, while inorganic modifications are often preferred for chemical and environmental applications, where chemical stability and magnetic properties are more important. MOF-coating MNPs can provide higher stability and selectivity, and they can be used in a variety of applications, including water treatment, drug delivery, catalysis, lithium-ion batteries, and luminescence [55].

■ MAGNETIC TEXTILE SOLID-PHASE EXTRACTION (MTSPE)

MTSPE is using magnetically modified textile materials as a new type of pre-concentration method. It Includes a piece of fabric textile 1×1 cm^2 with an office stapler, which is rapidly and easily separated magnetically by using an external magnetic field [56]. MTSPE is considered a green chemistry method due to its advantage of simplicity, readily, and low cost. Furthermore, this method is easy separation and recovery of the analytes, reducing the need for additional purification steps. Many materials were used for modified the textile fibers to provide a high surface area and a porous structure as a 1% chitosan solution was applied to determine azorubine, indigo carmine, tartrazine, and blue fountain ink dyes [57-58]. Polysaccharide κ-carrageenan combination with agarose was applied to determine Nile blue A, safranin O, and methylene blue [59].

■ APPLICATIONS AND OPTIMIZATION OF THE MSPE

MNPs are widely used in analytical chemistry, medicine, bioanalytical, environmental pollutants, and food samples. MSPE has been used to determine estrogens in milk [60], phthalic acid esters in carbonated soft drink [61], tetracyclines in milk [62], organophosphorus pesticides in water [63], phthalate monoesters in urine [64], Co(II) and Hg(II) in water and food [65], polycyclic aromatic hydrocarbons in grilled meat [66], lignans in sesame oil [67], a free fatty acid in edible oils [68], and

non-steroidal anti-inflammatory drugs (naproxen, ketoprofen, and diclofenac) in biological and water and samples [69]. However, the large surface area and high magnetic responsiveness of magnetic nanoparticles make them excellent sorbents for a variety of applications. To achieve the best extraction efficiency, various conditions, such as the sorbent categories, the pH, sorbent amount, extraction time, desorption solvent, the volume of desorption solvent, desorption temperature, and desorption time, were optimized (Table 3).

Table 3. Optimization factors of the MSPE procedure

Analyte	Magnetic material	Sample pH	Sorbent amount	Extraction time	Desorption solvent	Vol. of desorption solvent	Desorption temperature	Desorption time	Ref.
Basic violet 7, Basic red 13 and Basic orange 21	M-S-RGO	10	5.0 mg/mL	20 min	Acetone with 5% acetic acid	-	-	-	[73]
CV, MV, MB, and MG	MNPs-POLP	10	20.0 mg	15 min	Methanol	2 mL	Room temperature	10.0 min	[82]
MR and MO	MHNTs	7.5	60.0 mg	10 min	Methanol containing 1% acetic acid	2 mL	25 °C	-	[83]
MG(Cationic)	MWCNT@Fe_3O_4	6–8	60.0 mg	-	Acetonitrile	1 mL	Room temperature	2.0 min	[84]
Sudan I, II, III and IV(azo dye)	Fe_3O_4@PANI	7	8.0 mg	15 min	Ethanol	2 mL	Room temperature	4.0 min	[85]
MG	Fe_3O_4-NH_2@HKUST-1@PDES	4	5.0 mg	108 min	-	1 mL	31.65 °C	-	[74]
Sudan I, II, III and IV	MPCDPs(C)	7	4.0 mg	20 min	Methanol	3 mL	-	-	[75]
Sudan I-IV, Para Red and Sudan Red 7B	Fe_3O_4-NH_2@MIL-101	-	3.0 mg	2 min	Ethyl acetate	2 mL	-	10.0 min	[76]
Sudan Black B, Sudan Red 7B, Para Red and Sudan I, II, III, IV	cMWCNT-γ-Fe_2O_3	8	40.0 mg	15 min	Acetonitrile	0.3 mL	-	4.0 min	[77]
Sunset yellow, allure red and tartrazine	Fe_3O_4-fullerene-activated carbon	4.0	0.01 mg	15 min	Methanol solution containing NaOH 10^{-3} M	500 µL	-	5.0 min	[87]
Triphenylmethane dyes (MG and CV)	γ-Fe_2O_3@CNM	7	1.0 mg	5 min	Methanol containing 0.2% formic acid	1 mL	Room temperature	30.0 s	[87]
Sudan I, II, III and IV	magnetic Fe_3O_4 NPs	7	0.5 g	20 min	Methanol	5 mL	Room temperature	1.0 min	[78]
MG and CV	Fe_3O_4@SiO_2-Flu	5	30.0 mg	20 min	Methanol	0.5 mL	Room temperature	2.0 min	[88]
Rhodamine B	Fe_3O_4@SiO2@IL	3	0.1 g	10 min	Ethanol	4.0 mL	30 °C	5.0 min	[79]
Sudan red	Fe@NiAl-LDHs	7	80.0 mg	60 min	Acetone	7.5 mL	-	9.0 min	[89]
Sudan dyes (I, II, III, and IV)	Fe_3O_4 MNPs/PSt	4	70.0 mg	15 min	Acetonitrile	4.0 mL	Room temperature	1.5 min	[80]

Analyte	Magnetic material	Sample pH	Sorbent amount	Extraction time	Desorption solvent	Vol. of desorption solvent	Desorption temperature	Desorption time	Ref.
Sudan dyes (I, II, III, and IV)	Magnetic argan press cake nanocellulose (MNC)	3	50.0 mg	10 min	Methanol	2.0 mL	Room temperature	5.0 min	[81]
Congo Red and Basic Red 2	ZIF-8@$CoFe_2O_4$	7	10.0 mg	15 min	Methanol and water		Room temperature	1.0 min	[90]
Rose Bengal	C-MIONPs	6	0.5 g	-	Methanol	5.0 mL	25 °C	-	[91]
Acridine orange, Amido black 10B, Bismarck brown, Congo red, Crystal violet, Malachite green, Safranin O	Magnetically modified Spent coffee grounds	-	30.0 mg	90 min	Methanol	2.0 mL	Room temperature	20.0 min	[92]
Acridine orange, CV, MG, Safranin O, Methylene blue	Magnetically modified *S. horneri* biomass	-	-	-	-	-	-	-	[93]
MG and CV	Fe_3O_4/GO magnetic nanoparticles	6	0.13 mg	15 min	Acetonitrile/acetic acid	0.2 mL	Room temperature	15.0 min	[94]

■ FOOD ANALYSIS

Azo dyes are used for coloring food products due to their low cost and high stability to the oxygen, pH, and light compared to the dyes obtained from natural sources [70]. Many countries have forbidden synthetic azo dyes using in food products because they are shown to be genotoxic, potentially neurotoxic, and carcinogenic additives [71]. For example, Tartazin dye causes genotoxicity in rodents, and allura red and brilliant blue cause allergic reactions. Tartrazine, sunset yellow, erythrosine, and allura red can be carcinogenic [72]. MSPE was successfully used for the removal, analysis, and determination of cationic dyes from different samples (food and water) (Table 4). Cui et al. [73] developed a novel adsorbent magnetic sulfonated reduced graphene oxide (M-S-RGO) based on (M-S-RGO) with HPLC–MS/MS for analysis and determination of Basic violet7, Basic red 13 and Basic orange 21 in food samples. This method was applied for a wide range of basic dyes with lower LOD 0.01–0.2 μg/L [73]. A new Fe_3O_4-NH_2@HKUST-1@PDES-MSPE (Polymeric deep eutectic solvents (PDES)) based on 3-acrylamidopropyl trimethylammonium chloride/D-sorbitol functionalized amino-magnetic (Fe_3O_4-NH_2) metal-organic framework (HKUST-1-MOF) composites) was used for the extraction and determination of MG and CV cationic dyes from fish samples, with the successful recovery of 89.43–100.65% for MG and 95.29–98.03% for CV indicating that this method was a successful application in extracting cationic dyes in fish samples [74]. Sudan dyes are class 3 carcinogens, so using these dyes in food is considered illegal. Determination Sudan dyes were developed by using magnetically modified porous β-cyclodextrin polymers (MPCDPs) coupled with HPLC. MPCDPS was a good analytical adsorbent for the separation and concentration of Sudan dyes in food and water samples [75]. Magnetic trimeric chromium octahedral metal-organic framework (Fe_3O_4-NH_2@MIL-101) combined with HPLC was used to determine Sudan I-IV, Para Red, and Sudan Red 7B in tomato sauce with a good RSD of ≤ 9.2% [76]. Sudan Black B, Sudan Red 7B, Para Red, and Sudan I, II, III, IV were extracted by using γFe_2O_3 magnetic nanoparticle functionalized with carboxylated multiwalled carbon nanotube (cMWCNT-γ-Fe_2O_3) coupled with HPLC in chili products and ketchup [77]. Fe_3O_4 MNPs were used for the extraction of Sudan dyes from chili oil, chili powder, tomato paste, and different water samples coupled with HPLC for separation and determination of

Table 4. Application of MSPE

Analyte	Type of dye	Magnetic material	Sample	Technique	Limit of detection	Recovery	Ref.
Illegal basic dyes (Basic violet 7, Basic red 13 and Basic orange 21)	Cationic	M-S-RGO	Frozen grass carp, frozen yellow croaker, and tomato sauce	HPLC-MS/MS	0.01–0.2 μg/L	70–110%	[73]
MV, MB, MG, CV, and NR from MR	Cationic	MNPs-POLP	Aqueous solution	UV-Vis HPLC	-	-	[82]
and MO	Anionic azo dye	MHNTs	Water samples		MR: 0.042 μg/L MO: 0.050 μg/L	MR:85–87% MO: 89–93%	[83]
MG and GV	Cationic	MSPE method based on MWCNT@Fe_3O_4NPs	Water samples	HPLC-FLD	MG: 0.22 ng/mL GV: 0.09 ng/mL	87.0–92.8%	[84]
Sudan I, II, III and IV	Azo dye	Fe_3O_4@PANI	Water samples	UFLC-UV	0.041–0.151 ng/mL	92.4–106.9%	[85]
MG and CV	Cationic	Fe_3O_4-NH_2@HKUST-1@PDES-MSPE	Fish samples	UV-Vis	MG: 98.19 ng/mL CV: 23.97 ng/mL	MG: 89.43–100.65% CV: 95.29–98.03%	[74]
Sudan I, II, III and IV	Azo dye	MPCDPs(C) and MPCDPs(M)	Food samples and water samples	HPLC	MPCDPs(C): 0.013–0.054 ng/mL MPCDPs(M): 0.028–0.039 ng/mL	Food samples: 85.8–102.8% Water samples: 88.3–103.2%	[75]
Sudan I-IV, Para Red and Sudan Red 7B	Azo dye	Fe_3O_4-NH_2@MIL-101	Tomato sauce	HPLC-DAD	0.5-2.5 mg/kg	72.6–92.9%	[76]
Sudan Black B, Sudan Red 7B, Para Red and Sudan I, II, III, IV	Azo dye	cMWCNT-γ-Fe_2O_3	Chilli products and ketchup	HPLC	0.13-0.84 ng/mL	-	[77]
Sunset yellow, allure red and tartrazine	Anionic azo dye	Fe_3O_4-fullerene-activated carbon	Water samples	Capillary electrophoresis	1.0-2.0 mg/L	95–106%	[86]
Triphenylmethane dyes (MG and CV)	Cationic	γ-Fe_2O_3@CNM-based MSPE	Spring water, lake water, fishpond water, seawater, and mineral wastewater	LC-MS/MS	0.004 ng/mL	MG: 73.4–101.5% CV: 83.1–102.7%	[87]
Sudan I, II, III and IV	Azo dye	Magnetic Fe_3O_4 NPs	Food samples (chili oil, chili powder and tomato paste) and water samples (tap and river water)	HPLC	0.02 μg/L	Water samples: 91.9–98.1% Food samples: 92.9–109.9 %	[78]
MG and CV	Cationic	Fe_3O_4@SiO_2-Flu	Water samples	UV-Vis	2.82–3.27 ng/L	88–96%	[88]
Rhodamine B	Cationic	Fe_3O_4@SiO_2@IL	Chili powder	HPLC	0.08 μg/L	99.0–100.9%	[79]
Sudan red	Cationic	Fe@NiAl-LDHs	Water samples	HPLC	0.002–0.005 μg/L	97.6–105.7%	[89]
Sudan dyes (I, II, III, and IV)	Azo dye	Fe_3O_4 MNPs/PSt	Red wines, juices, and mature vinegar	UFLC-UV	0.0039, 0.0063, 0.0057, and 0.017 ng/mL	76.3–96.6%	[80]
Sudan dyes (I, II, III, and IV)	Azo dye	Magnetic argan press cake nanocellulose (MNC)	Barbeque and ketchup sauces	Capillary liquid chromatography	0.05–0.07 μg/L	93.4–109.6%	[81]
Congo Red and Basic Red 2	Congo red is azo dye and Basic Red 2 is cationic	ZIF-8@$CoFe_2O_4$	Aqueous solution	UV-Vis	-	-	[90]
Rose Bengal	Xanthenes dye	C-MIONPs	Brucella Antigen solution and water samples from the Karoon River	UV-Vis	5.91×10^{-3} μg/mL	95.7–98.9%	[91]

Analyte	Type of dye	Magnetic material	Sample	Technique	Limit of detection	Recovery	Ref.
Acridine orange, Amido black 10B, Bismarck brown, Congo red, Crystal violet, Malachite green, Safranin O	Acridine orange is a fluorescent dye. Black 10B, Congo red, CV, and MG are azo dyes. Safranin O is azonium compound	Magnetically modified Spent coffee grounds	Aqueous Solution	UV-Vis	-	-	[92]
Acridine orange, CV, MG, Safranin O, Methylene blue	Acridine orange isa fluorescent dye	Magnetically modified *S. horneri* biomass	Aqueous solution	UV-Vis	-	-	[93]
MG and CV	Cationic	Fe_3O_4/GO magnetic nanoparticles	Water samples	HPLC	MG: 0.091 μg/L CV: 0.120 μg/L	91.5–116.7%	[94]

dyes, with LOD values down to 0.02 μg/L for all samples [78]. Fe_3O_4@SiO_2NPs were coated with three ionic liquids [HMIM]PF_6, [BMIM]PF_6, and [OMIM]PF_6 to prepare fluconazole-functionalized Fe_3O_4@SiO_2 nanoparticles (Fe_3O_4@SiO_2@IL) coupled with HPLC for the determination of Rhodamine B in Chili powder, RSD value was 0.51%, and this MNPs could be reused up to 10 times [79]. Nanocomposite of polystyrene-coated magnetic nanoparticles (MNPs/PSt) coupled with UFLC-UV was used for the determination of Sudan dyes in different types of drinks and RSDs were lower than 9.6% [80]. Sudan dyes in the barbeque and ketchup sauces were extracted using magnetic/non-magnetic argan press cake nanocellulose coupled with capillary liquid chromatography and SD achieved was lower than 3.46% [81].

■ WATER ANALYSIS

Synthetic dyes are used to produce plastics, rubber and textiles which cause environmental pollution (water and soil). Most dyes are toxic and cause skin irritation, dermatitis, and allergy. They are harmful to humans and aquatic biota. MSPE is a new technique that has been used in the extraction of dyes from wastewater, tap water, and river water samples. MSPE was used for the extraction of dyes from water samples due to their selectivity, low volume of solvents, and high throughput (Table 4). Adsorption of cationic dyes (methyl violet (MV), methylene blue (MB), malachite green (MG), crystal violet (CV), and neutral red (NR)) from aqueous solution by using *Platanus orientalis* leaf powder (MNPs-POLP) coupled with UV-Vis spectrophotometer [82]. Mixed hemi micelle based on magnetic halloysite nanotubes and ionic liquids (MHMSPE) was prepared from ionic liquid [C16mimBr] and MHNTs to determination of anionic dyes (methyl red (MR) and methyl orange (MO)) in different water samples, lower RSD was achieved in this method, 2.5–5.4% for lake water, and 1.6–3.1% for tap water [83]. Multiwalled carbon nanotubes modified-Fe_3O_4 nanoparticles (MWCNT@Fe_3O_4 NPs) was used for extraction of MG and gentian violet (GV) dyes in water samples and followed by HPLC-FLD to give RSD values of 4.6–5.9% [84]. Sudan dyes were extracted by using Fe_3O_4@polyaniline particles (Fe_3O_4@PANI) coupled with UFLC-UV in water samples (lake water, rainwater, surface water, reservoir water and tap water) and RSD were found in the range of 1.6–6.8% [85]. Fe_3O_4-fullerene-activated carbon followed by capillary electrophoresis was used for extraction and analysis of anionic dyes (allure red, sunset yellow, and tartrazine) in water samples and RSD was found to be less than 10% [86]. Caramelized carbonaceous shell-coated γ-Fe_2O_3 (γ-Fe_2O_3@CNM-based MSPE) coupled with LC-MS/MS was used for the extraction and analysis of MG and CV dyes in spring water, fishpond, lake, sea, and industrial wastewater, RSD below 5.2% for MG and RSD below 5.5% for CV dyes [87]. Cationic dyes (MG and CV) were extracted and determined using Fe_3O_4@SiO_2-Flu followed by UV-Vis spectrophotometer in Caspian seawater and wastewater, and RSD was computed to be 4.77–4.17% [88]. Fe@NiAl-LDHs (layered double hydroxide) coupled with HPLC was used for the extraction and determination of Sudan red dyes in Ming Tombs Reservoir water, Changping Park water, and Binhe Park water, with low LOD from 0.002 to 0.005 μg/L [89]. Adsorption of Congo Red and Basic Red 2 was achieved using core–shell heterostructure of 24 $CoFe_2O_4$-Zeolitic

Imidazolate Framework-8 (ZIF-8@$CoFe_2O_4$) followed by a UV-Visible spectrometer with a high removal efficiency of 97% [90]. CTAB-coated magnetic iron oxide nanoparticles (C-MIONPs) coupled with a UV-Visible spectrometer were used for the separation and determination of RB dyes in Karoon river water and Brucella Antigen solution. RSD values were found to be 4.1 and 1.1% [91]. Adsorption of seven different types of dyes (Acridine orange, Amido black 10B, Bismarck brown, CR, CV, MG, Safranin O) was achieved by using a magnetically modified spent coffee grounds coupled with UV-Vis spectrometer in potable water [92]. Adsorption of acridine orange, CV, MG, Safranin O, and MB by using low-cost adsorbent magnetically modified *S. horneri* biomass followed by UV-Vis spectrometer [93]. Finally, Fe_3O_4/graphene oxide nanoparticles (Fe_3O_4/GO) coupled with HPLC were successfully applied to the extraction and determination of MG and CV dyes in the pond, lake, and river samples [94].

CONCLUSION

MSPE technique has the advantages of a simple synthesis of MNPs, selectivity to the target analyte, low cost due to using an external magnet which avoids the need for filtration or centrifugation steps, and avoiding using columns packed by sorbents that need to consume a long time to prepare these columns. Moreover, its ability to extract and pre-concentrate target analytes from complex matrices such as food and water samples. Dyes are often used in the food industry to enhance the appearance of food products. MSPE can be used to extract and quantify these compounds in food and water samples due to its high selectivity, sensitivity, and simplicity of operation. MSPE technique has been coupled with different analytical instruments such as UV-visible spectrometer, HPLC, LC-MS/MS, and capillary electrophoresis for the determination of dyes amount in food and water samples. Most past studies focus on the determination of dyes in the food or water samples, so efforts should be made to expand studies to soils, sediments, and other environmental samples. Future methods should seek to automate the MSPE method and couple it with the online system.

REFERENCES

[1] Berradi, M., Hsissou, R., Khudhair, M., Assouag, M., Cherkaoui, O., El Bachiri, A., and El Harfi, A., 2019, Textile finishing dyes and their impact on aquatic environments, *Heliyon*, 5 (11), e02711.

[2] de Campos Ventura-Camargo, B., and Marin-Morales, M.A., 2013, Azo dyes: Characterization and toxicity-A review, *Text. Light Ind. Sci. Technol.*, 2 (2), 85–103.

[3] El-Ashtoukhy, E.S.Z., and Fouad, Y.O., 2015, Liquid–liquid extraction of methylene blue dye from aqueous solutions using sodium dodecylbenzenesulfonate as an extractant, *Alexandria Eng. J.*, 54 (1), 77–81.

[4] Chen, J., Li, X., Huang, A., Deng, W., and Xiao, Y., 2021, Nonionic surfactants based hydrophobic deep eutectic solvents for liquid–liquid microextraction of Sudan dyes in tomato chili sauces, *Food Chem.*, 364, 130373.

[5] Bazregar, M., Rajabi, M., Yamini, Y., Arghavani-Beydokhti, S., and Asghari, A., 2018, Centrifugeless dispersive liquid-liquid microextraction based on salting-out phenomenon followed by high performance liquid chromatography for determination of Sudan dyes in different species, *Food Chem.*, 244, 1–6.

[6] Zocolo, G.J., Pilon dos Santos, G., Vendemiatti, J., Vacchi, F.I., Umbuzeiro, G.A., and Zanoni, M.V.B., 2015, Using SPE-LC-ESI-MS/MS analysis to assess disperse dyes in environmental water samples, *J. Chromatogr. Sci.*, 53 (8), 1257–1264.

[7] Sun, T., Wang, M., Wang, D., and Du, Z., 2020, Solid-phase microextraction based on nickel-foam@ polydopamine followed by ion mobility spectrometry for on-site detection of Sudan dyes in tomato sauce and hot-pot sample, *Talanta*, 207, 120244.

[8] del Nogal Sánchez, M., Santos, P.M., Sappó, C.P., Pavón, J.L.P., and Cordero, B.M., 2014, Microextraction by packed sorbent and salting-out-assisted liquid–liquid extraction for the determination of aromatic amines formed from azo dyes in textiles, *Talanta*, 119, 375–384.

[9] Móricz, Á.M., Lapat, V., Morlock, G.E., and Ott, P.G., 2020, High-performance thin-layer chromatography hyphenated to high-performance liquid chromatography-diode array detection-mass spectrometry for characterization of coeluting isomers, *Talanta*, 219, 121306.

[10] Zhou, J., Wang, R., and Chen, Z., 2019, Stir bar sorptive extraction with a graphene oxide framework-functionalized stainless-steel wire for the determination of Sudan dyes in water samples, *Anal. Methods*, 11 (15), 2050–2056.

[11] Wan Ibrahim, W.A., Nodeh, H.R., Aboul-Enein, H.Y., and Sanagi, M.M., 2015, Magnetic solid-phase extraction based on modified ferum oxides for enrichment, preconcentration, and isolation of pesticides and selected pollutants, *Crit. Rev. Anal. Chem.*, 45 (3), 270–287.

[12] Mundada, P., and Brighu, U., 2016, Remediation of textile effluent using siliceous materials: A review with a proposed alternative, *Int. J. Innovative Emerging Res. Eng.*, 3 (1), 1–5.

[13] Omer, O.S., Hussein, M.A., Hussein, B.H., and Mgaidi, A., 2018, Adsorption thermodynamics of cationic dyes (methylene blue and crystal violet) to a natural clay mineral from aqueous solution between 293.15 and 323.15 K, *Arabian J. Chem.*, 11 (5), 615–623.

[14] Pishgar, M., Gharanjig, K., Yazdanshenas, M.E., Farizadeh, K., and Rashidi, A., 2022, Photophysical properties of a novel xanthene dye, *Prog. Color, Color. Coat.*, 15 (2), 87–96.

[15] Teli, M.D., 2015, "Advances in the dyeing and printing of silk" in *Advances in Silk Science and Technology*, Eds. Basu, A., Woodhead Publishing, Cambridge, UK, 55–79.

[16] Nguyen, T.A., and Juang, R.S., 2013, Treatment of waters and wastewaters containing sulfur dyes: A review, *Chem. Eng. J.*, 219, 109–117.

[17] de Souza, J.C., Zanoni, M.V.B., and Oliveira-Brett, A.M., 2020, Genotoxic permanent hair dye precursors *p*-aminophenol and *p*-toluenediamine electrochemical oxidation mechanisms and evaluation in biological fluids, *J. Electroanal. Chem.*, 857, 113509.

[18] Da França, S.A., Dario, M.F., Esteves, V.B., Baby, A.R., and Velasco, M.V.R., 2015, Types of hair dye and their mechanisms of action, *Cosmetics*, 2 (2), 110–126.

[19] Kanthasamy, S., Hadibarata, T., Hidayat, T., Alamri, S.A., and Al-Ghamdi, A.A., 2020, Adsorption of azo and anthraquinone dye by using watermelon peel powder and corn peel powder: Equilibrium and kinetic studies, *Biointerface Res. Appl. Chem.*, 10 (1), 4706–4713.

[20] Kavcı, E., 2021, Adsorption of direct red 243 dye onto clay: Kinetic study and isotherm analysis, *Desalin. Water Treat.*, 212, 452–461.

[21] Mishra, L., Paul, K.K., and Jena, S., 2021, Coke wastewater treatment methods: Mini review, *J. Indian Chem. Soc.*, 98 (10), 100133.

[22] Jawad, A.H., Abdulhameed, A.S., and Mastuli, M.S., 2020, Acid-factionalized biomass material for methylene blue dye removal: A comprehensive adsorption and mechanism study, *J. Taibah Univ. Sci.*, 14 (1), 305–313.

[23] Yeum, J.H., Park, S.M., Kim, J.W., Choi, J.H., Han, S.I., Oh, W., Cheong, I.W., and Deng, Y., 2014, Effect of disperse dye on the preparation of poly(vinyl acetate)/poly(vinyl alcohol)/disperse dye composite microspheres, *J. Compos. Mater.*, 48 (18), 2265–2271.

[24] Benkhaya, S., El Harfi, S., and El Harfi, A., 2017, Classifications, properties and applications of textile dyes: A review, *Appl. J. Environ. Eng. Sci.*, 3 (3), 311–320.

[25] Mohtashim, Q., Rigout, M., and Yousfani, S.H.S.H., 2022, The development of a tannin-based after-treatment for cotton fabric dyed with sulphur dyes, *Pigm. Resin Technol.*, 51 (2), 227–235.

[26] Singh, J., Kaur, S., Kaur, G., Basu, S., and Rawat, M., 2019, Biogenic ZnO nanoparticles: A study of blueshift of optical band gap and photocatalytic degradation of reactive yellow 186 dye under direct sunlight, *Green Process. Synth.*, 8 (1), 272–280.

[27] Balu, S., Velmurugan, S., Palanisamy, S., Chen, S.W., Velusamy, V., Yang, T.C., and El-Shafey, E.S.I., 2019, Synthesis of α-Fe_2O_3 decorated g-C_3N_4/ZnO ternary Z-scheme photocatalyst for degradation of tartrazine dye in aqueous media, *J. Taiwan Inst. Chem. Eng.*, 99, 258–267.

[28] Marghussian, V., 2015, "Magnetic properties of nano-glass ceramics" in *Nano-Glass Ceramics*, William Andrew Publishing, Oxford, UK, 181–223.

[29] Amiri, M., Salavati-Niasari, M., and Akbari, A., 2019, Magnetic nanocarriers: Evolution of spinel ferrites for medical applications, *Adv. Colloid Interface Sci.*, 265, 29–44.

[30] Narang, S.B., and Pubby, K., 2021, Nickel spinel ferrites: A review, *J. Magn. Magn. Mater.*, 519, 167163.

[31] Safarik, I., Baldikova, E., Prochazkova, J., and Pospiskova, K., 2019, Smartphone-based image analysis for evaluation of magnetic textile solid phase extraction of colored compounds, *Heliyon*, 5 (12), e02995.

[32] Manousi, N., Rosenberg, E., Deliyanni, E., Zachariadis, G. A., &Samanidou, V., 2020, Magnetic solid-phase extraction of organic compounds based on graphene oxide nanocomposites, *Molecules*, 25 (5), 1148.

[33] Wierucka, M., and Biziuk, M, 2014, Application of magnetic nanoparticles for magnetic solid-phase extraction in preparing biological, environmental and food samples, *TrAC, Trends Anal. Chem.*, 59, 50–58.

[34] Öztürk Er, E., DalgıçBozyiğit, G., Büyükpınar, Ç., & Bakırdere, S, 2022, Magnetic nanoparticles based solid phase extraction methods for the determination of trace elements, *Crit. Rev. Anal. Chem.*, 52 (2), 231–249.

[35] Capriotti, A.L., Cavaliere, C., La Barbera, G., Montone, C.M., Piovesana, S., and Laganà, A, 2019, Recent applications of magnetic solid-phase extraction for sample preparation, *Chromatographia*, 82 (8), 1251–1274.

[36] Li, X.S., Zhu, G.T., Luo, Y.B., Yuan, B.F., and Feng, Y.Q., 2013, Synthesis and applications of functionalized magnetic materials in sample preparation, *TrAC, Trends Anal. Chem.*, 45, 233–247.

[37] Effenberger, F.B., Couto, R.A., Kiyohara, P.K., Machado, G., Masunaga, S.H., Jardim, R.F., and Rossi, L.M., 2017, Economically attractive route for the preparation of high quality magnetic nanoparticles by the thermal decomposition of iron(III) acetylacetonate, *Nanotechnology*, 28 (11), 115603.

[38] Lopez Perez, J.A., Lopez Quintela, M.A., Mira, J., Rivas, J., and Charles, S.W., 1997, Advances in the preparation of magnetic nanoparticles by the microemulsion method, *J. Phys. Chem. B.*, 101 (41), 8045–8047.

[39] de Carvalho, J.F., de Medeiros, S.N., Morales, M.A., Dantas, A.L., and Carriço, A.S., 2013, Synthesis of magnetite nanoparticles by high energy ball milling, *Appl. Surf. Sci.*, 275, 84–87.

[40] Takami, S., Sato, T., Mousavand, T., Ohara, S., Umetsu, M., and Adschiri, T., 2007, Hydrothermal synthesis of surface-modified iron oxide nanoparticles, *Mater. Lett.*, 61 (26), 4769–4772.

[41] Pinkas, J., Reichlova, V., Zboril, R., Moravec, Z., Bezdicka, P., and Matejkova, J., 2008, Sonochemical synthesis of amorphous nanoscopic iron(III) oxide from $Fe(acac)_3$, *Ultrason. Sonochem.*, 15 (3), 257–264.

[42] Predoi, D., 2007, A study on iron oxide nanoparticles coated with dextrin obtained by coprecipitation, *Dig. J. Nanomater. Biostruct.*, 2 (1), 169–173.

[43] Nguyen, M.D., Tran, H.V., Xu, S., and Lee, T.R., 2021, Fe_3O_4 nanoparticles: Structures, synthesis, magnetic properties, surface functionalization, and emerging applications, *Appl. Sci.*, 11 (23), 11301.

[44] Harisah, N., Siswanta, D., Mudasir, M., and Suyanta, S., 2022, Superparamagnetic composite of magnetite-CTAB as an efficient adsorbent for methyl orange, *Indones. J. Chem.*, 22 (2), 387–401.

[45] Zhang, W., Tu, J., Long, W., Lai, W., Sheng, Y., and Guo, T., 2017, Preparation of SiO_2 anti-reflection

coatings by sol-gel method, *Energy Procedia*, 130, 72–76.

[46] Ivanova, O.S., Edelman, I.S., Lin, C.R., Svetlitsky, E.S., Sokolov, A.E., Lukyanenko, K.A., Sukhachev, A.L., Shestakov, N.P., Chen, Y.Z., and Spivakov, A.A., 2023, Core–Shell Fe_3O_4@C nanoparticles for the organic dye adsorption and targeted magneto-mechanical destruction of Ehrlich ascites carcinoma cells, *Materials*, 16 (1), 23.

[47] Zare, F., Ghaedi, M., and Daneshfar, A., 2015, Solid phase extraction of antidepressant drugs amitriptyline and nortriptyline from plasma samples using core-shell nanoparticles of the type Fe_3O_4@ZrO_2@*N*-cetylpyridinium, and their subsequent determination by HPLC with UV detection, *Microchim. Acta*, 182 (11), 1893–1902.

[48] Maleki, S., Falaki, F., and Karimi, M., 2019, Synthesis of SDS micelles-coated Fe_3O_4/SiO_2 magnetic nanoparticles as an excellent adsorbent for facile removal and concentration of crystal violet from natural water samples, *J. Nanostruct. Chem.*, 9 (2), 129–139.

[49] Zhang, B.T., Zheng, X., Li, H.F., and Lin, J.M., 2013, Application of carbon-based nanomaterials in sample preparation: A review, *Anal. Chim. Acta,* 784, 1–17.

[50] Das, P.N., Jithesh, K., and Raj, K.G., 2021, Recent developments in the adsorptive removal of heavy metal ions using metal-organic frameworks and graphene-based adsorbents, *J. Indian Chem. Soc.*, 98 (11), 100188.

[51] Jiang, H.L., Li, N., Cui, L., Wang, X., and Zhao, R.S., 2019, Recent application of magnetic solid phase extraction for food safety analysis, *TrAC, Trends Anal. Chem.*, 120, 115632.

[52] Yang, J., Wang, Y., Pan, M., Xie, X., Liu, K., Hong, L., and Wang, S., 2020, Synthesis of magnetic metal-organic frame material and its application in food sample preparation, *Foods*, 9 (11), 1610.

[53] Ma, J., Wu, G., Li, S., Tan, W., Wang, X., Li, J., and Chen, L., 2018, Magnetic solid-phase extraction of heterocyclic pesticides in environmental water samples using metal-organic frameworks coupled to high performance liquid chromatography determination, *J. Chromatogr. A*, 1553, 57–66.

[54] Rösler, C., Aijaz, A., Turner, S., Filippousi, M., Shahabi, A., Xia, W., Van Tendeloo, G., Muhler, M., and Fischer, R.A., 2016, Hollow Zn/Co zeolitic imidazolate framework (ZIF) and yolk–shell metal@Zn/Co ZIF nanostructures, *Chem. Eur. J.*, 22 (10), 3304–3311.

[55] Sakamaki, Y., Tsuji, M., Heidrick, Z., Watson, O., Durchman, J., Salmon, C., and Beyzavi, H., 2020, Preparation and applications of metal–organic frameworks (MOFs): A laboratory activity and demonstration for high school and/or undergraduate students, *J. Chem. Educ.*, 97 (4), 1109–1116.

[56] Safarik, I., Baldikova, E., Safarikova, M., and Pospiskova, K., 2018, Magnetically responsive textile for a new preconcentration procedure: Magnetic textile solid phase extraction, *J. Ind. Text.*, 48 (4), 761–771.

[57] Safarik, I., Mullerova, S., and Pospiskova, K., 2019, Magnetically responsive textile for preconcentration of acid food dyes, *Mater. Chem. Phys.*, 232, 205–208.

[58] Safarik, I., and Pospiskova, K., 2018, A simple extraction of blue fountain ink dye (Acid blue 93) from water solutions using magnetic textile solid-phase extraction, *Sep. Sci. Plus*, 1 (1), 48–51.

[59] Safarik, I., Mullerova, S., and Pospiskova, K., 2020, Magnetic textile solid phase extraction of cationic dyes from water solutions, *Fibers Polym.*, 21 (12), 2836–2841.

[60] Li, N., Zhao, T., Du, L., Zhang, Z., Nian, Q., and Wang, M, 2021, Fast and simple determination of estrogens in milk powders by magnetic solid-phase extraction using carbon nitride composites prior to HPLC, *Anal. Bioanal. Chem.*, 413 (1), 215–223.

[61] Moazzen, M., Mousavi Khaneghah, A., Shariatifar, N., Ahmadloo, M., Eş, I., Baghani, A.N., Yousefinejad, S., Alimohammadi, M., Azari, A., Dobaradaran, S., Rastkari, N., Nazmara, S., Delikhoon, M., and Jahed Khaniki, G., 2019, Multi-walled carbon nanotubes modified with iron oxide

and silver nanoparticles (MWCNT-Fe_3O_4/Ag) as a novel adsorbent for determining PAEs in carbonated soft drinks using magnetic SPE-GC/MS method, *Arabian J. Chem.*, 12 (4), 476–488.

[62] Tang, H.Z., Wang, Y.H., Li, S., Wu, J., Gao, Z.X., and Zhou, H.Y., 2020, Development and application of magnetic solid phase extraction in tandem with liquid–liquid extraction method for determination of four tetracyclines by HPLC with UV detection, *J. Food Sci. Technol.*, 57 (8), 2884–2893.

[63] Nodeh, H.R., Wan Ibrahim, W.A., Kamboh, M.A., and Sanagi, M.M., 2017, New magnetic graphene-based inorganic–organic sol-gel hybrid nanocomposite for simultaneous analysis of polar and non-polar organophosphorus pesticides from water samples using solid-phase extraction, *Chemosphere*, 166, 21–30.

[64] Rastkari, N., and Ahmadkhaniha, R., 2013, Magnetic solid-phase extraction based on magnetic multi-walled carbon nanotubes for the determination of phthalate monoesters in urine samples, *J. Chromatogr. A*, 1286, 22–28.

[65] Özdemir, S., Mohamedsaid, S.A., Kılınç, E., and Soylak, M., 2019, Magnetic solid phase extractions of Co(II) and Hg(II) by using magnetized *C. micaceus* from water and food samples, *Food Chem.*, 271, 232–238.

[66] Moazzen, M., Shariatifar, N., Arabameri, M., Hosseini, H., and Ahmadloo, M., 2022, Measurement of polycyclic aromatic hydrocarbons in baby food samples in Tehran, Iran with magnetic-solid-phase-extraction and gas-chromatography/mass-spectrometry method: A health risk assessment, *Front. Nutr.*, 9, 833158.

[67] Wu, L., Yu, L., Ding, X., Li, P., Dai, X., Chen, X., Zhou, H., Bai, Y., and Ding, J. 2017, Magnetic solid-phase extraction based on graphene oxide for the determination of lignans in sesame oil, *Food Chem.*, 217, 320–325.

[68] Yang, C., Li, J., Wang, S., Wang, Y., Jia, J., Wu, W., Hu, J., and Zhao, Q., 2022, Determination of free fatty acids in Antarctic krill meals based on matrix solid phase dispersion, *Food Chem.*, 384, 132620.

[69] Wang, T., Liu, S., Gao, G., Zhao, P., Lu, N., Lun, X., and Hou, X., 2017, Magnetic solid phase extraction of non-steroidal anti-inflammatory drugs from water samples using a metal organic framework of type Fe_3O_4/MIL-101(Cr), and their quantitation by UPLC-MS/MS, *Microchim. Acta*, 184 (8), 2981–2990.

[70] Zahedi, M., Shakerian, A., Rahimi, E., and Sharafati Chaleshtori, R., 2020, Determination of synthetic dyes in various food samples of Iran's market and their risk assessment of daily intake, *Egypt. J. Vet. Sci.*, 51 (1), 23–33.

[71] Yamjala, K., Nainar, M.S., and Ramisetti, N.R., 2016, Methods for the analysis of azo dyes employed in food industry – A review, *Food Chem.*, 192, 813–824.

[72] Mishra, D., 2020, "Food Colors and Associated Oxidative Stress in Chemical Carcinogenesis" in *Handbook of Oxidative Stress in Cancer: Mechanistic Aspects*, Eds. Chakraborti, S., Ray, B.K., and Roychowdhury, S, Springer, Singapore, 1–14.

[73] Cui, S., Mao, X., Zhang, H., Zeng, H., Lin, Z., Zhang, X., and Qi, P., 2021, Magnetic solid-phase extraction based on magnetic sulfonated reduced graphene oxide for HPLC–MS/MS analysis of illegal basic dyes in foods, *Molecules*, 26 (24), 7427.

[74] Wei, X., Wang, Y., Chen, J., Xu, P., Xu, W., Ni, R., and Zhou, Y., 2019, Poly(deep eutectic solvent)-functionalized magnetic metal-organic framework composites coupled with solid-phase extraction for the selective separation of cationic dyes, *Anal. Chim. Acta*, 1056, 47–61.

[75] Duan, H.L., Mou, Z.L., Wang, J., Ma, S.Y., Zhan, H.Y., and Zhang, Z.Q., 2019, Magnetically modified porous β-cyclodextrin polymers for dispersive solid-phase extraction high-performance liquid chromatography analysis of Sudan dyes, *Food Anal. Methods*, 12 (6), 1429–1438.

[76] Shi, X.R., Chen, X.L., Hao, Y.L., Li, L., Xu, H.J., and Wang, M.M., 2018, Magnetic metal-organic frameworks for fast and efficient solid-phase extraction of six Sudan dyes in tomato sauce, *J. Chromatogr. B*, 1086, 146–152.

[77] Kılınç, E., Çelik, K.S., and Bilgetekin, H., 2018, γ-Fe_2O_3 magnetic nanoparticle functionalized with carboxylated multi walled carbon nanotube for magnetic solid phase extractions and determinations of Sudan dyes and Para Red in food samples, *Food Chem.*, 242, 533–537.

[78] Zhang, J., Shao, J., Guo, P., and Huang, Y., 2013, A simple and fast Fe_3O_4 magnetic nanoparticles-based dispersion solid phase extraction of Sudan dyes from food and water samples coupled with high-performance liquid chromatography, *Anal. Methods*, 5 (10), 2503–2510.

[79] Chen, J., and Zhu, X., 2016, Magnetic solid phase extraction using ionic liquid-coated core–shell magnetic nanoparticles followed by high-performance liquid chromatography for determination of Rhodamine B in food samples, *Food Chem.*, 200, 10–15.

[80] Yu, X., Sun, Y., Jiang, C.Z., Gao, Y., Wang, Y.P., Zhang, H.Q., and Song, D.Q., 2012, Magnetic solid-phase extraction and ultrafast liquid chromatographic detection of Sudan dyes in red wines, juices, and mature vinegars, *J. Sep. Sci.*, 35 (23), 3403–3411.

[81] Benmassaoud, Y., Villaseñor, M.J., Salghi, R., Jodeh, S., Algarra, M., Zougagh, M., and Ríos, Á., 2017, Magnetic/non-magnetic argan press cake nanocellulose for the selective extraction of Sudan dyes in food samples prior to the determination by capillary liquid chromatography, *Talanta*, 166, 63–69.

[82] Madrakian, E., Ghaemi, E., and Ahmadi, M., 2016, Magnetic solid phase extraction and removal of five cationic dyes from aqueous solution using magnetite nanoparticle loaded platanusorientalis waste leaves, *Anal. Bioanal. Chem. Res.*, 3 (2), 279–286.

[83] Liu, W., Fizir, M., Hu, F., Li, A., Hui, X., Zha, J., and He, H., 2018, Mixed hemimicelle solid-phase extraction based on magnetic halloysite nanotubes and ionic liquids for the determination and extraction of azo dyes in environmental water samples, *J. Chromatogr.* A, 1551, 10–20.

[84] Zhao, J., Wei, D., and Yang, Y., 2016, Magnetic solid-phase extraction for determination of the total malachite green, gentian violet and leucomalachite green, leucogentian violet in aquaculture water by high-performance liquid chromatography with fluorescence detection, *J. Sep. Sci.*, 39 (12), 2347–2355.

[85] Xu, B., Wang, Y., Jin, R., Li, X., Song, D., Zhang, H., and Sun, Y., 2015, Magnetic solid-phase extraction based on Fe_3O_4@polyaniline particles followed by ultrafast liquid chromatography for determination of Sudan dyes in environmental water samples, *Anal. Methods*, 7 (4), 1606–1614.

[86] Rodriguez, J.A., Ibarra, I.S., Miranda, J.M., Barrado, E., and Santos, E.M., 2016, Magnetic solid phase extraction based on fullerene and activated carbon adsorbents for determination of azo dyes in water samples by capillary electrophoresis, *Anal. Methods*, 8 (48), 8466–8473.

[87] Li, N., Li, R., Song, Y., Ma, L., Gao, C., Li, L., Cheng, S.B., Zhang, X., Chen, J., and Zhan, J., 2020, Caramelized carbonaceous shell-coated γ-Fe_2O_3 as a magnetic solid-phase extraction sorbent for LC-MS/MS analysis of triphenylmethane dyes, *Microchim. Acta*, 187 (7), 1–8.

[88] Mirzaei, F., Mohammadi Nilash, M., Sepahvand, H., Fakhari, A.R., and Shaabani, A., 2020, Magnetic solid-phase extraction based on fluconazole-functionalized Fe_3O_4@SiO_2 nanoparticles for the spectrophotometric determination of cationic dyes in environmental water samples, *J. Iran. Chem. Soc.*, 17 (7), 1591–1600.

[89] Zhou, Q., Wu, Y., Yuan, Y., Zhou, X., Wang, H., Tong, Y., Zhan, Y., Sun. L., and Sheng, X., 2019, Determination of Sudan red contaminants at trace level from water samples by magnetic solid-phase extraction using Fe@NiAl-layered double hydroxide coupled with HPLC, *Environ. Sci. Eur.*, 31 (1), 34.

[90] Xu, Y., Jin, J., Li, X., Han, Y., Meng, H., Wu, J., and Zhang, X., 2016, Rapid magnetic solid-phase extraction of Congo Red and Basic Red 2 from

aqueous solution by ZIF-8@$CoFe_2O_4$ hybrid composites, *J. Sep. Sci.*, 39 (18), 3647–3654.

[91] Parham, H., Zargar, B., Heidari, Z., and Hatamie, A., 2011, Magnetic solid-phase extraction of rose Bengal using iron oxide nanoparticles modified with cetyltrimethylammonium bromide, *J. Iran. Chem. Soc.*, 8 (1), S9–S16.

[92] Safarik, I., Horska, K., Svobodova, B., and Safarikova, M., 2012, Magnetically modified spent coffee grounds for dyes removal, *Eur. Food Res. Technol.*, 234 (2), 345–350.

[93] Angelova, R., Baldikova, E., Pospiskova, K., Maderova, Z., Safarikova, M., and Safarik, I., 2016, Magnetically modified *Sargassum horneri* biomass as an adsorbent for organic dye removal, *J. Cleaner Prod.*, 137, 189–194.

[94] Zhang, L., Zhang, Y., Tang, Y., Li, X., Zhang, X., Li, C., and Xu, S., 2018, Magnetic solid-phase extraction based on Fe_3O_4/graphene oxide nanoparticles for the determination of malachite green and crystal violet in environmental water samples by HPLC, *Int. J. Environ. Anal. Chem.*, 98 (3), 215–228.